Transactions of the ASME®

HEAT TRANSFER DIVISION
Chairman, J. R. LLOYD
Secretary, A. S. ADORJAN
Senior Technical Editor, G. M. FAETH
Technical Editor, J. V. BECK
Technical Editor, I. CATTON
Technical Editor, R. GREIF
Technical Editor, H. R. JACOBS
Technical Editor, P. J. MARTO
Technical Editor, D. M. McELIGOT
Technical Editor, R. H. PLETCHER
Technical Editor, W. A. SIRIGNANO
Technical Editor, R. VISKANTA

BOARD ON COMMUNICATIONS
Chairman and Vice President
K. N. REID, JR.

Members-at-Large
J. T. COKONIS
M. FRANKE
M. KUTZ
F. LANDIS
J. R. LLOYD
T. C. MIN
R. E. NICKELL
R. E. REDER
R. ROCKE
F. W. SCHMIDT
W. O. WINER

President, R. ROSENBERG
Executive Director,
D. L. BELDEN
Treasurer,
ROBERT A. BENNETT

PUBLISHING STAFF
Mng. Dir., Mktg., JOS. SANSONE
Managing Editor,
CORNELIA MONAHAN
Sr. Production Editor,
VALERIE WINTERS
Editorial Prod. Asst.,
MARISOL ANDINO

Transactions of the ASME, Journal of Heat Transfer (ISSN 0022-1481) is published quarterly (Feb., May, Aug., Nov.) for $150 per year by The American Society of Mechanical Engineers, 345 East 47th Street, New York, NY 10017. Second class postage paid at New York, NY and additional mailing offices. POSTMASTER: Send address changes to The Journal of Heat Transfer, c/o THE AMERICAN SOCIETY OF MECHANICAL ENGINEERS, 22 Law Drive, Box 2300, Fairfield, NJ 07007-2300.
CHANGES OF ADDRESS must be received at Society *headquarters seven weeks before they are to be* effective. Please send old label and new address.
PRICES: To members, $27.00, annually; to nonmembers, $150.00. Add $12.00 for postage to countries outside the United States and Canada.
STATEMENT from By-Laws. The Society shall not be responsible for statements or opinions advanced in papers or . . . printed in its publications (B7.1, para. 3).
COPYRIGHT © 1987 by the American Society of Mechanical Engineers. Reprints from this publication may be made on condition that full credit be given the TRANSACTIONS OF THE ASME, JOURNAL OF HEAT TRANSFER, and the author, and date of publication be stated.
INDEXED by Engineering Information

Journal of Heat Transfer

Published Quarterly by The American Society of Mechanical Engineers

VOLUME 109 • NUMBER 4 • NOVEMBER 1987

ANNOUNCEMENTS

TECHNICAL PAPERS

Downloaded 04 Feb 2011 to 194.85.80.107. Redistribution subject to ASME license or copyright; see http://www.asme.org/terms/Terms_Use.cfm

(Contents continued)

TECHNICAL NOTES

Downloaded 04 Feb 2011 to 194.85.80.107. Redistribution subject to ASME license or copyright; see http://www.asme.org/terms/Terms_Use.cfm

G. W. Barry
Research Assistant,
Physics Department,
Lehigh University,
Bethlehem, PA

J. S. Goodling
Professor,
Mechanical Engineering Department,
Auburn University,
Auburn, AL
Mem. ASME

A Stefan Problem With Contact Resistance

A Stefan problem in which a semi-infinite molten material at the fusion temperature solidifies as a result of imperfect thermal contact with a cooler semi-infinite solid is considered. The contact resistance, due to surface roughness, is modeled by a convective boundary condition. Biot's variational principle is used to reduce the coupled partial differential equations to a pair of coupled ordinary differential equations that are solved numerically. The position of the moving boundary as a function of time is given for both bismuth and aluminum solidifying on stainless steel.

Introduction

For phase-change or Stefan problems, the presence of a solid–liquid interface that moves as latent heat is absorbed or released introduces a nonlinearity into the boundary conditions of the one-dimensional conduction equation

$$\frac{\partial^2 T}{\partial x^2} = \frac{1}{\alpha}\frac{\partial T}{\partial t} \tag{1}$$

The position of this moving boundary is not known in advance and must be determined as part of the solution. Consequently, there are few exact analytical solutions available for phase-change problems, and approximate analytical or numerical solution techniques must often be used.

The phase-change problem discussed here involves a semi-infinite liquid, uniformly at its fusion temperature, which solidifies as a result of thermal contact with a cooler semi-infinite solid. If the contact is perfect, there is no resistance to heat transfer at the interface of the two media, and the temperature is continuous there. This idealized problem is straightforward to solve.

From an engineering standpoint, however, it is more realistic to include the effects of imperfect thermal contact due to surface roughness, which creates a resistance to heat transfer known as contact resistance. This can be modeled by a convective boundary condition, which gives rise to a discontinuity in temperature at the interface. The problem we solve here includes contact resistance, which better describes such situations as the solidification of a molten material by contact with a "thick" mold.

The case of imperfect thermal contact can be set in the context of the eight related problems displayed in Fig. 1. The problems on the right (2, 4, 6, and 8) involve a phase change, with 6 and 8 being the cases of perfect and imperfect thermal contact mentioned above. The four problems on the left are the non-phase-change analogies to 2, 4, 6, and 8. The first four problems (1–4) concern a semi-infinite material in contact with a constant-temperature heat sink. The last four problems (5–8) involve contact between two semi-infinite media, labeled solid 1 and solid 2, where the temperature field in each material is influenced by the field in the other material. Resistance to heat transfer is present at $x = 0$ in Problems 3, 4, 7, and 8. In particular, Problems 7 and 8 involve contact resistance at the interface of two different materials.

In all eight problems, the thermal conductivity k, density ρ, specific heat c, and thermal diffusivity $\alpha = k/\rho c$ are assumed constant. The heat transfer coefficient h at $x = 0$ is also taken to be constant. In the phase-change problems, it is assumed that solidification takes place at a single temperature T_f, the fusion temperature. The latent heat of fusion L is liberated at the moving phase-change interface $X(t)$. The dimensionless ratio of sensible heat to latent heat $\sigma = c(T_f - T_{ref})/L$, known as the Stefan number, is an important parameter in the phase-change problems.

Most of the problems in Fig. 1 can be viewed as limiting cases of some of the other problems. For example, taking $\sigma \to \infty$ effectively eliminates the liberation of heat at the moving boundary $X(t)$ and reduces each phase-change problem to the non-phase-change problem immediately to its left. Resistance to heat transfer at $x = 0$ is eliminated by taking $h \to \infty$, so that Problems 3, 4, 7, and 8 reduce to 1, 2, 5, and 6, respectively, for large h. Taking $k_2 \to \infty$ in Problems 5, 6, 7, and 8 reduces them to 1, 2, 3, and 4, by making solid 2 act like an isothermal heat sink. These limiting cases can be used to check solutions to problems for which no other solution is available.

Exact solutions to the non-phase-change problems in Fig. 1 can be obtained by several methods, including the use of the Laplace transform (Carslaw and Jaeger, 1959; Ozisik, 1980). Among the phase-change problems, 4 has been solved by assuming a series form (Lozano and Reemsten, 1981; Westphal, 1967), and Problems 2 and 6 by assuming an error function form for the temperature distribution (Carslaw and Jaeger, 1959; Ozisik, 1980) or by similarity transform (Lunardini, 1981). Ku and Chan (1984) have modified the Laplace transform method for use in phase-change problems and have applied it to five problems, including that of Neumann (a more general case of Problem 2 in which the liquid is initially superheated, so that the temperature profile in the liquid is also a function of position and time). Barry (1985) has used the Laplace transform method of Ku and Chan to solve Problem 6. In Problem 8, however, the presence of phase change, two media, and contact resistance makes solution by the methods mentioned above impossible. Alternative methods must therefore be used.

Biot's Variational Principle Applied to Problem 8

In a series of papers, Biot (1955, 1956, 1957, 1959) established a generalized theorem of minimum rate of entropy production and formulated a variational principle of irreversible thermodynamics similar to the Lagrangian equations of mechanics. This variational principle has been applied by Biot and others to problems in conduction heat transfer, including those involving temperature-dependent thermal properties and those in which melting or solidification occurs. For example, Biot and Daughaday (1962) have solved the case of ablation with a constant flux boundary condition and constant thermal properties, while Biot and Agrawal (1964) have treated the same problem assuming variable thermal properties. The case of melting due to constant flux without removal of melt has been considered by Prasad and Agrawal (1972). Lardner (1972) has solved the problem of melting with constant surface

Contributed by the Heat Transfer Division for publication in the JOURNAL OF HEAT TRANSFER. Manuscript received by the Heat Transfer Division June 16, 1986.

Copyright © 1987 by ASME

Downloaded 17 Dec 2010 to 193.140.21.150. Redistribution subject to ASME license or copyright; see http://www.asme.org/terms/Terms_Use.cfm

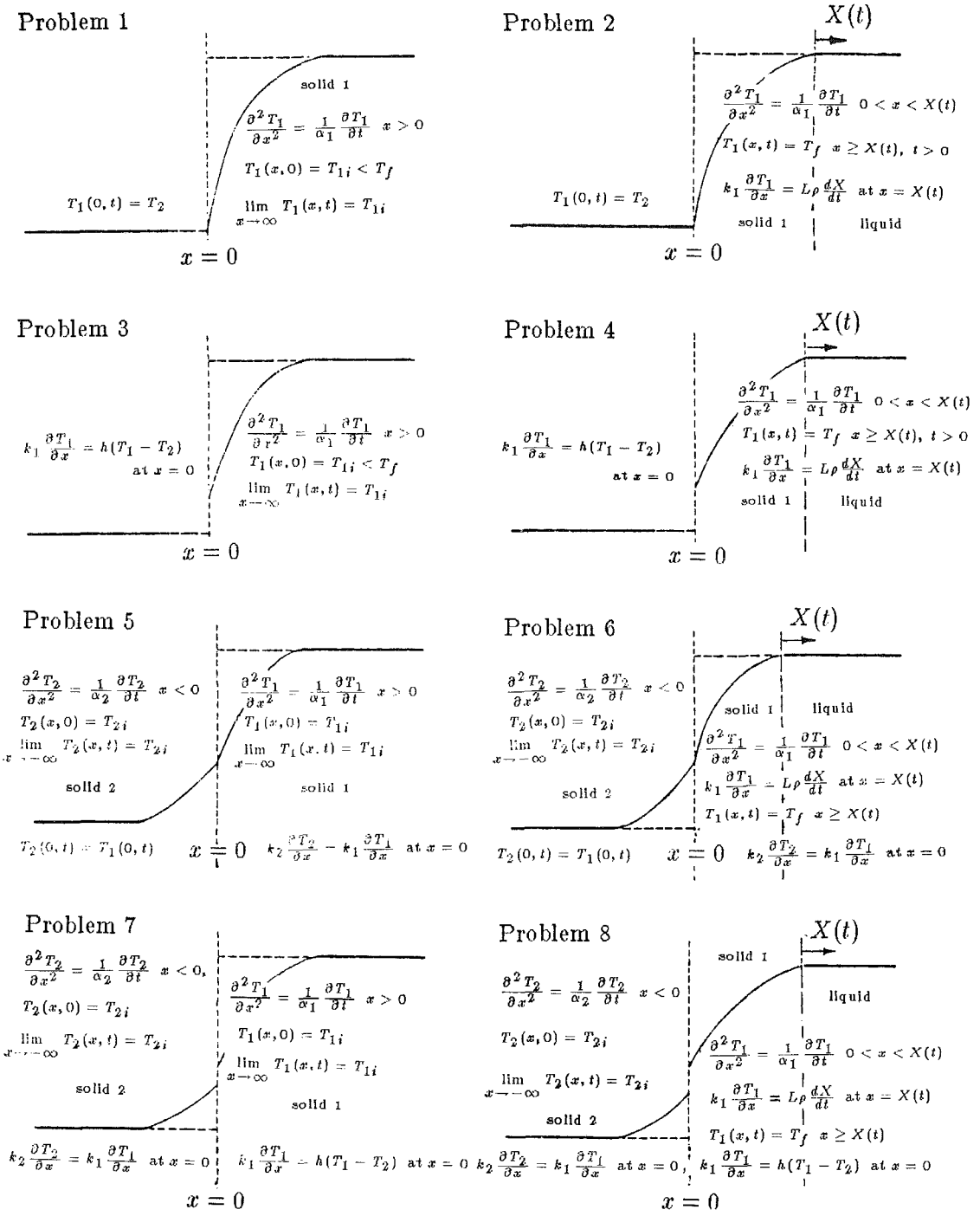

Fig. 1 The eight problems illustrated

Nomenclature

c = specific heat
D = dissipation function
$\mathbf{H}$ = heat flow vector
$\dot{\mathbf{H}}$ = heat flux
h = heat transfer coefficient
K = k_2/k_1
k = thermal conductivity
L = latent heat of fusion
Q = thermal driving force
q = generalized coordinate; temperature at $x = 0$
S = Xh/k_1 = dimensionless X
T = $T(x, t)$ = temperature
t = time
u = dimensionless $T = (T - T_{2i})/(T_{1i} - T_{2i})$
V = thermal potential
X = $X(t)$ = position of moving boundary
x = space variable
α = thermal diffusivity
β = dimensionless quantity = $nK(S + 1) - \Delta$
Δ = dimensionless $\delta = \delta h/k_1$
δ = $\delta(t)$ = penetration depth
θ = temperature displacement
θ_0 = defined in equation (22)
ρ = density
σ = Stefan number = $c(T_f - T_{ref})/L$

Subscripts

1 = solid 1
1i = solid 1 at $t = 0$
2 = solid 2
2i = solid 2 at $t = 0$
f = fusion

Downloaded 17 Dec 2010 to 193.140.21.150. Redistribution subject to ASME license or copyright; see http://www.asme.org/terms/Terms_Use.cfm

temperature as the boundary condition, and Agrawal (1975) has considered the case of melting due to "aerodynamic heating" (a convective boundary condition). These last two problems are virtually identical to Problems 2 and 4: The only difference between a melting problem and a solidification problem is the presence of a negative sign in the boundary condition at the phase front, equation (7). Further applications of Biot's principle to a vareity of heat transfer problems are mentioned in review articles by Kumar (1972) and by Muehlbauer and Sunderland (1965). A more general description of Biot's method is given by Biot (1970) and Lardner (1963).

Solution

In Problem 8, liquid initially at the fusion temperature T_f is confined to the semi-infinite region $x > 0$. At time $t = 0$, the liquid is brought into imperfect thermal contact at $x = 0$ with a semi-infinite solid occupying $x < 0$ and initially at a temperature $T_{2i} < T_f$. Solidification of the liquid begins at the surface $x = 0$, and the liquid–solid interface $X(t)$ moves in the positive x direction. The constants k_1, ρ_1, c_1, and α_1 are properties in the newly formed solid 1, while k_2, ρ_2, c_2, and α_2 are properties in solid 2 (see Fig. 1).

The following partial differential equations (PDE's) and boundary conditions apply for $t > 0$:

$$\frac{\partial^2 T_1}{\partial x^2} = \frac{1}{\alpha_1}\frac{\partial T_1}{\partial t} \qquad \text{for } 0 < x < X \tag{2}$$

$$\frac{\partial^2 T_2}{\partial x^2} = \frac{1}{\alpha_2}\frac{\partial T_2}{\partial t} \qquad \text{for } x < 0 \tag{3}$$

$$k_1\frac{\partial T_1}{\partial x} = h(T_1 - T_2) \qquad \text{at } x = 0,\ t > 0 \tag{4}$$

$$k_1\frac{\partial T_1}{\partial x} = k_2\frac{\partial T_2}{\partial x} \qquad \text{at } x = 0 \tag{5}$$

$$T_1(x, t) = T_f \qquad \text{at } x = X \tag{6}$$

$$k_1\frac{\partial T_1}{\partial x} = \rho_1 L\frac{dX}{dt} \qquad \text{at } x = X \tag{7}$$

The equation

$$k_2\frac{\partial T_2}{\partial x} = h(T_1 - T_2) \qquad \text{at } x = 0,\ t > 0 \tag{8}$$

can be immediately obtained from equations (4) and (5), and any two of equations (4), (5), and (8) may be used as the boundary conditions at $x = 0$. The initial condition in solid 2 is

$$T_2(x, 0) = T_{2i} \text{ for } x < 0 \tag{9}$$

Problem 8 differs from Problems 2 and 4 in that the medium occupying the region $x < 0$ is no longer an isothermal heat sink. This means that Biot's variational principle must be applied simultaneously but separately to two solids—solid 1, which is the newly solidified material occupying $0 < x < X$, and solid 2, which occupies $x < 0$. Also, the concept of a penetration depth (not needed in Problems 2 and 4) must now be introduced in this manner: We assume that the latent heat liberated at the moving boundary is transferred through solid 1 and into solid 2 to a depth $\delta(t)$, the penetration depth. Since the initial temperature distribution in solid 2 is undisturbed beyond $\delta(t)$, and since no energy is transferred at or beyond $\delta(t)$, the following two boundary conditions apply at $x = \delta(t)$:

$$T_2(x, t) = T_{2i} \qquad \text{at } x = \delta(t)$$

$$\frac{\partial T_2}{\partial x} = 0 \qquad \text{at } x = \delta(t) \tag{10}$$

The first step in applying Biot's method is to formulate the problem in terms of the displacements θ_i from the initial temperatures in the two regions. In solid 1,

$$\frac{\partial^2 \theta_1}{\partial x^2} = \frac{1}{\alpha_1}\frac{\partial \theta_1}{\partial t} \qquad \text{for } 0 < x < X(t) \tag{11}$$

$$\theta_1(x, t) = 0 \qquad \text{at } x = X(t) \tag{12}$$

$$k_1\frac{\partial \theta_1}{\partial x} = L\rho\frac{dX}{dt} \qquad \text{at } x = X(t) \tag{13}$$

Here

$$\theta_1(x, t) \equiv T_1(x, t) - T_f \tag{14}$$

is the temperature displacement in solid 1. Similarly for solid 2

$$\frac{\partial^2 \theta_2}{\partial x^2} = \frac{1}{\alpha_2}\frac{\partial \theta_2}{\partial t} \qquad \text{for } \delta(t) < x < 0 \tag{15}$$

$$\theta_2(x, t) = 0 \qquad \text{at } x = \delta(t) \tag{16}$$

$$\frac{\partial \theta_2}{\partial x} = 0 \qquad \text{at } x = \delta(t) \tag{17}$$

where

$$\theta_2(x, t) \equiv T_2(x, t) - T_{2i} \tag{18}$$

The discontinuity in temperature due to contact resistance at $x = 0$ is modeled by the convective boundary conditions

$$k_1\frac{\partial \theta_1}{\partial x} = h(q_1 - q_2 + \theta_0) \qquad \text{at } x = 0 \tag{19}$$

$$k_2\frac{\partial \theta_2}{\partial x} = h(q_1 - q_2 + \theta_0) \qquad \text{at } x = 0 \tag{20}$$

which can be combined to give

$$k_1\frac{\partial \theta_1}{\partial x} = k_2\frac{\partial \theta_2}{\partial x} \qquad \text{at } x = 0 \tag{21}$$

Here, θ_0 is the initial temperature difference across $x = 0$ at $t = 0$

$$\theta_0 = T_f - T_{2i} \tag{22}$$

and q_1 and q_2, defined as

$$q_i(t) \equiv \theta_i(0, t) \qquad \text{for } i = 1,\ 2 \tag{23}$$

represent the surface temperatures in each solid at the interface $x = 0$. Any two of equations (19), (20), and (21) may be used as the boundary conditions at $x = 0$.

Temperature profiles consistent with boundary conditions (12), (16), and (17) and with the definitions of q_1 and q_2 are assumed in each solid. Work done by Barry (1985) and by Hamm (1985) suggests that the temperature profile in the solidifying medium is approximately linear. For simplicity, a linear profile is assumed in solid 1 and an nth order polynomial in solid 2

$$\theta_1 = q_1\left(1 - \frac{x}{X}\right) \qquad 0 \le x \le X \tag{24}$$

$$\theta_2 = q_2\left(1 - \frac{x}{\delta}\right)^n \qquad \delta \le x \le 0 \tag{25}$$

Here, $X(t)$ and $\delta(t)$ constitute a proper set of generalized coordinates, and the temperatures $q_1(t)$ and $q_2(t)$ are related to X and δ through the convective boundary conditions at $x = 0$. In equation (25), n must be taken greater than one in order to satisfy the zero-flux boundary condition [equation (17)].

Downloaded 17 Dec 2010 to 193.140.21.150. Redistribution subject to ASME license or copyright; see http://www.asme.org/terms/Terms_Use.cfm

Biot's principle is applied separately to each solid. Let H_1 and H_2 represent the heat flow in solids 1 and 2, respectively. The energy equation $\nabla \cdot \mathbf{H} = -c\theta$ for each solid can be written as

$$\frac{\partial H_1}{\partial x} = -c_1 q_1 \left(1 - \frac{x}{X}\right) \qquad 0 \le x \le X \tag{26}$$

$$\frac{\partial H_2}{\partial x} = -c_2 q_2 \left(1 - \frac{x}{X}\right)^n \qquad \delta \le x \le 0 \tag{27}$$

Integrating and using equations (13) and (17) to solve for the constants of integration leads to expressions for the heat flow in each solid

$$H_1 = \frac{1}{2} c_1 q_1 X \left(1 - \frac{x}{X}\right)^2 - \rho L X \tag{28}$$

$$H_2 = \frac{1}{n+1} c_2 q_2 \delta \left(1 - \frac{x}{\delta}\right)^{n+1} \tag{29}$$

The expressions for θ_i and for the heat flux $\dot{H}_i$ are used to find the thermal potential V_i, which is related to the thermal energy of the system, and the dissipation function D_i, which is equal to the entropy production in the system

$$V_1 = \int_0^{X(t)} \frac{1}{2} c_1 \theta_1^2 dx = \frac{1}{6} c_1 q_1^2 X \tag{30}$$

$$D_1 = \int_0^{X(t)} \frac{1}{2k_1} \dot{H}_1^2 dx = \frac{X}{2k_1}\left[c_1^2\left(\frac{2}{15} q_1^2 \dot{X}^2 + \frac{3}{20} q_1 \dot{q}_1 X \dot{X} + \frac{1}{20} \dot{q}_1^2 X^2\right) - \frac{1}{3} c_1 \rho L (2 q_1 \dot{X}^2 + \dot{q}_1 X \dot{X}) + \rho^2 L^2 \dot{X}^2\right] \tag{31}$$

$$V_2 = \int_0^{\delta(t)} \frac{1}{2} c_2 \theta_2^2 dx = \frac{-c_2 \delta q_2^2}{2n+1} \tag{32}$$

$$D_2 = \int_0^{\delta(t)} \frac{1}{2k_2} \dot{H}_2^2 dx = -\frac{1}{2} \frac{\delta}{k_2} \frac{c_2^2}{(n+1)^2(2n+3)} \left(\dot{\delta}^2 q_2^2 \frac{5n+3}{2n+1} + 3\delta\dot{\delta} q_2 \dot{q}_2 + \delta^2 \dot{q}_2^2\right) \tag{33}$$

The thermal driving forces corresponding to the generalized coordinate X in solid 1 and δ in solid 2 are

$$Q_X = \frac{1}{2} c_1 q_1^2 - \rho L q_1 \tag{34}$$

$$Q_\delta = -\frac{c_2 q_2^2}{n+1} \tag{35}$$

Biot's variational principle is written in each solid as

$$\frac{\partial V_1}{\partial X} + \frac{\partial D_1}{\partial \dot{X}} = Q_X \tag{36}$$

$$\frac{\partial V_2}{\partial \delta} + \frac{\partial D_2}{\partial \dot{\delta}} = Q_\delta \tag{37}$$

Defining the dimensionless quantities $\Delta = \delta h/k_1$, $S = Xh/k_1$, $K = k_2/k_1$, $\beta = nK(S+1) - \Delta$, and $\sigma = c_1\theta_1/\rho L$ (the Stefan number) and using equations (20) and (21) to obtain

$$q_1 = -\frac{\theta_1 nKS}{\beta} \tag{38}$$

$$q_2 = \frac{\theta_1 \Delta}{\beta} \tag{39}$$

equations (36) and (37) can be rewritten in terms of the dimensionless generalized coordinates Δ and S and their dimensionless time derivatives

$$\frac{d\Delta}{d\tau} = \frac{P_1 + \frac{dS}{dr} P_2}{P_3}$$

$$P_1 = -\sigma\beta nK\left(\frac{1}{3}\sigma nKS + \beta\right)$$

$$P_2 = \beta^3 + \sigma nKS\left[(nK - \Delta)\left(\frac{1}{6}\beta + \frac{3}{40}\sigma nKS\right) + \beta\left(\frac{2}{3}\beta + \frac{2}{15}\sigma nKS\right)\right]$$

$$P_3 = -\sigma nKS^2\left(\frac{1}{6}\beta + \frac{3}{40}\sigma nKS\right) \tag{40}$$

and

$$\frac{d\Delta}{d\tau} = \frac{P_4 + \frac{dS}{dr} P_5}{P_6}$$

$$P_4 = -\beta \frac{\alpha_2}{\alpha_1}(n+1)(2n+3)(3n+1)$$

$$P_5 = 3nK\Delta^2(2n+1)$$

$$P_6 = \Delta[2\beta(5n+3) + 3nK(S+1)(2n+1)] \tag{41}$$

Here $\tau = th^2/k_1 c_1$ is dimensionless time, and all six P_i are functions of S, Δ, and the properties involved.

Thus, the use of Biot's principle has reduced the original PDE's for this problem to two coupled ordinary differential equations (ODE's), equations (40) and (41). These are the equations which must be solved simultaneously to obtain $X(t)$ and $\delta(t)$. In applying Biot's principle to Problems 2 and 4, only one ODE had to be solved, and in each case, it was simple enough to be solved analytically. However, the complexity of the expressions above makes the possibility of an analytical solution very unlikely for this problem. Therefore, a standard algorithm (IMSL, 1984) was used to obtain a numerical solution to equations (40) and (41). These results are presented in the following section.

Results

The position of the moving boundary $S(\tau)$ and the penetration depth $\Delta(\tau)$ are displayed graphically as functions of time in Figs. 2 and 3, respectively, for both bismuth ($K = 2.4$, $\sigma = 0.55$, $\alpha_1/\alpha_2 = 1.457$) and aluminum ($K = 0.1$, $\sigma = 2.5$, $\alpha_1/\alpha_2 = 20$) solidifying on stainless steel 304. The relationships shown there are nearly linear for large values of dimensionless time. In Fig. 4, the ratio $|\Delta(\tau)|/S(\tau)|$ appears to flatten out almost asymptotically as τ increases. The temperature profiles in the two solids for the case of bismuth on stainless steel are displayed in Fig. 5.

As mentioned earlier, the solution can be checked by considering limiting cases. In particular, the thermal conductivity in the nonsolidifying medium k_2 was taken to be large for Problem 8. In Table 1, the resulting position of the moving

Downloaded 17 Dec 2010 to 193.140.21.150. Redistribution subject to ASME license or copyright; see http://www.asme.org/terms/Terms_Use.cfm

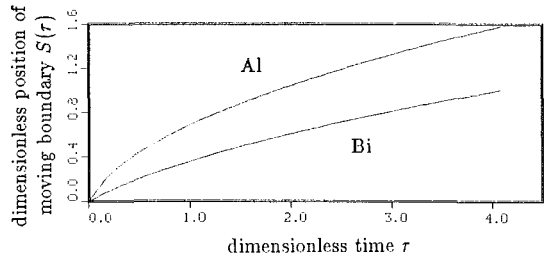

Fig. 2 Dimensionless position of moving boundary as a function of dimensionless time τ for bismuth/aluminum on stainless steel, $n = 2$

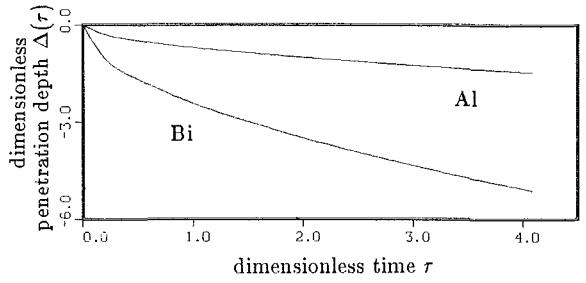

Fig. 3 Dimensionless penetration depth Δ as a function of dimensionless time τ for bismuth/aluminum on stainless steel, $n = 2$

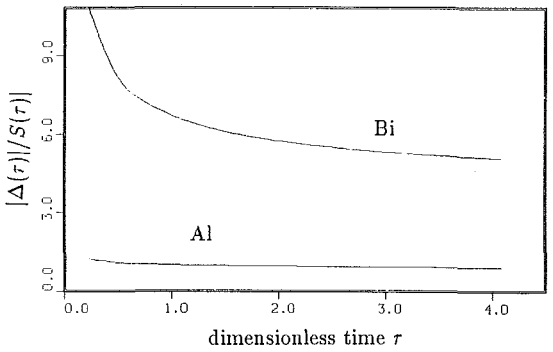

Fig. 4 Ratio $|\Delta(\tau)|/S(\tau)|$ as a function of dimensionless time τ for bismuth/aluminum on stainless steel, $n = 2$

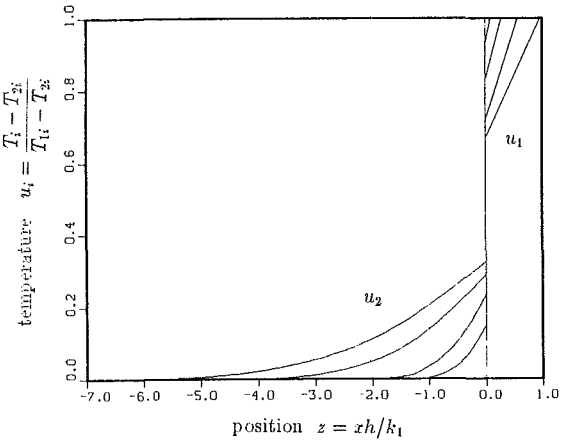

Fig. 5 Temperature as a function of position for various times (all quantities dimensionless) for bismuth/aluminum on stainless steel, $n = 2$

boundary is compared for various times with the position obtained in Problem 4 using Biot's method (Barry, 1985). As was expected, the values are in close agreement, particularly for large times. This confirms that Problem 8 reduces to Problem 4 as $k_2 \to \infty$.

The solution to Problem 8 was further checked by comparing it with the results of Hamm (1985), who has solved the original PDE's numerically using an implicit scheme and has obtained experimental results for the case of bismuth solidifying on stainless steel 304. A comparison of his numerical solution and the solution given here using Biot's principle appears in Table 2. The values for the dimensionless position of the moving boundary are in good agreement for all the assumed profiles in the table, with $n = 2$ giving a match to the nearest 0.01 for all values of dimensionless time listed. The temperature profiles shown in Fig. 5 also closely resemble those obtained by Hamm.

Table 1 Verification of collapse of Problem 8 to Problem 4 for large k_2; $\sigma = 0.5$

dimensionless time	dimensionless position of moving boundary — Biot's method	
	Problem 4	Problem 8: k_2 large, n=2
0.5063	0.20	0.22
1.0539	0.40	0.41
1.3642	0.50	0.51
2.4398	0.80	0.81
3.2768	1.00	1.01
4.2091	1.20	1.20
4.7110	1.30	1.30
5.7860	1.50	1.50
7.5762	1.80	1.80
8.8879	2.00	2.00

Table 2 Comparison of dimensionless position of moving boundary for bismuth solidifying on stainless steel 304: $K = 2.4$, $\sigma = 0.55$, $\alpha_1/\alpha_2 = 1.457$

dimensionless time	Biot's method				Hamm's numerical solution
	n=1.5	n=2	n=3	n=10	
0.2258	0.10	0.10	0.10	0.10	0.10
0.4941	0.20	0.20	0.21	0.21	0.20
0.8052	0.30	0.30	0.31	0.31	0.30
1.1569	0.39	0.40	0.41	0.42	0.40
1.5484	0.49	0.50	0.51	0.52	0.50
1.9790	0.59	0.60	0.62	0.63	0.60
2.4482	0.69	0.70	0.72	0.74	0.70
2.9558	0.78	0.80	0.82	0.85	0.80
3.5017	0.88	0.90	0.93	0.95	0.90
4.0855	0.98	1.00	1.03	1.06	1.00

Conclusions

We have presented the solution to a phase-change problem involving contact resistance. Using Biot's variational principle, we were able to reduce the problem to a pair of coupled ODE's, which are easier to solve numerically than are the original PDE's. It should be noted however that Biot's principle (like Goodman's heat balance method) is essentially an integral technique, since the conduction equation is satisfied on average over a body rather than at each point in the body. Thus, the most appropriate use for Biot's variational principle is in obtaining generalized coordinates (e.g., surface temperature, position of moving boundary) as functions of time, as we have done here.

Acknowledgments

This material is based upon work supported by the National Science Foundation under Grant MEA-8313296.

References

Agrawal, H. C., 1975, "Biot's Variational Principle for Moving Boundary Problems," in: *Moving Boundary Problems in Heat Flow and Diffusion*, J. R.

Downloaded 17 Dec 2010 to 193.140.21.150. Redistribution subject to ASME license or copyright; see http://www.asme.org/terms/Terms_Use.cfm

Ockendon and W. R. Hodgkins, eds., Oxford University Press, London, pp. 242–250.

Barry, G. W., 1985, "Application of Biot's Variational Principle to a Stefan Problem With Contact Resistance," M.S. Thesis, Department of Mechanical Engineering, Auburn University, Auburn, AL.

Biot, M. A., 1970, *Variational Principles in Heat Transfer*, Oxford University Press, London.

Biot, M. A., 1955, "Variational Principles in Irreversible Thermodynamics With Application to Viscoelasticity," *Physical Review*, Vol. 97, No. 6, pp. 1463–1469.

Biot, M. A., 1956, "Thermoelasticity and Irreversible Thermodynamics," *Journal of Applied Physics*, Vol. 27, No. 3, pp. 240–253.

Biot, M. A., 1957, "New Methods in Heat Flow Analysis With Application to Flight Structures," *Journal of the Aeronautical Sciences*, Vol. 24, No. 12, pp. 857–873.

Biot, M. A., 1959, "Further Developments of New Methods in Heat-Flow Analysis," *Journal of the Aerospace Sciences*, Vol. 26, No. 6, pp. 367–381.

Biot, M. A., and Daughaday, H., 1962, "Variational Analysis of Ablation," *Journal of the Aerospace Sciences*, Vol. 29, pp. 227–228.

Biot, M. A., and Agrawal, H. C., 1964, "Variational Analysis of Ablation for Variable Properties," ASME JOURNAL OF HEAT TRANSFER, Vol. 86, pp. 437–442.

Carslaw, H. S., and Jaeger, J. C., 1959, *Conduction of Heat in Solids*, Oxford University Press, Oxford, pp. 88, 89, 305–306, 285–286, 288–289.

IMSL, 1984, "Fortran Subroutine DREBS," IMSL Library, Edition 9.2, IMSL Inc., Houston, TX.

Hamm, M., 1985, "Numerical and Experimental Investigation of a Stefan Problem With Contact Conductance," M.S. Thesis, Department of Mechanical Engineering, Auburn University, Auburn, AL.

Ku, J. Y., and Chan, S. H., 1984, "A Systematic Approach to the Exact Solutions of Some Phase-Change Problems," ASME Paper No. 84-HT-1.

Kumar, I. J., 1972, "Recent Mathematical Methods in Heat Transfer," in: *Advances in Heat Transfer*, J. P. Harnett and T. F. Irvine, Jr., eds., Vol. 8, pp. 22–26.

Lardner, T. J., 1972, "Approximate Solutions to Phase-Change Problems," *AIAA Journal*, Vol. 5, pp. 2079–2080.

Lardner, T. J., 1963, "Biot's Variational Principle in Heat Conduction," *AIAA Journal*, Vol. 1, No. 1, pp. 196–206.

Lozano, C. J., and Reemtsen, R., 1981, "On a Stefan Problem With an Emerging Free Boundary," *Numerical Heat Transfer*, Vol. 4, pp. 239–245.

Lunardini, V. J., 1981, *Heat Transfer in Cold Climates*, Van Nostrand Reinhold Company, New York, pp. 381–386, 406–409.

Muehlbauer, J. C., and Sunderland, J. E., 1965, "Heat Conduction With Freezing or Melting," *Applied Mechanics Review*, Vol. 18, No. 12, pp. 951–959.

Ozisik, M. N., 1980, *Heat Conduction*, Wiley, New York, pp. 410–412, 416–423.

Prasad, A., and Agrawal, H. C., 1972, "Biot's Variational Principle for a Stefan Problem," *AIAA Journal*, Vol. 10, No. 3, pp. 325–327.

Westphal, K. O., 1967, "Series Solution of Freezing Problem With the Fixed Surface Radiating Into a Medium of Arbitrary Varying Temperature," *Int. J. Heat Mass Transfer*, Vol. 10, pp. 195–205.

Downloaded 17 Dec 2010 to 193.140.21.150. Redistribution subject to ASME license or copyright; see http://www.asme.org/terms/Terms_Use.cfm

Optimal Positioning of Tubes in Arbitrary Two-Dimensional Regions Using a Special Boundary Integral Method

M. Parang
Associate Professor.

R. V. Arimilli
Associate Professor.

S. P. Ketkar
Graduate Student.

Mechanical and Aerospace Engineering Department,
The University of Tennessee,
Knoxville, TN 37996

Two-dimensional steady conduction heat transfer from a set of parallel tubes located in a finite two-dimensional region enclosed by an arbitrarily shaped boundary is considered. A special boundary integral method is used in an optimization scheme where the tube sizes, positions, and surface temperatures can be determined in an iterative procedure with the objective of minimizing the variation of temperature over a specified segment of the boundary. Previous studies of this type were limited not only to rectangular regions but also to uniform heat flux results on the surface of each tube. However, the optimization scheme developed in this study is applicable to any arbitrarily shaped two-dimensional region and considers angular variation of heat flux on the surface of each tube. Results for three sample geometries are presented and discussed.

Introduction

In many conduction heat transfer problems, the behavior of the temperature or its normal derivative is of interest only on the boundary of the domain under consideration. In this type of problem it is often advantageous to use the boundary integral equation (BIE) method in which the problem can be formulated in terms of the unknowns on the boundary of the domain. The major advantage of this formulation is that only the boundary of the region of interest needs to be discretized. Therefore the BIE method involves a significantly smaller number of unknowns in this type of problem relative to such methods as finite difference or finite element, where the entire domain of interest must be discretized. A considerable amount of research using the BIE method has been reported in a variety of areas such as conduction heat transfer, potential flow, elastic torsion, and fracture mechanics. Problems governed by the Laplace equation have been successfully solved using the BIE method (Jaswon and Symm, 1977). Rizzo and Shippy (1977) and Fairweather et al. (1979) used the BIE method for the analysis of three-dimensional thermoelasticity and two-dimensional potential problems. Khader and Hanna (1981) presented a boundary integral iterative numerical solution for general steady heat conduction problems with a variety of different boundary conditions.

There are a variety of important problems where the solution of the Laplace equation in regions wth circular interior boundaries may be required. Some examples are two-dimensional conduction heat transfer through dies or molds in casting processes where cooling or heating lines are positioned in the mold to achieve the desired temperature distribution on the cavity surface. Other examples may include heat conduction in cooled gas turbine blades, flow of an incompressible inviscid fluid around circular cylinders, and buried heat-exchanger tubes of ground-coupled heat-pump systems.

In the application of numerical methods to steady-state conduction heat transfer problems, including the BIE method, the discretization of the boundaries internal to the region of interest may pose special problems. Specifically, when these internal boundaries are small relative to the outer boundary (e. g., small holes), a fine discretization needs to be implemented on the entire inner boundary to avoid numerical conditioning problems. Barone and Caulk (1981) developed a formulation in which the integrals around the circular interior boundaries were evaluated analytically using harmonic series expansions for boundary values of the dependent variable and its normal derivative, and by a clever choice of kernel functions. Arimilli and Parang (1983) and Arimilli et al. (1984) used this formulation to determine the conduction heat transfer from circular tubes embedded in semi-infinite medium with convective boundary conditions. Barone and Caulk (1981) applied their formulation, using only the constant term of the harmonic expansion for heat flux (called zeroth-order approximation), to the problem of a two-dimensional (2D) *rectangular* die with interior coolant lines. They applied the solution procedure developed to solve an optimization problem (Barone and Caulk, 1982).

The focus of the present study is the problem of optimal thermal design of two-dimensional molds with circular coolant lines. Here, the mold is modeled by a 2D arbitrary region with internal circular holes. The objective of an optimization process in a mold design could, as an example, be to minimize the variation of temperature over a segment of the mold (cavity) wall. The optimization parameters could be selected to include the locations, the number, and/or the sizes of the coolant lines (holes). This problem is solved by the use of the BIE method as modified by the special integral formulation proposed in Barone and Caulk (1981). More specifically, the present study allows the region which models the mold to be a specified but arbitrarily shaped region and, more importantly, considers the inclusion of higher order terms in the harmonic series expansions that were discussed earlier. This latter aspect of the solution makes it possible to determine the variation of normal heat flux (or temperature) on the boundaries of the coolant lines (holes).

Therefore, in the following section the analytical formulation leading to a particular numerical code, which has been developed based on the above special integral method, is discussed briefly. This code generates solutions of temperature and normal heat flux on the boundaries of any *arbitrary* 2D regions. It solves for the coefficients up to and including the first-order terms in the harmonic expansion of the heat transfer from circular holes. This code is then used in an optimization problem to determine the optimal locations and the

Contributed by the Heat Transfer Division and presented at the National Heat Transfer Conference, Denver, Colorado, August 4-7, 1985. Manuscript received by the Heat Transfer Division October 23, 1985.

Copyright © 1987 by ASME

Downloaded 17 Dec 2010 to 193.140.21.150. Redistribution subject to ASME license or copyright; see http://www.asme.org/terms/Terms_Use.cfm

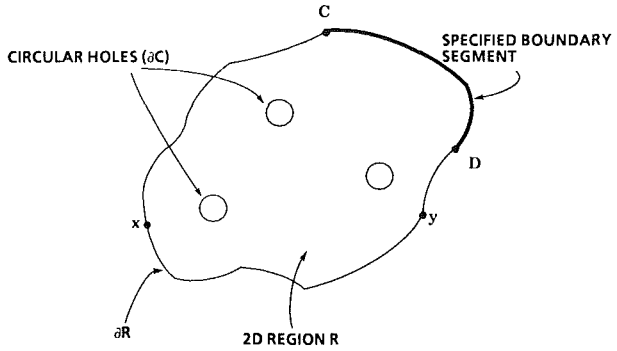

Fig. 1 The two-dimensional region with circular tubes

heat flux on the surface of the coolant lines in the 2D mold. This discussion is included in the section on optimization. Several configurations are used as illustrative examples and the results are presented and discussed in detail.

Analysis

Consider a two-dimensional region R as shown in Fig. 1 containing M circular holes, representing a cross section of tubes normal to the region. Assume the αth hole is centered at $\Gamma^\alpha(\xi^\alpha, \eta^\alpha)$ with radius a^α. The temperature ϕ in this region is governed by the Laplace equation. If the values of temperature or its normal derivative are only of interest on the boundaries of region R, an alternative integral method can be employed based on Green's identity (McMillan, 1930)

$$\lambda\phi(y)+\int_{\partial R}\left(\phi\frac{\partial g}{\partial n}-g\frac{\partial\phi}{\partial n}\right)ds + \sum_{\alpha=1}^{M}\int_{\partial c^\alpha}\left(\phi^\alpha\frac{\partial g}{\partial n}-g\frac{\partial\phi^\alpha}{\partial n}\right)ds=0 \tag{1}$$

where

$$\lambda=\begin{cases}1 & \text{when } y\in R\\ 1/2 & \text{when } y\in\{\partial R,\ \partial c^\alpha\}\\ 0 & \text{when } y\notin\{R,\ \partial R,\ \partial c^\alpha\}\end{cases}$$

and

$$g(x,y)=-\frac{1}{2\pi}\log|X-Y| \tag{2}$$

Equation (1) represents the value of ϕ at a point y on the boundary in terms of integrals of ϕ and its normal derivative over all boundaries of the domain. The solution for temperature or its normal derivative on the boundary of region R is obtained by evaluation of this integral over discrete intervals on this boundary.

The temperature and its normal derivative on the surface of circular tubes (∂c^α) can be expressed in a harmonic series

$$\phi^\alpha=\phi_0^\alpha+\sum_{m=1}^{\infty}\left(\phi_{1m}^\alpha\sin m\theta^\alpha+\phi_{2m}^\alpha\cos m\theta^\alpha\right) \tag{3}$$

$$\frac{\partial\phi^\alpha}{\partial n}=q^\alpha=q_0^\alpha+\sum_{m=1}^{\infty}\left(q_{1m}^\alpha\sin m\theta^\alpha+q_{2m}^\alpha\cos m\theta^\alpha\right) \tag{4}$$

where the coefficients of the above series can be obtained by employing the following special kernel functions:

$$g_0^\alpha(x)=g(X,\Gamma^\alpha) \tag{5a}$$

$$g_{2m}^\alpha=\frac{\cos m\theta^\alpha}{|X-\Gamma^\alpha|^m} \tag{5b}$$

$$g_{1m}^\alpha=\frac{\sin m\theta^\alpha}{|X-\Gamma^\alpha|^m} \tag{5c}$$

After equations (3)–(5) are substituted into equation (1), the integrals can be evaluated analytically over the circular holes, thus avoiding entirely the discretization of these boundaries (Barone and Caulk, 1981).

In this analysis we assume, following Barone and Caulk (1982), constant-temperature tube surfaces

$$\phi^\alpha=\phi_0^\alpha \tag{6}$$

For the harmonic expansion of heat transfer, the analysis was not limited to the inclusion of the zeroth-order term ($m = 0$) as in the previous reference. Instead the next higher order terms ($m = 1$) were also included

$$q^\alpha=q_0^\alpha+q_1^\alpha\sin\theta^\alpha+q_2^\alpha\cos\theta^\alpha \tag{7}$$

There are two reasons for including these higher order terms. First, the accuracy of the results can be significantly improved as illustrated in Barone and Caulk (1981). For the specific example used in that reference, the results for $m = 0$ were found less accurate by as much as 20 percent when compared to $m = 1$. The second, and more important, reason for including the higher order terms is that without them no information can be obtained on the angular variation of the normal heat flux on the surfaces of the coolant lines. Therefore such thermal properties of interest as estimates of maximum or minimum heat flux and their location on the tube walls can not be made without setting m equal to 1 or larger.

When equations (7) and (2) are substituted into equation (1), the integrals over each of the interior circular boundaries can be analytically evaluated. With the external boundary discretized into N segments, the first integral can be written as

Nomenclature

a^α = radius of tube α
∂c = hole boundary
g = harmonic function in Green's identity
M = number of holes
m = the order of the terms in harmonic expansions, equations (3) and (4)
n = unit normal vector at boundary
P = heat of reaction
q = normal derivative of temperature, see equation (4)
$q_0^\alpha, q_1^\alpha, q_2^\alpha$ = defined in equation (7)
$R, \partial R$ = region R and its boundary
ds = differential length on a boundary
X, Y = position vectors of points on the boundary
α = tube identification number
β = tube identification number in equation (11)
Γ^α = position vector of center of tube α
θ^α = azimuthal angle of tube α
λ = defined after equation (1)
ϕ = temperature
ϕ_0^α = constant temperature on the surface of holes
Φ = nondimensional temperature

Downloaded 17 Dec 2010 to 193.140.21.150. Redistribution subject to ASME license or copyright; see http://www.asme.org/terms/Terms_Use.cfm

N discrete integrals. The resultant discrete integrals over each segment can be evaluated analytically for segments on straight sections of the boundary, and numerically (using, for example, the trapezoid rule) for those on curved boundaries. Thus N algebraic equations can be generated corresponding to the N segments of the external boundary. Substitution of equations (7) and (5*a*), (7) and (5*b*), and (7) and (5*c*) into equation (1) yields three integral equations. The integrals can be evaluated in a manner similar to the one described above. For M circular interior boundaries, this procedure leads to $3M$ algebraic equations. The basic problem underlying the optimization problem is thus reduced to a set of $(N + 3M)$ linear algebraic equations involving N unknown temperatures of the discrete segments of the boundary $(\phi_1, \phi_2, \phi_3, \ldots, \phi_N)$ and the three unknown coefficients of the harmonic expansion for the normal temperature gradient for each tube

$$q_0^\alpha,\ q_1^\alpha, \text{ and } q_2^\alpha; \qquad \alpha = 1,2, \ldots, M$$

A computer code is developed to generate and solve the resultant set of equations. The code yields a boundary integral solution (BISOL) and is developed and presented in Ketkar (1985). This code is applied to four different 2D geometric configurations and some of the results are presented in Parang et al. (1985).

In the present paper we use BISOL to solve the optimization problem of determining the positions of a given number of tubes within a 2D mold with an arbitrarily shaped mold cavity surface with the objective that the temperature variation over the cavity surface be minimum. The problem involves steady-state conduction heat transfer from a finite body having, as its external boundaries, three normal plane surfaces and an arbitrarily shaped fourth surface. The interior of the body contains a specified number of circular boundaries maintained at a prescribed constant temperature. At each of the external boundaries either the temperature or a convective boundary condition may be specified. Three illustrative problems are solved and the results are presented and discussed.

Optimization

One of the objectives in the thermal design of molds or dies may be to achieve, as much as possible, a uniform temperature on the mold cavity surface. This objective can be achieved by optimization of several parameters that affect the cavity surface temperature. These parameters may include geometric contour of the external boundary, convective conditions on the external boundary, radius and surface temperature of the tubes, and location of the tubes. In this study we assume that the external boundary of the heat conductor is given and not subject to optimization. Although different sets of convective boundary conditions are considered in this study, they are also assumed known and not subject to parametric optimization. Assuming a given number of tubes, the design objective in this study is therefore selected to be the determination of optimal tube locations in the heat conductor (mold). Without a loss of generality in the application of the method, we assume the radii and surface temperatures of the tubes as given and select the tube locations as optimization parameters. Thus we consider two design variables for each tube, i.e., the coordinates of the center of the hole, ξ and η.

The objective of the optimization scheme is to minimize the distributed difference between the nodal temperature Φ_i and the desired temperature Φ_c over some portion of the outer boundary (the cavity surface). This distributed difference is expressed here, as in Barone and Caulk (1982), in the form of a least-square difference of the form

$$\text{OBJ} = \sum_{y_i \in \partial R} (\Phi_i - 1)^2 \tag{8}$$

where Φ_i is the nondimensional temperature given by

$$\Phi_i = \frac{\phi_i - \phi_a}{\phi_c - \phi_a}$$

and ϕ_a is the ambient temperature outside the heat conductor. The normal derivative of temperature q_i can be formulated in terms of temperature Φ_j at the boundaries. That is, the general boundary condition on ∂R can be expressed as

$$q_j = \frac{\partial \Phi_j}{\partial n} = -\text{Bi}\Phi_j + P \tag{9}$$

Here Bi is the Biot number and P is the heat of reaction absorbed by the heat conductor expressed as a uniform heat flux across the cavity surface.

The constraints on this optimization problem are: specified lower limits for the spacing between the tubes, and the spacing between each circular tube and the outer boundary. These constraints are expressed in the following explicit form:

$$\left| Y_i - \Gamma^\alpha \right| \geq a^\alpha + c_1; \qquad \alpha = 1,2, \ldots, M, \quad i = 1,2, \ldots, N \tag{10}$$

$$\left| \Gamma^\alpha - \Gamma^\beta \right| \geq a^\alpha + a^\beta + c_2; \quad \alpha, \quad \beta = 1,2, \ldots, M \tag{11}$$

where c_1 and c_2 are specified clearances and taken to be 0.05 in this study.

The nodal nondimensional temperatures Φ_i, which are represented in the objective function (8), depend on the location radii and the temperature of the tubes through the solution of the set of $(N + 3M)$ linear algebraic equations. Hence

$$\Phi_i = \Phi_i(\Gamma^\alpha, \alpha^\alpha, \phi_0^\alpha); \qquad \alpha = 1,2, \ldots, M \tag{12}$$

The optimization problem formulated above must be solved numerically. This objective is achieved with the use of the code CONMIN (Vanderplaats, 1973). CONMIN is a FORTRAN program in subroutine form for the minimization of a multivariable function subject to a set of inequality constraints. The main algorithm used in CONMIN is the method of feasible directions (Zoutendijk, 1960). The computer program BISOL developed and discussed earlier is used in conjunction with CONMIN for the determination of the optimal locations of cooling or heating lines in two-dimensional molds.

In order to illustrate the method and use the optimization scheme developed, several two-dimensional configurations are selected to represent different mold cross sections. The convective boundary conditions on the external boundary of the region are assumed known and Biot numbers specified. For illustration purposes the nondimensional temperature on the surface of all tubes are assumed to be constant and arbitrarily set to 1.24. Also all tube radii are assumed equal and have a dimensionless value of 1 for the cases considered here. It is important to note that the method and the code developed here are quite general and the tube radii and surface temperatures can also be subjected to the optimization scheme.

Initially the coordinates of the location of the tubes are assumed and BISOL and CONMIN are used in an iterative routine to establish the optimal locations of the tubes. The initial position of the tubes is found to affect the required optimization time. The significance of the initial guess for the tube locations on the computation time increases, not unexpectedly, with increase in the number of tubes in the two-dimensional region.

Results

The optimization scheme developed here is illustrated by applying it to a selected number of 2D configurations representing mold cross sections each with several coolant lines passing

Downloaded 17 Dec 2010 to 193.140.21.150. Redistribution subject to ASME license or copyright; see http://www.asme.org/terms/Terms_Use.cfm

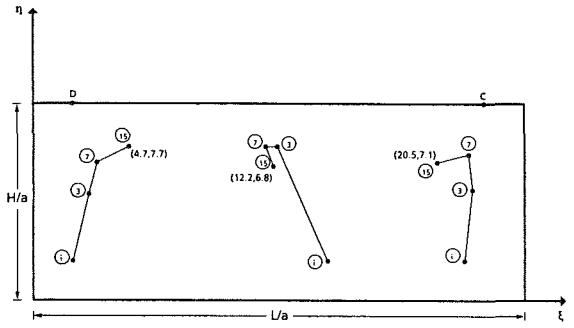

Fig. 2 Sketch of the two-dimensional rectangular region with circular holes and convective boundary conditions used in case I

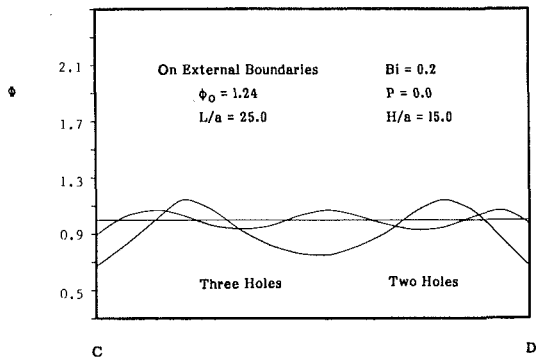

Fig. 3 Variation of the nondimensional temperature ϕ along the cavity surface: case I; optimal two hole locations: (7.2, 7.5), (18.5, 7.5); optimal three hole locations: (12.2, 6.8), (20.5, 7.1), (4.7, 7.7)

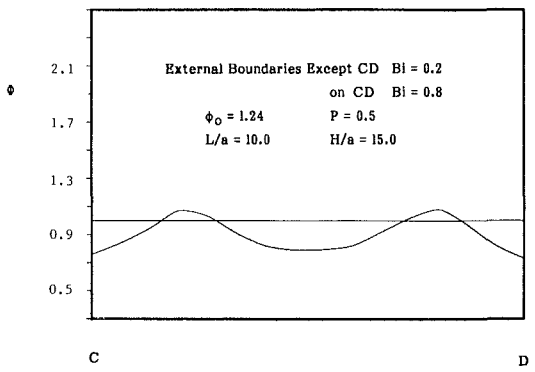

Fig. 4 Variation of the nondimensional temperature ϕ along the cavity surface: Case I; optimal two hole locations: (7.3, 7.7), (18.3, 7.7)

through them. Thus three different geometries are selected and are labeled Cases I, II, and III. The configurations are shown in Figs. 2, 5, and 7. In all cases tube sizes are assumed to be the same, $a_\alpha = 1.0$, and all tube surface temperatures are selected at $\Phi_I^\alpha = 1.24$. In all configurations the objective function defined by equation (8) is minimized over the mold cavity surface shown as the boundary segment between points C and D. These points are each assumed to be one tube diameter away horizontally from the vertical ends of the mold. In Figs. 2, 5, and 7 the initial guess for the center of each hole in the optimization process is shown by a circled i. The progression of the design is then described by indicating the location of the hole centers after the designated (circled) number of iterations. The optimal coordinates of the hole centers, (ξ, η), are also shown for each configuration.

Case I corresponds to the rectangular region shown in Fig 2. Assuming two and three heating lines, respectively, and

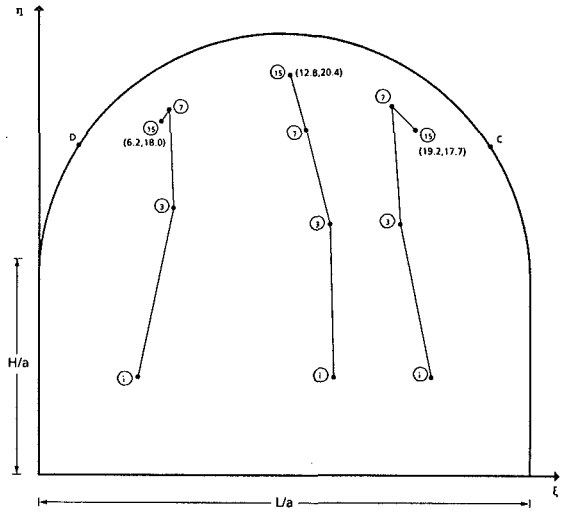

Fig. 5 Sketch of the two-dimensional region with circular holes and convective boundary conditions used in case II

uniform Bi = 0.2 on all external boundaries, $P = 0.0$, $L/a = 25.0$, and $H/a = 10.0$, optimal tube locations are calculated. The results of the cavity surface temperature and coordinates of tube locations are shown in Fig. 3. As expected, optimal tube locations and corresponding cavity temperature distribution are symmetric and temperature fluctuations are smaller for the three-hole problem. In this and other symmetric examples presented, a slight asymmetry may exist in the final optimal locations of the holes. This phenomenon is due to the manner in which the iteration process is carried out in CONMIN. That is, if in three consecutive iterations the change in the objective function is calculated and found to be less than a small specified limit (DELFUN), the process is terminated (Vanderplaats, 1973). In the examples used in this study, DELFUN is set equal to 0.001. Reducing this value will diminish the asymmetry in the final solution. However, the obvious disadvantage in reducing DELFUN is the increase in the required number of iterations needed to solve for the optimal hole locations.

Next the effect of a nonuniform convective condition on the optimal location of the tubes was considered. Assuming a different and nonuniform Biot number and $P = 0.5$, the results of the temperature distribution on the cavity surface and the optimal tube locations are given in Fig. 4. From Figs. 3 and 4 and other cases presented elsewhere (Ketkar, 1985), it is observed that the optimal tube locations are not significantly influenced by the changes introduced in the convective boundary conditions (i.e., for a range of Bi = 0.2 to 1.0; and a range of $P = 0.0$ to 0.5).

Case II corresponds to the configuration shown in Fig. 5. Here the cavity surface is assumed to be part of a semicircle. This geometry was used with both two and three tubes in the optimization problem and the temperature on the external boundary as well as the optimal locations of tubes in each case were determined. The results for temperature distribution on the cavity surface are shown in Fig. 6. The coordinates of the computed optimal tube locations are also given in Fig. 6. As in the rectangular region, the temperature distribution on the cavity surface has smaller fluctuations and is more uniform for the three-tube problem as compared to the two-tube problem.

Case III corresponds to the configuration shown in Fig. 7 where the semicircular cavity surface of the previous problem is replaced with an S-shaped contour. The progression of the iteration process for the two-hole system is also shown in this figure. The final results for the temperature and optimal hole locations for the three-hole system are presented in Fig. 8.

Downloaded 17 Dec 2010 to 193.140.21.150. Redistribution subject to ASME license or copyright; see http://www.asme.org/terms/Terms_Use.cfm

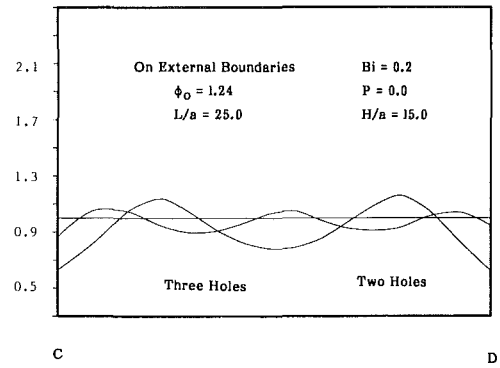

Fig. 6 Variation of the nondimensional temperature ϕ along the cavity surface: Case II; optimal two hole locations: (8.2, 19.5), (17.6, 18.9); optimal three hole locations: (6.2, 18.0), (12.8, 20.4), (19.2, 17.7)

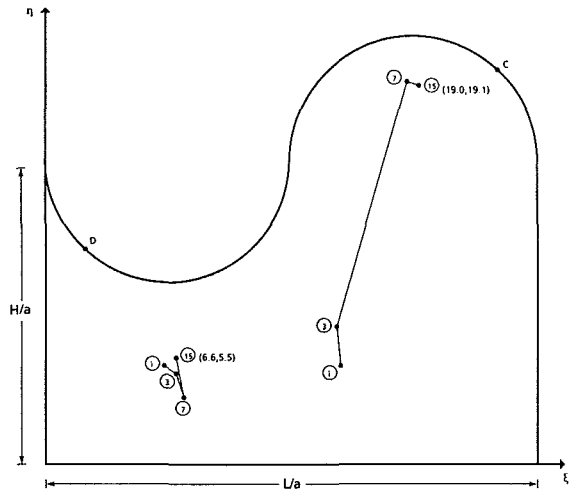

Fig. 7 Sketch of the two-dimensional region with circular holes and convective boundary conditions used in case III

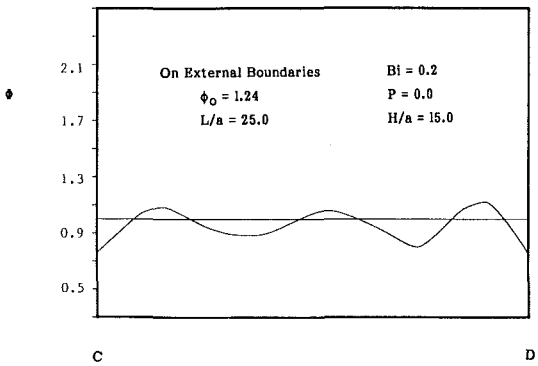

Fig. 8 Variation of the nondimensional temperature ϕ along the cavity surface: Case III; optimal two hole locations: (6.6, 5.5), (19.0, 19.1); optimal three hole locations: (6.3, 5.1), (15.3, 14.9), (19.0, 19.0)

The examples discussed above are illustrations of application of the general computer program developed for this study. As mentioned earlier, in this computer program, the tube size, convective boundary conditions, boundary of the region of interest, temperature imposed on circular holes, and the number of holes can all of course be conveniently varied for other two-dimensional applications.

The CPU time in the above numerical examples depended upon the number of tubes, initial tube locations, and the value of DELFUN used in the optimization scheme. The typical range of the computation time in the above illustrations is approximately 1 to 5 min on a DECsystem-10 Model 1090.

Conclusions

The computer program BISOL developed based on a special boundary integral method is used in an optimization scheme to determine the optimal locations of coolant lines in a two-dimensional mold. The method used and the optimization program developed are very general, and can be used to obtain quantitative results for any arbitrary two-dimensional region. In addition, the inclusion of higher-order terms in the harmonic expansions of heat flux in this numerical scheme makes it possible to consider angular variation of heat flux on the surface of each tube. Results for three sample geometries were presented and discussed. The maximum computational time required for the illustrative examples discussed was found to be less than 5 min.

References

Arimilli, R. V., and Parang, M., 1983, "Numerical Analysis of Heat Transfer in Buried Horizontal Heat Exchanger Tubes," *AIChE Symposium Series*, No. 225, Vol. 79, pp. 121–129.

Arimilli, R. V., Parang, M., and Surapaneni, P. R., 1984, "Numerical Boundary Integral Analysis of Heat Transfer From Circular Tubes in a Semi-infinite Medium," *Heat Transfer in Heat Rejection Systems*, ASME HTD-Vol. 37, New York, pp. 65–71.

Barone, M. R., and Caulk, D. A., 1981, "Special Boundary Integral Equations for Approximate Solution of Laplace's Equation in Two-Dimensional Region With Circular Holes," *The Quarterly Journal of Mechanics and Applied Mathematics*, Vol. XXXIV, pp. 265–286.

Barone, M. R., and Caulk, D. A., 1982, "Optimal Arrangement of Holes in a Two-Dimensional Heat Conductor by a Special Boundary Integral Method," *International Journal of Numerical Methods in Engineering*, Vol. 18, pp. 675–685.

Brebbia, C. A., Telles, J. C. F., and Wrobel, L. C., 1984, *Boundary Element Techniques—Theory and Applications in Engineering*, Springer-Verlag, New York.

Fairweather, G. F., Rizzo, J., Shippy, D. J., and Wu, Y. S., 1979, "On the Numerical Solution of Two-Dimensional Potential Problems by an Improved Boundary Integral Equation Method," *Journal of Computational Physics*, Vol. 31, pp. 96–112.

Jaswon, M. A., and Symm, G. T., 1977, *Integral Equation Methods in Potential Theory and Elastostatics*, Academic Press, New York.

Ketkar, S. P., 1985, "Determination of Optimal Hole Locations in a Two-Dimensional Heat Conductor Using Boundary Integral Method," M. S. Thesis, University of Tennessee, Knoxville, TN.

Khader, M. S., and Hanna, M. C., 1981, "An Iterative Numerical Solution for General Steady Heat Conduction Problems," *International Journal of Heat and Mass Transfer*, Vol. 103, pp. 26–31.

McMillan, W. D., 1930, *The Theory of Potential*, McGraw-Hill, New York.

Parang, M., Arimilli, R. V., and Ketkar, S. P., 1985, "Analysis of Conduction Heat Transfer Problems in Steady, 2D Regions With Circular Holes Using a Special Boundary Integral Method," *International Communications in Heat and Mass Transfer*, Vol. 12, No. 2, pp. 179–189.

Rizzo, F. J., and Shippy, D. J., 1977, "An Advanced Boundary Integral Equation Method for Three-Dimensional Thermoelasticity," *International Journal of Numerical Methods in Engineering*, Vol. 11, pp. 1753–1762.

Vanderplaats, G. N., 1972, "CONMIN—A FORTRAN Program for Constrained Function Minimization," NASA TM-X 62.282.11, pp. 1753–1768.

Zoutendijk, G., 1960, *Methods of Feasible Directions*, Elsevier, Amsterdam.

Downloaded 17 Dec 2010 to 193.140.21.150. Redistribution subject to ASME license or copyright; see http://www.asme.org/terms/Terms_Use.cfm

K. Kamiuto
Associate Professor.

M. Iwamoto
Graduate Student.

Faculty of Engineering,
Ohita University,
Dannoharu 700,
Ohita 870-11, Japan

Inversion Method for Determining Effective Thermal Conductivities of Porous Materials

An inversion method for determining the effective thermal conductivies of porous materials from observed mean effective thermal conductivities is presented. Its validity is confirmed by numerical simulations. The effective thermal conductivities of glass beads are determined by the proposed method successfully used to predict the temperature profiles within the glass beads.

Introduction

The guarded hot-plate method has been widely used in determining the effective thermal conductivities of porous materials. This method yields mean effective thermal conductivities defined by equation (1) alone

$$\bar{\lambda} = qy_0/(T_H - T_L). \tag{1}$$

Here, $\bar{\lambda}$ is the mean effective thermal conductivity, q is the heat flux across the porous material, y_0 is the thickness of the porous material, and T_H and T_L are the temperatures of hot and cold boundaries, respectively.

The mean effective thermal conductivity thus obtained can be used effectively for gross evaluation of heat transfer by conduction and radiation. However, based on the energy equation, an exact prediction of coupled conduction and radiation heat transfer in a thick porous medium calls for knowledge of its effective thermal conductivities. This includes the contribution of radiative heat transfer. Therefore it is necessary to determine effective thermal conductivity from information on mean effective thermal conductvities obtained experimentally. Two kinds of effective thermal conductivities are related by

$$\bar{\lambda}(\theta_L, \theta_H) = \int_{\theta_L}^{\theta_H} \lambda(\theta)d\theta/(\theta_H - \theta_L), \tag{2}$$

where $\lambda(\theta)$ denotes the effective thermal conductivity at temperature θ, $\theta = T/1000$, $\theta_H = T_H/1000$, and $\theta_L = T_L/1000$. Based on this relation, it may be possible to estimate $\lambda(\theta)$ from the data of $\bar{\lambda}(\theta_L, \theta_H)$, which freqeuntly entails error in the course of meaurement. However, to the authors' knowledge, no effective solution to this problem has yet been reported.

In the present study, an analytical method based on minimum AIC (Akaike's information criterion) estimation [1] for determining effective thermal conductivities of porous materials is presented, and is applied to some typical cases to confirm validity. Furthermore, the effective thermal conductivities of glass beads are determined.

Analytical Method

We suppose that $\lambda(\theta)$ is a continuous function of θ in the temperature zone of interest and that $\lambda(\theta)$ can be expanded as a polynomial of θ

$$\lambda(\theta) = \sum_{n=0}^{N} a_n \theta^n, \tag{3}$$

where N denotes the order of a polynomial and should be an integer less than about 6 so as to suppress undesirable oscillation induced by higher-order polynomials. Substitution of equation (3) into equation (2) yields

$$\bar{\lambda}(\theta_L, \theta_H) = a_0 + \sum_{n=1}^{N} \frac{a_n}{n+1} \sum_{i=1}^{n+1} \theta_L^{i-1} \theta_H^{n+1-i}. \tag{4}$$

The problem to be solved is converted to determine a_n (n = 0 to N) by utilizing observed values of $\bar{\lambda}(\theta_L, \theta_H)$. The number of data for $\bar{\lambda}(\theta_L, \theta_H)$ must be equal to or greater than N. Since $\bar{\lambda}(\theta_L, \theta_H)$ may contain some experimental error, the introduction of the least-squares method seems to be natural. Using to this method, we obtain a set of equations for a_n for n = 0 to N

$$\sum_{j=1}^{M} \frac{\theta_{Hj}^{k+1} - \theta_{Lj}^{k+1}}{(k+1)(\theta_{Hj} - \theta_{Lj})} \left\{ \bar{\lambda}(\theta_{Lj}, \theta_{Hj}) - a_0 - \sum_{n=1}^{N} \frac{a_n}{n+1} \sum_{i=1}^{n+1} \theta_{Lj}^{i-1} \theta_{Hj}^{n+1-i} \right\} = 0, \tag{5}$$

where M is the number of data on mean effective thermal conductivities and $k = 0, 1, 2, \ldots, N$. Equation (5) constitutes a set of simultaneous linear equations with degree $(N+1)$ and can be solved readily by a Gaussian eliminations method. It should be noted that the determination of the optimum value of N becomes crucial. In the present study, the optimum value of N is determined in order to achieve the minimum AIC [1].

The AIC is defined by

$$\mathrm{AIC} = M \ln(\delta) + 2(N+1), \tag{6}$$

where δ is the sum of squares of residuals, and is given by

$$\delta = \sum_{j=1}^{M} \left(\bar{\lambda}(\theta_{Lj}, \theta_{Hj}) - \int_{\theta_{Lj}}^{\theta_{Hj}} \lambda(\theta)d\theta/(\theta_{Hj} - \theta_{Lj}) \right)^2$$

$$= \sum_{j=1}^{M} \left(\bar{\lambda}(\theta_{Lj}, \theta_{Hj}) - a_0 - \sum_{n=1}^{N} \frac{a_n}{n+1} \sum_{i=1}^{n+1} \theta_{Lj}^{i-1} \theta_{Hj}^{n+1-i} \right)^2. \tag{7}$$

The minimum AIC estimation is thought to be a formulation of the principle of parsimony in model building. It works as follows: When δ is identical for two polynomial expansions of $\lambda(\theta)$ having different values of N, the polynomial expansion with the smaller number of parameters is selected. This is because it gives a smaller value of AIC. Here, equation (5) was solved by varying the value of N from 1 to 6, while simultaneously the value of AIC was evaluated from equation (6). The order of N for the minimum AIC was then picked up as the optimum order of N and the corresponding polynomial of $\lambda(\theta)$ was assumed to be the best one.

Numerical Simulations

Several synthetic cases were analyzed to test the proposed

Contributed by the Heat Transfer Division for publication in the JOURNAL OF HEAT TRANSFER. Manuscript received by the Heat Transfer Division July 8, 1985.

 Copyright © 1987 by ASME

Downloaded 17 Dec 2010 to 193.140.21.150. Redistribution subject to ASME license or copyright; see http://www.asme.org/terms/Terms_Use.cfm

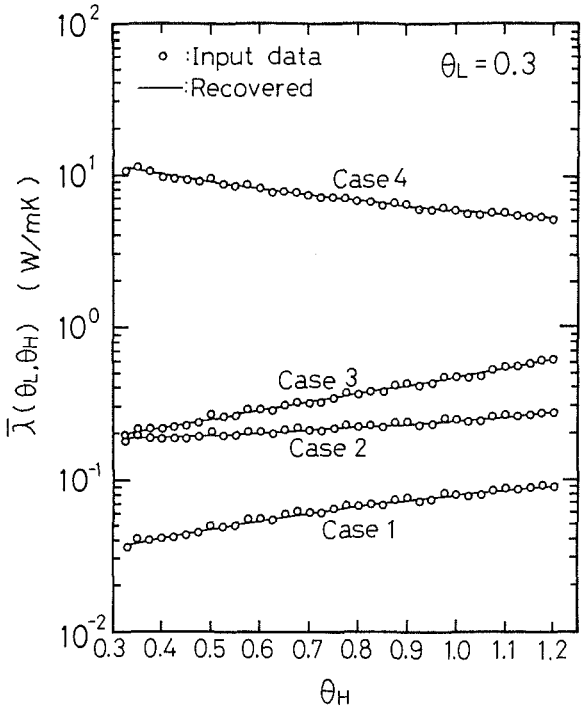

Fig. 1 Results of numerical simulations on inversion performed for some typical cases

method. The following expressions for $\lambda(\theta)$ were adopted to generate original data on mean effective thermal conductivities:

Case 1: $\lambda(\theta) = -0.001359 + 0.1234\theta$ (8)

Case 2: $\lambda(\theta) = 0.1747 - 0.0229\theta + 0.1781\theta^2$ (9)

Case 3: $\lambda(\theta) = -0.0678 + 1.2194\theta - 1.6008\theta^2 + 1.3654\theta^3$ (10)

Case 4: $\lambda(\theta) = 21.0014 - 40.7087\theta + 29.7208\theta^2 - 6.8558\theta^3$ (11)

These represent typical cases of variation in effective thermal conductivities. Cases 1, 2, 3 are models for increasing effective thermal conductivities against increasing temperature, whereas Case 4 is a model for decreasing effective thermal conductivities against increasing temperature.

Based on these expressions, the values of $\bar{\lambda}(\theta_{Lj}, \theta_{Hj})$ in equation (5) were first computed by utilizing equation (2) together with equations (8)–(11), where we tentatively assumed that θ_{Hj} is given by

$$\theta_{Hj} = \theta_{Lj} + 0.025j \tag{12}$$

for $j = 1$ to 36 and that $\theta_{Lj} = 0.3$. Subsequently, 5 percent random error was introduced to these data so as to simulate actual measurement. The 5 percent random error is thought to be corresponding to the lower limit of accuracy of mean effective thermal conductivities obtained by the guarded hot-plate method.

As a result of inversion, the following polynomials were obtained:

Case 1: $\lambda^*(\theta) = -0.0019085 + 0.1237\theta$ (13)

Case 2: $\lambda^*(\theta) = 0.1588 + 0.02762\theta + 0.1394\theta^2$ (14)

Case 3: $\lambda^*(\theta) = -0.09371 + 1.3174\theta - 1.7062\theta^2 + 1.3903\theta^3$ (15)

Case 4: $\lambda^*(\theta) = 18.7534 - 30.2768\theta + 14.585\theta^2$ (16)

Mean effective thermal conductivities computed from the recovered effective thermal conductivities $\lambda^*(\theta)$ are shown in Fig. 1. There is excellent agreement between the recovered results and the input data, meaning that the proposed method works very well.

Table 1 Some characteristic values of the glass beads used in the experiment

Mean radius (m)	4.95×10^{-4}
Number density (beads/m^3)	1.01×10^{9}
Porosity	0.409
Chemical composition (wt.%)	SiO_2 72 Al_2O_3 1 Na_2O, K_2O 14 MgO 4 CaO 8 others 1

Determination of Effective Thermal Conductivities of Glass Beads

Experimental Methods. The present inversion method was applied for estimating the effective thermal conductivities of glass beads. The mean radius of beads, number density, porosity of a layer of glass beads, and chemical composition

Nomenclature

AIC = Akaike's information criterion
a_n = coefficient of a series expansion, equation (3)
i, j = summation indices
k = index
M = number of data
N = order of a polynomial
n = variable
q = heat flux, W/m^2
T = temperature, K
T_H = hot boundary temperature of a porous material, K
T_L = cold boundary temperature of a porous material, K
y = distance from the hot boundary, m
y_0 = thickness of a porous material, m
δ = sum of squares of residuals
θ = $T/1000$
θ_H = $T_H/1000$
θ_L = $T_L/1000$
θ_m = $(\theta_H + \theta_L)/2$
$\lambda(\theta)$ = effective thermal conductivity at θ, W/mK
$\bar{\lambda}$ = mean effective thermal conductivity, W/mK
$\lambda^*(\theta)$ = recovered effective thermal conductivity, W/mK
$\lambda_G(\theta)$ = effective thermal conductivity of glass beads, W/mK

Downloaded 17 Dec 2010 to 193.140.21.150. Redistribution subject to ASME license or copyright; see http://www.asme.org/terms/Terms_Use.cfm

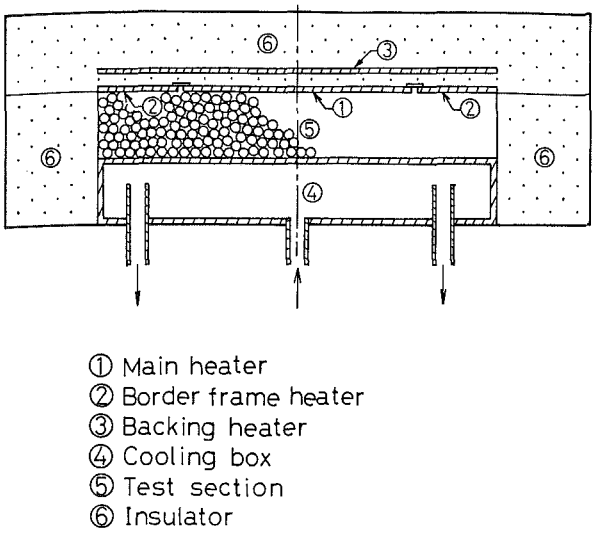

Fig. 2 Schematic diagram of the experimental apparatus

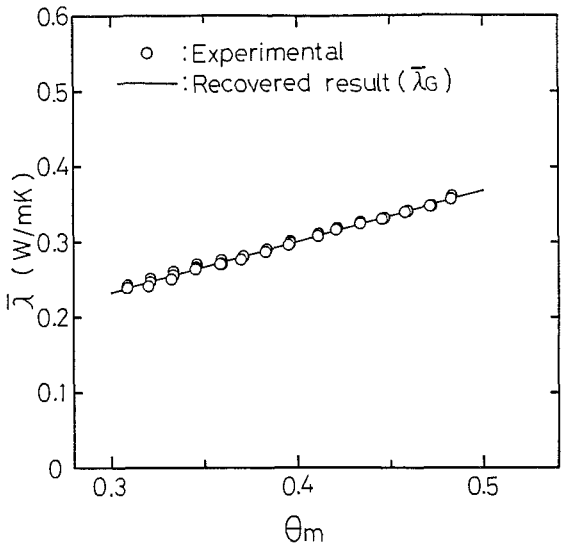

Fig 3 Relations between mean effective thermal conductivities of the glass bead and mean temperature

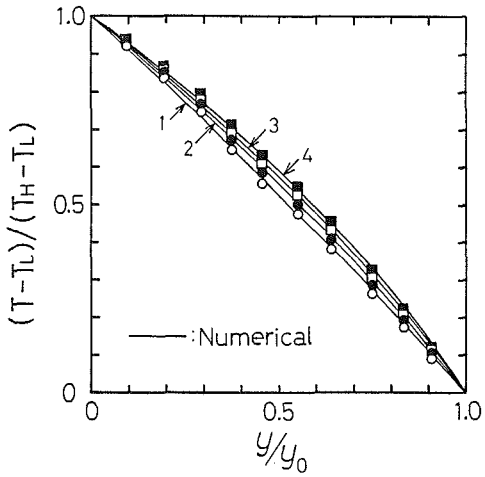

No.	Symbol	T_H(K)	T_L(K)	T_m(K)
1	o	374.1	293.2	333.7
2	●	473.1	293.7	383.4
3	□	574.1	293.2	434.6
4	■	673.4	294.0	483.7

Fig. 4 Temperature profiles within the glass bead layer

Table 2 Values of AIC

N	AIC
1	-384.19
2	-380.04
3	-362.78
4	-367.49
5	-366.56
6	-358.64

are shown in Table 1. Mean effective thermal conductivities were measured in air at 0.1 MPa by a parallel-plate-type apparatus. A schematic diagram of the experimental apparatus is shown in Fig. 2. The hot end unit, made of 0.5-cm-thick SUS316 platings, is divided into three parts: (*a*) the main hot plate, measuring 17×17 cm^2, (*b*) a bordering frame plate 6.2 cm wide around the main plate (*a*), and (*c*) a backing hot plate 30×30 cm^2 arranged behind and parallel to (*a*) and (*b*). Parts (*b*) and (*c*) constitute compensating heaters for the purpose of realizing one-dimensional heat flow through the test section from hot toward cold boundaries. The heating element (not shown in the drawing) was insulated kanthal wire, 0.14 cm in diameter, laid on parts (*a*), (*b*), and (*c*) to form three independent circuits. Each circuit was controlled manually to maintain the temperature of the hot end unit at the desired temperature in the range of 320 K to 680 K for each run. The temperature difference within the three parts (*a*), (*b*), and (*c*) of the hot end unit was regulated within 1 K. The cold end unit was a water-cooled box made of 0.5-cm-thick SUS316 plating and measuring $30 \times 30 \times 6$ cm^3. Its temperature was maintained within the approximate range of 290 to 295 K. Chromel-alumel sheathed thermocouples of 0.065 cm diameter were installed in the central part of the test section. The glass beads to be examined were then poured into the test section. The distance between the hot end unit and the cold end unit was 5.45 cm. The hot end unit was placed in position and the insulation was packed around the unit to prevent heat loss from the specimen sides. In each run, steady state was obtained in about 6 hr, and maintained thereafter for at least 2 hr before measurement.

Results. Typical experimental values of mean effective thermal conductivities of glass beads are shown in Fig. 3 as a function of mean temperature between the hot and cold walls. Using the proposed method with 47 values of mean effective thermal conductivities obtained, the effective thermal conductivities of glass beads at temperature θ were calculated. The values of AIC for various orders of N are shown in Table 2. From this table the first-order polynomial expansion of the effective thermal conductivities was found to be optimum. Consequently, the effective thermal conductivity of glass beads was determined to be

$$\lambda_G(\theta) = 0.02513 + 0.68644\theta \tag{17}$$

The mean effective thermal conductivity defined by $\bar{\lambda}_G = \int_{\theta_{Lj}}^{\theta_{Hj}}$

Downloaded 17 Dec 2010 to 193.140.21.150. Redistribution subject to ASME license or copyright; see http://www.asme.org/terms/Terms_Use.cfm

$\lambda_G(\theta)d\theta/(\theta_{Hj}-\theta_{Lj})$ is shown by a solid line in Fig. 3. The agreement between $\bar{\lambda}_G$ and the observed mean effective thermal conductivity is excellent, and this suggests the validity of the proposed method.

Calculation for Temperature Profile. Using $\lambda_G(\theta)$ thus determined, we can predict the temperature profile in the glass bead layer by solving the energy equation (18) utilizing the finite difference method.

$$\frac{d}{dy}\left[\lambda_G(T/1000)\frac{dT}{dy}\right]=0, \tag{18}$$

$$y=0: \quad T=T_H, \quad y=y_0: \quad T=T_L. \tag{19}$$

Predicted temperature profiles within the layer are shown by solid lines in Fig 4. Measured temperature profiles are also shown. As may be seen here, the predictions can be favorably compared with experimentally obtained results. This implies that temperature distributions within porous material can be accurately predicted, using the effective thermal conductivity determined by the proposed method.

Conclusions

An analytical method for estimating the effective thermal conductivities of porous materials from measured mean effective thermal conductivities was presented.

Results of numerical simultaneous performed for some typical cases showed the proposed method works well even in cases where input data used for inversion involves serious random error. Moreover, the effective thermal conductivities of glass beads were determined, and these effective thermal conductivities were applied successfully to predict temperature profiles within the glass bead layer.

References

1 Akaike, K., "A New Look at the Statistical Model Identification," *IEEE Transactions on Automatic Control*, Vol. AC-19, 1974, pp. 716–723.

Downloaded 17 Dec 2010 to 193.140.21.150. Redistribution subject to ASME license or copyright; see http://www.asme.org/terms/Terms_Use.cfm

ERRATA

Corrections to "Effect of Plate Inclination on Natural Convection From a Plate to Its Cylindrical Enclosure," by P. Singh and J. A. Liburdy, published in the November 1986 issue of the ASME JOURNAL OF HEAT TRANSFER, Vol. 108, pp. 770–775:

1 On page 771, Table 1, Listing of test conditions, the headings for the second and seventh columns should read ΔT (°C).

2 On page 775, the legend of Fig. 11 should be changed to read as follows: ○, $\theta = 90°$; ◇, $\theta = 60°$; △, $\theta = 30°$; □, $\theta = 0°$

Copyright © 1987 by ASME

Downloaded 17 Dec 2010 to 193.140.21.150. Redistribution subject to ASME license or copyright; see http://www.asme.org/terms/Terms_Use.cfm

Perturbation Solutions for the Shape of a Solidification Interface Subjected to a Spatially Periodic Heat Flux

A. K. Sen
Associate Professor,
Department of Mathematical Sciences,
Purdue University School of Science,
Indianapolis, IN 46223

In the manufacture of certain high-technology materials (such as strengthened composites for turbine and compressor blades) from a melt, it is essential to control the heat transfer conditions in such a way that a planar solidification interface is maintained within a given tolerance. Spatial nonuniformities in the heat flux imposed along the solidification interface may cause deformation. In this paper we analyze the interfacial shapes resulting from a periodic heat flux variation along the interface. Two cases of practical interest are examined. In case (a) the amplitude of heat flux variation is assumed small compared to the mean value, and in case (b) the wavelength of the imposed heat flux variation is considered to be much larger than a characteristic length in the transverse direction. In both cases, sensitivity of the interface shape with respect to heat flux nonuniformities is also determined.

Introduction

In many metal casting processes it is important to maintain a planar solidification interface because of its effect on the resulting crystal structure. Typical applications include manufacture of eutectic alloys and other composite materials (Flemings, 1974; Siegel, 1978a, b; 1982; 1984; Siegel and Sosoka, 1982). It is well known that the shape of the solidification interface is directly influenced by the rate of convective heat transfer from the liquid metal to the interface. Accordingly, the interface shape can be controlled by properly regulating this convective heat flux. The heat flux along the interface may, in general, vary from one point to another. The main purpose of this paper is to study the effect of a given heat flux variation on the shape of the solidification interface.

In an earlier work, Siegel (1982) examined this problem and determined the interface shape for a prescribed sinusoidal variation of the heat flux. He analyzed the case for which the amplitude of the heat flux variation Δq is much smaller than its mean value q_m and derived an analytical solution for the shape of the interface by means of a conformal mapping procedure. The primary objective of his analysis was to determine the sensitivity of the interface shape to the nonuniformity in the imposed heat flux, in terms of the wavelength and amplitude of the heat flux variation. In another paper, Siegel and Sosoka (1982) extended these results, with no restriction on the amplitude of heat flux variation. A further discussion of Siegel's (1982) work will be given later.

In the present paper we develop perturbation solutions for the interface shape for the following two cases: (*a*) when $M = \Delta q/q_m$ is much smaller than unity (the case considered by Siegel, 1982), and (*b*) when the wavelength of the imposed heat flux variation is much larger than a characteristic conduction length in the transverse (y) direction. In both cases we also derive solutions for the temperature distribution in the solidified region. We shall see that in case (*a*), i.e., for small M, it is possible to write the solutions for temperature and interface shape in the form of regular perturbation expansions in M. The situation in case (*b*) formally leads to a singular perturbation problem. However, it turns out that an appropriate outer expansion can be found which satisfies all of the boundary conditions of the problem. Thus, the outer solution itself constitutes the so-called composite solution, which is uniformly valid throughout the entire domain, and no boundary layer correction is required.

It should be emphasized that in free boundary problems of the type considered here, the temperature and the interface shape may, in general, be tightly coupled. As a consequence, it may be difficult to find a solution for one without solving for the other. We shall see however that when a small or a large parameter is involved, as in case (*a*) or case (*b*), the present perturbation technique enables us to uncouple the problem for temperature from that of the interface shape. In other words, it is possible to solve for the temperature independently at a certain order of approximation and then determine the shape of the solidification interface at that order or vice versa.

Formulation

For the present purpose we consider the same geometry as that used by Siegel (1982). The configuration shown in Fig. 1 displays a wavy interface between the liquid metal and the solidifying material. Along the cooled solid wall ($y = 0$), the temperature is maintained at T_w while the temperature along the interface remains at the freezing value T_s. The imposed heat flux on this interface is assumed to vary periodically in the x direction. Because of symmetry it is sufficient to analyze only the region between the vertical planes A–A and B–B (see Fig. 1). Since there is no heat transfer across these planes, they can be treated as insulating boundaries. Therefore, for the purpose of our analysis, we may consider the configuration shown in Fig. 2. This figure shows a rectangular container with insulated sidewalls. The bottom surface of the container is kept at a uniform temperature T_w. The unknown upper surface $y = h(x)$ is maintained at the freezing temperature T_s and is subjected to a heat flux which varies in a sinusoidal manner in the x direction. As pointed out by Siegel (1982), a similar configuration can be used as a model for a phase-change energy storage device where free convection in the liquid causes a variation in the heat transfer coefficient along the solidification interface.

In the solidified region, $0 \le x \le a$, $0 \le y \le h(x)$, the temperature satisfies the Laplace equation

$$T_{xx} + T_{yy} = 0 \tag{1}$$

Contributed by the Heat Transfer Division for publication in the JOURNAL OF HEAT TRANSFER. Manuscript received by the Heat Transfer Division January 6, 1987.

Copyright © 1987 by ASME
Downloaded 17 Dec 2010 to 193.140.21.150. Redistribution subject to ASME license or copyright; see http://www.asme.org/terms/Terms_Use.cfm

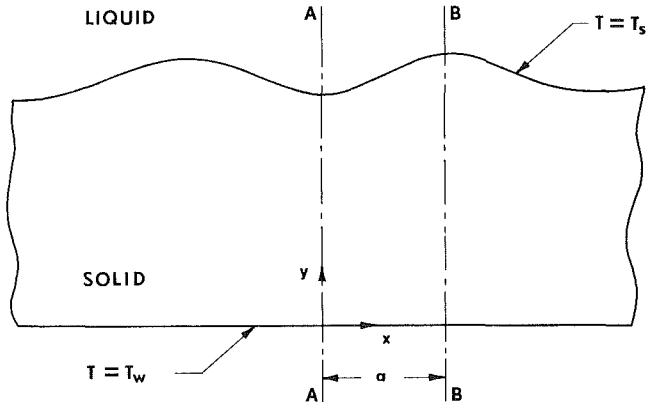

Fig. 1 Schematic diagram of a solidification interface subjected to a spatially periodic heat flux

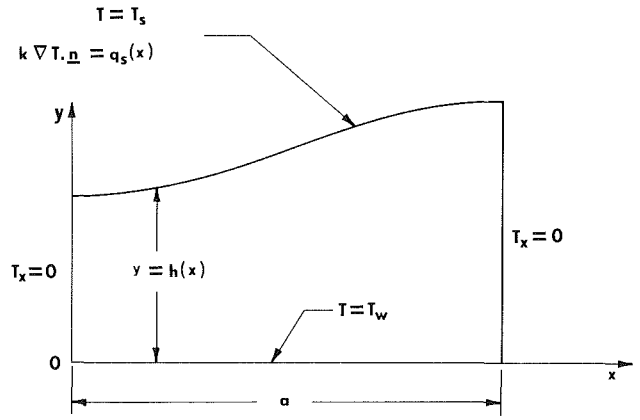

Fig. 2 Model configuration in the physical plane

This equation must be solved subject to the conditions

$$y=0: \quad T=T_w \tag{2a}$$

$$x=0,\ a: \quad T_x=0 \tag{2b}$$

$$y=h(x): \quad T=T_s \tag{2c}$$

$$\nabla T\cdot\mathbf{n}=q_s(x)/k \tag{2d}$$

where the shape of the interface, described by $h(x)$, is unknown and must be determined as part of the solution, along with the temperature distribution. The last condition prescribes the convective heat flux on the interface, where $q_s(x)$ is assumed to have a periodic variation given by

$$q_s(x)=q_m+\Delta q\cos(\pi x/a) \tag{3}$$

The normal vector $\mathbf{n}$ at the interface can be expressed as

$$\mathbf{n}=(1+h_x^2)^{-1/2}(-h_x\mathbf{i}+\mathbf{j}) \tag{4}$$

$\mathbf{i}$ and $\mathbf{j}$ being the unit vectors in the x and y directions, respectively. Using this, equation (2*d*) can be rearranged as

$$(1+h_x^2)^{-1/2}(T_y-h_xT_x)=k^{-1}[q_m+\Delta q\cos(\pi x/a)] \tag{5}$$

It is convenient to scale the above equations and boundary conditions by introducing the following dimensionless variables (denoted by primes):

$$x=\gamma x', \quad y=\gamma y', \quad h=\gamma h', \quad T=T_w+(T_s-T_w)T' \tag{6a}$$

where

$$\gamma=k(T_s-T_w)/q_m \tag{6b}$$

In these new variables, the dimensionless problem (after dropping the primes) can be written as follows:

$$T_{xx}+T_{yy}=0 \tag{7a}$$

$$y=0: \quad T=0 \tag{7b}$$

$$x=0,\ A: \quad T_x=0 \tag{7c}$$

$$y=h(x): \quad T=1 \tag{7d}$$

$$(1+h_x^2)^{-1/2}(T_y-h_xT_x)=1+M\cos(\pi x/A) \tag{7e}$$

Here

$$A=a/\gamma \tag{8}$$

and the quantity M in equation (7*e*), which was defined earlier, is a measure of the nonuniformity in the imposed heat flux.

As mentioned in the introduction, Siegel (1982) analyzed the problem given by equations (7) for small M, using a conformal mapping technique. By defining a complex-valued function $W(z)$ such that

$$\frac{dW}{dz}=-T_x+iT_y \tag{9}$$

where $z=x+iy$, he showed that for small M, the horizontal and vertical gradients of temperature at the solidification interface obey the equation of an ellipse in the complex dW/dz plane. The ellipse was then mapped into a rectangle via a conformal transformation and in the process the shape of the unknown interface was determined.

It should be pointed out that Siegel's (1982) analysis is based on the assumption that for small M, the interface shape can be described by a function of the form

$$h(x)=N_0-N_1\cos(\pi x/A)+0(N_1^2) \tag{10a}$$

where (in the present notation)

Nomenclature

A = dimensionless length in the horizontal direction
a = half-wavelength of heat flux variation along the solidification interface
$h(x)$ = function describing the interface shape
$\mathbf{i}$ = unit vector in the x direction
$\mathbf{j}$ = unit vector in the y direction
k = thermal conductivity of the solidified material
M = heat flux nonuniformity parameter $= \Delta q/q_m$
m = quantity defined by equation (16)
N_0, N_1 = coefficients in equation (10*a*), defined by equations (10*b*, *c*)
$\mathbf{n}$ = normal vector at the solidification interface
q = convective heat flux from the liquid to the interface
Δq = amplitude of periodic variation in q
T = temperature
x, y = horizontal and vertical coordinates
z = $x + iy$
γ = characteristic length, defined by equation (6*b*)
Γ = magnitude of interface distortion relative to the nonuniformity in the imposed heat flux

Subscripts

l = left sidewall at $x = 0$
m = mean value
r = right sidewall at $x = A$
s = solidification interface
w = cooled wall at $y = 0$

Downloaded 17 Dec 2010 to 193.140.21.150. Redistribution subject to ASME license or copyright; see http://www.asme.org/terms/Terms_Use.cfm

$$N_0 = (h_l + h_r)/2 \tag{10b}$$

and

$$N_1 = (h_r - h_l)/2 \tag{10c}$$

and h_l and h_r are the heights of the interface at the ends $x = 0$ and $x = A$, respectively. The quantities N_0 and N_1 may be interpreted as the average height and the average distortion of the deformed interface. Note that since the shape of the solidification interface is not known *a priori* and must be determined as part of the solution, its end-point values h_l and h_r are also not known beforehand. One of the objectives of the present study is to obtain a perturbation solution for the interface shape and the temperature for small M, in the form of a power series. We also construct a perturbation solution for the temperature and the interface shape for large A, with M not being restricted to values much less than unity.

Case (*a*): Solution for Small M

For small M, we look for a solution of the problem (7) in the form of the expansions

$$T = T_0(x, y) + MT_1(x, y) + M^2 T_2(x, y) + 0(M^3) \tag{11a}$$

$$h = h_0(x) + Mh_1(x) + M^2 h_2(x) + 0(M^3) \tag{11b}$$

Substitution of these expansions into equation (7*a*) and the boundary conditions (7*b–e*) leads to a sequence of problems in various orders in M. The problem at leading order is given by

$$T_{0xx} + T_{0yy} = 0 \tag{12a}$$

with

$$y = 0: \quad T_0 = 0 \tag{12b}$$

$$x = 0, A: \quad T_{0x} = 0 \tag{12c}$$

$$y = h_0(x): \quad T_0 = 1 \tag{12d}$$

$$(1 + h_{0x}^2)^{-1/2}(T_{0y} - h_{0x}T_{0x}) = 1 \tag{12e}$$

The boundary conditions at the interface, namely, (12*d*, *e*), are derived by using the expansions (11) in (7*d*, *e*) and expanding in Taylor series, in powers of M. It can be easily shown that a self-consistent solution of this problem is

$$T_0(x, y) = y, \qquad h_0(x) = 1$$

These results show that in the leading approximation, the solidification interface remains flat. The lowest order temperature field in the solidified region is horizontally uniform, but varies linearly along the vertical direction. In the next order we have

$$T_{1xx} + T_{1yy} = 0 \tag{13a}$$

$$y = 0: \quad T_1 = 0 \tag{13b}$$

$$x = 0, A: \quad T_{1x} = 0 \tag{13c}$$

$$y = 1: \quad T_1 = -h_1(x) \tag{13d}$$

$$T_{1y} = \cos(\pi x/A) \tag{13e}$$

The solution for T_1 satisfying equation (13*a*) and the boundary conditions (13*b*, *c*, *e*) is found to be

$$T_1(x, y) = \frac{A}{\pi} \frac{\cos(\pi x/A)\sinh(\pi y/A)}{\cosh(\pi/A)} \tag{14}$$

Applying this result in equation (13*d*), we find that the perturbation of the interface from its flat position is

$$h_1(x) = -\frac{Am}{\pi}\cos(\pi x/A) \tag{15}$$

where

$$m = \tanh(\pi/A) \tag{16}$$

At $0(M^2)$, we must solve the problem

$$T_{2xx} + T_{2yy} = 0 \tag{17a}$$

$$y = 0: \quad T_2 = 0 \tag{17b}$$

$$x = 0, A: \quad T_{2x} = 0 \tag{17c}$$

$$y = 1: \quad T_2 = -T_{1y}h_1 - h_2 \tag{17d}$$

$$T_{2y} = \tfrac{1}{2}h_{1x}^2 + T_{1x}h_{1x} - T_{1yy}h_1 \tag{17e}$$

$$= \frac{m^2}{4}[1 + 3\cos(2\pi x/A)]$$

The problem consisting of equation (17*a*) and the boundary conditions (17*b*, *c*, *e*) has the solution

$$T_2(x, y) = \frac{m^2}{4}\left[y + \frac{3A}{2\pi}\frac{\cos(2\pi x/A)\sinh(2\pi y/A)}{\cosh(2\pi/A)}\right] \tag{18}$$

Use of this result in the boundary condition (17*d*) then yields

$$h_2(x) = \frac{m}{2}\left\{\frac{A}{\pi}\left[1 + \frac{2 - m^2}{2(1 + m^2)}\cos(2\pi x/A)\right] - \frac{m}{2}\right\} \tag{19}$$

Higher order solutions for temperature and interface distortion can be obtained by proceeding in exactly the same manner. We shall not carry out these solutions any further.

From the solutions obtained so far, the height of the interface at the ends $x = 0$ and $x = A$ can be easily determined. We find

$$h_l = 1 - M\frac{Am}{\pi} + M^2\left\{\frac{m}{4}\left[\frac{A}{\pi}\frac{4 + m^2}{1 + m^2} - m\right]\right\} + 0(M^3) \tag{20a}$$

and

$$h_r = 1 + M\frac{Am}{\pi} + M^2\left\{\frac{m}{4}\left[\frac{A}{\pi}\frac{4 + m^2}{1 + m^2} - m\right]\right\} + 0(M^3) \tag{20b}$$

Therefore, the magnitude of interfacial distortion from a planar interface (which corresponds to $M = 0$) relative to the magnitude of nonuniformity in the imposed heat flux is given by

$$\Gamma = \frac{1}{2M}(h_r - h_l) = \frac{A}{\pi}\tanh(\pi/A) + 0(M^3) \tag{21}$$

Case (*b*): Analysis for Large A

The key to a proper asymptotic solution for large A is the fact that the characteristic length scale in the x direction is of $0(A)$. Accordingly, we introduce a new horizontal variable $\hat{x}$ defined by $\hat{x} = A^{-1}x$. In terms of this new variable, the governing equation (7*a*) for temperature becomes

$$A^{-2}T_{\hat{x}\hat{x}} + T_{yy} = 0 \tag{22a}$$

The associated boundary conditions (7*b–e*) transform into

$$y = 0: \quad T = 0 \tag{22b}$$

$$\hat{x} = 0, 1: \quad T_{\hat{x}} = 0 \tag{22c}$$

$$y = \tilde{h}(\hat{x}): \quad T = 1 \tag{22d}$$

$$(1 + A^{-2}\tilde{h}_{\hat{x}}^2)^{-1/2}(T_y - A^{-2}\tilde{h}_{\hat{x}}T_{\hat{x}}) = \tilde{q}_s(\hat{x}) \tag{22e}$$

where the solidification interface $y = h(x)$ is written as $y = h(A\hat{x}) = \tilde{h}(\hat{x})$ and

$$\tilde{q}_s(\hat{x}) = 1 + M\cos\pi\hat{x} \tag{22f}$$

(Note that M need not be restricted to values much smaller than unity in the present case.)

It is apparent from equation (22*a*) that for large A, the problem at hand is of the singular perturbation type. It can therefore be solved by the method of matched asymptotic expansions. The solution typically consists of an outer approximation valid away from the sidewalls and an inner approximation near each sidewall, which are joined together by means of an asymptotic matching procedure. However, we shall see that in the present case no inner approximation is

Downloaded 17 Dec 2010 to 193.140.21.150. Redistribution subject to ASME license or copyright; see http://www.asme.org/terms/Terms_Use.cfm

necessary and an appropriate outer solution satisfies all the boundary conditions, including those at the sidewalls. The outer solution is found by writing the expansions

$$T = \tilde{T}_0(\hat{x}, y) + A^{-1}\tilde{T}_1(\hat{x}, y) + A^{-2}\tilde{T}_2(\hat{x}, y) + 0(A^{-3}) \quad (23a)$$

$$\tilde{h} = \tilde{h}_0(\hat{x}) + A^{-1}\tilde{h}_1(\hat{x}) + A^{-2}\tilde{h}_2(\hat{x}) + 0(A^{-3}) \quad (23b)$$

Substituting these expansions into (22), we obtain at leading order, the equation

$$\tilde{T}_{0yy} = 0 \quad (24a)$$

with the boundary conditions

$$y = 0: \quad \tilde{T}_0 = 0 \quad (24b)$$

$$\hat{x} = 0,\ 1: \quad \tilde{T}_{0\hat{x}} = 0 \quad (24c)$$

$$y = \tilde{h}_0(\hat{x}): \quad \tilde{T}_0 = 1 \quad (24d)$$

$$\tilde{T}_{0y} = \tilde{q}_s(\hat{x}) \quad (24e)$$

Clearly the solution for $\tilde{T}_0$ satisfying (24*a*, *b*) and (24*e*) is given by

$$\tilde{T}_0(\hat{x}, y) = \tilde{q}_s(\hat{x})y \quad (25)$$

As a consequence, equation (24*d*) shows that the solidification interface, to leading order, is described by the function

$$\tilde{h}_0(\hat{x}) = 1/\tilde{q}_s(\hat{x}) \quad (26)$$

Note that since $\tilde{q}_s(\hat{x})$ has the value (22*f*), the solution (25) automatically satisfies the boundary conditions (24*c*). In other words, the leading order outer solution for temperature satisfies all the boundary conditions and therefore no boundary layer correction is needed near the sidewalls. Note also that unlike the case for small M of the previous section, the solidification interface (26) is nonplanar in the leading approximation.

The problem in the next order is given by

$$\tilde{T}_{1yy} = 0 \quad (27a)$$

$$y = 0: \quad \tilde{T}_1 = 0 \quad (27b)$$

$$\hat{x} = 0,\ 1: \quad \tilde{T}_{1\hat{x}} = 0 \quad (27c)$$

$$y = \tilde{h}_0(\hat{x}): \quad \tilde{T}_1 + \tilde{q}_s(\hat{x})\tilde{h}_1 = 0 \quad (27d)$$

$$\tilde{T}_{1y} = 0 \quad (27e)$$

It is straightforward to show that the above problem has only the trivial solution

$$\tilde{T}_1(\hat{x}, y) = \tilde{h}_1(\hat{x}) = 0 \quad (28)$$

At $0(A^{-2})$, the temperature satisfies the equation

$$\tilde{T}_{2yy} = -\tilde{T}_{0\hat{x}\hat{x}} \quad (29a)$$

and the boundary conditions

$$y = 0: \quad \tilde{T}_2 = 0 \quad (29b)$$

$$\hat{x} = 0,\ 1: \quad \tilde{T}_{2\hat{x}} = 0 \quad (29c)$$

$$y = \tilde{h}_0(\hat{x}): \quad \tilde{T}_2 = -\tilde{q}_s(\hat{x})\tilde{h}_2 \quad (29d)$$

$$\tilde{T}_{2y} = \tilde{h}_{0\hat{x}}\tilde{T}_{0\hat{x}} + \tfrac{1}{2}\tilde{T}_{0y}\tilde{h}_{0\hat{x}}^2. \quad (29e)$$

In view of the solution (25), equation (29*a*) can be simplified to

$$\tilde{T}_{2yy} = -\tilde{q}_s''(\hat{x})y \quad (30)$$

where a prime denotes $d/d\hat{x}$. Similarly the flux condition (29*e*) can be expressed as

$$y = \tilde{h}_0(\hat{x}): \quad \tilde{T}_{2y} = -\tfrac{1}{2}\frac{[\tilde{q}_s'(\hat{x})]^2}{[\tilde{q}_s(\hat{x})]^3} \quad (31)$$

Thus we need to solve equation (30) subject to conditions (29*b*) and (31). The solution is easily found to be

$$\tilde{T}_2(\hat{x}, y) = \frac{\tilde{q}_s\tilde{q}_s'' - \tilde{q}_s'^2}{2\tilde{q}_s^3}y - \frac{\tilde{q}_s''}{6}y^3 \quad (32)$$

An expression for $\tilde{h}_2(\hat{x})$ is then obtained from (29*d*). We have

$$\tilde{h}_2(\hat{x}) = \frac{3\tilde{q}_s'^2 - 2\tilde{q}_s\tilde{q}_s''}{6\tilde{q}_s^5}. \quad (33)$$

Once again, note that the solution (32) satisfies the boundary conditions (29*c*) at $\hat{x} = 0,\ 1$ as well. As a result, thermal boundary layers must be absent up to this order. Since $\tilde{q}_s(\hat{x})$ is given by (22*f*), we can write (33) in the form

$$\tilde{h}_2(\hat{x}) = \frac{M\pi^2}{12}\frac{4\cos\pi\hat{x} + M(5 - \cos 2\pi\hat{x})}{(1 + M\cos\pi\hat{x})^5} \quad (34)$$

Similarly, it follows from (32) that

$$\tilde{T}_2(\hat{x}, y) = \frac{M\pi^2}{6}(\cos\pi\hat{x})y^3 - \frac{M\pi^2}{2}\left[\frac{M + \cos\pi\hat{x}}{(1 + M\cos\pi\hat{x})^3}\right]y \quad (35)$$

From the solutions obtained above, the heights of the deformed interface at the two ends are given by

$$h_l = \frac{1}{1+M} + \frac{1}{A^2}\left[\frac{M\pi^2}{3(1+M)^4}\right] + 0\left(\frac{1}{A^3}\right) \quad (36a)$$

$$h_r = \frac{1}{1-M} - \frac{1}{A^2}\left[\frac{M\pi^2}{3(1-M)^4}\right] + 0\left(\frac{1}{A^3}\right) \quad (36b)$$

so that the amplitude of deformation relative to the amount of nonuniformity in the imposed heat flux becomes

$$\Gamma = \frac{1}{2M}(h_r - h_l) = \frac{1}{1-M^2} - \frac{\pi^2}{6A^2}\left[\frac{1}{(1-M)^4} + \frac{1}{(1+M)^4}\right] + 0\left(\frac{1}{A^3}\right). \quad (37)$$

Expanding the result (37) for small M, we find that

$$\Gamma \sim 1 - \frac{\pi^2}{3A^2} \quad (38)$$

which is asymptotically correct to $0(M^2)$. The same result can be deduced from equation (21) by expanding tanh (π/A) for large A, up to $0(1/A^3)$. Therefore, the solutions (21) and (37) yield identical results for Γ when M is small and A is large. Note also that up to these orders, Γ is independent of M.

Results and Discussion

Consider case (*a*) first, which applies for small M. For this case, the heights of the solidification interface at the two ends $x = 0$ and $x = A$ are given by equations (20*a*) and (20*b*), respectively. The values of h_l and h_r are listed in Table 1 for several choices of A and M. For comparison, the corresponding quantities derived by Siegel (1982) using a conformal mapping approach are also included in the table.

The interface shapes correct through $0(M^2)$ are plotted in Fig. 3 for $M = 0.3$ and various values of A. The horizontal line in this figure corresponds to a spatially uniform heat flux ($M = 0$) so that the interface remains plane for all A. Figure 4 shows the deformed interface shapes for A fixed ($A = 2$) and several values of M. It is apparent from this figure that a change in the value of M tends to alter the curvature of the solidification interface.

The quantity of most physical interest, namely, the amount of interface distortion relative to the magnitude of nonuniformity in the imposed heat flux is determined by equation (21). The values of this ratio Γ for selected values of A and M are given in Table 1. It can be readily seen from this table that for a given value of A, Γ is independent of M, consistent with equation (21). Furthermore, (21) shows that for small A, Γ becomes small, and is approximately equal to Am/π (or A/π since $m \to 1$ as $A \to 0$). This trend is also observed in Table 1. A comparison of these results with those of Siegel (1982) reveals

Downloaded 17 Dec 2010 to 193.140.21.150. Redistribution subject to ASME license or copyright; see http://www.asme.org/terms/Terms_Use.cfm

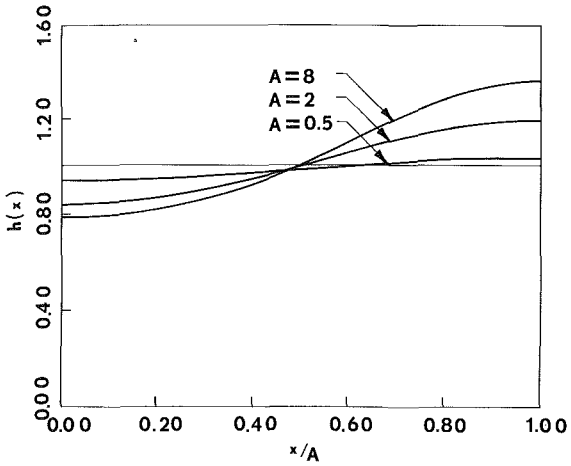

Fig. 3 Interface shapes for $M = 0.3$ and various values of A in case (a)

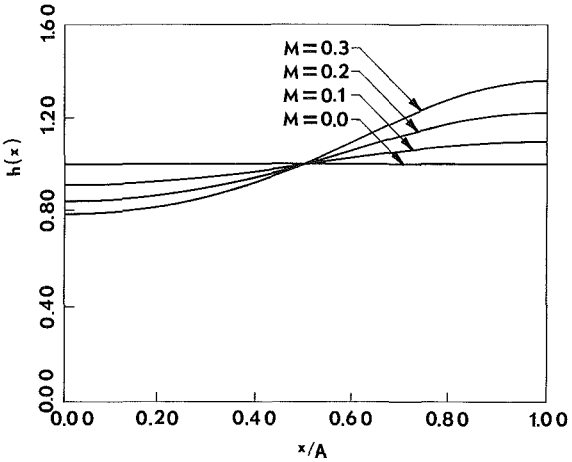

Fig. 4 Interface shapes for $A = 2$ and various values of M in case (a)

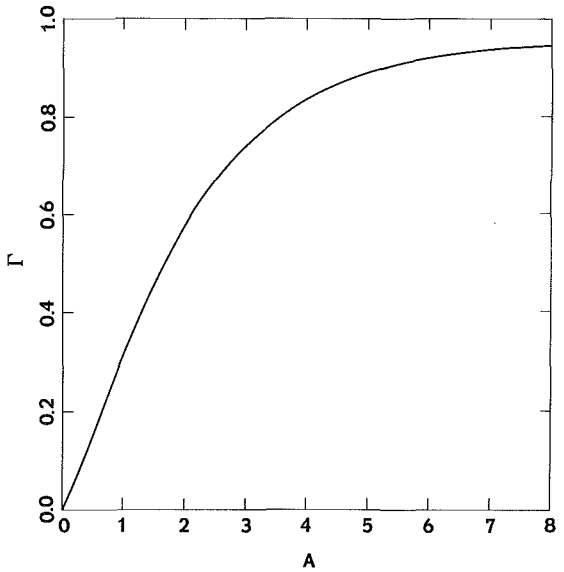

Fig. 5 Amplitude of interfacial distortion relative to the amplitude of heat flux variation in case (a)

that the present results for h_l, h_r, and Γ are typically lower than those obtained by Siegel (1982). However there seems to be general agreement between the results derived by these two analyses. The variation of Γ with A for small M is displayed in Fig. 5.

Table 1 Results for interface height and distortion in case (a)

A	M	h_ℓ		h_r		$\Gamma = (h_r - h_\ell)/2M$	
		Siegel (1982)	Present Work	Siegel (1982)	Present Work	Siegel (1982)	Present Work
	0.1	0.9924	0.990040	1.0084	1.005955	0.0798	0.07958
0.25	0.2	0.9855	0.976074	1.0178	1.007905	0.0807	0.07958
	0.3	0.9791	0.958103	1.0284	1.005849	0.0821	0.07958
	0.1	0.9848	0.982579	1.0168	1.014410	0.1597	0.15915
0.5	0.2	0.9710	0.962148	1.0355	1.025810	0.1613	0.15915
	0.3	0.9582	0.938707	1.0568	1.034199	0.1642	0.15915
	0.1	0.9698	0.967793	1.0335	1.031217	0.3182	0.31712
1.0	0.2	0.9423	0.934596	1.0709	1.061445	0.3215	0.31712
	0.3	0.9171	0.900409	1.1135	1.090683	0.3272	0.31712
	0.1	0.9451	0.943347	1.0623	1.060123	0.5861	0.58388
2.0	0.2	0.8965	0.890165	1.1337	1.123716	0.5930	0.58388
	0.3	0.8532	0.840454	1.2163	1.190780	0.6050	0.58388
	0.1	0.9230	0.921893	1.0911	1.088890	0.8402	0.83498
4.0	0.2	0.8574	0.854569	1.1999	1.188562	0.8562	0.83498
	0.3	0.8013	0.798027	1.3318	1.299017	0.8842	0.83498
	0.1	0.9131	0.913134	1.1051	1.103450	0.9640	0.95158
8.0	0.2	0.8403	0.842853	1.2346	1.223485	0.9856	0.95158
	0.3	0.7787	0.789156	1.3976	1.360104	1.0315	0.95158

Table 2 Results for interface height and distortion in case (b)

A	M	h_ℓ	h_r	$\Gamma = (h_r - h_\ell)/2M$
	0.1	0.909653	1.109858	1.001025
	0.2	0.834127	1.245984	1.029643
20	0.3	0.770095	1.418295	1.080333
	0.4	0.715142	1.641282	1.157675
	0.5	0.667479	1.934203	1.266724
	0.1	0.909181	1.110911	1.008650
	0.2	0.833460	1.249357	1.039743
50	0.3	0.769369	1.426927	1.095930
	0.4	0.714423	1.662605	1.185228
	0.5	0.666797	1.989472	1.322675
	0.1	0.909113	1.111061	1.009738
	0.2	0.833365	1.249839	1.041186
100	0.3	0.769265	1.428160	1.098158
	0.4	0.714320	1.665651	1.189164
	0.5	0.666699	1.997368	1.330669

The main results for case (b), which corresponds to $A >> 1$, are presented in Table 2. In this case, the heat flow tends to become locally one dimensional, consistent with equation (25), and the interface follows the prescribed heat flux in an "inverse" fashion, according to equation (26). The interface shapes correct through $0(A^{-2})$ are shown in Fig. 6 for $M = 0.5$ and various values of A. Observe from this figure that as A is changed through large values, the interface shape remains largely unaffected everywhere except in the vicinity of the right sidewall. This is also seen from equation (36) which shows that for a given value of M (with $M < 1$), the change of h_r with respect to A is much greater than that of h_l with respect to A. Interface shapes for $A = 20$ and various values of M are drawn in Fig. 7. The horizontal line in this figure corresponds to $M = 0$. The values of the amplitude ratio Γ, which are given in the last column of Table 2, indicate that the sensitivity of the interface shape with respect to M may be significant especially when M is not small. These values are

Downloaded 17 Dec 2010 to 193.140.21.150. Redistribution subject to ASME license or copyright; see http://www.asme.org/terms/Terms_Use.cfm

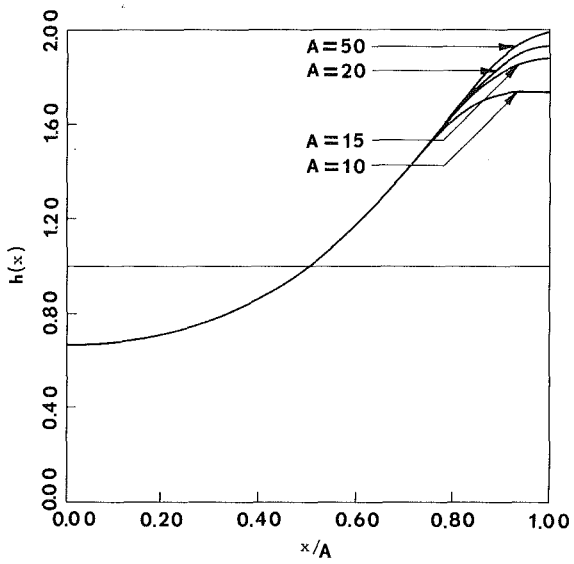

Fig. 6 Interface shapes for $M = 0.5$ and various values of A in case (b)

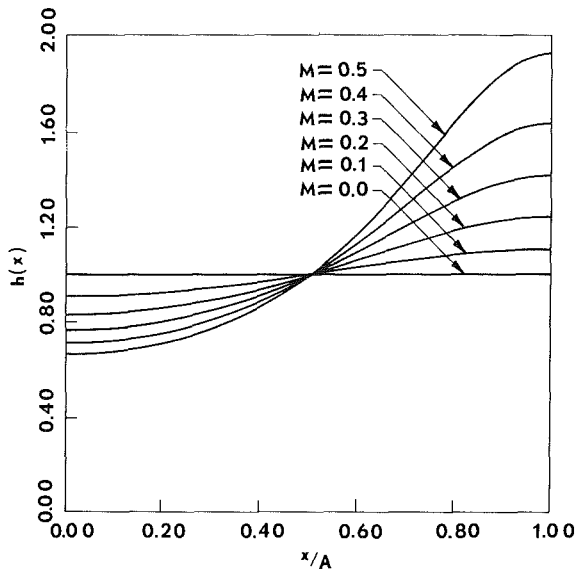

Fig. 7 Interface shapes for $A = 20$ and various values of M in case (b)

calculated using the formula (37) which exhibits an explicit dependence of Γ on M.

At this point it is appropriate to emphasize the nature of the asymptotic solution obtained here for large A. We have seen that when $A >> 1$, the outer solution, which is generally valid away from the sidewalls, satisfies all the boundary conditions of the problem, including those at the sidewalls. In other words, the large A limit, although formally singular, leads to a (regular) uniformly valid solution throughout the entire domain. Analogous results have been found in many other applications, for example, in the study of rivulet flows (Allen and Biggin, 1984; Rothfeld and Towell, 1966) and in the spreading of viscous liquid drops on a plane surface (Hocking, 1981).

Concluding Remarks

Using perturbation methods we have analyzed the solidification interface shapes for the cases (a) $M << 1$, $A = 0(1)$, and (b) $M = 0(1)$, $A >> 1$. In the first case the magnitude of interface distortion Γ, relative to the amplitude of heat flux nonuniformity, is found to be practically insensitive to M. In case (b) on the other hand, Γ is shown to be equal to $1/(1-M^2)$, to leading order. This means that when the wavelength of the imposed heat flux variation is large, the deformed interface responds rather significantly to the nonuniformities in heat flux variations, especially when M is not too small.

A major advantage of the present perturbation methods is the ease with which the successive approximations for the interface shape and temperature can be computed, in both cases. The results obtained here can be used to determine the extent to which the spatial nonuniformities in the imposed heat flux must be controlled in order to keep the interface distortion within a given tolerance.

References

Allen, R. F., and Biggin, C. M., 1974, "Longitudinal Flow of a Lenticular Liquid Filament Down an Inclined Plane," *The Physics of Fluids*, Vol. 17, No. 2, pp. 287–291.

Flemings, M. C., 1974, *Solidification Processing*, McGraw-Hill, New York.

Hocking, L. M., 1981, "Sliding and Spreading of Thin Two-Dimensional Drops," *Quarterly Journal of Mechanics and Applied Mathematics*, Vol. 34, pp. 37–55.

Rothfeld, L. B., and Towell, G. D., 1966, "Hydrodynamics of Rivulet Flow," *AIChE Journal*, Vol. 12, pp. 972–980.

Siegel, R., 1978a, "Shape of Two-Dimensional Solidification Interface During Directional Solidification by Continuous Casting," ASME JOURNAL OF HEAT TRANSFER, Vol. 100, pp. 3–10.

Siegel, R., 1978b, "An Analysis of Solidification Interface Shape During Continuous Casting of a Slab," *International Journal of Heat and Mass Transfer*, Vol. 21, pp. 1421–1430.

Siegel, R., 1982, "Analysis of Solidification Interface Shape Resulting From Applied Sinusoidal Heating," ASME JOURNAL OF HEAT TRANSFER, Vol. 104, pp. 13–18.

Siegel, R., and Sosoka, D. J., 1982, "Cauchy Integral Method for Two-Dimensional Solidification Interface Shapes," *International Journal of Heat and Mass Transfer*, Vol. 25, pp. 975–984.

Siegel, R., 1984, "Two-Region Analysis of Interface Shape in Continuous Casting With Superheated Liquid," ASME JOURNAL OF HEAT TRANSFER, Vol. 106, pp. 505–311.

Downloaded 17 Dec 2010 to 193.140.21.150. Redistribution subject to ASME license or copyright; see http://www.asme.org/terms/Terms_Use.cfm

C. P. Grigoropoulos[1]
R. H. Buckholz[2]

Columbia University,
Department of Mechanical Engineering,
New York, NY 10027

G. A. Domoto
Xerox, Palo Alto Research Center,
Mechanical Engineering Sciences,
North Tarrytown, NY 10591

A Thermal Instability in the Laser-Driven Melting and Recrystallization of Thin Silicon Films on Glass Substrates

This paper develops a conductive heat transfer stability theory for the laser-driven melting and recrystallization of thin silicon films deposited on conductive (glass) substrates. The important parameters are: laser power, laser intensity distribution, and beam scanning speed. Basic state temperature distributions are obtained for straight phase boundaries. These calculated temperature distributions show the origin of instability. A linear perturbation analysis is used to obtain the leading order corrections to the basic-state temperature fields. The perturbation time rate of growth, as a function of the disturbance wavelength, is then predicted.

1 Introduction

The trend in new semiconductor technology is toward smaller-sized and three-dimensional devices. Thus, it is of fundamental interest to produce single-crystal, thin silicon layers on amorphous substrates. In the electronics microfabrication technology, the most commonly used method to grow thin silicon layers is chemical vapor deposition (C.V.D.). The material obtained in this way has a definite crystalline structure, but it presents many imperfections, such as grain boundaries. These grain boundaries are known to reduce the value of the material significantly as an active component in electronic circuits.

The crystal structure has been improved by the method of laser heating. The basic experimental process requires sweeping a laser beam across a thin silicon layer. A molten spot of silicon is produced when the laser beam intensity is sufficiently high. Consequently, silicon material melts and then recrystallizes in the wake of the laser spot. A recrystallized material that is free of small grain boundaries is desired. The heat transfer associated with laser-induced silicon crystal growth has been delineated by experimental observations, mathematical analysis, and numerical simulations.

It has been experimentally observed that long, narrow crystallites propagate in a direction normal to the solidification boundary. It is evident that the temperature fields induced in the silicon layer by the sweeping laser beam determine the grain size and the quality of the crystal structure.

Bosch and Lemons (1981, 1982) studied the radiatively induced melting of thin silicon layers. In their experiments, the silicon molten spot was viewed by using the reflected, emitted, and transmitted light. They found that for a region of laser power, solid lamellae would penetrate into the molten spot. They suggested two possible explanations for the formation of these solid inclusions within the molten phase: (*i*) constitutional supercooling, originating from possible oxygen impurities; (*ii*) phase separation in liquid silicon. Lemons et al. (1983) used the Mullins–Sekerka (1964) type of linear stability analysis to predict the characteristic spacing of a straight silicon phase boundary, as a function of both the temperature gradient at the interface and an assumed impurity concentration. The same type of analysis was used by Narayan (1982) to study the formation of cellular growth patterns, induced in silicon alloys by pulsed laser irradiation.

Hawkins and Biegelsen (1982) investigated the coexistence of solid and liquid silicon phases. In their study no impurities could be detected. They showed the importance of the silicon reflectivity increase upon melting. Solid silicon absorbs twice as much heat as the neighboring liquid silicon. This appears as a very unusual phenomenon of superheated solid lamellae coexisting within the molten silicon. This effect has been studied experimentally by Nemanich et al. (1983a) and Biegelsen et al. (1983). It has been confirmed that small, solid regions initially occur at what appear to be random locations within the molten silicon. These inclusions tend to coalesce into larger regions, forming stable patterns coexisting with the liquid matrix. Patterns of aligned, alternating solid and liquid silicon stripes were observed by Nemanich et al. (1983b). These experimental results motivated an analysis by Jackson and Kurtze (1985). They used linear stability theory arguments to show that an infinitely wide stationary light source, having a uniform intensity distribution can generate stable patterns of alternating regions of superheated solid and supercooled liquid stripes. In their analysis they were not concerned with the temperature distribution in the glass substrate.

In this study, the temperature fields in both the silicon layer and the glass substrate are determined by solving the conductive heat transfer equations for the case of a moving heat source. Assuming that a time-independent, basic-state temperature solution has been obtained, departures from this temperature distribution will be examined. Linear stability analysis will be used to study the time rates of growth of small amplitude perturbations from the calculated basic-state solutions.

2 Analysis

A sketch of the silicon layer and the substrate structure is shown in Fig. 1; a silicon layer of thickness l_{si} is shown deposited on a glass substrate. A laser beam is focused on the layer. The beam moves at a uniform velocity V. A system of Cartesian coordinates (x, y, z) attached to the moving spot is considered. The solid silicon regions behind the solidification edge and ahead of the melting front are identified as I and II, respectively. In this mathematical model the external heating source is assumed to be of infinite length and is assumed to have a uniform intensity distribution in the y direction.

The silicon layer is sufficiently thin, so that it will not have a significant temperature variation in the vertical direction.

[1]Present address: Department of Mechanical Engineering, University of Washington, Seattle, WA 98195.

[2]Present address: Salomon Brothers Inc., One New York Plaza, New York, NY 10004.

Contributed by the Heat Transfer Division for publication in the JOURNAL OF HEAT TRANSFER. Manuscript received by the Heat Transfer Division August 20, 1985.

Copyright © 1987 by ASME

Downloaded 17 Dec 2010 to 193.140.21.150. Redistribution subject to ASME license or copyright; see http://www.asme.org/terms/Terms_Use.cfm

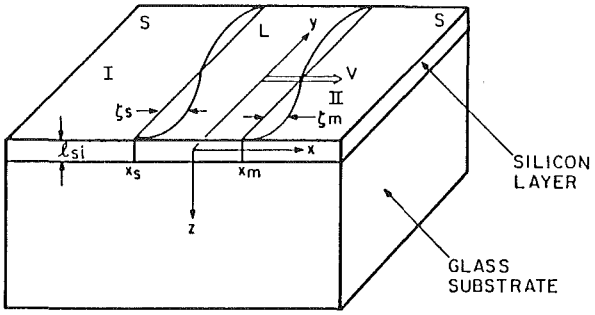

Fig. 1 Cross section through a thin silicon layer of thickness l_{si} = 0.5 μm deposited on a glass substrate; *S* and *L* are the solid and the liquid regions, respectively; the positions of the solidification edge and the melting front are x_s and x_m, respectively

However, it is necessary to consider the heat conducted to the glass substrate. The temperature field in the silicon layer depends upon the spatial coordinates (x, y) and upon time. The heat transfer in the silicon layer is represented by the integrated—across its thickness—heat conduction equation. Hot solid silicon, near the melting point, absorbs light almost entirely within a skin surface layer. This is also true for liquid silicon. At lower temperatures, the light penetration depth into the solid silicon layer is larger and the heat is more distributed through the thickness. The heat conduction equations are:

(*a*) *for the solid silicon:*

$$\frac{\partial T_{si,s}}{\partial t} - V\frac{\partial T_{si,s}}{\partial x} = \alpha_{si,s}\left(\frac{\partial^2 T_{si,s}}{\partial x^2} + \frac{\partial^2 T_{si,s}}{\partial y^2}\right) + \frac{(1-R_s)Q_{ext} - Q_{gl}}{\rho_{si}c_{p,si}l_{si}} \tag{1a}$$

(*b*) *for the liquid silicon*

$$\frac{\partial T_{si,l}}{\partial t} - V\frac{\partial T_{si,l}}{\partial x} = \alpha_{si,l}\left(\frac{\partial^2 T_{si,l}}{\partial x^2} + \frac{\partial^2 T_{si,l}}{\partial y^2}\right) + \frac{(1-R_l)Q_{ext} - Q_{gl}}{\rho_{si}c_{p,si}l_{si}} \tag{1b}$$

(*c*) *for the glass substrate*

$$\frac{\partial T_{gl}}{\partial t} - V\frac{\partial T_{gl}}{\partial x} = \alpha_{gl}\left(\frac{\partial^2 T_{gl}}{\partial x^2} + \frac{\partial^2 T_{gl}}{\partial y^2} + \frac{\partial^2 T_{gl}}{\partial z^2}\right) \tag{2}$$

in the above equations $T_{si,s}$, $T_{si,l}$ and T_{gl} represent the temperature differences above the ambient temperature. The unknown function $Q_{gl}(x, y, t)$ represents the heat conducted to the glass substrate.

The imposed external heating distribution is a function of the coordinate in the direction of motion. When the transient temperature effects disappear, quasi-static conditions are established. The change of phase boundaries could be expected to remain planar and fixed with respect to the moving heat source. The positions of the solidification and the melting interfaces are identified as x_s and x_m, respectively. The crystallization temperature at the solidification interface depends upon the local interface geometry and the nominal melting temperature in the following way:

$$T = T_m(1 + \Gamma\eta) \tag{3}$$

This is the general form of the Gibbs–Thomson boundary condition (Woodruff, 1973). The constant Γ is a surface tension parameter and η is the local curvature of the solidification interface that is in the direction of the outward normal to the crystal outer surface. The solidification interface is allowed to depart from a straight line

$$x = \zeta_s(y, t) + x_s \tag{4a}$$

Nomenclature

A = stiffness matrix of a linear system of algebraic equations
B = right-hand-side vector
c_p = heat capacity
K = thermal conductivity
K_0 = modified Bessel function of the second kind of zeroth order
K_1 = modified Bessel function of the second kind of first order
l_{si} = thickness of the silicon layer
L = latent heat of fusion
n = outward normal to the phase boundary directed into the liquid region
Q = rate of heat generation per unit volume
Q_{ext} = external heat source power density
Q_{gl} = heat conducted to the glass substrate
Q_T = total power of an infinitely wide laser beam per unit length
Q_0 = peak intensity of external heat source
r = $1/e$ irradiance half-span of an infinitely wide Gaussian beam
R = reflectivity of the silicon layer
r_s = ratio of the amplitude of solidification interface disturbance to the amplitude of melting interface disturbance
t = time
T = temperature
T_m = melting temperature
V = speed of light source
x = coordinate along the direction of motion
x_m = location of the melting interface
x_s = location of the solidification interface
y = coordinate in the lateral direction
z = coordinate into the glass substrate
w_n = speed of the phase boundary along the direction of the outward normal into the liquid region
α = thermal diffusivity
γ_{sl} = silicon solid–liquid interface free energy
Γ = capillary constant
ϵ_m = amplitude of the melting interface disturbance
ζ_m = disturbance of the melting interface
ζ_s = disturbance of the solidification interface
η = local radius of curvature
ξ = dummy variable of integration
ρ = density
σ = time rate of growth of the disturbance
ω = disturbance wavenumber

Subscripts

gl = glass
l = liquid silicon
si = silicon
s = solid silicon

Superscripts

0 = zeroth-order quantity
1 = first-order quantity
I, II = solid regions, see Fig. 1

Downloaded 17 Dec 2010 to 193.140.21.150. Redistribution subject to ASME license or copyright; see http://www.asme.org/terms/Terms_Use.cfm

The expression for the local radius of curvature is

$$\eta = \frac{d^2\zeta_s/dy^2}{\left[1+\left(\frac{d\zeta_s}{dy}\right)^2\right]^{3/2}} \tag{4b}$$

The heat flux boundary condition is applied at the solidification interface. The surface free energy contribution represents the work needed to form a curved interface Wollkind, 1976

$$K_{si,s}\frac{\partial T_{si,s}}{\partial n} - K_{si,l}\frac{\partial T_{si,l}}{\partial n} = w_n[\rho_{si}L + \gamma_{sl}\eta] \tag{5}$$

This equation is written in the following form:

$$\left[K_{si,s}\left(\frac{\partial T_{si,s}}{\partial x} - \frac{\partial T_{si,s}}{\partial y}\frac{\partial \zeta_s}{\partial y}\right) - K_{si,l}\left(\frac{\partial T_{si,l}}{\partial x} - \frac{\partial T_{si,l}}{\partial y}\frac{\partial \zeta_s}{\partial y}\right)\right]_{x=x_s+\zeta_s} = \left(V + \frac{\partial \zeta_s}{\partial t}\right)(\rho_{si}L + \gamma_{sl}\eta) \tag{6a}$$

A similar condition is applied at the melting front

$$\left[K_{si,s}\left(\frac{\partial T_{si,s}}{\partial x} - \frac{\partial T_{si,s}}{\partial y}\frac{\partial \zeta_m}{\partial y}\right) - K_{si,l}\left(\frac{\partial T_{si,l}}{\partial x} - \frac{\partial T_{si,l}}{\partial y}\frac{\partial \zeta_m}{\partial y}\right)\right]_{x=x_m+\zeta_m} = \left(V + \frac{\partial \zeta_m}{\partial t}\right)(\rho_{si}L + \gamma_{sl}\eta) \tag{6b}$$

A periodic perturbation is assumed at the melting front. This is the Mullins–Sekerka (1964) type of linear stability analysis

$$\zeta_m(y, t) = \epsilon_m \cos \omega y e^{\sigma t} \tag{7}$$

The solidification boundary will be perturbed at the same frequency, but at a different amplitude

$$\zeta_s(y, t) = \epsilon_m r_s \cos \omega y e^{\sigma t} \tag{8}$$

The following equations are obtained by applying the Gibbs–Thomson boundary conditions on the perturbed interfaces:

$$T_{si}(x_m + \zeta_m, y, t) = T_m + \epsilon_m \Gamma T_m \omega^2 \cos \omega y e^{\sigma t} \tag{9}$$

$$T_{si}(x_s + \zeta_s, y, t) = T_m - \epsilon_m r_s \Gamma T_m \omega^2 \cos \omega y e^{\sigma t} \tag{10}$$

The above boundary conditions imply a regular normal-mode small amplitude expansion for the temperature field

$$T_{si,l}(x, y, t) = T^0_{si,l}(x) + \epsilon_m T^1_{si,l}(x) \cos \omega y e^{\sigma t} \tag{11a}$$

$$T_{si,s}(x, y, t) = T^0_{si,s}(x) + \epsilon_m T^1_{si,s}(x) \cos \omega y e^{\sigma t} \tag{11b}$$

$$T_{gl}(x, y, z, t) = T^0_{gl}(x, z) + \epsilon_m T^1_{gl}(x, z) \cos \omega y e^{\sigma t} \tag{12}$$

The heat flux, conducted to the glass substrate, is also perturbed to determine the induced temperature field disturbances

$$Q_{gl}(x, y, t) = Q^0_{gl}(x) + \epsilon_m Q^1_{gl}(x) \cos \omega y e^{\sigma t} \tag{13}$$

The above temperature and heat flux expansions are used to order the heat conduction equations and the boundary conditions. The basic-state and leading order boundary value problems are then obtained.

2.1 Basic State Analysis. The construction of a mathematical model that will describe accurately the variation of the temperature field in the vicinity of the change of phase boundaries is sought. For this purpose it is necessary to define the location of the interfaces exactly.

The silicon and glass material properties appear in the governing equations; these material properties could be allowed to change with temperature. However, the thermal conductivity of the solid silicon does not change much for temperatures close to the melting point and for liquid silicon it is practically a constant. Therefore, it may be expected that the dependence of the material properties on temperature will act as a second-order effect on the temperature gradient distribution close to the solid–liquid interfaces; this effect will not grossly alter the character of the solution obtained. In the calculations the values of the silicon properties at the melting point were used. This simplifies the analysis by keeping the temperature field equations linear.

The laser heating is treated as being absorbed only in the thin silicon layer. The thermal radiation and convection losses through the top silicon surface are negligible compared to the high irradiance values, which are necessary to drive this process.

The basic-state temperature field equations are given below:

(*a*) *for the solid silicon*

$$\frac{d^2T^0_{si,s}}{dx^2} + \frac{V}{\alpha_{si,s}}\frac{dT^0_{si,s}}{dx} + \frac{(1-R_s)Q_{ext} - Q^0_{gl}}{K_{si,s}l_{si}} = 0 \tag{14a}$$

(*b*) *for the liquid silicon*

$$\frac{d^2T^0_{si,l}}{dx^2} + \frac{V}{\alpha_{si,l}}\frac{dT^0_{si,l}}{dx} + \frac{(1-R_l)Q_{ext} - Q^0_{gl}}{K_{si,l}l_{si}} = 0 \tag{14b}$$

(*c*) *for the glass substrate*

$$-\frac{V}{\alpha_{gl}}\frac{\partial T^0_{gl}}{\partial x} = \frac{\partial^2 T^0_{gl}}{\partial x^2} + \frac{\partial^2 T^0_{gl}}{\partial z^2} \tag{15}$$

The temperature far from the laser heating must vanish

$$T^0_{si,s}(\pm\infty) = 0 \tag{16}$$

$$T^0_{gl}(\pm\infty, z) = 0 \tag{17a}$$

$$T^0_{gl}(x, +\infty) = 0 \tag{17b}$$

The boundary conditions at the solidification and the melting interfaces are

$$T^0_{si,l}(x_s) = T^0_{si,s}(x_s) = T_m \tag{18a}$$

$$T^0_{si,l}(x_m) = T^0_{si,s}(x_m) = T_m \tag{18b}$$

$$K_{si,s}\frac{dT^0_{si,s}}{dx}\bigg|^{\mathrm{I}}_{x=x_s} - K_{si,l}\frac{dT^0_{si,l}}{dx}\bigg|_{x=x_s} = \rho_{si}LV \tag{19a}$$

$$K_{si,s}\frac{dT^0_{si,s}}{dx}\bigg|^{\mathrm{II}}_{x=x_m} - K_{si,l}\frac{dT^0_{si,l}}{dx}\bigg|_{x=x_m} = \rho_{si}LV \tag{19b}$$

The silicon temperature assumed identical to the glass top surface temperature

$$T^0_{si}(x) = T^0_{gl}(x, 0), \qquad -\infty < x < +\infty \tag{20}$$

Therefore, the quasi-static temperature distribution in the glass substrate can be expressed by an integral equation over the x-axis (Carslaw and Jaeger, 1959; Rosenthal, 1946):

$$T^0_{gl}(x, z) = \frac{1}{\pi K_{gl}}\int_{-\infty}^{+\infty} Q^0_{gl}(\xi)e^{-\frac{V(x-\xi)}{2\alpha_{gl}}} K_0\left[\frac{V\sqrt{[(x-\xi)^2+z^2]}}{2\alpha_{gl}}\right]d\xi \tag{21}$$

When the locations of the melting and the solidification interfaces x_s, x_m are fixed, then the zeroth-order temperature can be found. The boundary conditions (16)–(18) must be

Downloaded 17 Dec 2010 to 193.140.21.150. Redistribution subject to ASME license or copyright; see http://www.asme.org/terms/Terms_Use.cfm

satisfied. To arrive at solutions in the form of integral expressions a standard Green's function technique is applied.

The temperature in region I is given below:

$$T^0_{si,s}(x) = T_m - \frac{1}{V\rho_{si}c_{p,si}l_{si}}\left\{\int_{-\infty}^{x} [(1-R_s)Q_{ext}(\xi) - Q^0_{gl}(\xi)]\left[e^{\frac{V(\xi-x_s)}{\alpha_{si,s}}} - e^{\frac{V(\xi-x)}{\alpha_{si,s}}}\right]d\xi \right.$$

$$\left. + \int_{x}^{x_s} [(1-R_s)Q_{ext}(\xi) - Q^0_{gl}(\xi)]\left[e^{\frac{V(\xi-x_s)}{\alpha_{si,s}}} - 1\right]d\xi\right\} \quad (22)$$

The temperature in the liquid silicon region is given by

$$T^0_{si,l}(x) = T_m - \frac{1}{V\rho_{si}c_{p,si}l_{si}\left[e^{\frac{Vx_m}{\alpha_{si,l}}} - e^{\frac{Vx_s}{\alpha_{si,l}}}\right]}$$

$$\left\{\int_{x_s}^{x} [(1-R_l)Q_{ext}(\xi) - Q^0_{gl}(\xi)]\right.$$

$$\left[-e^{\frac{Vx_s}{\alpha_{si,l}}} + e^{\frac{-V[x-(x_m+x_s)]}{\alpha_{si,l}}} + e^{\frac{V\xi}{\alpha_{si,l}}} - e^{\frac{-V[x-(x_m+\xi)]}{\alpha_{si,l}}}\right]d\xi$$

$$+ \int_{x}^{x_m} [(1-R_l)Q_{ext}(\xi) - Q^0_{gl}(\xi)]$$

$$\left.\left[-e^{\frac{Vx_m}{\alpha_{si,l}}} + e^{\frac{-V[x-(x_m+x_s)]}{\alpha_{si,l}}} + e^{\frac{V\xi}{\alpha_{si,l}}} - e^{\frac{-V[x-(x_s+\xi)]}{\alpha_{si,l}}}\right]d\xi\right\} \quad (23)$$

Finally, the temperature in solid region II is given by

$$T^0_{si,s}(x) = T_m e^{\frac{-V(x-x_m)}{\alpha_{si,s}}} - \frac{1}{V\rho_{si}c_{p,si}l_{si}}\left\{\int_{x_m}^{x} [(1-R_s)Q_{ext}(\xi) - Q^0_{gl}(\xi)]\left[e^{\frac{-V(x-x_m)}{\alpha_{si,s}}} - e^{\frac{-V(x-\xi)}{\alpha_{si,s}}}\right]d\xi\right.$$

$$\left. + \int_{x}^{+\infty} [(1-R_s)Q_{ext}(\xi) - Q^0_{gl}(\xi)]\left[e^{\frac{-V(x-x_m)}{\alpha_{si,s}}} - 1\right]d\xi\right\} \quad (24)$$

By satisfying equation (20), three integral expressions—one for each silicon region—are obtained. They must be solved simultaneously for the unknown heat flux Q^0_{gl}. The x axis is discretized and the kernel is integrated over each interval, to obtain a system of linear algebraic equations

$$[A^0]\{Q^0_{gl}\} = \{B^0\} \quad (25)$$

The linear system given by equation (25) can be solved for the unknown average heat flux over each interval $[x_{l-1}, x_l]$, $l = 1, \ldots, n$. The zeroth-order temperature distributions are then determined. The thermal gradients are calculated by differentiating equations (22), (23), and (24) with respect to x using Leibniz's rule for an improved evaluation of the temperature gradients over that obtained by simply taking the finite difference. This is an advantage of the Green's function method. The heat balance conditions (19*a*) and (19*b*) give two simultaneous equations for the unknowns x_s and x_m. To determine whether the given laser power is sufficient to melt the silicon layer, uniformly solid material is assumed in the beginning

$$T^0_{si,s}(x) = \frac{1}{V\rho_{si}c_{p,si}l_{si}}\left\{\int_{-\infty}^{x} [(1-R_s)Q_{ext}(\xi) - Q^0_{gl}(\xi)]e^{\frac{-V(x-\xi)}{\alpha_{si,s}}}d\xi \right.$$

$$\left. + \int_{x}^{+\infty} [(1-R_s)Q_{ext}(\xi) - Q^0_{gl}(\xi)]d\xi\right\} \quad (26)$$

If the temperature exceeds T_m, melting can be assumed. Then a search for the location of the interfacial boundaries is made. In this first search, a rather coarse x-axis subdivision is used. Once the approximate positions are found, a finer grid spacing is applied. Newton's method is then used to locate the phase change boundaries exactly.

2.2 Linear Stability Analysis. The temperature perturbations are given by the following differential equations:

$$\frac{d^2T^1_{si,s}}{dx^2} + \frac{V}{\alpha_{si,s}}\frac{dT^1_{si,s}}{dx} - \left(\omega^2 + \frac{\sigma}{\alpha_{si.s}}\right)T^1_{si,s} = \frac{Q^1_{gl}}{K_{si,s}l_{si}} \quad (27)$$

$$\frac{d^2T^1_{si,l}}{dx^2} + \frac{V}{\alpha_{si,l}}\frac{dT^1_{si,l}}{dx} - \left(\omega^2 + \frac{\sigma}{\alpha_{si.l}}\right)T^1_{si,l} = \frac{Q^1_{gl}}{K_{si,l}l_{si}} \quad (28)$$

$$-\frac{V}{\alpha_{gl}}\frac{\partial T^1_{gl}}{\partial x} = \frac{\partial^2 T^1_{gl}}{\partial x^2} + \frac{\partial^2 T^1_{gl}}{\partial z^2} - \left(\omega^2 + \frac{\sigma}{\alpha_{gl}}\right)T^1_{gl} \quad (29)$$

Expanding the zeroth-order temperature field solution, the temperature perturbation boundary conditions are derived from equations (9) and (10)

$$T^1_{si,s}(x_s) = -r_s\left[\frac{dT^0_{si,s}}{dx}\Big|^{\mathrm{I}}_{x=x_s} + \Gamma T_m\omega^2\right] \quad (30)$$

$$T^1_{si,l}(x_s) = -r_s\left[\frac{dT^0_{si,l}}{dx}\Big|_{x=x_s} + \Gamma T_m\omega^2\right] \quad (31)$$

$$T^1_{si,l}(x_m) = -\left[\frac{dT^0_{si,l}}{dx}\Big|_{x=x_m} - \Gamma T_m\omega^2\right] \quad (32)$$

$$T^1_{si,s}(x_m) = -\left[\frac{dT^0_{si,s}}{dx}\Big|^{\mathrm{II}}_{x=x_m} - \Gamma T_m\omega^2\right] \quad (33)$$

The first derivatives of the temperature about x_s and x_m are also expanded in a similar manner.

The perturbation heat balance conditions across the interfaces are obtained from equations (6*a*) and (6*b*)

$$K_{si,s}\left\{\frac{dT^1_{si,s}}{dx}\Big|^{\mathrm{II}}_{x=x_m} + \frac{d^2T^0_{si,s}}{dx^2}\Big|^{\mathrm{II}}_{x=x_m}\right\} - K_{si,l}\left\{\frac{dT^1_{si,l}}{dx}\Big|_{x=x_m} + \frac{d^2T^0_{si.l}}{dx^2}\Big|_{x=x_m}\right\} = \rho_{si}L(\sigma + \Gamma\omega^2 V) \quad (34)$$

$$K_{si,s}\left\{\frac{dT^1_{si,s}}{dx}\Big|^{\mathrm{I}}_{x=x_s} + r_s\frac{d^2T^0_{si,s}}{dx^2}\Big|^{\mathrm{I}}_{x=x_s}\right\} - K_{si,l}\left\{\frac{dT^1_{si,l}}{dx}\Big|_{x=x_s} + r_s\frac{d^2T^0_{si,l}}{dx^2}\Big|_{x=x_s}\right\} = \rho_{si}Lr_s(\sigma - \Gamma\omega^2 V) \quad (35)$$

Downloaded 17 Dec 2010 to 193.140.21.150. Redistribution subject to ASME license or copyright; see http://www.asme.org/terms/Terms_Use.cfm

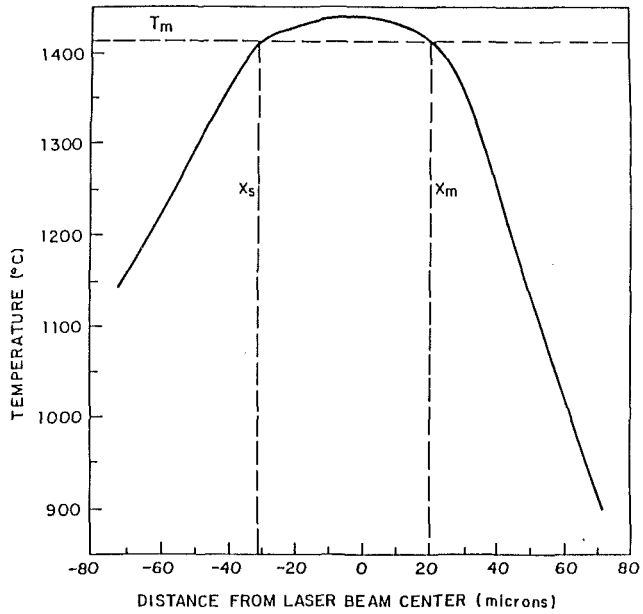

Fig. 2 Basic-state temperature distribution for a Gaussian beam of peak intensity $Q_0 = 0.65 \times 10^8$ W/m^2, $r = 40$ μm, and $V = 5$ mm/s

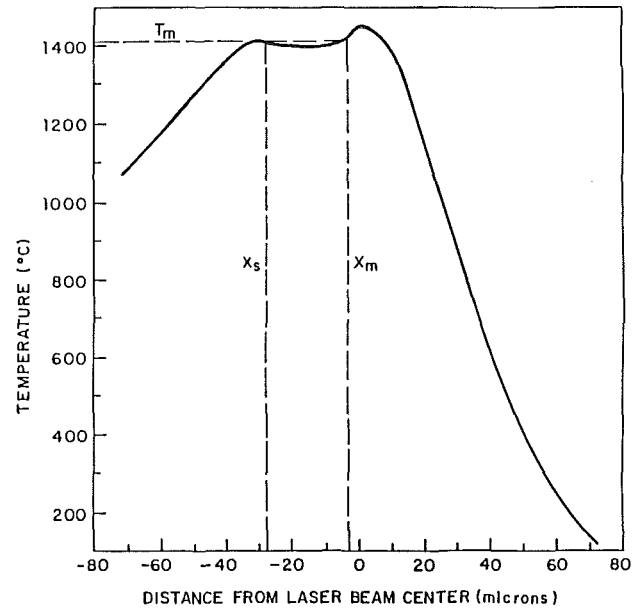

Fig. 3 Basic-state temperature distribution for a Gaussian beam of peak intensity $Q_0 = 1.60 \times 10^8$ W/m^2, $r = 40$ μm, and $V = 0.1$ m/s

The second derivatives of the basic-state temperature field are calculated analytically from equations (22), (23), and (24).

For given σ and r_s the leading order perturbation temperature field that satisfies boundary conditions (30)–(33) is found. The solution to equation (29) can be written in the form of an integral equation, according to Rosenthal (1946)

$$T^1_{gl}(x, z) = \frac{1}{\pi K_{gl}} \int_{-\infty}^{+\infty} Q^1_{gl}(\xi) e^{-\frac{V(x-\xi)}{2\alpha_{gl}}} K_0\left[\sqrt{\left\{\left[\left(\frac{V}{2\alpha_{gl}}\right)^2 + \omega^2 + \frac{\sigma}{\alpha_{gl}}\right]\left[(x-\xi)^2 + z^2\right]\right\}}\right] d\xi \quad (36)$$

A Green's function method is used to solve equations (27) and (28). This technique is very similar to the one used for the calculation of the zeroth-order temperature fields.

As in the case of the quasi-static solution, a linear system of algebraic equations is obtained

$$[A^1]\{Q^1_{gl}\} = \{B^1\} \quad (37)$$

The above system is solved for Q^1_{gl} and the solution is improved by the method of successive iterations to estimate the residuals. Equations (34) and (35) provide the additional conditions for the determination of σ and r_s. Newton's method is again used and it shows convergence after a few iterations.

3 Results

In the calculations, a Gaussian intensity profile is assumed for the external heat source

$$Q_{ext}(x) = Q_0 \exp\left(-\frac{x^2}{r^2}\right); \qquad -\infty < x < +\infty \quad (38)$$

The external adjustable parameters are Q_0, r, and V. The temperature distribution obtained for $r = 40$ μm, $Q_0 = 0.65 \times 10^8$ W/m^2, and $V = 5$ mm/s is shown in Fig. 2. As the beam scanning speed is increased to 10 cm/s, the liquid silicon region appears behind the center of the laser beam. Hence, due to the reflectivity rise upon melting, the difference between the heat absorbed by the adjacent solid and liquid phases will be larger. The basic-state solution has positive temperature gradients at the melting front and negative temperature gradients at the solidification trailing edge. The mechanism for the prediction of superheated solid in the neighborhood of the melting front can be seen by examining the following equation.

$$\left.\frac{dT^0_{si,s}}{dx}\right|^{II}_{x=x_m} = -T_m \frac{V}{\alpha_{si,s}} + \frac{1}{K_{si,s} l_{si}} \int_{x_m}^{+\infty} [(1-R_s)Q_{ext}(\xi) - Q^0_{gl}(\xi)] d\xi \quad (39)$$

The temperature derivative at the melting phase boundary is shown to depend on the local external heating and the heat loss to the glass substrate. This temperature gradient can be either negative or positive. The positive part of the solid silicon temperature gradient depends on the location of the phase boundary. The temperature gradient at the phase boundary will become steeper for the smaller heating values.

Basic-state temperature fields are shown in Figs. 2 and 3. The corresponding stability diagrams are shown in Figs. 4 and 5. The time rate of growth of the phase boundary disturbance is shown as a function of the disturbance wavenumber.

Figure 4 shows that the interface disturbance rate of growth is negative for all ω. This growth is monotonically decreasing for increasing wavelength. Thus, the corresponding system is stable for small interface disturbances.

A long-wavelength solid silicon protrusion formed at the melting front tends to absorb more heat. Consequently, this protrusion tends to remelt. Conversely, a liquid penetration into the solid must reject more heat and a return to the solid phase is then favored. This stabilizing effect can be expressed mathematically. In the case where the solid is superheated and the liquid supercooled, this is expressed by negative $d^2T^0_{si,s}/dx^2|^{II}_{x=x_m}$, $d^2T^0_{si,s}/dx^2|^{I}_{x=x_s}$ and positive $d^2T^0_{si,l}/dx^2|_{x=x_m}$ and $d^2T^0_{si,l}/dx^2|_{x=x_s}$. This temperature field property occurs when the temperature extrema are close to the phase boundaries. This effect gives a region of stability for long wavelength disturbances.

The area of the interface is increased for smaller wavelengths. The heat transfer between the solid protrusion and the neighboring supercooled melt is enhanced for these shorter disturbance wavelengths. This effect promotes growth of the solid protrusion. Likewise, heat transfer is enhanced for a liquid penetration into the superheated solid. This heat transfer promotes further growth of the liquid penetration. Therefore, there exists a region of instability. Curvature ef-

Downloaded 17 Dec 2010 to 193.140.21.150. Redistribution subject to ASME license or copyright; see http://www.asme.org/terms/Terms_Use.cfm

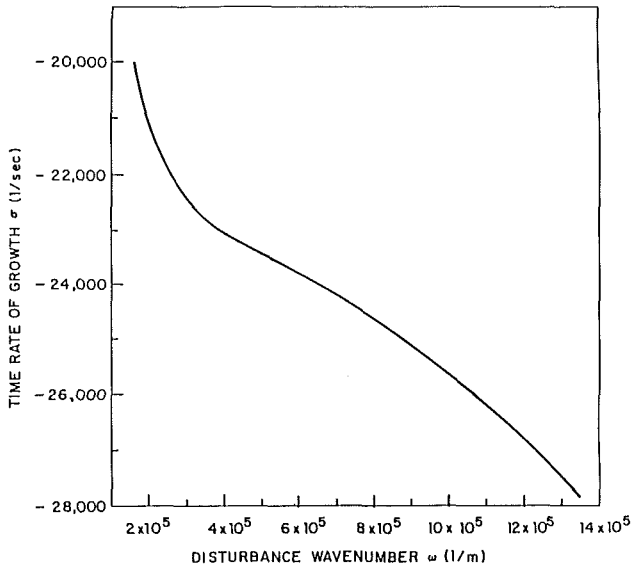

Fig. 4 Time rate of growth σ as a function of the disturbance wavenumber ω for the case of Fig. 2

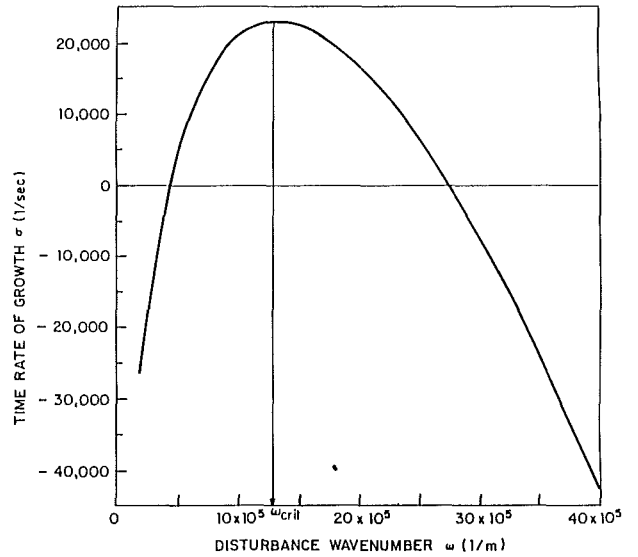

Fig. 5 Time rate of growth σ as a function of the disturbance wavenumber ω for the case of Fig. 3

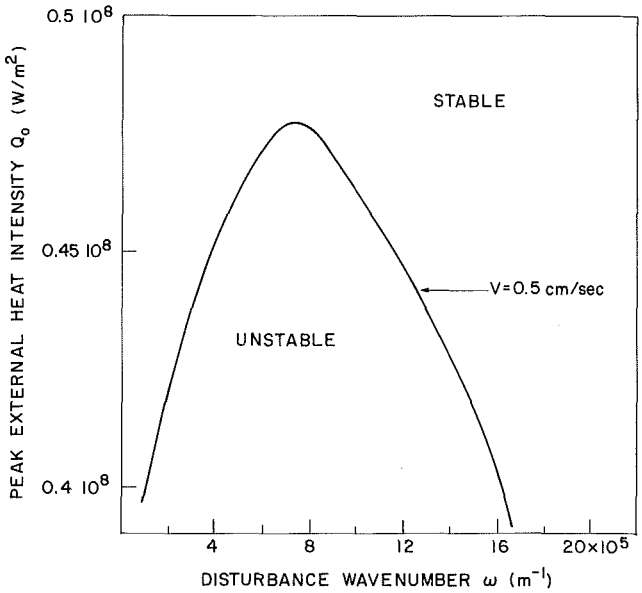

Fig. 6 Neutral stability curve for r = 40 μm, V = 5 mm/s

fects of the phase boundary tend to stabilize the growth of these protuberances. This effect is expressed by the Gibbs–Thomson boundary condition. The Gibbs–Thomson effect attenutates the growth of the smaller wavelength disturbances. There is a region of intermediate wavelengths between the small and long wavelengths where phase boundary instability occurs. Figure 5 illustrates a case where the basic-state temperature field drives the growth of intermediate wavelengths.

Figure 6 shows the neutral stability curve (σ = 0) for a scan rate V = 5 mm/s, holding r fixed. The adjustable parameter Q_0 is varied. As Q_0 is increased, more heat is incident on the silicon layer and the system is stabilized. The onset of instabilities occurs when both the real and the imaginary parts of σ are equal to zero. The occurrence of complex roots along the neutral stability curve indicates an oscillatory type behavior in time. This mode appears in the form of a traveling wave along the phase interface, when the observer is referenced to the moving laser beam. For the cases studied in this paper, the possibility of complex roots may occur for power densities and scan rates much higher than the range of the parameters examined.

The fastest growing wavelengths can be identified from the stability maps. Wavelengths near these values are believed to be related to the initial spacing of the interface disturbances. This analysis predicts wavelengths in the range of 5 to 10 μm. Experiments concurrent with this analysis show disturbances in this wavelength range. However, it must be recognized that the evolution of the interface instabilities for long times is a fundamentally nonlinear phenomenon, that cannot be treated within the framework of a linear (i.e., small amplitude) stability analysis.

4 Conclusions

A conductive heat transfer stability analysis, applied to the laser-induced melting and recrystallization of thin silicon films, has been presented. Basic-state temperature fields both in the silicon layer and in the glass substrate were obtained. The stability of these calculated temperature fields was investigated by using linear perturbation analysis. Unstable basic-state temperature fields were predicted. It was shown that the Gibbs–Thomson boundary condition tends to stabilize temperature disturbances at the solidification interface. On the contrary, the reflectivity increase upon melting enhances instability. The most dangerous wavenumbers for these unstable basic-state temperature distributions were obtained. These wavenumbers correlate with the finite amplitude crystal imperfections that have been measured.

Acknowledgment

The authors thank Dr. J. Pirvics of Xerox, Palo Alto Research Center, Mechanical Engineering Sciences, for supporting this work.

References

Abramowitz, M., and Stegun, J. A., 1964, *Handbook of Mathematical Functions*, N.B.S., Appl. Math. Series, Vol. 55.

Biegelsen, D. K., Johnson, N. M., Hawkins, W. G., Fennel, L. E., and Moyer, M. D., 1983, "Laser-Induced Crystallization of Silicon on Bulk Amorphous Substrates: An Overview," *Proceedings, Materials Research Society*, J. Narayan et al., eds., North Holland, New York, Vol. 13, pp. 537–548.

Bosch, M. A., and Lemons, R. A., 1981, "Laser Induced Melt Dynamics of Si and Silica," *Physical Review Letters*, Vol. 47, No. 16, pp. 1151–1156.

Carslaw, H. S., and Jaeger, J. C., 1959, *Conduction of Heat in Solids*, 2nd ed., Oxford University Press, Oxford, England, pp. 267–269.

Coriell, S. R., McFadden, G. B., and Sekerka, R. F., 1985, "Cellular Growth

Downloaded 17 Dec 2010 to 193.140.21.150. Redistribution subject to ASME license or copyright; see http://www.asme.org/terms/Terms_Use.cfm

During Directional Solidification," *Annual Review of Materials Science*, Vol. 15, pp. 119–145.

Hawkins, W. G., and Biegelsen, D. K., 1983, "Origin of Lamellae in Radiatively Melted Silicon Films," *Applied Physics Letters*, Vol. 42, No. 4, pp. 358–360.

Jackson, K. A., and Kurtze, D. A., 1985, "Instability in Radiatively Melted Silicon Films," *Journal of Crystal Growth*, Vol. 71, pp. 385–390.

Lemons, R. A., and Bosch, M. A., 1982, "Microscopy of Si Films During Laser Melting," *Applied Physics Letters*, Vol. 40, No. 8, pp. 703–706.

Lemons, R. A., Bosch, M. A., and Herbst, D., 1983, "Crystallization of Silicon Films on Glass: A Comparison of Methods," *Proceedings, Materials Research Society*, J. Narayan et al., eds., North Holland, New York, Vol. 13, pp. 581–592.

Mullins, W. W., and Sekerka, R. F., 1964, "Stability of a Planar Interface During Soldification of Dilute Binary Alloy," *Journal of Applied Physics*, Vol. 35, No. 2, pp. 444–451.

Narayan, J., 1982, "Development of Morphological Instability and Formation of Cells in Silicon Alloys During Pulsed Laser Irradiation," *Journal of Crystal Growth*, Vol. 59, pp. 583–598.

Nemanich, R. J., Biegelsen, D. K., and Hawkins, W. G., 1983a, "Aligned, Coexisting Liquid and Solid Regions in Laser-Annealed Si," *Physical Review B*, Vol. 27, No. 12, pp. 7817–7819.

Nemanich, R. J., Biegelsen, D. K., and Hawkins, W. G., 1983b, "Aligned, Coexisting Liquid and Solid Regions in Pulsed and CW Laser Annealing of Si," *Proceedings, Materials Research Society*, J. Narayan et al., eds., North Holland, New York, Vol. 13, pp. 211–216.

Rosenthal, D., 1946, "The Theory of Moving Sources of Heat and Its Application to Metal Treatments," *Trans. ASME*, Vol. 68, pp. 849–866.

Touloukian, Y. S., and Makita, T., 1970, *Thermophysical Properties of Matter*, Suppl. to Vol. 6, No. 83, IFI/Plenum, New York, Vol. 2.

Yaws, C. L., Dickens, L. L., Lutwack, R., and Hsu, G., 1981, "Semiconductor Industry Silicon—Physical and Mechanical Properties," *Solid State Technology*, Vol. 24, No. 1, pp. 87–92.

Wollkind, D. J., 1979, "A Deterministic Approach to Morphological Stability of the Solid–Liquid Interface," *Preparation and Properties of Solid State Materials*, W. R. Wilcox, ed., Marcel Dekker, New York, Vol. 4, p. 122.

Woodruff, D. P., 1973, *The Solid–Liquid Interface*, Cambridge University Press, London, p. 25.

APPENDIX

Material Properties Used in the Calculations

The silicon material properties were taken at the melting point (Yaws et al., 1981; Touloukian and Makita, 1970). The value of the capillary constant is the same as the one used by Jackson and Kurtze (1985).

(*a*) *Silicon*

Thermal conductivity, solid	$K_{si,s} = 22$ W/mK
Thermal conductivity, liquid	$K_{si,l} = 67$ W/m/K
Thermal diffusivity, solid	$\alpha_{si,s} = 0.96 \times 10^{-5}$ m^2/s
Thermal diffusivity, liquid	$\alpha_{si,l} = 2.64 \times 10^{-5}$ m^2/s
Heat capacity	$c_p = 1$ J/g/K
Density	$\rho_{si} = 2.533 \times 10^6$ g/m^3
Melting temperature	$T_m = 1412$°C
Latent heat	$L = 1106$ J/g
Refectivity, solid	$R_s = 0.3$
Reflectivity, liquid	$R_l = 0.7$
Capillary constant	$\Gamma = 0.3 \times 10^{-9}$ m

(*b*) *SiO_2*

Thermal conductivity	$K_{gl} = 1.3$ W/m/K
Thermal diffusivity	$\alpha_{gl} = 10^{-6}$ m^2/s

Downloaded 17 Dec 2010 to 193.140.21.150. Redistribution subject to ASME license or copyright; see http://www.asme.org/terms/Terms_Use.cfm

Analytical Solution of Transient Response of Gas-to-Gas Parallel and Counterflow Heat Exchangers

D. D. Gvozdenac
Institute of Fluid, Thermal, and Chemical Engineering, University of Novi Sad, Novi Sad, Yugoslavia

This paper shows how the transient response of gas-to-gas parallel and counterflow heat exchangers may be calculated by an analytical method. Making the usual idealizations for analysis of dynamic responses of heat exchangers, the problem of finding the temperature distributions of both fluids and the separating wall as well as the outlet temperatures of fluids is reduced to the solution of an integral equation. This equation contains an unknown function depending on two independent variables, space and time. The solution is found by using the method of successive approximations, the Laplace transform method, and special functions defined in this paper.

Introduction

In industrial installations, heat exchangers usually occur in continuous processes that, most of the time, operate at steady state. However, nonsteady operations also occur and they are of considerable practical interest. Any change, intentional or accidental, in the steady-state processes can cause a perturbation in system that can have important consequences. In these cases it is important to know the dynamic behavior of heat exchangers, in order to choose the most suitable design, control, and operation.

The intention of this paper is not to review the large number of preceding reports on the same subject that have led to the conclusions given by Kays and London (1984), but rather to present how transient temperatures in gas-to-gas parallel and counterflow heat exchangers may be calculated by analytical methods.

Nevertheless, some recently published papers dealing with similar problems should be mentioned here. Romie (1984) presented the outlet fluid temperature responses for a unit step increase in the inlet temperature of either of the fluids in a counterflow heat exchanger. The responses are found using a finite difference method and are represented by simple empirical equations. These solutions include the effect of the core thermal capacitance and are not restricted to the gas-to-gas heat exchanger, but are approximative. An exact analytical solution for the transient parallel flow heat exchanger for unit step increase in the inlet temperature of either of the fluids is presented by Romie (1985). This solution also includes the effect of core thermal capacitance but is restricted to the exchangers in which the two fluid velocities are equal or to exchangers in which both fluids are gases. Liapis and McAvoy (1981) defined the way in which analytical solutions for the transient behavior of a class of countercurrent heat and mass transfer systems can be obtained. Their solutions take into account flow forcing as well as the dependence of transfer coefficient on the velocities of flow streams but do not include the effect of core thermal capacitance. Li (1986) presented exact transient solutions of parallel flow heat exchanger in which the thermal capacitance of the core is negligible compared to the fluids contained in the exchanger. These solutions are valid for a finite or an infinite flow forcing.

In this work, analytical solutions to the energy equations governing convective heat transfer between a heat exchanger core, which is initially at an arbitrary temperature distribution, and a steady flow of fluids entering the exchanger at constant mass velocities with arbitrary time varying temperatures are presented. Solutions are restricted to the case when thermal capacities of the masses of two fluids contained in the exchanger are negligibly small relative to the thermal capacity of the heat exchanger core. They are found by using the method of successive approximations and the Laplace transform method, which leads to an extensive use of special functions defined in this paper.

As high-speed computing machines become more and more available to design engineers, the presented method for solving the addressed problem, hitherto of somewhat academic interest, will undoubtedly be found extremely useful.

Mathematical Formulation

On the basis of standard assumptions (Kays and London, 1984; Romie, 1983), one obtains three simultaneous partial differential equations in the coordinate system as shown in Fig. 1. If all quantities referring to the weaker fluid (W_{min}) flowing in the X direction are denoted with the subscript 1 and those referring to the stronger fluid (W_{max}) flowing in the X direction for parallel flow or the $-X$ direction for counterflow with the subscript 2 (Fig. 1), then the fluid temperatures T_1 (X, t) and T_2 (X, t) and the separating wall temperature T_w (X, t) of the heat exchanger are governed by the following equations:

$$M_w c_w \frac{\partial T_w}{\partial t} = (hA)_1(T_1 - T_w) - (hA)_2(T_w - T_2) \tag{1}$$

$$\dot{m}_1 c_{p1} L \frac{\partial T_1}{\partial X} = (hA)_1(T_w - T_1) \tag{2}$$

$$\pm \dot{m}_2 c_{p2} L \frac{\partial T_2}{\partial X} = (hA)_2(T_w - T_2) \tag{3}$$

In equation (3) and later, the upper part of the double sign is for the case of parallel flow and the lower part for the case of counterflow.

The space and time-independent variables, X and t, range from 0 to the heat exchanger length L, and from 0 to ∞, respectively.

In order to define dimensionless temperatures, it is appropriate to choose a reference temperature T_r and a characteristic temperature difference ΔT_r, so that

$$\theta_i(X, t) = \frac{T_i(X, t) - T_r}{\Delta T_r} \qquad (i = 1, 2, w) \tag{4}$$

Contributed by the Heat Transfer Division for publication in the JOURNAL OF HEAT TRANSFER. Manuscript received by the Heat Transfer Division September 10, 1986.

Copyright © 1987 by ASME

Downloaded 17 Dec 2010 to 193.140.21.150. Redistribution subject to ASME license or copyright; see http://www.asme.org/terms/Terms_Use.cfm

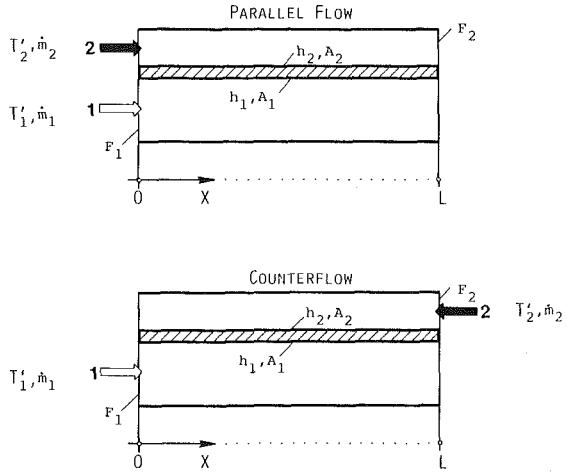

Fig. 1 Schematic description of parallel and counterflow heat exchangers

Introducing both the dimensionless distance and the dimensionless time

$$x=\frac{X}{L}\ \text{NTU}: \qquad z=\frac{t}{t^*} \tag{5}$$

and using the relations given by

$$\text{NTU}=\frac{(hA)_1(hA)_2}{(hA)_1+(hA)_2}\frac{1}{W_1}; \qquad \omega=\frac{W_1}{W_2} \tag{6}$$

$$t^*=\frac{c_w M_w}{(hA)_1+(hA)_2} \tag{7}$$

$$K_1=\frac{(hA)_1}{(hA)_1+(hA)_2}; \qquad K_2=1-K_1 \tag{8}$$

equations (1), (2), and (3) can now be written as follows:

$$\frac{\partial\theta_w}{\partial z}+\theta_w=K_1\theta_1+K_2\theta_2 \tag{9}$$

$$K_2\frac{\partial\theta_1}{\partial x}=\theta_w-\theta_1 \tag{10}$$

$$\pm\frac{K_1}{\omega}\frac{\partial\theta_2}{\partial x}=\theta_w-\theta_2 \tag{11}$$

The inlet and initial conditions for equations (9), (10), and (11) are

$$\left.\begin{aligned}&\theta_1(0,z)=\phi_1(z)\\&\theta_2(0,z)=\phi_2(z) \qquad \text{for parallel flow}\\&\theta_2(\text{NTU},z)=\phi_2(z) \qquad \text{for counterflow}\\&\theta_w(x,0)=\psi_w(x)\end{aligned}\right\} \tag{12}$$

Equations (12) represent arbitrary temperature distributions of the separating wall and arbitrary time varying inlet fluid temperatures.

It should be stressed that this model is valid if thermal capacities of the masses of the two fluids contained in the exchanger core are negligibly small relative to the thermal capacity of the core itself. The ratios of the thermal capacitance of the fluids contained in the exchanger to the

Nomenclature

A = matrix element, equation (34)
A_1, A_2 = total heat transfer area on side 1 and side 2, respectively, m^2
a, b = functions, equations (25) and (26), respectively
c = parameter $= \omega/K_1$
c_p = specific heat at constant pressure, J/(kg•K)
c_w = specific heat of core material, J/(kg•K)
d = parameter $= 1/K_2$
F = function defined in equations (21) and (23)
F_n = special function defined in the Appendix
f, g = functions defined in equations (28), (29), and (30)
$H_{n,m,k}$ = special function defined in the Appendix
h = heat transfer coefficient between fluid and the wall, W/(K•m^2)
$I_{n,m}$ = special function defined in the Appendix
K_1, K_2 = parameters, equations (8)
L = heat exchanger length, m
M_w = mass of exchanger core, kg
$\dot{m}$ = mass flow rate, kg/s
NTU = number of transfer units, equation (6)
$\binom{n}{r}$ = binomial coefficient $= n!/r!(n-r)!$
p, s = Laplace transform variable
T = temperature, K
t = time, s
t^* = parameter, equation (7), s
u, v = dummy variables
W = thermal capacity rate $= \dot{m}\, c_p$, W/K
X = distance from fluid 1 entrance, m
x, z = dimensionless independent variables, equation (5)
δ = parameter
θ = dimensionless temperature, defined in equation (4)
Φ = inlet temperature distribution, defined in equation (12)
ψ = initial temperature distribution of the separating wall, defined in equation (12)
ω = thermal capacity rate ratio, equation (6)

Subscripts

1 = refers to fluid 1
2 = refers to fluid 2
w = refers to the wall
i, j, k, m, n, r = integers

Superscripts

$'$ = at the inlet
$''$ = at the outlet
$\tilde{}$ = Laplace transform with respect to the variable x
$\bar{}$ = Laplace transform with respect to the variable z

Downloaded 17 Dec 2010 to 193.140.21.150. Redistribution subject to ASME license or copyright; see http://www.asme.org/terms/Terms_Use.cfm

thermal capacitance of the exchanger core are very small if the fluids are gases. The smallness of the capacity ratios means that the fluid transit or dwell times are small compared to the duration of the transient (Romie, 1984).

A general solution to this problem is developed in the following section.

General Solution

Since equations (9), (10), and (11) are linear in $\theta_1(x, z)$, $\theta_w(x, z)$, and $\theta_2(x, z)$, they can be solved by using the Laplace transform with respect to variable $z \to p$. This procedure yields

$$\tilde{\theta}_w = \frac{K_1\tilde{\theta}_1 + K_2\tilde{\theta}_2 + \psi_w}{p+1} \tag{13}$$

$$K_2\frac{d\tilde{\theta}_1}{dx} + \tilde{\theta}_1 = \tilde{\theta}_w \tag{14}$$

$$\pm\frac{K_1}{\omega}\frac{d\tilde{\theta}_2}{dx} + \tilde{\theta}_2 = \tilde{\theta}_w \tag{15}$$

Applying the convolution theorem on equation (13), one obtains

$$\theta_w(x, z) = \psi_w(x)\exp(-z) + K_1\int_0^z \theta_1(x, v)\exp[-(z-v)]dv + K_2\int_0^z \theta_2(x, v)\exp[-(z-v)]dv \tag{16}$$

and after integrating equations (14) and (15) with respect to x, satisfying equations (12), one finds

$$\theta_1(x, z) = \Phi_1(z)\exp\left(-\frac{x}{K_2}\right) + \frac{1}{K_2}\int_0^x \theta_w(u, z)\exp\left(-\frac{x-u}{K_2}\right)du \tag{17}$$

For parallel flow

$$\theta_2(x, z) = \Phi_2(z)\exp\left(-\frac{\omega x}{K_1}\right) + \frac{\omega}{K_1}\int_0^x \theta_w(u, z)\exp\left[-\frac{\omega(x-u)}{K_1}\right]du \tag{18}$$

For counterflow

$$\theta_2(x, z) = \Phi_2(z)\exp\left[-\frac{\omega(\mathrm{NTU}-x)}{K_1}\right] + \frac{\omega}{K_1}\int_x^{\mathrm{NTU}} \theta_w(u, z)\exp\left[-\frac{\omega(u-x)}{K_1}\right]du \tag{19}$$

The substitution of equations (17) and (18) for parallel flow and equations (17) and (19) for counterflow into equation (16) gives the following integral equations:

For parallel flow

$$\theta_w(x, z) = F(x, z) + \frac{K_1}{K_2}\int_0^z\int_0^x \theta_w(u, v)\exp\left(-\frac{x-u}{K_2}\right)\cdot\exp[-(z-v)]du\,dv + \frac{\omega K_2}{K_1}\int_0^z\int_0^x \theta_w(u, v)\exp\left[-\frac{\omega(x-u)}{K_1}\right]\cdot\exp[-(z-v)]du\,dv \tag{20}$$

where

$$F(x, z) = \psi_w(x)\exp(-z) + K_1\exp\left(-\frac{x}{K_2}\right)\int_0^z \Phi_1(v)\exp[-(z-v)]dv + K_2\exp\left(-\frac{\omega x}{K_1}\right)\int_0^z \Phi_2(v)\exp[-(z-v)]dv \tag{21}$$

For counterflow

$$\theta_w(x, z) = F(x, z) + \frac{K_1}{K_2}\int_0^z\int_0^x \theta_w(u, v)\exp\left(-\frac{x-u}{K_2}\right)\cdot\exp[-(z-v)]du\,dv + \frac{\omega K_2}{K_1}\int_0^z\int_x^{\mathrm{NTU}} \theta_w(u, v)\exp\left[-\frac{\omega(u-x)}{K_1}\right]\cdot\exp[-(z-v)]du\,dv \tag{22}$$

where

$$F(x, z) = \psi_w(x)\exp(-z) + K_1\exp\left(-\frac{x}{K_2}\right)\int_0^z \Phi_1(v)\exp[-(z-v)]dv + K_2\exp\left[-\frac{\omega(\mathrm{NTU}-x)}{K_1}\right]\int_0^z \Phi_2(v)\exp[-(z-v)]dv \tag{23}$$

From equations (21) and (23), one can see that the function $F(x, z)$ is expressible by

$$F(x, z) = \sum_{k=1}^{3} a_k(x)b_k(z) \tag{24}$$

where

$$\left.\begin{aligned} a_1(x) &= \psi_w(x)\\ a_2(x) &= K_1\exp\left(-\frac{x}{K_2}\right)\\ a_3(x) &= K_2\exp\left(-\frac{\omega x}{K_1}\right) \quad \text{for parallel flow}\\ a_3(x) &= K_2\exp\left[-\frac{\omega(\mathrm{NTU}-x)}{K_1}\right] \quad \text{for counterflow} \end{aligned}\right\} \tag{25}$$

and

$$\left.\begin{aligned} b_1(z) &= \exp(-z)\\ b_2(z) &= \int_0^z \Phi_1(v)\exp[-(z-v)]dv\\ b_3(z) &= \int_0^z \Phi_2(v)\exp[-(z-v)]dv \end{aligned}\right\} \tag{26}$$

It is interesting to note that only the function $a_1(x)$ depends on initial condition while the functions $b_2(z)$ and $b_3(z)$ depend on inlet conditions. Function $a_3(x)$ depends on flow arrangement (parallel or counterflow).

The known function $F(x, z)$ suggests that the unknown function $\theta_w(x, z)$ can be represented as

$$\theta_w(x, z) = \sum_{n=0}^{\infty}\sum_{k=1}^{3} f_{n,k}(x)g_{n,k}(z) \tag{27}$$

where the functions $f_{n,k}(x)$ and $g_{n,k}(z)$ depend only on x and z, respectively.

Substitution of equation (27) into equation (20) (for parallel flow) or into equation (22) (for counterflow) and application of the successive approximation method to solve integral equations gives the following integral recursion formulas:

Downloaded 17 Dec 2010 to 193.140.21.150. Redistribution subject to ASME license or copyright; see http://www.asme.org/terms/Terms_Use.cfm

For parallel flow

$$f_{0,k}(x) = a_k(x)$$

$$f_{n,k}(x) = \frac{K_1}{K_2}\int_0^x f_{n-1,k}(u)\exp\left(-\frac{x-u}{K_2}\right)du + \frac{\omega K_2}{K_1}\int_0^x f_{n-1,k}(u)\exp\left[-\frac{\omega(x-u)}{K_1}\right]du \tag{28}$$

For counterflow

$$f_{0,k}(x) = a_k(x)$$

$$f_{n,k}(x) = \frac{K_1}{K_2}\int_0^x f_{n-1,k}(u)\exp\left(-\frac{x-u}{K_2}\right)du + \frac{\omega K_2}{K_1}\int_x^{\text{NTU}} f_{n-1,k}(u)\exp\left[-\frac{\omega(u-x)}{K_1}\right]du \tag{29}$$

and (for both arrangements)

$$g_{0,k}(z) = b_k(z)$$

$$g_{n,k}(z) = \int_0^z g_{n-1,k}(v)\exp[-(z-v)]dv \tag{30}$$

Numerical values of the space-variable functions $f_{n,k}(x)$ ($k = 1, 2, 3$ and $n = 0, 1, 2, 3, \ldots$) are universal for all inlet conditions and depend only on the initial condition, independent heat exchanger parameters (NTU, ω, and K_1), and flow arrangement (parallel or counterflow). However, the time-variable functions $g_{n,k}(z)$ are universal for both flow arrangements and depend only on inlet conditions.

Taking the Laplace transform of equations (26) and (30) with respect to the variable z using p as the transform parameter, one obtains

$$\left.\begin{aligned} \bar{b}_1 &= \frac{1}{p+1} \\ \bar{b}_2 &= \bar{\Phi}_1\frac{1}{p+1} \\ \bar{b}_3 &= \bar{\Phi}_2\frac{1}{p+1} \end{aligned}\right\} \tag{31}$$

and

$$\left.\begin{aligned} \bar{g}_{0,k} &= \bar{b}_k \qquad (k=1,2,3) \\ \bar{g}_{n,k} &= \bar{g}_{n-1,k}\frac{1}{p+1} \qquad (n=1,2,3,\ldots) \end{aligned}\right\} \tag{32}$$

An explicit formula for the unknown function $g_{n,k}(z)$ can now be found using the last two equations as follows:

$$g_{n,k}(z) = L^{-1}_{p\to z}\left\{\frac{\bar{b}_k}{(p+1)^n}\right\} \tag{33}$$

A procedure similar to that used to find the unknown functions $g_{n,k}(z)$ can be used to find explicit formulas for the functions $f_{n,k}(x)$. That means, taking the Laplace transform of equation (28) for parallel flow, and equation (29) for counterflow, with respect to the variable x using s as the transform parameter, and using the method of successive substitution of functions $f_{n-1,k}(x)$ ($n = 1, 2, 3, \ldots$), one obtains formulas for finding the unknown functions $f_{n,k}(x)$.

For concise notation of explicit formulas, the matrix elements

$$A_{n,r} = \binom{n}{r}(dK_1)^{n-r}(cK_2)^r \qquad \begin{matrix} n=0,1,2,\ldots \\ 0\le r\le n \end{matrix} \tag{34}$$

and parameters $c = \omega/K_1$ and $d = 1/K_2$ are introduced.

For the case $\omega = 0$ (applies to exchangers of all configurations), one can find

$$f_{n,k}(x) = d^n K_1^n L^{-1}_{s\to x}\left\{\frac{\tilde{a}_k}{(s+d)^n}\right\} \tag{35}$$

For parallel flow if $\omega > 0$ and $c = d$

$$f_{n,k}(x) = d^n L^{-1}_{s\to x}\left\{\frac{\tilde{a}_k}{(s+d)^n}\right\} \tag{36}$$

and if $\omega > 0$ and $c \neq d$

$$f_{n,k}(x) = \sum_{r=0}^{n} A_{n,r} L^{-1}_{s\to x}\left\{\frac{\tilde{a}_k}{(s+d)^{n-r}(s+c)^r}\right\} \tag{37}$$

For counterflow

$$f_{n,k}(x) = \sum_{r=0}^{n}(-1)^r A_{n,r} L^{-1}_{s\to x}\left\{\frac{\tilde{a}_k}{(s+d)^{n-r}(s+c)^r}\right\} + \sum_{i=1}^{n} f_{i,k}(0)\sum_{r=0}^{n-i}(-1)^r A_{n-i,r} I_{n-i-r,r+1}(x,\, d,\, c+d) \tag{38}$$

where

$$f_{1,k}(0) = K_2 c L^{-1}_{s\to \text{NTU}}\left\{\frac{\tilde{a}_k(s+c)}{s}\right\}$$

$$f_{n,k}(0) = K_2 c\sum_{r=0}^{n-1}(-1)^r A_{n-1,r} L^{-1}_{s\to \text{NTU}}\left\{\frac{\tilde{a}_k(s+c)}{s^{r+1}(s+c+d)^{n-r-1}}\right\} + K_2 c\sum_{i=1}^{n-1} f_{i,k}(0)\sum_{r=0}^{n-i-1}(-1)^r A_{n-i-1,r}$$

$$I_{n-i-r-1,r+2}(\text{NTU}, c+d, c+d) \qquad (n = 2, 3, 4, \ldots) \tag{39}$$

Explicit relations for the function $I_{n,m}(x, c, d)$ appearing in equations (38) and (39) are given in the Appendix.

The functions $f_{n,k}(x)$ can also be calculated by integration of integral equations (28) and (29) using, for example, the trapezoidal rule. The functions $f_{n-1,k}(x)$ are evaluated at distinct values x_m ($m = 0, 1, 2, \ldots, M$) of x on the range $0 \le x \le$ NTU, that is, at distinct $x_m = m\cdot\Delta x$ from the fluid 1 entrance (Δx = NTU/M = step length).

That means that the values of the functions $f_{n,k}(x)$ may be calculated in two ways. The first way is to apply numerical integration of the recursion integral relations (28) and (29) and the second one is to apply explicit formulas for the functions $f_{n,k}(x)$ (equations (35), (36), (37), or (38)). Some aspects of applying both calculation methods of the functions $f_{n,k}(x)$ can be explained on the example of step change of inlet temperature of fluid 1 for counterflow heat exchanger having NTU = 1, ω = 1, and K_1 = 0.5. In this case, only the functions $f_{n,2}(x)$ shall be calculated as $f_{n,1}(x) = 0$ because of $\psi_w(x) = 0$ while the function $f_{n,3}(x)$ need not be calculated as $g_{n,3}(z) = 0$ because of $\Phi_2(z) = 0$. If only outlet fluid temperatures are to be determined, only $f_{n,2}(0)$ and $f_{n,2}$(NTU) shall be known. When the first calculation method is applied, functions $f_{n-1,2}(x)$ shall be calculated in 70 collocation points to obtain accuracy for the calculation of these functions to four significant figures. Calculating function $g_{n,2}(z)$ with the above accuracy, too, and wanting to obtain the outlet temperatures with the same accuracy, the products $g_{n,2}(z)\cdot f_{n+1,2}(x)$ ($x = 0$ or NTU) shall be added up to $n = 10$ for $z = 5$; $n = 14$ for $z = 10$; $n = 16$ for $z = 15$; and $n = 17$ for $z = 20$. The numerical integration has been performed resorting to an algorithm based on a trapezoidal rule and this procedure is very simple for use and can be easily programmed and quickly

Downloaded 17 Dec 2010 to 193.140.21.150. Redistribution subject to ASME license or copyright; see http://www.asme.org/terms/Terms_Use.cfm

done on a digital computer. The practical application of explicit analytical formulas is a little complicated. In the same example as mentioned above, the number of required functions $f_{n,2}(x)$ ($x = 0$ or NTU) is unchanged for the same accuracy of outlet temperatures, but the time period required for their computation is longer compared to the numerical method. The relation between the time periods required to calculate the functions $f_{n,k}(x)$ by use of the first/second method depends on the values of NTU, ω, and K_1 parameters as well as the flow arrangement and, of course, on the computer programs themselves. However, numerical aspects are not the subject of this paper and, therefore, they will not be discussed in more detail.

Similar analyses can also be carried out for other values of NTU, ω, and K_1 parameters as well as for the two different flow arrangements and various initial and inlet conditions. For the case when initial and inlet conditions are more complex, the functions $f_{n,1}(x)$, $f_{n,3}(x)$, $g_{n,1}(z)$, and $g_{n,3}(z)$ shall also be calculated. However, there are no considerable differences in the calculation procedure or the number of functions required to calculate outlet temperatures of a given accuracy.

It should be emphasized that all functions $f_{n,k}(x)$ and $g_{n,k}(z)$ are always less than or equal to one and that they are always positive or equal to zero which simplifies the analysis of calculation accuracy as well as the analysis of the influence of either initial or inlet conditions to the final calculation result. For example, the function $f_{n,1}(x)$ practically represents the influence of initial condition to the outlet fluid temperatures and the heat exchanger core which means that, taking the linearity of the subject mathematical formulation into account, an independent analysis of individual influences can also be carried out.

As the functions $f_{n,k}(x)$ and $g_{n,k}(z)$ are now known, the temperature distribution of the separating wall can be calculated by using equation (27) while temperature distributions of both fluids can be calculated by substituting the above functions in equations (17) and (18) or (19). This procedure gives

$$\theta_1(x,z) = \Phi_1(z)\exp(-dx) + d\sum_{n=0}^{\infty}\sum_{k=1}^{3} g_{n,k}(z)\int_0^x f_{n,k}(u)\exp[-d(x-u)]du \tag{40}$$

and

For parallel flow

$$\theta_2(x,z) = \Phi_2(z)\exp(-cx) + c\sum_{n=0}^{\infty}\sum_{k=1}^{3} g_{n,k}(z)\int_0^x f_{n,k}(u)\exp[-c(x-u)]du \tag{41}$$

For counterflow

$$\theta_2(x,z) = \Phi_2(z)\exp[-c(\mathrm{NTU}-x)] + c\sum_{n=0}^{\infty}\sum_{k=1}^{3} g_{n,k}(z)\int_x^{\mathrm{NTU}} f_{n,k}(u)\exp[-c(u-x)]du \tag{42}$$

The outlet fluid temperatures are

$$\theta_1'' = \theta_1(\mathrm{NTU}, z), \qquad \theta_2'' = \begin{cases}\theta_2(\mathrm{NTU}, z) & \text{for parallel flow}\\ \theta_2(0, z) & \text{for counterflow}\end{cases} \tag{43}$$

It is not difficult to show that the following relations are valid for both arrangements:

$$K_1\theta_1(x,z) + K_2\theta_2(x,z) = \Phi_1(z)a_2(x) + \Phi_2(z)a_3(x) + \sum_{n=0}^{\infty}\sum_{k=1}^{3} g_{n,k}(z)f_{n+1,k}(x) = \sum_{n=0}^{\infty}\sum_{k=1}^{3} g_{n-1,k}(z)f_{n,k}(x) \tag{44}$$

where

$$g_{-1,k}(z) = \frac{db_k(z)}{dz} \tag{45}$$

These relations are very suitable for the calculation of outlet temperatures in the counterflow heat exchanger because integral calculations in equations (40) and (42) are not required.

Calculation Results

The main purpose of this paper is to provide an analytical solution by which performances of the parallel and counterflow heat exchangers can be evaluated and compared. Because of the many parameters involved in the temperature distributions of fluids and separating walls, it is virtually impossible to present the quantitative influence of all of these parameters here. However, there is enough space in this paper to give one particular result showing the main characteristics of the solutions.

For the case of arbitrary and constant initial temperature of the separating wall and for inlet conditions given by exponential functions, i.e.,

$$\left.\begin{aligned}\theta_1(0,z) = \Phi_1(z) &= \begin{cases}1-(1-\beta)\exp(-\gamma_1 z) & \text{for } z\geq 0\\ \beta & \text{for } z<0\end{cases}\\ \theta_w(x,0) &= \beta\\ \left.\begin{matrix}\theta_2(0,z)\\ \theta_2(\mathrm{NTU},z)\end{matrix}\right\} &= \Phi_2(z) = \begin{cases}\beta\exp(-\gamma_2 z) & \text{for } z\geq 0\\ \beta & \text{for } z<0\end{cases}\end{aligned}\right\} \tag{46}$$

equations (25) and (26) are reduced to

$$\left.\begin{aligned}0a_1(x) &= \beta\\ a_2(x) &= K_1\exp(-dx)\\ a_3(x) &= K_2\exp(-cx) && \text{for parallel flow}\\ a_3(x) &= K_2\exp[-c(\mathrm{NTU}-x)] && \text{for counterflow}\end{aligned}\right\} \tag{47}$$

$$b_1(z) = \exp(-z)$$

$$b_2(z) = \begin{cases}1-\exp(-z) & \text{Step change} \quad (\gamma_1\to\infty)\\ 1-\exp(-z)-\dfrac{1-\beta}{1-\gamma_1}[\exp(-\gamma_1 z)-\exp(-z)] & (\gamma_1\neq 1)\\ 1-\exp(-z)-(1-\beta)z\exp(-z) & (\gamma_1 = 1)\end{cases}$$

Downloaded 17 Dec 2010 to 193.140.21.150. Redistribution subject to ASME license or copyright; see http://www.asme.org/terms/Terms_Use.cfm

$$b_3(z)=\begin{cases}0 & \text{Step change}\\ \dfrac{\beta}{1-\gamma_2}\left[\exp(-\gamma_2 z)-\exp(-z)\right] & (\gamma_2\to\infty)\\ \beta z\exp(-z) & (\gamma_2=1)\end{cases} \quad (\gamma_2\neq 1) \qquad (48)$$

It should be pointed out that for the $\gamma_1 \to \infty$ and $\gamma_2 \to \infty$ functions, $\Phi_1(z) \to 1$ and $\Phi_2(z) \to 0$, which corresponds to a step change of inlet fluid temperatures.

In order to determine outlet fluid temperatures of a parallel flow heat exchanger, equations (40) and (41) are used with x = NTU while outlet temperatures of counterflow heat exchanger are determined by equations (40) and (42) with x = NTU and $x = 0$, respectively. In that way, the following equations for outlet fluid temperatures are obtained

$$\left.\begin{aligned}\theta_1''&=\Phi_1(z)\exp(-d\text{NTU})\\ &\quad+d\sum_{n=0}^{\infty}\sum_{k=1}^{3}g_{n,k}(z)i_{n,k}(\text{NTU})\\ \theta_2''&=\Phi_2(z)\exp(-c\text{NTU})\\ &\quad+c\sum_{n=0}^{\infty}\sum_{k=1}^{3}g_{n,k}(z)j_{n,k}(\text{NTU})\end{aligned}\right\} \quad (49)$$

where the integrals in equations (40), (41), and (42) are as follows:

$$\left.\begin{aligned}i_{n,k}(\text{NTU})&=\int_0^{\text{NTU}}f_{n,k}(u)\exp[-d(\text{NTU}-u)]du\\ j_{n,k}(\text{NTU})&=\int_0^{\text{NTU}}f_{n,k}(u)\exp[-c(\text{NTU}-u)]du\\ &\qquad\qquad\text{for parallel flow}\\ j_{n,k}(\text{NTU})&=\int_0^{\text{NTU}}f_{n,k}(u)\exp(-cu)du\\ &\qquad\qquad\text{for counterflow}\end{aligned}\right\} \quad (50)$$

Taking the Laplace transform of equations (48), substituting these results into equation (33), and finding the inverse Laplace transform (see Appendix), exact formulas for functions $g_{n,k}(z)$ $(n = 1, 2, 3, \ldots)$ can be obtained in the following way:

$$\left.\begin{aligned}g_{n,1}(z)&=F_{n+1}(z,1)\\ g_{n,2}(z)&=\begin{cases}I_{n+1,1}(z,1,1)=1-\sum_{i=0}^{n}F_{i+1}(z,1) & (\gamma_1\to\infty)\\ I_{n+1,1}(z,1,1)-(1-\beta)I_{n+1,1}(z,1,1-\gamma_1)) & (0<\gamma_1<\infty)\end{cases}\\ g_{n,3}(z)&=\begin{cases}0 & (\gamma_2\to\infty)\\ \beta I_{n+1,1}(z,1,1-\gamma_2) & (0<\gamma_2<\infty)\end{cases}\end{aligned}\right\} \quad (51)$$

Exact formulas for the calculation of the functions $i_{n,k}$ (NTU) and $j_{n,k}$ (NTU) are obtained either by direct Laplace transform of equations (50) or by applying relations (A7), (A8), and (A9). This means that for the known functions $a_k(x)$ included in equations (47), the functions $f_{n,k}(x)$ have already been determined by use of the relevant equations (35)–(39).

For the functions $i_{n,k}$ (NTU) and $j_{n,k}$ (NTU), all calculation results are given in Table 1. The special functions $F_n(x, c)$, $I_{n,m}$ (x, c, d), and $H_{n,m,k}$ (x, c, d) appearing in Table 1 are given in the Appendix.

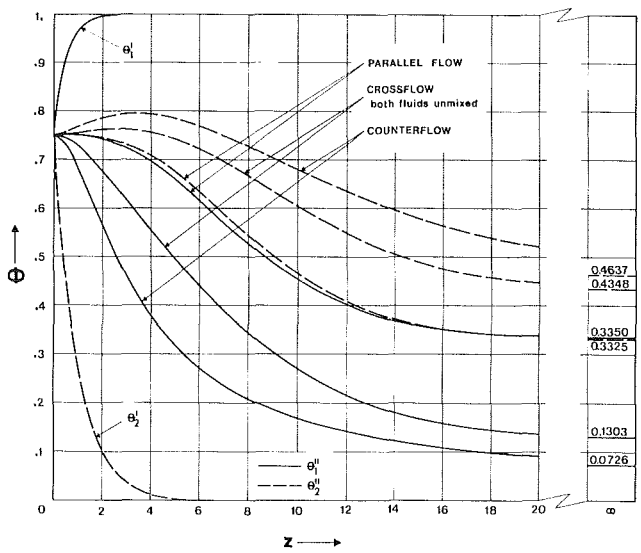

Fig. 2 Inlet and outlet temperatures for parallel, cross, and counterflow heat exchangers versus dimensionless time z: NTU = 4, ω = 0.5, K_1 = 0.25, β = 0.75, γ_1 = 2, and γ_2 = 1

For parallel flow, counterflow (results obtained in this paper), and crossflow heat exchangers with both fluids unmixed (Gvozdenac, 1986), outlet temperature θ_1'' and θ_2'' versus dimensionless time z are shown in Fig. 2.

Concluding Remarks

A method that provides analytical solutions to the transient response of gas-to-gas parallel and counterflow heat exchangers has been presented. The solution technique given in this paper allows for simultaneous and arbitrary forcing at both ends of the system.

A significant feature of the work presented is the approach which was taken to solve the integral equations (20) and (22). This solution procedure provides the necessary basis for the study of parameter estimation, model discrimination, and control of parallel and counterflow heat exchangers.

On the basis of presented results, a check of outlet temperatures has been made for special cases with a unit step increase in the inlet temperature of either gas given by Romie (1984, 1985) and these have been found correct.

Examination of these solutions reveals that they may be used effectively in practice for computer-aided design, control, and operation procedures.

References

Gvozdenac, D. D., 1986, "Analytical Solution of the Transient Response of Gas-to-Gas Crossflow Heat Exchanger With Both Fluids Unmixed," ASME JOURNAL OF HEAT TRANSFER, Vol. 108, pp. 722–727.

Kays, W. M., and London, A. L., 1984, *Compact Heat Exchangers*, 3rd ed., McGraw-Hill, New York.

Li, Ch. H., 1986, "Exact Transient Solutions of Parallel-Current Transfer Processes," ASME JOURNAL OF HEAT TRANSFER, Vol. 108, pp. 365–369.

Liapis, A. I., and McAvoy, T. J., 1981, "Transient Solutions for a Class of Hyperbolic Counter-current Distributed Heat and Mass Transfer Systems," *Trans. IChemE*, Vol. 59, pp. 89–94.

Downloaded 17 Dec 2010 to 193.140.21.150. Redistribution subject to ASME license or copyright; see http://www.asme.org/terms/Terms_Use.cfm

Table 1 Functions $i_{n,k}(\mathrm{NTU})$ and $j_{n,k}(\mathrm{NTU})$

	Parallel flow	Counterflow
$n=0$	$i_{n,1}(\mathrm{NTU})=\beta d i_{n,3}(\mathrm{NTU})$ $i_{n,2}(\mathrm{NTU})=K_1^n d^n F_{n+2}(\mathrm{NTU}, d)$ $i_{n,3}(\mathrm{NTU})=K_1^n d^{n-1} I_{n+1,1}(\mathrm{NTU}, d, d)$	$j_{n,1}(\mathrm{NTU})=0$ $j_{n,2}(\mathrm{NTU})=0$ $j_{n,3}(\mathrm{NTU})=0$
$1\le n<\infty$	$c=d$ $i_{n,1}(\mathrm{NTU})=j_{n,1}(\mathrm{NTU})=\beta d^n I_{n+1,1}(\mathrm{NTU}, d, d)$ $i_{n,2}(\mathrm{NTU})=j_{n,1}(\mathrm{NTU})=K_1 d^n F_{n+2}(\mathrm{NTU}, d)$ $i_{n,3}(\mathrm{NTU})=j_{n,3}(\mathrm{NTU})=\dfrac{1}{K_1 d} i_{n,2}(\mathrm{NTU})$	$i_{n,k}(\mathrm{NTU})=\dfrac{1}{K_1 d} f_{n+1,k}(\mathrm{NTU})$ $(k=1,2,3)$ $j_{n,k}(\mathrm{NTU})=\dfrac{d}{c} f_{n+1,k}(\mathrm{NTU})$ $f_{1,1}(0)=\beta K_2 c I_{1,1}(\mathrm{NTU}, c, c)$ $f_{n,1}(0)=\beta K_2 c \sum_{r=0}^{n-1}(-1)^r A_{n-1,r} H_{1,n-r-1,r+1}(\mathrm{NTU}, c, -d)$ $+K_2 c \sum_{i=1}^{n-1} f_{i,1}(0) \sum_{r=0}^{n-i-1}(-1)^r A_{n-i-1,r} I_{n-i-r-1,r+2}(\mathrm{NTU}, c+d, c+d)$ $f_{1,2}(0)=K_1 K_2 c I_{1,1}(\mathrm{NTU}, c+d, c+d)$ $f_{n,2}(0)=K_1 K_2 c \sum_{r=0}^{n-1}(-1)^r A_{n-1,r} I_{n-r,r+1}(\mathrm{NTU}, c+d, c+d)$ $+K_2 c \sum_{i=1}^{n-1} f_{i,2}(0) \sum_{r=0}^{n-i-1}(-1)^r A_{n-i-1,r} I_{n-i-r-1,r+2}(\mathrm{NTU}, c+d, c+d)$
$1\le n<\infty$	$c\neq d$ $i_{n,1}(\mathrm{NTU})=\beta \sum_{r=0}^{n} A_{n,r} H_{r,n-r+1,1}(\mathrm{NTU}, c, c-d)$ $i_{n,2}(\mathrm{NTU})=K_1 \sum_{r=0}^{n} A_{n,r} I_{r,n-r+2}(\mathrm{NTU}, c, c-d)$ $i_{n,3}(\mathrm{NTU})=K_2 \sum_{r=0}^{n} A_{n,r} I_{r+1,n-r+1}(\mathrm{NTU}, c, c-d)$ $j_{n,1}(\mathrm{NTU})=\beta \sum_{r=0}^{n} A_{n,r} H_{r+1,n-r,1}(\mathrm{NTU}, c, c-d)$ $j_{n,2}(\mathrm{NTU})=K_1 \sum_{r=0}^{n} A_{n,r} I_{r+1,n-r+1}(\mathrm{NTU}, c, c-d)$ $j_{n,3}(\mathrm{NTU})=K_2 \sum_{r=0}^{n} A_{n,r} I_{r+2,n-r}(\mathrm{NTU}, c, c-d)$	$f_{1,3}(0)=K_2^2 c F_2(\mathrm{NTU}, c)$ $f_{n,3}(0)=K_2^2 c \exp(-c\mathrm{NTU}) \sum_{r=0}^{n-1}(-1)^r A_{n-1,r} I_{n-r-1,r+2}(\mathrm{NTU}, c+d, c+d)$ $+K_2 c \sum_{i=1}^{n-1} f_{i,3}(0) \sum_{r=0}^{n-i-1}(-1)^r A_{n-i-1,r} I_{n-i-r-1,r+2}(\mathrm{NTU}, c+d, c+d)$ $f_{n,1}(\mathrm{NTU})=\beta \sum_{r=0}^{n}(-1)^r A_{n,r} H_{n-r,r,1}(\mathrm{NTU}, d, c+d)$ $+\sum_{i=1}^{n} f_{i,1}(0) \sum_{r=0}^{n-i}(-1)^r A_{n-i,r} I_{n-i-r,r+1}(\mathrm{NTU}, d, c+d)$ $f_{n,2}(\mathrm{NTU})=K_1 \sum_{r=0}^{n}(-1)^r A_{n,r} I_{n-r+1,r}(\mathrm{NTU}, d, c+d)$ $+\sum_{i=1}^{n} f_{i,2}(0) \sum_{r=0}^{n-i}(-1)^r A_{n-i,r} I_{n-i-r,r+1}(\mathrm{NTU}, d, c+d)$ $f_{n,3}(\mathrm{NTU})=K_2 \exp(-c\mathrm{NTU}) \sum_{r=0}^{n}(-1)^r A_{n,r} I_{n-r,r+1}(\mathrm{NTU}, d, c+d)$ $+\sum_{i=1}^{n} f_{i,3}(0) \sum_{r=0}^{n-i}(-1)^r A_{n-i,r} I_{n-i-r,r+1}(\mathrm{NTU}, d, c+d)$

Romie, F. E., 1983, "Transient Response of Gas-to-Gas Crossflow Heat Exchangers with Neither Gas Mixed," ASME JOURNAL OF HEAT TRANSFER, Vol. 105, pp. 563-570.

Romie, F. E., 1984, "Transient Response of the Counterflow Heat Exchanger," ASME JOURNAL OF HEAT TRANSFER, Vol. 106, pp. 620-626.

Romie, F. E., 1985, "Transient Response of the Parallel-Flow Heat Exchanger," ASME JOURNAL OF HEAT TRANSFER, Vol. 107, pp. 727-730.

APPENDIX

The functions $F_n(x, c)$, $I_{n,m}(x, c, d)$, and $H_{n,m,k}(x, c, d)$ and their Laplace transforms are given as described below ($x \ge 0$ and $-\infty < c, d < \infty$):

Downloaded 17 Dec 2010 to 193.140.21.150. Redistribution subject to ASME license or copyright; see http://www.asme.org/terms/Terms_Use.cfm

(*i*) $F_n(x, c) = \dfrac{x^{n-1}}{(n-1)!}\exp(-cx) \overset{L}{\Rightarrow} \dfrac{1}{(s+c)^n}$

$(n = 1, 2, 3, \ldots)$ (A1)

Particular values are

$F_1(0, c) = 1$

$F_n(0, c) = 0 \qquad (n = 2, 3, 4, \ldots)$

$F_1(x, 0) = 1$

$F_n(x, 0) = \dfrac{x^{n-1}}{(n-1)!} \qquad (n = 2, 3, 4, \ldots)$ (A2)

(*ii*) $I_{n,m}(x, c, d) = \sum_{i=0}^{\infty} \binom{m+i-1}{i} d^i F_{n+m+i}(x, c)$

$\overset{L}{\Rightarrow} \dfrac{1}{(s+c-d)^m (s+c)^n} \qquad (n, m = 1, 2, 3, \ldots)$ (A3)

Particular values are

$$I_{0,m}(x, c, d) = F_m(x, c-d)$$
$$I_{n,0}(x, c, d) = F_n(x, c)$$
$$I_{n,m}(0, c, d) = 0 \quad (A4)$$

(*iii*) $H_{n,m,k}(x, c, d) = \sum_{j=0}^{\infty} \binom{m+j-1}{j} d^j$

$I_{n+m+j,k}(x, c, c) \overset{L}{\Rightarrow} \dfrac{1}{s^k (s+c-d)^m (s+c)^n}$

$(n, m, k = 1, 2, 3, \ldots)$ (A5)

Particular values are

$$H_{0,m,k}(x, c, d) = I_{m,k}(x, c-d, c-d)$$
$$H_{n,0,k}(x, c, d) = I_{n,k}(x, c, c)$$
$$H_{n,m,0}(x, c, d) = I_{n,m}(x, c, d)$$
$$H_{0,0,k}(x, c, d) = F_k(x, 0)$$
$$H_{0,m,0}(x, c, d) = F_m(x, c-d)$$
$$H_{n,0,0}(x, c, d) = F_n(x, c)$$
$$H_{n,m,k}(0, c, d) = 0 \quad (n, m, k = 1, 2, 3, \ldots) \quad (A6)$$

(*iv*) Integrals

$$\int_0^x F_n(u, c)\exp(\delta u)\,du = \begin{cases} F_{n+1}(x, 0) & (\delta = c) \\ I_{n,1}(x, 2c, 2c) & (\delta = -c) \\ I_{n,1}(x, c-d, c-d) & (\delta = d) \\ I_{n,1}(x, c+d, c+d) & (\delta = -d) \end{cases} \quad (A7)$$

$$\int_0^x I_{n,m}(u, c, d)\exp(\delta u)\,du = \begin{cases} I_{m,n+1}(x, -d, -d) & (\delta = c) \\ H_{n,m,1}(x, 2c, d) & (\delta = -c) \\ H_{n,m,1}(x, c-d, d) & (\delta = d) \\ H_{n,m,1}(x, c+d, d) & (\delta = -d) \end{cases} \quad (A8)$$

$$\int_0^x H_{n,m,k}(u, c, d)\exp(\delta u)\,du = \begin{cases} H_{k,m,n-1}(x, -c, d-c) & (\delta = c) \\ \sum_{r=0}^{\infty} (-1)^r \binom{k+r-1}{r} c^r H_{n,m,k+r+1}(x, 2c, d) & (\delta = -c) \\ \sum_{r=0}^{\infty} \binom{k+r-1}{r} d^r H_{n,m,k+r+1}(x, c-d, d) & (\delta = d) \\ \sum_{r=0}^{\infty} (-1)^r \binom{k+r-1}{r} d^r H_{n,m,k+r+1}(x, c+d, d) & (\delta = -d) \end{cases} \quad (A9)$$

Downloaded 17 Dec 2010 to 193.140.21.150. Redistribution subject to ASME license or copyright; see http://www.asme.org/terms/Terms_Use.cfm

B. Vick

J. H. Beale

Mechanical Engineering Department,
Virginia Polytechnic Institute
and State University,
Blacksburg, VA 24061

J. I. Frankel

Department of Mechanical Engineering,
Florida Institute of Technology,
Melbourne, FL 32901

Integral Equation Solution for Internal Flow Subjected to a Variable Heat Transfer Coefficient

A solution methodology based on integral equations is presented for the problem of heat transfer to laminar duct flow subjected to an axial variation of the external heat transfer coefficient. The technique offers an efficient and accurate calculation procedure which combines standard analytical methods with a simple numerical integration. In order to examine the effect of external finning, results are calculated for the cases of a stepwise periodic and a harmonic variation of the heat transfer coefficient for both fully developed laminar flow and slug flow. The general procedure is applicable to a wide class of problems in heat and mass transfer involving variable boundary condition parameters.

Introduction

Numerous engineering applications exist for convective heat transfer to internal flow where the external heat transfer coefficient varies along the axial direction. An important example is a duct fitted with an array of external fins. Since each fin increases the effective coefficient of heat exchange between the fin base and ambient, a duct fitted with an array of external fins can be modeled as an unfinned duct with periodically low and high values of the heat transfer coefficient, corresponding to unfinned and finned regions, respectively.

Although a wealth of theoretical investigations concerning heat transfer to forced flow in ducts, heat conduction, and mass diffusion has appeared in the literature, almost all the existing works have considered boundary conditions of specified temperature, specified heat flux, or convection with an external environment via a constant heat transfer coefficient. Only a few theoretical studies involving a variable boundary condition parameter exist in the literature. This is perhaps due to the failure of standard analytical techniques for such problems and the demanding computational task required to implement purely numerical schemes in the presence of abruptly changing boundary conditions.

Heat conduction with a time-dependent heat transfer coefficient was considered by Ozisik and Murray [1], who used a variable eigenvalue technique, and by Thompson and Holy [2], who developed an approximate solution using integral equations. The only works available concerning heat transfer to forced flow in ducts subject to an axial variation in the external heat transfer coefficient appear to be those of Sparrow and Charmchi [3] and Vick and Wells [4]. In [3], a finite difference scheme was applied to the case of a stepwise periodic variation of the heat transfer coefficient. However, the discontinuous nature of the boundary condition made the computational task quite demanding and a complete parameter study was not feasible. In [4], an exact analytical scheme using a variable eigenvalue approach was developed where special consideration was required for each particular variation of the heat transfer coefficient.

The purpose of the current investigation is to present a solution methodology for the problem of forced convection with an axial variation of the heat transfer coefficient. The basic approach is to use the standard Green's function technique to obtain a singular Volterra integral equation of the second kind for the surface temperature, which can then be resolved numerically by any standard integration procedure such as the trapezoid rule. The proposed methodology provides an efficient and straightforward combination of analytical and numerical methods which can be applied to a wide range of problems involving variable boundary condition parameters occuring in heat and mass transfer.

Contributed by the Heat Transfer Division for publication in the JOURNAL OF HEAT TRANSFER. Manuscript received by the Heat Transfer Division August 1, 1986.

Formulation

The present investigation is concerned with the following dimensionless equations:

$$\frac{v(\eta)}{2}\frac{\partial\theta}{\partial\xi}=\frac{1}{\eta^i}\frac{\partial}{\partial\eta}\left(\eta^i\frac{\partial\theta}{\partial\eta}\right)+S(\eta,\xi),\quad 0<\eta<1,\quad \xi>0 \tag{1a}$$

$$\frac{\partial\theta}{\partial\eta}=0,\quad \eta=0 \tag{1b}$$

$$\frac{\partial\theta}{\partial\eta}+H(\xi)\theta=0,\quad \eta=1 \tag{1c}$$

$$\theta=1,\quad \xi=0 \tag{1d}$$

The various dimensionless quantities are defined as follows:

$$\eta=r/r_0,\quad \xi=\frac{z/r_0}{\mathrm{Pe}} \tag{2a}$$

$$\mathrm{Pe}=\frac{2r_0\bar{u}}{\alpha},\quad v(\eta)=\frac{u(r)}{\bar{u}} \tag{2b}$$

$$\theta(\eta,\xi)=\frac{T(r,z)-T_\infty}{T_0-T_\infty} \tag{2c}$$

$$H(\xi)=\frac{h(z)r_0}{k} \tag{2d}$$

$$S(\eta,\xi)=\frac{\left[g(r,z)+\mu\left(\frac{\partial u}{\partial r}\right)^2\right]r_0^2}{k(T_0-T_\infty)} \tag{2e}$$

These equations describe the thermal entry region in a duct with steady, fully developed flow entering at constant temperature T_0. The geometry is specified by

$$i=\begin{cases}0, & \text{parallel plates}\\ 1, & \text{circular tube}\end{cases}$$

and a choice of fully developed velocity profile is included by specifying the form of the dimensionless velocity $v(\eta)$. Also a

Copyright © 1987 by ASME

Downloaded 17 Dec 2010 to 193.140.21.150. Redistribution subject to ASME license or copyright; see http://www.asme.org/terms/Terms_Use.cfm

source term $S(\eta, \xi)$ is included, which accounts for heat generation and viscous dissipation.

The primary interest with the system defined by equations (1) is the boundary condition at $\eta = 1$, which represents convection with an external environment through a variable heat transfer coefficient or Biot number, $H(\xi)$. The variable boundary condition parameter allows for the modeling of a variety of situations of engineering interest, including the case of a duct with external fins. However, mathematical difficulties arise since the variable Biot number renders the problem nonseparable, and as a result a solution by any of the standard analytical techniques is not possible, except for the special case of a constant Biot number [5, 6]. In the following section, a straightforward and efficient solution methodology is proposed which is well suited to handle problems with variable boundary condition coefficients.

Analysis

The problem of interest, as described by equations (1), is now solved by employing the Green's function technique to convert the original problem into a singular Volterra integral equation of the second kind for the surface temperature. The resulting integral equation can then be numerically integrated by a suitable integration scheme.

A Green's function is chosen which is governed by the following system of equations:

$$\frac{v(\eta)}{2}\frac{\partial G}{\partial \xi} = \frac{1}{\eta^i}\frac{\partial}{\partial \eta}\left[\eta^i \frac{\partial G}{\partial \eta_i}\right] + \delta^i(\eta-\eta_0)\delta(\xi-\xi_0), \quad 0 \le \eta < 1, \quad \xi > 0 \tag{3a}$$

$$\frac{\partial G}{\partial \eta} = 0, \quad \eta = 0 \tag{3b}$$

$$\frac{\partial G}{\partial \eta} + H_0 G = 0, \quad \eta = 1 \tag{3c}$$

$$G = 0, \quad \xi < \xi_0 \tag{3d}$$

where $G = G(\eta, \xi \,|\eta_0, \xi_0)$ is the Green's function or response function to a concentrated heat source released at location (η_0, ξ_0). The arguments are written so as to emphasize their effect/cause relationship.

An important feature of this choice of the Green's function is that the boundary condition at $\eta = 1$ is taken with a constant coefficient H_0, which can be chosen for convenience. The solution to equations (3) is readily obtainable by the finite integral transform technique [6], as outlined in the Appendix. The delta function in the radial variable, $\delta^i(\eta-\eta_0)$, has the normal interpretation for $i = 0$ (parallel plate), but is interpreted as a cylindrical delta function for $i = 1$ (circular tube).

Following the procedure given in Ozisik [6], the general solution to the system of equations (1) can be expressed in terms of the Green's function in the form

$$\theta(\eta, \xi) = \int_{\xi_0=0}^{\xi} [H_0 - H(\xi_0)]G(\eta, \xi \,|1, \xi_0)\theta(1, \xi_0)d\xi_0 + \int_{\eta_0=0}^{1} \eta_0^i \frac{v(\eta_0)}{2} G(\eta, \xi \,|\eta_0, 0)d\eta_0 + \int_{\xi_0=0}^{\xi}\int_{\eta_0=0}^{1} \eta_0^i G(\eta, \xi \,|\eta_0, \xi_0)S(\eta_0, \xi_0)d\eta_0 d\xi_0 \tag{4}$$

The first integral represents the effect of the variable heat transfer coefficient, the second integral represents the effect of the inlet temperature, and the third integral is due to the source term.

Since the surface temperature $\theta(1, \xi)$ is still unknown, equation (4) is evaluated at $\eta = 1$ to get

$$\theta(1, \xi) = \int_{\xi_0=0}^{\xi} K(\xi, \xi_0)\theta(1, \xi_0)d\xi_0 + f(\xi) \tag{5}$$

where

$$K(\xi, \xi_0) = [H_0 - H(\xi_0)]G(1, \xi \,|1, \xi_0) \tag{6}$$

and

$$f(\xi) = \int_{\eta_0=0}^{1} \eta_0^i \frac{v(\eta_0)}{2} G(1, \xi \,|\eta_0, 0)d\eta_0 + \int_{\xi_0=0}^{\xi}\int_{\eta_0=0}^{1} \eta_0^i G(1, \xi \,|\eta_0, \xi_0)S(\eta_0, \xi_0)d\eta_0 d\xi_0 \tag{7}$$

Equation (5) is a Volterra integral equation of the second kind for the surface temperature which can be resolved using a suitable integration technique. A numerical difficulty that is inherent in equation (5) is the singularity of the kernel $K(\xi, \xi_0)$ when its arguments are equal, i.e., $\xi_0 = \xi$. Since the Green's function is the response to a concentrated heat source, it becomes unbounded at the location of the concentrated source, thus giving rise to the singular kernel defined by equation (6). The singularity can also be seen mathematically by examining the Green's function $G(1, \xi \,|1, \xi_0)$, given by equation (A1) in the Appendix.

In order to alleviate this difficulty, the following singularity subtraction procedure is used to rewrite equation (5) as

Nomenclature

$f(\xi)$ = function defined by equation (7)
$g(r, z)$ = energy source
$G(\eta, \xi \,|\eta_0, \xi_0)$ = Green's function
$h(z)$ = heat transfer coefficient
$H(\xi)$ = Biot number
k = thermal conductivity
$K(\xi, \xi_0)$ = kernel
Pe = Peclet number
$Q(\xi)$ = total heat transfer
r = radial variable
r_0 = tube radius
$S(\eta, \xi)$ = dimensionless energy source
$T(r, z)$ = temperature
T_∞ = environment temperature
T_0 = inlet temperature
$u(r)$ = velocity profile
$\bar{u}$ = average velocity
$v(\eta)$ = dimensionless velocity
z = axial variable
α = thermal diffusivity
η = dimensionless radial variable
$\theta(\eta, \xi)$ = dimensionless temperature
$\theta_b(\xi)$ = dimensionless bulk temperature
λ_m = eigenvalue
μ = viscosity
ξ = dimensionless axial variable
$\psi_m(\eta)$ = eigenfunction

Downloaded 17 Dec 2010 to 193.140.21.150. Redistribution subject to ASME license or copyright; see http://www.asme.org/terms/Terms_Use.cfm

$$\theta(1,\xi)=\int_{\xi_0=0}^{\xi-\Delta\xi} K(\xi,\xi_0)\theta(1,\xi_0)d\xi_0 + \int_{\xi_0=\xi-\Delta\xi}^{\xi} K(\xi,\xi_0)[\theta(1,\xi_0)-\theta(1,\xi)]d\xi_0 + \theta(1,\xi)\int_{\xi_0=\xi-\Delta\xi}^{\xi} K(\xi,\xi_0)d\xi_0 + f(\xi) \tag{8}$$

where $\Delta\xi$ is the axial step size used in the numerical integration. Equation (8) is now in a form suitable for direct numerical integration. The integrand in the first integral contains all bounded values over the range of integration and therefore provides no difficulties. The integrand in the second integral vanishes at the upper limit of integration, successfully canceling the singular point of the kernel. Although the kernel is singular, it is integrable and the third integral in equation (8) can be evaluated. In fact, this integral can be evaluated analytically for many variations of the convection coefficient. In the following section, numerical results are presented that were obtained by integrating equation (8) using the trapezoid rule with the integration beginning at the duct entrance and continuing downstream by increments of $\Delta\xi$.

Once values for the wall temperature are available, the bulk temperature can immediately be obtained from a numerical integration of the following energy balance:

$$\theta_b(\xi)=1-2^{i+1}\int_{\xi'=0}^{\xi} H(\xi')\theta(1,\xi')d\xi' + 2^{i+1}\int_{\xi'=0}^{\xi}\int_{\eta=0}^{1}\eta^i S(\eta,\xi')d\eta d\xi' \tag{9}$$

Another quantity of interest is the total heat transfer, which in the absence of energy sources ($S = 0$) is given by

$$Q(\xi)=1-\theta_b(\xi) \tag{10}$$

The quantity $Q(\xi)$ represents the total energy transferred from the fluid at location ξ, divided by the total energy transferred as a condition of thermal saturation is reached at sufficiently large ξ.

The solution is now complete with the wall temperature and bulk temperature available from equations (8) and (9), respectively. For the special case of $H(\xi) = H_0$, the kernel defined by equation (6) becomes zero and equations (4), (5), and (8) reduce to the exact analytical solution. In the following section, some representative results are presented.

Results and Discussion

Equations (8) and (9) for the wall and bulk temperature are now used to generate numerical results. A circular tube ($i = 1$) with no heat sources ($S = 0$) with either fully developed laminar flow or slug flow is considered. The dimensionless velocity profiles are

$$v(\eta)=\begin{cases}2(1-\eta^2), & \text{laminar flow (tube)}\\ 1, & \text{slug flow}\end{cases} \tag{11}$$

The influence of the velocity profile shows up directly in the eigenvalue problem, given by equations (A2) in the Appendix. The eigenfunctions generated from the eigenvalue problem are used in turn to generate the Green's function, given by equation (A1).

An important numerical consideration is the rate of convergence of the infinite series expression for the Green's function, equation (A1), which is required for the kernel defined by equation (6). Clearly, the slowest convergence will occur for $\xi-\xi_0 = \Delta\xi$, since the singularity subtraction employed in equation (8) alleviates the need to evaluate the Green's function at its singular point, $\xi-\xi_0 = 0$. Also, the case of laminar flow results in slightly slower convergence than slug flow since the eigenvalues do not grow as fast. The value chosen for H_0 does not play a significant role in the rate of convergence since it merely shifts the eigenvalues by a small amount. Results obtained on the computer indicate that the number of terms required for convergence is proportional to $(\Delta\xi)^{-1/2}$ for the laminar flow case. Specifically, for the sum to converge to within 99.9 percent of its final value, about 200 terms are required for $\Delta\xi = 0.00001$, 65 terms for $\Delta\xi = 0.0001$, and for $\Delta\xi = 0.001$ only 20 terms are needed.

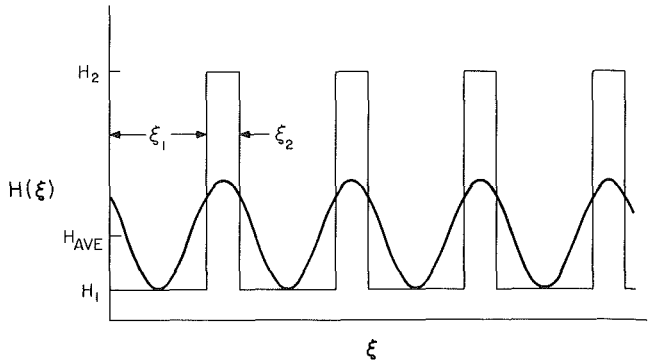

Fig. 1 External heat transfer coefficient variations

For the results which follow, consideration is given to both a stepwise periodic and a harmonic variation of the Biot number, as depicted in Fig. 1. The stepwise periodic model was considered in [3, 4] and serves as a model for a tube with external fins with regions of low Biot number H_1, corresponding to unfinned areas, and regions of high Biot number H_2, corresponding to finned areas. The harmonic variation has a minimum value of H_1 but the maximum value has been adjusted such that the average value of $H(\xi)$ over a cycle is the same for both variations. Although still somewhat arbitrary, this allows for a relevant comparison for heat transfer results using the two Biot number distributions. The harmonic variation is expected to be closer to the actual Biot number experienced by a duct fitted with fins since axial heat conduction in the walls tends to smooth out the abrupt changes between H_1 and H_2.

Numerical results were obtained using equations (8) and (9) by simply subdividing the integrals into regions of length $\Delta\xi$ and then using the trapezoid rule in each subdivision. Starting from the duct inlet, the wall temperature can be calculated by marching downstream and obtaining values at each successive location. This procedure produced results which were indistinguishable from those in [3, 4] for the bulk temperature in the stepwise periodic case. For the wall temperature in the periodic case and the harmonic case, no results appear to be available in the literature for comparison. If refined accuracy is desired, a higher order block-by-block method could be employed, at the expense of a more complicated computational algorithm.

The most critical numerical parameter is the axial step size $\Delta\xi$, since it affects both the convergence of the Green's function and the accuracy of the numerical integration. As the Biot number increases, $\Delta\xi$ must decrease in order to accommodate the rapidly changing wall temperature. Also, the step size must be small enough to pick up the effects of any variation in $H(\xi)$, like the harmonic function shown in Fig. 1 (typically 10 to 15 steps per cycle).

Figures 2 and 3 display the wall and bulk temperatures for both the stepwise and harmonic variations of the Biot number. The results are for fully developed laminar flow in a tube. Figure 2 displays results for the first few cycles with $H_1 = 1$, $\xi_1 = 0.003$, and $H_2 = 50$, $\xi_2 = 0.001$, which gives an average Biot number of $H_{av} = 13.25$. Each set of results in Fig. 2 took approximately 15 s on an IBM 3090 using an axial step size of $\Delta\xi = 0.0001$.

Downloaded 17 Dec 2010 to 193.140.21.150. Redistribution subject to ASME license or copyright; see http://www.asme.org/terms/Terms_Use.cfm

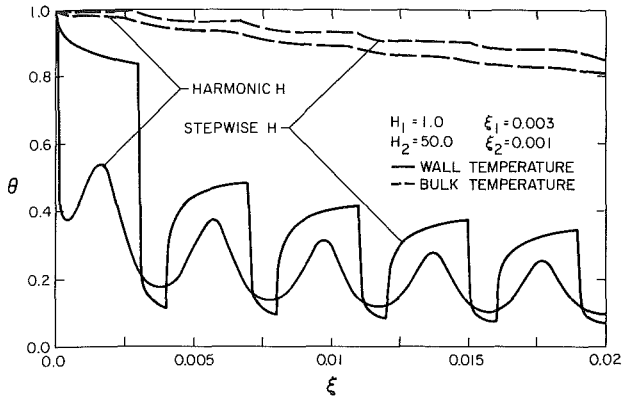

Fig. 2 Comparison of wall and bulk temperatures for stepwise and harmonic variations of the external convection coefficient for fully developed laminar flow in a tube

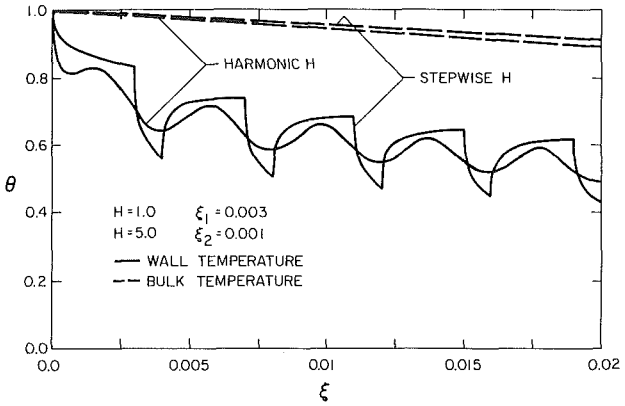

Fig. 3 Comparison of wall and bulk temperatures for stepwise and harmonic variation of the external convection coefficient for fully developed laminar flow in a tube

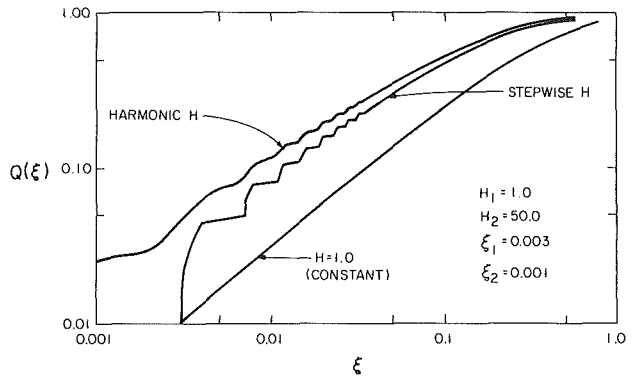

Fig. 4 Total heat transfer results, showing the effect of the convection coefficient for fully developed laminar flow in a tube

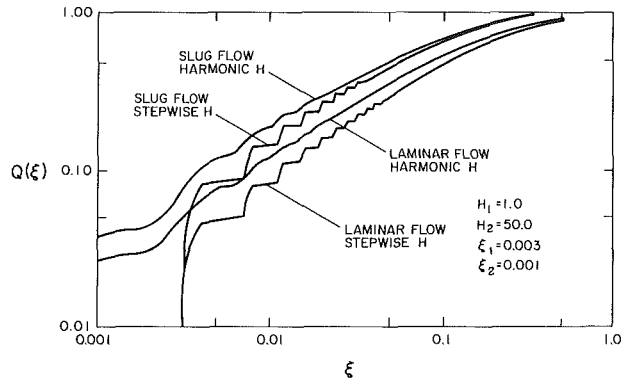

Fig. 5 Total heat transfer results, showing the effect of velocity profile and convection coefficient

The wall temperature for the stepwise periodic case drops sharply in regions of high H and then rises sharply in regions of low H. In this case, the value $H_1 = 1$ is low enough so as to cause an insulating effect. For the harmonic case, the wall temperature rises and falls more gradually, as would be expected from a gradually changing convection coefficient. The occurrence of the minimum and maximum values of the wall temperature, however, lags the occurrence of the minimum and maximum values of the Biot number. Although the wall temperature settles into a repetitive pattern, the magnitude is steadily dropping in each successive cycle as the fluid approaches the dimensionless ambient temperature of zero.

Consistent with basic energy considerations, the bulk temperatures shown in Fig. 2 decline continually. The stepwise periodic case shows a small drop in regions of low H and a larger drop in regions of high H. The most severe drops occur at the beginning of a high Biot number region, since the wall temperature has just risen to its greatest value during the cycle. The bulk temperature curve for the harmonic case drops in a more steady fashion in response to the more gradual changes in Biot number. Although the average Biot number is identical for both cases, the bulk temperature is lower in the harmonic case, indicating a greater amount of heat removed from the fluid. As a result, the effect of smoothing the heat transfer coefficient by axial conduction in the tube wall is expected to be advantageous for heat exchanger applications where external fins are required.

Figure 3 shows results similar to those of Fig. 2 except the value of H_2 has been lowered to 5, giving an average value of $H_{av} = 2$. The wall temperatures have the same characteristics as in Fig. 2, except that the magnitudes are higher due to a decrease in heat transfer. In this case, however, the bulk temperatures for the two variations are nearly identical, with the harmonic distribution still slightly lower. Thus the precise distribution of the heat transfer coefficient is more important in calculating heat transfer when a relatively large degree of enhancement (large H_2) or very effective fins are used.

In Figs. 4 and 5 the total heat transfer, which is defined by equation (10), is examined. The total heat transfer is a meaningful way to display the advantages of heat transfer enhancement due to finning. Figure 4 shows the effect of the assumed variation of the Biot number on the total heat transfer for fully developed laminar flow. Displayed along with the stepwise and harmonic variations is the constant case with $H(\xi) = H_1 = 1$, which represents a tube with no heat transfer enhancement. On the log scale used in Fig. 4, the abrupt changes caused by the stepwise periodic variation in the Biot number are clearly shown. The overall enhancement of the total heat transfer over the case of constant Biot number is quite significant for both the assumed distributions with the harmonic variation more effective. Thus, for heat exchange equipment where precise performance calculations or optimization is critical, an analysis coupling the fluid with the conduction in the wall and fin could be warranted.

Figure 5 shows the influence of the assumed velocity profile. The fully developed laminar and slug flow profiles give qualitatively similar results, but the total heat transfer with slug flow is greater due to the decreased internal resistance induced by greater velocity near the wall. The slug flow results are expected to be more representative of a turbulent flow due to the greater heat transport near the wall.

Downloaded 17 Dec 2010 to 193.140.21.150. Redistribution subject to ASME license or copyright; see http://www.asme.org/terms/Terms_Use.cfm

Summary and Conclusions

The purpose of this investigation is to propose a solution methodology and present results for the problem of fully developed internal flow subject to an axial variation of the heat transfer coefficient. This seemingly simple generalization to include a variable boundary condition parameter adds surprising complexity over the case of a constant coefficient since standard analytical schemes fail and purely numerical schemes can require excessive computer time to accommodate abruptly changing boundary conditions. The present solution offers an alternative using Green's functions to derive a singular Volterra integral equation of the second kind for the wall temperature, which is then integrated numerically with the aid of singularity subtraction. Although higher order integration schemes may be employed, a simple trapezoidal rule produces accurate results with very reasonable computer time.

Results are presented for both a stepwise periodic and a harmonic variation of the Biot number using both fully developed laminar flow and slug flow. With equal average Biot numbers over a cycle, the harmonic distribution gave a greater heat transfer rate. The difference in heat transfer predictions using the different Biot number models is significant for relatively large changes in Biot number (H_2/H_1 large) while for relatively small changes in Biot number over a cycle, the specific variation is unimportant as long as the average value remains constant. In all cases, the wall temperature is very sensitive to the Biot number distribution. The effect of the slug flow velocity profile is to give higher heat transfer rates than the fully developed laminar flow due to decreased thermal resistance near the wall.

In general, a large class of problems in heat and mass transfer involving variable boundary condition parameters can be solved efficiently using the proposed methodology.

Acknowledgments

This work was supported by the National Science Foundation through grant number MEA-8403964.

References

1 Ozisik, M. N., and Murray, R. L., "On the Solution of Linear Diffusion Problems With Variable Boundary Condition Parameters," ASME JOURNAL OF HEAT TRANSFER, Vol. 96, 1974, pp. 48–51.

2 Thompson, J. J., and Holy, Z. J., "Axisymmetric Thermal Response Problems for a Spherical Fuel Element With Time Dependent Heat Transfer Coefficient," *Nuclear Engineering and Design*, Vol. 9, 1969, pp. 29–44.

3 Sparrow, E. M., and Charmchi, M., "Laminar Heat Transfer in an Externally Finned Circular Tube," ASME JOURNAL OF HEAT TRANSFER, Vol. 102, 1980, pp. 605–611.

4 Vick, B., and Wells, R. G., "Laminar Flow With an Axially Varying Heat Transfer Coefficient," *International J. Heat Mass Transfer*, Vol. 29, 1986, pp. 1881–1890.

5 Javeri, V., "Heat Transfer in Laminar Entrance Region of a Flat Channel for the Temperature Boundary Condition of the Third Kind," *Wärme- und Stoffübertragung*, Vol. 10, 1977, pp. 137–144.

6 Ozisik, M. N., *Heat Conduction*, Wiley, New York, 1980.

7 Wells, R. G., "Laminar Flow With an Axially Varying Heat Transfer Coefficient," M. S. Thesis, VPI&SU, Blacksburg, VA, 1986, pp. 104–107.

8 Lauwerier, H. A., "The Use of Confluent Hypergeometric Functions in Mathematical Physics and the Solution of an Eigenvalue Problem," *Applied Science Research*, Vol. A.2, 1950, pp. 184–204.

APPENDIX

Determination of the Green's Function

A necessary ingredient required for equations (8) and (9) is the Green's function itself, as governed by equations (3). The finite integral transform technique, as described in [6], is employed to obtain the desired Green's function in the form

$$G(\eta, \xi \mid \eta_0, \xi_0) = \sum_{m=1}^{\infty} \frac{\psi_m(\eta)\psi_m(\eta_0)}{N(\lambda_m)} \exp[-\lambda_m^2(\xi - \xi_0)] \tag{A1}$$

The eigenvalues λ_m, and eigenfunctions $\psi_m(\eta)$, are obtained from the solution of the following:

$$\frac{d}{d\eta}\left[\eta^i \frac{d\psi_m}{d\eta}\right] + \lambda_m^2 \eta^i \frac{v(\eta)}{2} \psi_m = 0 \tag{A2a}$$

$$\frac{d\psi_m}{d\eta} = 0, \quad \eta = 0 \tag{A2b}$$

$$\frac{d\psi_m}{d\eta} + H_0 \psi_m = 0, \quad \eta = 1 \tag{A2c}$$

The normalization integral is defined as

$$N(\lambda_m) = \int_{n=0}^{1} \eta^i \frac{v(\eta)}{2} \psi_m^2(\eta) d\eta \tag{A3}$$

Calculations in the present investigation were performed for both laminar flow in a tube ($i = 1$, $v(\eta) = 2(1-\eta^2)$) and slug flow in a tube ($i = 1$, $v(\eta) = 1$). The details of the solution of eigenvalue problem (A2) for laminar flow in a tube can be found in [7], where eigenfunctions corresponding to the smaller eigenvalues were generated using confluent hypergeometric functions and the solutions for larger eigenvalues were generated using the asymptotic method of Lauwerier [8]. For the case of slug flow in a tube, the eigenvalue problem (A2) generates Bessel functions, as summarized in [6, Table 3-1, p. 92].

A characteristic of the eigenvalues is that the difference between two consecutive eigenvalues asymptotically approaches a constant. For slug flow this constant is $\pi\sqrt{2}$ and for laminar flow the constant is 4.0. Also, the square of the normalized eigenfunctions approaches a constant value asymptotically. In all cases these asymptotic values are independent of the value chosen for H_0.

Downloaded 17 Dec 2010 to 193.140.21.150. Redistribution subject to ASME license or copyright; see http://www.asme.org/terms/Terms_Use.cfm

A Wall Function for the Temperature Variance in Turbulent Flow Adjacent to a Diabatic Wall

Y. L. Sinai
R&D Technology Department,
National Nuclear Corporation Limited,
Risley, Warrington,
Cheshire WA3 6BZ, United Kingdom

By assuming simple initial conditions for a surface-renewal calculation of thermal coupling between a thick solid and a well-mixed, low-Prandtl-number fluid, it has been possible to approximate the temperature variance near the wall in terms of a straightforward quadrature. Comparisons have been made with several experiments. The results are aimed at numerical solutions of the turbulent variance transport equation, which has thus far been solved with ad-hoc boundary conditions applied at solid walls.

Introduction

There are several instances in which information about the magnitude of the temperature variance σ_T^2 $(=\overline{T'^2})$ is important. For example (Launder, 1978; Hirata et al., 1982), the turbulent heat-flux equation is coupled to σ_T in flows which are influenced by buoyancy, and there are circumstances in which σ_T affects the mechanical integrity of solid structures immersed in, or containing, the turbulent fluid.

Currently, there is apparently a dearth of methods for predicting temperature fluctuations near and at the surface of a wall that is in contact with a turbulent flow. One route which immediately springs to mind would utilize the simplest of all turbulent transport equations, that for σ_T^2, even if it is appreciated that the results would be of limited value in domains of low intermittency. The equation has been modeled and solved by many workers (Launder, 1978; Hirata et al., 1982), but it seems that usually, arbitrary boundary conditions have been applied at solid surfaces, like $\sigma_T = 0$ or $\partial\sigma_T/\partial n = 0$ (where n is a normal coordinate). Generally, such boundary conditions are incorrect, and under those circumstances in which a time-mean heat flux passes through the wall the present paper provides an approximation to the wall function of σ_T^2. Such a wall function is analogous to those which are widely employed in numerical solutions of the momentum and energy equations (Launder and Spalding, 1972), although it is confined to the inner region. The variance equation is

$$\frac{D\sigma_T^2}{Dt} = -2\overline{u_j T'}\frac{\partial T}{\partial x_j} - 2\lambda\overline{\left(\frac{\partial T'}{\partial x_j}\right)^2} - \frac{\partial}{\partial x_j}\left(\overline{u_j T'^2} - \lambda\frac{\partial \sigma_T^2}{\partial x_j}\right) \tag{1.1}$$

The terms on the right-hand side represent, respectively, production, dissipation, and diffusion, and the various closures which have been proposed for these terms have related them to the molecular properties, the turbulent viscosity, the mean temperature, and σ_T itself. Hence, the equation can be solved once the second and third of these quantities are known, although a strong coupling may be anticipated between the variance equation on the one hand and the turbulence and thermal energy equations on the other when buoyancy is significant. The wall function proposed here would provide the boundary condition at a solid surface, since it describes σ_T in terms of the local time-mean heat flux, shear stress, and distance from the wall, whether these quantities are the true values or approximations from numerical iterations.

The theory outlined here is based on the surface-renewal model, which has been revived and generalized in recent years because of mounting experimental evidence in its support. Only a brief outline will be given here and the reader is referred to Danckwertz (1970), Davies (1972), and Cantwell (1981) for more details.

Experiments on the flows in the wall regions of turbulent boundary layers, dating back to the 1930s, conflict with the classical view of steady laminar behavior in that region, and have led some workers to prefer the term "viscous" to "laminar."

The flow at a given point in the wall region is laminar-like but is punctuated by violent, rapid processes known as the burst and sweep, with a mean period between bursts around $250\nu/u_*^2$ (Thomas, 1982; Blackwelder and Haritonidis, 1983). During a burst, part of the low-speed fluid is ejected upward ($u' < 0$, $v' > 0$) toward the fluid bulk, and immediately afterward, during the "sweep" phase, high-momentum fluid ($u' > 0$, $v' < 0$) replenishes the ejected fluid. A long, tranquil period follows, during which molecular diffusion dominates, until the next burst signals a repetition of the cycle. As regards heat and mass transfer, researchers have found it necessary to include the influences of a thin, unreplenished layer at the wall in the so-called "surface rejuvenation" theory, when Prandtl or Schmidt numbers are moderate or high (e.g., Thomas, 1980).

In discussing these theoretical models it would probably be helpful to classify them into two categories. Both begin with a simplified governing equation, invariably of the diffusion type, and consider the deterministic problem representing molecular transfer from $t = 0$, the instant of in-rush, until $t = \theta$, the instant of bursting. Models in the "periodic" category, based on Higbie's work (1935), regard the process as purely harmonic with frequency ω, and calculate time-mean quantities over a period $t = \theta$. The "quasi-stochastic" methods, on the other hand, introduce an ergodic element to the calculation by accounting for the continuous distribution of eddy ages. The Danckwerts formalism (e.g., Hanratty, 1956; Davies 1972), used in this paper, has been popular and is particularly convenient because it leads to integrals resembling Laplace transforms, for which extensive tables are available.

In heat transfer analyses the vast majority of papers have assumed that during the deterministic calculation the boundary condition at the wall surface is one of either constant temperature or constant heat flux, so that with one exception thermal coupling between fluid and solid has generally been unrealistically modeled. That exception is the work of Meek and Baer (1973), in which a periodic surface-rejuvenation calculation accounts for the coupling in the correct manner, in the presence of a time-mean heat flux. Formally, Meek and Baer's analysis can be regarded as satisfactory and complete,

Contributed by the Heat Transfer Division for publication in the JOURNAL OF HEAT TRANSFER. Manuscript received by the Heat Transfer Division July 8, 1986.

 Copyright © 1987 by ASME

Downloaded 17 Dec 2010 to 193.140.21.150. Redistribution subject to ASME license or copyright; see http://www.asme.org/terms/Terms_Use.cfm

albeit with an emphasis on high Pr and Sc. As will be elaborated below, penetration theories require specification of "initial conditions," distributions of the dependent variables at the instant of sweep, and successful results have been obtained for the fluid by assigning a uniform distribution of momentum, temperature or concentration to the penetrating eddy. Of course, such a kinematic constraint cannot be utilized in the solid, where no eddies exist, and in the spirit of the period approach Meek and Baer searched for an initial temperature distribution $T_s(y)$ in the solid such that

$$T_s(y, \theta) = T_{s_0}(y) \tag{1.2}$$

where $T_s(y, t)$ is the transient distribution in the solid. T_{s_0} was determined by a numerical, iterative scheme which can contribute significantly to computational time and costs of typical engineering calculations, since the scheme has to be implemented at each boundary element in codes which themselves iterate on the whole flow field sometimes hundreds or thousands of times (e.g., Patankar, 1980). The present paper assumes a simple, if somewhat crude T_{s_0}, which is no more than Meek and Baer's initial guess for their numerical iteration, but this leads to closed-form solutions which sacrifice some accuracy for the sake of much greater convenience. The current theory is aimed at fluids having small Prandtl numbers and at heat transfer to a well-mixed fluid.

Theory

The prototype problem in the present calculation involves a plane interface separating the semi-infinite solid from the semi-infinite fluid (see Fig. 1). Only transport normal to the interface is considered, so that the processes in both the solid and the fluid are governed by the one-dimensional diffusion equation

$$\frac{\partial^2 T_f}{\partial y^2} - \frac{1}{\lambda_f}\frac{\partial T_f}{\partial t} = 0, \qquad y < 0 \tag{2.1}$$

$$\frac{\partial^2 T_s}{\partial y^2} - \frac{1}{\lambda_s}\frac{\partial T_s}{\partial t} = 0, \qquad y > 0 \tag{2.2}$$

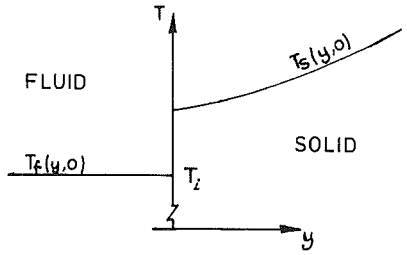

Fig. 1 General initial conditions for the surface-renewal calculation

The initial conditions are

$$T_f(y, 0) = 0, \qquad T_s(y, 0) = T_{s_0}(y) \tag{2.3}$$

The temperatures all use T_i as a datum, where T_i is the temperature assigned to the replenishing eddy. For moderate and high Pr, T_i may be taken to equal T_∞, but greater care is required when dealing with small Prandtl number (Thomas, 1980; Meek and Baer, 1973; and equation 2.6, which defines T_i in terms of the mean interfacial temperature $\bar{T}_w$ and the friction temperature T_*). Here, the assumption is made that T_{s_0} is linear for all $y > 0$

$$T_{s_0} = T_0 + \bar{q}_w y / k_s \tag{2.4}$$

where T_0 will be chosen shortly. Now the Danckwerts theory (Thomas, 1982) states that under steady conditions the time-averaged value of some quantity z is given by:

$$\bar{z} = \omega \hat{z}(\omega) \tag{2.5a}$$

$$\hat{z}(\omega) = L[z(t); t \to \omega] = \int_0^\infty e^{-\omega t} z(t) dt \tag{2.5b}$$

Here L denotes a Laplace transform, with t being mapped to ω in the specific case of equation (2.5*b*).

The classical result (Davies, 1972) then follows

$$\bar{q}_w = (\omega \alpha_f)^{1/2} \bar{T}_w \tag{2.6}$$

With equation (2.4) the solution is particularly simple, and by

Nomenclature

c = specific heat (at constant pressure for a fluid)
k = thermal conductivity
Pr = laminar Prandtl number = ν/λ
Pr_t = turbulent Prandtl number
q = heat flux
Re = Reynolds number
R_0 = tube radius
Sc = Schmidt number
s = Laplace transform variable
t = time
T = temperature, using T_i as a datum
T_i = reference temperature of sweeping eddy
$T_{s_0}(y)$ = initial temperature distribution in the solid
T_0 = $T_{s_0}(0)$
T_∞ = free-stram temperature (external flow)
T_* = friction temperature = $\bar{q}_w/\rho_f c_f u_*$
u, v, w = fluid velocity components
u_* = friction velocity = $(\tau_w/\rho_f)^{1/2}$
x, y, z = Cartesian coordinate system
Y = $-y$
Y_T = nondimensional height of inner region
Y_+ = $u_* Y/\nu_f$
α = $\rho c k$
β = $\Gamma_f/\Gamma_s(\alpha_f/\alpha_s)^{1/2}$
γ = $1/\beta$
Γ = thermal responsivity = $\alpha^{1/2}$
Δ = $\Gamma_f + \Gamma_s$
η = $(\Omega \mathrm{Pr})^{1/2}$
θ = mean burst period = $1/\omega$
λ = thermal diffusivity = $k/\rho c$
μ = $(s/\lambda)^{1/2}$
ν = momentum diffusivity
ξ = ηY_+
ρ = density
σ_z = rms value of z', $(\overline{z'^2})^{1/2}$
$\tilde{\sigma}_{T_f}$ = $\sigma_{T_f}/\sigma_{T_w}$, equation (2.11)
σ_{T_∞} = $\tilde{\sigma}_{T_f}$ as $\xi \to \infty$, equation (2.13)
τ = mean shear stress
ψ = equation (2.11*b*)
ω = mean burst frequency, Hz
Ω = $\nu_f \omega / u_*^2$

Superscripts

$\bar{}$ = time average
$'$ = flluctuation component
$\hat{}$ = transform with respect to time, with t mapped to s

Subscripts

f = fluid
j = f or s
s = solid
w = at solid/fluid interface

Downloaded 17 Dec 2010 to 193.140.21.150. Redistribution subject to ASME license or copyright; see http://www.asme.org/terms/Terms_Use.cfm

imposing consistency on $\bar{T}_w$ within the framework of equation (2.5), T_0 is found to be equal to $\bar{T}_w$, leading to

$$\frac{\sigma_{T_w}}{T_*} = \frac{\beta}{(1+\beta)}\left[\frac{(4-\pi)\mathrm{Pr}}{\pi\Omega}\right]^{1/2}; \quad \beta = \Gamma_f/\Gamma_s \tag{2.7}$$

where T_* is the friction temperature and the bursting frequency has been normalized as $\omega = \Omega u_*^2/\lambda_f$ (Thomas, 1982; Blackwelder and Haritonidis, 1983), where $\Omega \simeq 0.004$. Now consider $y<0$; taking Laplace transforms of equations (2.1) and (2.2), mapping t to s, leads to:

$$\hat{T}_f(y, s) = Ae^{\lambda_f y} \tag{2.8a}$$

$$\hat{T}_s(y, s) = \frac{1}{s}(\bar{T}_w + \bar{q}_w y/k_s) + Be^{-\lambda_s y} \tag{2.8b}$$

where

$$A(s) = \frac{\bar{q}_w}{\Delta}\left(\frac{1}{s^{3/2}} + \frac{1}{\beta\omega^{1/2}s}\right)$$

$$B(s) = \frac{\bar{q}_w}{\Delta}\left(\frac{1}{s^{3/2}} - \frac{1}{\beta\omega^{1/2}s}\right) \tag{2.8c}$$

$$\mu_j^2 = s/\lambda_j; \quad \Delta = \Gamma_f + \Gamma_s$$

Inverting equation (2.8a)

$$T_f(y, t) = \frac{\bar{q}_w}{\Delta}\left\{\phi + \frac{1}{\beta\omega^{1/2}}\,\mathrm{erfc}\left[\frac{Y}{2(\lambda_f t)^{1/2}}\right]\right\} \tag{2.9a}$$

$$\phi(y, t) = \frac{\eta Y_+}{(4\pi\omega)^{1/2}}\Phi\left(\frac{\eta^2 Y_+^2}{4\omega t}\right) \tag{2.9b}$$

$$\Phi(z) = 2z^{-1/2}e^{-z} - 2\pi^{1/2}\mathrm{erfc}(z^{1/2}) \tag{2.9c}$$

Here η equals $(\Omega\mathrm{Pr})^{1/2}$. Substituting in the relation

$$\sigma_{T_f}^2 = \omega\int_0^\infty e^{-\omega t}T_f^2(Y, t)dt - \omega^2\hat{T}_f^2(Y, \omega) \tag{2.10}$$

finally yields

$$\tilde{\sigma}_{T_f}^2 = \frac{\pi}{(4-\pi)}[\psi(\xi) - (\gamma+1)^2e^{-2\xi}] \tag{2.11a}$$

where erfc is the complementary error function (Abramowitz and Stegun, 1965)

$$\psi(\xi) = \int_0^\infty e^{-x}\left[2\left(\frac{x}{\pi}\right)^{1/2} + (\gamma-\xi)\mathrm{erfc}\left(\frac{\xi}{2x^{1/2}}\right)\right]^2 dx \tag{2.11b}$$

and $\tilde{\sigma}_{T_f}$ is σ_{T_f} normalized with respect to its value at the wall.

Two asymptotic results are useful; for small ξ

$$\tilde{\sigma}_{T_f} \sim 1 + \gamma\left(\frac{\pi-2}{4-\pi}\right)\xi + 0(\xi^2), \quad \xi \to 0 \tag{2.12}$$

On the other hand, for large ξ

$$\tilde{\sigma}_{T_f} \sim \sigma_{T_\infty}, \quad \sigma_{T_\infty} = \left(\frac{4}{4-\pi}\right)^{1/2} \simeq 2.16, \quad \xi \to \infty \tag{2.13}$$

It must be emphasized, though, that $\tilde{\sigma}_{T_f}$ does not necessarily increase monotonically between 1 and σ_{T_∞}. Equation (2.11) constitutes the principal result of this paper. It relates the variance to the physical properties of the two media and to the local shear stress and heat flux. Ω may reflect a Reynolds number dependence, as discussed below.

Discussion

Generally, ψ cannot be determined analytically, but it is easily evaluated as a quadrature on a computer, provided the lower limit is replaced by a finite, small number. This has been done, and the results are shown in Fig. 2, as $\tilde{\sigma}_{T_f}$ versus ξ for several values of β.

As predicted by equation (2.13), all the curves are asymptotic to σ_{T_∞} as $\xi \to \infty$, but it should be remembered that the

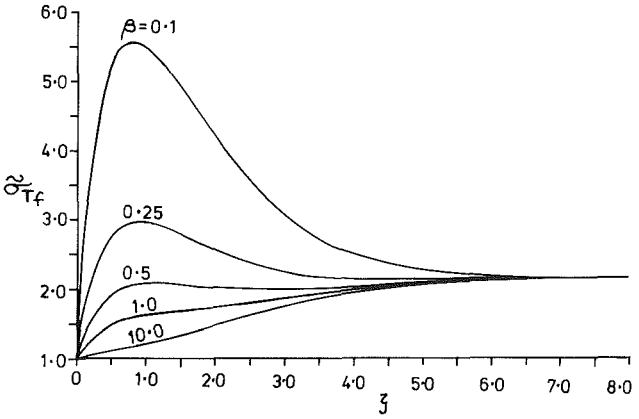

Fig. 2 The fluid rms temperature fluctuation, normalized with respect to its value at the solid/fluid interface, as a function of nondimensional distance from the wall

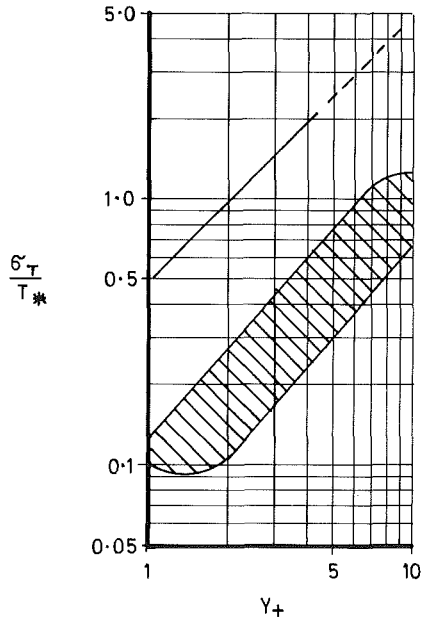

**Fig. 3 Comparison of equation (2.12) with the measurements of Tanimoto and Hanratty (1963) in air: theory: _____; experiment: **

present theory only applies within an inner region. The extent of the inner region can, in principle, be determined by invoking the proposition made by Thomas (1980), whereby the inner law is matched to the classical intermediate region by considering the mean fluid temperature. This leads to

$$(1 + K\mathrm{Pr}_t^{-1}\mathrm{Pr}\,Y_T)e^{-\eta Y_T} = 1 \tag{3.1}$$

where Y_T denotes the value of Y_+ representing the limit of the present model's domain of validity.

It turns out that equation (3.1) does not always possess a solution: Indeed, examination of the expression for small Y_T shows that no solution will exist if

$$\mathrm{Pr} < \Omega(\mathrm{Pr}_t/K)^2; \quad \text{no solution} \tag{3.2}$$

To the author's knowledge, the bursting frequencies for flow of low-Prandtl-number fluids have not been measured extensively, but if the value quoted above is true, then equation (3.2) indicates that for some liquid metals no solution to equation (3.1) will exist. However, the absence of a solution to equation (3.1) under certain circumstances is a minor issue as far as the present theory is concerned, although it does merit investigation; certainly, restricting the proposed wall function,

Downloaded 17 Dec 2010 to 193.140.21.150. Redistribution subject to ASME license or copyright; see http://www.asme.org/terms/Terms_Use.cfm

Table 1 Experimental conditions (Hochreiter and Sesonske, 1969)

Re	Pe	U_b, ft s^{-1}	u_*, ft s^{-1}	$\bar{q}_w$, Btu s^{-1} ft^{-2}	T_b, °F	T_*, °F
26,800	690	2.1	0.12	3.406	216	2.10
41,500	1160	3.5	0.18	3.297	171	1.27
56,900	1300	4.2	0.21	3.314	256	1.14

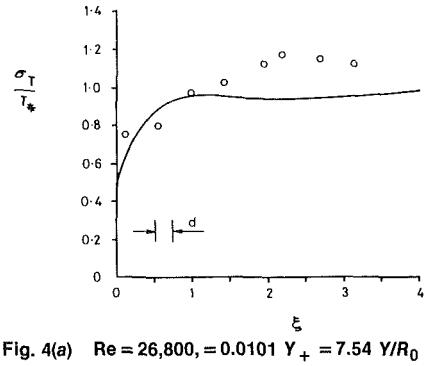

Fig. 4(a) Re = 26,800, = 0.0101 Y_+ = 7.54 Y/R_0

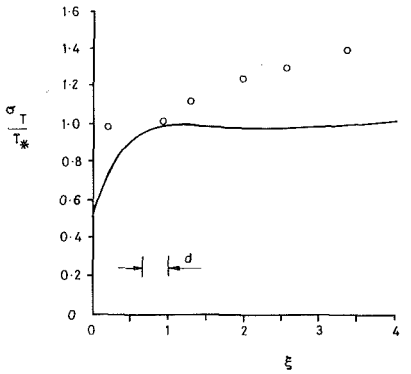

Fig. 4(b) Re = 41,500, = 0.0106 Y_+ = 11.5 Y/R_0

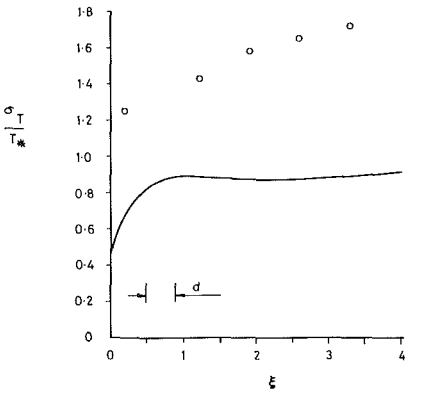

Fig. 4(c) Re = 56,900, = 0.00955 Y_+ = 13.7 Y/R_0

Fig. 4 Comparison of theory with the measurements of Hochreiter and Sesonske (1969) for NaK-56 flowing in a stainless steel tube. Theory: ———; experiment: ○; *d* is the probe diameter

equation (2.11), to $Y_+ < 100$ for liquid metals would be a safe step to take (see Thomas, 1970).

Considerable data for the wall region in air have been given by Tanimoto and Hanratty (1963), although no details were given of the tubing. Their measurements at different axial locations in developing pipe flow exhibited a near-linear profile qualitatively similar to equation (2.12). The latter equation predicts (assuming mild steel tubing, Pr = 0.7, $\gamma = 3620$, $\eta \simeq 0.053$)

$$\sigma_{T_f}/T_* \sim 1.9 \times 10^{-3} + 0.49 Y_+, \quad Y_+ << 19 \tag{3.3}$$

This asymptotic result is compared with Tanimoto and Hanratty's measurements in Fig. 3; while the prediction may be regarded as qualitatively adequate, there are significant discrepancies in amplitude and this suggests that the surface-renewal theory should only be applied to fluids having small Pr when considering rms fluctuations of temperature (or concentration), even though it has been found to be quite acceptable for moderate Pr and Sc as regards mean velocity, temperature and concentration (Thomas, 1980, 1982). This conclusion may be confirmed by examining the classical "decay length" or "skin depth" $\lambda_f/(2\pi\omega)^{1/2}$ for harmonic temperature fluctuations of frequency ω imposed at the boundary of a semi-infinite medium having thermal diffusivity λ_f. This depth is a measure of the distance at which the fluctuation amplitude falls to e^{-1} of its value at the boundary. Assuming frequency scaling as dictated by Thomas (1982) and Blackwelder and Haritonidis (1983), this depth is found to be $L_+ = (2\pi\Omega \mathrm{Pr})^{-1/2}$ in wall units. Thus, for liquid metals having $\mathrm{Pr} \simeq 0.02$, the skin depth is about 45, which is much greater than the "penetration depth" $Y_+ \simeq 3$ to 5 used in the surface-rejuvenation theory, and the thermal resistance of the unreplenished layer is therefore deduced to be negligible. For moderate Pr, however, the skin depth is $Y_+ \simeq 6$, which is comparable to the penetration depth, and the influence of the unreplenished layer is seen to be significant.

Equation (2.7) is in fairly good agreement with accurate numerical computations performed by Meek and Baer (1973) for Tetralin flowing in a pyrex tube; for a value of 0.24 assigned to β, equation (2.7) predicts $\sigma_T/T_w = 0.10$, with no dependence on Reynolds number, and Meek and Baer's full computations yielded $\sigma_T/T_w \simeq 0.07$, with only a very weak variation with Re. Further comments will be made below on the role of uncertainties in the value of Ω.

A useful quantitative comparison can also be made with the work reported by Hochreiter and Sesonske (1969), who measured temperature fluctuations by NaK-56 flowing in a tube made of type 304 stainless steel. Three of their tests have been chosen to encompass most of the range of Reynolds numbers which they covered, and Table 1 lists the relevant parameters for these tests (in Imperial units).

It should be emphasized that u_* and T_* have both been deduced from Hochreiter and Sesonske's paper, the former on the basis of the standard Blasius correlation $c_f = 0.079\ \mathrm{Re}^{-1/4}$, and the latter from sodium-potassium properties quoted in Foust (1972). Hochreiter and Sesonske's measurements are shown in Fig. 4(*a* – *c*), plotted as σ_T/T_* versus ξ, and the solid curves show the theoretical predictions, which are given by

$$\frac{\sigma_{T_f}}{T_*} = \frac{8.26\ \mathrm{Pr}^{1/2}}{(1+\gamma)}\ \bar{\sigma}_{T_f} \tag{3.4}$$

Based on stainless steel properties listed in the *Metals Handbook*. (1961), the corresponding theoretical parameters are delineated in Table 2.

The comparisons are encouraging, although the discrepancies in Fig. 4(*c*) are significant. Several points should be made.

(*i*) The experimental measurements were made inside a tube, whereas the present theory is intended for planar flows and should therefore only be applied when $Y/R_0 << 1$. Some feel for the scale can be acquired by noting that $\xi = 1$ corresponds, in all three tests, to $Y_+ = 0(100)$ and $Y/R_0 = 0$ (1/10).

(*ii*) There is some uncertainty about the values of the thermodynamic properties of both the fluid and the wall. It is recommended that in future experimental programs these parameters are noted, or measured and reported.

Downloaded 17 Dec 2010 to 193.140.21.150. Redistribution subject to ASME license or copyright; see http://www.asme.org/terms/Terms_Use.cfm

Table 2 Theoretical conditions

Test number	β	σ_{T_w}/T_*
1	0.58	0.486
2	0.58	0.507
3	0.56	0.448

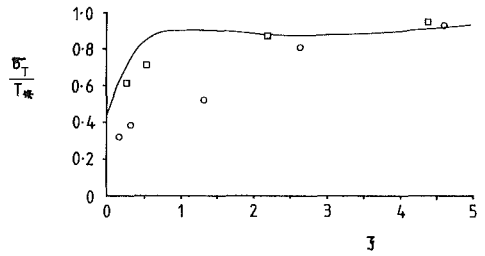

Fig. 5 Comparison of theory with measurements of Bobkov et al. (1965) in mercury: theory: ———; experiment: ○ Re = 7 × 10⁴, □ Re = 1.25 × 10⁵

(*iii*) Ω has been assumed to be equal to 0.004 (Thomas 1982). This may be inaccurate.

(*iv*) The theory predicts a high gradient of σ_T in the region $\xi \leq 0.5$. However, the thickness of this region is comparable to the probe diameter and the thermocouple readings are probably unreliable in that vicinity (Hochreiter and Sesonske assumed that the measurement closest to the wall was at a distance of one-half the probe diameter, or 0.0075 in.). A more definitive judgment must await detailed measurements within this zone.

No comparisons will be made with Rust and Sesonske (1966) because buoyancy effects were significant in those experiments. Figure 5 compares the present theory with measurements made in mercury by Bobkov et al. (1965), at Reynolds numbers of 7×10^4 and 1.25×10^5. As with most of the papers, insufficient information was provided on the tube material and properties, and for the theoretical predictions stainless steel type 304 was assumed. The agreement is good at the higher Re but the theory overestimates σ_T at and below the former Re. The most likely explanation is a deviation of Ω from the assumed value of 0.004; as noted in the introduction, there is considerable scatter of experimental data about this value in Fig. 2 of Thomas (1982), and moreover some of the measurements reflect a dependence on Reynolds number. Thus, there is clearly a need for experimental data on for low-Pr fluids, and in fact equation (2.7) is being proposed here as a convenient means of measuring Ω, for specific fluid/wall pairs.

Finally, the prediction shown in Fig. 5 can be compared with the near-wall experimental correlation for mercury flow provided in a recent paper by de Lemos and Sesonske (1985)

$$\sigma_T/T_* = 8.7 \times 10^{-6}\mathrm{Re} + \mathrm{Re}^{0.0258} y_+ \qquad (3.5)$$

The Reynolds number of the experiments ranged between 3×10^4 and 9×10^4. The first term on the RHS reflects a dependence on Re which is qualitatively similar to Bobkov et al. (1965). However, the second term is too large, since the coefficient of y_+ is 0 (1) and y_+ may acquire values up to 100. The present asymptotic prediction (equation (2.12), assuming constant Ω again) is $\sigma_T/T_* \sim 0.44 + 0.006\, y_+$.

Conclusions

The paper has outlined a simple technique for approximating the wall function for the temperature variance when heat is transferred, in the time-mean, between a thick solid and a well-mixed, turbulent fluid. By assuming a linear initial temperature distribution in the solid, as part of a surface-renewal model, the problem degenerates to a straightforward quadrature, equation (2.11). Attention has been confined to low-Prandtl-number fluids; comparisons with the measurements reported by Hochreiter and Sesonske (1969) and Bobkov et al. (1965) are encouraging.

Clearly, scope for improvement of the method does exist, particularly in relation to the initial conditions assumed for the surface-renewal calculation. This aspect is being addressed and will have particular bearing on configurations in which the time-mean heat flux is small.

Note Added in Proof

In another recent paper (*Proc. Third Int. Topical Meeting on Reactor Thermal Hydraulics*, Newport, RI, Oct. 15–18, 1985, C. Chiu and G. J. Brown, eds., ANS, Paper No. 21.F), de Lemos gives a coefficient of y_+ in equation (3.5) that reads $\mathrm{Re}^{-0.528}$, in closer agreement with the present theory. Such correlations can be used for estimating the variation of Ω with Re, although equation (3.5) was provided for only one pair of substances.

Acknowledgments

The assistance of the NNC library staff is gratefully acknowledged. This paper is published by permission of the National Nuclear Corporation.

References

Abramowitz, M., and Stegun, I. A., 1965, *Handbook of Mathematical Functions*, Dover, New York.

Blackwelder, R. F., and Haritonidis, J. H., 1983, "Scaling of the Bursting Frequency in Turbulent Boundary Layers, *J. Fluid Mech.*, Vol. 132, pp. 87–103.

Bobkov, P. V., Gribanov, Yu. I., Hragimov, M. Kh., Nomofilov, E. V., and Subbotin, V. I., 1965, "Measurement of Intensity of Temperature Fluctuations in Turbulent Flow of Mercury in a Tube," *Teplofizika Vysokikh Temperature*, Vol. 3, pp. 708–716.

Cantwell, B. J., 1981, "Organized Motion in Turbulent Flow," *Ann. Rev. Fluid Mech.*, Vol. 13, pp. 457–515.

Danckwerts, P. V., 1951, "Significance of Liquid-Film Coefficients in Gas Absorption," *Ind. Eng. Chem.*, Vol. 43, pp. 1460–1467.

Danckwerts, P. V., 1970, *Gas-Liquid Reactions*, McGraw-Hill, New York.

Davies, J. T., 1972, *Turbulence Phenomena*, Academic Press, New York.

Foust, O. J., ed., 1972, *Sodium-NaK Engineering Handbook*, Vol. 1, Gordon and Breach, New York.

Hanratty, T. J., 1956, "Turbulent Exchange of Mass and Momentum With a Boundary," *AIChE Journal*, Vol. 2, pp. 359–362.

Higbie, R., 1935, "The Rate of Absorption of a Pure Gas Into a Still Liquid During Short Periods of Exposure," *Trans. AIChE*, Vol. 31, p. 365.

Hirata, M., Tanaka, H., Kawamura, H., and Kasagi, N., 1982, "Heat Transfer in Turbulent Flows," *Proc. Seventh International Heat Transfer Conference*, U. Grigull, ed., Vol. 1, Hemisphere, Washington, pp. 31–57.

Hochreiter, L. E., and Sesonske, A., 1969, "Thermal Turbulence Characteristics in Sodium–Potassium," *Int. J. Heat Mass Transfer*, Vol. 12, pp. 114–118.

Launder, B. E., 1978, "Heat and Mass Transport," in: *Turbulence, Topics in Applied Physics*, P. Bradshaw, ed., Vol. 12, Springer-Verlag, New York.

Launder, B. E., and Spalding, D. B., 1972, *Mathematical Models of Turbulence*, Academic, London.

de Lemos, M. J. S., and Sesonske, A., 1985, "Turbulence Modeling in Combined Convection in Mercury Pipe Flow," *Int. J. Heat Mass Transfer*, Vol. 28, pp. 1067–1088.

Meek, R. L., and Baer, A. D., 1973, "Turbulent Heat Transfer and the Periodic Viscous Sublayer," *Int. J. Heat Mass Transfer*, Vol. 16, pp. 1385–1396.

Metals Handbook, 1961, 8th ed., Vol. 1, American Society for Metals.

Patankar, S. V., 1980, *Numerical Heat Transfer and Fluid Flow*. Hemisphere/McGraw-Hill, New York.

Rust, J. H., and Sesonske, A., 1966, "Turbulent Temperature Fluctuations in Mercury and Ethylene Glycol in Pipe Flow," *Int. J. Heat Mass Transfer*, Vol. 9, pp. 215–227.

Tanimoto, S., and Hanratty, T. J., 1963, "Fluid Temperature Fluctuations Accompanying Turbulent Heat Transfer in a Pipe," *Chem. Eng. Sci.*, Vol. 18, pp. 307–311.

Thomas, L. C., 1970, "Temperature Profiles for Liquid Metals and Moderate Prandtl-Number Fluids," ASME JOURNAL OF HEAT TRANSFER, Vol. 92, pp. 565–567.

Thomas, L. C., 1980, "The Surface Rejuvenation Model of Wall Turbulence. Inner Laws for $u+$ and $T+$," *Int. J. Heat Mass Transfer*, Vol. 23, pp. 1099–1104.

Thomas, L. C., 1982, "A Turbulent Burst Model of Wall Turbulence for Two-Dimensional Turbulent Boundary Layer Flow," *Int. J. Heat Mass Transfer*, Vol. 25, pp. 1127–1136.

Downloaded 17 Dec 2010 to 193.140.21.150. Redistribution subject to ASME license or copyright; see http://www.asme.org/terms/Terms_Use.cfm

Forced Convective Heat Transfer in Curved Diffusers

J. Rojas

J. H. Whitelaw

Imperial College of Science and Technology,
Mechanical Engineering Department,
Fluids Section,
London SW7 2BX, England

M. Yianneskis

King's College London,
Mechanical Engineering Department,
London WC2R 2LS, England

Measurements of the velocity characteristics of the flows in two curved diffusers of rectangular cross section with **C** *and* **S***-shaped centerlines are presented and related to measurements of wall heat transfer coefficients along the heated flat walls of the ducts. The velocity results were obtained by laser-Doppler anemometry in a water tunnel and the heat transfer results by liquid crystal thermography in a wind tunnel. The thermographic technique allowed the rapid and inexpensive measurement of wall heat transfer coefficents along flat walls of arbitrary boundary shapes with an accuracy of about 5 percent. The results show that an increase in secondary flow velocities near the heated wall causes an increase in the local wall heat transfer coefficient, and quantify the variation for maximum secondary-flow velocities in a range from 1.5 to 17 percent of the bulk flow velocity.*

Introduction

Curved passages with changes in cross-sectional area are frequently employed in aircraft turbine intake and exhaust ducts and in turbomachinery blade passages. Knowledge of the velocity and heat transfer characteristics of the flows in such ducts is desirable in order to enhance understanding of the processes involved and aid the design of relevant turbine components. The present paper is primarily concerned with the convective cooling effects of secondary flows on curved duct walls and the processes in singly and doubly curved diffusing ducts are investigated.

The characteristics of developing flows in constant-area **C**-shaped ducts have been investigated in detail by Taylor et al. (1982), Enayet et al. (1982), and others, and in **S**-shaped ducts by Bansod and Bradshaw (1972) and Anderson et al. (1984). The results have shown that the secondary flows present in **C** and **S**-shaped ducts of mild curvature reach maxima of 0.25 and 0.15 of the bulk flow velocity (V_b), respectively, in turbulent flow. Stronger duct curvature results in higher cross-stream velocities, of up to around 0.4 V_b, and in general there are two pairs of counter-rotating vortices in **S**-ducts as opposed to the single pair present in unidirectional bends. Measurements in a 45-deg curved diffuser have been reported by McMillan (1982) and showed that a deceleration of the secondary flows is produced by the area expansion. Graziani et al. (1980) used thermocouples to measure the heat transfer on the walls of a turbine blade passage and reported that the secondary flows and the thickness of the endwall boundary layer greatly influenced the heat transfer process.

The use of thermocouples is relatively inefficient when localized three-dimensional effects are to be investigated over a comparatively large area, and liquid crystal thermography provides a rapid, inexpensive, and accurate alternative for such measurements. The suitability of liquid crystals for convective heat transfer work has been demonstrated by Cooper et al. (1975) and others. The technique developed for the present investigation made use of a heating element/liquid crystal sheet assembly designed to enable measurements in a variety of passages of complex geometries.

In the present study, the flows in **C** and **S**-shaped diffusers were investigated, with one of the flat walls of the ducts heated for the heat transfer experiment. The choice of this thermal boundary condition was made in order to facilitate interpretation of the heat transfer results in view of the complexity of the flows studied. Results were also obtained in a straight square duct and in a **C**-shaped diffuser with a pair of vortex generators at the inlet to enable comparisons with both simpler and more complex flows.

Contributed by the Heat Transfer Division and presented at the ASME Winter Annual Meeting, Miami Beach, Florida, November 1985. Manuscript received by the Heat Transfer Division June 30, 1986.

The flow configurations investigated are described in the following section, together with the laser velocimeter used for the mean flow results in the water tunnel and the liquid crystal bed used for the heat transfer results in the wind tunnel. The flow and heat transfer results are then presented in the two following subsections and discussed in the penultimate section. The paper closes with a list of the main findings.

Flow Configurations and Experimental Procedures

Curved Diffusers. The test sections were constructed of Plexiglas to allow optical access through all walls and consisted of two 22.5-deg bends, with a radius of curvature of 280 mm, in series. The cross section of the bends expanded linearly with the downstream distance on both curved surfaces. The geometry of the **C**-shaped diffuser is shown in Fig. 1(*a*). The **S**-shaped diffuser was assembled by turning the second 22.5-deg bend by 180 deg about the centerline at the $\theta = 22.5$-deg plane. The inlet cross section of the diffusers was square (40 ± 0.1 mm $\times$ 40 ± 0.1 mm) and the exit cross section rectangular (40 ± 0.1 mm $\times$ 60 ± 0.1 mm) with an exit-to-inlet area ratio of 1.5. The effective total divergence angle for an equivalent straight diffuser is 5.2 deg. The dimensions of the upstream and downstream tangents matched those of the diffuser inlet and exit, respectively, to ± 0.1 mm. The donwstream tangent was 2 m long in the water tunnel and in the wind tunnel it was kept to 5 cm since it had no influence on the flow in the ducts. The short length of the upstream tangents and the small expansion ratio (and, in the case of the **S**-duct, the small centerline displacement) were chosen to have developing flows and conditions similar to those encountered in aircraft intake ducts. Both the water and the air tunnel had inlet contractions of 12:1 area ratios to ensure smooth entrance flows and there were no discontinuities on the duct walls. A 0.5-mm boundary layer trip was incorporated at the entrance to the inlet tangent. The water tunnel has been described in detail by Taylor et al. (1982) and the wind tunnel by Rojas and Yianneskis (1984).

The coordinate system is also shown in Fig. 1(*a*). Streamwise distance is measured in hydraulic diameters of the upstream tangent (D_H = 0.04 m). Water was employed as the working fluid for the velocity measurements so that the same Reynolds number (Re) could be obtained at a velocity much smaller than that achieved in air and to allow high measurement accuracy. Measurements were made at Re = 40,000 in the water flow and at Re = 35,000 in the air flow, based on D_H and on the bulk flow velocity in the upstream tangent V_b, which was 1.0 m/s for the water flow and 12.5 m/s for the air flow. Velocity measurements were made on both sides of the symmetry plane and it was established that the flows were symmetric to within the precision of the measurements. The

Copyright © 1987 by ASME

Downloaded 17 Dec 2010 to 193.140.21.150. Redistribution subject to ASME license or copyright; see http://www.asme.org/terms/Terms_Use.cfm

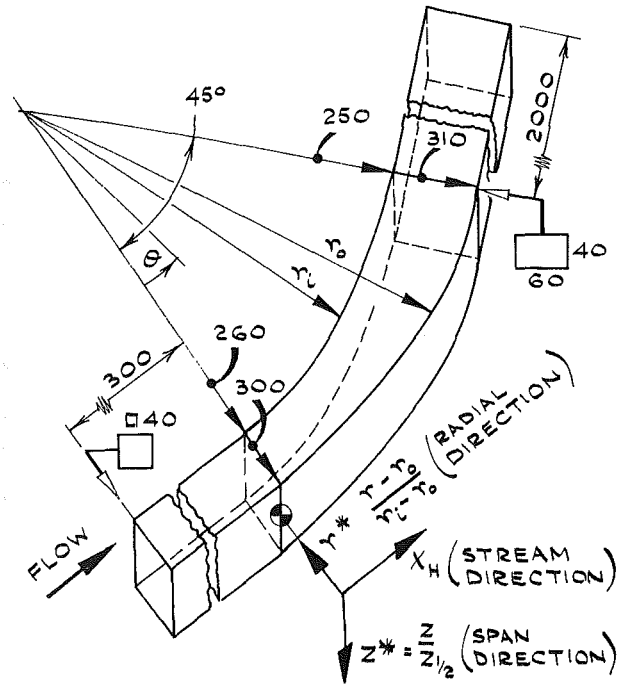

Fig. 1(*a*) C-diffuser flow configuration, dimensions, and coordinate system; all dimensions in mm

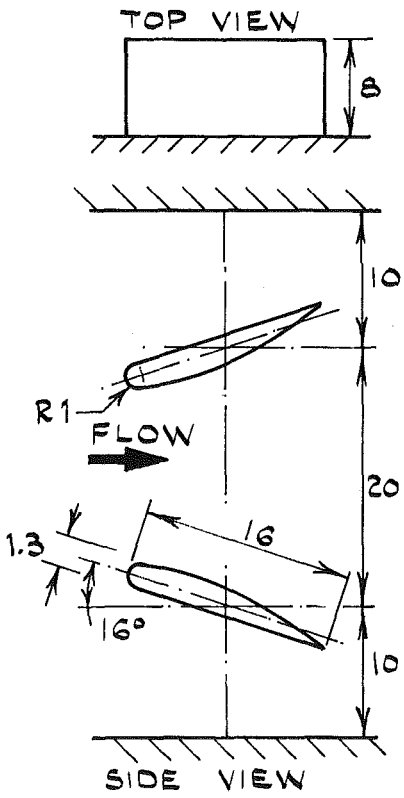

Fig. 1(*b*) Vortex generators: all dimensions in mm

similarity of the air and water flows was also established by measurements.

In order to investigate the influence of a typical inlet mixing device on the flow, a pair of vortex generators was installed on the inside wall of the C-diffuser (at $r^* = 1.0$, $X_H = 0.0$). The blade pair is shown in Fig. 1(*b*) in the X–r^* (top view) and X–z^* (side view) planes.

The Laser-Doppler Velocimeter. The laser-Doppler velocimeter was of the dual-beam fringe type and operated in forward scatter. Measurements in three directions (0, ±45 deg to the local streamwise direction) were made with the beams entering through the side wall to provide the local streamwise ($\bar{U}$ and $\tilde{u}$) and radial ($\bar{V}$ and $\tilde{v}$) mean velocities and turbulence levels, in the manner described by Melling and Whitelaw (1976). Frequency-tracking demodulation was used for the processing of the measured Doppler frequencies. The optical and signal processing system have been described in detail by Taylor et al. (1982), together with the sources and estimates of experimental error. In brief, systematic errors are generally of the order of 1 percent of the local velocity values shown, rising to 2–3 percent in the regions of steep velocity gradients near the walls.

Liquid Crystal and Heating Element Assembly. The heating element assembly consisted of an acrylic plastic base on which an expanded polystyrene insulating sheet and two copper bus bars were attached with a stainless steel foil 25 μm thick stretched on them. A roller mechanism was used to stretch and hold the foil in place, and a pair of contact blocks and clamps was employed to ensure a good and uniform contact between the bus bars and the foil. The free area of the foil was 0.3 m × 0.3 m and the part of this area not covered by the duct was insulated to minimize heat losses. A uniform heat flux condition was obtained by passing an a-c electrical current through the bus bars and foil.

The liquid crystals (organic materials which exhibit a mesophase, i.e., an intermediate phase between a pure crystalline solid and a pure liquid phase) respond to changes in temperature by exhibiting different colors due to Bragg diffraction of light from the molecular layers in the crystals. A cholesteric liquid crystal sheet was used, and consisted of a 0.092-mm-thick crystal layer embedded on a 0.137-mm-thick mylar sheet, with a black absorptive background. The sheet was attached to the foil with a double-sided adhesive tape. The sensitivity (color response) of the crystal sheet was in the range of 35–36°C and it was calibrated to 0.1°C in a constant-temperature bath immediately before the measurements were made. Photographs of the crystals during calibration and during the experiments were taken with the same film, illumination and angle of view. The green color corresponding to 35.7°C was chosen as the isotherm indicator for the wall temperature measurements.

The whole assembly was placed so as to form the lower (flat) side wall of the duct investigated, and the heating was applied from the inlet of the diffusers to the end of the ducts (50 mm downstream of the diffuser exit plane). Current was applied to the bus bars at first without flow in the ducts, and photographic recordings of the isotherms were made for different current settings. In this manner the green isotherms would be placed in a multitude of locations, enough to describe the "no-flow" heat flux (q_1) distribution over the wall. Heat fluxes were calculated from the measurement of the current and of the resistance of the heating element, by $q = I^2R$. But $q_1 = q_L + q_N$, where q_L is the heat lost by conduction and radiation and q_N the amount of heat maintaining natural convection in the duct. An accurate estimate of q_N can be obtained in the manner described by O'Toole and Silveston (1961). Subsequently the flow was turned on and the mapping of the green isotherms for different current settings was repeated. The heat flux measured was then $q_2 = q_f + q_L$ where q_f is the forced convection heat flux, and $q_f = q_2 - q_1 + q_N$.

The bulk air temperature T_b was constantly monitored and recorded during the experiments. The local bulk temperature was determined by measuring T_b at the duct inlet and exit under flow conditions with a thermocouple and by assuming a linear increase in T_b through the duct, as suggested by Barrow

Downloaded 17 Dec 2010 to 193.140.21.150. Redistribution subject to ASME license or copyright; see http://www.asme.org/terms/Terms_Use.cfm

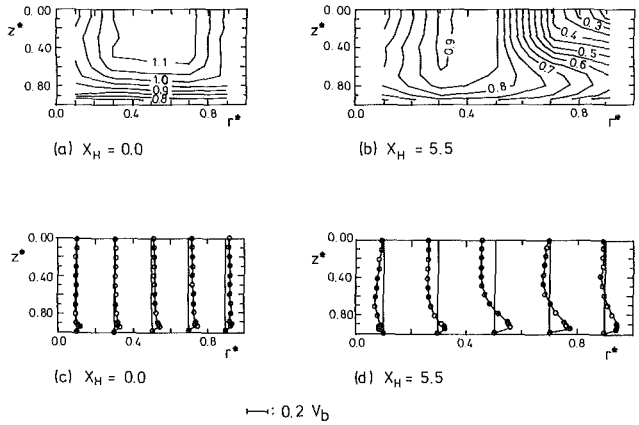

Fig. 2 C-diffuser velocity results: (*a*), (*b*) contours of $\bar{U}/V_b$; (*c*), (*d*) profiles of $\bar{V}/V_b$

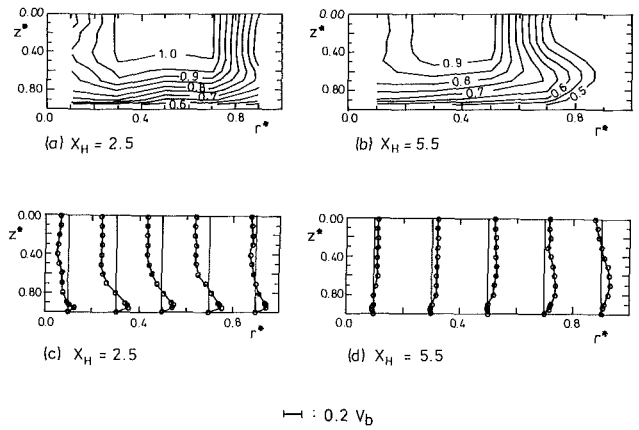

Fig. 3 S-diffuser velocity results: (*a*), (*b*) contours of $\bar{U}/V_b$; (*c*), (*d*) profiles of $\bar{V}/V_b$

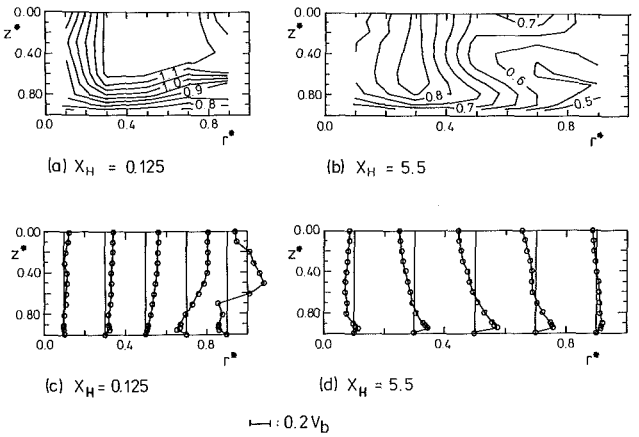

Fig. 4 Velocity results for C-diffuser with vortex generators: (*a*), (*b*) contours of $\bar{U}/V_b$; (*c*), (*d*) profiles of $\bar{V}/V_b$

(1962). As the wall temperature at each point is known from the crystal colors, the wall heat transfer coefficient at each point can be found from $h = q_f/(T_w - T_b)$.

The total experimental error in h in the procedure described above was estimated in the manner suggested by Brady and Odorizzi (1981) and was found to be, typically, 5 percent of the h value calculated. Effects such as the crystal viewing angle, conduction through the mylar sheet (causing a difference in temperature between that at the wall surface and that indicated by the crystals), lateral conduction, heat losses from the part of the foil not covered by the duct, and that of the different rates of heating have been estimated to be either negligible or well within the total error quoted above.

Results

Velocity Results. The turbulent flow streamwise and radial mean velocity component results obtained in the water tunnel are shown in Figs. 2–4; those of Figs. 2(*b*) and (*d*) and 3(*b*) and (*d*) have been reported previously by Rojas et al. (1982). The results are presented as contours of $\bar{U}/V_b$ and profiles of $\bar{V}/V_b$ in r^*–z^* planes below the plane of symmetry, with the left and right-hand side walls being the $r^* = 0$ and $r^* = 1.0$ walls, respectively, and the bottom wall being the side wall.

It is useful to distinguish two characteristic regions, a high-velocity "core" region where the flow is akin to potential flow, and a near-wall region of boundary layer flow where most of the secondary flow activity takes place. The streamwise velocities in the **C**-diffuser show a slight asymmetry and a large potential core at the inlet plane (Fig. 2*a*), and a large redistribution of the isotachs by the exit (Fig. 2*b*). The core region migrates toward the outside ($r^* = 0.0$) wall in its passage through the diffuser, and a large region of slow-moving fluid is found near the inside wall at the exit. The radial velocities are small, of the order of 0.05 V_b at the inlet (Fig. 2*c*) and show a displacement of the flow toward the inside wall. A counterclockwise rotation can be observed in the $\bar{V}$ profiles in Fig. 2(*d*), as a result of the curvature-induced secondary flows, with maxima of 0.15 V_b near the sidewall. At $r^* = 0.1$, the velocities are always directed toward the outside wall, probably as a result of the area-expansion-related cross flows superimposed on the curvature-induced ones.

The measurements obtained in the inlet of the **S**-diffuser were identical to those shown in Figs. 2(*a*) and (*c*), as the effects due to the differences in geometry do not travel upstream by more than about one hydraulic diameter. Different velocity patterns were recorded though near the plane of inflection (Fig. 3*a*, at a plane 20.5 deg downstream of the inlet) and in the exit plane (Fig. 3*b*). The core region is located further away from the $r^* = 0.0$ wall than in the **C**-diffuser, and it follows an **S**-shaped path through the duct. The radial velocities in Figs. 3(*c*) and (*d*) show that the secondary flow vortex has been established by the $X_H = 2.5$ station with a maximum of 0.17 V_b near its side wall at $r^* = 0.8$. However, two distinct and opposite rotations can be observed in the exit plane cross flows, a counterclockwise one near $r^* = 0.9$, $z^* = 0.3$ and a clockwise one near $r^* = 0.1$, $z^* = 0.8$. The former is due to the persistence of the secondary flow generated in the first bend and the latter is due to the curvature of the second bend, in agreement with the findings in uniform-area S-ducts (Anderson et al., 1984).

The results obtained with the pair of vortex generators at the inlet of the **C**-diffuser are shown in Fig 4. Significant changes in the $\bar{U}$ and $\bar{V}$ distributions can be observed in comparison to the results of Fig. 2, especially near the inlet. The data in Fig. 4(*a*) and (*c*) were taken at $X_H = 0.125$, as the presence of the blades prohibited measurements at $X_H = 0.0$. A strong clockwise-rotating vortex is produced behind each generator blade as shown in Fig. 4(*c*), with $\bar{V}$ reaching 0.4 V_b. The vortex is about 0.25 D_H in diameter and the flow from $r^* = 0.5$ to the inside wall is dominated by its presence. The effect of the vortex on the exit plane $\bar{V}$ profiles is not as strong (compare Fig. 2*d* to 4*d*) as near the inlet, but the redistribution of the streamwise isotachs in Fig. 4(*b*) is markedly different from that in the **C**-diffuser.

Turbulence level and cross-correlation results are not shown for economy of presentation, as no firm conclusions could be drawn about the influence of turbulence characteristics on the wall heat transfer. Detailed velocity results, together with

Downloaded 17 Dec 2010 to 193.140.21.150. Redistribution subject to ASME license or copyright; see http://www.asme.org/terms/Terms_Use.cfm

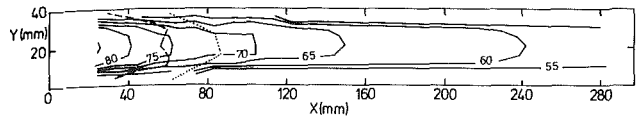

Fig. 5 Contours of constant Nusselt number on lower wall of straight square duct; flow direction is from left to right; — — —: results from straight duct, and, ...: results downstream of a 90-deg bend, from Rojas and Yianneskis (1984)

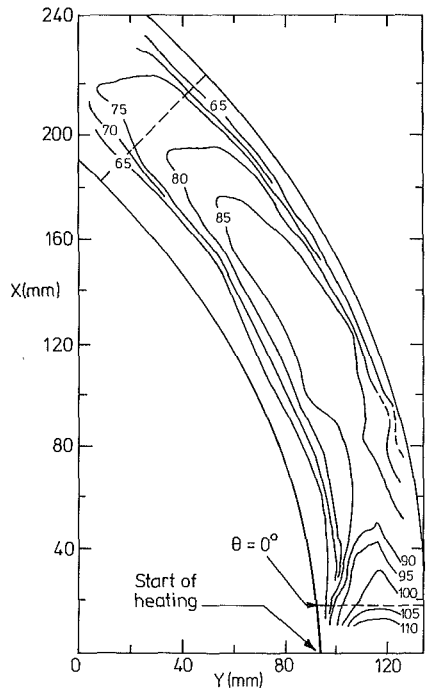

Fig. 6 Contours of constant Nusselt number on lower side wall of C-diffuser; flow direction is from bottom right to top left

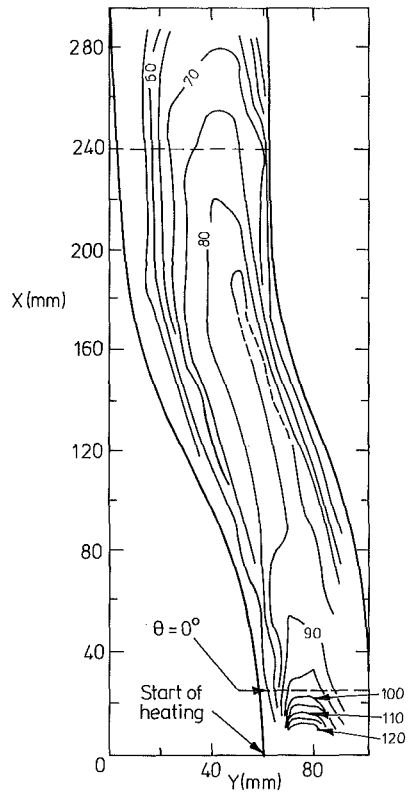

Fig. 7 Contours of constant Nusselt number on lower side wall of S-diffuser; flow direction is from bottom right to top left

associated pressure measurements, flow visualization, and laminar flow data can be found in reports by Rojas et al. (1983, 1985). The data are available on magnetic tape for ease of comparison with numerical calculations of the flows.

Heat Transfer Results. The h values calculated from the heat transfer measurements were used to plot contours of Nusselt number, defined as $\mathrm{Nu} = hD/k$, where k is the thermal conductivity of the convecting fluid (air in this case). The data are presented as contours of Nu to allow comparisons with data reported in the references quoted. Contours of Nu (or of the Stanton number St) are, in effect, lines of constant, non-dimensional heat transfer coefficient and provide an indication of heat transfer characteristics irrespective of duct size.

As the flows in the diffusers are complex, the technique was first employed to measure the wall heat transfer in a straight duct of square cross section, in order to enable comparisons with previously obtained data and to facilitate the interpretation of the results by reference to a simpler geometry. Contours of Nu in fully developed turbulent flow along the bottom wall of a 40-mm square duct are shown in Fig. 5. Heating was applied from $X = 0$ mm to 280 mm (7.0 D_H downstream), where the duct exit was located. Novotny et al. (1964) measured fully developed Nusselt numbers $\mathrm{Nu}_f = 70$ in a symmetrically heated square duct at Re = 35,000 and the analysis of Sparrow et al. (1966) suggests that Nu_f is 15 percent lower in the case of ducts with only the bottom wall heated, i.e., $\mathrm{Nu}_f = 59$ for the present duct. As Nu tends asymptotically to the Nu_f value, thermally fully developed conditions are not reached by the exit of the duct. The variation of the ratio of the local to the fully developed Nusselt number $\mathrm{Nu}/\mathrm{Nu}_f$ in the present case follows that measured by Davies et al. (1984) in a two-dimensional duct at Re = 32,000 to within 2 percent. The straight duct results indicate the viability of the technique for accurate measurements of local wall heat transfer coefficients. The dashed and dotted lines on Fig. 5 refer to the data of Rojas and Yianneskis (1984) and are discussed in the following section.

Contours of Nu over the **C** and **S**-diffuser heated side walls are presented in Figs. 6 and 7, respectively. The inlet planes of the diffusing part of the ducts are located in the bottom right-hand corner of the plots and the exit planes are denoted by a dashed line. Nu is higher in both geometries, by about 25 percent on average, in comparison to the values in the straight duct. Higher values of Nu are found near the inlet and near the $r^* = 0.0$ wall in both ducts.

The heat transfer results obtained with the vortex generators in the inlet of the **C**-diffuser yielded similar Nu values to those of Fig. 6, but their distribution was markedly different in the first half of the duct. A qualitative comparison of typical isotherms (traced directly from the photographs) obtained with (dashed line) and without (solid line) the vortex generators is shown in Fig. 8. The heat fluxes were identical in both flow configurations. The shaded regions are the cooler ones. The convective cooling produced by the vortex behind the blade is evident as a sharp peak separated from the main flow cooling by a region of low convection. The cooling patterns are however very similar near the diffuser exit. The overall area kept at the lower temperature is smaller with the vortex generators.

Discussion

The results presented in the preceding section allow the evaluation of the effect of secondary flows of various

Downloaded 17 Dec 2010 to 193.140.21.150. Redistribution subject to ASME license or copyright; see http://www.asme.org/terms/Terms_Use.cfm

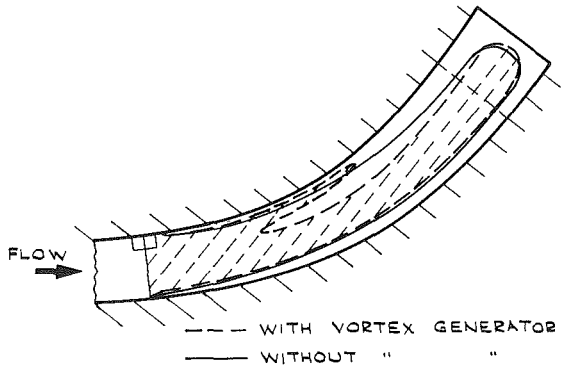

Fig. 8 Diagram showing the location of the blue/green line isotherm on liquid crystal sheet for the same heat flux condition in the C-diffuser with and without the vortex generators: $q'' = 450$ W/m^{2}K, $T = 35.7$°C

magnitudes on the convective cooling of duct walls. The Reynolds and Rayleigh numbers of the flows examined are such as to place the flows in the turbulent, forced-convection regime.

The straight duct heat transfer results can be considered in conjunction with the velocity measurements of Melling and Whitelaw (1976) in an identical duct geometry. The Reynolds-stress-induced secondary flows in the duct of Melling and Whitelaw reached maxima of 0.015 V_b near the walls at distances of about 0.3 D_H away from the corners: These are the same locations where maxima of the streamwise velocity component were measured. In the present results (Fig. 5) the maximum Nu region is located in the central one-third of the wall but only a single peak can be distinguished. However, in the experiment of Rojas and Yianneskis (1984) the same h values were obtained but with two peaks with values approximately 2 percent higher than in the center in the locations of the velocity maxima. This difference arises from the smaller number of points used to plot the present result (196 over 280 mm as opposed to over 100 mm in the investigation of Rojas and Yianneskis), and indicates the detail of measurement required to resolve such effects. Typical results from Rojas and Yianneskis (1984) are reproduced in Fig. 5 to enable comparison. The dashed and dotted lines show the measurements in the straight duct and 2.5 diameters downstream of a 90-deg bend, respectively; by comparison of the latter Nu profile with those of Figs. 6 and 7 it can be expected that all significant features of the Nu distributions in the present curved geometries have been resolved.

In the case of the curved ducts, previous investigations by Mori et al. (1971) have reported that wall heat transfer in uniform-area curved ducts increased because of the secondary flows and Graziani et al. (1980) reported that the heat transfer in turbine cascade passages was largely determined by the secondary flows between the blades and by the inlet boundary layer thickness. As has been reported by Taylor et al. (1982), thicker boundary layers result in stronger secondary flows in curved ducts and the two effects will be considered as one in the following discussion. The present results show that curved diffuser flows with secondary flow maxima of 0.15–0.17 V_b result in higher wall heat transfer than in straight duct flow (h and Nu values are 40–50 percent higher in some locations) where the cross flows are smaller by an order of magnitude of V_b. The corresponding Stanton numbers, defined with the bulk velocity at the inlet and wall-to-local-bulk temperature difference, were in the ranges 0.028–0.048 and 0.019–0.051 in the **C** and **S**-diffusers respectively, compared with 0.02–0.04 in the straight duct.

Variations of Nu (and of h and temperature) across the duct wall are present in all configurations and they may result from reasons other than convective cooling. In the corner regions Nu variations are partly due to the smaller convective heat transfer capability (because of the slower-moving fluid present there) than in the central region of the wall, an effect which is not present in circular-cross-section pipes. Conduction to the unheated walls is not expected to be important to the heat transfer in the corner region, partly due to a layer of insulation installed at the end of these walls. Longitudinal variations of wall temperature (and Nu) result partly because a thermally developed state is not achieved in any configuration in the curved ducts by virtue of the developing nature of the flows. Although in straight circular pipes thermally developed regimes can be achieved after 10–20 D_H, there is no evidence about thermal entry lengths in asymmetrically heated rectangular ducts (Sparrow et al., 1966).

The increase in the bulk flow temperature due to the heating of the wall was about 0.5°C in the centerline of the curved ducts and its rise with longitudinal distance was similar to that of the heated wall temperature, in accordance with the findings of Sparrow et al. (1966).

Apart from the aforementioned sources of h and Nu variations, the curved duct Nu distributions of Figs. 6 and 7 appear to be influenced first by the core flow with the Nu contours following in general the shape of the centerlines of the ducts, and secondly by the secondary flow activity. The most striking evidence of the latter effect can be observed in the qualitative results of Fig. 8. However, the complexity of the three-dimensional flow patterns does not allow a clear distinction of the core flow and of the secondary flow influences. The radial locations where the streamwise mean velocity gradients are higher, in general near the side wall under the core regions, and the locations of the near-wall V maxima can be mostly found in all cross sections in close proximity to the high heat transfer regions (e.g., at $X_H = 5.5$ in the **C** and $X_H = 2.5$ in the **S**-diffuser).

Concluding Remarks

1 Velocity measurements obtained by laser-Doppler velocimetry and wall heat transfer measurements obtained by liquid-crystal thermography of the turbulent, forced-convection flows in two curved diffusers with **C** and **S**-shaped centerlines were reported.

2 The liquid-crystal technique enabled the rapid and inexpensive measurement of local wall heat transfer coefficients over a heated flat wall in the ducts with an uncertainty of 5 percent.

3 Secondary flows resulting from the curvature of the ducts and from the expansions in area are present in both diffusers and reach maxima of 0.17 of the bulk flow velocity V_b.

4 The wall heat transfer results quantify the effects of secondary flow in a range of 0.015–0.17 V_b and indicate that stronger convective cooling takes place in the diffusers than in a straight duct of similar cross section. Higher Nusselt numbers were recorded in locations where the near-wall streamwise velocity gradients and the radial mean velocity components were higher.

Acknowledgments

The velocity measurements were obtained with financial support from NASA under grant NASW-3631. The heat transfer measurements were undertaken as part of a collaborative project with the University of Minnesota; we are grateful to Professor R. J. Goldstein for useful discussions.

References

Anderson, B. H., Taylor, A. M. K. P., Whitelaw, J. H., and Yianneskis, M., 1984, "Developing Flow in S-Shaped Ducts," in: *Laser Anemometry in Fluid Mechanics*, R. J. Adrian et al., eds., Ladoan, Lisbon, pp. 66–78.

Bansod, P., and Bradshaw, P., 1972, "The Flow in S-Shaped Ducts," *Aeronautical Quarterly*, Vol. 23, pp. 131–140.

Barrow, H., 1962, "An Analytical and Experimental Study of Turbulent Gas

Downloaded 17 Dec 2010 to 193.140.21.150. Redistribution subject to ASME license or copyright; see http://www.asme.org/terms/Terms_Use.cfm

Flow Between Two Smooth Parallel Walls With Unequal Heat Fluxes," *Int. Journal of Heat and Mass Transfer*, Vol. 5, pp. 469–487.

Brady, D. D., and Odorizzi, D. J., 1981, "Statistical Tolerancing: Optimise Component-Tolerance Budgets," in: *Advanced Test and Measurement Instrumentation*, Hayden Book Co., pp. 313–317.

Cooper, T. E., Field, R. J., and Meyer, J. F., 1975, "Liquid Crystal Thermography and Its Application to the Study of Convective Heat Transfer," ASME JOURNAL OF HEAT TRANSFER, Vol. 97, pp. 442–450.

Davies, R. M., Rhines, J. M., and Sidhu, B. S., 1984, "The Application of the Liquid Crystal Technique to the Experimental Modelling of Forced Convective Heat Transfer in Industrial Heating Processes," *Proc. First U.K. National Heat Transfer Conference*, Leeds, July 3–5.

Enayet, M. M., Gibson, M. M., and Yianneskis, M., 1982, "Measurements of Turbulent Developing Flows in a Moderately Curved Square Duct," *Int. Journal Heat and Fluid Flow*, Vol. 3, pp. 221–224.

Graziani, R. A., Blair, M. F., Taylor, J. R., and Mayle, R. E., 1980, "An Experimental Study of Endwall and Airfoil Surface Heat Transfer in a Large Scale Turbine Blade Cascade," ASME *Journal of Engineering for Power*, Vol. 102, pp. 257–267.

McMillan, O. J., 1982, "Mean-Flow Measurements of the Flow Field Diffusing Bend," NASA Contractor Report No. 3634.

Melling, A., and Whitelaw, J. H., 1976, "Turbulent Flow in a Rectangular Duct," *Journal of Fluid Mechanics*, Vol. 78, pp. 289–315.

Mori, Y., Uchida, Y., and Ukon, T., 1971, "Forced Convective Heat Transfer in a Curved Channel With a Square Cross-Section," *International Journal of Heat and Mass Transfer*, Vol. 14, pp. 1787–1805.

Novotny, J. L., McComas, S. T., Sparrow, E. M., and Eckert, E. R. G., 1964, "Heat Transfer for Turbulent Flow in Rectangular Ducts With Two Heated and Two Unheated Walls," *AIChE Journal*, Vol. 10, pp. 466–470.

O'Toole, J. L., and Silveston, P. L., 1961, "Correlations of Convective Heat Transfer in Confined Horizontal Layers," Chemical Engineering Symposium Series, Vol. 57, *Heat Transfer*, Buffalo, pp. 81–86.

Rojas, J., and Yianneskis, M., 1984, "The Development of Liquid Crystal Techniques for the Measurement of Wall Heat Transfer Coefficients in Ducts," Imperial College, Mechanical Engineering Department Report No. FS/84/27, London.

Rojas, J., Whitelaw, J. H., and Yianneskis, M., 1982, "Flow in Sigmoid Diffusers of Moderate Curvature," Fourth Symposium on Turbulent Shear Flows, Karlsruhe, Germany.

Rojas, J., Whitelaw, J. H., and Yianneskis, M., 1983, "Developing Flow in S-Shaped Diffusers: Part I: Square-to-Rectangular Cross-Section Diffuser," NASA Contractor Report.

Rojas, J., Whitelaw, J. H., and Yianneskis, M., 1985, "Inlet Condition Effects on Incipient Separation in Curved Diffusers," NASA Contractor Report.

Sparrow, E. M., Lloyd, J. R., and Hixon, C. W., 1966, "Experiments in Heat Transfer in an Asymmetrically Heated Rectangular Duct," ASME JOURNAL OF HEAT TRANSFER, Vol. 88, pp. 170–174.

Taylor, A. M. K. P., Whitelaw, J. H., and Yianneskis, M., 1982, "Curved Ducts With Strong Secondary Motion: Velocity Measurements of Developing Laminar and Turbulent Flow," ASME *Journal of Fluids Engineering*, Vol. 104, pp. 350–359.

Downloaded 17 Dec 2010 to 193.140.21.150. Redistribution subject to ASME license or copyright; see http://www.asme.org/terms/Terms_Use.cfm

Impingement Heat Transfer Within Arrays of Circular Jets: Part 1—Effects of Minimum, Intermediate, and Complete Crossflow for Small and Large Spacings

N. T. Obot
Associate Professor.
Mem. ASME

T. A. Trabold
Research Assistant.
Student Mem. ASME

Fluid Mechanics, Heat and Mass Transfer Laboratory,
Department of Chemical Engineering,
Clarkson University,
Potsdam, NY 13676

An experimental study of the effects of three jet-induced crossflow schemes on impingement heat transfer was made. The schemes, referred to as minimum, intermediate, and maximum crossflow correspond, successively, to unrestricted flow of spent air away from the target surface, restriction of the flow to leave through two opposite sides, and through one side of a rectangular impingement surface. The study covered jet Reynolds number, jet-to-surface spacing, and open area of 1000–21,000, 2–16 jet hole diameters, and 1–4 percent, respectively. The best heat transfer performance is obtained with the minimum scheme, intermediate and complete crossflow being associated with varying degrees of degradation. For a given blower power, heat transfer can be enhanced markedly by having greater number of jets over a fixed target area; notably when working with the minimum scheme at narrow jet-to-target spacings.

1 Introduction

Heat transfer characteristics within arrays of circular jets have been studied quite extensively, especially in connection with the design of internal cooling schemes for gas turbine air foils. Of the numerous other applications, mention is made here of cooling of planar VLSI circuits, evaporation from exposed liquid surfaces, and drying of various materials. The last two applications provided the motivation for the present study.

The flow field for any multiple jet system is very complex and is characterized by two types of interaction: interference between neighboring jets prior to impingement and collision of the developing wall flows from adjacent nozzles, the latter being referred to hereafter as the crossflow. Depending, of course, on jet-to-jet spacing (X_n, Y_n), and jet-to-surface spacing ($\overline{Z}_n$), the effects of either or both of these on impingement transfer rates can be quite pronounced. In the case of crossflow, its influence on transfer rates can be further accentuated by restricting the spent flow to leave through one or two sides of a rectangular impingement surface. For brevity, complete (or maximum) and intermediate crossflow, as used hereafter, refer to the former and latter situations, respectively, while unrestricted flow of spent air away from the heat transfer surface is associated with minimum crossflow (Fig. 1).

From the brief summary of some of the relevant literature (Table 1) it may be noted that, although complete or maximum crossflow has been studied by previous researchers, notably by Metzger et al. (1979), very limited investigations were carried out with intermediate crossflow. In fact, for impingement on flat surfaces, the only study with intermediate crossflow (Friedman and Mueller, 1951) considered one standoff spacing. Later, Huang (1963) considered impingement on a convex drum with partial restriction of the spent air, but the magnitude of the effect of crossflow cannot be determined from his results.

Table 1 Summary of relevant previous studies

Author(s)	$\overline{Z}_n$ (range)	flow scheme
Friedman and Mueller (1951)	3–10	intermediate, maximum
Allander (1961)	2–8	minimum
Gardon and Cobonpue (1961)	4–32	minimum
Kercher and Tabakoff (1970)	1–4.8	maximum
Chance (1974)	2–8	maximum
Cole (1978)	1–3	maximum
Hollworth and Berry (1978)	1–25	minimum
Metzger et al. (1979)	1–4	maximum
Florschuetz et al. (1980)	1–3	maximum
Saad et al. (1980)	1–3	maximum
Florschuetz et al. (1981)	1–3	maximum
Florschuetz et al.(1984)	1–3	intermediate, with initial crossflow

Previous researchers were concerned mainly with separation distances in the range one to five jet hole diameters, as this is the range of interest in the aforementioned gas turbine applications. The works by Hollworth and Berry (1978) and Gardon and Cobonpue (1962) complement one another, in that the spent air flowed freely away from the heat transfer surface, a situation that is associated with minimum crossflow effects (Fig. 1). However, use of the correlation proposed by Gardon and Cobonpue is conditioned by knowledge of the dependence of arrival velocity on nozzle details, while the results of Hollworth and Berry are valid for large jet-to-jet spacings. Even for the case of complete crossflow, the standoff spacing of eight jet hole diameters represents the maximum that has been tested (Chance, 1974).

The present paper, the first part of a larger research program on impingement heat and mass transfer, is devoted to a comprehensive study of the effects of crossflow for small and

Contributed by the Heat Transfer Division for publication in the JOURNAL OF HEAT TRANSFER. Manuscript received by the Heat Transfer Division September 12, 1986.

Copyright © 1987 by ASME

Downloaded 17 Dec 2010 to 193.140.21.150. Redistribution subject to ASME license or copyright; see http://www.asme.org/terms/Terms_Use.cfm

large jet-to-surface spacings. The subsequent papers will consider the role of crossflow in the presence of roughness elements, and evaporation from small and large liquid surfaces exposed to impinging heated air jets.

In this paper, results are presented for the three flow schemes depicted in Fig. 1. The standoff distance and jet Reynolds number were varied between 2 and 16 jet hole diameters and 1000 to 21,000, respectively. At least 250 test runs were carried out during this phase of the research program. It should perhaps be noted at the outset that, since the present results were averaged over large segmented test plates, they do not reveal highly localized trends. However, some of the gross effects of crossflow and geometric variables are very important and, on this basis, the results should be of some interest in applications other than those that motivated this study.

2 Test Facility and Procedure

The experimental facility, essentially the same as that presented elsewhere (Obot et al., 1984), will be briefly described here. It consisted basically of a blower which delivered room temperature air through a calibrated orifice, a 203-mm-square plenum chamber containing layers of screen and aluminum honeycomb, and interchangeable nozzle plates. Average air temperature in the plenum was determined from the readings of a chromel-constantan thermocouple, its installation being such that it could be moved transversely through a threaded fitting located on the side of the plenum. Plenum static pressure, and hence pressure drop across each nozzle plate, was averaged from the readings of 12 taps using a manifold assembly. The nozzles were fabricated by boring square-edged holes, 3.175 mm in diameter, in 305-mm-square aluminum plates of thickness 9.53-mm, giving a thickness-to-diameter ratio of 3.02. The layout of the inline jet holes is also illustrated in Fig. 1. Expressed in terms of the relative nozzle (or open) area A_f, the values for the 48, 90, and 180-jet-hole plates could be stated as 0.0098, 0.0196, and 0.0352, successively. The jet hole arrangement for the latter was such that the same number of jets impinged on each segment of a test plate (smooth or rough).

The impingement surface consisted of a 609-mm-square Plexiglas plate, the central portion of which contained the assembled aluminum heat transfer surface. The latter is formed by cementing six aluminum plates of thickness 5.5 mm. Each plate segment of width and length 35 and 204 mm, respectively, is insulated from the next using a 2 mm strip of asbestos. Six thermocouples were installed in each segment with the objective of determining the average surface temperature. The couples were lined with two-hole ceramic tubings and then epoxied into holes drilled from the back of the plate to within 1 mm of the heat transfer surface. All couples were connected to a 40-port rotary switch to facilitate monitoring of surface temperatures.

Each aluminum segment was heated separately with 30-gage insulated nichrome wires located in small grooves machined in the back surface. Each was powered with a separate d-c power supply, and the heating circuit included a fixed resistor, a variable resistor, and a shunt of known resistance. The electrical power input to each unit was evaluated from the current, as determined from the voltage across the shunt, and the voltage measured directly across each segment. To minimize heat conduction from the back surface of the plates, a

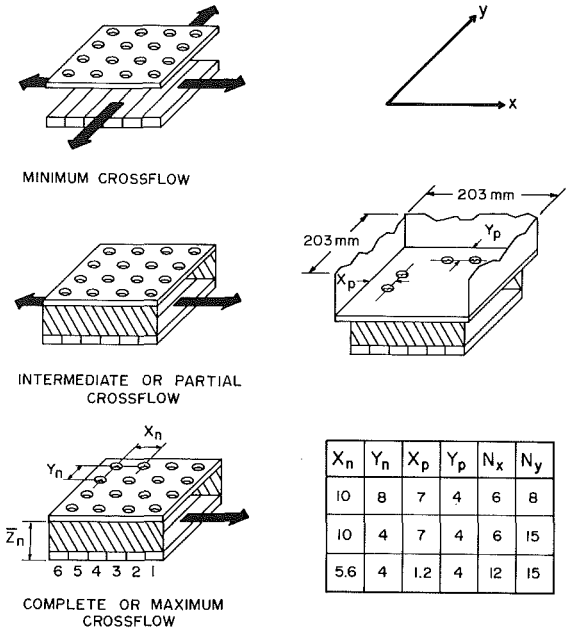

X_n	Y_n	X_p	Y_p	N_x	N_y
10	8	7	4	6	8
10	4	7	4	6	15
5.6	4	1.2	4	12	15

Fig. 1 Definitions of flow schemes and geometric variables

Nomenclature

A = heat transfer area, m^2
A_f = open area = $\pi d^2(4x_n y_n)^{-1}$
A_n = total jet flow area, m^2
A_0 = regression coefficient
d = jet hole diameter, m
E = blower power, W
h = individual plate heat transfer coefficient, $W/m^2°C$
$\bar{h}$ = transfer coefficient averaged over the entire heat transfer surface, $W/m^2°C$
k_f = thermal conductivity based on film temperature, W/m°C
L = width of heat transfer surface in x direction, m
$\dot{m}$ = total air mass flow rate, kg/s
Nu = individual plate Nusselt number = hd/k_f
$\overline{\text{Nu}}$ = average Nusselt number = $\bar{h}d/k_f$
$\overline{\text{Nu}}_y$ = average Nusselt number = $\bar{h}y_n/k_f$
N_x = number of rows in the x direction
N_y = number of rows in the y direction
Q_c = convective heat transfer, W
Re = Reynolds number = $\dot{m}d/A_n\mu$
Re_y = Reynolds number = $\dot{m}y_n/A_n\mu$
$\overline{\text{Re}}$ = Reynolds number = Re • A_f
T_{aw} = average adiabatic wall temperature, °C
T_b = bulk mean temperature = $(T_p + T_e)/2$, °C
T_e = average exhaust air temperature, °C
T_p = average air temperature in plenum chamber, °C
T_R = reference temperature, °C
T_s = average temperature of heated surface, °C
X = location in the x direction along heat transfer surface measured from upstream end of plate No. 6, m
x_n = jet hole spacing in the x direction, m
X_n = nondimensional jet hole spacing = x_n/d
y_n = spanwise jet hole spacing (y direction), m
Y_n = nondimensional jet hole spacing = y_n/d
z_n = jet-to-surface spacing, m
Z_n = nondimensional jet-to-surface spacing = z_n/d
μ = fluid viscosity, Pa•s

Downloaded 17 Dec 2010 to 193.140.21.150. Redistribution subject to ASME license or copyright; see http://www.asme.org/terms/Terms_Use.cfm

25.4-mm layer of Kaowool insulation was taped to this side of the plate.

Provision was made (in the form of three 12.7-mm-square grooves in the Plexiglas plate and bordering the heat transfer surface) to facilitate boxing in of two or three sides of the rectangular test plate. Flat wooden spacers were prepared for all standoff spacings to be tested. By sliding the appropriate spacers into place, the spent air was constrained to leave through one or two sides of the test plate (Fig. 1). For tests with no restriction of the spent air flow direction, 12.7-mm-square wooden strips were inserted in the grooves, and the clearance between the plexiglass and the test plate was neatly lined with epoxy, to give a smooth continuous surface for air flow away from the heat transfer surface.

Expressed as values of Nusselt number, individual plate results were computed from

$$\mathrm{Nu} = (Q_c d)/(k_f A)(T_s - T_R) \tag{1}$$

where the convective contribution Q_c is the difference between the power input and the losses. The latter, determined experimentally in the absence of the flow, represented the total electrical power input required to maintain the plates at the same surface temperature as in tests with flow. With this method, the losses ranged from 2 to 31 percent of the power input to the segments.

The validity of the above method was also verified experimentally for the case with complete crossflow. The Q_c values determined by the above technique were compared with those calculated from the mass flowrate of exiting air, the nearly constant specific heat, and ΔT_e. Here, ΔT_e is the difference in the average temperatures of the exiting air, one set of steady-state temperature measurements being taken just before power was supplied to the plates and the other when isothermal conditions were established with power. These readings (25 to 50 depending on the value of $\overline{Z}_n$ tested) were obtained by traversing a dual capability pitot static probe (i.e., measures total temperature as well as total and static pressures) across the entire exhaust exit. For example, with a jet Reynolds number of 4800, the differences between the two sets of Q_c data at $\overline{Z}_n$ = 2, 4, and 6 were 6, 0.4, and 1.2 percent successively. In fact, for each of the eight qualification runs carried out for several Re and $\overline{Z}_n$ in the ranges 4800–20,000 and 2–8, respectively, the two sets of data differed by no more than 8 percent.

A final comment, one that is of considerable importance to the design engineer, deals with the choice of reference temperature T_R for use in equation (1). Many researchers use the plenum or jet exit temperature. Although this is strictly incorrect, the advantages are that either can be measured quite easily and is, insofar as isothermal jets are concerned, essentially independent of axial location. In principle, T_R should be the average recovery temperature measured at the target surface, but this depends on several variables: jet-to-surface spacing, Re, spanwise and streamwise locations at the surface, notably when working with complete crossflow. For the latter situation, T_R may also be defined by $(T_p + T_e)/2$, where T_p and T_e are the steady-state plenum and initial exhaust air temperatures. Suffice it, for the moment, to state that the present experiment was designed to permit a thorough evaluation of use of all of these reference temperatures, and this will be explored in the next section.

3 Results and Discussion

In view of the observations in the last paragraph of the preceding section, we begin this presentation by considering the effect the choice of T_R has on the calculated heat transfer coefficients, a typical trend of which is displayed in Fig. 2 for the case with maximum crossflow and A_f = 0.0352. It can be seen that use of the average adiabatic wall (T_{aw}) or plenum

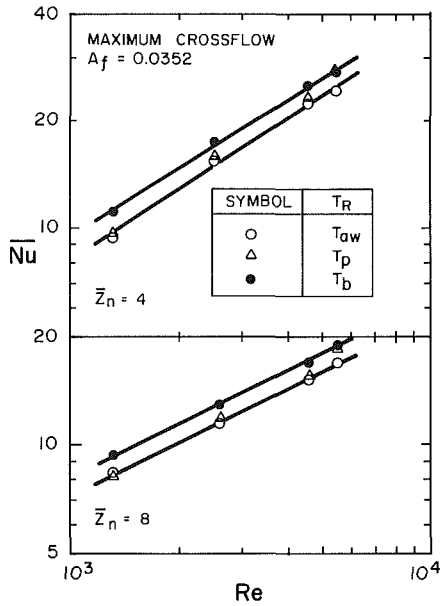

Fig. 2 Effect of choice of reference temperature

temperature yields about the same results while, relative to the other two, the choice of the bulk mean temperature can be expected to give results that are higher by about 15 percent. Similar differences were computed for results obtained for spacings in the range of $\overline{Z}_n$ between 2 and 8. To provide a consistent basis for evaluation of the effects of the various flow schemes on heat transfer, especially since the bulk mean temperatures are not readily determined for minimum crossflow, adiabatic wall temperatures were used for calculations of all results presented hereafter. It should be mentioned that, since these temperatures were taken at least one and a half hours after the establishment of the air flowrate for a run, they correspond to the steady-state values in the absence of power input to the plates.

It must not be inferred from Fig. 2, however, that the choice of T_p as the reference temperature will always give about the same heat transfer coefficients as with T_{aw}, for obviously the nominal temperature difference ($T_p - T_{aw}$) does depend on the range of Reynolds number tested. For example, whereas this temperature difference was within 1°C for Re < 10,000 (Fig. 2), it ranged from 2°C to 4°C when Re was increased over the range of values between 10,000 and 21,000. Depending, of course, then on the mean surface temperature (T_s), the use of T_p may result in $\overline{\mathrm{Nu}}$ values that are larger than those obtained with T_{aw} as the reference temperature. In this study, the mean temperature difference ($T_s - T_R$) was held close to 15°C for most of the trials.

Local Mean Nusselt Numbers. Figures 3–5 show trends for heat transfer coefficients averaged over each segment of the test plate. Although the compact presentations in Figs. 3 and 4 for Re = 11,000 and 5,500 are intended to illustrate the variation with increasing $\overline{Z}_n$, there is one common feature between the figures: Due to doubling the number of jet holes from 90 to 180, the air mass flowrate is the same. Here, X is the distance measured from the upstream end of the sixth test plate (i.e., farthest from the exhaust in the case of complete crossflow), while L is the width (streamwise) of the assembled test plate, exclusive of the small allowances taken up by the strips of insulation. The location of each data point corresponds closely to the center plane of each segment. For complete crossflow, the Nu trend with increasing Re is illustrated in Fig. 5 for $\overline{Z}_n$ = 4.

A study of the results in Figs. 3–5 reveals many interesting

Downloaded 17 Dec 2010 to 193.140.21.150. Redistribution subject to ASME license or copyright; see http://www.asme.org/terms/Terms_Use.cfm

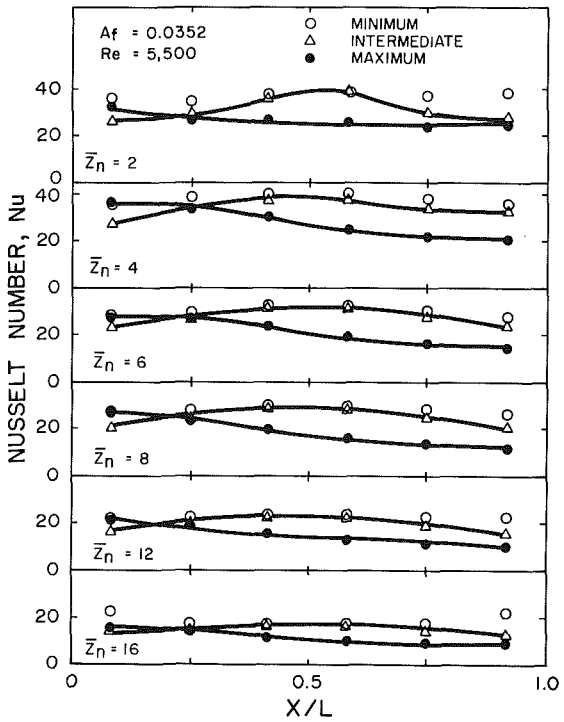

Fig. 3 Local mean Nusselt number profiles for A_f = 0.0196 and Re = 11,000

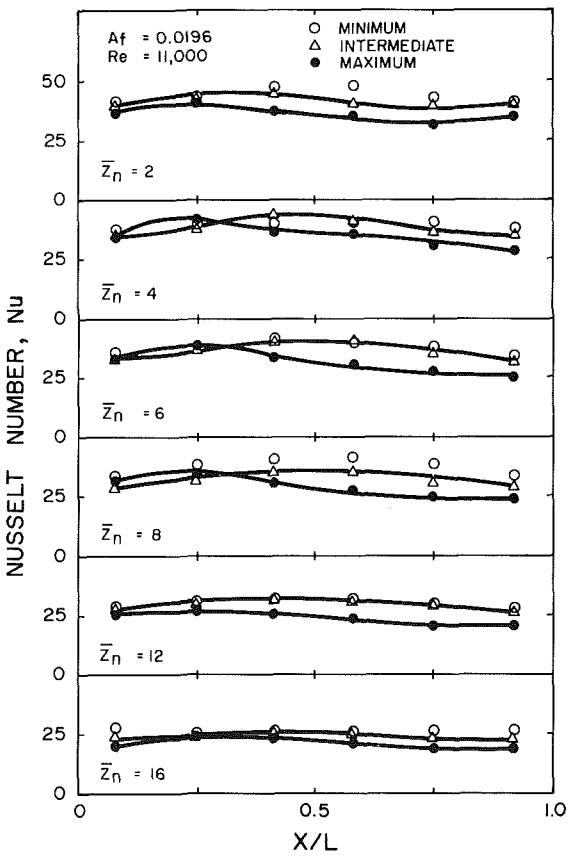

Fig. 4 Local mean Nusselt number profiles for A_f = 0.0352 and Re = 5500

features. One of the most obvious is the significant downstream degradation in heat transfer due to maximum jet-induced crossflow, a finding that is in complete agreement with virtually all of the published literature on the subject

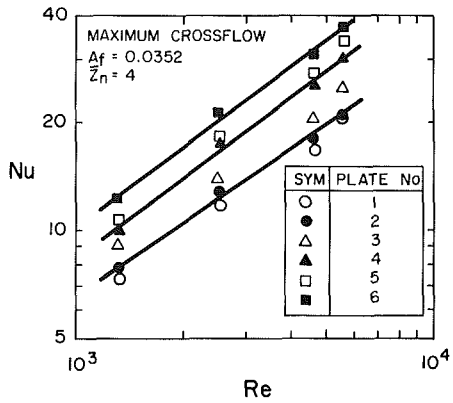

Fig. 5 Variation of Nu with Re for maximum crossflow and A_f = 0.0352

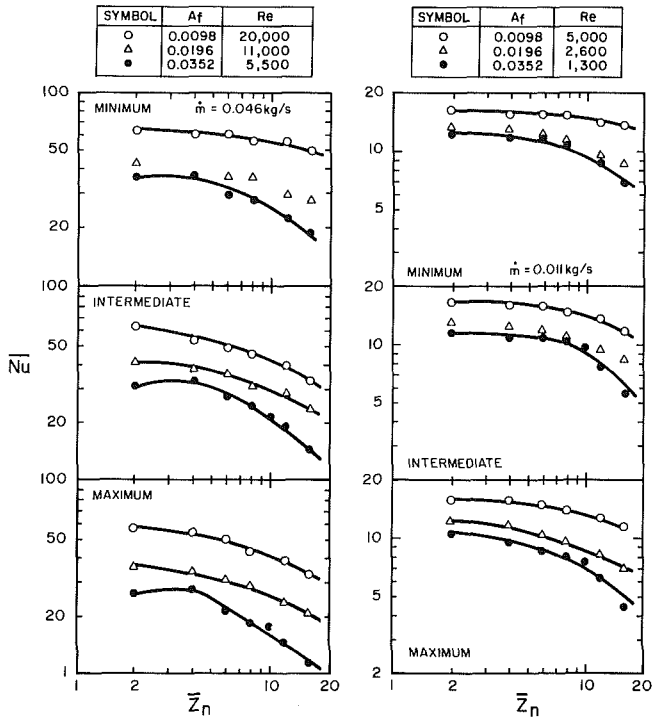

Fig. 6 Effect of jet-to-surface spacing on Nu for m = 0.011 and 0.046 kg/s

(Metzger et al., 1979; Florschuetz et al., 1981; Chance, 1974; to mention but a few). It is often speculated that, in the presence of maximum crossflow, the area-integrated heat transfer coefficient for the region farthest from the exhaust is not significantly affected by the crossflow originating from that region. Figures 3 and 4 show quite conclusively that this is indeed the case, this being true for the three nozzle configurations tested and for all Re in the range 1000 to 20,000.

When the spent air is discharged through two opposite sides of the rectangular impingement surface, a symmetric flow distribution is expected which, in turn, should result in nearly symmetric distribution curves for heat transfer coefficients. This is verified by the results in Figs. 3 and 4 which show Nu values that are generally higher over the central portion of the impingement surface than near the two exhaust openings. It is also quite evident from Figs. 3 and 4 that a fairly uniform cooling occurs when the spent air flows freely away from the heat transfer surface, and that any departure from this consistent pattern is due to directional discharge of the flow.

A closer examination of Figs. 3 and 4 reveals a marked effect of maintaining a fixed air flowrate and doubling the

Downloaded 17 Dec 2010 to 193.140.21.150. Redistribution subject to ASME license or copyright; see http://www.asme.org/terms/Terms_Use.cfm

number of jets over a given surface. It will there be observed that, for any particular exhaust scheme, the results in Fig. 3 with the (10, 4) arrangement are significantly higher than those obtained with the (5.6, 4) nozzle plate, the latter being characterized by more closely spaced jets in the streamwise direction. This is of course consistent with expectations because, for a given flowrate, the exit velocity, as well as that at impingement, decreases with increasing jet holes in an array. This observation is in agreement with the findings of Hollworth and Berry (1978) and Metzger et al. (1979). It is also especially noticeable that the absolute effect of crossflow is more pronounced in Fig. 4 than in Fig. 3, notably for the scheme with one exhaust opening. For example, at $\overline{Z}_n$ = 2, 4, 6, and 8, the complete crossflow results averaged over the three downstream plates are, successively, 28, 28, 36, and 49 percent (Fig. 3), and 47, 69, 80, and 106 percent (Fig. 4) lower than those obtained with the minimum scheme. In fact, even for the case of intermediate crossflow, the percentage differences in Fig. 4 are larger than in Fig. 3, especially for the last plate segments at each exhaust opening. The trend with increasing $\overline{Z}_n$, documented here for complete crossflow, is in agreement with that of Chance (1974).

It might appear at first, from the presentation in the preceding paragraph (as well as that of either of the references cited therein, where Nu or $\overline{\text{Nu}}$ was plotted against the Reynolds number based upon the mass flowrate per unit heat transfer surface area $\overline{\text{Re}}$) that there may be no real advantage in doubling the number of jets over a given surface area, except of course for the attendant more uniform cooling or heating. Kercher and Tabakoff (1970) provided extensive results for a square array of round jets. For a constant jet hole diameter, as is the case in the present study, they varied X_n and reported increased heat transfer by having a greater number of jets over a given surface. The basis for their observation will be examined in the next section.

Average Nusselt Numbers. It is important to note that average Nu values were computed from the total convective contribution for all six plates. Figure 6 is an alternative representation of the data in Figs. 3 and 4, the data for A_f = 0.0098 being included for completeness, and show the variation of $\overline{\text{Nu}}$ with $\overline{Z}_n$ for all flow schemes. It is strikingly apparent that, at low flowrates corresponding to Re = 5000, 2600, and 1300 for A_f = 0.0098, 0.0196, and 0.0352, respectively, $\overline{\text{Nu}}$ decreases steadily with increasing spacing for any particular flow scheme. It can be established that $\overline{\text{Nu}} \propto \overline{Z}_n^n$, where n depends on the exhaust scheme. With a fourfold increase in air flowrate, although the results for the widely spaced arrays still exhibit the same general trend as noted above, each of the three $\overline{\text{Nu}}$ profiles for the tightest jet hole arrangement passes through a maximum around $\overline{Z}_n$ = 4. Hollworth and Berry (1978) reported a similar trend for their most compact array. It is of some interest to note that the results of Metzger et al. (1979), Saad et al. (1980), and Kercher and Tabakoff (1970) also show an increasing trend with $\overline{Z}_n$ up to about $\overline{Z}_n$ = 4, the maximum $\overline{Z}_n$ range for which extensive data were reported by these investigators.

The different trends outlined above with increasing $\overline{Z}_n$ and A_f appear to be primarily the result of jet interference prior to impingement, a phenomenon which has received relatively little attention in the past. For a given array and prior to impingement, interference in all directions with the neighboring jets can be expected when X_n and Y_n values are about the same as the nondimensional axial distance in the free jet (z/d). One clear consequence of this interaction and mixing with neighboring jets is a reduction in the axial velocity in the downstream direction. Also, the intensity of this interference, and its effect on heat or mass transfer, must be expected to depend on the turbulence level at the nozzle exit and at locations downstream, both of which do vary with Reynolds number.

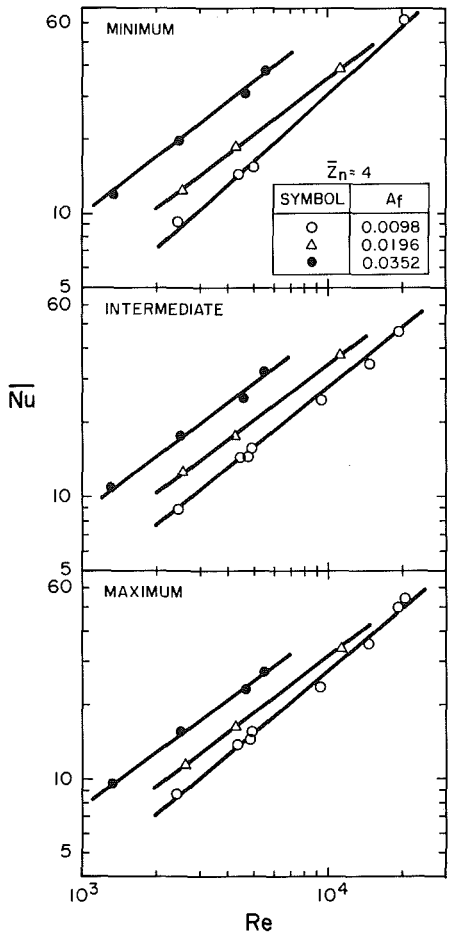

Fig. 7 Variation of $\overline{\text{Nu}}$ with Re at $\overline{Z}_n$ = 4

At large X_n, Y_n, and for a given Re, jet interaction occurs at larger downstream distances, and the attendant mixing process associated with the reduced axial velocity and low turbulence level is not so intense as to produce any measurable effect on a typical $\overline{\text{Nu}}$ versus $\overline{Z}_n$ trend, this being equally true in the case of closely spaced jets with low Re. At large Re with A_f = 0.0352, the high turbulence levels both at the nozzle exit and downstream locations, together with that induced by the interacting jets, combine to bring about a maximum in heat transfer. Consistent with the lowering of the axial velocity in the downstream direction due to jet interference, it will be observed that, beyond the spacing which affords the maximum, there is an appreciable drop in $\overline{\text{Nu}}$ with further increases in $\overline{Z}_n$. The views advanced here may help explain the marked drop in $\overline{\text{Nu}}$ with $\overline{Z}_n$ as reported by Hollworth and Berry for their tightest array and Re > 3000.

The effects of Reynolds number on average heat transfer are shown differently in Figs. 7–9, the first of which is simply a plot of $\overline{\text{Nu}}$ versus Re with the nozzle diameter as the characteristic length. In the second figure, the length scale is the appropriate spanwise jet hole spacing for (10, 4) and (10, 8), similar to Figs. 10 and 11 of Kercher and Tabakoff (1970), which formed the basis for their observation that the greater the number of jets over a given area, the higher the heat transfer coefficient for a fixed jet hole diameter. In Fig. 9, $\overline{\text{Nu}}$ is plotted against $\overline{\text{Re}}$, where $\overline{\text{Re}}$ = Re • A_f (Hollworth and Berry, 1978; Metzger et al., 1979).

Figure 7 shows that, for a specified Re (or same jet hole plate pressure drop), $\overline{\text{Nu}}$ increases with increasing A_f, in agreement with the observation of nearly all investigators. A change of slope with increasing Re is clearly in evidence for

Downloaded 17 Dec 2010 to 193.140.21.150. Redistribution subject to ASME license or copyright; see http://www.asme.org/terms/Terms_Use.cfm

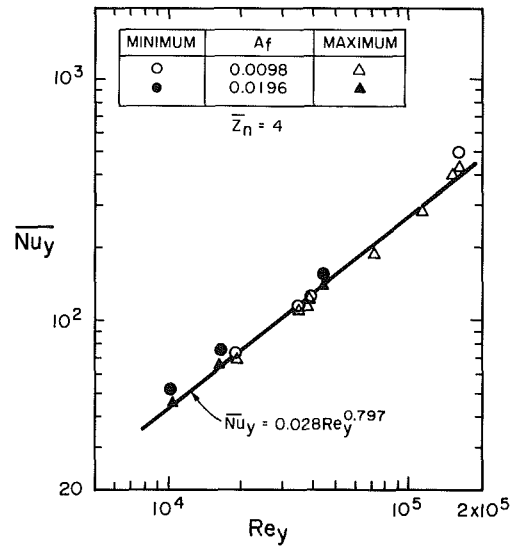

Fig. 8 Effect of jet hole spacing on average Nusselt number

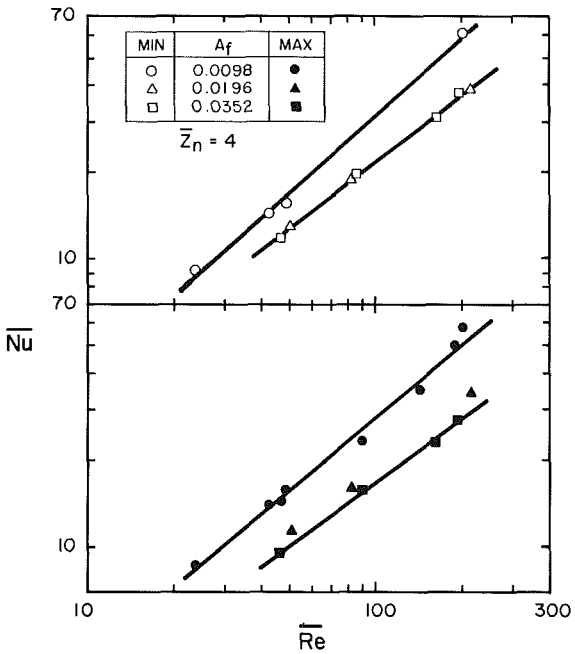

Fig. 9 Average Nusselt number versus Reynolds number based on flow rate per unit heat transfer area

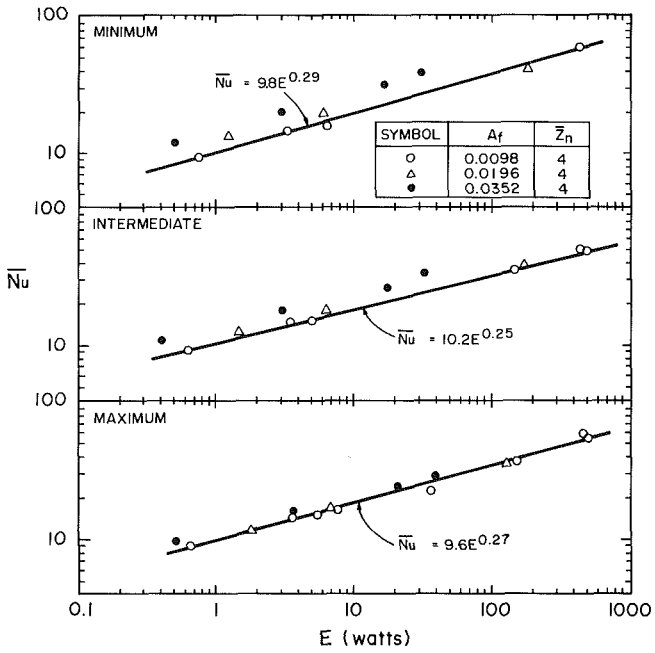

Fig. 10 Variation of $\overline{Nu}$ with blower power

some of the test conditions which are given in Fig. 7. This expected trend is also in agreement with the results of previous studies. The presentation on Fig. 8, while suppressing the differences due to nozzle geometric configurations or exhaust scheme, provides little evidence to support the view that the 90-hole jet plate is more effective than the 48-hole arrangement. In fact, all results in this figure are closely approximated by a single equation with an exponent on Re$_y$ of 0.797 (correlation coefficient = 0.992), suggesting that correlation of all data at $\overline{Z}_n = 4$ may be accomplished with a constant value for the exponent on Reynolds number. Kercher and Tabakoff based their conclusion on results averaged over the plate segment located farthest from the exhaust opening. However, countering this upstream enhancement is the significant downstream degradation with increased jet holes in the array. Clearly, their observation is not of general validity. In terms of Re or Re$_y$ (Figs. 7 and 8), it is quite apparent that the basis for the comparison is that of unequal air mass flowrate.

It was noted in the previous section that comparison between Figs. 3 and 4 might lead one to conclude that some benefits could be obtained by maintaining widely spaced hole arrangement in an array. The use of $\overline{Re}$ (Fig. 9), i.e., based on the mass flowrate per unit heat transfer area, does not modify that view. For a given mass flowrate and fixed jet hole diameter, the picture that emerges then from Figs. 7–9 is one of no clear definitive statement concerning the advantage of increasing the number of jets over a given area.

To carry the analysis and discussion to a satisfactory conclusion, at least insofar as the real advantage of greater over fewer jet holes is concerned, it is more instructive to consider the blower power requirements. For a given flowrate, this power is simply the product of the pressure drop across the nozzle plate and the corresponding volumetric flowrate based on the actual flow area. Naturally, since this pressure drop decreases significantly wth increasing number of holes over the given area, it was envisaged that plots of $\overline{Nu}$ versus E should provide realistic perspectives for examining the effectiveness of the different arrangements. The results of such calculations are illustrated in Fig. 10. The relations which are quoted therein represent logarithmic best fits through the data for the most widely spaced jets with $A_f = 0.0098$. In each case, the correlation coefficient was between 0.99 and 1.0, and the exponents on E are quite consistent with the available literature. It is of interest to note that the alternative approach, which involves plots of $\overline{Nu}$ versus the blower power per unit heat transfer area, leads one to the same conclusion as already mentioned in connection with Fig. 9.

It can be seen that, for a given E, better heat transfer performance is realized with a greater number of jets over a fixed target area, the least improvement being obtained when working with the complete crossflow scheme. In view of the marked degradation in heat transfer with increasing A_f, discussed already in connection with Figs. 3–5, this outcome is not surprising. Also, since the absolute effect of complete crossflow is more pronounced at larger spacing ($\overline{Z}_n > 5$) than for $\overline{Z}_n < 5$, it can be readily appreciated that there is no advantage to using closely spaced jets when designing for large jet-to-surface situations.

Comparison of the present results with some of the published data obtained with segmented test plates is given in Fig.

Downloaded 17 Dec 2010 to 193.140.21.150. Redistribution subject to ASME license or copyright; see http://www.asme.org/terms/Terms_Use.cfm

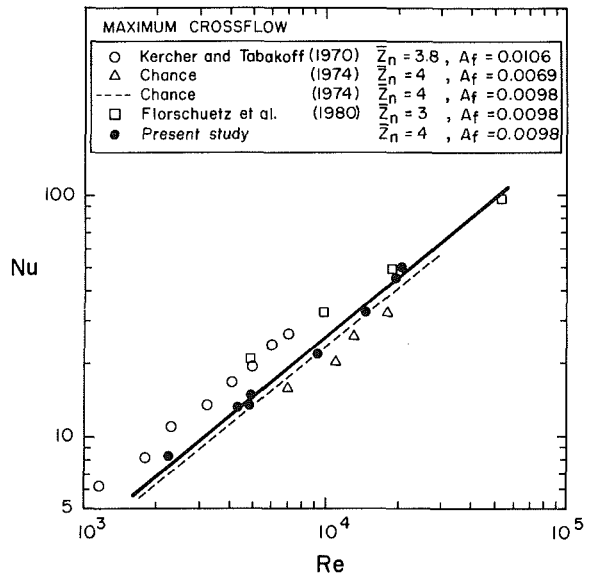

Fig. 11 Comparison of present results with published data

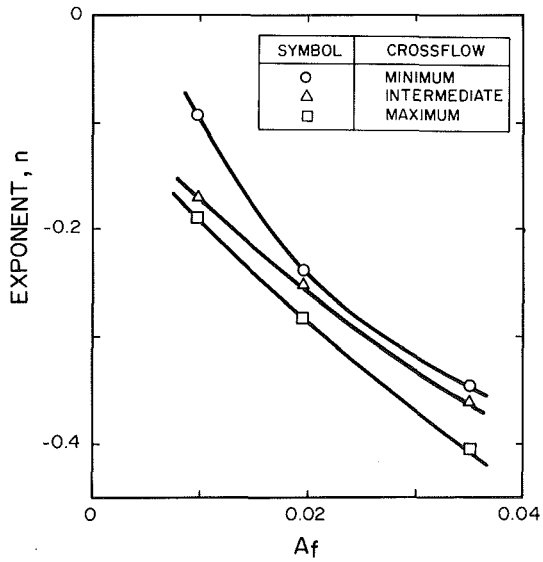

Fig. 12 Variation of exponent on $\overline{Z}_n$ with open area

Table 2 Summary of predictive equations

Flow scheme	A_0	m	n	x
Minimum	0.863	0.8	Fig. 12	0.815
Intermediate	0.484	0.8	Fig. 12	0.676
Maximum	0.328	0.8	Fig. 12	0.595

11 for the most widely studied maximum crossflow scheme. In each case, the results are for the plate segment located farthest from the exhaust opening, with minimum crossflow effects. The solid line corresponds to a logarithmic best fit of our data, while the dashed line is obtained from the Chance correlation for $A_f = 0.0098$. The differences which are observed here can be attributed largely to the residual effects of nozzle geometric details, mass flowrate, and averaging area. Chance's data for $A_f = 0.0069$ follow the expected trend, being about 24 percent lower than ours; but his correlation gives about the same results. The results of Kercher and Tabakoff are higher than ours by roughly a constant factor of 1.25. A Prandtl number of 0.7 was used to scale down their results. To gain insight on the possible sources of this disagreement (since differences in A_f and $\overline{Z}_n$ are minimal), it is instructive to compare the number of jets in the array (N_T), exit hole velocity (V_0) range, and averaging area (A), as these are clearly the most important parameters. For their study, $N_T = 256$, $V_0 =$ 68–415 m/s, and $A = 645$ mm^2, in sharp constrast with (in the same order) 48, 12–105 m/s, and 7140 mm^2 of the present study. On the basis of this information, the trend on Fig. 11 is exactly as would be expected. The moderate differences between our results and the types A and B plenum data of Metzger et al. (1979) and Florschuetz et al. (1980) are due to the same reasons as outlined above.

Correlation of Average Nusselt Numbers. In principle, for a constant Prandtl number, $\overline{\mathrm{Nu}}$ can be represented by the relation

$$\overline{\mathrm{Nu}} = A_0 \mathrm{Re}^m \overline{Z}_n^n A_f^x \tag{2}$$

where A_0 is a regression coefficient. In practice, however, the determination of A_0, m, n, and x is complicated by their dependence on flow and geometric conditions. As can be inferred from Fig. 8, although the exponent on Re is a function of $\overline{Z}_n$ or A_f, there is only mild dependence on the exhaust scheme. For a fixed jet hole opening, as is usually the case in many practical situations, the variations with $\overline{Z}_n$ or A_f is such

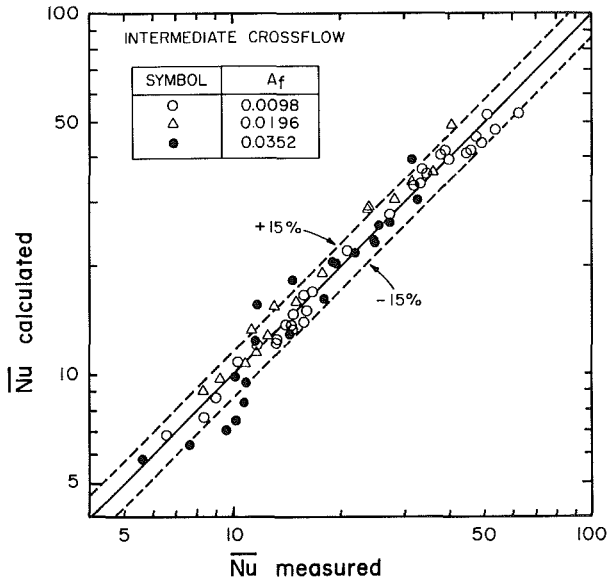

Fig. 13 Calculated versus experimental $\overline{\mathrm{Nu}}$ for intermediate crossflow

that a single value would suffice. For example, using data for all $\overline{Z}_n$ and A_f, the present m values could be stated as 0.82 ± 0.08, 0.72 ± 0.08, and 0.77 ± 0.09 for minimum, intermediate, and maximum crossflow, successively, with an average value of 0.77 ± 0.09, which is about as good as the rounded value of 0.8 reported by other investigators. For the exponent on $\overline{Z}_n$, the situation was quite different and, as would be expected, there is a marked variation with A_f and exhaust scheme as shown in Fig. 12. Likewise, a constant x value for all exhaust schemes would result in about a 20 percent variation about such a mean regression value. For Re = 1000–21,000, $A_f = 0.0098$–0.0352 and $\overline{Z}_n = 2$–16, the recommended values of A_0, m, and n for each predictive equation are summarized in Table 2. To calculate average heat transfer coefficient for any particular flow scheme, the pertinent information is provided in Table 2 and Fig. 12. For each flow scheme, individual differences between measured and calculated values are under 10 percent for 85 percent of the nearly 80 data points. A typical fit of the proposed correlation to the experimental data is illustrated graphically in Fig. 13 for intermediate crossflow. For clarity, coincident data points are not so identified in Fig. 13.

Downloaded 17 Dec 2010 to 193.140.21.150. Redistribution subject to ASME license or copyright; see http://www.asme.org/terms/Terms_Use.cfm

4 Concluding Remarks

This experimental investigation was carried out to determine the effects of three crossflow schemes on impingement heat transfer from smooth surfaces. The schemes tested include unrestricted flow of spent air away from the target surface, restriction of the flow to leave through two opposite sides, and through one side of a rectanglar impingement surface. For brevity, these are referred to as minimum, intermediate, and complete crossflow, successively.

It has been established that the best heat transfer performance (with respect to magnitude and uniformity of cooling) occurs with minimum crossflow, with moderate and substantial reductions in average heat transfer with intermediate and complete schemes, respectively. For a given mass flowrate of air, the results show quite conclusively that the greater the number of jets over a fixed target area, the more pronounced the degradation in heat transfer with intermediate or complete crossflow and that, relative to the minimum scheme, the magnitude of this effect increases with increasing jet-to-surface spacing.

For a given Re, the larger the open area (i.e., the greater the number of jets over a fixed target area at constant d), the higher the heat transfer coefficient. This is clearly a natural consequence of maintaining about the same pressure drop across the nozzle plate with varying flowrate. The real advantage of using a denser hole arrangement comes from consideration of the blower power requirement. For a specified flowrate and hole diameter, the jet can be generated using fewer holes with a large pressure drop, or a larger number of holes with substantially lower pressure drop; but, for a given blower power and at narrow jet-to-target spacings, the latter gives better heat transfer performance, regardless of the spent air flow scheme used. At larger spacings and in spite of jet interference prior to impingement, the preceding observation is still true for the minimum scheme. However, due to the marked effect of crossflow with increasing spacing, no benefits can be established from our results for use of a more compact in place of a widely spaced arrangement.

Acknowledgments

This work was supported by the Chemical Research and Development Center of the US Army under Contract DAAK11-85-C-0001. Technical liaison for this project was provided by Paul Grasso, Operational Sciences Section, Physics Branch, CRDC, Aberdeen, MD.

References

Allander, C. G., 1969, "Air Impingement Drying," *TAPPI*, Vol. 44, pp. 332–337.

Chance, J. L., 1974, "Experimental Investigation of Air Impingement Heat Transfer Under Arrays of Round Jets," *TAPPI*, Vol. 57, pp. 108–112.

Cole, G. H., 1978, "Heat Transfer to Arrays of Impinging Jets in a Crossflow," M.S. Thesis, Clarkson University, Potsdam, NY.

Florschuetz, L. W., Metzger, D. E., Takeuchi, D. I., and Berry, R. A., 1980, "Multiple Jet Impingement Heat Transfer Characteristics—Experimental Investigation of In-Line and Staggered Arrays with Crossflow," NASA Contractor Report 3217.

Florschuetz, L. W., Truman, C. R., and Metzger, D. E., 1981, "Streamwise Flow and Heat Transfer Distributions for Jet Array Impingement with Crossflow," ASME JOURNAL OF HEAT TRANSFER, Vol. 102, pp. 337–342.

Florschuetz, L. W., Metzger, D. E., Su, C. C., Isoda, Y., and Tseng, H. H., 1984, "Heat Transfer Characteristics for Jet Array Impingement With Initial Crossflow," ASME JOURNAL OF HEAT TRANSFER, Vol. 106, pp. 34–41.

Friedman, S. J., and Mueller, A. C., 1951, "Heat Transfer to Flat Surfaces," *Proceedings, ASME General Discussion on Heat Transfer*, pp. 138–142.

Gardon, R., and Cobonpue, J., 1962, "Heat Transfer Between a Flat Plate and Jets of Air Impinging on It," *Proceedings, 2nd International Heat Transfer Conference*, ASME, New York, pp. 454–460.

Hollworth, B. R., and Berry, R. D., 1978, "Heat Transfer From Arrays of Impinging Jets With Large Jet-To-Jet Spacing," ASME JOURNAL OF HEAT TRANSFER, Vol. 100, pp. 352–357

Huang, G. C., 1963, "Investigations of Heat Transfer Coefficients for Air Flow Through Round Jets Impinging Normal to a Heat Transfer Surface," ASME JOURNAL OF HEAT TRANSFER, Vol. 85, pp. 237–243

Kercher, D. M., and Tabakoff, W., 1970, "Heat Transfer by a Square Array of Air Jets Impinging Perpendicular to a Flat Surface Including the Effect of Spent Air," ASME *Journal of Engineering for Power*, Vol. 92, pp. 73–82.

Metzger, D. E., Florschuetz, L. W., Takeuchi, D. I., Behee, R. D., and Berry, R. A., 1979, "Heat Transfer Characteristics for Inline and Staggered Arrays of Circular Jets With Crossflow of Spent Air," ASME JOURNAL OF HEAT TRANSFER, Vol. 101, pp. 526–531

Obot, N. T., Graska, M. L., and Trabold, T. A., 1984, "The Near Field Behavior of Round Jets at Moderate Reynolds Numbers," *Canadian Journal of Chemical Engineering*, Vol. 62, pp. 587–593.

Saad, N. R., Mujumdar, A. S., Abdel Messeh, W., and Douglas, W. J. M., 1980, "Local Heat Transfer Characteristics for Staggered Arrays of Circular Jets With Crossflow of Spent Air," ASME Paper No. 80-HT-23.

Downloaded 17 Dec 2010 to 193.140.21.150. Redistribution subject to ASME license or copyright; see http://www.asme.org/terms/Terms_Use.cfm

Forced Convection in a Channel Filled With Porous Medium, Including the Effects of Flow Inertia, Variable Porosity, and Brinkman Friction

D. Poulikakos

K. Renken

Department of Mechanical Engineering,
University of Illinois at Chicago,
Chicago, IL 60680

This paper presents a series of numerical simulations which aim to document the problem of forced convection in a channel filled with a fluid-saturated porous medium. In modeling the flow in the channel, the effects of flow inertia, variable porosity and Brinkman friction are taken into account. Two channel configurations are investigated: parallel plates and circular pipe. In both cases, the channel wall is maintained at constant temperature. It is found that the general flow model predicts an overall enhancement in heat transfer between the fluid/porous matrix composite and the walls, compared to the predictions of the widely used Darcy flow model. This enhancement is reflected in the increase of the value of the Nusselt number. Important results documenting the dependence of the temperature and flow fields in the channel as well as the dependence of the thermal entry length on the problem parameters are also reported in the course of the study.

Introduction

Porous media heat transfer has been attracting the attention of an increasingly large number of investigators in recent years. The need for fundamental studies in porous media heat transfer stems from the fact that a better understanding of a host of thermal engineering applications in which porous materials are present is required. The accumulated impact of these studies is twofold: first to improve the performance of existing porous-media-related thermal systems, and second to generate new ideas and explore new avenues with respect to the use of porous media in heat transfer applications. Some examples of thermal engineering disciplines which stand to benefit from a better understanding of heat and fluid flow processes through porous materials are geothermal systems, thermal insulations, grain storage, solid matrix heat exchangers, oil extraction and the manufacturing of numerous products in the chemical industry.

The overwhelming majority of existing studies pertinent to heat and fluid flow in porous media makes use of the Darcy flow model [1]. This model features a linear momentum equation, which states that the volumetrically averaged velocity in any direction in space is proportional to the pressure gradient in that direction. The popularity of the Darcy flow model in convective heat transfer studies is justified: The model is simple and has performed well within the range of its validity [1]. The main limitations of the Darcy flow model are the following:

(*a*) It is not appropriate for "fast" flows, i.e., flows for which the Reynolds number based on the local velocity and pore diameter is greater than 0(1).

(*b*) It does not satisfy the no-slip condition on a solid boundary: In convective heat transfer problems, heat is often transferred to (or from) the fluid saturating the porous matrix through a solid boundary. In such cases the predictions of the Darcy model have been challenged [2, 3].

(*c*) It does not account for the spatial variation of the matrix porosity. It has been shown [4–9] that high porosity regions in a porous matrix (exemplified by regions near solid walls) are more penetrable by the fluid flowing in the porous matrix. As a result, "channels" of fast flowing fluid are created in these regions with significant effects on the heat transfer characteristics of the system [8, 9].

Even though limited, there exist studies of convective heat transfer in porous media, which make use of flow models that relax some or all of the above limitations. To this end, the works of Vafai and Tien [2], Vafai et al. [9], and Vafai [8] are relevant. Reference [2] in particular constitutes one of the first theoretical attempts to account for boundary and inertia effects in porous media forced convection. The studies in [8, 9] thoroughly document, theoretically and experimentally, the effect of flow channeling in flat plate forced convection. Significant differences were found both in the flow field and in the temperature field and heat transfer, caused by the presence of variable porosity, flow inertia, and Brinkman friction. The effect of flow channeling was to enhance the heat transfer from the wall. On the other hand, increasing the flow inertia reduced the heat transfer, relative to the Darcy flow model. The impact of flow inertia in natural convection problems has been investigated by Poulikakos [10] and Bejan and Poulikakos [11]. With reference to natural convection Georgiadis and Catton [12] reported interesting theoretical results relevant to flow instability in a horizontal porous layer in the non-Darcian regime. The numerical findings for the Prandtl number effect on the overall heat transfer through a horizontal porous layer [12] were found to be in good agreement with experiments performed later by Jonsson and Catton [13]. Pertinent to enclosure natural convection in non-Darcy porous media is [14]. In addition to the above, a study of laminar flow through a porous channel bounded by isothermal parallel plates, based on the Brinkman-extended flow model and for constant matrix porosity, was recently reported [15]. In this study, it is shown that the velocity field changes gradually from parabolic (classical fluids limit) to uniform (Darcy limit) as the Darcy number decreases. Results are reported for the hydrodynamic entry and the thermal entry regions as well as for the fully developed regions.

Contributed by the Heat Transfer Division for publication in the JOURNAL OF HEAT TRANSFER. Manuscript received by the Heat Transfer Division October 10, 1985.

Copyright © 1987 by ASME

Downloaded 17 Dec 2010 to 193.140.21.150. Redistribution subject to ASME license or copyright; see http://www.asme.org/terms/Terms_Use.cfm

The present paper focuses on an interesting problem which is of both fundamental and practical value, for it relates to several of the abovementioned thermal engineering applications, namely, the problem of forced convection in a channel filled with porous material. The model used to describe the flow in the channel accounts for all the phenomena neglected in the Darcy flow model: variable porosity, Brinkman friction, and flow inertia. It is worth noting that unlike the hydrodynamic entry length, which is usually short in porous media channel flows, very little is known about the thermal entry length. One of the goals of this study is to present detailed results on the thermal entry length by using the general flow model. Two channel geometries are investigated extensively: (*a*) parallel plates, and (*b*) circular pipe. Comparisons of the results of the general flow model to the results of the Darcy flow model are also reported in the course of the study. As will be shown in the following sections, these comparisons reveal significant differences of engineering importance in the heat and fluid flow characteristics of the configurations of interest. Finally, the range of the problem parameters in which the non-Darcy terms in the momentum equation (such as inertia terms) are significant for the present problem is identified.

Mathematical Formulation

The system of interest is shown schematically in Fig. 1. More specifically, Fig. 1(*a*) depicts a channel filled with fluid-saturated porous medium and bounded by two solid horizontal walls. Both these walls are kept at constant temperature T_w. The fluid at the inlet of the channel is isothermal at temperature T_i with $T_i \neq T_w$. In the spirit of the Graetz problem in classical fluids, a fully developed velocity profile is assumed at the channel inlet. This assumption is much more justified in porous media flows than it is in classical fluid flows for it has been shown [2] that the velocity boundary layer growth in porous media takes place over a distance of order 0 (KV/ν). Therefore, in most practical cases the hydrodynamic entrance length is negligible. Figure 1 also illustrates the fact that regions of high porosity exist near the solid walls. The exact variation of porosity with the distance from the walls will be discussed in detail later in this section. Figure 1(*b*) shows the second duct configuration of interest to the present study, namely, a circular pipe of diameter D. The previous discussion pertinent to the parallel plate configuration holds in this case as well. Assuming that the fluid and the

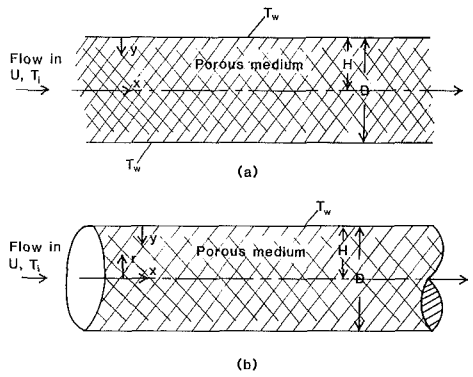

Fig. 1 Schematic of the configurations of interest: (*a*) a channel filled with fluid saturated porous medium and bounded by two horizontal solid walls; (*b*) a circular pipe filled with a fluid-saturated porous medium

porous medium are in local thermal equilibrium, and that the effective thermal diffusivity is constant, yields the following energy equation governing the convection phenomenon in the channel

$$u\frac{\partial T}{\partial x} = \alpha_e \frac{1}{r^m}\frac{\partial}{\partial y}\left(r^m \frac{\partial T}{\partial y}\right) \tag{1}$$

Note that $m = 0$ corresponds to the parallel plate case (Fig. 1*a*) while $m = 1$ is relevant to the circular pipe configuration (Fig. 1*b*). The coordinate systems are defined in Fig. 1. The effective thermal diffusivity is denoted by α_e. The effective thermal diffusivity of the porous medium is assumed to be constant in the course of this study, for simplicity. The variation of porosity is expected to have an effect on the thermal diffusivity. This effect will be minimal when the thermal diffusivity of the porous matrix is of the same order of magnitude as the thermal diffusivity of the fluid. Taking into account the variation of the effective thermal diffusivity with porosity will greatly complicate the problem and make any theoretical solution unattractive. This seems unnecessary since significant knowledge on the effect of channeling on heat transfer can be acquired by assuming that α_e remains constant. It is worth noting that the viewpoint that α_e remains constant when the porosity decreases exponentially with distance from a solid wall is shared unanimously by all authors of papers relevant to

Nomenclature

A = Forchheimer's function, equation (5)
B = dimensionless parameter, equation (9)
c_i = dimensionless coefficients, equation (9)
c_p = fluid specific heat at constant pressure
D = channel width or diameter, Fig. 1
d_* = dimensionless sphere diameter = d/H
H = channel half-width or radius, Fig. 1
K = permeability, equation (4)
k_e = effective thermal conductivity of porous medium
m = exponent defining the channel geometry, equations (1), (2)
Nu = Nusselt number, equation (13)
P = pressure
Pr = Prandtl number = ν/α_e
r = radial coordinate, Fig. 1
S = channel cross section
T = temperature
T_m = average temperature = $(\int \rho u T dS)/\rho VS$
u = horizontal velocity component
V = average velocity = $(\int u dS)/S$
x = horizontal Cartesian coordinate, Fig. 1
y = vertical Cartesian coordinate, Fig. 1
$(\Delta y)_j$ = size of the jth mesh interval in y
α_e = effective thermal diffusivity of porous medium
γ = constant in the relation for the compound interest grid
η = similarity variable, equation (10)
$(\Delta\eta)_j$ = size of the jth mesh interval in η
θ = dimensionless temperature
θ_m = invariant temperature = $(T_w - T)/(T_w - T_m)$
λ_i = constants in equation (3)
μ = viscosity
ν = kinematic viscosity
ρ = density
ϕ = porosity, equation (3)

Subscripts

i = pertaining to the channel inlet
w = pertaining to the wall
$*$ = denoting dimensionless quantity

Downloaded 17 Dec 2010 to 193.140.21.150. Redistribution subject to ASME license or copyright; see http://www.asme.org/terms/Terms_Use.cfm

the effect of channeling on porous media heat transfer (see, for example, [8, 9, 16]).

To obtain the temperature field from equation (1), knowledge of the velocity distribution is necessary. The fully developed velocity field is described by the x-momentum equation

$$0 = -\frac{1}{\rho}\frac{dP}{dx} + \nu\frac{1}{r^m}\frac{d}{dy}\left[r^m\frac{du}{dy}\right] - \frac{\nu}{K(y)}u - A(y)u^2 \quad (2)$$

In the above equation, A is an empirical function which depends on the structure of the porous medium. It is worth noting that the term multiplied by A in equation (2) was first introduced by Forchheimer in an empirical manner for the special case of one-dimensional flows through porous media, in order to account for inertial effects [1]. Similarly, the second term on the right-hand side of equation (2) accounts for friction due to macroscopic shear and was introduced first by Brinkman [1, 3] again in an heuristic manner. Both the Brinkman term and the Forchheimer term in the momentum equation for porous media flows were derived rigorously in later studies, exemplified by [17], which relied on the formalism of volumetric averaging along with physically acceptable assumptions.

The porosity of the matrix is assumed to be dependent on location to account for the high porosity regions near the walls (porosity variations in the horizontal are neglected). It has been shown [6–9, 16] that for a bed of randomly well-packed spheres, the porosity decreases exponentially with the distance from a solid wall. The most commonly used equation for this exponential variation is [6–9, 16]

$$\phi = \phi_\infty[1 + \lambda_1 e^{-\lambda_2 y/d}] \quad (3)$$

where ϕ is the porosity, d is the sphere diameter and λ_1 and λ_2 are constants depending on the sphere diameter. In the present study, the results will be illustrated by using spheres 3 mm and 5 mm in diameter. These sphere sizes are commonly used in laboratory experiments. We believe that using other bead diameters of comparable size will not alter the results qualitatively. An indication for the quantitative effect that the bead size has on the results will be revealed by comparing the results for $d = 3$ mm to the results for $d = 5$ mm. Reliable experimental values for the constants in the porosity equation (3) exist in the literature for the two bead sizes under investigation. In the case where $d = 3$ mm the values of the parameters in equation (3) are $\phi_\infty = 0.37$, $\lambda_1 = 0.35$, and $\lambda_2 = 3$[6]. For $d = 5$ mm, on the other hand, the values $\phi_\infty = 0.37$, $\lambda_1 = 0.43$, and $\lambda_2 = 3$ were used [6]. Both the permeability K and parameter A in equation (2) depend on the sphere diameter and the matrix porosity as follows [23]:

$$K = \frac{d^2\phi^3}{175(1-\phi)^2} \quad (4)$$

$$A = \frac{1.75(1-\phi)}{\phi^3 d} \quad (5)$$

In the momentum equation (2) the buoyancy term has been neglected, since the present study deals with forced convection in a channel filled with a porous medium. Forced convection is a common heat transfer mode in porous media [8, 9, 16]. The boundary conditions necessary to complete the problem formulation are that the temperature on the channel wall is a constant T_w, that the velocity on the wall is zero, and that at the centerline both the temperature and the velocity gradients in y are zero. Since studying the thermal entry region is of primary interest to this investigation, boundary conditions for the temperature field at the edge of the thermal boundary layer are necessary. The temperature at the edge of the boundary layer was kept constant at T_i and the temperature gradient zero within prescribed error, throughout the extent of the thermal entry region. More details on the boundary conditions at the edge of the thermal boundary layer will be given in the next section.

Numerical Solution

The heat and fluid flow characteristics in the configurations of interest will be revealed after solving numerically the mathematical model outlined in the previous section. Before proceeding with the discussion relevant to the numerical solution, it is convenient to cast the governing equations (1) and (2) in dimensionless form. The nondimensionalization is carried out based on the following definitions:

$$u_* = u/(\nu/H),\ y_* = y/H,\ x_* = \frac{x - x_i}{H\mathrm{Pr}},\ \theta = \frac{T_w - T}{T_w - T_i} \quad (6)$$

$$r_* = \frac{r}{H} = 1 - y_*$$

The dimensionless momentum and energy equations are

$$u_* + c_1(y_*)u_*^2 = Bc_2(y_*) + c_2(y_*)\frac{1}{r_*^m}\frac{\partial}{\partial y_*}\left(r_*^m\frac{du_*}{dy_*}\right) \quad (7)$$

$$u_*\frac{\partial\theta}{\partial x_*} = \frac{1}{r_*^m}\frac{\partial}{\partial y_*}\left(r_*^m\frac{\partial\theta}{\partial y_*}\right) \quad (8)$$

In writing equation (7), relations (4) and (5) were taken into account. The definitions of the coefficients B (dimensionless pressure gradient) and $c_i(y_*)$, $i = 1, 2$ read

$$c_1(y_*) = 10^{-2}\frac{d_*}{1-\phi},\quad B = -\frac{\partial P}{\partial x}\frac{H^3}{\rho\nu^2}$$

$$c_2(y_*) = \frac{d_*^2\phi^3}{175(1-\phi)^2} \quad (9)$$

The spatial variation of porosity ϕ is given by equation (3). Note that since explicit expressions were used to describe the variation of porosity and permeability with y for the spherical beads, familiar dimensionless parameters (such as the Darcy number) often used in theoretical convection studies in porous media did not appear in the present dimensionless equations (7) and (8). This fact does not restrict the generalization of the present formulation. However, our results are tailored to describe accurately the phenomenon of forced convection inside a channel filled with *spherical beads*. If other types of porous matrix are to be studied, the appropriate expressions for the porosity, the permeability, and the Forchheimer coefficient need to be used in place of equations (3)–(5) in the analysis. In summary, the present model offers a significant improvement over other simple models (such as the Darcy model or the Darcy–Brinkman model with constant porosity) for the case of a matrix consisting of spherical beads. On the other hand, simple flow models in which the *nature* of the porous matrix is not taken into account yield (naturally) more general, although less accurate, results.

Since the present study pertains to forced convection, equation (7) can be solved independently to yield the velocity field. With this information in hand, the temperature field can be obtained from the energy equation (8).

The momentum equation was solved based on finite differencing, linearization, and by following an iterative process. The finite difference form of the momentum equation was obtained by using a variable grid for accurate resolution of the important near-wall region. In particular, the so-called "compound interest grid" in which each interval is a constant multiple of the preceding one ($(\Delta y_*)_j = \gamma(\Delta y_*)_{j-1}$) was used. Clearly, $\gamma > 1$ yields finer resolution of small values of y_*. The value of $\gamma = 1.05$ yielded accurate results for most runs in the present investigation. Both the first and second-order derivatives were discretized by using central difference for-

Downloaded 17 Dec 2010 to 193.140.21.150. Redistribution subject to ASME license or copyright; see http://www.asme.org/terms/Terms_Use.cfm

mulas [19]. Since the Forchheimer term in the momentum equation is nonlinear, a linearization process proved necessary. To this end, initial values of the velocity field were guessed at all the grid points. The nonlinear term was written as the product of the unknown velocity and the guessed velocity. In finite difference form, after the above linearization, equation (7), together with the boundary conditions, transforms into an equivalent tridiagonal set of algebraic equations. This set of equations was solved by using Gauss elimination [19] to yield the velocity field for one iteration. The above process was repeated until convergence was achieved within prescribed errors.

The numerical solution of the energy equation was carried out based on an implicit method, namely, the Keller Box method [20, 21]. This method has several desirable features that make it appropriate for the solution of partial differential equations. For example, it provides second-order accuracy with nonuniform grids in both the x and y directions, it allows for very fast x variations, and allows easy programming for the solution of large numbers of coupled equations. One problem encountered in the numerical solution of thermally developing regions in channels is that near the origin ($x = x_i$), the thermal boundary layer is very thin compared to the channel half-width H. To achieve computational accuracy the following similarity variable is introduced [20]:

$$\eta = \frac{y_*}{\sqrt{x_*}} \tag{10}$$

In terms of η the energy equation (8) and the boundary conditions read

$$\frac{\partial}{\partial \eta}\left[(1-y_*)^m \frac{\partial \theta}{\partial \eta}\right] + (1-y_*)^m u_* \frac{\eta}{2}\frac{\partial \theta}{\partial \eta} = (1-y_*)^m u_* x_* \frac{\partial \theta}{\partial x} \tag{11}$$

$$\theta = 0 \text{ at } \eta = 0, \quad \theta = 1 \text{ at } \eta = \eta_{\text{edge}} \tag{12}$$

The details of finite differencing a parabolic partial differential equation of the type of equation (11) exist in the numerical heat transfer literature (see, for example, [20]). Hence, they are not repeated here in the interest of brevity. The final set of linear algebraic equations was solved by using the block elimination method to yield the temperature field at each x_* station. The discretization in η was performed by using a variable compound interest grid identical to that used for the solution of the momentum equation. The grid size in the x direction was very fine near the channel inlet and coarser downstream. The reason behind the use of a very fine grid near the channel entrance was to be able to capture the steep changes in the temperature field near the entrance. In the downstream region keeping the same grid would yield prohibitively large computation times. Therefore, a coarser grid was used downstream. This grid was fine enough to produce accurate results while decreasing the computational time. An important issue is that of the "numerical" definition of the edge of the thermal boundary layer [20]. After a trial and error procedure we chose $\eta_{\text{edge}} = 7 - 10$ for most of the numerical simulations, to start the numerical solution. In addition, the values $\gamma = 1.05$, $\Delta\eta_1 = 0.01$ yielded initially around 60 grid points across the thermal boundary layer. Increasing the number of grid points further had no visible effect on the numerical results. For example, for $B = 10^5$, $d_* = 0.1$, increasing the number of grid points in the vertical from 29 to 38 yielded an increase in the value of the fully developed Nusselt number of only 0.8 percent. Increasing the number of vertical grid points further to 45 and to 60 left the Nusselt number value practically unchanged. The numerical solution of equation (11) started at the wall and proceeded toward the edge of the thermal boundary layer. When the edge of the boundary layer was reached, the temperature gradient was checked. If the temperature gradient was found to be less than 10^{-4} the solution was advanced to the next x station. In the opposite situation η_{edge} was gradually increased until the above criterion for the temperature gradient at η_{edge} was satisfied. The value of the temperature at the edge of the boundary layer was kept constant at $\theta = 1$ according to equation (12) within the thermal entry length. When the thickness of the thermal boundary layer became equal to the half-width (or radius) of the channel the above procedure used to define the edge of the boundary layer was abandoned. Instead, for the remaining x stations, the temperature gradient at the centerline was set equal to zero and the temperature at the centerline was evaluated numerically much like the temperature at any other grid point.

The local heat flux at the channel wall was also evaluated numerically and cast in dimensionless form by means of the conduction-referenced Nusselt number. The definition of this Nusselt number is based on the channel width (or diameter) D and not on the hydraulic diameter.

$$\text{Nu} = -\left(\frac{\partial T}{\partial y}\right)_{y=0} \frac{D}{T_w - T_m} \tag{13}$$

In the above equation, T_m is the mixed mean fluid temperature defined in the nomenclature in a manner similar to that for classical fluid duct flows.

The numerical code outlined above was tested against existing results for the Graetz problem in classical fluids (i.e., in the absence of the solid matrix) for both configurations of interest: the parallel plates and the circular pipe [20–23]. In all cases, excellent agreement (within one percent) between our findings and those reported in the literature was found.

Results and Discussion

In this section, the main results of the numerical simulations are reported and discussed. The impact of the "flow channeling" phenomenon on the velocity field, caused by the high-porosity regions near the solid walls, is illustrated in Fig. 2(*a*) for the parallel plate geometry. Clearly, near the duct wall the velocity field departs dramatically from its uniform distribution. A channel of fast flowing fluid is thus created in the near wall region. The extent of this region is approximately 15 percent of the channel half-width for the parametric domain in this study. It is reasonable to expect that the channeling phenomenon shown in Fig. 2 will affect the heat transfer from the fluid to the wall. Increasing the sphere-diameter-to-channel-half-width ratio, $d_* = d/H$, yields an overall increase in the fluid velocity with no other significant qualitative difference. This result makes sense physically: Noting that the solid lines in Fig. 2(*a*) all correspond to $d = 3$ mm, we realize that increasing d_* is equivalent to decreasing H or the channel cross section which, in turn, yields an increase in the fluid velocity at all points. Using spheres of diameter $d = 5$ mm (dashed line in Fig. 2) resulted in a faster flow in the channel compared to the case $d = 3$ mm, for the same value of the sphere-diameter-to-channel-half-width ratio, $d_* = 0.1$.

In Fig. 2(*b*) the impact of the separate effects included in the general flow model on the velocity field is identified. Clearly, flow inertia has a negligible impact on the velocity profile for $B = 10^5$ and $d_* = 10^{-1}$ ($d = 3$ mm). Comparing curves *a* and *c*, on the other hand, proves that omitting the Brinkman term in the momentum equation enhances the channeling phenomenon and yields even faster flow near the channel wall. This result is correct physically since in the absence of Brinkman friction the no-slip condition on the wall is not satisfied. Overall, the use of the general flow model takes into account several phenomena that significantly alter the velocity field predicted by the popular Darcy flow model (Fig. 2*b*).

Downloaded 17 Dec 2010 to 193.140.21.150. Redistribution subject to ASME license or copyright; see http://www.asme.org/terms/Terms_Use.cfm

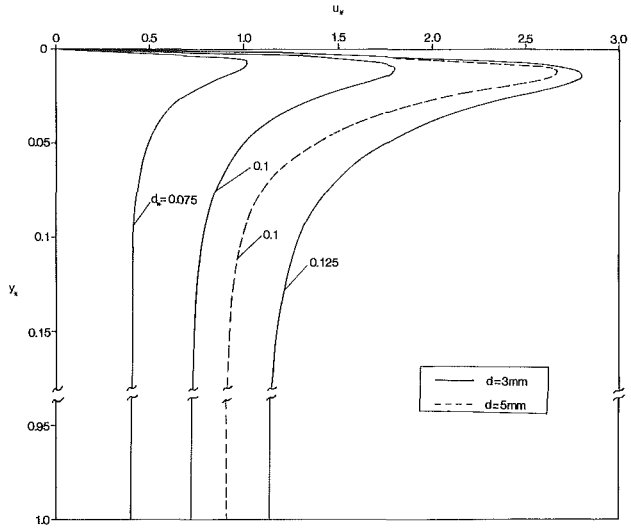

Fig. 2(*a*) Velocity distribution across the channel half-width for the parallel plate configuration and $B = 10^5$

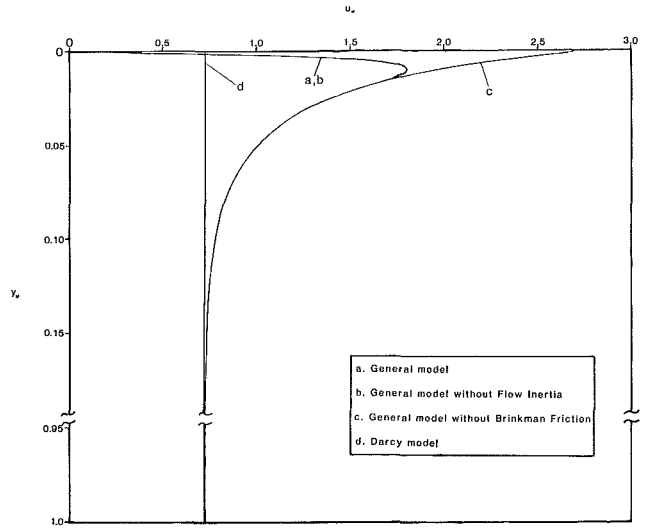

Fig. 2(*b*) Relative contribution of the various effects in the general flow model on the velocity profile for parallel plates; $B = 10^5$, $d = 3$ mm, $d_* = 0.1$

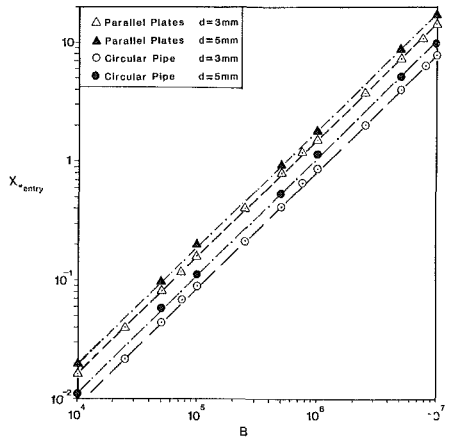

Fig. 3 Dependence of the thermal entry length on parameter B for $d_* = 0.1$

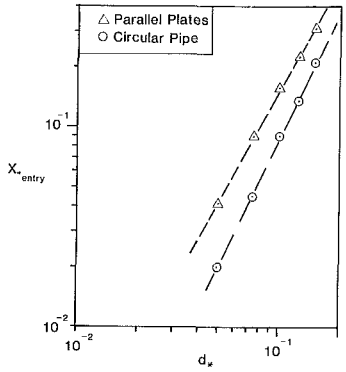

Fig. 4 Dependence of the thermal entry length on the sphere-diameter-to-channel-half-width ratio d_*, for $B = 10^5$

It is worth clarifying that using the present realistic flow model removes some of the "arbitrariness" in varying the parameters affecting the velocity field. Once the nature of the porous matrix is decided upon (spherical beads) the relative contributions of the Brinkman term and the Darcy term in equation (7) are practically fixed. It is not possible, nor is it physically justified to vary arbitrarily the relative contribution of these terms and show that the velocity profile changes between the Poiseuille profile (classical fluids, no Darcy terms) and the plug profile (Darcy flow no Brinkman terms). In this respect, the present velocity profiles differ from those reported in the literature [15] obtained with the help of the Brinkman flow model with constant porosity.

Figures 3 and 4 as well as Tables 1 and 2 pertain to a heat transfer result of engineering interest, namely, the dependence of the thermal entry length on the problem parameters. The thermal entry length was defined as the distance between the entrance of the channel and the point at which the mixed mean (invariant) fluid temperature and the Nusselt number became independent of the x location. The dependence of the thermal entry length on parameter B (note that in equation (9) this parameter is, in effect, the dimensionless pressure gradient) is linear on the logarithmic graph shown in Fig. 3. Increasing the value of B and the bead diameter yielded an increase in thermal entry length. This result is correct from a physical standpoint since increasing B and the bead diameter yields faster flow in the channel, and therefore thinner thermal boundary layers that require a longer distance to develop. The circular pipe configuration yielded consistently shorter thermal entry lengths than the parallel plates. Similar behavior to what was just described in conjunction with parameter B was observed when the dependence of the thermal entry length on the sphere-diameter-to-half-channel-width ratio (Fig. 4) was investigated. The data points shown in Figs. 3 and 4 were correlated by the following equations:

$$x_{*\text{entry}} = 1.83 \times 10^{-6} B^{0.99}$$

parallel plates, $d = 3$ mm, $d_* = 0.1$ (14*a*)

$$x_{*\text{entry}} = 1.78 \times 10^{-6} B$$

parallel plates, $d = 5$ mm, $d_* = 0.1$ (14*b*)

$$x_{*\text{entry}} = 1.03 \times 10^{-6} B^{0.98}$$

circular pipe, $d = 3$ mm, $d_* = 0.1$ (15*a*)

$$x_{*\text{entry}} = 1.02 \times 10^{-6} B$$

circular pipe, $d = 5$ mm, $d_* = 0.1$ (15*b*)

$$x_{*\text{entry}} = 10.11 d_*^{1.84}$$

parallel plates, $d = 3$ mm, $B = 10^5$ (16)

$$x_{*\text{entry}} = 10.29 d_*^{2.08}$$

circular pipe, $d = 3$ mm, $B = 10^5$ (17)

Figures 5(*a*, *b*) exemplify the temperature variation across

Downloaded 17 Dec 2010 to 193.140.21.150. Redistribution subject to ASME license or copyright; see http://www.asme.org/terms/Terms_Use.cfm

Table 1 Dependence of the thermal entry length and the Nusselt number on parameters B and d_* for forced convection in a channel between two parallel plates, filled with a porous matrix consisting of packed spheres

B	d(mm)	d_*	x_{*entry}	Nu
10^4	3	0.1	0.016	5.57
2.5×10^4	3	0.1	0.04	5.57
5×10^4	3	0.1	0.08	5.57
7.5×10^4	3	0.1	0.12	5.57
10^5	3	0.1	0.16	5.57
2.5×10^5	3	0.1	0.4	5.57
5×10^5	3	0.1	0.78	5.57
7.5×10^5	3	0.1	1.21	5.57
10^6	3	0.1	1.56	5.57
2.5×10^6	3	0.1	3.8	5.57
5×10^6	3	0.1	6.25	5.57
7.5×10^6	3	0.1	11	5.57
10^7	3	0.1	14.5	5.57
10^5	3	0.05	0.04	5.45
10^5	3	0.075	0.09	5.50
10^5	3	0.125	0.22	5.60
10^5	3	0.15	0.31	5.62
10^4	5	0.1	0.019	5.67
5×10^4	5	0.1	0.098	5.67
10^5	5	0.1	0.2	5.67
5×10^5	5	0.1	0.87	5.67
10^6	5	0.1	1.78	5.67
5×10^6	5	0.1	8.47	5.67
10^7	5	0.1	17.0	5.67

Table 2 Dependence of the thermal entry length and the Nusselt number on parameters B and d_* for forced convection in a circular pipe filled with a porous matrix consisting of packed spheres

B	d(mm)	d_*	x_{*entry}	Nu
10^4	3	0.1	0.009	7.35
2.5×10^4	3	0.1	0.022	7.35
5×10^4	3	0.1	0.044	7.35
7.5×10^4	3	0.1	0.065	7.35
10^5	3	0.1	0.09	7.35
2.5×10^5	3	0.1	0.21	7.35
5×10^5	3	0.1	0.42	7.35
7.5×10^5	3	0.1	0.65	7.35
10^6	3	0.1	0.85	7.35
2.5×10^6	3	0.1	2	7.35
5×10^6	3	0.1	4	7.35
7.5×10^6	3	0.1	6.4	7.35
10^7	3	0.1	8	7.35
10^5	3	0.05	0.02	7.00
10^5	3	0.075	0.045	7.20
10^5	3	0.125	0.135	7.51
10^5	3	0.15	0.21	7.66
10^4	5	0.10	0.011	7.6
5×10^4	5	0.10	0.058	7.6
10^5	5	0.10	0.11	7.6
5×10^5	5	0.10	0.53	7.6
10^6	5	0.10	1.14	7.6
5×10^6	5	0.10	5.11	7.6
10^7	5	0.10	8.56	7.6

the channel half-width at several downstream locations for the parallel plates and the circular pipe, respectively. The cooling effect of the wall propagates faster in the fluid-saturated porous medium in the circular pipe than in the parallel plates. The invariant temperature distribution in the fully developed region is shown in Fig. 6. In the same figure, the mixed mean temperature distribution obtained based on the Darcy flow model is reported. It is worth noting that since the Darcy flow model does not satisfy the no-slip condition on the wall and since it assumes constant porosity (ϕ_∞), it yields a uniform (slug) velocity profile. The solution of the Graetz problem with a "slug" velocity profile is reported extensively in the literature [22, 23]. In both configurations of interest (Fig. 1), the general flow model yields a more effective thermal communication between the fluid and the solid boundary compared to the Darcy model (Fig. 6). The invariant temperature in the fully developed region was also found to be independent of parameter B.

Figures 7 and 8 report the variation of the Nusselt number along the thermal entry region for a wide range of parameter

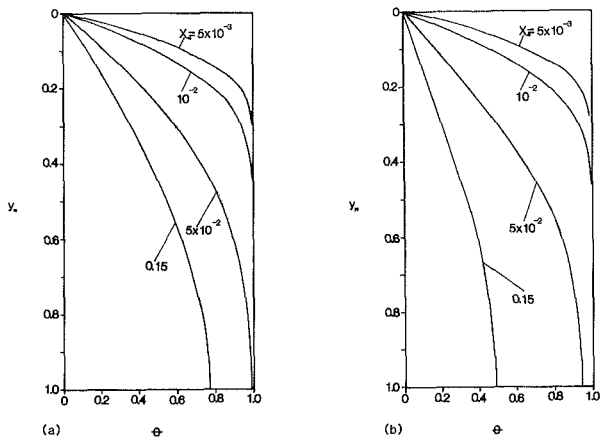

Fig. 5 Dimensionless temperature distribution across the channel half-width for $B = 10^5$, $d = 3$ mm, $d_* = 0.1$: (*a*) parallel plates; (*b*) circular pipe

Downloaded 17 Dec 2010 to 193.140.21.150. Redistribution subject to ASME license or copyright; see http://www.asme.org/terms/Terms_Use.cfm

B. Increasing B (faster flow) yields larger values of Nu throughout the thermal entry region. However, it is interesting to note that the various curves corresponding to different values of B in the thermal entry region converge toward a single value in the thermally fully developed region. The value of Nu in the fully developed region, including the effects of Brinkman friction, flow inertia, and variable porosity, is approximately 12 percent higher than the value predicted by the Darcy model for the parallel plate geometry (Fig. 7) and 22 percent higher than the value predicted by the Darcy model for the circular pipe geometry (Fig. 8). As indicated in Tables 1 and 2 increasing the bead diameter to 5 mm has a marginal effect on the value of Nu.

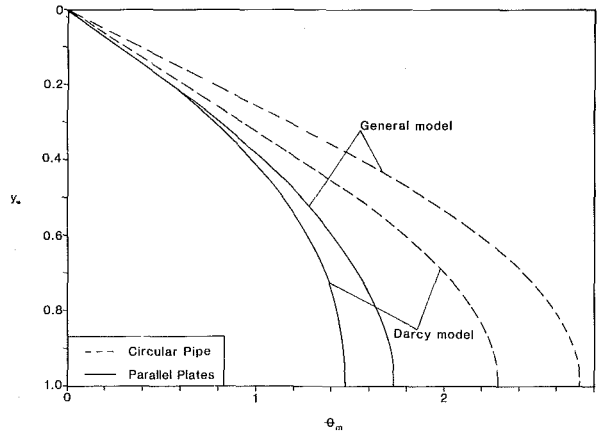

Fig. 6 Mixed mean (invariant) temperature distribution across the channel half-width for the fully developed region for $B = 10^5$, $d = 3$ mm, $d_* = 0.1$; comparison with the predictions of the Darcy model

The next two figures aim to identify the contribution of each of the various effects included in the momentum equation (7) on the Nusselt number for the parallel plate channel (Fig. 9) and for the circular pipe (Fig. 10). For both channel configurations the effect of flow inertia on Nu is negligible for $B = 10^5$. Excluding the Brinkman friction term (curve *c*) yields a noticeable increase in the value of Nu especially near the channel entrance for both configurations of interest. Overall, taking into account the variation of porosity in the near-wall region, as well as the Brinkman friction, yielded results significantly different from the Darcy model (curve *d*).

It is expected the flow inertia will have a significant impact on the value of Nu at larger values of B (dimensionless pressure gradient). Indeed, as Figs. 11 and 12 indicate for the parallel plates and the circular pipe, respectively, as B increases beyond approximately $B = 10^6$, the inertia terms

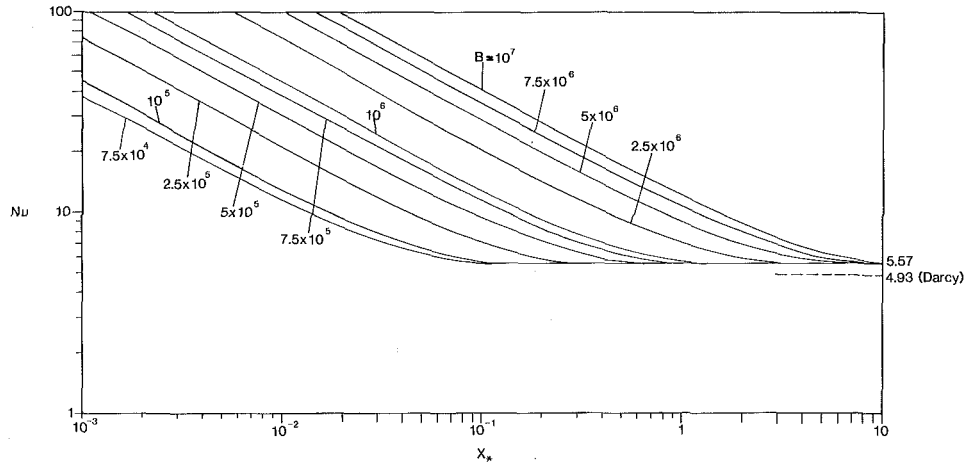

Fig. 7 Nusselt number variation with the horizontal coordinate in the thermal entry region for the parallel plate configuration for a host of B values, $d_* = 0.1$, $d = 3$ mm

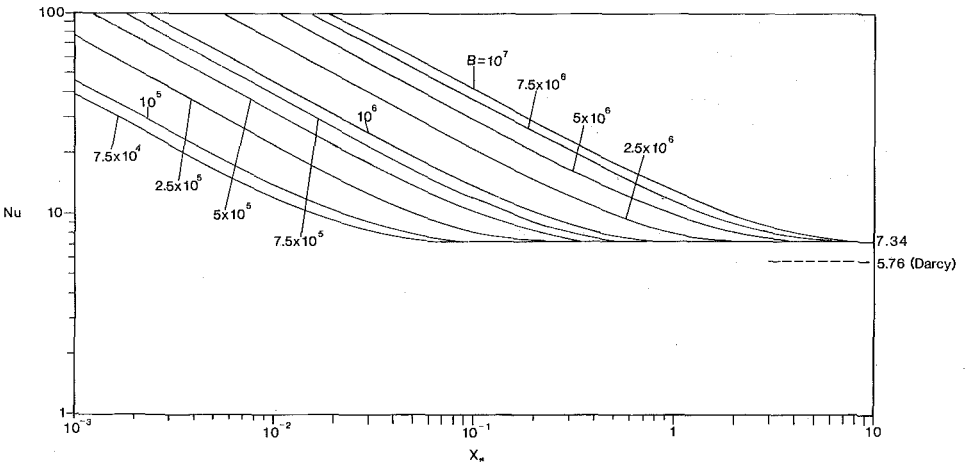

Fig. 8 Nusselt number variation with the horizontal coordinate in the thermal entry region for the circular pipe configuration for a host of B values, $d_* = 0.1$, $d = 3$ mm

Downloaded 17 Dec 2010 to 193.140.21.150. Redistribution subject to ASME license or copyright; see http://www.asme.org/terms/Terms_Use.cfm

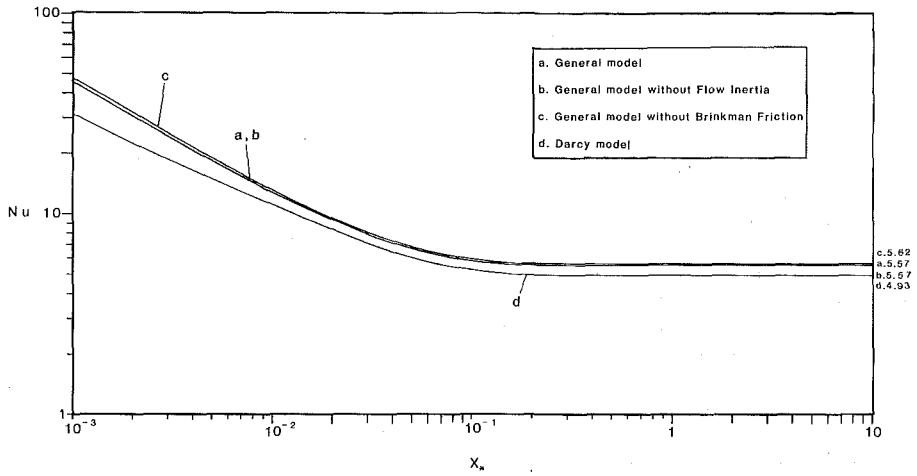

Fig. 9 Nusselt number variation with the horizontal coordinate in the thermal entry region for the parallel plate configuration, for four different flow models; $B = 10^5$, $d_* = 0.1$, $d = 3$ mm

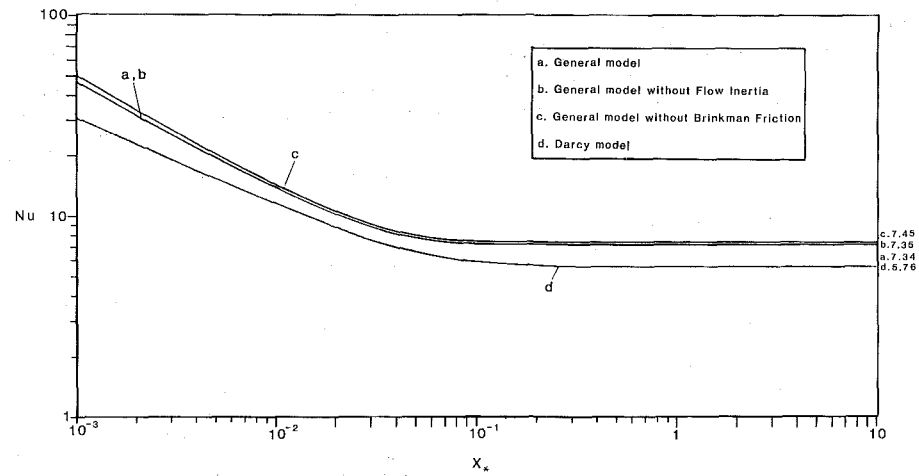

Fig. 10 Nusselt number variation with the horizontal coordinate in the thermal entry region for the circular pipe configuration, for four different flow models; $B = 10^5$, $d_* = 0.1$, $d = 3$ mm

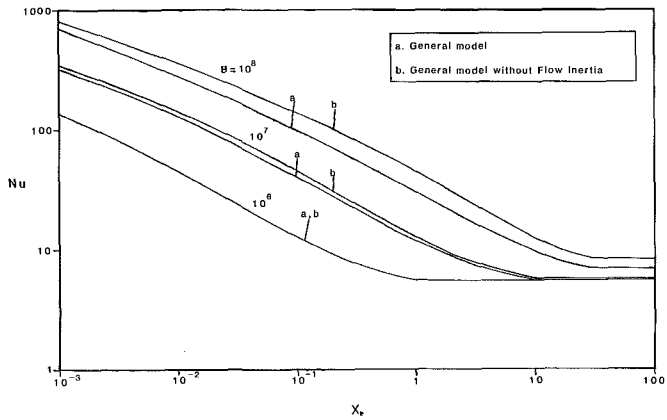

Fig. 11 Effect of flow inertia on Nu in the thermal entry region for the parallel plate channel; $d_* = 0.1$, $d = 3$ mm

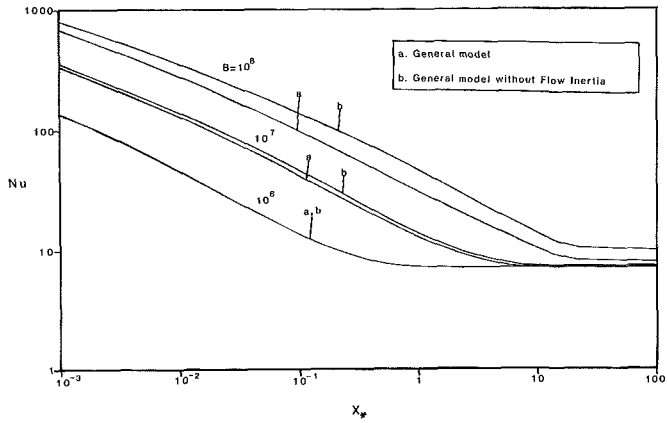

Fig. 12 Effect of flow inertia on Nu in the thermal entry region for the circular pipe; $d_* = 0.1$, $d = 3$ mm

become significant. The effect of increasing the relative contribution flow inertia is to decrease the value of Nu, especially in the entrance region. The fact that increasing the magnitude of Forchheimer inertia decreases Nu has been reported in the literature, for example, in [15] for the case of natural convection from a vertical plate in a porous medium.

Conclusion

This paper presented a numerical investigation of forced convection in a channel filled with a fluid-saturated porous material. The temperature at the channel walls was assumed to be constant. Two channel configurations were investigated extensively, namely, two parallel plates and a circular pipe. The

Downloaded 17 Dec 2010 to 193.140.21.150. Redistribution subject to ASME license or copyright; see http://www.asme.org/terms/Terms_Use.cfm

main novelty of this study lies in the fact that the general model for flow in porous medium was used, including the effects of variable porosity, flow inertia, and Brinkman friction. A porous bed consisting of packed spheres was used to illustrate the results. It was found that the velocity field resulting from the solution of the general momentum equation (Fig. 2) significantly altered the heat transfer characteristics in the system compared to the predictions of the widely used Darcy flow model. The "channeling" phenomenon near the walls of both duct configurations enhanced the thermal communication between the fluid/solid matrix composite and the walls. This fact yielded an overall 12 percent increase in the value of the Nusselt number in the fully developed region for the parallel plate channel, compared to the value predicted when the Darcy model was used. Similarly, a 22 percent increase in the value of the fully developed Nusselt number for the circular channel geometry was observed. The main reason for this heat transfer enhancement is attributed to the existence of a high porosity region near the channel wall. As discussed in connection with Figs. 11 and 12, increasing parameter B beyond approximately $B = 10^6$ increases the contribution of the inertia terms on the value of Nu. The effect of increasing inertia is actually to decrease Nu. The effect of flow channeling is even more pronounced when Brinkman friction is not taken into account (Figs. 2*b*, 9, 10). Useful correlations reporting the dependence of the thermal entry length on the problem parameters were also reported in the course of the study.

Acknowledgments

Financial support for this research provided by NSF through Grant ENG-8451144 is greatly appreciated.

References

1 Cheng, P., "Heat Transfer in Geothermal Systems," *Advances in Heat Transfer*, Vol. 14, 1979, pp. 1–105.

2 Vafai, K., and Tien, C. L., "Boundary and Inertia Effects on Flow and Heat Transfer in Porous Media," *Int. J. Heat Mass Transfer*, Vol. 24, 1984, pp. 195–203.

3 Brinkman, H. C., "A Calculation of the Viscous Force Exerted by a Flowing Fluid on a Dense Swarm of Particles," *Appl. Sci. Res.*, Vol. A1, 1947, pp. 27–34.

4 Schwartz, C. E., and Smith, J. M., "Flow Distribution in Packed Beds," *Ind. Eng. Ch.*, Vol. 45, 1958, pp. 1209–1218.

5 Schertz, W. M., and Bischoff, K. B., "Thermal and Material Transport in Non-Isothermal Packed Beds," *AIChE J.*, Vol. 15, 1969, pp. 597–604.

6 Benenati, R. F., and Brosilow, C. B., "Void Fraction Distribution in Packed Beds," *AIChE J.*, Vol. 8, 1962, pp. 359–361.

7 Chandrasekhara, B. C., and Vortmeyer, D., "Flow Model for Velocity Distribution in Fixed Beds Under Isothermal Conditions," *Th. Fluid Dynamics*, Vol. 12, 1979, pp. 105–111.

8 Vafai, K., "Convective Flow and Heat Transfer in Variable Porosity Media," *J. Fluid Mechanics*, Vol. 147, 1984, pp. 233–259.

9 Vafai, K., Alkire, R. L., and Tien, C. L., "An Experimental Investigation of Heat Transfer in Variable Porosity Media," ASME JOURNAL OF HEAT TRANSFER, Vol. 107, 1985, pp. 642–647.

10 Poulikakos, D., "A Departure From the Darcy Model in Boundary Layer Natural Convection in a Vertical Porous Layer With Uniform Heat Flux From the Side," ASME JOURNAL OF HEAT TRANSFER, Vol. 107, 1985, pp. 716–720.

11 Bejan, A., and Poulikakos, D., "The Non-Darcy Regime for Vertical Boundary Layer Natural Convection in a Porous Medium," *Int. J. Heat Mass Transfer*, Vol. 27, 1984, pp. 717–722.

12 Georgiadis, J., and Catton, I., "Prandtl Number Effect on Benard Convection in Porous Media," ASME Paper No. 84-HT-115, 1984.

13 Jonsson, T., and Catton, I., "Prandtl Number Dependence of Natural Convection in Porous Medium," *Heat Transfer in Porous Media and Particulate Flows*, L. S. Yao, M. M. Chen, C. E. Hickox, P. G. Simpkins, L. C. Chow, M. Kaviany, P. Cheng, and L. R. Davis, eds., HTD-Vol. 46, 1985, pp. 21–27.

14 Prasad, V., Kulacki, F. A., and Keyhani, M., "Natural Convection in Porous Media," *Journal of Fluid Mechanics*, Vol. 150, 1985, pp. 89–119.

15 Kaviany, M., "Laminar Flow Through a Porous Channel Bounded by Isothermal Parallel Plates," *Int. J. Heat Mass Transfer*, Vol. 28, 1985, pp. 851–858.

16 Tien, C. L., and Hong, J. T., "Natural Convection in Porous Media Under Non-Darcian and Non-uniform Permeability Conditions," in: *Natural Convection*, Kakac et al., eds., Hemisphere, Washington, DC, 1985.

17 Witaker, S., "Advances in Theory in Fluid Motion in Porous Media," *Ind. Eng. Chem.*, Vol. 61, 1969, pp. 14–28.

18 Ergun, S., "Fluid Flow Through Packed Columns," *Chem. Eng. Progr.*, 1952, pp. 89–94.

19 Ferziger, J. H., *Numerical Methods for Engineering Applications*, Wiley, New York, 1981.

20 Cebeci, T., and Bradshaw, P., *Physical and Computational Aspects of Convective Heat Transfer*, Springer-Verlag, New York, 1984.

21 Keller, H. B., "A New Difference Scheme for Parabolic Problems," in: *Numerical Solutions of Partial Differential Equations*, J. Bramble, ed., Vol. 11, Academic Press, New York, 1970.

22 Shah, R. K., and London, A. K., "Supplement 1 – Laminar Flow Forced Convection in Ducts," *Advances in Heat Transfer*, T. F. Irvine and J. P. Hartnett, eds., Academic Press, New York, 1978.

23 Rohsenow, W., and Hartnett, J. P., eds., *Handbook of Heat Transfer*, McGraw-Hill, New York, 1973.

Downloaded 17 Dec 2010 to 193.140.21.150. Redistribution subject to ASME license or copyright; see http://www.asme.org/terms/Terms_Use.cfm

Stability of Thermal Convection in a Vertical Porous Layer

L. P. Kwok

C. F. Chen

Department of Aerospace and Mechanical Engineering, University of Arizona, Tucson, AZ 85721

Experiments were carried out to study the stability of thermal convection generated in a vertical porous layer by lateral heating in a tall, narrow tank. The porous medium, consisting of glass beads, was saturated with distilled water. It was found that the flow became unstable at a critical ΔT *of 29.2°C (critical Rayleigh number of 66.2). Linear stability analysis was applied to study the effects of the Brinkman term and of variable viscosity separately using a quadratic relationship between the density and temperature. It was found that with the Brinkman term, no instability could occur within the allowable temperature difference across the tank. With the effect of variable viscosity included, linear stability theory predicts a critical* ΔT *of 43.4°C (Rayleigh number of 98.3).*

1 Introduction

Thermal convection in a vertical porous layer has been the subject of investigation by a number of researchers. Gill (1966) studied the stability of convection generated by a lateral temperature difference in an infinite, vertical porous layer. Weber (1975) applied a boundary layer analysis to a finite, vertical porous layer using the method developed by Gill (1966) for convection in a viscous fluid. Bejan (1983) extended Weber's analysis to include the uniform heat flux conditions of the side walls, and the results were obtained both by analytic solution and numerical study. More recently, Trevisan and Bejan (1986) considered the problem of mass transfer as well as heat transfer in porous vertical layers. Experimental heat transfer characteristics in a rectangular porous region with moderate aspect ratio have been investigated by Seki et al. (1978), who obtained a correlation between the Nusselt number and the Rayleigh number. Experimental results in a vertical annulus with an aspect ratio of nearly one have been reported by Prasad et al. (1985) for a number of fluid–solid combinations.

In this paper, we report the results of experimental investigation and linear stability consideration of thermal convection generated in a vertical porous layer by lateral heating. The results show that there exists a critical temperature difference, 29.2°C, across the tank beyond which the convective flow becomes unstable.

According to Gill (1969), thermal convection generated by a lateral temperature difference in an infinite, vertical layer saturated with a constant-property fluid is always stable. However, in the laboratory system, there are a number of conditions which are different from what Gill had assumed: (*i*) The fluid, being viscous, must satisfy nonslip conditions at the wall. (*ii*) For the temperature range experienced in the experiment, the effect of temperature-dependent property values may be of importance. (*iii*) The height of the layer is finite. (*iv*) The properties of the porous medium may not be constant.

Using the linear stability theory, we have considered the effects of the first two factors separately for an infinite, vertical porous layer. For the effect of the nonslip condition, we used Darcy's equation with the Brinkman term included. In the variable property case, we assumed that the viscosity is a function of temperature and all other properties are constant. In both of these cases, a quadratic relationship between the density and temperature was assumed since a linear relationship would incur too much error in the temperature range used in the experiment. Results show that with the addition of the Brinkman term, no instability can occur within reasonable temperature differences across the tank. For the variable viscosity effect, the linear stability analysis shows that the onset of instability occurs at $\Delta T = 43.4°C$. The details of the experimental investigation and the linear stability analysis are presented within the following sections.

2 Experimental Investigation

The experiment was conducted in a tall, narrow box, 30 cm high × 2 cm wide × 11.5 cm deep. The two lateral sides (30 cm × 11.5 cm) of the box were made of milled brass plates in which water passages were provided, and the rest of the box was made of plexiglass. Two constant-temperature baths were used to create a temperature difference across the 2-cm gap: a Haake A80 circulator and a Lauda K-2/R circulator. The temperature of the water in the baths could be controlled to within ±0.02°C of the desired temperature. The hot wall was of a sandwich construction with a 1-mm-thick Bakelite sheet between two brass plates. Th outer plate was provided with water passages and the inner one was a plain brass plate. At the midheight of the hot wall, a Microfoil thin foil heat flux meter was installed between the outer brass plate and the Bakelite sheet. In this manner, the heat flux across the tank was monitored.

On each of the two heat transfer walls, two copper-constantan thermocouples were installed along the centerline very close to the inner surface. One thermocouple was installed 10 cm from the top, and the other at 10 cm from the bottom. In all tests, the maximum difference between the two readings was less than 0.2°C. Therefore, the average of the two readings was taken as the wall temperature.

The porous medium, consisting of 3-mm-dia glass beads, was saturated with distilled water. Before the beads were placed into the tank, they were cleaned with detergent. Care was taken in filling the tank with distilled water and glass beads so that no air bubbles were trapped among the beads. After the tank was filled, a plexiglass cover was placed on the top of the tank. Then, the entire tank was covered with styrofoam insulation approximately 5 cm thick.

Before starting any experiment, it was first established that the porous medium and the walls of the tank were all at the ambient temperature. A temperature difference across the tank was then established by increasing the temperature of the hot wall and reducing the temperature of the cold wall by the same amount so that the mean temperature remained at the ambient temperature. Property values needed to evaluate the Rayleigh number were all determined at the ambient temperature. After each new setting of the temperature difference, the wall temperatures and the heat flux were

Contributed by the Heat Transfer Division and presented at the ASME/JSME Thermal Engineering Joint Conference, Honolulu, Hawaii, March 22–27, 1986. Manuscript received by the Heat Transfer Division November 12, 1986.

 Copyright © 1987 by ASME

Downloaded 17 Dec 2010 to 193.140.21.150. Redistribution subject to ASME license or copyright; see http://www.asme.org/terms/Terms_Use.cfm

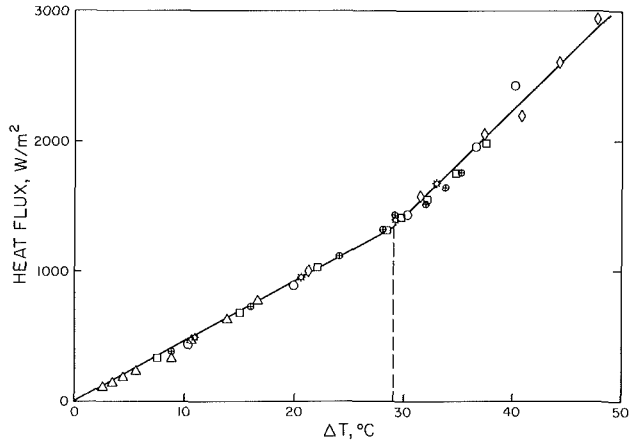

Fig. 1 Heat flux across the porous layer

monitored in 3- to 5-min intervals until equilibrium was reached, which was usually less than 30 min. Re-adjustment of the temperature difference was made in 1-hr intervals, approximately four diffusion times, to ensure that a steady-state condition was obtained.

A total of six test runs were made and the data are presented in Fig. 1, in which the heat flux is shown as a function of the temperature difference ΔT across the tank. Different symbols are used for the six different tests. The data show that there is a change of slope at 29.2°C, indicating a change in the heat transfer process signifying the onset of instabilities. Based on our previous measurements of the temperature distribution at the center of the tank (Kianjah and Chen, 1982), the convection pattern, after the onset of instabilities, consists of a number of cells stacked in the vertical direction. This critical ΔT of 29.2°C corresponds to a critical Rayleigh number of 66.2. The definition of the Rayleigh number is given in the next section; the property values are evaluated at the reference temperature of 25°C. The permeability was measured in a cylindrical column 8.15 cm in diameter and 55 cm in height. The value of 0.85×10^{-8} m^2, as reported by Chen and Murray (1985). The porosity was measured in a graduated cylinder 6 cm in diameter, and the value is 0.40.

3 Formulation of the Linear Stability Problem

3.1 General Equations. The governing equations for a porous layer saturated with an incompressible fluid including the Brinkman effect and the variable viscosity effect with the Boussinesq approximation are

Continuity:

$$\frac{\partial u_i}{\partial x_i} = 0 \tag{1}$$

Momentum:

$$\frac{\rho_0}{\epsilon}\left(\frac{\partial u_i}{\partial t} + u_j \frac{\partial u_i}{\partial x_j}\right) + \frac{\mu}{k} u_i = -\frac{\partial p}{\partial x_i} + \frac{\partial}{\partial x_j}\left(\mu \frac{\partial u_i}{\partial x_j}\right) + \rho g_i \tag{2}$$

Energy:

$$(\rho c)_m \frac{\partial T}{\partial t} + (\rho c)_f u_j \frac{\partial T}{\partial x_j} = \lambda_m \frac{\partial^2 T}{\partial x_j \partial x_j} \tag{3}$$

The properties of the medium are defined as follows:

$$\lambda_m = (1-\epsilon)\lambda_s + \epsilon\lambda_f$$
$$(\rho c)_m = (1-\epsilon)(\rho c)_s + \epsilon(\rho c)_f \tag{4}$$

The density of the fluid in the body force term is given by Ruddick and Shirtcliffe (1979) as

$$\rho = \rho_0[1 - \alpha_1(T-T_0) - \alpha_2(T-T_0)^2 - \alpha_3(T-T_0)^3] \tag{5}$$

in which $\alpha_1 = 2.539 \times 10^{-4}$, $\alpha_2 = 4.968 \times 10^{-6}$, and $\alpha_3 = -2.7 \times 10^{-8}$.

Based on our knowledge of the instability occurring in a viscous fluid confined within a narrow slot (Chen and Thangam, 1985; Thangam and Chen, 1986), we assume the motion is two dimensional. Let the x axis be horizontal and extend across the narrow gap of the tank, and let the z axis be vertical; we denote the velocity components in their respective directions by u and w. With the introduction of the stream function

$$u = \frac{\partial \psi}{\partial z}, \qquad w = -\frac{\partial \psi}{\partial x}$$

the continuity equation is satisfied identically.

The momentum and energy equations are then rendered dimensionless by the following characteristic quantities: length L, temperature difference ΔT, time $L^2(\mathrm{Ra}\kappa^*)^{-1}$, stream function $(\mathrm{Ra}\kappa^*)^{-1}$, viscosity μ_0, density ρ_0, and pressure $k(\mathrm{Ra}\mu_0\kappa^*)^{-1}$. In these expressions, L is the width of the tank, $\kappa^* = \lambda_m(\rho c)_f^{-1}$, and the Rayleigh number is defined as

Nomenclature

A, B = constants in equation (9)
b = constants of viscosity model, equation (16)
c = specific heat
C_2, C_3 = defined in equation (6a)
D = constants in equation (17)
g = gravitational constant
k = permeability of the porous medium
L = width of the slot
$\tilde{L}$ = L/k
p = pressure
Ra = $g\alpha_1 \Delta T k L/\nu_0\kappa^*$ = Rayleigh number
T = temperature
t = time
u, w = velocity in the x and z directions
x, y, z = coordinates
α = wavenumber in the z direction
$\alpha_1, \alpha_2, \alpha_3$ = constants in the density function of water
ΔT = temperature difference across the slot
ϵ = porosity
θ = perturbed temperature
κ^* = $\lambda_m/(\rho c)_f$
λ = heat conductivity
μ = absolute viscosity
ν = kinematic viscosity
ρ = density
σ = growth rate of disturbance
ϕ = perturbed stream function
ψ = stream function

Subscripts

b = denotes base solution
f = denotes fluid property
m = denotes property of the porous medium
0 = denotes reference state
s = denotes property of solid matrix

Superscripts

$'$ = perturbed quantity

Downloaded 17 Dec 2010 to 193.140.21.150. Redistribution subject to ASME license or copyright; see http://www.asme.org/terms/Terms_Use.cfm

$$\mathrm{Ra}=\frac{g\alpha_1\Delta TLk}{\nu_0\kappa^*}$$

The equations can be obtained by substitution and they need not be presented here.

In the following, two speical cases are studied in detail. First, we consider the effect of the addition of the Brinkman term while the properties of the medium are kept constant. Next, we consider the effect of variable viscosity without the Brinkman term while all other properties are kept constant. In both cases, the density is considered a nonlinear function of the temperature.

3.2 Effect of the Brinkman Term. Eliminating the pressure term in the momentum equation, we obtain

$$\mathrm{Ra}\left\{C_1\frac{\partial}{\partial t}+C_3\left(\frac{\partial\psi}{\partial z}\frac{\partial}{\partial x}-\frac{\partial\psi}{\partial x}\frac{\partial}{\partial z}\right)\right\}\nabla^2\psi$$

$$\nabla^2\psi=\frac{k}{L^2}\nabla^2(\nabla^2\psi)+\frac{1}{\alpha_1\Delta T}\frac{\partial\rho}{\partial x} \tag{6}$$

in which

$$C_2=\frac{k}{\epsilon L^2}\frac{\kappa_m}{\nu_0},\quad C_3=\frac{(\rho c)_m}{(\rho c)_f}C_2,\quad \kappa_m=\frac{\lambda_m}{(\rho c)_m}$$

It is noted here that C_2 and C_3 are of order 10^{-4}, and the effect of the inertial terms is negligible. The energy equation becomes

$$\frac{\partial T}{\partial t}+\frac{\partial\psi}{\partial z}\frac{\partial T}{\partial x}-\frac{\partial\psi}{\partial x}\frac{\partial T}{\partial z}=\frac{1}{\mathrm{Ra}}\nabla^2T \tag{7}$$

Due to the inclusion of the Brinkman term, the nonslip condition at the walls needs to be imposed. Therefore, the appropriate boundary conditions for equations (6) and (7) are

$$\left.\begin{aligned}u=\frac{\partial\psi}{\partial z}=0\\ w=-\frac{\partial\psi}{\partial x}=0\\ T=\pm\frac{1}{2}\end{aligned}\right\}\text{at } x=\pm\frac{1}{2} \tag{8}$$

It is reasonable to assume that the basic steady-state solution to equations (6) and (7) subjected to the boundary conditions (8) consists of

$$u=0,\quad w=w_b(x),\quad T=T_b(x),\quad \psi=\psi_b(x)$$

With this assumption, equation (7) becomes a linear, second-order ordinary differential equation and equation (6) becomes a linear, fourth-order ordinary differential equation. The solutions are

$$T_b=x \tag{9a}$$

$$\psi_b=A_1\cosh\tilde{L}x+A_2\sinh\tilde{L}x+\sum_{j=0}^{4}B_jx^j \tag{9b}$$

$$w_b=-\frac{d\psi_b}{dx}=-\left\{A_1\tilde{L}\sinh\tilde{L}x+A_2\tilde{L}\cosh\tilde{L}x+B_1+2B_2x+3B_3x^2+4B_4x^3\right\} \tag{9c}$$

in which $\tilde{L}=L/k$ and A and B are constants, which are listed in the Appendix. In the density-temperature relationship given by Ruddick and Shirtcliffe (1979), the value of α_3 is approximately $10^{-2}\alpha_2$. We have used the cubic and the quadratic relationships to evaluate the critical conditions for the variable viscosity case. The differences are barely discernible. In view of this fact, we have carried out all calculations

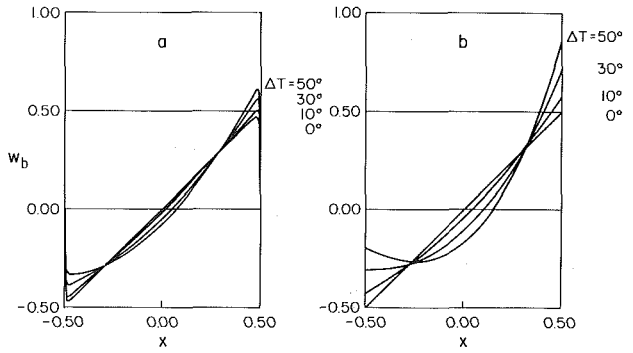

Fig 2 Nondimensional vertical velocity: (*a*) Brinkman term; (*b*) variable viscosity

assuming $\alpha_3 = 0$. Using the property values corresponding to a reference temperature of 25°C, the basic velocity w_b has been evaluated and is shown in Fig. 2(*a*). It is noted here that w_b is nondimensionalized with respect to $\mathrm{Ra}\kappa^*L^{-1}$. Because of the quadratic dependence of ρ on T, the flow is nonsymmetric. The velocity is higher near the hot wall and becomes more so as ΔT increases. The viscous effects are confined to the regions very close to the two walls. The boundary layer thickness in this case is constant and is equal to $\tilde{L}^{-1}\ln(\tilde{L}/2)$, which is proportional to $k^{1/2}$.

Linearized stability equations are obtained by introducing small perturbations to the basic flow

$$\psi=\psi_b+\psi',\quad T=T_b+T'$$

When these are substituted back into equations (6) and (7) and terms of higher order are neglected, we obtain

$$\frac{\partial T'}{\partial t}+\frac{\partial\psi'}{\partial z}-\frac{d\psi_b}{dx}\frac{\partial T'}{\partial x}=\frac{1}{\mathrm{Ra}}\nabla^2T' \tag{10}$$

and

$$\mathrm{Ra}\left\{C_2\frac{\partial}{\partial t}\nabla^2\psi'+C_3\left(\frac{\partial\psi'}{\partial z}\frac{d^3\psi_b}{dx^3}-\frac{d\psi_b}{dx}\frac{\partial}{\partial z}\nabla^2\psi'\right)\right\}$$

$$+\nabla^2\psi'=\frac{1}{\tilde{L}^2}\nabla^2(\nabla^2\psi')+\frac{1}{\alpha_1\Delta T}\frac{\partial\rho'}{\partial x} \tag{11}$$

Following Thangam and Chen (1986), we introduce the perturbation temperature and stream function defined as

$$T'=\theta(x)\exp(i\alpha z+\sigma t)$$

$$\psi'=\phi(x)\exp(i\alpha z+\sigma t)$$

in which α is the wavenumber in the z direction and σ is, in general, complex. When these are substituted into equations (10) and (11), we obtain two ordinary differential equations with appropriate boundary conditions. Solution of these equations is effected by using the Galerkin method. The following trial functions which satisfy the given boundary conditions are employed:

$$\theta_n=\begin{cases}\sin n\pi x \text{ when } n \text{ is even}\\ \cos n\pi x \text{ when } n \text{ is odd}\end{cases} \tag{12}$$

$$\phi_n=\begin{cases}\dfrac{(\cosh\rho_nx)}{\cosh\rho_n/2}-\dfrac{\cos\rho_nx}{\cos\rho_n/2},\ \tanh\dfrac{\rho_n}{2}+\tan\dfrac{\rho_n}{2}=0\\ \qquad\text{when } n \text{ is odd}\\ \dfrac{\sinh\rho_nx}{\sinh\rho_n/2}-\dfrac{\sin\rho_nx}{\sin\rho_n/2},\ \coth\dfrac{\rho_n}{2}-\cot\dfrac{\rho_n}{2}=0\\ \qquad\text{when } n \text{ is even}\end{cases} \tag{13}$$

The procedure is to expand

Downloaded 17 Dec 2010 to 193.140.21.150. Redistribution subject to ASME license or copyright; see http://www.asme.org/terms/Terms_Use.cfm

$$\Theta = \sum_{n=1}^{\infty} a_n \theta_n \text{ and } \phi = \sum_{n=1}^{\infty} b_n \phi_n$$

in equations (12) and (13), which are then multiplied by θ_m and ϕ_m, respectively, and integrated from $x = -1/2$ to $x = 1/2$. After some algerbraic manipulation, we obtain the following eigenvalue problem:

$$\underline{\underline{A}}\,\underline{x} = \sigma \underline{\underline{B}}\,\underline{x} = 0 \tag{14}$$

with the coefficient vector $\underline{x} = \{a_1, \ldots, a_n, \ldots, b_1, \ldots, b_n, \ldots,\}^T$ where T denotes the transpose. The matrices $\underline{\underline{A}}$ and $\underline{\underline{B}}$ are not presented here because of space limitations. Readers interested in their values are welcome to correspond with the authors.

The numerical solution will be obtained in Section 4 for the critical wavenumber and Rayleigh number. Before presenting the numerical results, we turn to the formulation of the case for variable viscosity.

3.3 Effect of Variable Viscosity. In this case, the vorticity equation becomes

$$\mu \nabla^2 \psi + \left(\frac{\partial \mu}{\partial z} \frac{\partial \psi}{\partial z} + \frac{\partial \mu}{\partial x} \frac{\partial \psi}{\partial x} \right) + C_2 \mathrm{Ra} \frac{\partial}{\partial t} \Delta^2 \psi = \frac{1}{\alpha_1 \Delta T} \frac{\partial \rho}{\partial x} \tag{15}$$

It is noted here that the nondimensional μ is assumed to be a function of temperature only and is given by the equation

$$\mu = \frac{1}{\mu_0 (b_1 + b_2 T \Delta T)} \tag{16}$$

in which $b_1 = 0.511 \times 10^3$ m^2/(N − s) and $b_2 = 0.248 \times 10^2$ m^2/(N − s − °C). They were chosen to give the best fit of the viscosity data as given by the NBS (Weast, 1974) in the temperature range of 5°C to 45°C. This special functional form of $\mu(T)$ was chosen so that the basic velocity profile may be obtained analytically.

Since the order of the equations has been reduced due to the omission of Brinkman terms, the nonslip condition can no longer be entered. Therefore, the appropriate boundary conditions are

$$\left.\begin{aligned} u &= 0 \\ T &= \pm \frac{1}{2} \end{aligned}\right\} \text{at } x = \pm \frac{1}{2}$$

The basic steady state can be found to be

$$T_b = x \tag{17a}$$

$$\psi_b = \sum_{j=0}^{5} D_j x^j \tag{17b}$$

$$w_b = -\frac{d\psi_b}{dx} = -\sum_{j=0}^{5} j D_j x^{j-1} \tag{17c}$$

The constant coefficients D_j are given in the Appendix.

In Fig. 2(*b*), the vertical velocity across the layer is shown with ΔT as a parameter. Because of the effect of the variable viscosity, the velocity profile is even more asymmetric than in the previous case shown in Fig. 2(*a*). As ΔT approaches zero, the viscosity of the fluid approaches a constant value and the velocity profile approaches a straight line. As ΔT increases, the variable viscosity effect augments the effect of the quadratic density and temperature relationship in producing a velocity profile which is skewed toward the hot wall. By comparing with Fig. 2(*a*), we see that at the same ΔT, the maximum velocity in this case is larger than the previous case. At $\Delta T = 40$°C, because of the viscosity variations, the location for the maximum downward velocity shifted from the cold wall into the interior of the layer. It is conjectured that such abnormal behavior of the velocity profile is responsible for the growth of instabilities in an infinite vertical porous layer.

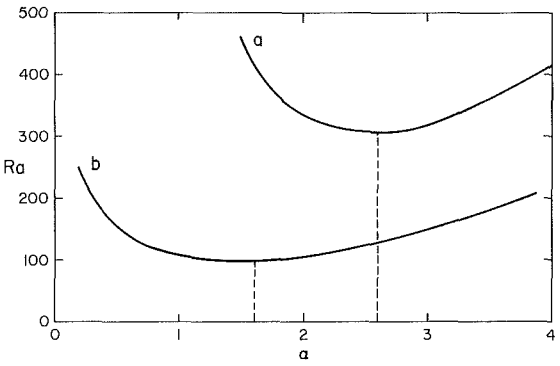

Fig. 3 Marginal stability curves: (*a*) Brinkman term; (*b*) variable viscosity

The linear perturbation equation for the stream function is

$$\mu_b \nabla^2 \psi' + \mu' \frac{d^2 \psi_b}{dx^2} + C_2 \mathrm{Ra} \frac{\partial}{\partial t} \nabla^2 \psi' + \frac{d\mu_b}{dx} \frac{\partial \psi'}{\partial x} + \frac{\partial \mu'}{\partial x} \frac{d\psi_b}{dx} = \frac{1}{\alpha_1 \Delta T} \frac{\partial \rho'}{\partial x} \tag{18}$$

while the temperature perturbation equation remains the same as equation (10). It is noted that μ' and T' are related by

$$\mu' = \frac{d\mu}{dT}\bigg|_{T=T_b} T' = -\frac{b_2 \Delta T}{\mu_0 (b_1 + b_2 T_0 + b_2 \Delta T x)^2} T' \tag{19}$$

Following the same procedure as in Section 3.2 and expanding both $\theta(x)$ and $\phi(x)$ into sinusoidal functions as in equation (12), a similar set of eigenvalue problems can be derived. Both eigenvalue problems were solved by truncating the series representation for θ and ϕ after convergence had been achieved. In both cases, the relative change in the critical Rayleigh number from an eight-term expansion to a ten-term expansion is 2 percent, and that from a ten-term expansion to a twelve-term expansion is 0.2 percent. All results, therefore, are obtained with ten-term expansions.

4 Results and Conclusions

Th eigenvalue σ was determined by using the IMSL subroutine EIGCC available at the University of Arizona Computer Center. When the real part of σ was less than 10^{-8}, we considered that the marginal state had been reached. The corresponding Rayleigh number for a given wavenumber was found. The imaginary part of σ was found to be nonzero, thus indicating an oscillatory onset.

The neutral curve for the case with the Brinkman term included is shown as curve (*a*) in Fig. 3. It is seen that the critical Rayleigh number is 308.0, corresponding to an unrealistic ΔT of 135.9°C. Inertial effect was found to be negligible. Since T_0 is taken to be 25°C, the cold wall would have been at −43°C. This means that for the physically reasonable range of temperature differences <50°C, no instability can exist.

The neutral curve for the variable viscosity case is shown as curve (*b*) in Fig. 3, and it is seen that the critical Rayleigh number is 98.3, corresponding to a critical ΔT of 43.4°C at a wavenumber of 1.6. It is noted that at this ΔT the basic flow velocity profile shows an inward shift of the maximum downward velocity from the boundary wall. The difference in the critical Rayleigh numbers between the experiment and the theory may be attributed to (*a*) the finite extent of the experimental apparatus and (*b*) possible nonuniformity of the permeability k in the layer. Convection in a porous layer of

Downloaded 17 Dec 2010 to 193.140.21.150. Redistribution subject to ASME license or copyright; see http://www.asme.org/terms/Terms_Use.cfm

finite geometry at high Reynolds numbers has been treated by Bejan (1979) and Daniels et al. (1982). However, the effects of finite geometry, as well as variable k, on the onset of instabilities are difficult to assess at the present time.

It may be concluded that for a vertical layer of water-saturated porous medium, the effect of variable viscosity has a profound influence on the stability of thermal convection, whereas the effect of the nonslip condition at the wall has minimal influence on the stability.

Acknowledgments

The financial support of the National Science Foundation through Grant MEA 82-06087 is gratefully acknowledged.

References

Bejan, A., 1979, "On the Boundary Layer Regime in a Vertical Enclosure Filled With a Porous Medium," *Let. Heat Mass Trans.*, Vol. 6, pp. 93–102.

Bejan, A., 1983, "The Boundary Layer Regime in a Porous Layer With Uniform Heat Flux From the Side," *Int. J. Heat Mass Trans.*, Vol. 26, pp. 1339–1346.

Chen, C. F., and Murray, B., 1985, "Double Diffusive Convection in a Porous Medium," *Double Diffusive Motions*, ASME FED, Vol. 24, pp. 47–55.

Chen, C. F., and Thangam, S., 1985, "Convective Stability of a Variable Viscosity Fluid in a Vertical Slot," *J. Fluid Mech.*, Vol. 161, pp. 161–173.

Daniels, P. G., Blythe, P. A., and Simpkins, P. G., 1982, "Thermally Driven Cavity Flows in Porous Media, II. The Horizontal Boundary Layer Structure," *Proc. Roy. Soc.*, Vol. A382, pp. 135–154.

Gill, A. E., 1966, "The Boundary-Layer Regime for Convection in a Rectangular Cavity," *J. of Fluid Mech.*, Vol. 26, pp. 515–536.

Gill, A. E., 1969, "A Proof that Convection in a Porous Vertical Slab is Stable," *J. Fluid Mech.*, Vol. 35, pp. 545–547.

Kianjah, H., and Chen, C. F., 1982, "Convection in a Vertical Layer of Water Saturated Porous Medium," *Bull. Amer. Phys. Soc.*, Vol. 27, p. 1171.

Prasad, V., Kulacki, F. A., and Keyhani, M., 1985, "Natural Convection in Porous Media," *J. Fluid Mech.*, Vol. 150, pp. 89–119.

Ruddick, B. R., and Shirtcliffe, T. G. L., 1979, "Data for Double-Diffusers: Physical Properties of Aqueous Salt–Sugar Solutions," *Deep-Sea Research*, Vol. 26, pp. 775–787.

Seki, N., Fukusako, S., and Inaba, H., 1978, "Heat Transfer in a Confined Rectangular Cavity With Porous Media," *Int. J. Heat Mass Trans.*, Vol. 21, pp. 985–989.

Thangam, S., and Chen, C. F., 1986, "Stability Analysis on the Convection of a Variable Viscosity Fluid in an Infinite Vertical Slot," *Physics of Fluids*, Vol. 29, pp. 1367–1372.

Trevisan, O. V., and Bejan, A., 1986, "Mass and Heat Transfer by Natural Convection in a Vertical Slot Filled With Porous Medium," *Int. J. Heat Mass Trans.*, Vol. 29, pp. 403–415.

Weast, R. C., ed., 1974, *Handbook of Chemistry and Physics*, CRC Press, p. F-49.

Weber, J. E., 1975, "The Boundary-Layer Regime for Convection in a Vertical Porous Layer," *Int. J. Heat Mass Trans.*, Vol. 18, pp. 569–573.

APPENDIX

The constants A_j and B_j appearing in equation (9) are

$$A_1 = \left[1 - \frac{\alpha_3}{\alpha_1}\Delta T^2\left(\frac{6}{\tilde{L}^2} + \frac{1}{4}\right)\right] \Big/ 2\tilde{L}\sinh\frac{\tilde{L}}{2}$$

$$A_2 = \frac{\alpha_2}{\alpha_1}\frac{\Delta T}{12} \Big/ \left(\frac{\tilde{L}}{2}\cosh\frac{\tilde{L}}{2} - \sinh\frac{\tilde{L}}{2}\right)$$

$$B_0 = \frac{1}{8} - \left[\frac{\alpha_3}{\alpha_1}\Delta T^2\left(\frac{1}{4} + \frac{6}{\tilde{L}^2}\right) + 1\right] \Big/ 2\tilde{L}\tanh\frac{\tilde{L}}{2} + \frac{\alpha_3}{\alpha_1}\frac{\Delta T^2}{4}\left(\frac{1}{16} + \frac{3}{\tilde{L}^2}\right)$$

$$B_1 = \frac{\alpha_2}{\alpha_1}\Delta T\left[\frac{1}{4} - \frac{1}{6\left(1 - \frac{2}{\tilde{L}}\tanh\frac{\tilde{L}}{2}\right)}\right]$$

$$B_2 = -\frac{1}{2} - \frac{3\alpha_3}{\tilde{L}\alpha_1}\Delta T^2, \quad B_3 = -\frac{\alpha_2}{3\alpha_1}\Delta T$$

$$B_4 = -\frac{\alpha_3}{4\alpha_1}\Delta T^2$$

The constants D_j appearing in equation (17) are

$$D_0 = \frac{\mu_0 g_2}{}\left\{1 + \left(\frac{b_2}{6g_2}\frac{\alpha_2}{\alpha_1} - \frac{b_2^2}{3g_2^2} + \frac{\alpha_3}{2\alpha_1}\right)\frac{\Delta T^2}{4} - \frac{\alpha_3}{\alpha_1}\frac{b_2^2}{20g_2^2}\Delta T^4\right\}$$

$$D_1 = \frac{\mu_0 g_2}{12}s_1\Delta T, \quad D_2 = \frac{\mu_0 g_2}{2}\left\{\frac{s_1}{16}\frac{b_2}{g_2}\Delta T^2 - 1\right\}$$

$$D_3 = -\frac{\mu_0 g_2}{3}\left\{\frac{b_2}{g_2} + \frac{\alpha_2}{\alpha_1}\right\},$$

$$D_4 = -\frac{\mu_0 g_2}{4}\left\{\frac{b_2}{g_2}\frac{\alpha_2}{\alpha_1} + \frac{\alpha_3}{\alpha_1}\right\}\Delta T^2$$

$$D_5 = -\frac{\mu_0}{5}\frac{b_2\alpha_3}{\alpha_1}$$

and

$$s_1 = \frac{b_2}{g_2} + \frac{\alpha_2}{\alpha_1} + \frac{b_2}{g_2}\frac{\alpha_3}{\alpha_1}\frac{3}{20}\Delta T^2$$

$$g_2 = b_1 + b_2 T_0$$

Downloaded 17 Dec 2010 to 193.140.21.150. Redistribution subject to ASME license or copyright; see http://www.asme.org/terms/Terms_Use.cfm

Hopf Bifurcation in the Double-Glazing Problem With Conducting Boundaries

K. H. Winters
Theoretical Physics Division,
Harwell Laboratory,
Didcot, Oxon OX11 0RA, United Kingdom

Oscillatory convection has been observed in recent experiments in a square, air-filled cavity with differentially heated sidewalls and conducting horizontal surfaces. We show that the onset of the oscillatory convection occurs at a Hopf bifurcation in the steady-state equations for free convection in the Boussinesq approximation. The location of the bifurcation point is found by solving an extended system of steady-state equations. The predicted critical Rayleigh number and frequency at the onset of oscillations are in excellent agreement with the values measured recently and with those of a time-dependent simulation. Four other Hopf bifurcation points are found near the critical point and their presence supports a conjectured resonance between traveling waves in the boundary layers and interior gravity waves in the stratified core.

1 Introduction

In recent years there have been many studies of the natural convection inside a two-dimensional rectangular cavity with differentially heated sidewalls, over wide ranges of aspect ratio and Prandtl number. The particular case of steady, laminar flow in a square, air-filled cavity with adiabatic horizontal surfaces was proposed as a comparison problem by Jones (1979). It attracted a large number of contributions and these were compared with an accurate "benchmark" solution by de Vahl Davis and Jones (1983). This "double-glazing" problem, a term which we extend to include the case where the horizontal surfaces may be either conducting or adiabatic, is an excellent test problem since it is increasingly difficult to obtain accurate solutions for increasing Rayleigh number; within current computer resources it is possible to obtain a benchmark solution accurate to within 1 percent at a Rayleigh number of 10^6, but solutions at 10^7 are much less reliable.

As predictions of the double-glazing and related problems in free convection are obtained at increasingly higher Rayleigh number, it is natural to question the physical reality of the solutions. By solving the steady Navier–Stokes and energy equations we are able to predict laminar convective flows at any Rayleigh number, in principle. Yet all convective flows become turbulent at sufficiently high Rayleigh number, and many are oscillatory over a range of Rayleigh numbers which usually lies between the laminar and turbulent regimes. This question of the reality of the steady solutions was addressed recently by Briggs and Jones (1985) in an experimental study of the double-glazing problem with conducting horizontal surfaces. They found a transition from steady to oscillatory free convection in a square, air-filled cavity at a Rayleigh number of 3×10^6 with a simple periodicity of about 0.5 Hz at onset. The regime of periodic convection was found to persist to a Rayleigh number of at least 1.2×10^7 and there were abrupt changes in the frequency of oscillation within this range. The flow was observed to be predominantly two dimensional.

In this paper we show that the behavior observed by Briggs and Jones arises as a Hopf bifurcation in the two-dimensional steady-state equations for free convection in the Boussinesq approximation. We locate several Hopf bifurcation points by solving a specific extended system of *steady-state* equations and obtain the critical Rayleigh number and frequency for the onset of oscillations. The predicted critical values are in reasonable agreement with the measurements of Briggs and Jones. Our approach predicts also the oscillatory flow arising at the Hopf bifurcation and we confirm that it has the form of traveling waves in the boundary layers. The presence of several Hopf bifurcation points at similar Rayleigh numbers supports the conjecture of Briggs and Jones that the oscillations are the result of a resonance phenomenon between the traveling waves and gravity waves in the stratified interior of the cavity.

We note that the term "double-glazing" problem is also used in a related context to describe convection in a cavity of large aspect ratio with differentially heated walls, in contrast to the square cavity considered here. In future work we intend to consider this large-aspect-ratio case also, using parameter continuation to trace the variation of the Hopf bifurcation with aspect ratio.

2 Problem Description

We consider natural convection in a square, air-filled cavity with differentially heated sidewalls and conducting horizontal surfaces, corresponding to a section of the apparatus of Briggs and Jones in which the flow was observed to be predominantly two dimensional. We assume that the convection is described by the Navier–Stokes and energy equations in the Boussinesq approximation and we express these equations in nondimensional form using the following scales:

- temperature scale S_T, the temperature difference between the hot and cold sidewalls;
- length scale S_L, the width of the cavity;
- velocity scale κ/S_L, where κ is the thermal diffusivity of the fluid.

We obtain the following set of equations for the velocity components u and v, the temperature T, and pressure p:

$$\frac{\partial u}{\partial t}+u\frac{\partial u}{\partial x}+v\frac{\partial u}{\partial y}+\frac{\partial p}{\partial x}-\mathrm{Pr}\,\nabla^2 u=0 \tag{1}$$

$$\frac{\partial v}{\partial t}+u\frac{\partial v}{\partial x}+v\frac{\partial v}{\partial y}+\frac{\partial p}{\partial y}-\mathrm{Pr}\,\nabla^2 v=\mathrm{RaPr}T \tag{2}$$

$$\frac{\partial u}{\partial x}+\frac{\partial v}{\partial y}=0 \tag{3}$$

$$\frac{\partial T}{\partial t}+u\frac{\partial T}{\partial x}+v\frac{\partial T}{\partial y}-\nabla^2 T=0 \tag{4}$$

Contributed by the Heat Transfer Division for publication in the JOURNAL OF HEAT TRANSFER. Manuscript received by the Heat Transfer Division July 21, 1986.

Copyright © 1987 by ASME

Downloaded 17 Dec 2010 to 193.140.21.150. Redistribution subject to ASME license or copyright; see http://www.asme.org/terms/Terms_Use.cfm

where the Laplacian is defined as

$$\nabla^2 = \frac{\partial^2}{\partial x^2} + \frac{\partial^2}{\partial y^2}$$

The above equations contain two nondimensional groups, the Rayleigh number

$$\mathrm{Ra} = g\beta S_T S_L^3 / \kappa\nu$$

and the Prandtl number

$$\mathrm{Pr} = \nu/\kappa$$

where g is the acceleration due to gravity; β is the coefficient of volumetric expansion; ν is the kinematic viscosity; κ is the thermal diffusivity. Fuller details of the formulation are given in Winters (1983).

The thermal boundary conditions are:

- $T=1$ on the left vertical wall;
- $T=0$ on the right vertical wall;
- $T=1-x$ on the floor and roof,

where x is the horizontal coordinate with origin at the lower left corner. Both horizontal and vertical components of velocity were set to zero on all four walls.

3 Numerical Techniques

Steady-state equations are obtained from equations (1)–(4) by setting the time derivatives equal to zero. We discretize these steady equations using the finite-element method (Winters, 1983) and we denote the resulting set of discrete equations as

$$\mathbf{f}(\mathbf{x}, \lambda, \mathbf{a}) = \mathbf{0} \qquad (\mathbf{x} \epsilon \mathbf{X}) \tag{5}$$

where $\mathbf{f}$ is a smooth nonlinear function, $\mathbf{X}$ is the space of solutions $\mathbf{x}$ ($\mathbf{R}^n$ in this case, where n is the number of degrees of freedom in the discretization), λ is a bifurcation parameter, and $\mathbf{a}$ is a vector of control parameters. We distinguish the bifurcation parameter λ from the control parameters $\mathbf{a}$ because we seek the change of behavior as this parameter is varied. In the present problem the Rayleigh number Ra is chosen as the bifurcation parameter and we seek the onset of oscillatory flow as Ra varies. The control parameters are the Prandtl number Pr and the aspect ratio γ of the cavity; we fix their values at $\mathrm{Pr}=0.71$ and $\gamma=1$.

We now consider the linear stability of a steady solution $\mathbf{x}_0$ of equation (5) with respect to a small perturbation $\mathbf{x}_1$. The equation is derived from the time-dependent form

$$M\frac{\partial \mathbf{x}}{\partial t} + \mathbf{f}(\mathbf{x}, \lambda, \mathbf{a}) = \mathbf{0} \tag{6}$$

where M is a linear operator on $\mathbf{X}$ defined by the time-derivative terms in equations (1)–(4). The behavior of the perturbation $\mathbf{x}_1$ is governed to lowest order by the linear equation

$$M\frac{\partial \mathbf{x}_1}{\partial t} + \mathbf{f}_\mathbf{x}(\mathbf{x}_0, \lambda, \mathbf{a})\mathbf{x}_1 = \mathbf{0} \tag{7}$$

Thus, if ξ is a generalized eigenvector of $\mathbf{f}_\mathbf{x}(\mathbf{x}_0, \lambda, \mathbf{a})$ with eigenvalue σ such that

$$\mathbf{f}_\mathbf{x}\xi = \sigma M\xi \tag{8}$$

then the perturbation behaves as

$$\mathbf{x}_1(t) = \epsilon e^{-\sigma t}\xi \tag{9}$$

where ϵ is the component of $\mathbf{x}_1$ along ξ at $t=0$. The steady solution $\mathbf{x}_0$ is linearly stable if all the eigenvalues σ have $\mathrm{Re}(\sigma)>0$. We note that since $\mathbf{f}_\mathbf{x}$ is real the eigenvalues in equation (8) are either real or else occur in complex conjugate pairs.

As the bifurcation parameter λ varies, the linear stability of the steady solution $\mathbf{x}_0$ changes when one or more eigenvalues in equation (8) cross the imaginary axis. Thus there is a critical value of λ for which $\mathrm{Re}(\sigma)=0$ and $\mathbf{f}_\mathbf{x}$ is singular; this critical value is called a singular or bifurcation point of equation (5). Moreover, if σ is purely imaginary at the critical point, so that $\sigma=\pm i\omega$, then equation (5) has a Hopf bifurcation which gives rise to periodic solutions of angular frequency ω at the critical value of λ.

In the present problem we suppose that the observed oscillatory convection arises at a Hopf bifurcation point in the steady equations. To confirm this hypothesis we implement a technique proposed by Jepson (1981) and Griewank and Reddien (1983) for locating Hopf bifurcation points which involves the solution of the following extended set of equations:

$$\begin{aligned}
&\mathbf{f}(\mathbf{x}, \lambda, \mathbf{a}) = \mathbf{0}\\
&\mathbf{f}_\mathbf{x}(\mathbf{x}, \lambda, \mathbf{a})\xi_R + \omega M\xi_I = \mathbf{0}\\
&\mathbf{f}_\mathbf{x}(\mathbf{x}, \lambda, \mathbf{a})\xi_I - \omega M\xi_R = \mathbf{0}\\
&\mathbf{I}\xi_R = 0\\
&\mathbf{I}\xi_I = 1
\end{aligned} \tag{10}$$

The functions ξ_R and ξ_I are the real and imaginary parts of the right eigenvector of $\mathbf{f}_\mathbf{x}$ and the last two equations in the set are normalization conditions. The solution of these nonlinear equations by Newton's method gives successive approximations to $\mathbf{x}$, ξ_R, ξ_I, λ, and ω that converge quadratically to their values at the Hopf bifurcation point $\lambda=\lambda_H$. This technique has been applied successfully by Winters et al. (1984, 1987) to locate the onset of oscillatory convection in a semiconductor crystal melt and the onset of vortex shedding in flow past a cylinder.

From the above extended system of equations (10) it is clear that we are solving basically a linear stability problem to locate the Hopf bifurcation point. However, there are two important differences between our approach and the linear stability and weakly nonlinear analyses of Busse and others (see review by Busse, 1978). Firstly, by solving (10) in a finite-element formulation we are able to locate bifurcations in finite regions of arbitrary shape and with arbitrary boundary conditions. Secondly, in the extended-systems approach the basic governing equations are solved simultaneously with conditions satisfied at the singular point; this provides a framework for systematically identifying and computing different types of singular points of increasing codimension (Jepson and Spence, 1984). It is the combination of the extended systems approach with the finite-element approximation which makes the present method novel and gives it great generality, allowing for example the possibility of locating instabilities in much more complex configurations than that considered here. Other applications of this approach to different bifurcation problems in fluid mechanics and heat transfer are discussed by Winters et al. (1984, 1987).

It is natural in the finite-element method to use a direct solver which makes available the Jacobian matrix $\mathbf{f}_\mathbf{x}$; this is particularly appropriate for bifurcation studies where the Jacobian can be used for parameter continuation (Keller, 1977) and for assessing stability (either by monitoring the sign of its determinant, which equals $(-1)^n$ where n is the number of negative eigenvalues, or by direct calculation of its lowest eigenvalues). Against the advantages of the finite-element method discussed above we must balance the cost; the method is generally slower than finite difference or spectral methods, although this did not impede the present investigation in any way. The cost of solving the extended system (10) is of the order of nine times that of solving the steady equations (5) alone, with an appropriate two-step Newton-Raphson linearization (Jackson, 1987).

We note from equation (9) that in the neighborhood of the Hopf point the solution is approximately of the form:

$$\mathbf{x}(t) = \mathbf{x}_0 + \epsilon\{\cos(\omega t)\xi_R - \sin(\omega t)\xi_I\} \tag{11}$$

Downloaded 17 Dec 2010 to 193.140.21.150. Redistribution subject to ASME license or copyright; see http://www.asme.org/terms/Terms_Use.cfm

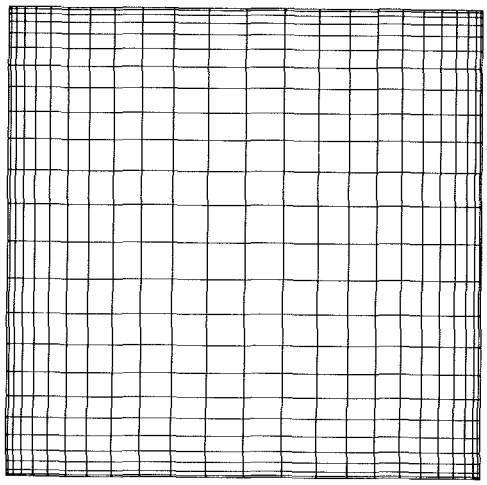

Fig. 1 Finite-element grid of 24 x 24 nine-noded quadrilateral elements

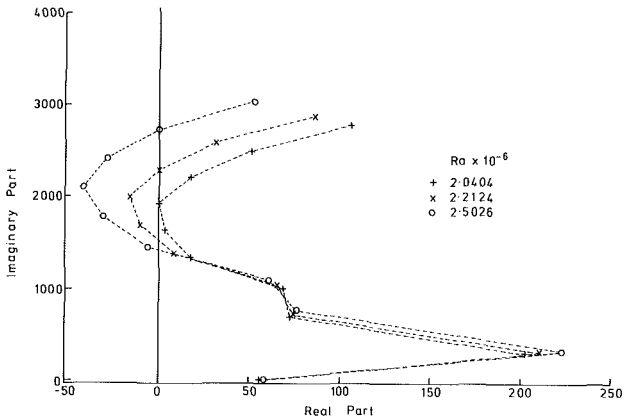

Fig. 2 Part of the complex eigenvalue spectrum at three critical values of the Rayleigh number. Only eigenvalues of positive imaginary part are shown. Dashed lines join eigenvalues computed at the same Rayleigh number.

with the amplitude ϵ behaving as $\sqrt{\lambda-\lambda_H}$ (Joseph and Sattinger, 1972). We use the relationship (11) to visualize the oscillatory flow arising at the Hopf bifurcation with an assumed value of ϵ.

4 Results

The discretized steady equations (5) and the extended set of equations (10) were solved with the ENTWIFE finite-element code developed at Harwell. All calculations were carried out on a CRAY S-2200. A typical grid consisting of 24×24 nine-noded quadrilateral elements with quadratic interpolation for the velocity and temperature and linear discontinuous interpolation for the pressure is shown in Fig. 1. One Newton–Raphson iteration in the solution of the extended set of equations (10) required around 45 s of CPU time for this grid, and typically four Newton–Raphson iterations were required for convergence.

The procedure for locating the Hopf bifurcation points was as follows. Steady solutions were obtained at Rayleigh numbers of 10^6, 2×10^6, and 3×10^6. Then at each of the Rayleigh numbers the eigenvalue spectrum of the Jacobian matrix was explored. A set of sample points was chosen along the imaginary axis and the nearest eigenvalue to each of the sample points was found by inverse iteration (Jackson, 1987). In this way five distinct complex eigenvalues were found in the left half plane at Ra $= 3\times10^6$ and five complex eigenvalues were found about to cross the imaginary axis into the left half plane at Ra $= 2\times10^6$. This indicates that five Hopf bifurcations from the steady solution occur for Rayleigh numbers between 2×10^6 and 3×10^6. The base solution at 2×10^6 and each of the five eigenvectors were used as the initial guess for the solution of the extended system (10) by Newton's method; in each case this converged to a distinct Hopf bifurcation point.

Table 1 Critical Rayleigh number Ra at the first five Hopf bifurcation points for different grids

Grid	Ra_{P1} x10^{-6}	Ra_{P2} x10^{-6}	Ra_{P3} x10^{-6}	Ra_{P4} x10^{-6}	Ra_{P5} x10^{-6}
12x12	2.0041	2.0111	2.2015	2.2568	2.4947
14x14	2.0404	2.0834	2.2124	2.3869	2.5026
16x16	2.0986	2.1453	2.2678	2.4525	2.5366
24x24	2.1102	2.1660	2.2799	2.4989	2.5563
28x28	2.1092	–	–	–	2.5538
32x32	–	–	–	–	2.5517

Table 2 Critical angular frequency ω at the first five Hopf bifurcation points for different grids. The corresponding dimensional frequency is $\omega\kappa/S_L^2$ rad/s.

Grid	w_{P1}	w_{P2}	w_{P3}	w_{P4}	w_{P5}
12x12	1915.3	1629.4	2290.3	1394.5	2727.7
14x14	1922.8	1646.3	2286.5	1420.7	2721.0
16x16	1948.9	1668.3	2317.6	1439.0	2749.5
24x24	1950.0	1671.9	2318.7	1448.5	2753.0
28x28	1949.4	–	–	–	2751.4
32x32	–	–	–	–	2750.4

Figure 2 shows part of the eigenvalue spectrum at three of the critical Rayleigh numbers. Only the eigenvalues of positive imaginary part are plotted; each complex eigenvalue has a complex conjugate with an equal imaginary part of opposite sign. Although the five eigenvalues cross the imaginary axis for only a small increase in Rayleigh number, their imaginary parts are well separated so that no difficulty was encountered in converging the extended system to each of the Hopf points. The five eigenvalues show a remarkable coherence as the Rayleigh number changes, and this would seem to indicate that their behavior arises from a common physical phenomenon. Briggs and Jones have hypothesized that the onset of oscillations occurs as a resonance between the traveling waves in the boundary layers and internal gravity waves in the stratified core of the cavity. We would then expect each of the five Hopf bifurcation points to arise from this same resonance phenomenon. Since more than one mode is expected in disturbances giving rise to internal gravity waves, each mode having a distinct frequency (Turner, 1973), it is natural to identify each Hopf point with a resonance between the traveling waves in the boundary layers and a particular mode of the internal gravity waves.

A characteristic feature of the numerical study of bifurcations is the appearance of spurious bifurcations when the discretization of the exact continuum equations is too coarse. In view of this we took special care to ensure grid convergence of our predicted Hopf bifurcation points. The critical Rayleigh numbers and angular frequencies at the Hopf points are summarized in Tables 1 and 2 for a series of different grids; the notation $n\times m$ is used to denote n quadrilateral elements in the horizontal direction and m in the vertical direction. We know of no theoretical derivation of the asymptotic rate of convergence of Hopf bifurcation points computed from discrete equations for decreasing mesh spacing. However, for turning points and symmetry-breaking bifurcation points Brezzi et al. (1981) have shown that the rate of convergence of the predicted critical parameter is the square of the rate of convergence of the variables. If the same result holds

Downloaded 17 Dec 2010 to 193.140.21.150. Redistribution subject to ASME license or copyright; see http://www.asme.org/terms/Terms_Use.cfm

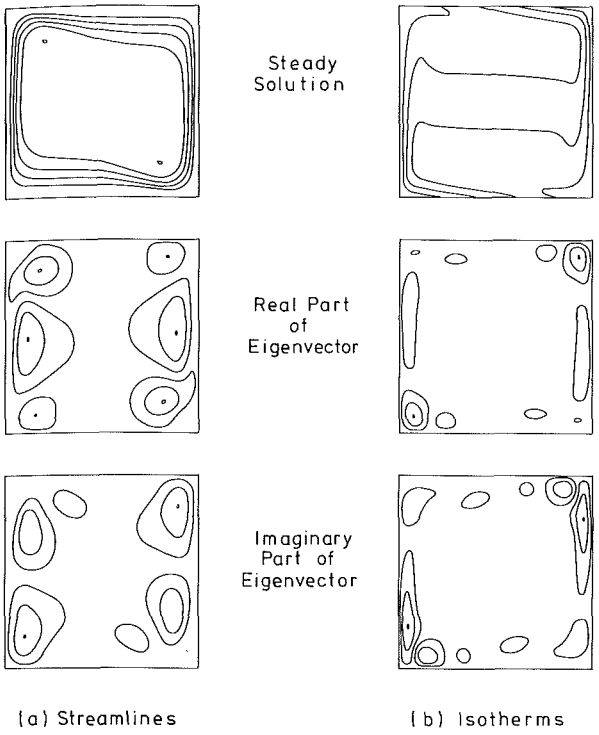

Fig. 3 (*a*) Streamlines and (*b*) isotherms for the steady solution and the real and imaginary parts of the critical eigenvector at the first Hopf bifurcation point. Note that the functions plotted have so-called centrosymmetry on reflection about the horizontal and vertical axes which pass through the center of the cavity.

for Hopf bifurcations then the asymptotic rate of convergence of the critical Rayleigh numbers and angular frequencies is expected to be h^4, where h is the mesh spacing, for the quadratic elements used here (Winters and Cliffe, 1985).

Although we predict five Hopf bifurcations from the steady convective state, only the bifurcation with lowest Rayleigh number is physical and marks the transition to oscillatory convection. Thus, we predict the onset of oscillations at a Rayleigh number of 2.109×10^6 which is in reasonable agreement with the value of 3×10^6 measured by Briggs and Jones. The angular frequency of the oscillations at onset is predicted to be 1949.4, based on a frequency scale of κ/S_L^2. Since the thermal diffusivity κ of air is 2.11×10^{-5} at 20°C (Cornwell, 1977) and the length scale S_L is 0.15 m in the experiment, the corresponding dimensional frequency is 0.29 Hz at onset, in fair accord with the value of around 0.5 Hz quoted by Briggs and Jones. Two points should be considered when making this comparison. Firstly, the oscillatory flow at the exact point of bifurcation has zero amplitude and is not observable; in the experiment the value of the Rayleigh number giving rise to oscillations of *finite* amplitude is measured, and this is taken to be the threshold value. We have no estimate of the error involved in this assumption, although in principle it could be found by measuring the amplitude of oscillation as a function of Rayleigh number near the threshold and extrapolating back to zero amplitude, a technique used in a recent simulation (Le Quéré and Alziary de Roquefort, 1986). Secondly, a slight three dimensionality of the flow in the center midplane was observed and this, together with the effect of the lateral sidewalls, introduces further uncertainties into the comparison.

Very recently, Le Quéré and Alziary de Roquefort (1986) have simulated the convective flow for the present problem in a time-dependent finite-difference calculation. They find that the onset of oscillations occurs at a Rayleigh number between

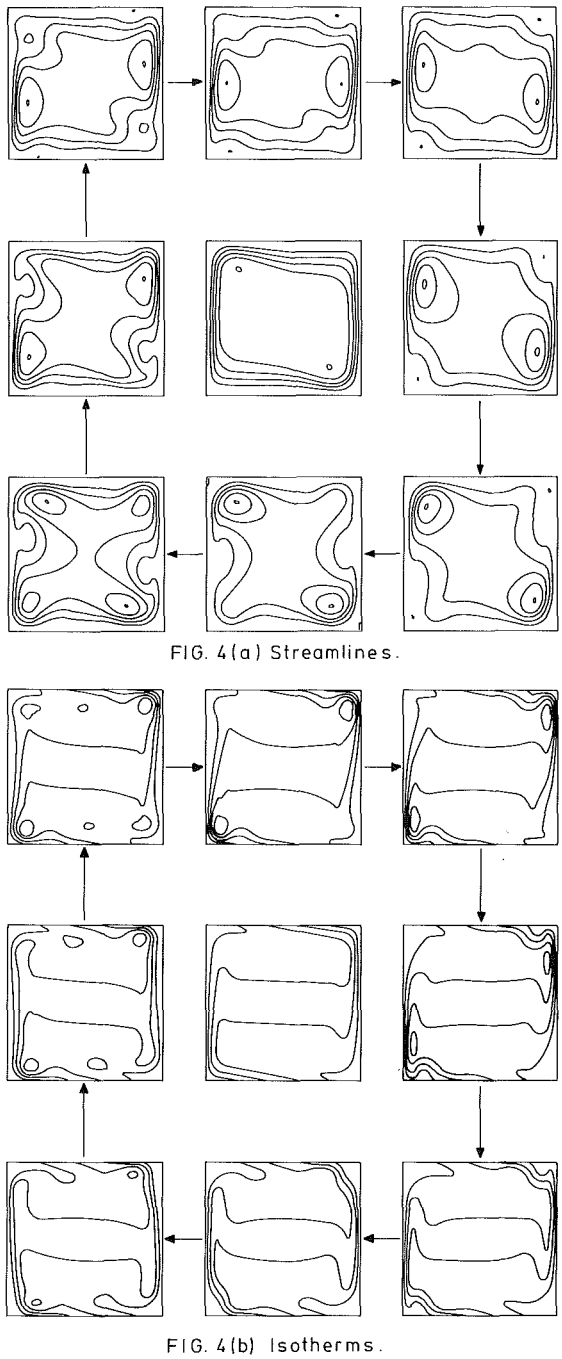

Fig. 4 (*a*) Streamlines and (*b*) isotherms for the steady solution at the first Hopf bifurcation point (center plot) compared with one cycle of the oscillatory solution arising at the bifurcation (outer plots). The time intervals between each plot of the oscillatory solution are equal.

2×10^6 and 2.2×10^6, in good agreement with our predicted critical value of 2.109×10^6. They obtain an angular frequency of 1895 at the supercritical Rayleigh number of 2.2×10^6, compared with the present critical frequency of 1949.

Figure 3 shows the streamlines and isotherms for the steady solution and real and imaginary parts of the eigenvector at the first Hopf bifurcation point. It is apparent that while the boundary layers in temperature and momentum for the base solution are narrow, those for the eigenvectors are much broader. Thus, the variation of velocity as the periodic convection develops will be greater on the centerline side of the peak velocity, and this was measured by Briggs and Jones.

The nature of the oscillatory convection at a Rayleigh number near the critical value can be determined from equa-

Downloaded 17 Dec 2010 to 193.140.21.150. Redistribution subject to ASME license or copyright; see http://www.asme.org/terms/Terms_Use.cfm

tion (11). Figure 4 shows the change in flow and temperature distribution during one oscillation with ϵ assumed to be 0.5. The flow is represented by streamlines computed from the instantaneous velocity field. The instability clearly takes the form of traveling waves in the boundary layers adjacent to both the vertical and horizontal surfaces. The oscillatory convection which arises at the higher (unstable) Hopf points was also visualized and found to have a similar form.

It should be emphasized that once the first complex conjugate pair of eigenvalues has crossed the imaginary axis then the solutions of the steady equations are unstable. The other complex pairs which cross the axis at higher Rayleigh number correspond to Hopf bifurcations from the (now unstable) steady solution branch to unstable periodic orbits, regardless of whether they branch sub- or supercritically from the steady solution. Thus, only the first bifurcated solution can be stable. We note that the time-dependent simulation of Le Quéré and Alziary de Roquefort (1986) indicates that this bifurcation is supercritical, but we are unable to verify this at present.

Briggs and Jones found in their experiment that as the Rayleigh number increases above its critical value for periodic convection there are abrupt changes in the frequency of oscillation up to $\mathrm{Ra} = 1.2 \times 10^7$, but only a single frequency is ever observed at a particular Rayleigh number. It is tempting to identify this behavior with the existence of the four Hopf bifurcations from the unstable steady solution branch, since each of the bifurcations gives rise to a distinct frequency of oscillation. It is conceivable that a transition from steady flow to an *unstable* periodic orbit of one of these higher Hopf points might be observed in the experiment, but only if the time scale for the development of the instability is much greater than the observation time. This time scale is determined by the magnitude of the real part of the eigenvalue and at a Rayleigh number of 3×10^6 it is typically less than 10 s for the four higher Hopf points, which is far smaller than the observation time of more than half an hour. It is more likely that the distinct frequencies observed by Briggs and Jones are the result of some interaction, not yet understood, between the periodic orbits arising at the different Hopf points. This could be verified by continuation of each of the periodic orbits, but the techniques required are beyond the scope of the present paper.

5 Conclusions

We have applied a technique for locating Hopf bifurcations in steady-state equations to the problem of free convective flow in a square, air-filled cavity in the Boussinesq approximation, and we have found five bifurcation points at similar Rayleigh number. The lowest point corresponds to the loss of stability of steady solutions and the development of time-periodic behavior, and we predict a critical Rayleigh number and frequency for the onset of oscillatory convection in reasonable agreement with the measurements of Briggs and Jones (1985).

We note that the present technique locates the onset of instability exactly, unlike transient studies where there may be considerable uncertainty in distinguishing true oscillatory behavior from transient oscillations which tend to a steady state over a long time scale. A further advantage of the present approach is that, having located a bifurcation point for a particular set of control parameters **a**, we can obtain by parameter continuation the variation of the critical Rayleigh number as one or more of the control parameters vary. In this way the onset of oscillatory convection can be predicted as both the Prandtl number and aspect ratio change. As an extension of this approach we can introduce a homotopy parameter into the boundary conditions to study the effect of insulating rather than conducting surfaces on the instability.

Acknowledgment

The work described in this report is part of the longer term research carried out within the Underlying Programme of the United Kingdom Atomic Energy Authority.

References

Brezzi, F., Rappaz, J., and Raviart, P. A., 1981, "Finite Dimensional Approximation of Nonlinear Problems, Part III: Simple Bifurcation Points," *Numer. Math.*, Vol. 38, pp. 1–30.

Briggs, D. G., and Jones, D. N., 1985, "Two-Dimensional Periodic Natural Convection in a Rectangular Enclosure of Aspect Ratio One," ASME JOURNAL OF HEAT TRANSFER, Vol. 107, pp. 850–854.

Busse, F. H., 1978, "Non-linear Properties of Thermal Convection," *Rep. Prog. Phys.*, Vol. 41, pp. 1929–1967.

Cornwell, K., 1977, *The Flow of Heat*, Van Nostrand Reinhold, New York.

Griewank, A., and Reddien, G., 1983, "The Calculation of Hopf Points by a Direct Method," *IMA J. Numer. Anal.*, Vol. 3, pp. 295–303.

Jackson, C. P., 1987, "A Finite-Element Study of the Onset of Vortex Shedding in Flow Past Variously Shaped Bodies," Harwell Report TP. 1154; *J. Fluid Mech.*, in press.

Jepson, A. D., 1981, "Numerical Hopf Bifurcation," Thesis, Part 2, California Institute of Technology, Pasadena, CA.

Jepson, A. D., and Spence, A., 1984, "Singular Points and Their Computation," in: *Numerical Methods for Bifurcation Problems*, T. Küpper, H. D. Mittlemann, and H. Weber, eds., International Series of Numerical Mathematics, Vol. 70, Birkhäuser Verlag.

Jones, I. P., 1979, "A Comparison Problem for Numerical Methods in Fluid Dynamics: the 'Double-Glazing' Problem," *Numerical Methods in Thermal Problems*, R. W. Lewis and K. Morgan, eds., Pineridge Press, Swansea, UK, pp. 338–348.

Joseph, D. D., and Sattinger, D. H., 1972, "Bifurcating Time Periodic Solutions and Their Stability," *Arch. Rational Mech. Anal.*, Vol. 45, pp. 79–109.

Keller, H. B., 1977, "Numerical Solutions of Bifurcation and Nonlinear Eigenvalue Problems," *Applications of Bifurcation Theory*, P. H. Rabinowitz, ed., Academic Press, New York, pp. 359–384.

Le Quéré, P., and Alziary de Roquefort, T., 1986, "Transition to Unsteady Natural Convection of Air in Vertical Differentially Heated Cavities: Influence of Thermal Boundary Conditions on the Horizontal Walls," *Eighth International Heat Transfer Conference*, San Francisco, CA.

Turner, J. S., 1973, *Buoyancy Effects in Fluids*, Cambridge University Press, Cambridge, UK.

de Vahl Davis, G., and Jones, I. P., 1983, "Natural Convection in a Square Cavity: A Comparison Exercise," *Int. J. Numer. Methods Fluids*, Vol. 3, pp. 227–248.

Winters, K. H., 1983," Predictions of Laminar Natural Convection in Heated Cavities," *Numerical Methods in Heat Transfer*, Vol. 2, R. W. Lewis, K. Morgan, and B. A. Schrefler, eds., Wiley, Chichester, pp. 179–204.

Winters, K. H., and Cliffe, K. A., 1985, "Convergence Properties of the Finite-Element Method for Bénard Convection in an Infinite Layer," *J. Comp. Phys.*, Vol. 60, pp. 346–351.

Winters, K. H., Cliffe, K. A., and Jackson, C. P. 1984, "A Review of Extended Systems for Finding Critical Points in Coupled Problems," *Proceedings of Conference on Numerical Methods for Transient and Coupled Problems*, R. W. Lewis, E. Hinton, P. Bettess, and B. A. Schrefler, eds., Pineridge Press, Swansea, UK, pp. 949–959.

Winters, K. H., Cliffe, K. A., and Jackson, C. P., 1987, "The Prediction of Instabilities Using Bifurcation Theory," *Numerical Methods for Transient and Coupled Problems*, R. W. Lewis, E. Hinton, P. Bettess, and B. A. Schrefler, eds., Wiley, New York, pp. 179–198.

Downloaded 17 Dec 2010 to 193.140.21.150. Redistribution subject to ASME license or copyright; see http://www.asme.org/terms/Terms_Use.cfm

D. S. Lin
Research Assistant.

M. W. Nansteel
Assistant Professor.

Department of Mechanical Engineering
and Applied Mechanics,
University of Pennsylvania,
Philadelphia, PA 19104

Natural Convection in a Vertical Annulus Containing Water Near the Density Maximum

Steady natural convection of water near the density extremum in a vertical annulus is studied numerically. Results for flow in annuli with aspect ratio $1 \leq A \leq 8$ and varying degrees of curvature are given for $10^3 \leq Ra \leq 10^5$. It is shown that both the density distribution parameter R and the annulus curvature K have a strong effect on the steady flow structure and heat transfer in the annulus. A closed-form solution for the vertical flow in a very tall annulus is compared with numerical results for finite-aspect-ratio annuli.

Introduction

Most studies of natural convection in enclosures concern fluids for which density decreases roughly linearly with increasing temperature. This linear behavior gives rise to the second part of the Boussinesq approximation. For a number of fluids, however, such as water, molten bismuth, antimony, gallium and tellurium (Grant, 1968; Lankford and Bejan, 1986) the density-temperature relationship exhibits an extremum. For water, this density maximum occurs at about 4°C at atmospheric pressure. A number of experimental and analytical studies have been carried out for the steady natural convection of water near 4°C in a rectangular enclosure with vertical walls maintained at two different temperatures while the horizontal walls are adiabatic. Watson (1972) seems to have been the first to investigate natural convection in a differentially heated enclosure filled with cold water. It was found that the anomalous density-temperature relationship may result in a dual, counterrotating cell flow pattern which significantly inhibits cross-cavity heat transfer such that the Nusselt number attains a minimum when the two convective cells are of the same size. The effect of temperature-dependent viscosity was also addressed and was found to result in changes in magnitude rather than in the character of the flow. Seki et al. (1978) carried out experimental and numerical work on a cold water-filled rectangular enclosure with a height of 100 mm. Aspect ratios of 1, 2, 5, 10, and 20 were considered. It was found that aspect ratios near unity resulted in the maximum heat transfer. Inaba and Fukuda (1984a, b) investigated the effect of inclination angle on the natural convection of cold water in a rectangular enclosure both experimentally and numerically. Discrepancies between numerical and experimental results were observed for hot wall temperatures in excess of 8°C for some inclination angles. These differences were attributed to imperfect thermal boundary conditions in the experiment and to incipient transition to three-dimensional behavior in the experiment. The inclination angle was found to affect the rate of heat transfer differently depending on the relationship between the wall temperatures and the extremum temperature. Very recently, Nansteel et al. (1987) used a perturbation technique to study the natural convection of cold water in a rectangular enclosure for small Rayleigh number. Additional work for rectangular enclosures containing cold water has been carried out by Desai and Forbes (1971), Robillard and Vasseur (1981, 1982), Poulikakos (1984), Forbes and Cooper (1975), Vasseur and Robillard (1980), Blake et al. (1984), and Lin and Nansteel (1987).

The investigations discussed above addressed the convection of cold water in rectangular enclosures. However, natural convection heat transfer in annular passages is encountered in a variety of engineering situations including heat exchangers, the food industry, biomedical applications, and nuclear reactors. The natural convection of water in the annular space between two horizontal cylinders with density inversion has also been studied. Seki et al. (1975) experimentally and numerically studied flow patterns and heat transfer for cold water confined between two horizontal cylinders with a radius ratio K (outer radius/inner radius) in the range $1.18 \leq K \leq 6.39$, with the temperature of the outer cylinder varying from 1 to 15°C while the inner cylinder was maintained at 0°C. Nguyen et al. (1982) examined the same problem for $K=2$ for small Rayleigh numbers using a perturbation technique. As in the rectangular enclosure, it was found that density inversion may result in a dual-cell flow pattern which prohibits fluid in a given convective cell from simultaneously contacting both the heated and cooled surfaces and hence limits heat transfer.

Buoyancy-induced flow in vertical annular passages has received relatively little attention. What is known about Boussinesq fluid convection is due to the numerical work of Schwab and DeWitt (1970), de Vahl Davis and Thomas (1969), Thomas and de Vahl Davis (1970), and Lee et al. (1982). Most of the results reported in these investigations are for tall annuli only. de Vahl Davis and Thomas (1969) and Thomas and de Vahl Davis (1970) studied free convection in a differentially heated vertical annulus with upper and lower horizontal surfaces insulated. They considered a wide range of parameters: $10^2 \leq \mathrm{Ra} \leq 2 \times 10^5$, $0.5 \leq \mathrm{Pr} \leq 10^4$, $1 \leq A \leq 33$, and $1 \leq K \leq 10$. The aspect ratio A is the ratio of the annulus height H to the gap width D. The majority of the results were for $\mathrm{Pr}=1$ and $1 \leq K \leq 4$. Their results indicate that the temperature and velocity fields, and consequently heat transfer rate, are not only functions of Ra and A, but strongly depend on the radius ratio. They classified the flow regimes as being either conduction, transition, or boundary layer using the horizontal temperature gradient at the annulus midplane as a criterion. Thomas and de Vahl Davis (1970) have also reported multicellular flow behavior depending on the Rayleigh number and aspect ratio. The numerical heat transfer results of Schwab and DeWitt (1970) are not in agreement with the findings of Thomas and de Vahl Davis (1970). The reason for this discrepancy is not clear although the numerical methods used are essentially the same. Keyhani et al. (1983) conducted experiments for the case when a constant heat flux is applied on the inner wall of the annulus with air and helium as test fluids for $K=4.33$ and $A=2.76$ for a wide range of Rayleigh numbers. They reported that in the conduction regime the heat transfer rate for a constant flux boundary condition is 10 percent higher than for the isothermal case. Recently, Prasad and Kulacki (1985) performed experiments with a liquid-filled vertical annulus for $K=5.338$, aspect ratio

Contributed by the Heat Transfer Division for publication in the JOURNAL OF HEAT TRANSFER. Manuscript received by the Heat Transfer Division October 3, 1986.

 Copyright © 1987 by ASME

Downloaded 17 Dec 2010 to 193.140.21.150. Redistribution subject to ASME license or copyright; see http://www.asme.org/terms/Terms_Use.cfm

$A = 0.5$, 1, and 1.5, and $8 \times 10^6 \leq \mathrm{Ra} \leq 3 \times 10^{10}$. Water and ethylene glycol were used as the working fluids. Other investigations of Boussinesq convection in vertical annuli include the work of Shaaban and Ösizik (1982), Hanzawa and Kato (1984), and Bhushan et al. (1983). It appears to the present authors that no work has been done on the convection in a vertical annulus with cold water effects.

The objective here is systematically to investigate the effects of density inversion, curvature, and aspect ratio on the steady natural convection of cold water in a vertical annulus. Because the effects of density inversion, in the absence of curvature, have been discussed elsewhere, the primary emphasis here will be on curvature and its consequences with respect to the flow structure and heat transfer in the annulus.

Formulation

Consider the cold water-filled annular region of height H, and inner and outer radii $\bar{r}_i$ and $\bar{r}_o$, respectively (gap width $= \bar{r}_o - \bar{r}_i = D$) shown in Fig. 1. The outer wall is at temperature $\bar{T}_c$ and the inner wall is maintained at temperature $\bar{T}_h > \bar{T}_c$ while the horizontal surfaces are insulated. Assuming that the flow in the gap is laminar and axisymmetric, and all fluid properties are constant except for density in the buoyancy term of the vertical momentum balance, the governing equations for conservation of mass, momentum, and energy in the annulus expressed in unsteady form are

$$\frac{\partial(\bar{r}\bar{u})}{\partial \bar{r}} + \frac{\partial(\bar{r}\bar{v})}{\partial \bar{z}} = 0 \tag{1}$$

$$\frac{D\bar{u}}{D\bar{t}} = -\frac{1}{\rho_c}\frac{\partial \bar{p}'}{\partial \bar{r}} + \nu_c\left(\frac{\partial^2 \bar{u}}{\partial \bar{r}^2} + \frac{1}{\bar{r}}\frac{\partial \bar{u}}{\partial \bar{r}} + \frac{\partial^2 \bar{u}}{\partial \bar{z}^2} - \frac{\bar{u}}{\bar{r}^2}\right) \tag{2}$$

$$\frac{D\bar{v}}{D\bar{t}} = -\frac{1}{\rho_c}\frac{\partial \bar{p}'}{\partial \bar{z}} - \frac{\rho}{\rho_c}g + \nu_c\left(\frac{\partial^2 \bar{v}}{\partial \bar{r}^2} + \frac{1}{\bar{r}}\frac{\partial \bar{v}}{\partial \bar{r}} + \frac{\partial^2 \bar{v}}{\partial \bar{z}^2}\right) \tag{3}$$

$$\frac{D\bar{T}}{D\bar{t}} = \alpha_c\left(\frac{\partial^2 \bar{T}}{\partial \bar{r}^2} + \frac{1}{\bar{r}}\frac{\partial \bar{T}}{\partial \bar{r}} + \frac{\partial^2 \bar{T}}{\partial \bar{z}^2}\right) \tag{4}$$

where viscous dissipation has been neglected and properties have been evaluated at the cold wall temperature. Conditions on the boundary are

$$\bar{u} = \bar{v} = 0$$

$$\bar{T}(\bar{r}_i, \bar{z}) = \bar{T}_h, \qquad \bar{T}(\bar{r}_o, \bar{z}) = \bar{T}_c$$

$$\frac{\partial \bar{T}}{\partial \bar{z}}(\bar{r}, 0) = \frac{\partial \bar{T}}{\partial \bar{z}}(\bar{r}, H) = 0$$

In the past, many correlations have been proposed to represent the density of cold water as a function of temperature such as rational function (see Kell, 1967; Seki et al., 1978) and polynomial approximation (see Watson, 1972). Other correlations include Chen and Millero (1976), Poulikakos (1984), and Gebhart and Mollendorf (1977). Although most of these correlations are in close agreement, the relation from Gebhart and Mollendorf will be used here due to its high precision and simple form. The density of pure water at atmospheric pressure is given as (Gebhart and Mollendorf, 1977)

$$\rho = \rho_m[1 - \alpha_1 |\bar{T} - \bar{T}_m|^q] \tag{5}$$

where $\bar{T}_m = 4.029325°\mathrm{C}$ is the temperature corresponding to the density maximum, $\rho_m = 999.9720\ \mathrm{kg/m^3}$, $\alpha_1 = 9.297173 \times 10^{-6}\ °\mathrm{C}^{-q}$ and $q = 1.894816$.

Defining the modified pressure $\bar{p} = \bar{p}' + \rho_c g \bar{z}$, introducing equation (5) and the nondimensional variables

$$r = \frac{\bar{r} - \bar{r}_i}{D}, \quad z = \bar{z}/D, \quad u = \bar{u}D/\nu_c, \quad v = \bar{v}D/\nu_c$$

$$t = \nu_c \bar{t}/D^2, \quad p = \frac{\bar{p}D^2}{\rho_c \nu_c^2}, \quad \phi = (\bar{T} - \bar{T}_c)/(\bar{T}_h - \bar{T}_c)$$

equations (1)–(4) become

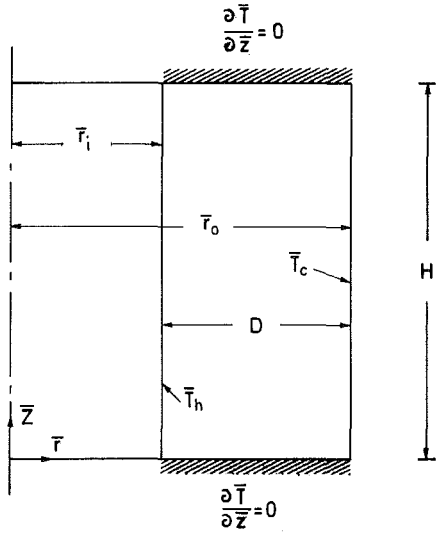

Fig. 1 Vertical annulus, coordinate system, and thermal boundary conditions

Nomenclature

A = aspect ratio $= H/D$
D = gap width
g = gravitational acceleration
H = annulus height
k = thermal conductivity
K = radius ratio $= \bar{r}_o/\bar{r}_i$
Nu = Nusselt number $= q''D/k(\bar{T}_h - \bar{T}_c)$
p = dimensionless pressure $= \bar{p}D^2/\rho_c \nu_c^2$
$\bar{p}$ = modified pressure $= \bar{p}' + \rho_c g \bar{z}$
$\bar{p}'$ = pressure
Pr = Prandtl number $= \nu_c/\alpha_c$
q = constant in equation (5)
q'' = heat flux
r = dimensionless radial coordinate $= (\bar{r} - \bar{r}_i)/D$
$\bar{r}$ = radial coordinate
R = density distribution parameter $= (\bar{T}_m - \bar{T}_c)/(\bar{T}_h - \bar{T}_c)$
Ra = Rayleigh number $= g\rho_m \alpha_1 (\bar{T}_h - \bar{T}_c)^q D^3/\rho_c \nu_c \alpha_c$
t = dimensionless time $= \nu_c \bar{t}/D^2$
$\bar{t}$ = time
$\bar{T}$ = temperature
u = dimensionless radial velocity $= \bar{u}D/\nu_c$
$\bar{u}$ = radial velocity
v = dimensionless axial velocity $= \bar{v}D/\nu_c$
$\bar{v}$ = axial velocity
z = dimensionless axial coordinate $= \bar{z}/D$
$\bar{z}$ = axial coordinate
α = thermal diffusivity
α_1 = constant in equation (5)
ν = kinematic viscosity
ξ = dimensionless vorticity
ρ = density
ϕ = dimensionless temperature $= (\bar{T} - \bar{T}_c)/(\bar{T}_h - \bar{T}_c)$
ψ = dimensionless stream function

Subscripts

c = cold wall
h = hot wall
i = inner wall
m = extremum temperature
o = outer wall

Downloaded 17 Dec 2010 to 193.140.21.150. Redistribution subject to ASME license or copyright; see http://www.asme.org/terms/Terms_Use.cfm

Table 1 Convergence of heat transfer and ψ with mesh size: $R=1/2$, $K=2$, $A=1$

Ra	Mesh	Nu_i	Nu_o	KNu_o	ψ_{max}
10^3	21*21	1.446	0.723	1.446	0.0304
	21*21	1.738	0.868	1.736	0.282
10^4	31*31	1.740	0.870	1.740	0.281
	41*41	1.738	0.871	1.742	0.281
	21*21	3.551	1.806	3.612	0.997
10^5	31*31	3.518	1.763	3.526	0.997
	41*41	3.521	1.762	3.524	0.998
	21*21	10.858	4.670	9.340	2.238
10^6	31*31	8.408	3.815	7.630	2.077
	41*41	7.420	3.682	7.364	2.048
	61*61	7.136	3.543	7.086	2.043

$$\frac{\partial u}{\partial r}+\frac{\partial \cdot}{\partial z}+\frac{(K-1)}{(K-1)r+1}u=0 \tag{6}$$

$$\frac{Du}{Dt}=-\frac{\partial p}{\partial r}+\frac{\partial^2 u}{\partial r^2}+\frac{(K-1)}{(K-1)r+1}\frac{\partial u}{\partial r}+\frac{\partial^2 u}{\partial z^2}-\left[\frac{K-1}{(K-1)r+1}\right]^2 u \tag{7}$$

$$\frac{Dv}{Dt}=-\frac{\partial p}{\partial z}+\frac{\mathrm{Ra}}{\mathrm{Pr}}[\,|\phi-R\,|^q-|-R\,|^q]+\frac{\partial^2 v}{\partial r^2}+\frac{(K-1)}{(K-1)r+1}\frac{\partial v}{\partial r}+\frac{\partial^2 v}{\partial z^2} \tag{8}$$

$$\frac{D\phi}{Dt}=\frac{1}{\mathrm{Pr}}\left[\frac{\partial^2\phi}{\partial r^2}+\frac{(K-1)}{(K-1)r+1}\frac{\partial\phi}{\partial r}+\frac{\partial^2\phi}{\partial z^2}\right] \tag{9}$$

where

$$u=v=0, \text{ on the boundary}$$

$$\phi(0,z)=1, \quad \phi(1,z)=0$$

$$\frac{\partial\phi}{\partial z}(r,0)=\frac{\partial\phi}{\partial z}(r,A)=0$$

Additional parameters appearing in equations (6)–(9) are the radius ratio $K=\bar{r}_o/\bar{r}_i$, which characterizes the degree of curvature, the Prandtl number $\mathrm{Pr}=\nu_c/\alpha_c$, the aspect ratio $A=H/D$, the Rayleigh number

$$\mathrm{Ra}=\frac{g\rho_m\alpha_1(\bar{T}_h-\bar{T}_c)^q D^3}{\rho_c\nu_c\alpha_c}$$

and the density distribution parameter

$$R=\frac{\bar{T}_m-\bar{T}_c}{\bar{T}_h-\bar{T}_c}$$

which fixes the orientation of the maximum density temperature with respect to the wall temperatures $\bar{T}_h$ and $\bar{T}_c$ (see also Gebhart and Mollendorf, 1978; Nansteel et al., 1987). Note that the case $R=1/2$ corresponds to the circumstance in which the hot and cold wall temperatures perfectly straddle the maximum density temperature. For values of R in the range $0<R<1$, water density in the annulus increases with increasing temperature to a maximum $\rho=\rho_m$ at $\bar{T}=\bar{T}_m$ and then decreases with any further increase in temperature. On the other hand $R=0$ corresponds to the case in which the cold wall is at temperature $\bar{T}_m$ so that fluid density decreases monotonically with temperature everywhere in the annulus. In the instance $R=0$ flow in the annulus is similar to the flow of a Boussinesq fluid but only in a qualitative sense since density is a nonlinear function of temperature. When $R=1$ the hot wall is at the maximum density temperature so density increases monotonically with temperature everywhere in the annulus.

Eliminating p between equations (7) and (8) and introducing the vorticity ξ

$$\xi=\frac{\partial v}{\partial r}-\frac{\partial u}{\partial z}$$

and the stream function ψ

$$u=\frac{(K-1)}{(K-1)r+1}\frac{\partial\psi}{\partial z}, \qquad v=-\frac{(K-1)}{(K-1)r+1}\frac{\partial\psi}{\partial r}$$

yields

$$\frac{D\xi}{Dt}-\frac{(K-1)}{(K-1)r+1}u\xi=\frac{\mathrm{Ra}}{\mathrm{Pr}}q\,|\phi-R\,|^{q-2}(\phi-R)\frac{\partial\phi}{\partial r}+\frac{\partial^2\xi}{\partial r^2}+\frac{\partial^2\xi}{\partial z^2}+\frac{(K-1)}{(K-1)r+1}\frac{\partial\xi}{\partial r}-\left[\frac{K-1}{(K-1)r+1}\right]^2\xi \tag{10}$$

with

$$\xi=-\frac{1}{(K-1)r+1}\left(\frac{\partial^2\psi}{\partial r^2}+\frac{\partial^2\psi}{\partial z^2}-\frac{(K-1)}{(K-1)r+1}\frac{\partial\psi}{\partial r}\right) \tag{11}$$

Note that in the case of a vanishingly small annular gap (i.e., vanishingly small curvature effects) $K\to 1$ and the above equations reduce to those appropriate for a cold water-filled rectangular enclosure with differentially heated vertical walls and adiabatic horizontal surfaces (see Lin and Nansteel, 1987). The Nusselt numbers at the inner and outer wall are given by

$$\mathrm{Nu}_i=\frac{q_i'' D}{k(\bar{T}_h-\bar{T}_c)}=-\int_0^A\frac{\partial\phi}{\partial r}(0,z)dz$$

$$\mathrm{Nu}_o=\frac{q_o'' D}{k(\bar{T}_h-\bar{T}_c)}=-\int_0^A\frac{\partial\phi}{\partial r}(1,z)dz$$

Also, since the areas for heat transfer at the outer and inner walls are in the ratio K, under steady conditions,

$$\mathrm{Nu}_i=K\mathrm{Nu}_o \tag{12}$$

Numerical results were obtained by solving equations (9)–(11) subject to the accompanying boundary conditions by a finite difference method. A false-transient approach was used to obtain steady-state solutions. First-order forward differences were used to approximate time derivatives while central difference approximations were used for spatial derivatives. The resulting set of algebraic equations was solved by the Alternating Direction Implicit (ADI) technique, which yields a system of algebraic equations in tridiagonal form to which the Thomas algorithm (Householder, 1979) can be applied. Results for the lowest Rayleigh number considered ($\mathrm{Ra}=10^3$) were obtained from a rest initial condition ($\psi=\xi=u=v=0$, $\phi=1/2$). For higher values of Ra, the steady solution for a somewhat smaller Rayleigh number was used as the initial state. In this way, computation time is minimized and stability criteria are somewhat relaxed. It is also noted that the steady-state solution was found to be independent of the choice of initial condition. For each case (Ra, K, R, A) mesh refinement was continued until adequate pointwise convergence was observed in ψ, ξ, and ϕ, as well as convergence of global heat transfer. The mesh size required for satisfactory convergence was found to be strongly dependent on Ra, as shown in Table 1, for the case $R=1/2$, $K=2$, and $A=1$. All results were obtained with $\mathrm{Pr}=13.0$.

Results and Discussion

Flow Structure. The two most important parameters influencing the structure of the flow in the vertical annulus are the density distribution parameter R and the radius ratio K. First, the effect of R in the absence of curvature ($K=1$) will be briefly discussed. Figure 2 shows contour values of ψ and ϕ for a unit-aspect-ratio annulus in the case $\mathrm{Ra}=10^5$, $K=1$, and

Downloaded 17 Dec 2010 to 193.140.21.150. Redistribution subject to ASME license or copyright; see http://www.asme.org/terms/Terms_Use.cfm

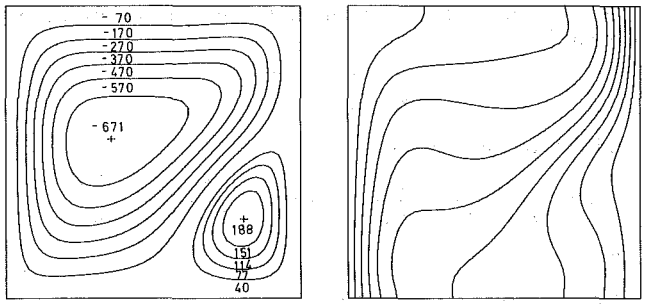

Fig. 2(a) $R = 0.4$

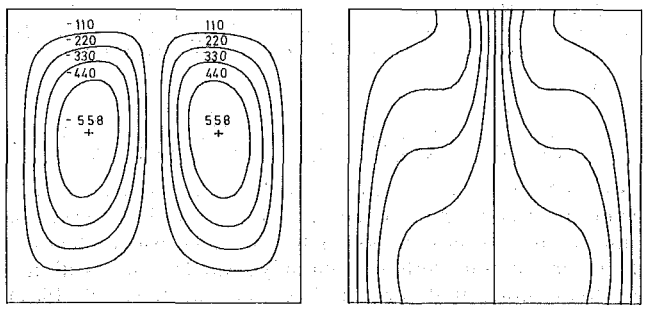

Fig. 2(b) $R = 0.5$

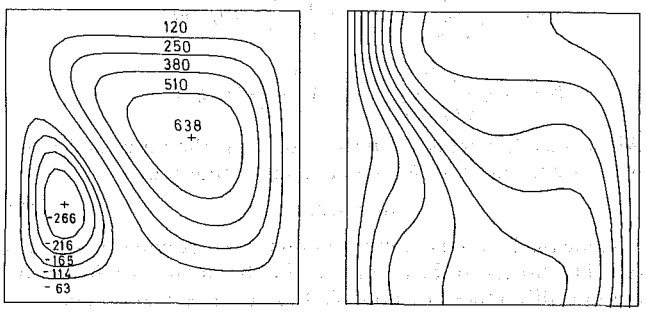

Fig. 2(c) $R = 0.55$

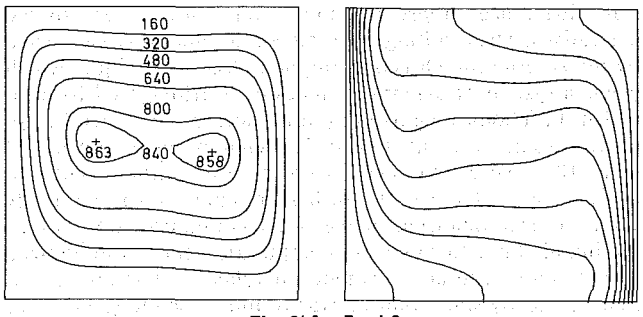

Fig. 2(d) $R = 1.0$

Fig. 2 Stream function ($\psi \times 10^3$) and temperature ($\phi = 0(0.1)1$) contours for the unit-aspect-ratio ($A = 1$) vertical annulus with no curvature, $K = 1$: $Ra = 10^5$

$R = 0.4$, 0.5, 0.55, and 1.0.[1] In Fig. 2(*a*), $R = 0.4$, the two counterrotating cells are separated, roughly, by the maximum density isotherm $\phi = R = 0.4$. In the small counterclockwise rotating cell in the lower right-hand quadrant of Fig. 2(*a*) relatively light fluid ascends adjacent to the cold wall while fluid of maximum density $\bar{T} = \bar{T}_m$, $\phi = R$ falls near the line of demarcation between the two cells. In Fig. 2(*b*), $R = 1/2$, the hot and cold wall temperatures perfectly straddle the extremum temperature; hence, relatively light fluid rises adjacent to the heated and cooled walls, while dense fluid $\rho \simeq \rho_m$,

[1] In Figs. 2-4 the notation $\phi = 0(0.1)1$ indicates that contours of ϕ are plotted for nine equally spaced values of ϕ between zero and unity.

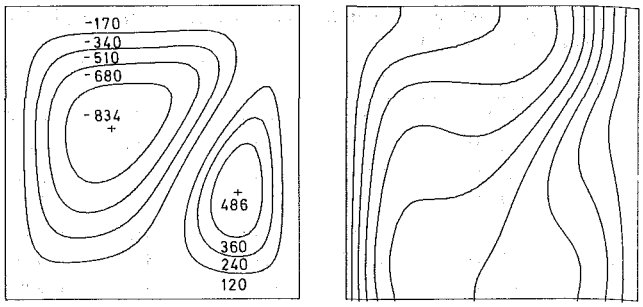

Fig. 3(a) $K = 2$

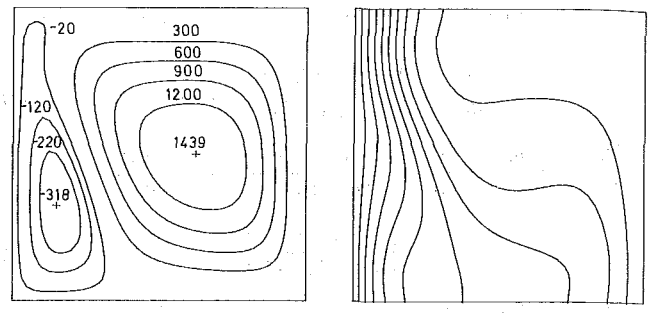

Fig. 3(b) $K = 4$

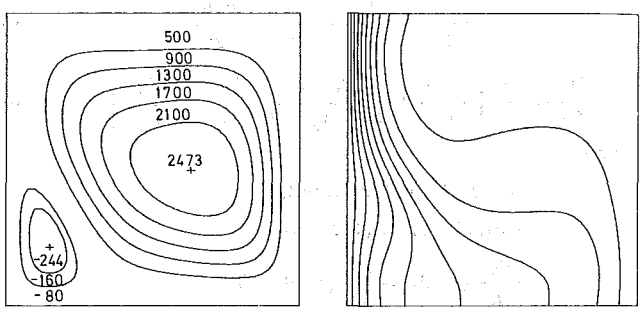

Fig. 3(c) $K = 8$

Fig. 3 Stream function ($\psi \times 10^3$) and temperature ($\phi = 0(0.1)1$) contours for the unit-aspect-ratio annulus: $R = 0.4$, $Ra = 10^5$

$\bar{T} \simeq \bar{T}_m$ falls near the enclosure vertical midplane in a symmetric dual-cell pattern. In Fig. 2(*c*), $R = 0.55$, the counterclockwise rotating cell near the cold wall has grown substantially in size and strength (compared with the case $R = 1/2$) at the expense of the clockwise rotating cell near the hot wall. In the case $R = 1$ (Fig. 2*d*) the maximum density temperature $\bar{T}_m = \bar{T}_h$ so that density increases with temperature everywhere in the enclosure resulting in a single counterclockwise vortex. This flow pattern is qualitatively similar to the convection of a Boussinesq fluid except for the sense of circulation. Evidently the size and orientation of the cell(s) in the enclosure with $K = 1$ (corresponding to a vertical rectangular enclosure) are critically dependent upon the relationship between the wall temperatures and $\bar{T}_m$ (i.e., the parameter $R = (\bar{T}_m - \bar{T}_c)/(\bar{T}_h - \bar{T}_c)$). It has been shown (Lin and Nansteel, 1987) that Ra has a relatively minor influence on the cell structure.

It will be seen that curvature also may have a profound effect on the resulting flow structure in the annulus. Recall that under steady-state conditions conservation of energy requires the average heat flux at the inner wall to be a factor K times the average flux at the outer wall (equation (12)). This is due to the smaller area available for heat transfer at the inner wall. As a result, with increasing K, isotherms will become increas-

Downloaded 17 Dec 2010 to 193.140.21.150. Redistribution subject to ASME license or copyright; see http://www.asme.org/terms/Terms_Use.cfm

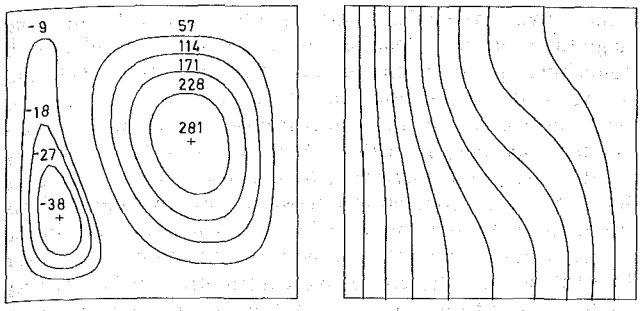

Fig. 4(a) $A = 1$

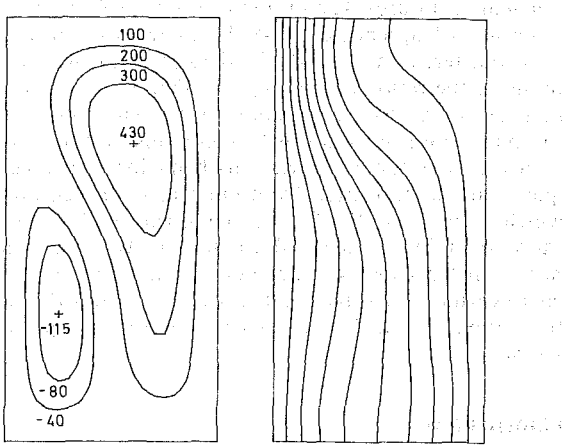

Fig. 4(b) $A = 2$

ingly crowded near the inner cylinder. The resulting effect on the ψ and ϕ fields is shown in Fig. 3 again for $A = 1$ for the case $R = 0.4$, $\mathrm{Ra} = 10^5$. Note that increasing curvature (K) tends to shift isotherms (including the maximum density isotherm) toward the inner cylinder. As maximum density fluid shifts toward the inner cylinder so does the line of demarcation between the outer counterclockwise-rotating cell and the inner clockwise-rotating cell. Hence for fixed wall temperature (fixed R) the outer cell strengthens and the inner cell weakens with increasing curvature of the annulus. Note (Figs. 2 and 3) that increasing the curvature from $K = 1$ to $K = 8$ has resulted in a complete reversal in the relative size of the two cells. Also, from Fig. 3, fluid in the upper portion of the annulus is becoming more nearly isothermal ($\bar{T} \simeq \bar{T}_c$) as K increases. In general, it is observed that increasing curvature increases the size and strength of the outer cell.

Figure 4 shows contours of ψ and ϕ for tall enclosures ($A \geq 1$) for the case $K = 2$, $R = 1/2$, and $\mathrm{Ra} = 10^4$. Note that increasing aspect ratio tends to increase the convective intensity of the large outer cell. This is because the quenching effect of the unheated horizontal surfaces becomes less as A is increased. Also, the temperature field becomes dominated by conduction over much of the vertical span of the annulus when $A \geq 4$ (Fig. 4). Only near the top of the annulus where the counterclockwise outer cell sweeps cool fluid from the outer wall onto the heated inner wall does the contribution of convection become significant. A similar phenomenon is not observed near the bottom of the annular space since the dual-cell structure there precludes contact of the inner cell with the outer, cooled wall. The flow structure in the central portion (i.e., away from the horizontal end walls) of the vertical annulus with $A = 8$ is already reasonably well approximated by the flow in an infinitely tall ($A \to \infty$) annulus. An expression for the vertical velocity in an infinitely tall annulus is given in Appendix A. Figure 5 shows vertical velocity profiles at the annulus midheight, $z = A/2$, for $\mathrm{Ra} = 10^4$, $R = 1/2$, and $A = 2$,

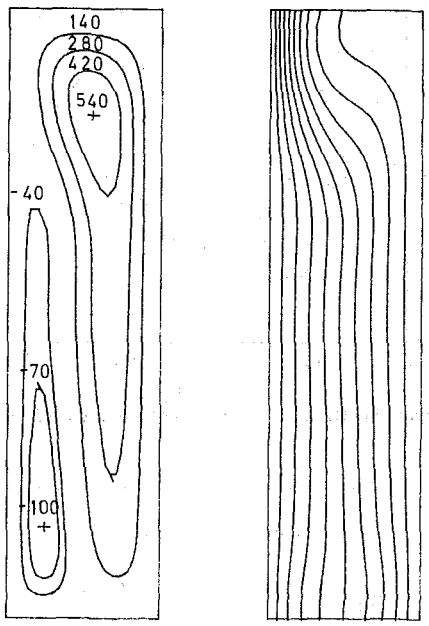

Fig. 4(c) $A = 4$

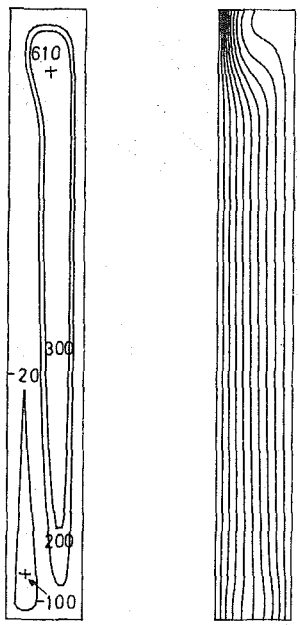

Fig. 4(d) $A = 8$

Fig. 4 Stream function ($\psi \times 10^3$) and temperature ($\phi = 0(0.1)1$) contours for tall annuli: $R = 0.5$, $K = 2$, $\mathrm{Ra} = 10^4$

4, 8, and ∞. For $R = 1/2$ the finite aspect ratio results approach the $A \to \infty$ results quite rapidly with increasing A. This is probably due to the dual-cell structure which makes the "apparent" aspect ratio of each of the cells larger than if a single cell occupied the annulus.

Heat Transfer. The variation of heat transfer at the inner wall, Nu_i, with K for $R = 0.4$, $A = 1$, and $10^3 \leq \mathrm{Ra} \leq 10^5$ is shown in Fig. 6. Recall (Fig. 3) that $R = 0.4$ leads to a transition from inner to outer cell dominance as curvature of the annulus is increased. This transition occurs in the range $2 \lesssim K \lesssim 5$ for $10^3 \leq \mathrm{Ra} \leq 10^5$. Hence in this approximate range there is a smooth transition from a circumstance in which the inner (clockwise-rotating) cell wets both walls of the annulus to one

Downloaded 17 Dec 2010 to 193.140.21.150. Redistribution subject to ASME license or copyright; see http://www.asme.org/terms/Terms_Use.cfm

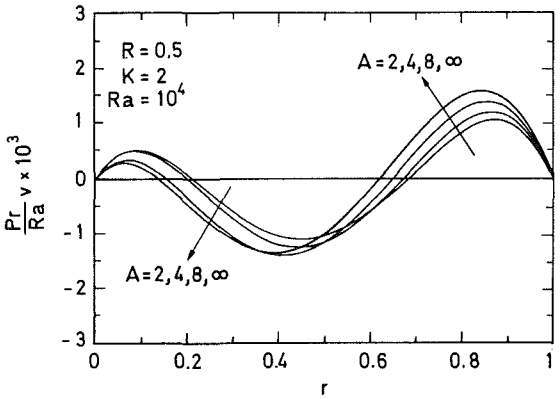

Fig. 5 Vertical velocity at the annulus midheight ($z = A/2$): $R = 0.5$, $K = 2$, $Ra = 10^4$

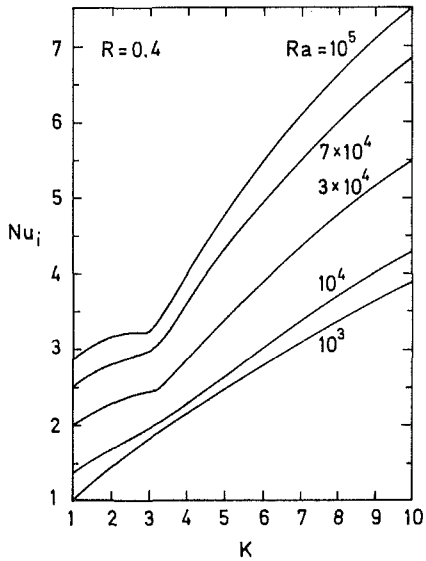

Fig. 6 Heat transfer at the inner wall, Nu_i: $R = 0.4$, $A = 1$

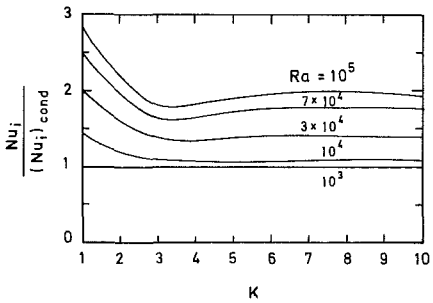

Fig. 7 Heat transfer at the inner wall relative to conduction, $Nu_i/(Nu_i)_{cond}$: $R = 0.4$, $A = 1$

in which the outer (counterclockwise-rotating) cell wets both walls. Over much of this range of K then, the cells are of roughly equal strength and the inner cell is effectively insulated from the outer wall by the outer cell and vice versa. This in turn leads to a diminished rate of convective heat transfer from the inner to the outer wall. In Fig. 6 this results not in a minimum heat transfer rate near $K = 3.5$ but only a minimum rate of increase of Nu_i with K since conduction heat transfer increases quite rapidly with increasing K. It is easily shown that

$$(Nu_i)_{cond} = \frac{K-1}{\log(K)} \tag{13}$$

Hence two mechanisms are involved in affecting the magnitude of Nu_i. One is curvature which results in a "bunching-up" of isotherms near the inner (hot) wall and always tends to increase Nu_i as K increases. The second mechanism is due to the configuration of the two counterrotating cells changing with K. As the two cells become nearly equal in size, with increasing K, convective heat transfer is diminished. The competition between these two mechanisms results in the locally diminished heat transfer rate seen in the curves of Fig. 6. Note that no point of inflection appears for $Ra = 10^3$ because the convective contribution to Nu_i is very small. As seen from equation (13) the conduction component of Nu_i is in general not unity as it is in the case $K = 1$ (rectangular enclosure). Therefore the heat transfer representation in terms of Nu_i tends to mask the contribution of convective heat transfer. Consequently the data of Fig. 6 are replotted in terms of the ratio $Nu_i/(Nu_i)_{cond}$ in Fig. 7. This figure shows that the convective contribution to the heat transfer (relative to conduction) decreases with increasing K for $K \lesssim 3.5$ and then increases for larger K. This behavior is a direct consequence of the transition from inner to outer cell dominance which occurs near $K = 3.5$. For large values of K (Fig. 7) the ratio $Nu_i/(Nu_i)_{cond}$ again decreases slowly since conduction heat transfer grows without bound (equation (13)) as K increases while convective heat transfer is bounded. Hence, all the curves in Fig. 7 will approach unity asymptotically as $K \to \infty$.

Conclusions

The steady natural convection of cold water in a vertical annulus has been studied. It is found that density inversion phenomena are altered substantially by curvature of the annulus. It is the combination of the inversion parameter R and the curvature K which ultimately gives rise to a particular steady flow structure in the annulus. A transition from inner to outer convective cell dominance can be effected by either increasing R (shifting the extremum temperature toward $\bar{T}_h$) or by increasing the curvature K of the annulus. When this transition takes place a decrease in convective heat transfer occurs since each of the two counterrotating cells is effectively isolated from the opposite wall. An expression for the vertical velocity in an infinitely tall vertical annulus has been shown to yield a good approximation to the flow in finite ($A \gtrsim 8$) annuli away from the horizontal end walls when $R = 1/2$.

Acknowledgments

The authors wish to thank Professor B. Gebhart for his invaluable advice during the course of this work.

References

Bhushan, R., Keyhani, M., Christensen, R. N., and Kulacki, F. A., 1983, "Correlation Equations for Free Convection in a Vertical Annulus With Constant Heat Flux on the Inner Wall," ASME JOURNAL OF HEAT TRANSFER, Vol. 105, pp. 910-912.

Blake, K. R., Bejan, A., and Poulikakos, D., 1984, "Natural Convection Near 4°C in a Water Saturated Porous Layer Heated From Below," *Int. J. Heat Mass Transfer*, Vol. 27, pp. 2355-2364.

Chen, C. T., and Millero, F. J., 1976, "The Specific Volume of Sea Water at High Pressures," *Deep Sea Res.*, Vol. 23, pp. 595-612.

Desai, V. S., and Forbes, R. E., 1971, "Free Convection in Water in the Vicinity of Maximum Density," *Environ. Geophys. Heat Transfer*, pp. 41-47.

de Vahl Davis, G., and Thomas, R. W., 1969, "Natural Convection Between Concentric Vertical Cylinders, High Speed Computing in Fluid Dynamics," *Physics of Fluids*, Supplement II, pp. 198-207.

Forbes, R. E., and Cooper, J. W., 1975, "Natural Convection in a Horizontal Layer of Water Cooled From Above to Near Freezing," ASME JOURNAL OF HEAT TRANSFER, Vol. 97, pp. 47-53.

Gebhart, B., and Mollendorf, J. C., 1977, "A New Density Relation for Pure and Saline Water," *Deep Sea Res.*, Vol. 24, pp. 831-848.

Gebhart, B., and Mollendorf, J. C., 1978, "Buoyancy Induced Flows in a

Downloaded 17 Dec 2010 to 193.140.21.150. Redistribution subject to ASME license or copyright; see http://www.asme.org/terms/Terms_Use.cfm

Liquid Under Conditions in Which Density Extrema May Arise," *J. Fluid Mech.*, Vol. 89, pp. 673-707.

Grant, J., 1968, "The Liquid State Densities of Metals, Alloys and Intermetallic Compounds," Ph.D. Thesis, Syracuse University, Syracuse, NY.

Hanzawa, T., and Kato, K., 1984, "Heat Transfer by Natural Convection Between Vertical, Enclosed, Concentric Cylinders With the Inner Cylinder Heated Locally," *Int. Chem. Engng.*, Vol. 24, pp. 696-701.

Householder, A. S., 1979, *The Theory of Matrices in Numerical Analysis*, Blaisdell, New York.

Inaba, H., and Fukuda, T., 1984a, "An Experimental Study of Natural Convection in an Inclined Rectangular Cavity Filled With Water at Its Density Extremum," ASME JOURNAL OF HEAT TRANSFER, Vol. 106, pp. 109-115.

Inaba, H., and Fukuda, T., 1984b, "Natural Convection in an Inclined Square Cavity in Regions of Density Inversion of Water," *J. Fluid Mech.*, Vol. 142, pp. 363-381.

Kell, G. S., 1967, "Precise Representation of Volume Properties of Water at One Atmosphere," *J. Chem. Engng. Data*, Vol. 12, pp. 66-69.

Keyhani, M., Kulacki, F. A., and Christensen, R. N., 1983, "Free Convection in a Vertical Annulus With Constant Heat Flux on the Inner Wall," ASME JOURNAL OF HEAT TRANSFER, Vol. 105, pp. 454-459.

Lankford, K. E., and Bejan, A., 1986, "Natural Convection in a Vertical Enclosure Filled With Water Near 4°C," ASME JOURNAL OF HEAT TRANSFER, Vol. 108, pp. 755-763.

Lee, Y., Korpela, S. A., and Horne, R. N., 1982, "Structure of Multicellular Natural Convection in a Tall Vertical Annulus," *Proceedings of the 7th International Heat Transfer Conference*, Munich.

Lin, D. S., and Nansteel, M. W., 1987, "Natural Convection Heat Transfer in a Square Enclosure Containing Water Near Its Density Maximum," *Int. J. Heat and Mass Transfer*, to appear.

Nansteel, M. W., Medjani, K., and Lin, D. S., 1987, "Natural Convection of Water Near Its Density Maximum in a Rectangular Enclosure: Low Rayleigh Number Calculations," *Physics of Fluids*, Vol. 30, No. 2, pp. 312-317.

Nguyen, T. Hung, Vasseur, P., and Robillard, L., 1982, "Natural Convection Between Horizontal Concentric Cylinders With Density Inversion of Water for Low Rayleigh Number," *Int. J. Heat Mass Transfer*, Vol. 25, pp. 1559-1568.

Poulikakos, D., 1984, "Maximum Density Effects on Natural Convection in a Porous Layer Differentially Heated in the Horizontal Direction," *Int. J. Heat Mass Transfer*, Vol. 27, pp. 2067-2075.

Prasad, V., and Kulacki, F. A., 1985, "Free Convective Heat Transfer in a Liquid-Filled Vertical Annulus," ASME JOURNAL OF HEAT TRANSFER, Vol. 107, pp. 596-602.

Robillard, L., and Vasseur, P., 1981, "Transient Natural Convection Heat Transfer of Water With Maximum Density Effect and Supercooling," ASME JOURNAL OF HEAT TRANSFER, Vol. 103, pp. 528-534.

Robillard, L., and Vasseur, P., 1982, "Convective Response of a Mass of Water Near 4°C to a Constant Cooling Rate Applied on its Boundaries," *J. Fluid Mech.*, Vol. 118, pp. 123-141.

Schwab, T. H., and DeWitt, K. J., 1970, "Numerical Investigation of Free Convection Between Two Vertical Coaxial Cylinders," *AIChE J.*, Vol. 16, pp. 1005-1010.

Seki, N., Fukusako, S., and Nakaoka, M., 1975, "Experimental Study on Natural Convection Heat Transfer With Density Inversion of Water Between Horizontal Concentric Cylinders," ASME JOURNAL OF HEAT TRANSFER, Vol. 97, pp. 555-561.

Seki, N., Fukusako, S., and Inaba, H., 1978, "Free Convective Heat Transfer With Density Inversion in a Confined Rectangular Vessel," *Wärme- und Stoffübertragung*, Vol. 11, pp. 145-156.

Shaaban, A. H., and Özisik, M. N., 1982, "Effect of Curvature on the Thermal Stability of a Fluid Between Two Long Vertical Coaxial Cylinders," *Proceedings of the 7th International Heat Transfer Conference*, Munich.

Thomas, R. W., and de Vahl Davis, G., 1970, "Natural Convection in Annular and Rectangular Cavities – A Numerical Study," *Proceedings of the 4th International Heat Transfer Conference*, Amsterdam.

Vasseur, P., and Robillard, L., 1980, "Transient Natural Convection Heat Transfer in a Mass of Water Cooled Through 4°C," *Int. J. Heat Mass Transfer*, Vol. 23, pp. 1195-1205.

Watson, A., 1972, "The Effect of Inversion Temperature on the Convection of Water in an Enclosed Rectangular Cavity," *Q. J. Mech. Appl. Math.*, Vol. 25, pp. 423-446.

APPENDIX A

The flow in an infinitely tall annulus ($A \to \infty$) is purely vertical, i.e., $u \equiv 0$, $v = v(r)$. From equations (7) and (8) then, $\partial p/\partial z = \text{const}$, hence equation (8) becomes

$$\frac{d^2v}{dr^2} + \frac{K-1}{(K-1)r+1}\frac{dv}{dr} = -\frac{\text{Ra}}{\text{Pr}}|\phi - R|^q + C$$

where the constant

$$C \equiv -\frac{\partial p}{\partial z} + \frac{\text{Ra}}{\text{Pr}}|-R|^q$$

Using

$$\phi = 1 - \frac{\log(r(K-1)+1)}{\log K}$$

and the mass conservation condition

$$\int_0^1 v\,dr = 0$$

the velocity distribution in the annulus becomes

$$\frac{\text{Pr}}{\text{Ra}}v(r) = B(r) - \frac{B(1)}{\log K}\log((K-1)r+1) + C^*\left[\frac{r^2}{4} + \frac{r}{2(K-1)} - \frac{1}{2(K-1)^2}\log((K-1)r+1) - J\frac{\log((K-1)r+1)}{\log K}\right]$$

where

$$C^* = \left[\frac{K(\log K - 1)+1}{(K-1)\log K}B(1) - \int_0^1 B(r)\,dr\right]\Big/\left[\frac{1}{12} + \frac{1}{4(K-1)} - \frac{K(\log K-1)+1}{2(K-1)^3} - \frac{K(\log K-1)+1}{(K-1)\log K}J\right]$$

$$J = \frac{1}{4} + \frac{1}{2(K-1)} - \frac{1}{2(K-1)^2}\log K$$

$$B(r) = \begin{cases} \dfrac{-\tau_1}{2(K-1)}\displaystyle\sum_{k=0}^{\infty}(-1)^k\frac{(2\log K)^{q+k+2}}{(q+k+1)(q+k+2)k!} \\ \left[1 - R - \dfrac{\log((K-1)r+1)}{\log K}\right]^{q+k+2} + \dfrac{\tau_1\tau_3}{2(K-1)} \\ -\dfrac{\tau_1\tau_2}{(K-1)}\log((K-1)r+1), \qquad r \le \dfrac{K^{1-R}-1}{K-1} \\ \dfrac{\tau_1\tau_3}{2(K-1)} - \dfrac{\tau_1\tau_2}{(K-1)}\log((K-1)r+1) - \dfrac{\tau_1}{2(K-1)} \\ \displaystyle\sum_{k=0}^{\infty}\frac{(2\log K)^{q+k+2}}{(q+k+1)(q+k+2)k!}\left[R-1 + \frac{\log((K-1)r+1)}{\log K}\right]^{q+k+2}, \qquad r > \dfrac{K^{1-R}-1}{K-1} \end{cases}$$

$$\tau_1 = -\frac{K^{2(1-R)}}{(K-1)2^{q+1}(\log K)^q}$$

$$\tau_2 = \sum_{k=0}^{\infty}(-1)^k\frac{(2(1-R)\log K)^{q+k+1}}{(q+k+1)k!}$$

$$\tau_3 = \sum_{k=0}^{\infty}(-1)^k\frac{[2(1-R)\log K]^{q+k+2}}{(q+k+1)(q+k+2)k!}$$

Downloaded 17 Dec 2010 to 193.140.21.150. Redistribution subject to ASME license or copyright; see http://www.asme.org/terms/Terms_Use.cfm

Prediction of the Natural Convective Heat Transfer From a Horizontal Heated Disk

S. B. Robinson

J. A. Liburdy

Thermal Fluids Laboratory,
Department of Mechanical Engineering,
Clemson University,
Clemson, SC 29631

A thin-layer approximation is applied to the laminar momentum and energy equations governing the natural convection above an isothermal heated disk in air. Using the Boussinesq assumption the equations are nondimensionalized in terms of a stream function, pressure and temperature difference. The variables are expanded in a series solution and the resulting set of equations are solved numerically. The solution is cast in terms of the nondimensional radial position and the disk Grashof number. These two parameters are shown to define the outer boundary conditions which are uniquely determined from a point source solution. The outer velocity boundary condition is shown to decrease in relative magnitude as the disk Rayleigh number increases. Beyond a Rayleigh number of approximately 10^6 the outer flow may be ignored in calculating the disk heat transfer rate. The radial variation of the outer flow is to the $-1/5$ power measured inward from the leading edge. This is a result of the scaling difference of the thin layer flow, and the outer, plume entrainment flow. The local heat transfer rate is increased by including the entrainment effects on the outer flow and varies as the Grashof number to the power $(1/5-\epsilon)$, where ϵ is a decreasing function of inward radial distance.

Introduction

Natural convective heat transfer from a finite-size, horizontal disk is complicated by the interaction of entrained flow along the disk with the separated flow from the surface. Two important parameters that affect the structure are the geometry and an appropriately defined Grashof number. Limits can be identified as (*i*) a point heat source which releases thermal energy in the form of an axisymmetric plume, and (*ii*) a large horizontal disk which, in the limit, neglects the radial geometry over a large portion of the disk and assumes that the central region, where flow separation occurs, is of minor importance to the heat transfer.

The first limit has been analytically and numerically solved, in terms of similarity variables, by Yih (1951) and Fujii (1963). The results show a (-1) power law dependence on the temperature decay with elevation. Also, the similarity transformation indicate a (1/4) power law dependence of the plume width on the source Grashof number. This Grashof number is defined in terms of a steady heat release rate and elevation above the heat source. The plume width decreases (at a given elevation) with increased source strength.

The second limit, that of a very large disk, is fundamentally quite different from the first. The radial geometry effects become insignificant except near the disk center; this could then be treated similarly to a semi-infinite heated flat plate. Analyses by Stewartson (1958), Rotem and Claassen (1969), and several others indicate scaling for the Boussinesq form of the governing equations for a flat plate. The appropriate stretching of the y coordinate (upward normal to a heated disk, downward normal to a cooled disk) is proportional to $\mathrm{Gr}_l^{-1/5}$. Here, Gr_l is the Grashof number based on an appropriate length scale l for the boundary layer development. An upper bound on l, measured from the disk edge inward in the primary flow direction, represents a measure of the extent of validity of the boundary layer analysis. This critical value of the length scale is inherently dependent on the relationship between the local buoyancy force and resulting pressure gradient driving the flow.

The present problem, that of a finite-size heated surface, addresses the development of the inward, entrained flow, taking into account the existence of flow separation. Zakerullah and Ackroyd (1979) use a series expansion solution to solve the nearly parallel flow equations. They treat the radial effects as a perturbation on the governing equations, thus being valid near the edge of the disk. Variable property effects are included but their predicted heat transfer rates are less than the experimentally determined overall heat transfer rates found in the literature. In an earlier paper Ackroyd (1976) suggests the order of the error when using first-order boundary layer approximations. Merkin (1985, 1983) extends the previous analyses for a uniformly heated surface and an isothermal heated surface. In both of these studies Merkin obtains a solution near the disk center where he shows the existence of a thin viscous region below an inviscid region. All of these analyses assume that the nearly parallel flow condition, which neglects normal stress components and axial diffusion, is valid very near the disk center. Additionally, the outer boundary conditions neglect the effects of entrainment by the plume that exists near the disk center.

The overall agreement between analyses and experimental results for natural convective heat transfer above horizontal disks is fair, at best. Suggested reasons for this lack of agreement are (*i*) the assumption that the proper value of l is significantly less than the disk radius in the governing equations, (*ii*) the neglect of the importance of entrainment by the separated flow on the thin layer, and (*iii*) the application of the boundary layer analysis over the entire disk surface to determine the overall heat transfer rate. There is a lack of experimental data available to determine the effects of disk size, Grashof and Prandtl numbers, and reference temperature difference conditions. Detailed temperature profiles do not exist which would substantiate the extent of validity of the boundary layer analysis and identify the appropriate relationship between the length scale l and the heat transfer parameters.

This paper addresses the natural convection of air above a horizontal, heated disk, facing upward. This includes the development of the disk boundary layer and proper scaling of the entrainment flow relative to the disk boundary layer. The flow and temperature fields near the disk can be segmented into two domains as shown in Fig. 1. The heat transfer

Contributed by the Heat Transfer Division for publication in the JOURNAL OF HEAT TRANSFER. Manuscript received by the Heat Transfer Division March 4, 1986.

Copyright © 1987 by ASME

Downloaded 17 Dec 2010 to 193.140.21.150. Redistribution subject to ASME license or copyright; see http://www.asme.org/terms/Terms_Use.cfm

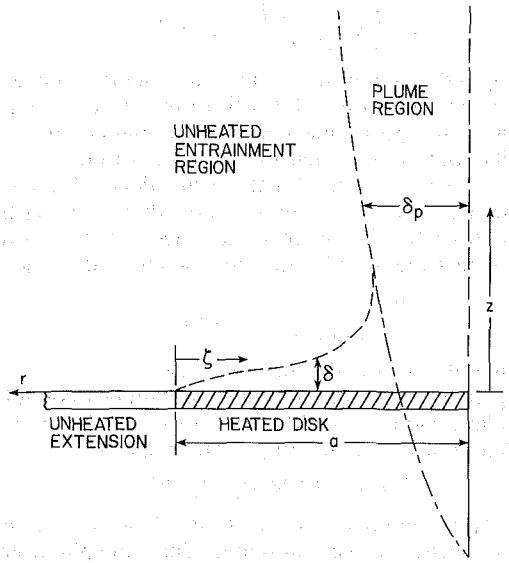

Fig. 1 Flow geometry and coordinate system; note that the z axis is a line of symmetry

mechanism is assumed to occur over a sufficiently large disk surface such that a boundary layer can develop prior to separation. The separation may result from either the collision of radially inward flow occurring near the center of the disk, or a sufficiently large local buoyancy force which overcomes the radial momentum resulting in separation prior to the center portion of the disk.

We put forth in this paper a method to determine boundary conditions for the solution of the thin layer region and thus better predict the local heat transfer rate from the disk surface. The analysis assumes a point source plume behavior of the central upward flow from the disk. This assumption is supported by experimental evidence. Results of the predicted local heat transfer rate from the disk are presented, and compared to previously published experimental results.

Mathematical Model

The convective heat transfer from the heated surface is assumed to be a result of the radially inward heated flow, which results in a central plume as shown in Fig. 1.

The analysis is limited to a region on the disk surface which has not experienced flow separation. If we assume that the local buoyancy force is not sufficient to cause separation then the flow has a thin layer developing inward along the surface. Near the center of the disk the flow must separate to form a plume. If undisturbed, the plume will be a steady flow whose energy transport rate is equal to the heat transfer rate from the disk surface. The outer edge of the thin layer is defined as the point vertically above the surface where the temperature has decayed to the ambient value and the shear stress is zero. At some radial location near the center of the disk the boundary layer approximations break down and there is the transition to the plume.

The strength of the central plume depends on the buoyancy forces generated by the relative disk temperature. If the heating rate is very high the local buoyancy forces may be large, causing flow separation from the surface. This condition will not result in plume development as previously described, but will rather cause bursting of heated fluid from the surface. This has been documented by Yousef et al. (1982) for square surfaces, and Liburdy et al. (1987) for a heated disk. In this latter case, only a very small region near the edge of the disk may adhere to the thin-layer approximations.

The governing equations for the thin layer, using the Boussinesq approximation, are

$$\frac{\partial(ru_z)}{\partial z}+\frac{\partial(ru_r)}{\partial r}=0 \tag{1a}$$

$$\frac{\partial P}{\partial z}=(\rho-\rho_\infty)g \tag{1b}$$

$$u_z\frac{\partial u_r}{\partial z}+u_r\frac{\partial u_r}{\partial r}=-\frac{1}{\rho}\frac{\partial P}{\partial r}+\nu\frac{\partial^2 u_r}{\partial r^2} \tag{1c}$$

$$\rho C_p\left(u_z\frac{\partial T}{\partial z}+u_r\frac{\partial T}{\partial r}\right)=k\frac{\partial^2 T}{\partial r^2} \tag{1d}$$

These equations are nondimensionalized based on the following definitions:

$$\zeta=\left(1-\frac{r}{a}\right) \tag{2a}$$

$$\eta=\mathrm{Gr}_a^{1/5}\frac{z}{a}\zeta^{-2/5} \tag{2b}$$

$$F(\zeta,\eta)=\frac{\psi}{\nu a\rho_\infty}\mathrm{Gr}_a^{-1/5}\zeta^{-3/5} \tag{2c}$$

Nomenclature

a = disk radius
C_p = specific heat at constant pressure
f = similarity variable, stream function for the point source plume
F = similarity variable, stream function for the thin layer region
G = similarity variable, pressure function for the thin layer region
g = acceleration of gravity, positive downward
Gr_a = Grashof number based on risk radius
Gr_d = Grashof number based on disk diameter
k = thermal conductivity
Nu_d = Nusselt number based on disk diameter
P = perturbation pressure
Pr = Prandtl number
Q_p = heat source strength
Ra = Rayleigh number
r = radial coordinate
T = temperature
T_c = centerline temperature
T_s = disk surface temperature
T_∞ = ambient temperature
u_r = velocity in the r direction
u_z = velocity in the z direction
z = vertical coordinate
z_0 = location of the virtual origin relative to the disk elevation
β = coefficient of thermal expansion
ζ = dimensionless distance from the disk edge toward the center
η = independent pseudosimilarity variable for the thin layer region
θ = similarity variable, temperature for the thin layer region
θ_c = nondimensional centerline temperature
ν = kinematic viscosity
ξ = similarity variable for the point source plume
ρ = density
ρ_∞ = density of the ambient fluid
ψ = stream function

Downloaded 17 Dec 2010 to 193.140.21.150. Redistribution subject to ASME license or copyright; see http://www.asme.org/terms/Terms_Use.cfm

$$G(\zeta, \eta) = \frac{aP}{\nu^2 \rho_\infty} \mathrm{Gr}_a^{-4/5} \zeta^{-2/5} \tag{2d}$$

$$\theta(\zeta, \eta) = \frac{T - T_\infty}{T_s - T_\infty} \tag{2e}$$

where T_s is the disk surface temperature and Gr_a is defined as

$$\mathrm{Gr}_a = \frac{g\beta(T_s - T_\infty)a^3}{\nu^2} \tag{3}$$

The stream function ψ for the thin layer is defined by

$$\frac{\partial \psi}{\partial z} = \rho r u_r \tag{4a}$$

$$\frac{\partial \psi}{\partial r} = -\rho r u_z \tag{4b}$$

Based on the above, the horizontal and vertical velocity components become

$$\frac{u_r r}{\nu} = \frac{\rho_\infty}{\rho} F'(\zeta, \eta) \mathrm{Gr}_a^{2/5} \zeta^{1/5} \tag{5a}$$

and

$$\frac{u_z r^2}{z\nu} = \frac{2}{5} \frac{\rho_\infty}{\rho} F'(\zeta, \eta) \mathrm{Gr}_a^{2/5} \zeta^{1/5} \tag{5b}$$

where a prime denotes differentiation with respect to η. The resulting governing equations for conservation of radial momentum, vertical momentum, and thermal energy are

$$(1-\zeta)^2 F''' + (1-\zeta)\left(\frac{3}{5} FF'' - \frac{1}{5} F'^2\right) - \frac{2}{5}(1-\zeta)^3 \cdot \left[G + \frac{\zeta}{2} \frac{\partial G}{\partial \zeta} + \frac{5a}{2} \zeta \frac{\partial \eta}{\partial r} G'\right] = \zeta(1-\zeta)\left(F' \frac{\partial F'}{\partial \zeta} - F'' \frac{\partial F}{\partial \zeta}\right) + \zeta F'^2 \tag{6a}$$

$$G'(\zeta, \eta) = 0 \tag{6b}$$

$$\frac{1}{\mathrm{Pr}}(1-\zeta)\theta'' + \frac{3}{5} F\theta' = \zeta\left(F' \frac{\partial \theta}{\partial \zeta} - \theta' \frac{\partial F}{\partial \zeta}\right) \tag{6c}$$

The boundary conditions, expressed in nondimensional form, are a result of the no-slip velocity condition, the isothermal surface temperature, the ambient temperature and pressure, and the plume entrainment. The first three conditions result in

$$F(\zeta, 0) = F'/\zeta(\zeta, 0) = \theta(\zeta, \infty) = G(\zeta, \infty) = 0, \quad \theta(\zeta, 0) = 1 \tag{7}$$

By definition the thin layer extends from the disk surface to the height where the temperature decays to T_∞. The entrainment velocity is used to specify the boundary condition for F' at the edge of the thin layer $F'(\infty)$. The plume-like behavior near the disk center establishes an entrainment condition which influences the thin-layer flow over the outer portion of the disk. Since the region above the thermal boundary layer is driven by the plume entrainment it is a nonheated, essentially inviscid, flow. An expression for the entrainment can be determined by assuming a virtual origin for the plume. The resulting horizontal velocity component can be expressed in terms of a nondimensional stream function, $f = \psi/\nu z$, that is valid in the region radially beyond the thermal plume. The entrainment velocity for the point source plume is (see Fujii, 1963)

$$\left.\frac{u_r r}{\nu}\right|_{\text{limit } \xi \to \infty} = -\xi\left(\frac{f}{\xi} - \frac{f'}{2}\right) \tag{8}$$

Here f is the dependent similarity variable, a function of ξ which is defined as

$$\xi = \left[\frac{g\beta Z^2 Q_p}{2\pi\rho C_p \nu^3}\right]^{1/4} \left(\frac{r}{z}\right) \tag{9}$$

where Q_p is the total heat transfer rate from the source and f' represents the derivative of f with respect to ξ. A numerical solution of the governing point source plume equations in similarity form was carried out using a fifth-order Hamner predictor-corrector method with results identical to those obtained by Fuji (1963). Our results show that the outer boundary conditions for the plume are satisfied to within $\pm 10^{-4}$ at $\xi = 10$. Thus equation (8) can safely be reduced to the form

$$\left.\frac{u_r r}{\nu}\right|_{\text{limit } \xi \to \infty} = -f(\infty) \tag{10}$$

The value of $f(\infty)$ for $\mathrm{Pr} = 0.72$ is 7.528.

Using these results, the entrainment boundary condition for the thin layer along the disk surface for F' can be specified independently of the plume origin. The result is

$$F'(\infty) = 7.528 \mathrm{Gr}_a^{-2/5} \zeta^{-1/5} \tag{11}$$

where $F'(\infty)$ represents the value of F' outside of the thin layer and outside the central plume. Since the plume entrainment velocity varies as r^{-1} to satisfy the continuity relationship, then $F'(\infty)$ varies as $r^{-1/5}$. The dependence of $F'(\infty)$ on Gr_a is a result of the velocity scaling and is consistent with the scaling for a semi-infinite heated surface (Rotem and Claassen, 1969).

The governing equations (6) with boundary conditions (7) and (11) for the thin layer were solved assuming a series expansion for ζ similar to the procedure used by Zakerullah and Ackroyd (1979). The approach is valid for small values of ζ and has the following form:

$$V(\eta, \zeta) = \sum_{n=0}^{\infty} \zeta^n V_n(\eta) \tag{12}$$

where V represents any dependent variable and $V_n(\eta)$ is the nth-order expansion term, which is only a function of η. The values of V_n are obtained by solving the system of equations for the zero through n order equations consecutively.

The disk heat transfer is evaluated from the local surface temperature gradient. In nondimensional form the local convective coefficient h is

$$\left(\frac{2ah}{k\Delta t}\right)_{\text{local}} = -2\zeta^{-2/5} \mathrm{Gr}_a^{1/5} \sum_{n=0}^{\infty} \zeta^n \theta_n'(0) \tag{13}$$

For comparison, the average Nusselt number based on the disk diameter, assuming $F'(\infty) = 0$, is

$$\overline{\mathrm{Nu}}_d = -2.749 \mathrm{Gr}_d^{1/5} \sum_{n=0}^{\infty} \theta_n'(0) \tag{14}$$

where $-\theta_0'(0) = 0.3573$.

The numerical solution of equations (6) requires specifying $F''(0)$, $\theta'(0)$, and $G(0)$, which are initially unknown. An iterative multivariate search was developed which simultaneously updates iterative initial values. This scheme is based on maximizing the total rate of convergence using a gradient vector formed from the partial derivatives of the unknown initial conditions with the outer boundary values for $F'(\infty)$, $\theta(\infty)$, and $G(\infty)$. Solutions were determined satisfying a least-squares error of the outer boundary conditions. Details are provided by Liburdy and Robinson (1985).

Experimental Procedure and Results

An experimental apparatus was designed and tests performed to determine whether or not the thermal structure above the heated surface is as described in the mathematical model. A schematic of the test apparatus is shown in Fig. 2. The apparatus consisted of a 50.8-mm-dia copper disk heated from below, an insulation and support assembly, and a

Downloaded 17 Dec 2010 to 193.140.21.150. Redistribution subject to ASME license or copyright; see http://www.asme.org/terms/Terms_Use.cfm

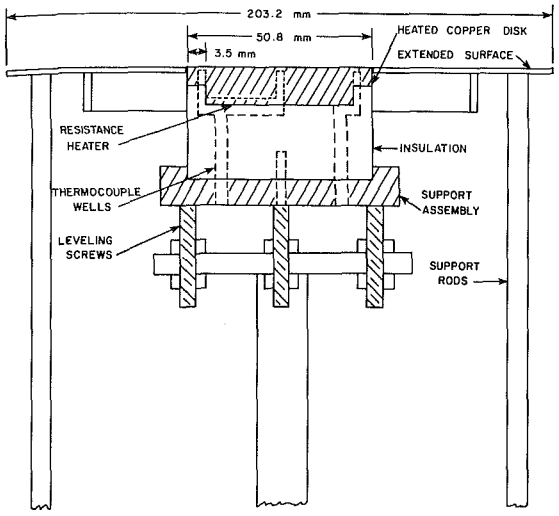

Fig. 2 Schematic of the heat transfer apparatus, which was supported on an isolation vibration table

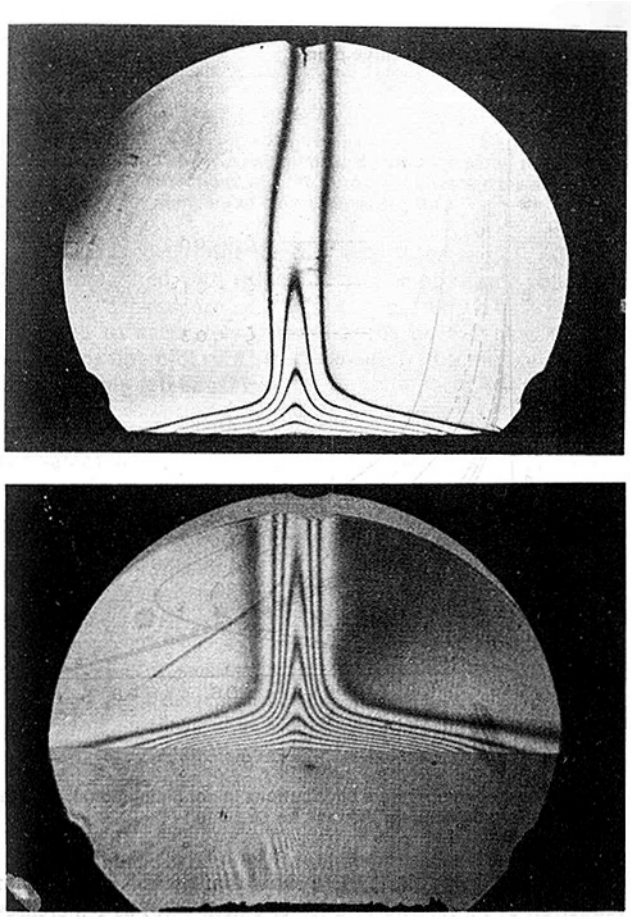

Fig. 3 Holographic inteferograms of the axisymmetric thin layer and plume development above a heated disk in air at two Grashof numbers: top, $Gr_a = 7.7 \times 10^4$; bottom, $Gr_a = 1.2 \times 10^5$

traverser for a thermocouple probe. A horizontal edge extension of thin (1.5 mm) balsa wood protruded radially 76 mm beyond the disk edge with a beveled leading edge. This extension was insulated from the heated copper disk with a ceramic glass lip and a thin layer of silicon paste. The purpose of the extension was to assure a predominantly horizontal flow near the edge of the disk to establish the thin layer flow. The disk was instrumented with three thermocouples embedded within

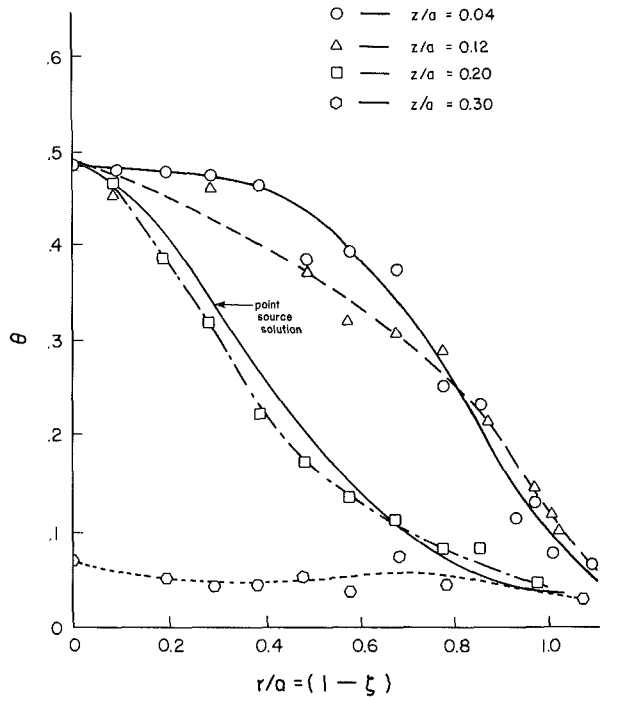

Fig. 4 Radial temperature distributions at four elevations above the disk surface for $Gr_a = 6.0 \times 10^4$

0.8 mm from the disk surface to assure constant and uniform temperature conditions throughout each experiment. The copper disk was heated with a thin foil resistance heater, and was insulated on the bottom and sides with a low-conductivity ceramic glass. Further details concerning the apparatus are given by Robinson (1985).

The air temperature above the disk was measured with a fine wire thermocouple (0.25 mm dia) attached to a traverser accurate to ± 0.05 mm. Radial traverses were made at various elevations above the disk. The temperature data were recorded and stored with a PDP data acquisition system. The millivolt signal from the thermocouple circuit, referenced to the ice point, was amplified and then sampled at several different rates to determine the mean temperature. Each mean temperature presented was evaluated from 1024 data points which were recorded at 3 samples per second.

Interferograms were also obtained using a holographic interferometer for qualitative information about the nature of the temperature distribution above the disk. Figure 3 shows two interferograms of the convective pattern in air above the heated disk for $Gr_a = 7.7 \times 10^4$ and 1.2×10^5. Note that this is an axisymmetric structure; therefore the fringe patterns represent the Abel transform of the temperature distribution. It is evident that a well-defined narrow plume exists above the disk center. A thin layer develops inward from the edge of the heated surface with a rapid transition to the central plume. The case of the larger Grashof number results in a somewhat better-defined thin layer and stronger plume.

Figure 4 shows radial temperature distributions measured at four different elevations above the disk surface. At lower elevations, the temperature is fairly constant up to $r/a = 0.4$ and then decreases rapidly to the ambient value. At $z/a = 0.2$, the temperature profile very nearly matches the numerically obtained distribution for an ideal point source, where the ideal point source solution is matched to the measured centerline temperature. Observing the structure in Fig. 3 shows that $z/a = 0.2$ is approximately twice as high as the thin layer where it begins to form the plume. At larger z/a, the temperature profile quickly decays to nearly the ambient temperature. The

Downloaded 17 Dec 2010 to 193.140.21.150. Redistribution subject to ASME license or copyright; see http://www.asme.org/terms/Terms_Use.cfm

Table 1 Numerical results

Gr_a	ζ	$F_0'(\infty)$*	$F_0'(\infty)$	$F''(0)$	$-\theta'(0)$	$-G(0)$
10^4	0.0	0.1884	0.1862	0.9808	0.3633	1.7011
	0.1	0.1924	0.1912	0.8779	0.3590	1.7522
	0.2	0.1970	0.1991	0.7750	0.3540	1.8180
	0.3	0.2023	0.2023	0.6568	0.3460	1.8610
	0.4	0.2087	0.2060	0.5262	0.3351	1.8567
10^5	0.0	0.0750	0.0726	0.9810	0.3600	1.7247
	0.1	0.0766	0.0773	0.8688	0.3553	1.7592
	0.2	0.0784	0.0794	0.7404	0.3478	1.7702
	0.3	0.0805	0.0809	0.6530	0.3435	1.8651
	0.4	0.0831	0.0848	0.5262	0.3344	1.8630
10^6	0.0	0.0299	0.0296	0.9582	0.3489	1.7392
	0.1	0.0305	0.0312	0.8838	0.3550	1.7917
	0.2	0.0312	0.0322	0.7435	0.3471	1.7838
	0.3	0.0321	0.0335	0.6330	0.3407	1.8218
	0.4	0.0331	0.0341	0.5667	0.3337	1.8695

*Values from equation (9).

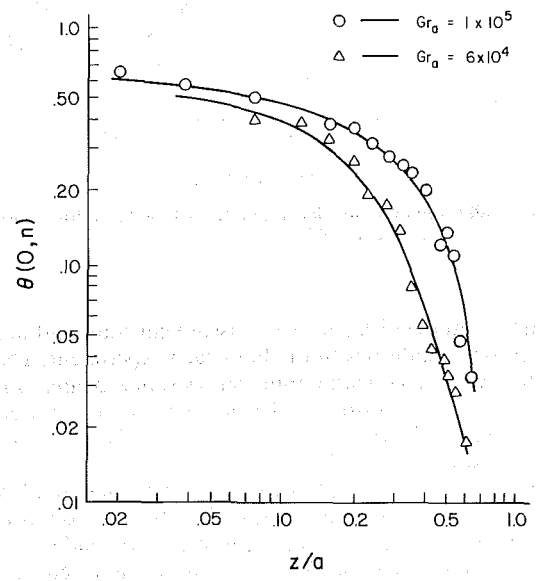

Fig. 5 Centerline temperature decay for two Grashof numbers

uniform temperature near the center portion is a result of the inward flow mixing of the heated air.

The centerline temperature decay is shown in Fig. 5 for two different Grashof numbers. Near the disk surface the slow decay rate is due to mixing of the inward heated flow along the disk. As ambient fluid is entrained, the decay rate increases. Based on the similarity solution of a point source plume, the temperature difference between the centerline and ambient temperatures decays as $(z)^{-1}$, where z is the height above the source. By specifying a virtual origin at a distance z_0 from the disk surface, the centerline temperature decay rate can be expressed as

$$\frac{T_c - T_\infty}{T_s - T_\infty} = \theta \simeq \left(\frac{z - z_0}{a}\right)^{1/n} \tag{15}$$

Data for $Gr_a = 6 \times 10^4$ and 10^5 for $n = 1$ yield virtual origins, z_0/a, of 0.27 and 0.45, respectively. In Fig. 6 the data are presented according to equation (15) showing that the plume decay rate is consistent with a point source plume which supports the boundary condition specified by equation (11).

Numerical Results

Numerical results are presented for the nondimensional stream function F, temperature difference θ, and pressure G, for Grashof numbers between 10^4 and 10^6. Results for $n = 0$

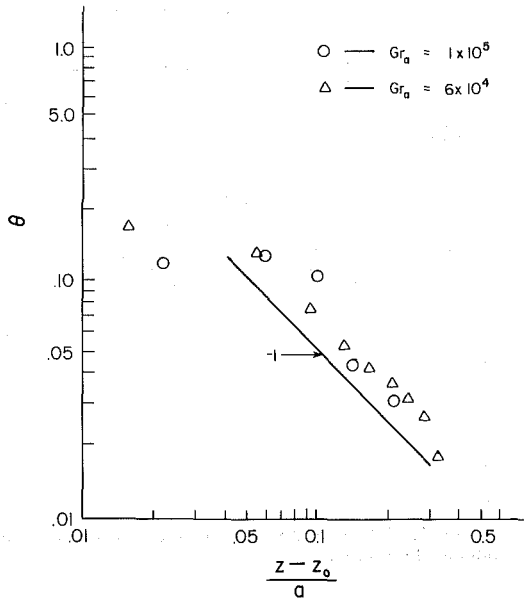

Fig. 6 Centerline temperature decay using a virtual origin; the −1 slope is that of a point source plume

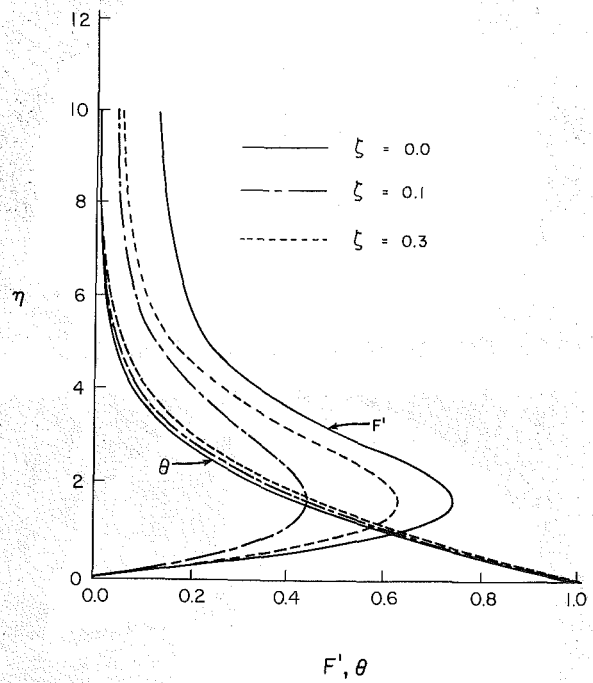

Fig. 7 Flow and temperature distributions in nondimensional variables at three radial positions on the disk for $Gr_a = 10^6$

are presented in Table 1; these show that there is a significant reduction of $F_0''(0)$ and to a lesser extent $\theta_0'(0)$ as ζ increases. The magnitude of the outer boundary condition $F_0'(\infty)$ falls rapidly with increasing Grashof number yet is still significant up to $Gr_a = 10^6$.

Profiles of $F'(\eta, \zeta)$ as a function of η for $Gr_a = 10^4$ are shown in Fig. 7. To satisfy conservation of mass, $F'\zeta^{1/5}$ remains constant for a given Grashof number. For increasing ζ the inner layer thickness, measured to the maxima of F', remains nearly constant. Although not shown, profiles for larger values of Gr_a show the same trend. Also contained in Fig. 7 are the nondimensional temperature profiles for $Gr_a = 10^4$ and various ζ values. The magnitude of the effect of increasing Gr_a on the surface temperature gradient is indicated in Table 1.

Downloaded 17 Dec 2010 to 193.140.21.150. Redistribution subject to ASME license or copyright; see http://www.asme.org/terms/Terms_Use.cfm

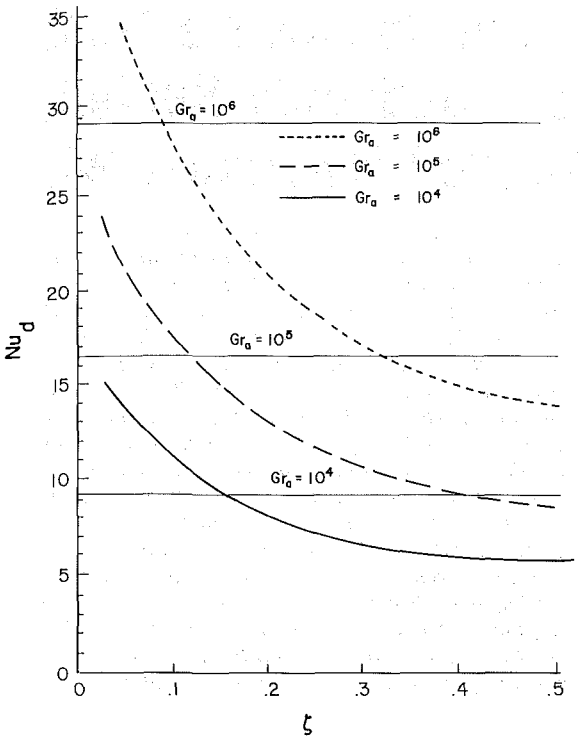

Fig. 8 Predicted local Nusselt number distribution along the disk surface for three Grashof numbers; the horizontal lines are the experimental mean Nusselt numbers of Goldstein et al., 1973

In order to determine the disk heat transfer rate, equation (13) is integrated with respect to ζ. The preceding results indicate the dependence of $\theta'(0)$ on ζ and Gr_a which must be evaluated to accurately determine the overall heat transfer rate. A log-log plot of $\theta'(0, \zeta)$ versus Gr_a for various ζ yields the following relationship:

$$-\theta'(0, \zeta) = C(\zeta) Gr_a^{-\epsilon(\zeta)} \tag{16}$$

The values of $\epsilon(\zeta)$ are small; for example, $\epsilon = 0.006$ at $\zeta = 0.02$ and 0.0033 at $\zeta = 0.4$. The function $C(\zeta)$ decreases with increasing ζ, as implied in Table 1.

A generalized equation can be written for the local heat transfer coefficient as

$$Nu_d = \left(\frac{2ah}{k}\right)_{\text{local}} = -2\zeta^{-2/5} C(\zeta) Gr_a^{1/5-\epsilon(\zeta)} \tag{17}$$

Figure 8 shows the results of equation (17) using the values of $C(\zeta)$ and $\epsilon(\zeta)$ determined from the numerical calculation. These results indicate that by imposing the plume entrainment condition the overall heat transfer rate does not vary with Gr_a to a constant power but varies with location on the disk. Experimental results of Goldstein and Lau (1983) using naphthalene sublimation yield a 0.195 power law relationship for the mean transfer rate versus Rayleigh number. Their experiments were run using square plates in air with extended side surfaces. The data were correlated using a length scale calculated from the surface area divided by the surface perimeter which was shown by Goldstein et al. (1973) and Lloyd and Moran (1974) to correlate results for different shapes. The 0.195 power law is in agreement with our prediction of $1/5 - \epsilon(\zeta)$, where $\epsilon(\zeta)$ is shown to be of the order 0.0033 up to $\zeta = 0.4$ and increases as ζ increases.

Conclusions

Solutions of the laminar boundary layer equations have been obtained for $Pr = 0.72$, subject to an outer entrainment velocity. The entrainment velocity was determined from the point source plume solution, which is assumed to characterize the central plume rising from the disk. This condition is supported by experimental data used to determine a virtual origin for the disk generated plume. The results show better agreement with experimental results when compared to the solution, which neglects the plume entrainment velocity. The local Nusselt number has a reduced power law dependence on the Grashof number due to the outer entrainment. For a Grashof number based on a disk radius greater than 10^6, the plume entrainment velocity becomes insignificant, but for high Grashof numbers the thermal structure will most likely be significantly altered and the analysis presented would no longer apply. Detailed experimental study of the problem is required.

Acknowledgments

The authors would like to thank Mr. S. Bahl for assistance with the interferograms and NSF for partial financial support under Grnt No. ISP-8011451 and Grant No. CBT-8415360.

References

Ackroyd, J. A. D., 1976, "Laminar Natural Convection Boundary Layers on Near-Horizontal Plates," *Proc. R. Soc. Lond.*, Vol. 352, pp. 249–274.

Fujii, T., 1963, "Theory of the Steady Laminar Natural Convection Above a Horizontal Line Heat Source on a Point Heat Source," *Int. J. Heat Mass Transfer*, Vol. 6, pp. 597–606.

Goldstein, R. J., Sparrow, E. M., and Jones, D. C., 1973, "Natural Convection Mass Transfers Adjacent to Horizontal Plates," *Int. Journal Heat Mass Transfer*, Vol. 16, pp. 1025–1035.

Liburdy, J. A., Dorrah, R. L., and Bahl, S., 1987, "Experimental Investigation of Natural Convection From a Horizontal Disk," ASME/JSME Thermal Engineering Conference, Honolulu, HI, Mar. 22–27.

Liburdy, J. A., and Robinson, S. B., 1985, "Solution Procedure for Determining Initial Conditions for a Multivariate Boundary Value Problem," Technical Report, Department of Mechanical Engineering, Clemson University, Clemson, SC.

Lloyd, J. R., and Moran, W. R., 1974, "Natural Convection Adjacent to Horizontal Surfaces of Various Planforms," ASME JOURNAL OF HEAT TRANSFER, Vol. 96, pp. 443–449.

Merkin, J. H., 1983, "Free Convection Above a Heated Horizontal Circular Disk," *J. of Applied Math and Physics (ZAMP)*, Vol. 34, pp. 596–608.

Merkin, J. H., 1985, "Free Convection Above a Uniformly Heated Horizontal Circular Disk," *Int. J. Heat Mass Transfer*, Vol. 28, No. 6, pp. 1157–1163.

Robinson, S. B., 1985, "Natural Convection Heat Transfer From a Horizontal Heated Disk," M.S. Thesis, Clemson University, Clemson, SC.

Rotem, Z., and Claassen, L., 1969, "Natural Convection Above Unconfined Horizontal Surfaces," *J. Fluid Mechanics*, Vol. 9, pt. 1, pp. 173–192.

Stewarton, K., 1958, "On the Free Convection From a Horizontal Plate," *ZAMP*, Vol. 9, pp. 276–282.

Yih, C., 1951, "Free Convection Due to a Point Source of Heat," *Proceedings of the First National Congress of Applied Mechanics*, pp. 941–947.

Yousef, W. W., Tarasuk, J. D., and McKeen, W. J., 1982, "Free Convection Heat Transfer from Upward Facing Isothermal Horizontal Surfaces," ASME JOURNAL OF HEAT TRANSFER, Vol. 104, pp. 493–500.

Zakerullah, M. D., and Ackroyd, J. A. D., 1979, "Laminar Natural Convection Boundary Layers on Horizontal Circular Discs," *ZAMP*, Vol. 30, pp. 427–435.

Downloaded 17 Dec 2010 to 193.140.21.150. Redistribution subject to ASME license or copyright; see http://www.asme.org/terms/Terms_Use.cfm

Development of Convective Heat Transfer Near Suddenly Heated, Vertically Aligned Horizontal Wires

J. R. Parsons, Jr.
Mem. ASME

M. L. Arey, Jr.[1]
Student Mem. ASME

Department of Mechanical and Aerospace Engineering,
University of Tennessee,
Knoxville, TN 37996-2210

Experiments have been performed which describe the transient development of natural convective flow from both a single and two vertically aligned horizontal cylindrical heat sources. The temperature of the wire heat sources was monitored with a resistance bridge arrangement while the development of the flow field was observed optically with a Mach–Zehnder interferometer. Results for the single wire show that after an initial regime where the wire temperature follows pure conductive response to a motionless fluid, two types of fluid motion will begin. The first is characterized as a local buoyancy, wherein the heated fluid adjacent to the wire begins to rise. The second is the onset of global convective motion, this being governed by the thermal stability of the fluid layer immediately above the cylinder. The interaction of these two motions is dependent on the heating rate and relative heat capacities of the cylinder and fluid, and governs whether the temperature response will exceed the steady value during the transient (overshoot). The two heat source experiments show that the merging of the two developing temperature fields is hydrodynamically stabilizing and thermally insulating. For small spacing-to-diameter ratios, the development of convective motion is delayed and the heat transfer coefficients degraded by the proximity of another heat source. For larger spacings, the transient behavior approaches that of a single isolated cylinder.

Introduction

Arrays of horizontal cylinders occur in numerous heat exchange and storage devices. Transfer of heat by natural convection about these cylinders can eliminate the need for a fluid moving device and therefore simplify and enhance the reliability of a particular design. Heat storage exchangers that are driven by periodic sources typical of alternate energy applications may require detailed knowledge of the transient natural convective response of multiple cylinder geometries.

The problem of steady-state natural convection for multiple cylinders has received some attention in the literature. Eckert and Soehngen (1948) measured heat transfer from a three-tube array of cylinders, one configuration with the tubes directly above each other, and another configuration in which the middle tube was offset by one half diameter. For the first configuration, the Nusselt number for the bottom cylinder agreed with single-cylinder results, while the Nu number decreased for the other two, the explanation being that for tubes located in a heated wake, the local temperature difference was less, therefore decreasing the heat transfer. For the staggered arrangement, the middle tube exhibited a higher Nu number than the lowest one, showing that the velocity of the fluid in the wake tends to increase the heat transfer. Solid copper cylinders of 0.878-in. diameter were used in the experiment. Lieberman and Gebhart (1969) studied an array of heated wires. The spacing and inclination of the plane array could be varied. For the vertical array, the Nu number of each wire decreased in the vertical direction for small spacing, while the opposite was true for larger spacings. The spacing (S/D) and Gr_D for this experiment were much higher and lower, respectively, than one would expect in practical devices due to the use of small wires. Marsters (1972) recognized this and did a detailed study of the heat transfer of a plane array of heated 6.35 mm o.d. tubes with variable spacing. Although all of his S/D values were much smaller than Lieberman and Gebhart's the same sort of trend was noted, i.e., Nu number decreasing in the vertical direction for the smaller spacings tested and the opposite for the larger spacings. The "transition" occurred at Grashof numbers (based on length from bottom of the array) of 10^6–10^7, and some success was had with correlating the Nu number behavior with a Gr number defined in this way. Clearly the wake effect(s) makes cylinder spacing an important and not fully understood variable in this problem. Recently, this important problem has begun to receive significant attention with more precisely controlled experiments. Sparrow and Niethammer (1981) conducted experiments on the heat transfer from a pair of heated cylinders with diameters of 37.9 mm in vertical alignment. They reported upper cylinder Nusselt number approximately 15 percent less than single cylinder values for a spacing-to-diameter ratio of 2 increasing and reaching a maximum value of about 20 percent in excess of the single value for a spacing-to-diameter ratio of 7 to 9. Later, with a similar apparatus, Sparrow and Boessneck (1983) examined the effect of misalignment on heat transfer from this pair of cylinders. One of their principal conclusions was that offset of the cylinders tends to moderate the spacing effects. That is, an increase in offset makes the ratio of upper cylinder Nusselt number to single cylinder Nusselt number approach one from the enhanced or degraded values quoted above. In all cases, the misalignment had no further effect for offset to diameter ratios exceeding 2. Tokura et al. (1983) extended the work of Sparrow and Niethammer by testing spacing effects on two, three, and five-cylinder vertical arrays. They showed an average Nu number for the entire array which was degraded for S/D of less than 2 and enhanced for S/D up to about 10, where a maximum was reached. For fine wires, Honda et al. (1983) show the same trends but the crossover between degradation and enhancement occurs at S/D of about 20, increasing to a maximum at a value of S/D of about 100.

For a vertical element, the transient following a step change in wall temperature or heat flux is known to consist of three relatively distinct regimes. The initial regime is characterized by pure conduction. The fluid motion begins as the diffusion of heat from the body establishes variations in the density

[1]Presently at Duke Power Co., Charlotte, NC.

Contributed by the Heat Transfer Division for publication in the JOURNAL OF HEAT TRANSFER. Manuscript received by the Heat Transfer Division May 3, 1985.

Copyright © 1987 by ASME

Downloaded 17 Dec 2010 to 193.140.21.150. Redistribution subject to ASME license or copyright; see http://www.asme.org/terms/Terms_Use.cfm

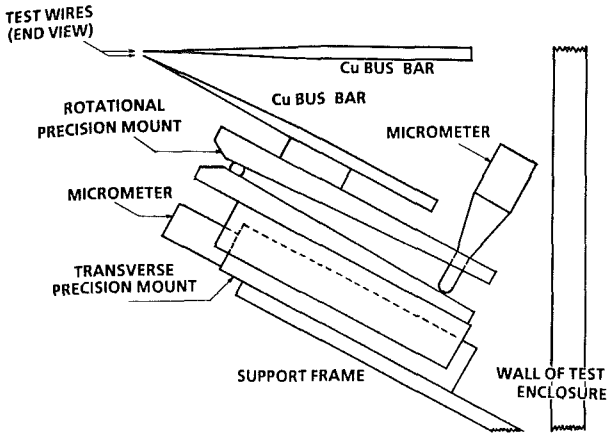

Fig. 1 Test wire holder

field. Finally, the convection currents become established and dominate the heat transfer. The limit of pure conduction and the minimum (overshoot) which sometimes occurs in the heat transfer coefficient are well-known characteristics of these transient problems and have been clearly related to the existence of a sharp leading edge (Nanbu, 1971; Mahajan and Gebhart, 1978). Unlike the vertical element problem, determining the onset of convective motion for a horizontal bluff geometry requires consideration of the thermal stability of the surrounding fluid (Vest and Lawson, 1972; Parsons and Mulligan, 1978). The conduction regime breaks down at a critical Rayleigh number defined on the basis of temperature penetration depth. Although movement of the fluid on the side of the cylinder is also present, the stability layer appears to control the transient for a wide range of conditions. This work is summarized by Parsons and Arey (1984).

The purpose of this study was to examine the transient convective response of both a single and two vertically aligned horizontal wires, suddenly and equally heated. The temperatures of the wires were monitored with an unbalanced resistance bridge arrangement while observing the development of the surrounding fluid temperature field with a Mach-Zehnder interferometer. This gave the clearest physical picture yet of the onset of convection under these circumstances. It was expected that the cylinder interactions would significantly alter the convective transition between pure conduction and steady convection.

Experiments

A Mach-Zehnder interferometer was used with a He-Ne laser light source. The test section was constructed of 1.2-cm-thick plexiglass with an outer insulation blanket, providing a sealed enclosure approximately 35 cm high by 35 cm wide and 45 cm deep. The thermal environment inside the enclosure was well monitored at three separate levels to assure thermal equilibrium between test runs. A system of gear and slide adjustments, which attached the test section to an optical table, provided three degrees of linear freedom and two degrees of rotational freedom. This was necessary to adjust the horizontal wires parallel to the optical path accurately.

The wire holder is seen in Fig. 1. A main brace was attached to the sides of the test section to hold four solid copper bus bars between which two 0.076 mm ± 0.003 mm diameter platinum wires were stretched. The length of the heated wires was 9.2 cm. Grooves of approximately 0.050-mm depth were cut into the sides of the bus bars to set the wires and ensure minimal contact resistance. The mounting arrangement allowed the bottom wire to be raised or lowered by angular rotation and then placed vertically under the top wire by the translation of the linear table. The alignment measuring arrangement could make horizontal measurements to 0.025 mm and vertical measurements to 0.0125 mm. The cylinder offset and S/D ratio were checked before and after each test run was made.

Radiation heat loss from the two-wire arrangement was considered using the same procedure as Sparrow and Niethammer (1981). For this study's worst case, radiation losses were calculated at less than 2 percent of input heat rate. Therefore, radiation losses were considered negligible for all cases.

The wire length-to-diameter ratio (L/D) for these test sections was approximately 1200 and was limited to this value by space requirements of the Mach-Zehnder interferometer. As pointed out by Gebhart and Pera (1970) and Morgan (1975), an L/D of approximately 10^4 is necessary to neglect completely end effects in the measurement of steady-state natural con-

Nomenclature

c = specific heat at constant pressure
d = diameter of wire
g = gravitational accceleration
Gr = Grashof number = $g\beta(T_w - T_\infty)d^3\rho^2/\mu^2$
h = convective heat transfer coefficient = $q'/\pi d(T_w - T_\infty)$
k = thermal conductivity
L/D = length of wire to diameter of wire ratio
Nu = Nusselt number = hd/k
Nu_{ss} = Nusselt number at steady-state conditions
Pr = Prandtl number = $c\mu/k$
q' = cylinder linear heat rate
Ra = Rayleigh number = Gr•Pr
Ra* = modified Rayleigh number based on heat rate = Ra•Nu
Ra_δ = Rayleigh number based on penetration depth δ
S/D = spacing of wires to diameter of wire ratio
t = time
T = temperature
T_w = wire temperature
T_∞ = bulk fluid temperature
α = thermal diffusivity = $k/\rho c$
β = coefficient of thermal expansion of fluid
δ = penetration depth of temperature field around cylinder
μ = dynamic viscosity of fluid
ρ = density
τ = Fourier number = $4\alpha t/d^2$
τ_B = Fourier number at the beginning of fluid movement as designated by the deviation of top and bottom isotherm measurements
τ_{CD} = Fourier number at the beginning of fluid movement as designated by the deviation of wire temperature from pure conduction response
τ_D = Fourier number at the onset of global convection, as predicted by stability theory
τ_P = Fourier number corresponding to the peak of wire temperature response
τ_S = Fourier number designating the time of distinct change in slope for the wire temperature profile
τ_{ss} = Fourier number at beginning of steady conditions
τ_{TH} = Fourier number at the beginning of significant heated layer thinning as designated by side and bottom isotherm measurements

Subscripts

B = bottom wire
T = top wire

Downloaded 17 Dec 2010 to 193.140.21.150. Redistribution subject to ASME license or copyright; see http://www.asme.org/terms/Terms_Use.cfm

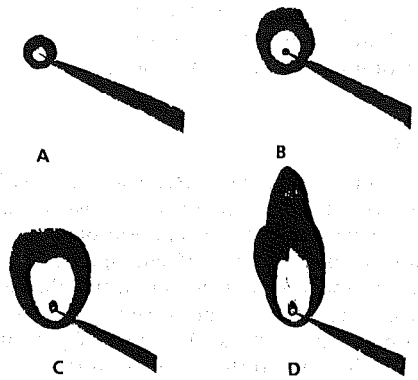

Fig. 2 Typical sequence of Mach-Zehnder photographs showing (A) pure conduction, (B) local buoyancy regime, (C) beginning of global convection, and (D) approaching steady convection

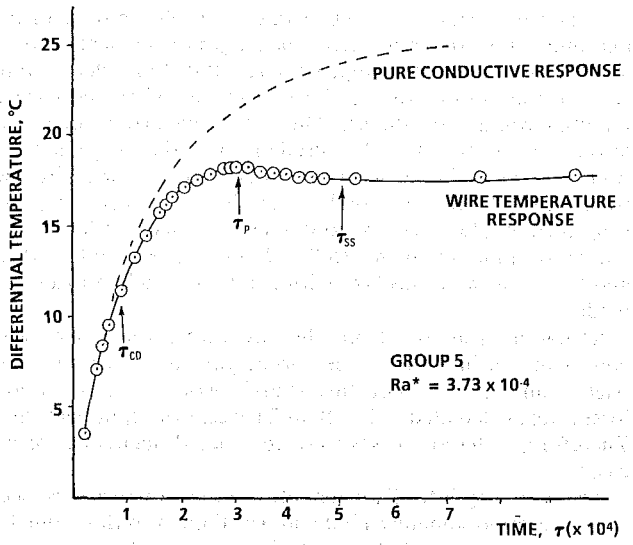

Fig. 3 Example of wire temperature response for overshoot transient

Table 1

Group Number	Heat Load, q' (W/M)	Ra* (x 10⁻⁴)	Nu_{ss}	τ_{CD} (x10⁴)	τ_P (x10⁴)	τ_{SS} (x10⁴)	τ_B (x10⁴)	τ_{TH} (x10⁴)	τ_D (x10⁴)	τ_P/τ_{CD}	τ_{TH}/τ_{CD}
1	.144	.723	.433	---	3.9	---	---	---	4.7	---	---
2	.289	1.45	.460	---	2.82	7.77	1.5	2.5	2.95	---	---
3	.420	2.12	.486	1.0	2.56	6.45	1.3	2.4	2.57	2.6	2.4
4	.568	2.87	.490	.98	2.43	6.04	1.0	2.3	2.25	2.5	2.35
5	.734	3.73	.505	.93	2.22	5.13	.97	2.2	1.95	2.4	2.35
6	.895	4.55	.535	.88	2.12	4.68	.93	2.3	1.82	2.4	2.6
7	1.02	5.19	.540	.86	2.06	4.49	.89	2.2	1.72	2.4	2.55
8	1.17	5.97	.556	.77	1.96	4.30	.73	2.0	1.67	2.5	2.6
9*	1.32	6.76	.551	.74	---	4.23	.68	1.7	1.55	---	2.3
10*	1.47	7.53	.557	.71	---	3.88	.68	1.5	1.48	---	2.15

* NO OVERSHOOT OBSERVED

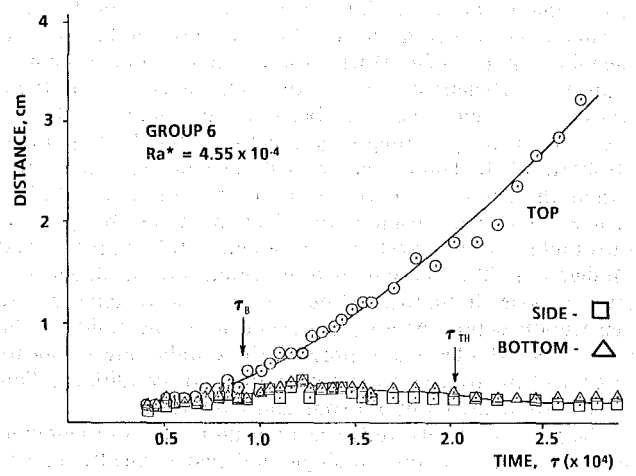

Fig. 4 Example of fringe position measurements for overshoot transient

vection Nusselt numbers in air. Some small systematic error due to end effects could thus be expected but was not further considered in these studies of transient cylinder interactions.

A wheatstone bridge/power supply unit was used to heat the test wires. A high-speed chart recorder provided a time versus bridge unbalance (temperature) curve to be correlated with the film frame by frame. For these experiments, both wires were heated identically in all cases. This was confirmed by heating each wire independently and matching the temperature profiles prior to each test run. The power supply system was on continuously ensuring that the components were at a steady-state operating temperature. A timer, accurate to 0.01 s, was mounted on the screen and photographed along with the interferometric image. This procedure allowed each frame to be correlated to the actual time from the start of the heating process.

Results

Single Wire. Forty acceptable runs were made using power levels of 0.14 to 1.5 W/m. Steady-state temperature levels were confirmed by comparison with an established Nusselt number correlation (Churchill and Chu, 1975). A typical series of Mach-Zehnder photographs is shown in Fig. 2. As expected, the development of the temperature field can be described as occurring in three stages. In the first photograph, heat is being conducted radially from the wire as evidenced by the concentric growth of the temperature fringes. As time proceeds, a temperature fringe, while retaining its circular shape, drifts upward by buoyancy. Finally, large-scale convective fluid motion begins and the fringe pattern is distorted significantly.

The data obtained are portrayed in the next two figures. The wire temperature-time response as measured by the resistance bridge circuit is shown in Fig. 3. An analytical pure conduction solution for a small cylinder subjected to constant heating at zero time and dissipating heat to an infinite medium has been described by Carslaw and Jaeger (1959) for the case of infinite cylinder thermal conductivity and finite cylinder heat capacity. The solution is shown plotted in Fig. 3. The time to 2 percent deviation of wire temperature from pure conduction (τ_{CD}), time to peak of temperature response (τ_P), the steady-state temperature difference and corresponding time (τ_{ss}) were noted and are tabulated in Table 1.

Measurements of fringe position from the Mach-Zehnder photographs are shown in Fig. 4. The exposure time and timer image on each photograph allowed time resolution to approximately 0.005 s. Fringe position measurements were taken from the movies using frame-by-frame projection with an estimated accuracy of ± 0.03 cm. Time to beginning of fluid movement (τ_B), designated by the deviation of the top and bottom isotherm measurements, and the time to significant thinning of the side and bottom measured isotherms (τ_{TH}) were noted and recorded in Table 1.

Comparison of these data reveals a clear picture of the transient. The time to end of conduction τ_{CD} corresponds to the beginning of fluid motion τ_B; the difference between these

Downloaded 17 Dec 2010 to 193.140.21.150. Redistribution subject to ASME license or copyright; see http://www.asme.org/terms/Terms_Use.cfm

points is typically 6-8 percent. This is considered to be within experimental accuracy.

After τ_{CD}, a local buoyancy motion begins in which the heated cylinder of fluid around the wire begins to rise. Ostroumov (1956) partially formulated a theory for this movement based on slow viscous motion around a solid cylinder. In the simplest case, suggested by the measured movement of the isotherms (Fig. 4), he assumed a uniform acceleration of the cylinder until the cylinder broke away from the wire with a constant ascent velocity at 2 τ_{CD}. He could then solve his approximate equation for an effective heated cylinder radius of $r = (4\alpha t)^{1/2}$. His data, however, indicated a larger effective radius than this; the wire retarded the motion of the hot fluid cylinder. The data from this experiment support this observation. The ratio of time to attainment of constant ascent velocity to time of beginning motion was observed to be approximately 2.5. Significantly, it is also observed that the point 2.5 τ_{CD} predicts the point of peak temperature response to within 5 percent. As local motion starts after τ_{CD}, this local velocity of the buoyant cylinder enhances heat transfer and the temperature of the wire decreases away from the pure conductive response. The fluid moving past the cylinder, though, is "locally thick" relative to the steady convective boundary layer, and has been heated above ambient, depressing the local temperature difference and heat transfer. This latter effect continues until the still thickening heated cylinder moves through the wire and this should correspond to the peak of the temperature response, as the data indicate. After this point, global fluid motion has clearly started, the locally heated layer thins down, and a temperature difference predicted by steady convective motion is approached.

It is assumed that the process occurring at the uppermost point on a heated cylinder is essentially the Bénard thermal stability problem of a fluid layer heated from below. This problem generally applies for a constantly imposed temperature difference with one fixed and one free boundary, the instability occurring at the critical Rayleigh number of 1100. While the Bénard instability criteria may not be perfectly representative of the physical boundary conditions of the present problem, a computational procedure employing it was found to be successful by Vest and Lawson (1972) and Parsons and Mulligan (1978). This thermal stability criterion, using a critical Ra_δ of 1100., predicts a delay time τ_D as shown in Fig. 5. Even with the small wires used here, corrections for cylinder heat capacity are necessary for experiments in air. The Vest and Lawson results are equivalent to the no heat capacity effect prediction line shown on this figure. Comparing these predictions with the time to peak temperature response shows very good agreement, with a maximum deviation of 10 percent, with most runs agreeing to 3-4 percent. Stability appears to be a remarkable predictor of onset of global fluid motion.

As the heating rate is increased, a fundamental change in the nature of this transient occurs. As the time to onset of global motion decreases, the wire temperature and radial temperature penetration may not have reached steady convective values when global convection begins. The temperature will then approach its steady value from below and no temperature overshoot will occur. The local buoyancy regime will be interrupted in this case; no locally thick cylinder of fluid moves past the wire before stability causes convection to begin. A simple theory and criterion for predicting this transition as a function of the ratio of heat capacities of heater to fluid media and the Prandtl number was presented by Parsons and Mulligan (1978). This criterion would predict a critical heating rate corresponding to a Ra* of $4. \times 10^{-4}$ for these experiments. The data show overshoot not occurring for Ra* greater than $6. \times 10^{-4}$, the difference attributed to ignoring heat capacity effects in the delay time prediction method. The interrupted buoyancy regime was best observed in these experiments by comparing the time to significant thinning of the bottom and side measured isotherm (τ_{TH}) to the beginning of fluid motion. Although the small changes in slope make τ_{TH} a difficult measurement, the data show a marked decrease in this ratio for the nonovershoot transient. The photographic data for these runs do not show a clear local buoyancy period.

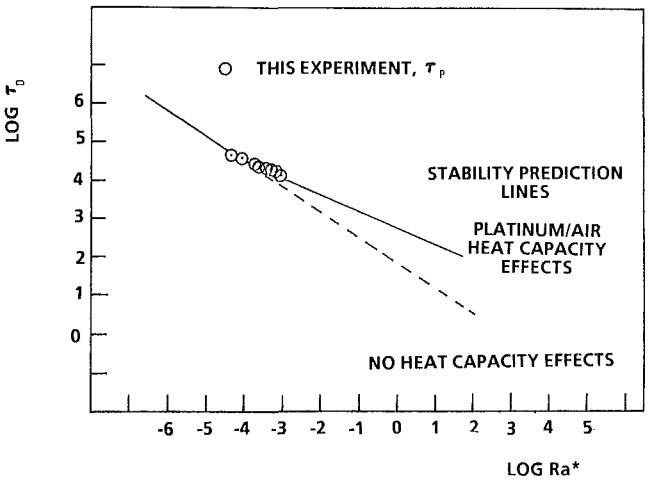

Fig. 5 Thermal stability prediction for onset of global convection

Table 2

Ra* = 3.73 X 10-4

S/D	τ_D (x10⁴)	Nu_{ss}	Nu_{SST}	Nu_{SSB}	τ_{SB} (x10⁴)	τ_{ST} (x10⁴)
83	1.95	.505	.431	.480	1.85	1.96
50	1.95	.505	.413	.474	1.90	1.99
33	1.95	.505	.389	.456	1.93	1.90
17	1.95	.505	.384	.454	2.01	2.41
4.7	1.95	.505	.342	.378	2.41	2.73

Ra* 5.19 x 10-4

S/D	τ_D (x10⁴)	Nu_{ss}	Nu_{SST}	Nu_{SSB}	τ_{SB} (x10⁴)	τ_{ST} (x10⁴)
83	1.72	.540	.451	.523	1.69	1.77
50	1.72	.540	.451	.523	1.69	1.77
33	1.72	.540	.418	.497	1.69	2.10
17	1.72	.540	.407	.495	1.69	2.56
4.7	1.72	.540	.361	.406	1.69	3.37

Ra* = 6.76 x 10-4

S/D	τ_D (x10⁴)	Nu_{ss}	Nu_{SST}	Nu_{SSB}	τ_{SB} (x10⁴)	τ_{ST} (x10⁴)
83	1.55	.551	.490	.544	1.50	1.61
50	1.55	.551	.471	.534	1.49	1.94
33	1.55	.551	.432	.526	1.93	2.25
17	1.55	.551	.420	.514	2.39	2.65
4.7	1.55	.551	.377	.427	2.38	2.73

Downloaded 17 Dec 2010 to 193.140.21.150. Redistribution subject to ASME license or copyright; see http://www.asme.org/terms/Terms_Use.cfm

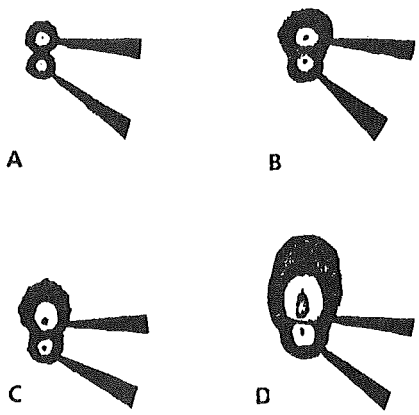

Fig. 6 Typical sequence of Mach-Zehnder photographs showing (*A*) pure conduction, (*B*) pseudo-conduction, (*C*) local buoyancy, (*D*) approaching steady convection

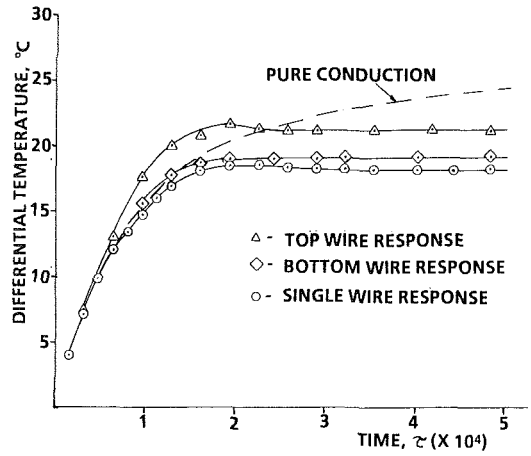

Fig. 7 Two-wire temperature response, Ra* = 3.73 × 10^{-4}, *S/D* = 83

Two Wire. Five different spacings and three heat rates were chosen for study in the two-wire experiments. Tabular results are presented in Table 2. Typical Mach–Zehnder photographs for a two-wire experiment (Fig. 6) showed the same three distinct regimes as could be seen in a single-wire experiment. In addition, however, another occurrence was observed and labeled the pseudo-conduction regime (Fig. 6(B)). This term describes the fluid shortly after the thermal penetration fields from each wire merged. After this point the lower wire's thermal penetration depth remained constant, while the upper wire's thermal penetration continued to increase essentially radially like a conduction pattern. After some distinct period of time, the local buoyancy motion begins around the upper cylinder and eventually leads to full-scale convective motion. For wider spacings where the local buoyancy motion began before the thermal penetration fields met, the pseudo-conduction regime did not occur. For most spacings, the thermal penetration depth of the upper cylinder visibly decreased from a maximum value during the onset of convection motion. This maximum in penetration depth correlated very well ($\pm 5-10$ percent) with the time and magnitude of the temperature "overshoot" that was observed on the time versus temperature graphs discussed below. As would be expected, then, with the stable penetration depth, no overshoot was seen on the temperature versus time graphs for the lower cylinder.

The essential elements of the transient mode of the two wire experiments can be observed in Figs. 7 and 8. These figures show, at a particular input heat rate and spacing, the differential temperature response $(T_w - T_\infty)$ of the two vertically aligned wires compared to the temperature response of a single wire at the same heat rate and an analytical pure conductive response for a single wire. These curves can also be considered the reciprocal of transient Nusselt number response (by the relation $\mathrm{Nu} = q'/\pi k(T_w - T_\infty)$).

For the lowest heat rate, Ra* = 3.73 × 10^{-4}, and widest spacing, *S/D* = 83, Fig. 7 shows that the lower wire results matched the single-wire results within approximately 5 percent over the entire range, which was within experimental accuracy. The steady-state values, the initial slope of the curves, the deviation from the pure conduction curve, and the overshoot were essentially identical on the lower and single wire curves. It is also shown that the initial slope of the top wire curve matches the single-wire experimental values; however, the steady-state values are higher for the top wire and the overshoot is earlier and somewhat enhanced. The top wire temperature is at a higher value than the pure conduction case for an extended period of time, crossing over only after the top wire approaches steady-state conditions. This can be attributed to the heating effects from the lower wire's thermal

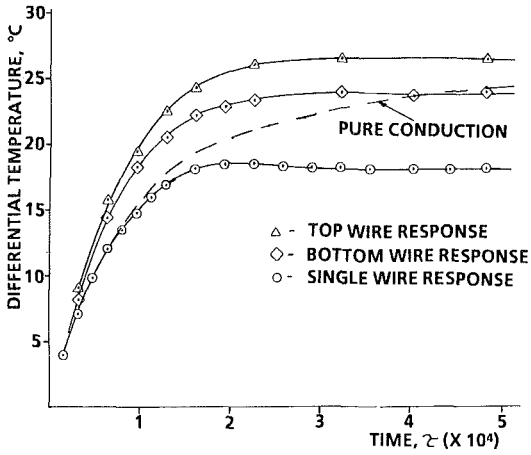

Fig. 8 Two-wire temperature response, Ra* = 3.73 × 10^{-4}, *S/D* = 4.7

plume. A delay in this effect on the upper wire is caused by the wide spacing, thus the initial slopes are the same.

Maintaining this low heat rate and narrowing the spacing to its smallest value, *S/D* = 4.7, it is shown in Fig. 8 that both the top and bottom cylinders' initial temperature slopes have been increased; the overshoot has disappeared for the top cylinder and the steady-state temperatures for the top and bottom are higher than the single wire, 33 and 24 percent, respectively. This corresponds to an equivalent decrease in steady-state Nusselt number. The top wire again has the higher slope and steady-state temperatures. As can be observed from the change in initial slopes and confirmed by the Mach–Zehnder photographs, the interaction effects are almost instantaneous at this spacing.

As the heat rate is increased, the profiles for the *S/D* = 83 spacing remain relatively the same. The lower wire again shows an absence of overshoot but otherwise equivalent response to the single-wire data. For the upper wire curve, the overshoot occurs earlier and has been further enhanced. The initial regime slope for the top wire has increased and thus the top wire curve is initially farther away from the conduction curve. However, the top wire's temperature profile crosses the pure conduction curve sooner than for the lower heating rate.

As the spacing is decreased for the higher heat rates, the same relative movements in the curves are noticed as for the lower heat rate. The upper wire's temperature overshoot disappears at a wider spacing than before, indicating that the total heat rate into the fluid surrounding the upper wire has caused global convection to begin prior to the local buoyancy,

Downloaded 17 Dec 2010 to 193.140.21.150. Redistribution subject to ASME license or copyright; see http://www.asme.org/terms/Terms_Use.cfm

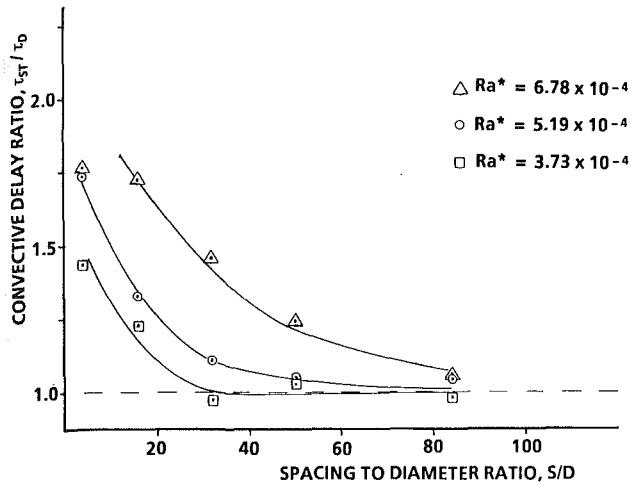

Fig. 9 Convection delay, top wire

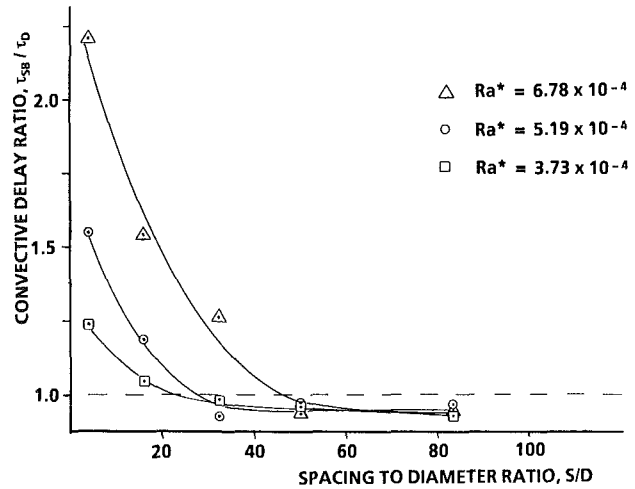

Fig. 10 Convective delay, bottom wire

and thus the upper wire's temperature approaches steady state from below. The time required for the top and bottom wires' temperature profiles to cross back over the pure conduction curve, an indication of the insulating effect of the adjacent wire, decreases for increasing heat rate and increases for decreasing spacing, as would be expected.

In previous steady-state multiwire and multicylinder experiments, the lower cylinder was assumed to have the same temperature as a single cylinder. While at relatively wide spacings this is accurate, in some cases it may have been somewhat in error. The limiting factor is the thermal penetration depth of the two cylinders with respect to their spacing. Sparrow and Boessneck (1983) used a cylinder diameter of 37.87 mm with a closest S/D ratio of 2. Even though this was a very low S/D ratio, the physical spacing was greater than twice the steady convective thermal penetration depth at their high Grashof number. Therefore there was no effect of the top cylinder on the lower cylinder. Conversely, Honda et al. (1983) used wires with diameter of 0.485 mm and the closest S/D ratio of 4.1. At their highest heat rates and thus the deepest penetration by the upper wire's isotherms, they noticed a decrease in the Nusselt number of the lower wire. They attributed this to the geometry of the problem, that the convective flow of the lower wire was restricted by the upper wire. What they apparently observed was the "insulating" effect of the upper wire's thermal penetration field on the lower wire.

One key objective of this study was to identify the end of pure conduction, thus signaling the beginning of the transient

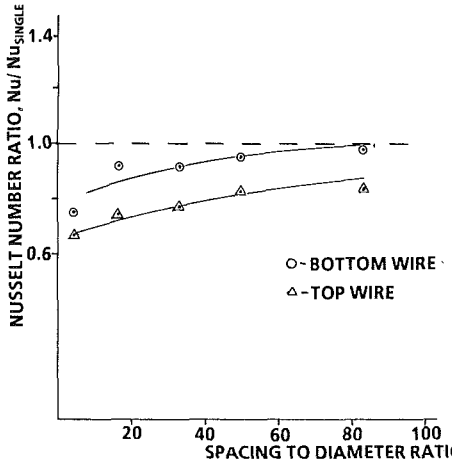

Fig. 11 Steady-state Nusselt number ratio, Ra* = 5.19 x 10^{-4}

regime. The time to distinct change in slope of the top and bottom cylinder's temperature profile was recorded and labeled as τ_{ST} and τ_{SB} in Table 2. As seen from these data, the values steadily increase for identical heat rates as the S/D ratio is lowered, thus identifying again a stabilizing effect on the cylinder temperature response. By comparing the ratio of τ_{ST} and τ_{SB} to τ_D (the stability delay time which predicted onset of global motion in the single-wire experiments), and plotting it versus S/D, it is seen that all cases approach a value of 1.0 as the spacing is increased (Figs. 9 and 10). This indicates that for the transient regimes, the spacings and heat rates chosen do represent two single wires at the widest spacings. The increase of this ratio as the spacing is decreased is also the strongest suggestion of the stabilizing effect of the pseudo-conduction regime. This effect is seen to produce delay in onset of convective motion of 50–100 percent at small spacings and to persist to higher spacings for higher heat rates, as would be expected.

The ratios of the steady-state Nusselt numbers, Nu_{ssT} and Nu_{ssB}, to the steady Nusselt number for a single wire, Nu_{ss}, were plotted versus the S/D ratio (Fig. 11). When the Nu/Nu_{ss} ratio has departed from the value of 1.0, it indicates that the cylinder temperature has been either increased or decreased by the presence of another cylinder. All bottom wire steady-state Nusselt number ratios approached 1.0 within 3 percent for the wider spacings at all heat rates, thus indicating no effect of the upper wire. This is compared to a 0.77 value for the Nu_{ssB}/Nu_{ss} ratio at close spacings and the highest heat rate tested. This clearly shows the insulating effects that the thermal penetration field of the upper wire has on the lower wire. Previous studies indicate that at greater than some S/D value, the upper cylinder Nusselt number will be enhanced by the mixed convection effect of the lower cylinder's thermal plume. This transition is reported at S/D of 5 with a cylinder of 37.87 mm diameter (Sparrow and Niethammer, 1981) steadily increasing with decreasing cylinder diameter to a value of 20 with wires of 0.485 mm diameter (Honda et al., 1983). These experiments continue this trend with no enhancement seen for S/D of 83 with a diameter of 0.076 mm. The lack of enhancement observed may also be partially due to the critical nature of the alignment at large spacings using very small wires such as those utilized in these experiments. As pointed out by Sparrow and Boessneck (1983), misalignments on the order of 2 diameters were sufficient to eliminate most of the enhancement effect of aligned cylinder spacing.

Summary

Single Wire

A The initial motion observed has been characterized as a

Downloaded 17 Dec 2010 to 193.140.21.150. Redistribution subject to ASME license or copyright; see http://www.asme.org/terms/Terms_Use.cfm

local buoyancy motion of the heated cylinder of fluid surrounding the wire.

B Applying a thermal stability criterion with a critical value of $Ra_\delta = 1100$ to the fluid layer on top of the heated wire provides good correlation for the onset of bulk convection motion.

C The interaction of the local and global motions is dependent on the heating rate and heat capacity ratio of cylinder to fluid. For low heating rates, the local buoyancy movement develops fully, retards the heat transfer relative to a convective development, and is ended abruptly by the onset of global convection. The temperature response peaks at this point. For heating rates greater than a value chiefly predictable from the heat capacity ratio, this local buoyancy regime is interrupted by the onset of convective motion and no wire temperature overshoot occurs.

Two Wire

A These experiments are the first to observe successfully the transient interaction of developing convection fields near heated horizontal cylinders.

B For certain spacings and heat rates, a "pseudo-conduction" regime occurs after the first merging of the thermal penetration fields. This effect is hydrodynamically stabilizing and thermally insulating relative to a single-cylinder transient.

C Evidence of the stabilizing effect is a 50–100 percent increase in the time to onset of global convection for the smaller spacings tested.

D The insulating effect of this transition temperature pattern is seen by observing that for all spacings tested the top cylinder temperature exceeds the pure conductive response at sometime during the transient. For small spacings, the bottom cylinder also shows this effect.

Acknowledgments

This work was supported by the National Science Foundation under Grant No. MEA-82-04884.

References

Carslaw, H. S., and Jaeger, J. C., 1959, *Conduction of Heat in Solids*, 2nd ed., Oxford University Press, London, pp. 342-345.

Churchill, S. W., and Chu, H. H. S., 1975, "Correlating Equations for Laminar and Turbulent Free Convection From a Horizontal Cylinder," *International Journal of Heat and Mass Transfer*, Vol. 18, pp. 1049-1053.

Eckert, E. R. G., and Soehngen, E., 1948, "Studies of Heat Transfer in Laminar Free Convection With the Zehnder–Mach Interferometer," Technical Report No. 5747, USAF AMC, Dayton, OH.

Gebhart, B., and Pera, L., 1970, "Mixed Convection From Long Horizontal Cylinders," *Journal of Fluid Mechanics*, Vol. 45, Part 1, pp. 49-64.

Honda, T., Fujii, M., and Fujii, T., 1983, "Free Convection Around Vertical Arrays of Two Horizontal Wires," *Proceedings of the ASME/JSME Thermal Engineering Conference*, Honolulu, HI, March.

Lieberman, J., and Gebhart, B., 1969, "Interactions in Natural Convection From an Array of Heated Elements, Experimental," *International Journal of Heat and Mass Transfer*, Vol. 12, pp. 1385-1396.

Mahajan, R. L., and Gebhart, B., 1978, "Leading Edge Effects in Transient Natural Convection Flow Adjacent to a Vertical Surface," ASME JOURNAL OF HEAT TRANSFER, Vol. 100, pp. 731-733.

Marsters, G., 1972, "Arrays of Heated Horizontal Cylinders in Natural Convection," *International Journal of Heat and Mass Transfer*, Vol. 15, pp. 921-933.

Morgan, V. F., 1975, "The Overall Convective Heat Transfer From Smooth Circular Cylinders," *Advances in Heat Transfer*, Vol. 11, Academic Press, New York, pp. 199-264.

Nanbu, K., 1971, "Limit of Pure Conduction for Unsteady Free Convection on a Vertical Plate," *International Journal of Heat and Mass Transfer*, Vol. 4, pp. 1531-1534.

Ostroumov, G. A. 1956, "Unsteady Heat Convection Near a Horizontal Cylinder," *Soviet Technical Physics*, Vol. 1, pp. 2627-2641.

Parsons, J. R., and Arey, M. L., 1984, "Development of Convective Heat Transfer Near a Suddenly Heated Horizontal Wire in a Still Fluid," presented at the ASME Winter Annual Meeting, New Orleans, LA, Paper No. 84-WA/HT-50.

Parsons, J. R., and Mulligan, J. C., 1978, "Transient Free Convection From a Suddenly Heated Horizontal Wire," ASME JOURNAL OF HEAT TRANSFER, Vol. 100, pp. 423-428.

Sparrow, E. M., and Boessneck, D. S., 1983, "Effect of Transverse Misalignment on Natural Convection From a Pair of Parallel, Vertically Stacked, Horizontal Cylinders," ASME JOURNAL OF HEAT TRANSFER, Vol. 105, pp. 241-247.

Sparrow, E. M., and Niethammer, J. E., 1981, "Effect of Vertical Separation Distance and Cylinder-to-Cylinder Temperature Imbalance on Natural Convection From a Pair of Horizontal Cylinders," ASME JOURNAL OF HEAT TRANSFER, Vol. 103, pp. 638-644.

Tokura, J., Hakaur, S., Kishinami, K., and Muramoto, K., 1983, "An Experimental Study of Free Convection Heat Transfer From a Horizontal Cylinder in a Vertical Array Set in Free Space Between Parallel Walls," ASME JOURNAL OF HEAT TRANSFER, Vol. 105, pp. 102-107.

Vest, C. M., and Lawson, M. L., 1972, "Onset of Convection Near a Suddenly Heated Horizontal Wire," *International Journal of Heat and Mass Transfer*, Vol. 15, pp. 1281-1283.

Downloaded 17 Dec 2010 to 193.140.21.150. Redistribution subject to ASME license or copyright; see http://www.asme.org/terms/Terms_Use.cfm

Steady and Transient Analyses of Natural Convection in a Horizontal Porous Annulus With the Galerkin Method

Y. F. Rao
K. Fukuda
S. Hasegawa
Department of Nuclear Engineering,
Kyushu University,
Fukuoka, Japan

Steady and transient analytical investigation with the Galerkin method has been performed on natural convection in a horizontal porous annulus heated from the inner surface. Three families of convergent solutions, appearing one after another with increasing RaDa numbers, were obtained corresponding to different initial conditions. Despite the fact that the flow structures of two branching solutions are quite different, there exists a critcal RaDa number at which their overall heat transfer rates have the same value. The bifurcation point was determined numerically, which coincided very well with that from experimental observation. The solutions in which higher wavenumber modes are dominant agree better with experimental data of overall heat transfer.

Introduction

Natural convection in a horizontal annular porous layer heated from the inner surface and cooled from the outer surface has become a subject receiving increasing attention due to its practical importance in the problems of insulators, such as the ducting system in a high-temperature gas-cooled reactor, the storage system of thermal energy, underground cable system, etc. A number of works on the subject have been published. Caltagirone (1976) investigated the problem experimentally and numberically. Two-dimensional steady solutions were obtained numerically and utilizing the perturbation technique as well. It was demonstrated by their experiment that there existed a different flow pattern at higher RaDa numbers. Burns and Tien (1979) examined the variations of the overall heat transfer coefficients with the external heat transfer coefficient and radius ratio by a steady-state two-dimensional analysis with the finite difference method and the perturbation method. It was indicated that a maximum value of the overall heat transfer coefficient existed depending upon the radius ratio. Using the finite difference method, Echigo et al. (1978a,b) also obtained two-dimensional steady-state numerical results taking into account the radiation effect. Masuoka et al. (1980) investigated the secondary flow in narrow annuli ($R \leq 1.5$) experimentally and numerically, and showed that the appearance of the secondary flow could enhance the overall heat transfer. Takata (1984) investigated the natrual convection in an inclined porous annulus experimentally and numerically, and obtained three-dimensional results for the inclined case, using the finite difference method. Bau (1984a,b), in recent works, took eccentricity into consideration and demonstrated that heat transfer in the annulus could be optimized by a proper choice of eccentricity.

As mentioned above, although several works have been presented on the problem, most of them were restricted to one flow pattern, the unicellular one, except for the case of a narrow annulus (Masuoka et al., 1980). However, as experimental measurements (Caltagirone, 1976) show, the flow pattern is unlike and not as simple as the unicellular one, and mainly because of this, the overall heat transfer rates predicted numerically disagree by a wide margin with the experimental data (Caltagirone, 1976). It is widely known that the solution of the nonlinear Navier–Stokes differential system is not necessarily unique. The fact that more than one flow pattern exists depending upon initial conditions or initial perturbations is often resported in both experimental and numerical works on natural convection. Experimental works about typical Benard convection in a fluid layer heated from below (Krishnamurti, 1970, 1973) and a numerical work on natural convection between two concentric spheres (Caltagirone et al., 1980) can be taken as examples. For more information on bifurcation, readers are referred to Joseph (1985). Depsite the differences in the geometric configuration and medium nature, there is similarity between the problem considered here and that treated in the works of Caltagirone et al. (1980), and it is natural to assume that the bifurcation would also occur in the numerical solutions dealing with natural convection in a cylindrical porous annulus.

In the present study, the Galerkin method, or spectral expansion method, is utilized. The velocity and temperature are expanded with a series of orthogonal eigenfunctions determined by the nature of the space and boundary conditions; this makes it possible to focus our attention of a few of the main dominant modes whose amplitudes are fairly large compared with the others. In the steady-state analysis small perturbations are given at the beginning of iterations, while in the transient analysis they serve as the perturbed initial condition possibly corresponding to real perturbed experimental conditions. The perturbation are expected to determine which of the branches the solution will finally be led to, although the steady-state solutions are not dependent on perturbations in a sense of one-to-one correspondence. By observing the growing or damping of the perturbations or speical modes, we can verify the change of flow patterns and obtain information about stability of the flow patterns. The radius ratio is set at 2 for the convenience of comparing with other data; this will not lose the generality from the engineering point of view. The results of overall heat transfer corresponding to different flow patterns are expected to give a better interpretation of the problem.

Analyses

The problem considered in the present study is the convection in an annular porous layer enclosed between two horizontal concentric cylinders with dimensionless inner and outer radii 1 and R, and with their inner and outer dimensionless

Contributed by the Heat Transfer Division and presented at the 4th AIAA/ASME Thermophysics and Heat Transfer Conference, Boston, Massachusetts, June 1–4, 1986. Manuscript received by the Heat Transfer Division August 26, 1986.

Copyright © 1987 by ASME

Downloaded 17 Dec 2010 to 193.140.21.150. Redistribution subject to ASME license or copyright; see http://www.asme.org/terms/Terms_Use.cfm

surface temperature 1 and 0, respectively. Due to the symmetry of the boundary conditions and gravitational force, the flow in the annulus is assumed to be two-dimensional and symmetric about the vertical symmetry plane.

Steady Analysis. The dimensionless grovering equations of two-dimensional convection, the conservation of mass, Darcy's law and the conservation of energy, are given in equations (1), (2) and (3) as derived by Caltagirone (1976)

$$\nabla \cdot \mathbf{v} = 0 \tag{1}$$

$$\frac{1}{\mathrm{RaDa}} \nabla P - \lambda\Theta + \mathrm{Ga}\lambda + \frac{\mathbf{v}}{\mathrm{RaDa}} = 0 \tag{2}$$

$$-(\mathbf{v}\cdot\nabla)\Theta + \nabla^2\Theta = \partial\Theta/\partial t \tag{3}$$

where $\lambda = [-\cos\phi, \sin\phi]$. The boundary conditions to be satisfied are $V_r = 0$ at $r = 1$, R; $V_\phi = \partial\Theta/\partial\phi = 0$ at $\phi = 0$, π; $\Theta = 1$ at $r = 1$; and $\Theta = 0$ at $r = R$.

Substituting $\Theta = 1 - \ln r/\ln R + \theta$ in equations (2) and (3), we obtain

$$\nabla P^* + \begin{bmatrix} \cos\phi/\ln R \\ 0 \end{bmatrix} - \lambda\theta + \frac{1}{\mathrm{RaDa}}\mathbf{v} = 0, \tag{4}$$

$$-(\mathbf{v}\cdot\nabla)\theta + \frac{V_r}{r\ln R} + \nabla^2\theta = \partial\theta/\partial t, \tag{5}$$

where $P^* = P/\mathrm{RaDa} - Ga \times r\cos\phi + r(1 - \ln r/\ln R)\cos\phi$. Velocity $\mathbf{v}$ and temperature θ are expanded as follows:

$$\mathbf{v} = \sum_{\substack{i=1 \\ j=1}}^{N,N} S_{ij}\mathbf{v}_{ij} \qquad \theta = \sum_{\substack{i=1 \\ j=0}}^{N,N} T_{ij}\theta_{ij} \tag{6}$$

The trail functions $\mathbf{v}_{ij}$ and θ_{ij} are chosen to satisfy the continuity equation and boundary conditions

$$V_{r_{ij}} = -\frac{j}{r}\sin\left(\frac{i}{a}\ln r\right)\cos j\phi$$

$$V_{\phi_{ij}} = \frac{i}{ar}\cos\left(\frac{i}{a}\ln r\right)\sin j\phi$$

$$\theta_{ij} = \sin\left(\frac{i}{a}\ln r\right)\cos j\phi \tag{7}$$

where $a = \ln R/\pi$. In the ϕ direction, trigonometric functions are used, while in the r direction, orthogonal functions satisfying boundary conditions are adopted, obtained from the following eigenfunction problem:

$$\frac{d}{dr}\, r\, \frac{d}{dr}\, ry(r) + \gamma^2 y(r) = 0 \quad (y = 0 \text{ at } r = 1, R). \tag{8}$$

The solution of equation (8) is $1/r \sin(i/a \ln r)$, which is used to form V_r, while V_ϕ is obtained from the continuity equation (1). In the group of trial functions in equation (7), to which we will refer as trial function 1, $\sin(i/a \ln r)\cos(j\phi)$ instead of $1/r\sin(i/a \ln r)\cos(j\phi)$ is used as the temperature trial function for reasons mentioned below. First, it will yield equal average Nusselt numbers on the inner and the outer surfaces of the annulus when we consider an effective first-term approximation, as will be shown later. Second, it is expected to be more efficient in describing overall heat transfer because of satisfying the condition

$$\frac{\partial}{\partial r}\, r\, \frac{\partial\theta}{\partial r} = 0 \qquad (\text{at } r = 1, R) \tag{9}$$

which is derived from equation (5). As an indirect condition, equation (9) is not necessarily required to be satisifed by each term of the trial functions; it can be satisifed, as a result, by the summation of them, equation (6). However, as will be discussed later, using trial functions satifying equation (9) will actually speed up the convergence of series for the heat transfer coefficient.

The formulation of the Galerkin method (Finlason, 1972; Gottlieb and Orszag, 1977) is completed by inserting equations (6) and (7) into equations (4) and (5), multiplying them by $\mathbf{v}_{mn}$ and θ_{pg}, respectively, and integrating over the annulus. The term ∇P^* is eliminated by applying the divergence theorem and by taking into account the continuity equation and boundary conditions which $\mathbf{v}_{mn}$ satisfies. We finally obtain

Nomenclature

a = $\ln R/\pi$
C, C' = constants defined in appendix
D = Dirichelet function (see equation (A8)
g = gravitational acceleration
Ga = $1/[\beta(\hat{T}_{in} - \hat{T}_o)]$
N = truncating number
Nu = local Nusselt number
$\overline{\mathrm{Nu}}$ = average Nusslet number
P = pressure
R = ratio of inner to outer radius
r = radial distance
RaDa = $g\beta\kappa r_{in}(\hat{T}_{in} - \hat{T}_o)/\alpha_{eq}\nu$
S_{ij} = amplitude of velocity mode (i, j)
$\hat{T}$ = temperature
T_{ij} = amplitude of the mode (i, j) of the dimensionless temperature θ
t = time
$\mathbf{v}$ = velocity vector $[V_r, V_\phi]$
V_r = velocity component in r direction
V_ϕ = velocity component in ϕ direction
α_{eq} = equivalent thermal diffusivity of the saturated porous medium
β = thermal expansion coefficient
γ = eigenvalue used in equation (8)
Θ = dimensionless expansion temperature = $(\hat{T} - \hat{T}_o)/(\hat{T}_{in} - \hat{T}_o)$
θ = dimensionless temperature defined by $\Theta - (1 - \ln r/\ln R)$
κ = permeability
λ = direction vector $[-\cos\phi, \sin\phi]$
ν = kinematic viscosity
ϕ = angular coordinate measured from downward vertical axis
ψ = stream function

Subscripts

in = inner
o = outer
(I, J); (i, j); (m, n); (p, q) = modes of dimensionless temperature

Downloaded 17 Dec 2010 to 193.140.21.150. Redistribution subject to ASME license or copyright; see http://www.asme.org/terms/Terms_Use.cfm

$$S_{mn} = C_1 + \sum_{i=1}^{N} (C_2 T_{i,n+1} + C_3 T_{i,n-1})$$
$$m = 1, 2, \ldots, N; \quad n = 1, 2, \ldots, N \tag{10}$$

$$\sum_{\substack{i=p-N \\ j=q-N}}^{N,N} C_5 S_{|i|,|q-j|} T_{|p-i|,|j|} + C_6 S_{pq} + C_7 T_{pq} = 0$$
$$p = 1, 2, \ldots, N; \quad q = 0, 1, \ldots, N \tag{11}$$

where $C_1, \ldots, C_7$ are coefficients whose values are given in Appendix A. The Nusselt numbers are defined as follows:

$$\overline{\mathrm{Nu}}_{in} = -\frac{1}{\pi}\int_0^{\pi} \ln R \left.\frac{\partial \Theta}{\partial r}\right|_{r=1} d\phi = 1 - \pi \sum_{i=1}^{N} i T_{i0}$$

$$\overline{\mathrm{Nu}}_{0} = -\frac{1}{\pi}\int_0^{\pi} R \ln R \left.\frac{\partial \Theta}{\partial r}\right|_{r=R} d\phi = 1 - \pi \sum_{i=1}^{N} (-1)^i i T_{i0} \tag{12}$$

With the limitation of $m+n \le 2$ and $p+q \le 2$, equations (10), and (11), and (12) reduce to their simplest form as follows:

$$T_{10} = 0$$

$$1 + \frac{2\pi(3-a^2)}{a^2+9} T_{20} - \frac{\pi^2(a^2+1)^2}{2\mathrm{RaDa}(R+1)a} S_{11} = 0$$

$$S_{11} T_{11} - \frac{8}{a} T_{20} = 0$$

$$T_{20} S_{11} + \frac{1}{\pi} S_{11} + \left(a + \frac{1}{a}\right) T_{11} = 0$$

$$\overline{\mathrm{Nu}} = \overline{\mathrm{Nu}}_{in} = \overline{\mathrm{Nu}}_{o} = 1 - 2\pi T_{20} \tag{13}$$

Equation (13), which we call the first-term approximation since only one term of the velocity expansion series is considered, is transformed to a one-dimensional third-order algebraic equation and will be solved exactly. This exact solution will give a convenient and effective interpretation of the problem at low RaDa numbers.

When $N > 2$, equations (10) and (11) constitute a nonlinear algebric system and must be solved by an interation method. The iteration is continued until $\Sigma |f_{ij}(\theta)| < 10^{-3}$ is satisfied. For higher RaDa numbers, we have to conduct several runs by increasing the RaDa number step by step because the scheme is unstable for large RaDa variations.

Transient Analysis. With the exception of the time differential term $\partial\theta/\partial t$ in the energy conservation equation, the main procedure of formulation in the transient analysis is similar to that described above and is omitted here. The trial function θ_{ij} must be orthogonal in this case if we want to avoid matrix inversion for integrating with time using the explicit method. Therefore, the trial function $\theta_{ij} = 1/r \sin(i/a \ln r)\cos j\phi$, the unmodified one as obtained from equation (8), is used; we will later refer to it as trial function 2. The equations thus obtained are as follows:

$$S_{mn}(t) = C_1' + \sum_{i=1}^{N} [C_2' T_{i,n+1}(t) + C_3' T_{i,n-1}(t)]$$
$$m = 1, 2, \ldots, N; \quad n = 1, 2, \ldots, N \tag{14}$$

$$\frac{d}{dt} T_{pq}(t) = -\sum_{\substack{i=1 \\ I=1 \\ j=q-N}}^{N,N,N} C_5' S_{I,|q-j|}(t) T_{i,|j|}(t)$$
$$+ \sum_{i=1}^{N} [C_6' S_{iq}(t) + C_7' T_{iq}(t)]$$
$$p = 1, 2, \ldots, N; \quad q = 0, 1, \ldots, N \tag{15}$$

where $C_1', \ldots, C_7'$ are coefficients whose values are given in Appendix B. It should be noted that trial function 2 does not satisfy the indirect condition (9) as trial function 1 does, so that larger truncating numbers are required to obtain the results of heat transfer with good coincidence of $\overline{\mathrm{Nu}}_{in}$ and $\overline{\mathrm{Nu}}_{o}$, which deviate from each other by about 3 percent using trial function 2 with $N = 10$, compared to within 1 percent using trial function 1 with the same N. However, the deviation is proved to decrease with increasing N, and it is found that the two trial functions yield nearly equal $\overline{\mathrm{Nu}} = 1/2(\overline{\mathrm{Nu}}_{in} + \overline{\mathrm{Nu}}_{o})$, which is used as the evaluation of the overall heat transfer. In the calculations, truncating the series by $i+j \le N+1$ and $p+q \le N+1$ was found to be efficient and was utilized in most of the calculating runs. In this case the summations take different forms; for exmaple, the summation of the convection term in equation (15) should be changed to

$$\sum_{i=1}^{N} \sum_{I=1}^{N} \sum_{j=j_1}^{j_2}$$

where

$$j_1 = \max[q-N, -(N+1-i), -(N+1-I)+q]$$

and

$$j_2 = \min[N, N+1-i, N+1-I+q] \tag{16}$$

Equations (14) and (15) constitute the first-order nonlinear ordinary differential equation system and are solved by the so-called rational Runge–Kutta method (RRK) developed by Wambecq (1978) as a nonlinear explicit method for solving stiff ordinary differential system, which is stable at much larger time step than the usual explicit methods. Its two-stage form is adopted. The values of variable parameters taken in the present study are the same as those used by Wambecq in a simple testing problem of four dimensions; this makes the scheme of the second order to the time interval. Compared with the conventional Runge–Kutta method (CRK), the scheme is found to be almost free from stability restriction to which CRK and most explicit methods are subject. At higher RaDa numbers and with a large truncating number N, the time interval of CRK was restricted to 0.001, while the calculation with RRK did not diverge even with a time interval ten times larger. However, if beside the final steady-state solutions we also want the transient one, the time interval cannot be taken too large due to numerical oscillation occurring during the transient process. Generally, time intervals two or three times larger can be taken using RRK than using CRK; this will save much computer cost because the CPU time by RRK for one time step is comparable with that by CRK. The time intervals used are between 0.002–0.01. The CPU time for an average run is about 20 s with a FACOM-382 digital computer.

Results and Discussion

Exact Solutions of First-Term Approximation. Exact solutions of equation (13), numerical solutions of equations (10) and (11) and of equations (14) and (15) were obtained with aspect ratio $R = 2$ and RaDa ranging from 1 to 300. It is important to note that the first-term approximation, equation (13), can serve as an effective assessment of the flow configuration and heat transfer at low RaDa numbers, and this also confirms that the scheme developed is highly efficient. The flow pattern obtained from equation (13) is shown in Fig. 1, where the kidney-shaped flow circulation, often reported in literature, is well depicted. Because only one term, the mode

Downloaded 17 Dec 2010 to 193.140.21.150. Redistribution subject to ASME license or copyright; see http://www.asme.org/terms/Terms_Use.cfm

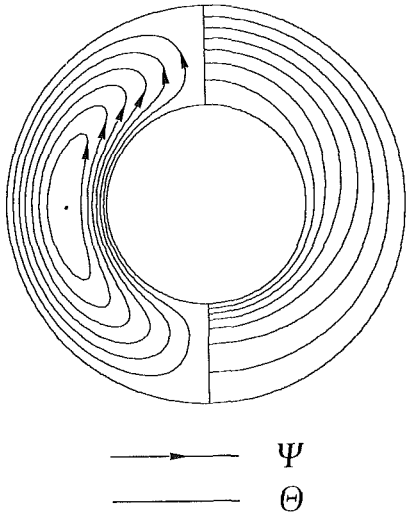

Fig. 1 Flow pattern obtained from the first-term approximation, RaDa = 50, $\Delta\Theta = 1/7$, $\Delta\psi = \psi_{max}/7$, $\psi_{max} = 5.489$

(1, 1), of velocity is used, the streamline pattern becomes symmetric about the horizontal symmetry (i.e., $\phi = \pi/2$) plane. This locates the center of the circulation flow at $\phi = \pi/2$ rather than at a higher place as it should be. The resulting error, however, is negligible at low RaDa numbers when the center is near $\phi = \pi/2$. In Table 1, the Nusselt numbers from the first-term approximation are compared with those from higher-order approximations of equations (10) and (11). The results are reasonably consistent with the convergent ones (at $N = 8$ or 10) at the range of RaDa numbers which is of importance from the engineering point of view; the maximum error is about 3 percent at RaDa numbers up to 50.

Branching Solutions: Three Flow Patterns. It should be noted that there is no general way for choosing initial conditions, especially in the problems that involve stability. Instability expected to occur in the present problem is mainly due to a reverse temperature gradient at the top of the annulus, which is similar to the case of the well-known Benard problem. In such problems, initial perturbation is necessary since the unstable change of flow patterns, as well as the onset of convection, is usually caused by small perturbations in the nature; the use of conduction solutions or uniform temperature distribution as initial conditions may prevent these solutions from being obtained. The number of steady-state branching solutions at a given RaDa number is an intrinsic feature of the problem and should be independent of initial conditions. However, and again, there is no general method to determine the number in such complicated nonlinear problems; analysis has to be done case by case, and empirically in most cases. The simplicity of the geometric and boundary conditions in the present case allows us to assume that the possible branching solutions take the form of secondary (multiple) cell patterns extending, at the top region of the annulus, in either circumferential or axial directions; the latter involves the three-dimensional branching solutions which will be discussed in a subsequent paper.

On solving the problem at higher RaDa numbers, three types of initial conditions, shown in Table 2, were adopted at the beginning of iterations or integration. The initial condition of Type 1, which always generates unicellular flow, corresponds to the state of pure conduction, i.e., $\theta = 0$; that of Type 2 corresponds to a disturbed distribution of Type 1, with temperature being slightly lower at the top of the annulus, where a down-forward flow will be generated to form the secondary flow. The condition of Type 3 corresponds to a disturbance resulting in a higher temperature at the top and including higher wave number modes; it will generate tricellular flow at higher RaDa numbers. Since velocities are set to zero, these conditions are not in conflict with any of the governing equations, and the perturbations are so small that the temperature distribution of conduction is just slightly disturbed; this can be verified later by the temperature distribution at the first time step in Fig. 4 and Fig. 5.

Table 1 Comparison of exact solution of the first-term approximation with numerical solutions of higher order at low RaDa numbers

RADA	exact sol. of (13)	N=4	N=6	N=8	N=10
5	1.0043	1.00432*	1.00432	1.00431	1.00431
		1.00428**	1.00430	1.00430	1.00431
10	1.017	1.01723	1.01714	1.01712	1.01712
		1.01697	1.01707	1.01709	1.01710
20	1.064	1.0671	1.0666	1.0665	1.0665
		1.0657	1.0663	1.0664	1.0665
25	1.097	1.1027	1.1019	1,1018	1.1017
		1.1002	1.1013	1.1015	1.1016
50	1.30	1.3491	1.3443	1.3434	1.3430
		1.3285	1.3390	1.3415	1.3422

* : $\overline{Nu}_i$; ** : $\overline{Nu}_o$.

Table 2 Initial conditions for generating three flow patterns

Type 1 for unicellular flow or MODE 1	Type 2 for bicellular flow or MODE 2	Type 3 for tricellular flow or MODE 3
all $T_{ij}=0$	all $T_{ij}=0$ except $T_{13}=\varepsilon$, $T_{14}=-\varepsilon$, and $T_{15}=\varepsilon$.	all $T_{ij}=0$ except $T_{16}=\varepsilon$, $T_{17}=-\varepsilon$, $T_{18}=\varepsilon$, $T_{19}=-\varepsilon$.

Where ε (>0)=0.01-0.1.

Three MODEs of solutions were obtained corresponding to these different initial conditions. Here, by the term "MODE" we mean a flow pattern or a family of branching solutions, while by "mode" a special wavenumber combination, i.e., (i,j), which specifies the wavenumbers in the r and ϕ directions, respectively. One case is shown in Fig. 2, where the flow pattern of MODE 1, the unicellular flow, is the same as in previous works for this aspect ratio, while those of MODE 2 and MODE 3 can be recognized as bicellular and tricellular ones, respectively. Besides the same solutions as obtained in transient analysis, an additional flow pattern, MODE 4, was obtained in the steady-state analysis over a wide range of RaDa numbers. This flow pattern is stable, easy to converge and gives quite good total energy balance (coincidence of $\overline{Nu}_{in}$ and $\overline{Nu}_o$). However, as will be shown later, it is unstable when transient analysis is conducted. Attention therefore will be focused here on the other three flow patterns.

Listed in Table 3 are the dominant modes of temperature whose absolute values are above 3 percent of the mean-square root of all modes (i, j). It was found that the higher wavenumber modes are involved for higher MODE, and that besides the common modes describing the main flow circulation of the three flow patterns, those appearing in higher MODEs are of $(1, j)$ which generally, if not absolutely, are more apt to become dominant than those having the same total wavenumber $i+j$. These special modes were compared in Fig. 3 for the three flow patterns, where one can find that the values of $(-1)^j T_{1j}$ vary quite regularly and with distinct characteristics for each of the three MODEs. The unicellular flow, MODE 1, has its plus values of $(-1)^j T_{1j}$ for all j; this

Downloaded 17 Dec 2010 to 193.140.21.150. Redistribution subject to ASME license or copyright; see http://www.asme.org/terms/Terms_Use.cfm

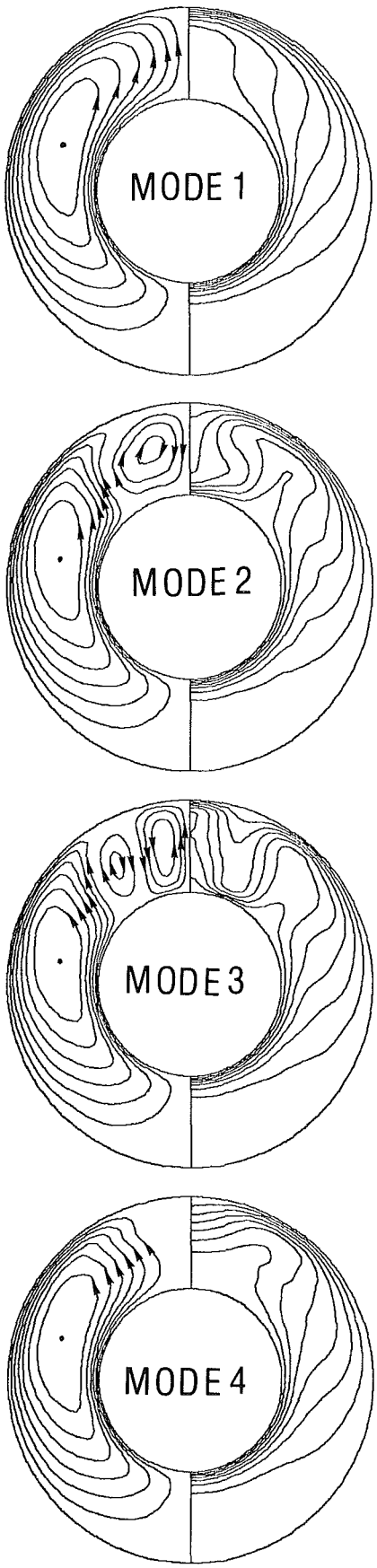

Fig 2 Flow patterns of branching solutions for RaDa = 200, $\Delta\Theta = 1/7$, $\Delta\psi = \psi_{max}/7$: MODE 1, unicellular flow, $N = 11$, $\psi_{max} = 16.33$, MODE 2, bicellular flow, $N = 14$, $\psi_{max} = 15.42$, MODE 3, tricellular flow, $N = 14$, $\psi_{max} = 15.02$, MODE 4, an additional flow pattern only stable in steady-state analysis, $N = 10$, $\psi_{max} = 15.73$

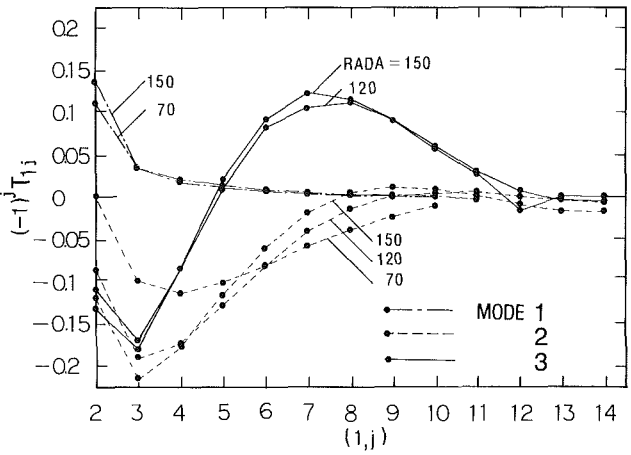

Fig. 3 Comparison of dominant modes (1, *j*) for three flow patterns

Table 3 Dominant modes of three flow patterns for RaDa = 120

MODE 1 or unicellular flow N=11		MODE 2 or bicellular flow N=14		MODE 3 or tricellular flow N=14	
mode	T_{ij}	mode	T_{ij}	mode	T_{ij}
1,1	-0.659	1,1	-0.508	1,1	-0.487
2,0	-0.165	1,3	0.191	1,3	0.170
2,1	0.141	2,0	-0.185	2,0	-0.166
1,2	0.134	1,4	-0.173	2,1	0.118
3,1	-0.103	2,1	0.161	1,7	-0.115
2,2	-0.081	1,5	0.128	1,8	0.113
1,0	-0.061	3,1	-0.110	1,2	-0.112
		1,0	-0.109	1,0	-0.108
		1,2	-0.085	3,1	-0.092
		1,6	-0.081	1,9	-0.090

forms a temperature distribution peak at the top of the annulus which corresponds to an upward flow there. The bicellular flow, MODE 2, has minus values of $(-1)^j T_{1j}$ for all j except for $j=1$ if thoses of small values near zero are neglected. This forms a temperature distribution valley at the top and the peak consequently shifts to a lower angular place, generating a counterrotating secondary flow at the top region. The exception of mode (1, 1) is due to the fact that the main circulation is common to all three MODEs. The case of tricellular flow, MODE 3, is slightly different. Its temperature distribution has a peak at the top which is similar to MODE 1, while another peak also exists at a lower angular place, which is similar to MODE 2. So the values of $(-1)^j T_{1j}$ have the nature of both MODE 1 and MODE 2. In addition, higher modes are involved owing to increasing vortex numbers. The results show that it is difficult to determine the proper truncating number N not knowing the flow structure. In Fig. 4, one can find that $N=8$ is sufficient to MODE 1 and nearly sufficient to MODE 2, but $N>9$ is necessary for generating MODE 3.

Figure 5 shows the time variation of special dominant modes of temperature from an initial condition of Type 2 with $N=8$. We find that mode (1, 1) has an overshoot and the other secondary flow modes become dominant at the same time about 0.09, when the flow pattern begins to change. It is found that MODE 4 appears firstly and then transits to MODE 2 as time elaspses. This fact is confirmed by integrating the results of MODE 4 obtained from steady-state analysis, with the RaDa and N unchanged, showing that MODE 4 is unstable in the transient analysis. This shows the

Downloaded 17 Dec 2010 to 193.140.21.150. Redistribution subject to ASME license or copyright; see http://www.asme.org/terms/Terms_Use.cfm

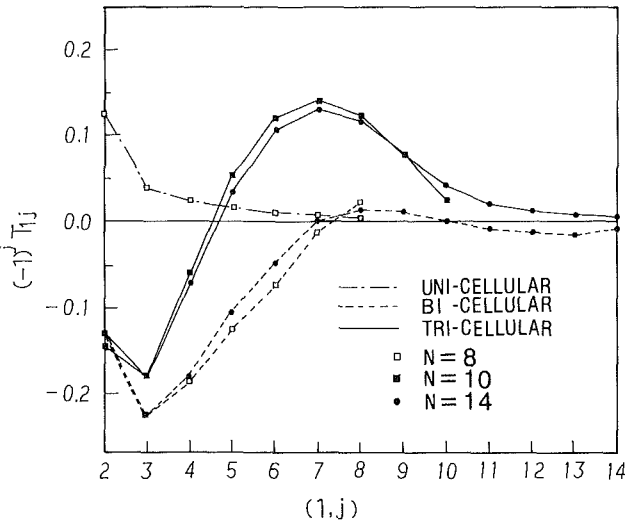

Fig. 4 Comparison of dominant modes (1, *j*) with different *N*; RaDa = 200

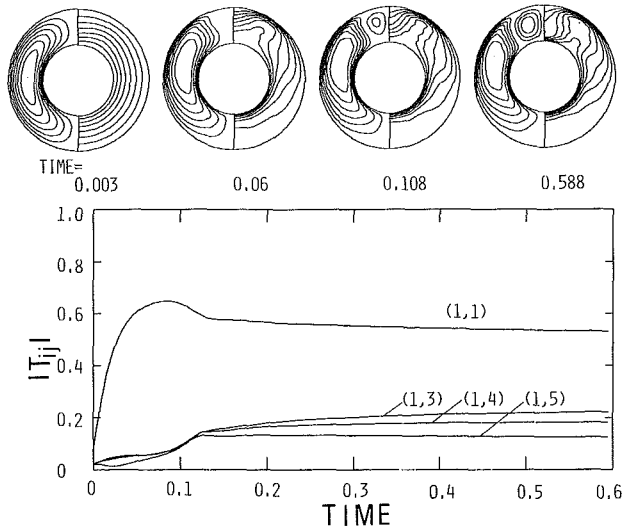

Fig. 5 Time variation of the flow pattern and dominant modes for RaDa = 200, *N* = 8, Δ*t* = 0.003: MODE 4 is an unstable one

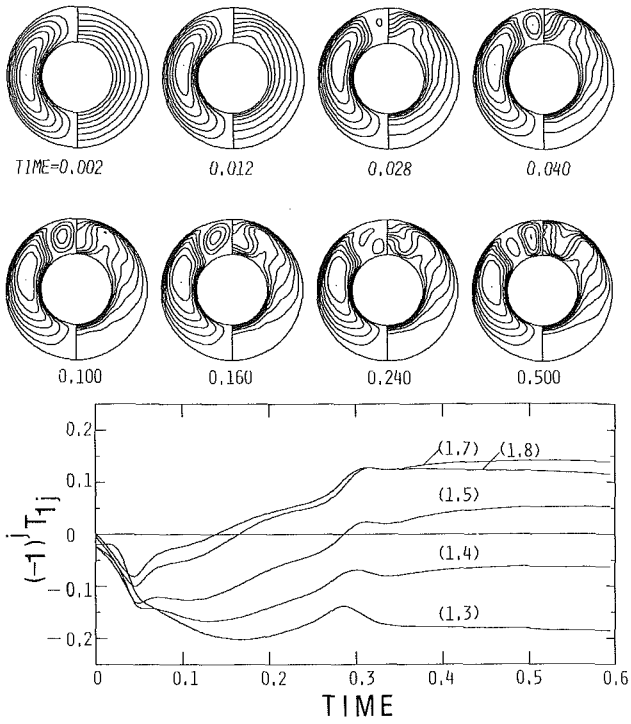

Fig. 6 Time variation of the flow pattern and dominant modes for RaDa = 200, *N* = 10, Δ*t* = 0.002: MODE 2 transits to MODE 3

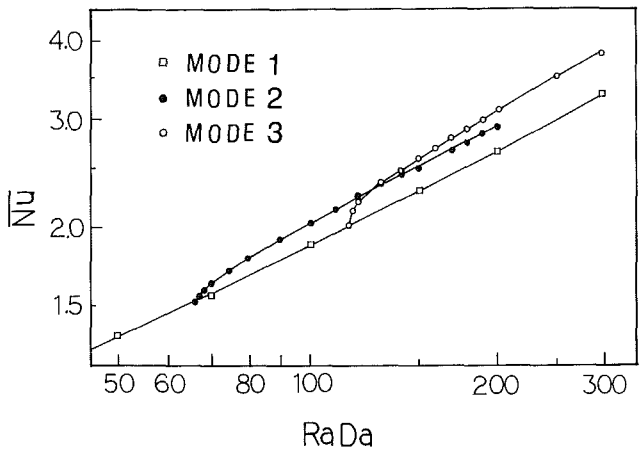

Fig. 7 Average Nusselt numbers for three branching solutions

case in which steady-state analysis gives more branching solutions than transient analysis does. From Fig. 6 (with $N=10$), we can find that a bicellular flow is generated and then transits to a tricellular one through a unstable process, which sets in when the dominant modes (1, 7) and (1, 8) change their signs at a time about 0.16. It is true that, for RaDa > 150, we cannot obtain bicellular flow from the perturbed conduction solution, but we can obtain it from the steady solurions for lower RaDa numbers by increasing RaDa step by step. This shows us that MODE 2 is less stable than MODE 3 at higher RaDa numbers, and the latter can be considered to be more apt to become dominant.

Although MODE 3 is proved to be more stable than MODE 2 at higher RaDa numbers, we could not obtain it with a truncating number less than 9 under any perturbations tried. This indicates that insufficient N (in the present case $N<9$) is not just a problem of accuracy; it will lead to the problem of losing important branching solutions at higher RaDa numbers.

It is also worth noting that there are two options of initial conditions usually adopted, pure (or perturbed) conduction and uniform distribution of temperature. The pure (or perturbed) condition distribution of temperature was used as the initial condition in present study because it is simplest for the spectral method and also because it can avoid an overshoot in the early steps of time integrating from the initial uniform temperature distribution. Calculations, however, were also performed with the pure (or perturbed) uniform temperature distribution as the initial condition, and it was proved that the results about branching solutions given in the context remained essentially the same. The initial condition is shown in Appendix C, and the time-dependent results are compared with the previous work (Facas and Farouk, 1983).

Bifurcation Point: Critical RaDa Number. In Fig. 7 the average Nusselt numbers of the three MODEs are plotted. It can be noted that, of the three branching solutions, the higher MODE appears at higher RaDa regions and has higher Nusselt numbers than the lower MODE. If "the maximum heat of flux assumption" proposed by Malkus (1954) holds, the most dominant one at high RaDa numbers should be MODE 3, which is supported by Fig. 6 where MODE 2 transmitted to MODE 3. In Fig. 7, emphasis is placed on the fact that,

Downloaded 17 Dec 2010 to 193.140.21.150. Redistribution subject to ASME license or copyright; see http://www.asme.org/terms/Terms_Use.cfm

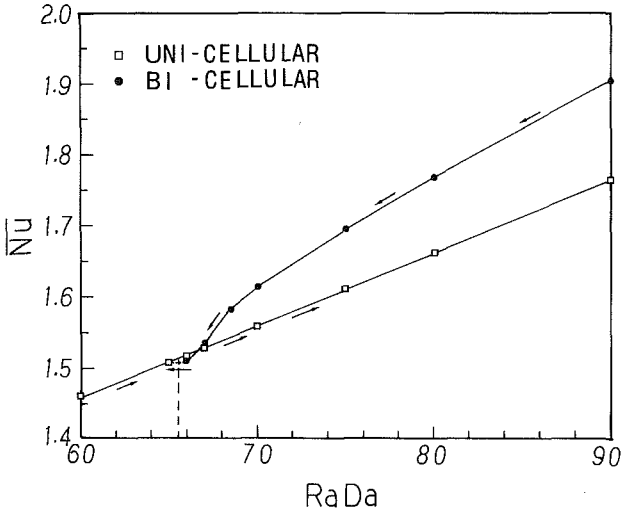

Fig. 8 Determination of the bifurcation point of the branching solutions

Table 4 Comparison of overall heat transfer rates for three flow patterns with values from other numerical works

RaDa	MODE 1	MODE 2	MODE 3	other numerical works
50	1.341	---	---	1.328[*1], 1.335[*2] 1.363[*3], 1.358[*4]
100	1.861	2.030	---	1.829[*1], 1.844[*2] 1.876[*4]
150	2.295	2.516	2.601	2.26[*2], 2.30[*4]
200	2.657	2.903	3.106	2.626[*1], 2.63[*2] 2.69[*4]

*1 : Caltagirone (1976)
*2 : Bau (1984b)
*3 : Burns and Tien (1979)
*4 : Echigo el al. (1978a)

despite the change of flow pattern itself being an abrupt, unstable process, the difference between the overall heat transfer rates is continuous; this contrasts to the reported case of a spheric annulus (Caltagirone, 1980) in which two MODEs were shown. Although there is the same final restriction of the computer capacity as the current turbulence investigation encounters, it is interesting to consider that we may obtain even higher MODEs with even finer flow structures by increasing the RaDa numbers and, at the same time, involving higher modes, which is equal to increasing grid numbers in a finite difference scheme. The process of determining the bifurcation point is shown in Fig. 8. From converged bicellular solutions obtained using the initial condition in Table 2, RaDa number is decreased step by step and at every step the converged steady-state solutions are obtained for the next step. This process is continued until the secondary flow at the top region disappears and the flow transits to the unicellular one; this transition is verified by the abrupt change in the values of dominant modes and by the plotting of the flow pattern as well. At the last step, much computing time was used because of the change of flow patterns. However, as the RaDa number approaches the bifurcation point, the difference between the Nusselt numbers of the two MODEs decreases continuously to zero, if the numerical error of about 0.2 percent is neglected. Thus, there exists a critical RaDa number at which the two MODEs have the same Nusselt numbers so that at that critical point the change of flow patterns will not exert any influence on the surroundings of the annulus as a whole when we consider the total energy balance. This bifurcation point, therefore, might be a critical one for the onset of unstable phenomenon. Compared with experimental data 65 ± 4 (Caltagirone, 1976), the numerically determined critical value corresponding to the onset of secondary flow in the present study is 65.5 ± 0.5. The value is slightly smaller than that at which a perturbation of the one-dimensional periodic wave along the direction of the axis of the annulus becomes unstable, 67.0, as estimated by a simplified stability analysis (Caltagirone, 1976).

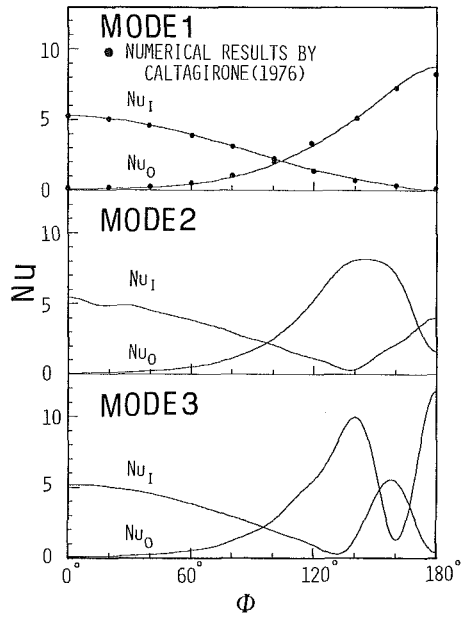

Fig. 9 Local Nusselt numbers for three branching solutions, MODE 1, MODE 2, and MODE 3, as shown in Fig. 2

It is necessary to be noted that in Caltagirone's experiment the flow was reported to have changed to a three-dimensional fluctuating spiral one rather than the bicellular one, so the critical value obtained here agrees with his experimental data in a sense that both represent the critical value under which two-dimensional unicellular flow is the unique flow pattern. There is, however, no reason to exclude the possibility that this bicellular flow occurs in the experiment at a RaDa number above but not far from the critical one, with the experimental perturbations minimized.

Another bifurcation point in Fig. 7 is obtained with a similar procedure. MODE 3 is found to transit to MODE 1 rather than MODE 2 when RaDa is decreased step by step; this can be explained by the similarity of their flow structures at the top region of the annulus. There also exists an intersection point of MODE 2 and 3. The Nusselt numbers of MODE 2 becomes smaller than those of MODE 3 when the RaDa number exceeds that point, and MODE 2 becomes apt to change to MODE 3 under perturbations; this needs verification by experiments that take bifurcation into consideration.

Influence of Flow Patterns on Overall Heat Transfer. In Table 4, the overall heat transfer rates are listed for the three MODEs and compared with the data from previous works by finite-difference methods. The Nusselt numbers for MODE 1, the unicellular flow, agree very well with those from previous works and will be taken to represent them later. No data, however, are available to compare with those for MODE 2 and MODE 3, which deviate from MODE 1 by a large margin, up to 14 percent.

In Fig. 9 local heat transfer rates are plotted. MODE 1 is compared with solutions by Caltagirone (1976); the agreement is satisfactory. MODE 2 and MODE 3, depending upon the

Downloaded 17 Dec 2010 to 193.140.21.150. Redistribution subject to ASME license or copyright; see http://www.asme.org/terms/Terms_Use.cfm

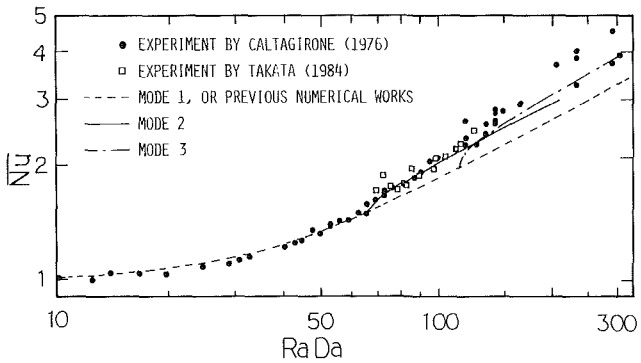

Fig. 10 Comparison of overall heat transfer rates for three branching solutions with experimental data

flow structure, give more peaks and valleys in distributions of local heat transfer rates, which enhances overall heat transfer. These numerical results are compared with experimental data in Fig. 10, where we can find that the Nusselt numbers for MODE 1, or previous works, depart from the experimental data when the RaDa number exceeds about 65.5, and the deviation increases with the increasing of the RaDa number. The values for MODE 2 and MODE 3, the bicellular and tricellular flows, agree better with experimental results in the moderate and higher RaDa regions, respectively.

Although the present study is restricted by the limitation of two-dimensional analysis and by the symmetry conditions, it gives major characteristics of flow patterns and heat transfer, and is very informative, since the transient, asymmetric three-dimensional numerical analysis in this system would be, if not impossible, formidably costly considering the current capacity of computers.

Conclusion

Numerical results have been presented for an inner-heated horizontal cylinderical porous annulus of radius ratio 2.0, with RaDa numbers ranging from 1 to 300, which covers the experimental data available. Through investigation of flow patterns, the dominant modes, and the bifurcation phenomenon, the following conclusions were obtained:

1 Branching solutions in which higher modes are dominant appear one after another with increasing RaDa numbers; this causes the flow pattern to change to a finer structure. Three MODEs of flow patterns were found corresponding to different initial conditions.

2 The bifurcation is not abrupt but continuous on the Nu-RaDa plane. There exists a critical RaDa number at which two MODEs of quite different flow structure have the same overall heat transfer rates so that the unstable phenomenon can be considered to occur easily.

3 The numerically determined bifurcation point at which the secondary flow occurs agrees remarkably well with the critical RaDa number from experimental observations.

4 In the higher RaDa region, overall heat transfer rates calculated from multicellular flows agree much better with experiment data than those from previous works or from unicellular flow.

5 The exact solutions from first-term approximation can be used as a convenient and effective evaluation of flow configuration and heat transfer rates at lower RaDa numbers.

6 The steady-state analysis is found to produce additional branching solutions that are unstable in transient analysis.

7 By using an insufficient truncating number N, we will risk losing the branching solutions of the higher MODE important at high RaDa number regions.

8 The rational Runge-Kutta methods has a very attractive feature due to its stability at much larger time intervals, and is highly efficient to the nonlinear ordinary differential systems derived from natural convection problem.

Acknowledgments

The authors would like to acknowledge the financial support of the Japan Atomic Energy Research Institute (JAERI) and to express their gratitude to Dr. K. Sanokawa, JAERI, for his valuable suggestions and supports.

The authors are also grateful to Mr. K. Kiku for his assistance in conducting the calculations.

Finally the authors thank the reviewers for their helpful comments.

References

Bau, H. H., 1984a, "Low Rayleigh Number Thermal Convection in a Saturated Porous Medium Bounded by Two Horizontal, Eccentric Cylinders," ASME JOURNAL OF HEAT TRANSFER, Vol. 106, pp. 166–175.

Bau, H. H., 1984b, "Thermal Convection in a Horizontal, Eccentric Annulus Containing a Saturated Porous Medium—an Extended Perturbation Expansion," *Int. J. Heat Mass Transfer*, Vol. 27, pp. 2277–2287.

Burns, P. J., and Tien, C. L., 1979, "Natural Convection in Porous Media Bounded by Concentric Spheres and Horizontal Cylinders," *Int. J. Heat Mass Transfer*, Vol. 22, pp. 929–939.

Caltagirone, J. P., 1976, "Thermoconvective Instabilities in a Porous Medium Bounded by Two Concentric Horizontal Cylinders," *J. Fluid Mech.*, Vol. 76, pp. 337–362.

Caltagirone, J. P., Combarnous, M., and Mojtabi, A., 1980, "Natural Convection Between Two Concentric Spheres: Transition Toward a Multicellular Flow," *Num. Heat Transfer*, Vol. 3, pp. 107–114.

Echigo, R., Hasegawa, S., Tottori, S., Shimomura, H., and Okamoto, Y., 1978a, "An Analysis on the Radiative and Free Convective Heat Transfer in a Horizontal Annulus With Permeable Insulator," *Proc. 6th International Heat Transfer Conf.*, Vol. 3, pp. 385–390.

Echigo, R, Hasegawa, S. Tottori, S., Shimomura, H., and Okamoto, Y., 1978b, "Studies on Thermal Insulation for a Horizontal Annulus at High Temperature and High Pressure (1st Report, Free Convection in a Horizontal Annulus With Constant Wall Temperature" [in Japanese], *Transactions of JSME*, Vol. 45, pp. 91–98.

Finlayson, B. A., 1972, *The Method of Weighted Residual and Variational Principle*. Academic Press, New York.

Facas, G. N., and Farouk, B., 1983, "Transient and Steady-State Natural Convection in Porous Medium Between Two Concentric Cylinders," ASME JOURNAL OF HEAT TRANSFER, Vol. 105, pp. 660–663.

Gollub, P., and Orszag, S. A., 1977, "Numerical Analysis of Special Method: Theory and Applications," Regional Conf. Series in Applied Maths, Vol. 26, Arrowsmith.

Joseph, D. D., 1985, "Hydrodynamic Stability and Bifurcation," in: *Hydrodynamic Instabilities and the Transition to Turbulence*, 2nd ed., H. L. Swiney, and J. P. Gottlub, eds., Springer-Verlag, Berlin, pp. 27–76.

Krishnamurti, R., 1970, "On the Transition to Turbulent Convection," *J. Fluid Mech.*, Vol. 42, pp. 295–307.

Krishnamurti, R., 1973, "Some Further Studies on the Transition to Turbulent Convection," *J. Fluid Mech.*, Vol. 60, pp. 285–303.

Malkus, W. V. R., 1964, "The Heat Transport and Specturm of Thermal Turbulence," *Proc. Roy. Soc. A.*, Vol. 225, pp. 196–212.

Masuoka, T., Sakamoto, N., and Katsuhara, T., 1980, "Free Convection Heat Transfer in a Porous Medium Between Horizontal Concentric Cylinders" [in Japanese], *Transactions of JSME*, Vol. 46, pp. 919–926.

Takata, Y., 1984, "Three Dimensional Natural Convection in Cylindric Annuli" [in Japanese], Doctoral Thesis, Kyushu University, Japan.

Wambecq, A., 1978, "Rational Runge–Kutta Methods for Solving Systems of Ordinary Differential Equations," *Computing*, Vol. 20, pp. 333–342.

APPENDIX A

The coefficients of equations (10) and (11), corresponding to trial function 1, are

$$C_1(m, n) = \frac{m}{2(a^2+m^2)} [1 - R(-1)^m]\delta_{n1}/C_4 \tag{A1}$$

$$C_2(i, m, n) = \frac{im[R(-1)^{i-m} - 1]}{4[a^2+(i+m)^2)][a^2+(i-m)^2]} (2a^2n + a^2 + i^2 - m^2)/C_4 \tag{A2}$$

Downloaded 17 Dec 2010 to 193.140.21.150. Redistribution subject to ASME license or copyright; see http://www.asme.org/terms/Terms_Use.cfm

$$C_3(i, m, n) = \frac{im[R(-1)^{i-m} - 1]}{4[a^2 + (i+m)^2)][a^2 + (i-m)^2]} (2a^2 n - a^2 - i^2 - m^2)(1 + \delta_{n1})/C_4 \quad \text{(A3)}$$

where

$$C_4 = \frac{\pi^2}{4\text{RaDa}}\, a\left(n^2 + \frac{m^2}{a^2}\right) \quad \text{(A4)}$$

$$C_5(i, j, p, q) = \left(\frac{\pi}{4}\right)^2 D_{p-i} D_i D_{q-j} [(1 + \delta_{0j})(p-i)(q-j) - ij] \quad \text{(A5)}$$

$$C_6(q) = -\frac{\pi}{4}\, q \quad \text{(A6)}$$

$$C_7(p, q) = -\left(\frac{p^2}{a^2} + q^2\right) a\, \frac{\pi^2}{4}\, (1 + \delta_{0q}) \quad \text{(A7)}$$

where

$$D_x = \begin{cases} 1 & (x > 0) \\ 0 & (x = 0) \\ -1 & (x < 0) \end{cases} \quad \text{(A8)}$$

stands for the Dirichlet function.

APPENDIX B

The coefficients of equations (14) and (15), corresponding to trial function 2, are

$$C_1'(m, n) = \frac{m}{2(a^2 + m^2)} [1 - R(-1)^m]\delta_{n1}/C_4' \quad \text{(B1)}$$

$$C_2'(i, m, n) = \left\{\frac{\pi^2}{8}\, na\delta_{im} + [(-1)^{i+m} - 1] \frac{im\pi}{4(i^2 - m^2)}\right\}(1 - \delta_{nN})/C_4' \quad \text{(B2)}$$

$$C_3'(i, m, n) = \left\{\frac{\pi^2}{8}\, na\delta_{im} - [(-1)^{i+m} - 1] \frac{im\pi}{4(i^2 - m^2)}\right\}(1 + \delta_{n1})/C_4' \quad \text{(B3)}$$

where

$$C_4' = \frac{\pi^2}{4\text{RaDa}}\, a\left(n^2 + \frac{m^2}{a^2}\right) \quad \text{(B4)}$$

$$C_5'(I, i, p, j, q) = D_{q-j} X_0 ap(1 + \delta_{0j})\left\{\frac{1}{8}\,(q-j)[(X_2 - X_1)(4a^2 + p^2 + 3I^2 + 3i^2) - 6Ii(X_2 + X_1)] - Iq[I(X_2 - X_1) - i(X_2 + X_1)]\right\}, \quad \text{(B5)}$$

$$C_6'(I, p, q) = \frac{-pqaI\left[1 - \frac{1}{R}(-1)^{I+p}\right]}{[a^2 + (I+p)^2][a^2 + (I-p)^2]} \quad \text{(B6)}$$

$$C_7'(i, p, q) = -(1 + \delta_{0q})\pi pi(p^2 + 2a^2q^2 + 2a^2 + i^2) \frac{\left[1 - \frac{1}{R^2}(-1)^{I+p}\right]}{[4a^2 + (p+i)^2][4a^2 + (p-i)^2]} \quad \text{(B7)}$$

where

$$X_0 = \left[1 - \frac{1}{R^2}(-1)^{I+i+p}\right] \quad \text{(B8)}$$

$$X_1 = \{[4a^2 + (p + I + i)^2][4a^2 + (p - I - i)^2]\}^{-1} \quad \text{(B9)}$$

$$X_2 = \{[4a^2 + (p + I - i)^2][4a^2 + (p - I + i)^2]\}^{-1} \quad \text{(B10)}$$

APPENDIX C

The initial condition of the uniform temperature distribution is $\Theta = 0$ (at $t = 0$), i.,e.,

$$\theta + 1 - \frac{\ln r}{\ln R} = 0 \quad \text{(C1)}$$

Expanding ($\ln r/\ln R - 1$) with the trial function series $1/r \sin (1/a \ln r/\ln R)\cos j\phi$, we obtain the resulting condition as follows:

all $T_{ij} = 0$ except

$$T_{i0} = -\frac{2i}{\pi(a^2 + i^2)}\left\{1 + \frac{2a[(-1)^i R - 1]}{\pi(a^2 + i^2)}\right\} \quad \text{(C2)}$$

In Fig. C1, the time-dependent results are compared with the previous data (Facas and Farouk, 1983). The time interval here is taken as 0.001, the same as that used in their work.

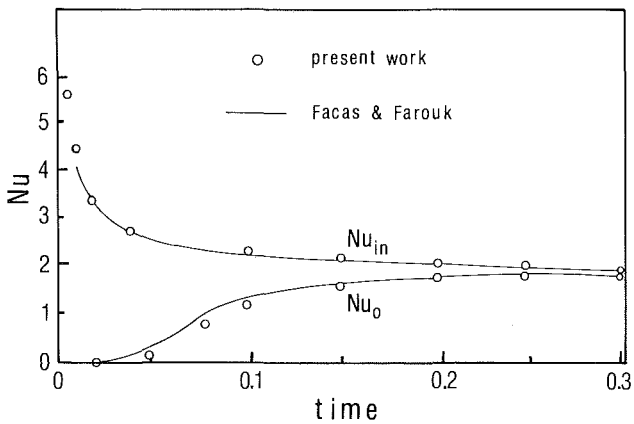

Fig. C1 Time variation of mean Nusselt numbers for both inner and outer boundaries, RaDa = 100

Downloaded 17 Dec 2010 to 193.140.21.150. Redistribution subject to ASME license or copyright; see http://www.asme.org/terms/Terms_Use.cfm

A Numerical Model of the Flow and Heat Transfer in a Rotating Disk Chemical Vapor Deposition Reactor

G. Evans
Computational Mechanics Division,
Sandia National Laboratories,
Livermore, CA 94550

R. Greif
Mechanical Engineering Department,
University of California,
Berkeley, CA 94720

Steady, laminar, axisymmetric, and circumferentially uniform flow and heat transfer, including the effects of variable properties and buoyancy, have been modeled within a rotating disk chemical vapor deposition (CVD) reactor. The reactor is oriented vertically, with the hot, isothermal, spinning disk facing upward. The Navier–Stokes and energy equations have been solved for the carrier gas helium. The solutions have been obtained over a range of parameters, which is of importance in CVD applications. The primary parameters are the ratio of the disk temperature to the free stream temperature T_w/T_∞, *the disk Reynolds number* $Re = r_d^2\omega/\nu_\infty$, *a mixed convection parameter* $Gr/Re^{3/2} = g(\rho_\infty - \rho_w)/(\rho_w\omega\sqrt{\omega\nu_\infty})$, *the dimensionless inlet velocity* $u_\infty/\sqrt{\omega\nu_\infty}$, *and two geometric parameters* r_o/r_d *and* L/r_d. *Results are obtained for the velocity and the temperature fields and for the heat flux at the surface of the rotating disk. Comparisons are made with the one-dimensional, variable-property (excluding buoyant effects), infinite rotating disk solutions of Pollard and Newman. Results are presented in terms of a local Nusselt number. The potential uniformity of CVD in this geometry can be inferred from the variation of the Nusselt number over the surface of the rotating disk. The effects of buoyancy and the finite size of the rotating disk within the cylindrical reactor are clearly evident in the present work.*

Introduction

Chemical vapor deposition (CVD) is an important process for fabricating microelectronic circuits. A wide variety of semiconductors can be made using this process, and a large degree of control can be exerted over the deposition by altering the composition and concentration of active species in the gas phase. Individual layers of materials can be deposited on a substrate by introducing various active species into the gas stream in the desired sequence and the rates of deposition with CVD can be of the order of microns/minute. Although the potential exists for obtaining uniform deposition, the deposition process is dependent on the flow and the heat transfer from the heated substrate to the gas, especially when deposition occurs near atmospheric pressure. Convection in the gas phase becomes a consideration of increasing importance, especially when high deposition rates are desired. The geometry of the reactor is important because, in order to replenish the reactants, the gas must be continuously passed over the heated substrate. Recirculation of the gas due to geometry or buoyant effects has a strong effect on the uniformity of the heat transfer and consequently the mass transfer. Because of the importance of gas phase chemistry in the CVD process, as pointed out by Coltrin et al. (1984) for the deposition of Si from SiH_4, understanding the convection and diffusion processes also becomes important. Most CVD reactors consist of a forced flow past a heated substrate in a channel. The growth of the momentum, energy, and concentration boundary layers along the substrate leads to nonuniform surface fluxes and research is being conducted to understand and quantify the phenomena (Giling, 1982; Kapur et al., 1985; Stock and Richter, 1986).

Two geometries that ideally yield uniform boundary layers and uniform deposition are the infinite planar or axisymmetric stagnation flow and the infinite rotating disk flow (see White, 1974). Hitchman and Curtis (1982) examined epitaxial deposition of Si from $SiCl_4$ in a rotating disk reactor and developed a simple one-dimensional theory to explain their results. They noted, however, that the flow in the reactor could not be described in terms of the infinite disk solutions. Pollard and Newman (1980) performed a theoretical study of CVD of Si from $SiCl_4$ near a rotating disk. They used the von Karman (1921) similarity transformation to obtain an ODE boundary value problem describing the transport of mass, momentum, and energy. Their study included the effects of variable gas properties. However, the effects of geometry and buoyancy were not considered due to the one dimensionality of the study. Recently, Houtman et al. (1986) performed a numerical study of two-dimensional, axisymmetric, steady transport within a stagnation flow reactor. The effects of buoyancy and finite geometry on the heat transfer were obtained and results were presented in terms of the region over which a one-dimensional solution would apply.

Analysis

In many cases of CVD the active species exist in only small concentrations relative to the carrier gas so that the solution of the continuity, momentum, and energy equations for the carrier gas can be separated from the solution of the species mass conservation equations. For certain system operating parameters the heat flux at the surface may be essentially uniform. The equations governing the transport of mass (for Fickian diffusion) and energy are similar and, provided that the boundary conditions for species transport are uniform over the surface, these same system parameters that result in uniform heat transport would also be expected in many cases to produce uniform mass transport (deposition). The purpose of this paper is to obtain the local heat transfer for the carrier

Contributed by the Heat Transfer Division for publication in the JOURNAL OF HEAT TRANSFER. Manuscript received by the Heat Transfer Division July 22, 1986.

Copyright © 1987 by ASME

Downloaded 17 Dec 2010 to 193.140.21.150. Redistribution subject to ASME license or copyright; see http://www.asme.org/terms/Terms_Use.cfm

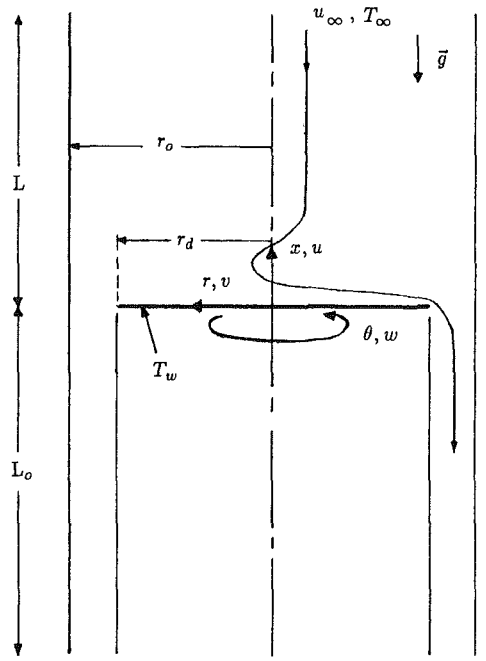

Fig. 1 Geometry and coordinate system of rotating disk reactor

gas over a range of the operating parameters that are important in CVD. By determining the domain of these parameters that yields uniform surface heat flux, an understanding of the operating regime that produces uniform deposition can be obtained.

The present study is similar to that of Houtman et al. (1986); however, this work considers a rotating, heated, circular disk (Fig. 1). The disk of radius r_d is centered within a larger, stationary cylindrical tube of radius r_o. The spin axis of the disk is aligned with the axis of the tube and with the gravitational vector. As shown in Fig. 1, $\vec{g}$ is in the $-x$ direction (the heated disk faces vertically upward). The gas is helium and the flow field is assumed to be laminar, steady, axisymmetric, and circumferentially uniform. Boundary layer assumptions are not made since recirculating flow may occur due to the finite geometry and the buoyancy associated with the heated surface facing upward. Helium at ambient temperature, $T_\infty = 300$ K, enters the reactor at $x = L$ with no rotation and as it moves toward the disk at $x = 0$ begins to rotate. At the edge of the disk ($r = r_d$) the gas turns downward and leaves the reactor through the annular region ($r_d < r < r_o$) below the disk ($-L_o \le x < 0$). For the purposes of the analysis the disk is assumed to have zero thickness and the region directly underneath the disk ($0 \le r \le r_d$, $-L_o \le x < 0$) does not rotate and is not part of the solution domain. The local heat transfer on the surface of the rotating disk has been determined to be insensitive to the thickness of the disk.

The governing equations in cylindrical coordinates are:

Continuity:

$$\frac{1}{r}\frac{\partial}{\partial r}(\rho r v) + \frac{\partial}{\partial x}(\rho u) = 0 \tag{1}$$

Axial (x) component of momentum:

$$\frac{1}{r}\frac{\partial}{\partial r}(r\rho v u) + \frac{\partial}{\partial x}(\rho u u) = -\frac{\partial p^*}{\partial x} - \rho g + \frac{1}{r}\frac{\partial}{\partial r}\left[r\mu\left(\frac{\partial u}{\partial r} + \frac{\partial v}{\partial x}\right)\right] + \frac{\partial}{\partial x}\left[2\mu\frac{\partial u}{\partial x} - \frac{2}{3}\mu(\vec{\nabla}\cdot\vec{v})\right] \tag{2}$$

Radial (r) component of momentum:

$$\frac{1}{r}\frac{\partial}{\partial r}(r\rho v v) + \frac{\partial}{\partial x}(\rho v u) - \frac{\rho w^2}{r} = -\frac{\partial p^*}{\partial r} + \frac{1}{r}\frac{\partial}{\partial r}\left\{r\mu\left[2\frac{\partial v}{\partial r} - \frac{2}{3}(\vec{\nabla}\cdot\vec{u})\right]\right\} - \frac{\mu}{r}\left[2\frac{v}{r} - \frac{2}{3}(\vec{\nabla}\cdot\vec{v})\right] + \frac{\partial}{\partial x}\left[\mu\left(\frac{\partial u}{\partial r} + \frac{\partial v}{\partial x}\right)\right] \tag{3}$$

Nomenclature

c_p = specific heat, J/(kg-K)
F = dimensionless radial velocity
G = dimensionless circumferential velocity
g = acceleration of gravity, m/s^2
Gr = Grashof number = $g(1-\bar{\rho}_w)r_d^3/(\bar{\rho}_w\nu_\infty^2)$
Gr/Re$^{3/2}$ = mixed convection parameter = $g(1-\bar{\rho}_w)/(\bar{\rho}_w\omega\sqrt{\omega\nu_\infty})$
H = dimensionless axial velocity
k = thermal conductivity, W/(m-K)
$\bar{k}$ = dimensionless thermal conductivity
L = distance from reactor inlet to rotating disk, m
L_o = distance from rotating disk to reactor outlet, m
Nu = Nusselt number = $\partial\Theta/\partial\bar{x}\,|_{\bar{x}=0}$
P = dimensionless dynamic and hydrostatic pressure
p = pressure, Pa
p^* = dynamic and hydrostatic pressure, Pa
p_m = dynamic pressure = $p^* + \rho_\infty gx$, Pa
$\bar{p}_m$ = dimensionless motion pressure
Pr = Prandtl number = $(c_p\mu/k)\,|_\infty$
R = gas constant, J/(kg-K)
r = radial coordinate, m
$\bar{r}$ = dimensionless radial coordinate
Re = disk Reynolds number = $r_d^2\omega/\nu_\infty$
T = temperature, K
u = axial velocity, m/s
$\bar{u}$ = dimensionless axial velocity
v = radial velocity, m/s
$\bar{v}$ = dimensionless radial velocity
w = circumferential velocity, m/s
$\bar{w}$ = dimensionless circumferential velocity
x = axial coordinate, m
$\bar{x}$ = dimensionless axial coordinate
η = dimensionless axial coordinate
Θ = dimensionless temperature
θ = circumferential coordinate
μ = dynamic viscosity, kg/(m-s)
$\bar{\mu}$ = dimensionless dynamic viscosity
ν = kinematic viscosity, m^2/s
ρ = density, kg/m^3
$\bar{\rho}$ = dimensionless density
ω = disk spin rate, s^{-1}

Subscripts

d = evaluated at the radius of the disk
o = evaluated at the radius of the reactor
w = evaluated at the surface of the disk
∞ = evaluated at the inlet of the reactor

Downloaded 17 Dec 2010 to 193.140.21.150. Redistribution subject to ASME license or copyright; see http://www.asme.org/terms/Terms_Use.cfm

Circumferential (θ) component of momentum:

$$\frac{1}{r}\frac{\partial}{\partial r}(r\rho vw)+\frac{\partial}{\partial x}(\rho uw)$$

$$=-\frac{\rho vw}{r}+\frac{1}{r^2}\frac{\partial}{\partial r}\left[r^3\mu\frac{\partial}{\partial r}\left(\frac{w}{r}\right)\right]+\frac{\partial}{\partial x}\left(\mu\frac{\partial w}{\partial x}\right) \tag{4}$$

Energy equation:

$$\frac{1}{r}\frac{\partial}{\partial r}(r\rho vT)+\frac{\partial}{\partial x}(\rho uT)$$

$$=\frac{1}{r}\frac{\partial}{\partial r}\left(r\frac{k}{c_p}\frac{\partial T}{\partial r}\right)+\frac{\partial}{\partial x}\left(\frac{k}{c_p}\frac{\partial T}{\partial x}\right) \tag{5}$$

In the above energy equation, viscous dissipation and compressibility effects have been neglected, and the specific heat is assumed to be constant at 5192.6 J/(kg-K). The equation of state for an ideal gas is used in the analysis

$$\rho=p/RT \tag{6}$$

In equations (2) and (3), p^* includes the dynamic and hydrostatic components of the pressure. The pressure p, which appears in equation (6), is assumed to be constant. This method of treating pressure is valid for flows with a small Mach number (Paolucci, 1982). The dynamic viscosity and the thermal conductivity are determined from the Chapman-Enskog equations[1]

$$\mu=26.69\times10^{-7}\sqrt{MT}/(\sigma^2\Omega_v),\ \mu \text{ in kg/(m-s)} \tag{7}$$

$$k=8.326\times10^{-2}\sqrt{T/M}/(\sigma^2\Omega_v),\qquad k \text{ in W/(m-K)} \tag{8}$$

The set of parameters which will be used to characterize the gas flow and the heat transfer within the rotating disk reactor of Fig. 1 are obtained from the nondimensionalization of equations (1)-(5) and from the geometry and the boundary conditions of the problem. The similarity transformation of van Karman (1921) has been used with the finite radius of the disk replacing the variable radial coordinate. The viscous length scale for the axial coordinate allows for adequate resolution of the important gradients of velocity and temperature at the surface of the disk. The radial coordinate is scaled with the radius of the disk. The gas properties are scaled with their values at the inflow boundary.

Specifically, the transformation $\bar{r}=r/r_d$, $\bar{x}=x\sqrt{\omega/\nu_\infty}$, $\bar{u}=u/\sqrt{\omega\nu_\infty}$, $\bar{v}=v/(r_d\omega)$, $\bar{w}=w/(r_d\omega)$, $\bar{p}_m=p_m/(\mu_\infty\omega)$, $\Theta=(T-T_\infty)/(T_w-T_\infty)$, $\bar{\rho}=\rho/\rho_\infty$, $\bar{\mu}=\mu/\mu_\infty$, $\bar{k}=k/k_\infty$ applied to equations (1)-(5) results in the following dimensionless equations:

$$\frac{1}{\bar{r}}\frac{\partial}{\partial\bar{r}}(\bar{\rho}\bar{r}\bar{v})+\frac{\partial}{\partial\bar{x}}(\bar{\rho}\bar{u})=0 \tag{9}$$

$$\frac{1}{\bar{r}}\frac{\partial}{\partial\bar{r}}(\bar{r}\bar{\rho}\bar{v}\bar{u})+\frac{\partial}{\partial\bar{x}}(\bar{\rho}\bar{u}\bar{u})=-\frac{\partial\bar{p}_m}{\partial\bar{x}}+\frac{\mathrm{Gr}}{\mathrm{Re}^{3/2}}\frac{\bar{\rho}_w(1-\bar{\rho})}{(1-\bar{\rho}_w)}$$

$$+\frac{1}{\bar{r}}\frac{\partial}{\partial\bar{r}}\left[\bar{r}\bar{\mu}\left(\frac{1}{\mathrm{Re}}\frac{\partial\bar{u}}{\partial\bar{r}}+\frac{\partial\bar{v}}{\partial\bar{x}}\right)\right]+\frac{\partial}{\partial\bar{x}}\left\{2\bar{\mu}\frac{\partial\bar{u}}{\partial\bar{x}}\right.$$

$$\left.-\frac{2}{3}\bar{\mu}\left[\frac{1}{\bar{r}}\frac{\partial}{\partial\bar{r}}(\bar{r}\bar{v})+\frac{\partial\bar{u}}{\partial\bar{x}}\right]\right\} \tag{10}$$

$$\frac{1}{\bar{r}}\frac{\partial}{\partial\bar{r}}(\bar{r}\bar{\rho}\bar{v}\bar{v})+\frac{\partial}{\partial\bar{x}}(\bar{\rho}\bar{v}\bar{u})-\frac{\bar{\rho}\bar{w}^2}{\bar{r}}=-\frac{1}{\mathrm{Re}}\frac{\partial\bar{p}_m}{\partial\bar{r}}$$

$$+\frac{1}{\mathrm{Re}}\frac{1}{\bar{r}}\frac{\partial}{\partial\bar{r}}\left\{\bar{r}\bar{\mu}\left[2\frac{\partial\bar{v}}{\partial\bar{r}}-\frac{2}{3}\left(\frac{1}{\bar{r}}\frac{\partial}{\partial\bar{r}}(\bar{r}\bar{v})+\frac{\partial\bar{u}}{\partial\bar{x}}\right)\right]\right\}$$

$$-\frac{1}{\mathrm{Re}}\frac{\bar{\mu}}{\bar{r}}\left\{2\frac{\bar{v}}{\bar{r}}-\frac{2}{3}\left[\frac{1}{\bar{r}}\frac{\partial}{\partial\bar{r}}(\bar{r}\bar{v})+\frac{\partial\bar{u}}{\partial\bar{x}}\right]\right\}$$

$$+\frac{\partial}{\partial\bar{x}}\left[\bar{\mu}\left(\frac{1}{\mathrm{Re}}\frac{\partial\bar{u}}{\partial\bar{r}}+\frac{\partial\bar{v}}{\partial\bar{x}}\right)\right] \tag{11}$$

$$\frac{1}{\bar{r}}\frac{\partial}{\partial\bar{r}}(\bar{r}\bar{\rho}\bar{v}\bar{w})+\frac{\partial}{\partial\bar{x}}(\bar{\rho}\bar{u}\bar{w})=-\frac{\bar{\rho}\bar{v}\bar{w}}{\bar{r}}$$

$$+\frac{1}{\mathrm{Re}}\frac{1}{\bar{r}^2}\frac{\partial}{\partial\bar{r}}\left[\bar{r}^3\bar{\mu}\frac{\partial}{\partial\bar{r}}\left(\frac{\bar{w}}{\bar{r}}\right)\right]+\frac{\partial}{\partial\bar{x}}\left(\bar{\mu}\frac{\partial\bar{w}}{\partial\bar{x}}\right) \tag{12}$$

$$\frac{1}{\bar{r}}\frac{\partial}{\partial\bar{r}}(\bar{r}\bar{\rho}\bar{v}\Theta)+\frac{\partial}{\partial\bar{x}}(\bar{\rho}\bar{u}\Theta)$$

$$=\frac{1}{\mathrm{Re}}\frac{1}{\mathrm{Pr}}\frac{1}{\bar{r}}\frac{\partial}{\partial\bar{r}}\left(\bar{r}\bar{k}\frac{\partial\Theta}{\partial\bar{r}}\right)+\frac{1}{\mathrm{Pr}}\frac{\partial}{\partial\bar{x}}\left(\bar{k}\frac{\partial\Theta}{\partial\bar{x}}\right) \tag{13}$$

The boundary conditions are:

$$\bar{u}=\bar{v}=\bar{w}=\frac{\partial\Theta}{\partial\bar{r}}=0 \text{ for } \bar{r}=r_o/r_d$$

$$\text{and } -L_o\sqrt{\omega/\nu_\infty}\le\bar{x}\le L\sqrt{\omega/\nu_\infty}$$

$$\bar{u}=\bar{v}=\bar{w}=\frac{\partial\Theta}{\partial\bar{r}}=0 \text{ for } \bar{r}=1 \text{ and } -L_o\sqrt{\omega/\nu_\infty}\le\bar{x}<0$$

$$\bar{v}=\bar{w}=\frac{\partial(\bar{u},\,\Theta)}{\partial\bar{r}}=0 \text{ for } \bar{r}=0 \text{ and } 0<\bar{x}\le L\sqrt{\omega/\nu_\infty} \tag{14}$$

$$\bar{u}=\bar{v}=0,\quad \bar{w}=\bar{r},\quad \Theta=1 \text{ for } \bar{x}=0 \text{ and } 0\le\bar{r}\le1$$

$$\bar{v}=\bar{w}=\Theta=0,\quad \bar{u}=H|_{\eta\to\infty} \text{ for } \bar{x}=L\sqrt{\omega/\nu_\infty}$$

$$\text{and } 0<\bar{r}<r_o/r_d$$

$$\frac{\partial(\bar{u},\,\bar{v},\,\bar{w},\,\Theta)}{\partial\bar{x}}=0 \text{ for } \bar{x}=-L_o\sqrt{\omega/\nu_\infty}$$

$$\text{and } 1<\bar{r}<r_o/r_d$$

where $H|_{\eta\to\infty}$ is the dimensionless axial inflow velocity from the one-dimensional solution to be presented. Note that the inlet velocity distribution is uniform over the inlet plane.

The dimensionless parameters appearing in these equations are the disk Reynolds number $\mathrm{Re}=r_d^2\omega/\nu_\infty$, the mixed convection parameter $\mathrm{Gr}/\mathrm{Re}^{3/2}=g(1-\bar{\rho}_w)/(\bar{\rho}_w\omega\sqrt{\omega\nu_\infty})$, where $\mathrm{Gr}=g(1-\bar{\rho}_w)r_d^3/(\bar{\rho}_w\nu_\infty^2)$, and the Prandtl number $\mathrm{Pr}=(c_p\mu/k)|_\infty$. The temperatures of the disk and the inlet stream are also parameters which determine the variable property ratios: μ/μ_∞, k/k_∞, and ρ/ρ_∞. The geometric parameters are r_o/r_d and L/r_d. It will be shown later that for small values of $\mathrm{Gr}/\mathrm{Re}^{3/2}$ there is no recirculation of the flow above the rotating disk. In this situation, L/r_d is not an important parameter in the problem, provided the inflow boundary is sufficiently far from the disk (greater than a boundary layer thickness). However, when $\mathrm{Gr}/\mathrm{Re}^{3/2}$ is large enough for recirculation to occur L/r_d will be shown to be an important parameter. Houtman et al. (1986) have shown that L/r_d is a significant parameter in the study of axisymmetric stagnation flow reactors. The effect of the geometric ratio L_o/r_d that specifies the outflow region has not been considered in this study; the outflow length L_o has been taken large enough for fully developed flow conditions to apply at the outflow boundary. The inlet velocity distribution is an additional parameter that enters the problem through the specification of the boundary conditions. By varying the parameters over ranges of interest in CVD, operating regimes which would result in uniform heat transport, and by analogy, uniform

[1] The collision integral, Ω_v, is given by Reid et al. (1977) as $\Omega_c\approx\frac{A}{T^{*B}}$, $A=1.16145$, $B=0.14874$, $T^*=\frac{\kappa}{\epsilon}T$, $\frac{\epsilon}{\kappa}=10.22$ K $\sigma=2.551$ Å is the collision diameter and M is the molecular weight.

Downloaded 17 Dec 2010 to 193.140.21.150. Redistribution subject to ASME license or copyright; see http://www.asme.org/terms/Terms_Use.cfm

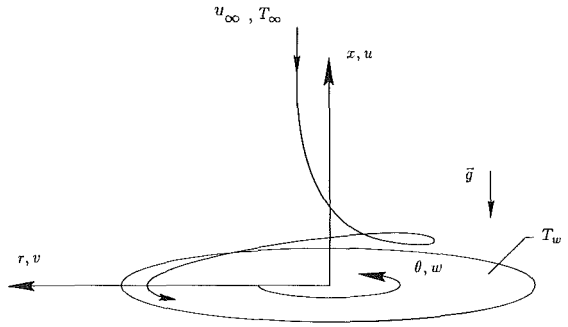

Fig. 2 Geometry and coordinate system of infinite rotating disk

mass transport, in a rotating disk reactor can be determined. Equations (9)–(13) have been solved numerically, subject to the boundary conditions (14).

Solution Method and Convergence Criteria

Equations (9)–(13) are integrated over control volumes and finite differences are used to discretize derivatives on the cylindrical grid. A combination central/upwind difference method is used for convective terms, with central differences applied to the diffusive derivatives. The solution method is semi-implicit and is based on the TEACH code (see Gosman and Pun, 1973). The method is semi-implicit because the solution algorithm consists of a tridiagonal "one variable at a time" solution, which is repeated until convergence criteria are satisfied. The SIMPLER method described by Patankar (1980) is used to determine the pressure field. The criteria for convergence are: For each equation i, where i represents one of the dependent variables $\bar{u}$, $\bar{v}$, $\bar{w}$, Θ, $\bar{p}_m$

$$\frac{1}{N}\sum_{j=1}^{N} |\text{res}_i|_j \le 0.01\,|\text{term}|_i \tag{15}$$

where $|\text{res}_i|_j$ is the absolute value of the residual of the ith equation for the jth control volume, and N is the number of control volumes. In this inequality, $|\text{term}|_i$ is the absolute value of a characteristic term in the ith equation, evaluated near the edge of the rotating disk. When these criteria are satisfied, the change per iteration proved negligible (with the change for 500 iterations being less than 1.0 percent).

One-Dimensional Solution

The von Karman (1921) transformation reduces the three-dimensional Navier–Stokes equations governing the isothermal flow about an infinite rotating disk to a system of coupled, ordinary, nonlinear differential equations. Millsaps and Pohlhausen (1952) extended the analysis to include heat transfer from an isothermal disk and Sparrow and Gregg (1960) included mass injection or suction from the disk surface. Pollard and Newman (1980) allowed variable fluid properties in their study of CVD of Si from $SiCl_4$ near a rotating disk; however, the effects of buoyancy could not be included since only the pressure distribution in the axial direction, which is uncoupled from the determination of the velocity and temperature field in such an analysis, would have been affected. The solution of the equations of Pollard and Newman (1980), restricted to a single component gas, will be used for comparison purposes when the local heat transfer results are presented. This solution will also be used in the following section to verify the two-dimensional computer code. Utilizing the similarity transformation for the infinite rotating disk (see Fig. 2), equations (1), (3)–(5) yield the following:

$$2F + H' + H\frac{d(\ln\bar{\rho})}{d\eta} = 0 \tag{16}$$

$$F^2 - G^2 + F'H - \frac{1}{\bar{\rho}}\frac{d}{d\eta}(\bar{\mu}F') = 0 \tag{17}$$

$$2FG + G'H - \frac{1}{\bar{\rho}}\frac{d}{d\eta}(\bar{\mu}G') = 0 \tag{18}$$

$$H\Theta' - \frac{1}{\text{Pr}_\infty}\frac{1}{\bar{\rho}}\frac{d}{d\eta}(\bar{k}\Theta') = 0 \tag{19}$$

where $\eta = \bar{x} = x\sqrt{\omega/\nu_\infty}$, $F(\eta) = v/(r\omega)$, $G(\eta) = w/(r\omega)$, $H(\eta) = u/\sqrt{\omega\nu_\infty}$, $\Theta(\eta) = (T - T_\infty)/(T_w - T_\infty)$. The boundary conditions are

$$F = H = 0, \quad \Theta = G = 1 \text{ for } \eta = 0$$
$$\Theta, F, G \to 0 \text{ for } \eta \to \infty \tag{20}$$

Primes denote differentiation with respect to η. Since equations (16)–(19) are restricted to a single component gas and are a subset of the equations solved by Pollard and Newman (1980) and the conditions of interest are different from those presented in their paper, we have solved equations (16)–(19) with a block tridiagonal, finite difference scheme, employing Newton's method. Properties have been evaluated using equations (7) and (8). Values of $H|_{\eta\to\infty}$ and $-\Theta'(0)$ obtained from the solution of equations (16)–(19) for helium have been given in Table 1 for several disk temperatures.

Verification of Computer Code and Adequacy of Grid Resolution

Although an experiment is being planned, there are no experimental data available for comparison with the numerical results to be presented in the next section. In order to evaluate the two-dimensional computer code, the continuity, Navier–Stokes, and energy equations (9)–(13) were solved over the domain shown in Fig. 2. Note that the geometry of Fig. 2 is a limiting case of that of Fig. 1, which is obtained by letting $r_o/r_d \to \infty$ and restricting the solution domain to the region: $0 \le r \le r_d$, $0 \le x \le L$. The boundary conditions that are used at the inflow boundary, along the symmetry axis, and on the rotating disk are the same as conditions (14). The outflow boundary conditions are

$$\frac{\partial\bar{u}}{\partial\bar{r}} = \frac{\partial\bar{w}}{\partial\bar{r}} = \frac{\partial\Theta}{\partial\bar{r}} = \frac{\partial}{\partial\bar{r}}(\bar{\rho}\bar{r}\bar{v}) = 0 \text{ for } \bar{r} = 1$$
and $$0 < \bar{x} < L\sqrt{\omega/\nu_\infty} \tag{21}$$

The numerical solution of equations (9)–(13) with boundary conditions (21), over the domain of Fig. 2, referred to as the $2D_{\text{inf}}$ solution, has been compared with the numerical solution of equations (16)–(19), referred to as the $1D$ solution. Detailed comparisons have been made but, due to space limitations, are not presented here. As a specific example, for $T_w = 1100$ K, $\text{Re} = 1000$, $\text{Gr}/\text{Re}^{3/2} = 2.2$, and $L/r_d = 2.16$, the local heat flux and the local values of the radial and the axial shear stresses obtained from the $2D_{\text{inf}}$ solution agree with the result from the $1D$ solution to within 0.2 percent at any radial position on the disk. For the geometry of Fig. 2, even at this nonzero value of the mixed convection parameter, the flow is essentially one-dimensional. It is noted that for this disk temperature and Re, the $1D$ disk heat flux agrees with the $2D_{\text{inf}}$ solution to within 0.5 percent for $\text{Gr}/\text{Re}^{3/2}$ as large as 7.7. This is not the case for a rotating disk within a cylindrical tube, as will be shown later.

For the domain of Fig. 1, where the rotating disk is situated within the cylindrical reactor, equations (9)–(13) with boundary conditions (14), referred to as the $2D$ solution, were solved on an equally spaced radial grid with $\Delta\bar{r} = 0.0256$ and a nonuniform axial grid with grid lines concentrated near the disk, with the value of $\Delta\bar{x}$ near the disk equal to 0.002882. This grid spacing resulted in 4420 control volumes. The adequacy of this grid was checked. For $T_w = 800$ K, $\text{Re} = 1000$,

Downloaded 17 Dec 2010 to 193.140.21.150. Redistribution subject to ASME license or copyright; see http://www.asme.org/terms/Terms_Use.cfm

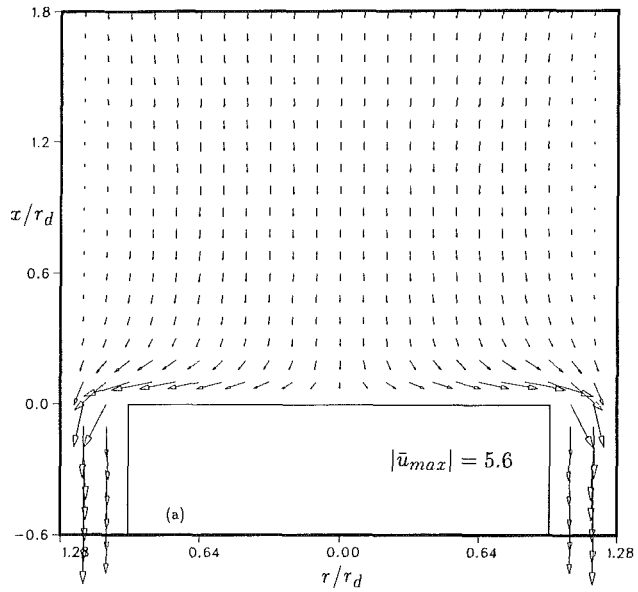

Fig. 3(*a*)

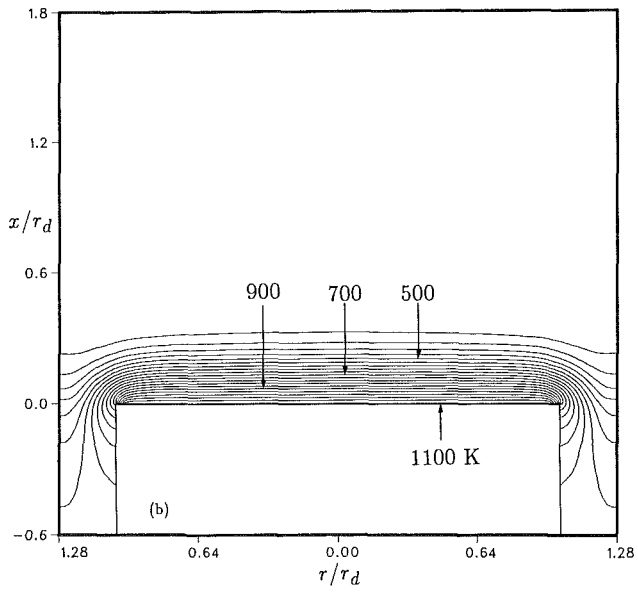

Fig. 3(*b*)

Fig. 3 Dimensionless radial and axial velocity vector field (*a*) and temperature contours (*b*) in rotating disk reactor: $T_w = 1100$ K, Re = 1000, $Gr/Re^{3/2} = 2.2$, $r_o/r_d = 1.28$, $L/r_d = 2.16$

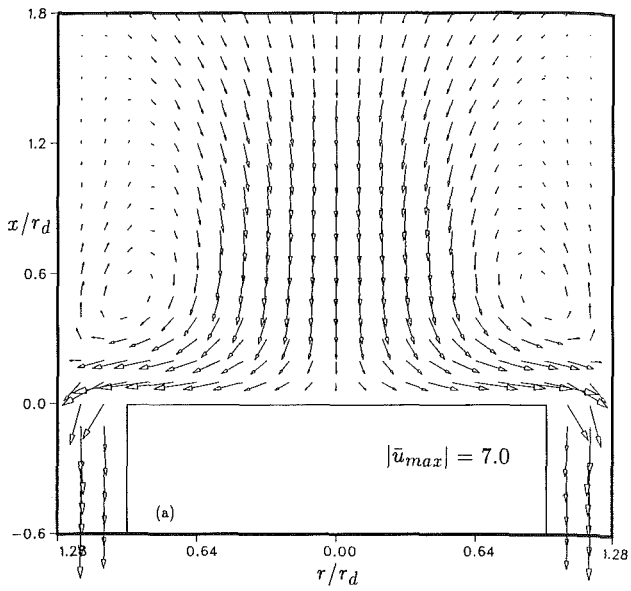

Fig. 4(*a*)

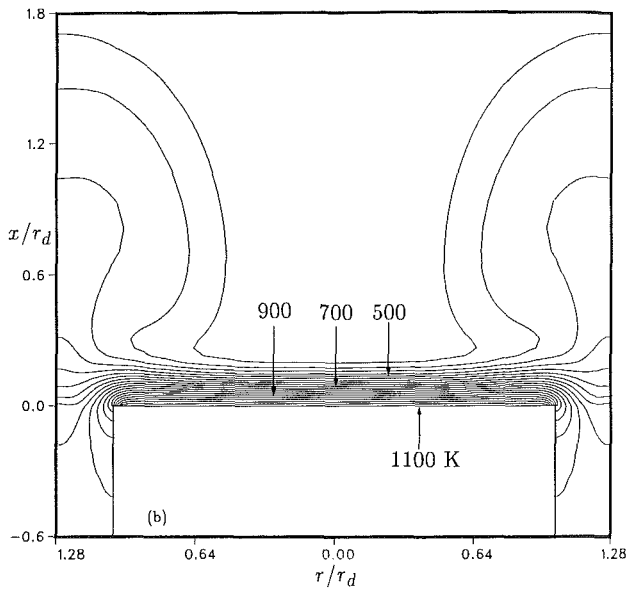

Fig. 4(*b*)

Fig. 4 Dimensionless radial and axial velocity vector field (*a*) and temperature contours (*b*) in rotating disk reactor: $T_w = 1100$ K, Re = 1000, $Gr/Re^{3/2} = 6.2$, $r_o/r_d = 1.28$, $L/r_d = 2.16$

$Gr/Re^{3/2} = 4.0$, $r_o/r_d = 1.28$, and $L/r_d = 2.16$, calculations of the local values of the disk heat flux and the disk radial shear stress changed by only 0.01 to 0.07 percent (compared at all radial locations on the surface of the disk) when the axial grid spacing was doubled to 0.00576. For the same values of the parameters, the local values of the disk heat flux and the disk shear stress changed by only 0.01 to 0.1 percent when the radial grid spacing was decreased by 20 percent to 0.020408.

Results

The velocity and the temperature fields and the local heat transfer from the solution of the two-dimensional equations (9)–(13) with boundary conditions (14), over the domain of Fig. 1, referred to as the 2*D* solution, are presented in this section. The dimensionless parameters that influence the heat transfer from the rotating disk are varied to determine the operating regimes that result in uniform surface heat flux and by analogy uniform mass flux. The regimes which yield agreement with the 1*D* solution of Pollard and Newman (1980) are also determined. An understanding of the ranges of the operating parameters that yield agreement with the 1*D* solution is valuable not only for the prediction of uniform surface heat flux, but also because research reactors operating within the one-dimensional regime can be used to study complex chemical reaction mechanisms.

Figures 3(*a*) and 3(*b*) show the radial and axial velocity vector field (the circumferential component is not included) and the temperature field in a region near the rotating disk for $T_w = 1100$ K, Re = 1000, $Gr/Re^{3/2} = 2.2$, $r_o/r_d = 1.28$, and $L/r_d = 2.16$. It is noted that the number of arrows displayed in Fig. 3(*a*) does not correspond to the number of grid points used to obtain the solution. Rather, the number of arrows shown is limited for clarity and the vectors are obtained by in-

Downloaded 17 Dec 2010 to 193.140.21.150. Redistribution subject to ASME license or copyright; see http://www.asme.org/terms/Terms_Use.cfm

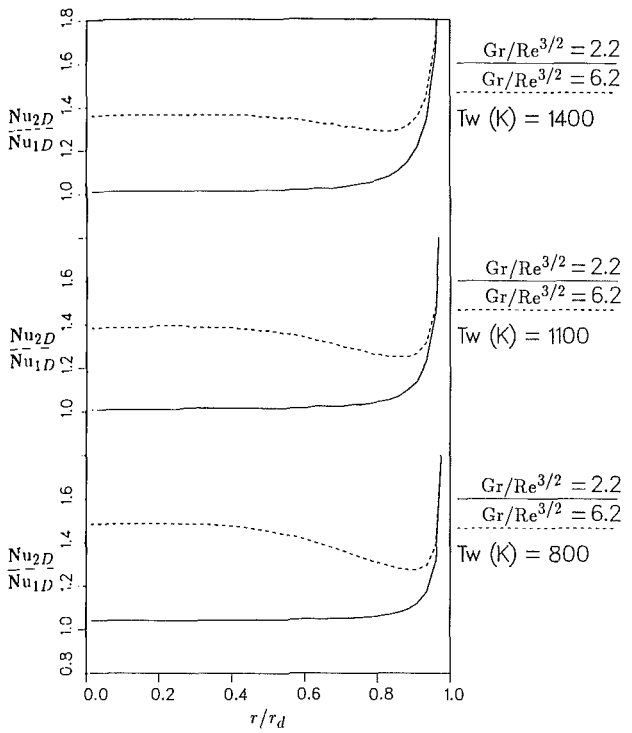

Fig. 5 Variation of local Nusselt number with radial position as a function of disk temperature for small and large values of $Gr/Re^{3/2}$; Re = 1000, $r_o/r_d = 1.28$, $L/r_d = 2.16$

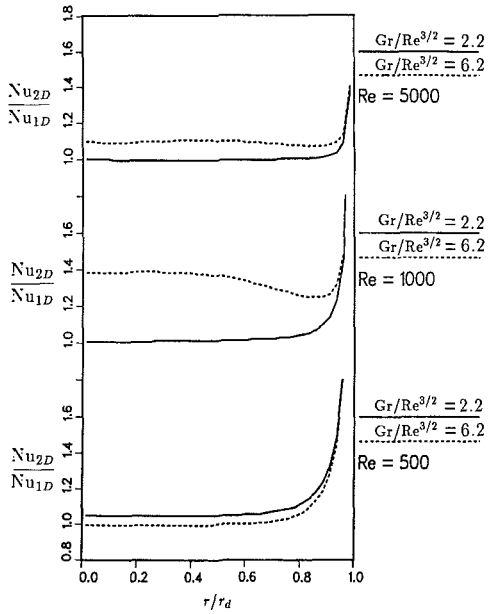

Fig. 6 Variation of local Nusselt number with radial position as a function of disk Reynolds number for two values of $Gr/Re^{3/2}$; $T_w = 1100$ K, $r_o/r_d = 1.28$, $L/r_d = 2.16$ for $Gr/Re^{3/2} = 6.2$; various L/r_d used for $Gr/Re^{3/2} = 2.2$

terpolation of the calculated data. There is no recirculation of fluid in the region above the disk and the temperature field is highly uniform, indicating that most of the disk (except for the region close to the edge) is uniformly accessible for mass transfer. The local disk heat flux is 1 percent larger than the 1*D* value at $\bar{r} = 0.1$, increases to 10 percent larger than the 1*D* value at $\bar{r} = 0.9$, and then rapidly increases for $\bar{r} > 0.9$ (see Fig. 6 for this case). Figures 4(*a*) and 4(*b*) show the results that are obtained with the same parameters as in Figs. 3(*a*) and 3(*b*) except that the mixed convection parameter, $Gr/Re^{3/2}$, is now

Table 1 $H|_{\eta\to\infty}$ and Nusselt number for the 1*D* situation for helium

T_w (K)	$H\|_{\eta\to\infty}$	$Nu_{1D} = -\Theta'(0)$
800	-0.8043	0.14543
1100	-0.7754	0.11282
1400	-0.7529	0.09292

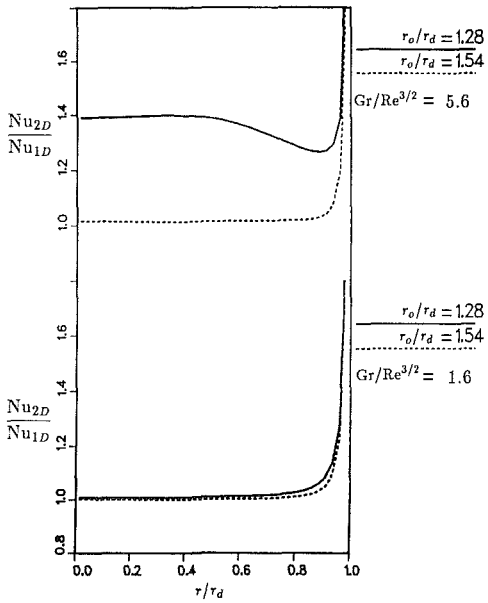

Fig. 7 Variation of local Nusselt number with radial position as a function of the radial aspect ratio, r_o/r_d, for two values of $Gr/Re^{3/2}$; $T_w = 800$ K, Re = 1000, $L/r_d = 2.16$

6.2, a value large enough for recirculation to occur. For this recirculating flow, the local disk heat flux is 42 percent larger than the 1*D* value at $\bar{r} = 0.1$, decreasing to a value that is 28 percent larger than the 1*D* value at $\bar{r} = 0.9$.

In Figs. 5–9 the dimensionless heat transfer is presented in terms of the Nusselt number based on the viscous length scale $\sqrt{\nu_\infty/\omega}$ divided by the one-dimensional Nusselt number $Nu_{1D} = -\Theta'(0)$ (Table 1) as a function of the radial position on the rotating disk. The local variation of the Nusselt number for $T_w = 800$, 1100, and 1400 K is shown in Fig. 5 (Re = 1000, $r_o/r_d = 1.28$, $L/r_d = 2.16$). For each disk temperature, the heat transfer is presented for two values of the mixed convection parameter. For the smaller value of $Gr/Re^{3/2}$, there is no recirculation of the gas and the heat transfer is very uniform over most of the disk except close to the edge where the flow turns the corner and leaves the reactor. However, for the higher value of $Gr/Re^{3/2}$, a recirculation region does exist near the reactor wall. This results in an acceleration of the incoming flow near the axis of symmetry and leads to higher heat fluxes. Note that the heat transfer is still reasonably uniform over the central portion of the disk. When a recirculation zone exists the local heat transfer is larger for a smaller value of T_w. This is due to the proximity of the recirculation zone to the surface of the disk (the zone being closer to the disk for a lower disk temperature) which leads to higher gas velocities between the rotating disk and the recirculation zone and thus higher heat fluxes.

The local variation of the Nusselt number over a Reynolds number range from 500 to 5000 for $T_w = 1100$ K and $r_o/r_d = 1.28$ is shown in Fig. 6. For $Gr/Re^{3/2} = 6.2$, the value of L/r_d was 2.16 for all Re, whereas various values of L/r_d were used for $Gr/Re^{3/2} = 2.2$. It will be shown later that the results are insensitive to this aspect ratio for small $Gr/Re^{3/2}$.

Downloaded 17 Dec 2010 to 193.140.21.150. Redistribution subject to ASME license or copyright; see http://www.asme.org/terms/Terms_Use.cfm

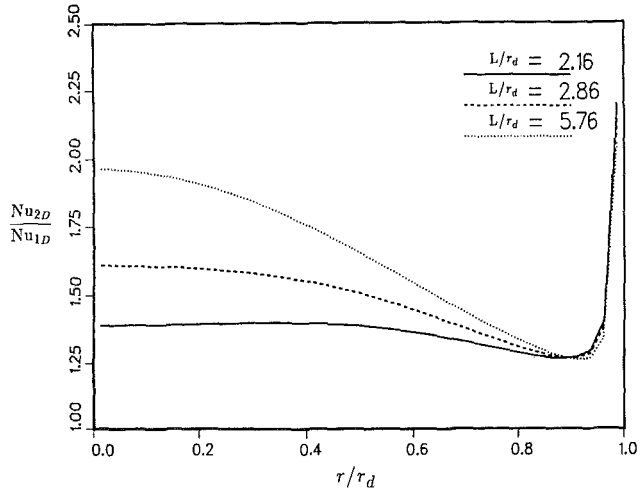

Fig. 8 Variation of local Nusselt number with radial position as a function of the axial aspect ratio, L/r_d; $T_w = 800$ K, Re = 1000, $Gr/Re^{3/2} = 5.6$, $r_o/r_d = 1.28$

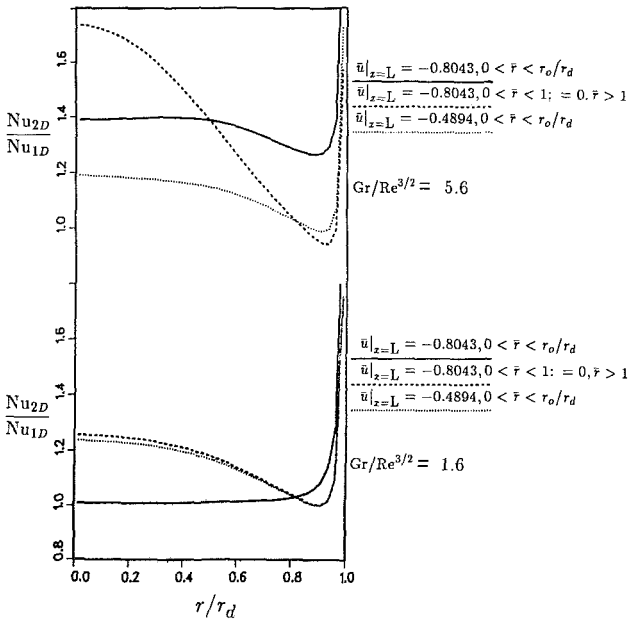

Fig. 9 Variation of local Nusselt number with radial position as a function of the inlet velocity, $\bar{u}|_{x=L}$, for two values of $Gr/Re^{3/2}$; $T_w = 800$ K, Re = 1000, $r_o/r_d = 1.28$, $L/r_d = 2.16$

For Re = 500, there is no recirculation for either of the two values of $Gr/Re^{3/2}$. The heat transfer is reasonably uniform over most of the disk and the 1*D* solution is valid except close to the edge of the disk. However, for Re = 1000, there is a large recirculation region for $Gr/Re^{3/2} = 6.2$. Even with the recirculation region, the heat transfer is uniform over the central portion of the disk but the magnitude of the heat flux is significantly larger than that given by the 1*D* solution. For Re = 5000, the recirculation region for $Gr/Re^{3/2} = 6.2$ is smaller and the heat flux is more uniform over the disk and in better agreement with the 1*D* result. This trend of decreasing size of the recirculation region with increasing Re above 1000 was also obtained for intermediate values of Re between 1000 and 5000.

The effect of radial aspect ratio, r_o/r_d, on the local Nusselt number is shown in Fig. 7 for two values of $Gr/Re^{3/2}$. The results are for $T_w = 800$ K, Re = 1000, and $L/r_d = 2.16$. For $Gr/Re^{3/2} = 1.6$, the Nusselt number variation over the disk is only slightly larger as r_o/r_d is decreased from 1.54 to 1.28 and the agreement with the 1*D* solution is excellent over most of the disk except for a small region close to the edge of the disk. However, for $Gr/Re^{3/2} = 5.6$, the effect of decreasing the radial aspect ratio is dramatic. For $r_o/r_d = 1.54$, agreement with the 1*D* solution is again excellent over the central region of the disk. However, for $r_o/r_d = 1.28$, the heat transfer is much larger than the 1*D* result (about 40 percent) and a significant variation in the heat transfer occurs for $r/r_d > 0.5$.

The effect of the axial aspect ratio, L/r_d, on the local Nusselt number is shown in Fig. 8 for three values of L/r_d. The results are obtained for $T_w = 800$ K, Re = 1000, $r_o/r_d = 1.28$, and $Gr/Re^{3/2} = 5.6$. As L/r_d is increased from 2.16 to 5.76, the variation of the local Nusselt number becomes much larger. Analysis of the velocity fields for these aspect ratios shows that the recirculation region becomes more vigorous as L/r_d increases. As $Gr/Re^{3/2}$ is decreased there is a smaller effect of the axial aspect ratio on the heat transfer. For example, although not shown, there is no effect of the axial aspect ratio on the local Nusselt number for $Gr/Re^{3/2} = 1.6$, provided that L/r_d is greater than the thickness of the boundary layers on the rotating disk.

For the results previously discussed, the specified inlet velocity, $\bar{u}|_{x=L}$, was uniform over the reactor radius, r_o (case I), with a magnitude given by the solution for the infinite disk as listed in Table 1 ($\bar{u}|_{x=L} = H|_{\eta\to\infty}$). The sensitivity of the local Nusselt number to the inlet velocity was determined by considering two additional inlet velocities. For one condition, the distribution of the inlet velocity was changed by applying the infinite disk inlet velocity uniformly from $\bar{r} = 0$ to $\bar{r} = 1$ and setting the inlet velocity to zero for $\bar{r} > 1$ (case II). For the other condition, the inlet velocity was uniform over the entire cross section ($0 < \bar{r} < r_o/r_d$), with a value determined from

$$\bar{u}|_{x=L} = H|_{\eta\to\infty}/(r_o/r_d)^2 \qquad \text{(case III)} \qquad (22)$$

The effect of inlet velocity on the local Nusselt number is shown in Fig. 9 for these three cases and for two values of $Gr/Re^{3/2}$. These results are obtained for $T_w = 800$ K, Re = 1000, $r_o/r_d = 1.28$, and $L/r_d = 2.16$. For $Gr/Re^{3/2} = 1.6$, case I yields uniform heat transfer over most of the disk (and agrees with the 1*D* solution), but the other two inlet velocities result in large variations over the disk. For $Gr/Re^{3/2} = 5.6$, all the curves show significant variations over the disk radius, the most dramatic variation corresponding to case II. A uniform inlet velocity distribution would be relatively easy to produce experimentally and it is fortunate that this distribution (case I) results in uniform heat flux over most of the rotating disk and also yields good agreement with the 1*D* solution for small and moderate values of $Gr/Re^{3/2}$.

Summary and Conclusions

Numerical solutions of the Navier-Stokes equations and the energy equation have been obtained to predict the heat transfer and fluid flow in a rotating disk CVD reactor. The effects of buoyancy, variable properties, and finite geometry have been included. The dimensionless parameters that influence the heat transfer from the rotating disk have been varied to determine the operating regimes that result in uniform surface heat flux and by analogy uniform mass flux. The results should be useful for the design and operation of similar CVD reactors. The regimes which yield agreement with the 1*D* solution of Pollard and Newman (1980) have also been determined. The determination of the ranges of the system parameters that yield agreement with the 1*D* solution provides the operating conditions for research reactors that can be used to study complex chemical reaction mechanisms.

For values of the mixed convection parameter $Gr/Re^{3/2}$, less than approximately 3 the heat transfer is uniform over most of the disk and the solution of equations (16)–(19) yields results that are in good agreement with the 1*D* values except for a small region close to the edge of the disk. For values of

Downloaded 17 Dec 2010 to 193.140.21.150. Redistribution subject to ASME license or copyright; see http://www.asme.org/terms/Terms_Use.cfm

the mixed convection parameter $Gr/Re^{3/2}$ greater than approximately 3 a recirculation region appears which leads to heat transfer rates that are larger than the 1*D* value. Significant variations in the heat transfer also occur, especially for $r/r_d > 0.5$.

The local heat transfer and the fluid flow have been obtained over a Reynolds number range from 500 to 5000. For sufficiently large values of $Gr/Re^{3/2}$, as the Reynolds number increases from 500 to 1000, a large recirculation zone appears and the heat transfer becomes nonuniform and significantly larger than the 1*D* value. However, for Re greater than 1000, this recirculation zone becomes smaller and the heat transfer then becomes more uniform and decreases.

For $Gr/Re^{3/2} = 1.6$ the local Nusselt number is only slightly dependent on r_o/r_d and is independent of L/r_d. For the larger value of $Gr/Re^{3/2} = 5.6$, the local Nusselt number becomes greatly dependent on both r_o/r_d and L/r_d; as r_o/r_d becomes smaller the local Nusselt number variation over the disk becomes larger, but decreasing L/r_d results in a smaller variation of the local Nusselt number.

The effect of the inlet velocity on the local Nusselt number has also been obtained. For $Gr/Re^{3/2} = 1.6$, only the case of the inlet velocity given by the 1*D* solution applied uniformly over the radius of the reactor (case I) yielded uniform heat transfer. For $Gr/Re^{3/2} = 5.6$, all three of the inlet velocity distributions exhibited significant variations for the local heat transfer. We also note that for $Gr/Re^{3/2} = 5.6$ the Nusselt number is significantly larger than the 1*D* result.

Acknowledgments

This work was supported by the US Department of Energy.

References

Coltrin, M. E., Kee, R. J., and Miller, J. A., 1984, "A Mathematical Model of the Coupled Fluid Mechanics and Chemical Kinetics in a Chemical Vapor Deposition Reactor," *J. Electrochem. Soc.*, Vol. 131, No. 2, pp. 425–434.

Giling, L. J., 1982, "Gas Flow Patterns in Horizontal Epitaxial Reactor Cells Observed by Interference Holography," *J. Electrochem. Soc.*, Vol. 129, No. 3, pp. 634–644.

Gosman, A. D., and Pun, W. M., 1973, "Calculation of Recirculating Flow," Lecture Notes, Imperial College of Science and Technology, London, England.

Hitchman, M. L., and Curtis, B. J., 1982, "Heterogeneous Kinetic and Mass Transfer in Chemical Vapour Deposition Processes. III. The Rotating Disc Reactor," *J. Crystal Growth*, Vol. 60, pp. 43–56.

Houtman, C., Graves, D. B., and Jensen, K. F., 1986, "CVD in Stagnation Point Flow," *J. Electrochem. Soc.*, Vol. 133, No. 5, pp. 961–970.

Kapur, D., Lee, P., and Jensen, K. F., 1985, "Metal Organic CVD in Stagnation Point Flow," AIChE Annual Meeting, Nov. 10–15, Chicago, IL, Paper No. 105a.

Millsaps, K., and Pohlhausen, K., 1952, "Heat Transfer by Laminar Flow From a Rotating Plate," *J. of Aero. Sci.*, Vol. 19, pp. 120–126.

Paolucci, S., 1982, "On the Filtering of Sound from the Navier-Stokes Equations," Sandia National Laboratories Report SAND82-8257.

Patankar, S. V., 1980, *Numerical Heat Transfer and Fluid Flow*, McGraw-Hill, New York.

Pollard, R., and Newman, J., 1980, "Silicon Deposition on a Rotating Disk," *J. Electrochem. Soc.*, Vol. 127, No. 3, pp. 744–752.

Reid, R. C., Prausnitz, J. M., and Sherwood, T. K., 1977, *The Properties of Gases and Liquids*, 3rd ed., McGraw-Hill, New York, pp. 394–397, 470–473, 678–679.

Sparrow, E. M., and Gregg, J. L., 1960, "Mass Transfer, Flow, and Heat Transfer About a Rotating Disk," ASME JOURNAL OF HEAT TRANSFER, Vol. 82, pp. 294–302.

Stock, L., and Richter, W., 1986, "Vertical Versus Horizontal Reactor: An Optical Study of the Gas Phase in a MOCVD Reactor," International MOCVD Conference, Los Angeles, CA.

von Karman, T., 1921, "Uber laminare und turbulent Reibung," *Z. f. a. M. M.*, Vol. 1, No. 4, pp. 233–252, also available as NACA-TM-1092.

White, F. M., 1974, *Viscous Fluid Flow*, McGraw-Hill, New York, pp. 163–184.

Downloaded 17 Dec 2010 to 193.140.21.150. Redistribution subject to ASME license or copyright; see http://www.asme.org/terms/Terms_Use.cfm

Effect of Wall Conduction on Combined Free and Forced Laminar Convection in Horizontal Rectangular Channels

G. J. Hwang
Professor.
Mem. ASME

F. C. Chou[1]

Department of Power Mechanical Engineering,
National Tsing Hua University,
Hsinchu, Taiwan 30043

This paper presents a numerical study of the effect of peripheral wall conduction on combined free and forced laminar convection in hydrodynamically and thermally fully developed flow in horizontal rectangular channels with uniform heat input axially, In addition to the Prandtl number, the Grashof number Gr^+, and the aspect ratio γ, a parameter K_p indicating the significance of wall conduction plays an important role in heat transfer. A finite-difference method utilizing a power-law scheme is employed to solve the system of governing partial differential equations coupled with the equation for wall conduction. The numerical solution covers the parameters: $Pr = 7.2$ and 0.73, $\gamma = 0.5$, 1, and 2, $K_p = 10^{-4}$–10^4, and $Gr^+ = 0$–1.37×10^5. The flow patterns and isotherms, the wall temperature distribution, the friction factor, and the Nusselt number are presented. The results show a significant effect of the conduction parameter K_p.

Introduction

Combined free and forced laminar convection in ducts is encountered in a wide variety of engineering situations, including heat exchangers designed for viscous fluids in chemical processes, solar collectors, food industries, and biomedical applications. In the past decades, the combined convection in tubes and channels has been treated extensively. Analyses have been performed via finite-difference schemes in the fully developed region of horizontal tubes [1–3], inclined tubes [4, 5], and the entrance region with or without a large Prantdl number assumption [6–10]. Numerous experiments [11–14] were carried out for the approximate thermal boundary conditions of uniform heat flux or circumferentially uniform wall temperature.

The boundary conditions posed for the analytical and experimental studies in the fully developed flow area are: axially and circumferentially uniform heat flux [2, 11, 12], and uniform wall temperature at any axial position and linear axial wall temperature [1, 3–5, 13]. It is noted that the former corresponds to the case of thin wall and small wall thermal conductivity, and the latter corresponds to the case of thick wall and large wall thermal conductivity. In the thermal entrance region, the boundary conditions are: axially and circumferentially uniform heat flux [6] and uniform wall temperature [7–10, 14].

Patankar and his co-workers [15] studied the effect of circumferentially nonuniform heating on laminar combined convection in a horizontal tube. The boundary conditions considered are a uniform heat flux on the upper or lower half of the tube wall and an insulated condition on the other half. This circumferentially nonuniform boundary condition did not take into account the effect of wall conduction. Sparrow and Patankar [16] examined the relationships among boundary conditions and Nusselt numbers for thermally developed forced flow. Considering the axial wall conduction and the external convective heat transfer coefficient of the tube, the thermal boundary conditions depend on the Biot number. The boundary conditions of uniform heat flux and wall temperature are two limiting cases for the Biot number varying from zero to infinity. Faghri and Sparrow [17] investigated the simultaneous wall and fluid axial conduction in laminar forced convection in which the upstream portion of the wall is externally insulated while the downstream portion of the wall is uniformly heated.

The effect of heat conduction in the peripheral direction along the duct wall for purely forced convection has been discussed by Shah and London [18, 23]. Data including Nusselt numbers for uniform heat flux and wall temperature in rectangular ducts $\gamma = 1$, 2, 4, 8 and other ducts were reported. Iqbal et al. [24] investigated the conjugate problem of laminar combined free and forced convection through vertical noncircular ducts. Morcos and Bergles [19] studied experimentally the combined free and forced laminar convection in horizontal tubes with wall conduction as a correlation parameter.

In many engineering applications, the boundary conditions in combined free and forced laminar convection cannot be considered either uniform wall temperature or uniform heat flux. To the best of the authors' knowledge, the effect of wall conduction on the mixed convection in channel flows has not been studied in the literature. This paper presents a theoretical investigation on the effect of finite wall conduction on the combined free and forced laminar convection in both hydrodynamically and thermally fully developed regions of horizontal channels. A finite-difference power-law scheme was employed to solve this problem.

Theoretical Analysis

Consider a steady laminar flow in the hydrodynamically and thermally fully developed region of a horizontal rectangular channel under an axially and peripherally uniform heat flux q_w on the outer surface of the channel wall. The physical configuration is shown in Fig. 1. This situation can be realized as a steady laminar flow in a long rectangular channel with finite values of thermal conductivity and wall thickness heated electrically from the outer surface of the channel wall. The viscous dissipation and compressibility effects in the energy equation are neglected. The Boussinesq approximation [20] is valid.

[1] Associate Professor, Department of Mechanical Engineering, National Central University, Chungli, Taiwan.

Contributed by the Heat Transfer Division and presented at the 23rd National Heat Transfer Conference, Denver, Colorado, August 1985. Manuscript received by the Heat Transfer Division May 15, 1985.

Copyright © 1987 by ASME

Downloaded 17 Dec 2010 to 193.140.21.150. Redistribution subject to ASME license or copyright; see http://www.asme.org/terms/Terms_Use.cfm

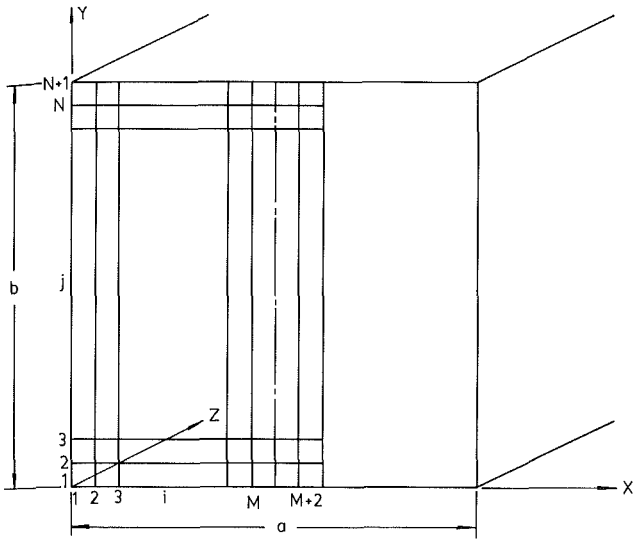

Fig. 1 Physical configuration and grid points

With the foregoing assumptions and introducing the dimensionless variables

$$x = X/D_e, \quad y = Y/D_e, \quad u = UD_e/\nu, \quad v = VD_e/\nu$$
$$w = WD_e/(\nu C), \quad \theta = (T - T_r)k_f/(q_w D_e)$$
$$C = -(dP_0/dZ)D_e^3/(4\mu\nu), \quad \mathrm{Gr}^+ = g\beta q_w D_e^4/(\nu^2 k_f) \tag{1}$$

and the vorticity and stream function

$$u = \partial\psi/\partial y, \quad v = -\partial\psi/\partial x$$
$$\xi = \partial v/\partial x - \partial u/\partial y \tag{2}$$

the governing equations expressing the conservation of mass, momentum, and energy become

$$\xi = -\nabla^2\psi = -(\partial^2/\partial x^2 + \partial^2/\partial y^2)\psi \tag{3}$$
$$u\partial\xi/\partial x + v\partial\xi/\partial y = \nabla^2\xi + \mathrm{Gr}^+ \partial\theta/\partial x \tag{4}$$
$$u\partial w/\partial x + v\partial w/\partial y = \nabla^2 w + 4 \tag{5}$$
$$\mathrm{Pr}(u\partial\theta/\partial x + v\partial\theta/\partial y) = \nabla^2\theta - 4w/\bar{w} \tag{6}$$

Equation (3), indicating the circulation of the fluid per unit area at each point, is derived directly from equation (2). Equation (4) is the vorticity transport equation and it is obtained by cross differentiation of the X and Y-direction momentum equations. It is seen from equation (4) that the vorticity is generated by the temperature gradient in the horizontal direction. Equation (5) is the axial momentum equation. The value 4 on the right-hand side of the equation (5) is the axial pressure gradient. The average w will decrease with the increase in the secondary flow intensity. Equation (6) is the energy equation. The term $4w/\bar{w}$ in the right-hand side of the equation is the axial advective term. The advective terms in the cross-sectional directions are on the left-hand side of equation (6). The effect of the secondary motion on the temperature distribution depends also on the Prandtl number.

Equations (3)–(6) contain two independent parameters: Gr^+ and Pr. For a fluid of fixed Pr, Gr^+ alone governs the flow and heat transfer characteristics. Gr^+ based on a prescribed heat flux is a modified Grashof number which can be easily related to a conventional parameter ReRa employed in [1]

$$\mathrm{ReRa}^* = 4\,\mathrm{Gr}^+ \tag{7}$$

where $\mathrm{Re} = \bar{W}D_e/\nu$ is the Reynolds number and $\mathrm{Ra}^* = g\beta(\partial T/\partial Z)D_e^4/(\nu\alpha)$ is the Rayleigh number based on the axial temperature gradient.

Nomenclature

A = cross-sectional area
a = width of rectangular channel
b = height of a rectangular channel
C = constant $= -C_1 D_e^3/4\nu\mu = \mathrm{Re}/\bar{w}$
C_1 = axial pressure gradient $= dP_0/dZ$
C_2 = axial temperature gradient $= \partial T/\partial Z$
D_e = equivalent hydraulic diameter $= 4A/S$
f = friction factor $= 2\bar{\tau}_w/(\rho\bar{W}^2)$
Gr^+ = modified Grashof number $= g\beta q_w D_e^4/\nu^2 k_f$
g = gravitational acceleration
$\bar{h}$ = average heat transfer coefficient
K_p = wall heat conduction parameter $= k_w t/(k_f D_e)$
k = thermal conductivity
k_w = thermal conductivity of channel wall
k_f = thermal conductivity of fluid
M = number of divisions in the X direction
N = number of divisions in the Y direction
Nu = Nusselt number $= \bar{h}D_e/k_f$
n = dimensionless inward-drawn normal
P_0 = axial pressure which is a function of Z only
Pr = Prandtl number $= \nu/\alpha$
q_w = prescribed uniform heat flux on the outside surface of the channel wall
Ra = Rayleigh number = Pr Gr^+
Ra^* = Rayleigh number based on the axial temperature gradient $= g\beta(\partial T/\partial Z)D_e^4/\nu\alpha$
Re = Reynolds number $= D_e\bar{W}/\nu$
S = circumference of cross section
s = dimensionless circumference of cross section
T = local temperature
T_r = reference temperature, selected as the temperature at the upper corner of the wall
T_w = wall temperature
t = thickness of channel wall
U, V, W = velocity components in X, Y, and Z directions
u, v, w = dimensionless velocity components in x, y, and z directions
X, Y, Z = rectangular coordinates
x, y, z = dimensionless rectangular coordinates
α = thermal diffusivity
β = coefficient of thermal expansion
γ = aspect ratio of a rectangular channel $= a/b$
θ = dimensionless temperature difference $= (T - T_r)/(q_w D_e/k_f)$
μ = viscosity
ν = kinematic viscosity
ρ = density
τ_w = wall shear stress
ψ = dimensionless stream function
ξ = vorticity

Subscripts

0 = condition for pure forced convection
i, j = nodal point

Downloaded 17 Dec 2010 to 193.140.21.150. Redistribution subject to ASME license or copyright; see http://www.asme.org/terms/Terms_Use.cfm

Table 1 Nusselt number versus conduction ratio for pure forced convection

γ \ K_p	10^{-4}	10^{-3}	10^{-2}	10^{-1}	1	10	10^2	10^3	10^4
1	3.098 3.08*	3.098	3.138	3.324	3.548 3.50*	3.599	3.610 3.606*	3.610	3.610 3.608*
0.5, 2	3.035 3.08*	3.039	3.084	3.337	3.864 3.87*	4.093	4.121	4.123	4.123 4.12*

*From Table 4(*b*) of the book by Shah and London [23].

Because of symmetry, it is necessary to consider only half of the region. Consequently, the boundary conditions are

$$\partial\psi/\partial x = \partial\psi/\partial y = w = 0$$

on the channel walls

$$\partial\psi/\partial y = \partial^2\psi/\partial x^2 = \partial w/\partial x = \partial\theta/\partial x = 0 \tag{8}$$

along the center line, $X = a/2$

In the present study, the values of the streamfunction on the channel walls and along the center line are taken as zero for simplicity. The derivation of thermal boundary condition along the channel wall can be found in Shan and London [23] and the dimensionless thermal boundary condition is

$$1 + (\partial\theta/\partial n)_\Gamma + K_p(\partial^2\theta/\partial s^2)_\Gamma = 0 \tag{9}$$

where condition Γ denotes the inside surface of the channel wall, n is inward normal, s is the circumference of cross section, and $K_p = k_w t/(k_f D_e)$ is a parameter indicating the relative importance of heat conduction along the channel wall and in the fluid. Two limiting cases, $K_p = 0$ and ∞, yield the boundary conditions of uniform heat flux and uniform wall temperature, respectively. It is reported in [18] that the values of the parameter K_p ranging from 0.1 to 10 are generally of interest to study the effect of wall conduction in a pipe flow. For instance, for a glass channel of $t/D_e = 0(0.1)$ with water, gases and engine oils, or for a metal channel of $t/D_e = 0(0.01\text{–}0.1)$ with liquid metals, the effect of wall conduction is important.

Method of Solution

The details regarding the formulation of finite-difference equations for equations (2)–(6) and the related boundary conditions (8) and (9) are omitted here for simplicity. In order to have a convergent solution in a higher Gr^+ region, the power-law scheme of [21] was employed. The procedure for solving the finite-difference equations is:

1 Assign values for Pr, Gr^+ and K_p, and initial values for ψ, ξ, w, and θ in equations (3)–(6).

2 New values of the streamfunction ψ can be found by solving equation (3) from the assigned value of ξ at each node.

3 The velocity components u and v are then computed by using equation (2).

4 Values of the vorticity on the boundary are calculated from equation (3) and the associated boundary condition for ψ.

5 With the assigned Gr^+, the values of u and v from step 3 and the boundary vorticity from step 4, equation (4) can be solved for ξ.

6 Equations (5) and (6) are solved for w and θ, respectively, with the velocity components u and v and the given Pr.

7 The wall temperature can then be solved from equation (9) and temperatures at interior nodal points.

8 Repeat steps 2 to 7 until the following convergence criterion is satisified:

$$\epsilon = \sum_{i,j} |(\theta_{i,j}^{(n+1)} - \theta_{i,j}^{(n)})|/\theta_{i,j}^{(n+1)}|/(M\times N) < 8\times 10^{-5} \tag{10}$$

9 Compute the friction factor and the Nusselt number.

Results and Discussion

Following the usual definitions, the expressions for the product of the friction factor and the Reynolds number $f\cdot$Re and the Nusselt number Nu can be written based on the overall force and energy balances in the axial direction

$$f\cdot \mathrm{Re} = (2\bar{\tau}_w/\rho\bar{W}^2)(\bar{W}D_e/\nu) = 2/\bar{w}$$
$$\mathrm{Nu} = \bar{h}D_e/k_f = \bar{w}/\overline{w(\tilde{\theta}_w - \theta)} \tag{11}$$

where the dimensionless quantities w, $\tilde{\theta}_w$, and $w(\tilde{\theta}_w - \theta)$ are the cross-sectional average values which can be evaluated by using Simpson's rule. A computation experiment for the case of $\mathrm{Pr} = 7.2$ and $K_p \to \infty$ was made to determine the mesh size required for sufficient accuracy. The differences for both the friction factor and the Nusselt numbers between mesh sizes 14×28 and 16×32 are less than 0.07 percent for the case of $Gr^+ = 0$ and $\gamma = 1$ and less than 0.13 percent for the case of $Gr^+ = 2.56\times 10^4$ and $\gamma = 1$. The mesh sizes 14×28 for $\gamma = 1$ and 0.5, and 20×20 for $\gamma = 2$, are taken in the present study. A comparison between the results from the power-law scheme and the central-difference scheme for the case of $\gamma = 1$, $K_p \to \infty$ can be seen also in [22].

Table 1 shows the Nusselt numbers with the wall conduction parameter K_p ranging from 10^{-4} to 10^4 for forced convection in channels of aspect ratios $\gamma = 1$, 0.5, and 2. The relevant results given in Table 4(*b*) of the book by Shah and London [23] are also presented for comparison. It is seen that the Nusselt number increases with K_p for all values of γ. Furthermore, for a small value of K_p, the Nusselt number approaches an asymptotic value of 3.098 at $K_p \le 10^{-3}$, which shows only a 0.23 percent difference from the known value Nu = 3.091 [18] for the case of $\gamma = 1$ and peripherally uniform wall heat flux. Similarly, for a large value of K_p, the Nusselt number approaches an asymptotic value of 3.610 at $K_p \ge 10^2$, which also shows a small difference of 0.55 percent from the known value of 3.63 [18] for the case of $\gamma = 1$ and uniform wall temperature. For the cases of $\gamma = 0.5$ and 2, and large K_p, the value 4.123 at $K_p \ge 10^3$ also agrees with the value in the literature [1]. This observation confirms the accuracy and convergence properties of the present numerical solution.

To illustrate the effects of peripheral wall heat conduction and buoyancy force on flow and heat transfer characteristics, the streamlines and isotherms are shown in Figs. 2(*a*), 2(*b*), and 2(*c*) for the cases of $K_p = 10^{-4}$, 10^{-1}, and 10^4, respectively. $\mathrm{Pr} = 7.2$ and $Gr^+ = 10^4$ are chosen for this illustration. The values of the streamfunction are zero on the channel wall and the center symmetry line. Therefore it can be seen from equation (2) that the speed of secondary motion is proportional to the normal gradient of the streamfunction. It is seen from Figs. 2(*a–c*) that the secondry flow patterns are almost similar for K_p ranging from 10^{-4} to 10^4. Thus the maximum absolute value of the streamfunction may be regarded as the intensity of secondary flow. The maximum absolute value of the streamfunction is 0.56 for $K_p = 10^{-4}$ and is 0.761 for $K_p = 10^4$. A 36 percent increase in the maximum value of the streamfunction is observed from the case of constant heat flux

Downloaded 17 Dec 2010 to 193.140.21.150. Redistribution subject to ASME license or copyright; see http://www.asme.org/terms/Terms_Use.cfm

($K_p = 10^{-4}$) to the case of uniform wall temperature ($K_p = 10^4$). This observation depicts the importance of the wall conduction in the present study.

It is also seen on the left-hand side of Figs. 2(*a–c*) that the isotherms change drastically with the wall conduction parameter K_p. In Fig. 2(*a*), $K_p = 10^{-4}$, the isotherms $\theta = -0.05$, -0.15, and -0.25 start at the left vertical wall. In Fig. 2(*b*), $K_p = 10^{-1}$, two isotherms $\theta = -0.05$ and -0.15 start at the left vertical wall. For the case of $K_p = 10^4$ in Fig. 2(*c*), none of the isotherms start at the side wall and a uniform temperature along the channel wall is observed. It is shown in equation (4) that the secondary flow is driven by the horizontal temperature gradient which increases with increase in the parameter K_p. This explains why the intensity of secondary flow is stronger in the case of uniform wall temperature than in the case of uniform heat flux. In the numerical computation, the temperature at the upper corner is assigned zero as a reference. The difference between the reference temperature and the minimum temperature is 0.286 in the case of $K_p = 10^4$, but the difference is 0.537 for $K_p = 10^{-4}$. This is also a result of stronger secondary flow in the case of uniform wall temperature.

For the varying wall conduction parameter K_p, the temperature distribution along the channel wall is of practical interest. Figures 3(*a*), 3(*b*), and 3(*c*) show the wall temperature distributions for the case of Pr = 7.2, and $Gr^+ = 0$, 10^3, and 10^4, respectively, in a square channel. It is seen that in the case of purely forced convection $Gr^+ = 0$, the highest temperature appears at the corners, and the temperature distribution is symmetric with respect to the horizontal center line $Y = b/2$. As the conduction parameter K_p increases, the wall temperature distributions become more and more uniform. For the cases of $Gr^+ = 10^3$ and 10^4, the secondary flow carries the fluid heated along the lower horizontal wall CD, vertical side wall BC, and then the upper horizontal wall AB. The fluid temperature becomes higher and higher. Therefore the location of the highest wall temperature appears at the upper corner B in the case of $Gr^+ = 10^3$ or on the upper horizontal wall in the case of $Gr^+ = 10^4$. Furthermore, it is seen that the difference between the highest and lowest wall temperature increases with increase in Gr^+ for the same value of K_p.

To confirm the present numerical solution, Fig. 4 shows the comparison of Nusselt numbers for the limiting cases of small and large conduction parameter K_p. The dashed line is the result presented in Cheng and Hwang [1] for the case of uniform wall temperature at small and intermediate values of Gr^+. The dash-dot line is the result presented in Chou and Hwang [22] for the case of uniform wall temperature at larger values of Gr^+. The present solution for the case of $\gamma = 1$ and $K_p = 10$ agrees closely with the results in [1, 22]. The data indicated by solid circles are obtained from [6] with a large Prandtl number assumption for mixed laminar convection in the thermal entrance region of horizontal rectangular channels with uniform heat flux. These data agree reasonably well with the present solution for the case of small values of K_p.

It may be interesting to know under what wall conduction parameter the thermal boundary condition may be considered as circumferentially uniform heat flux or circumferentially

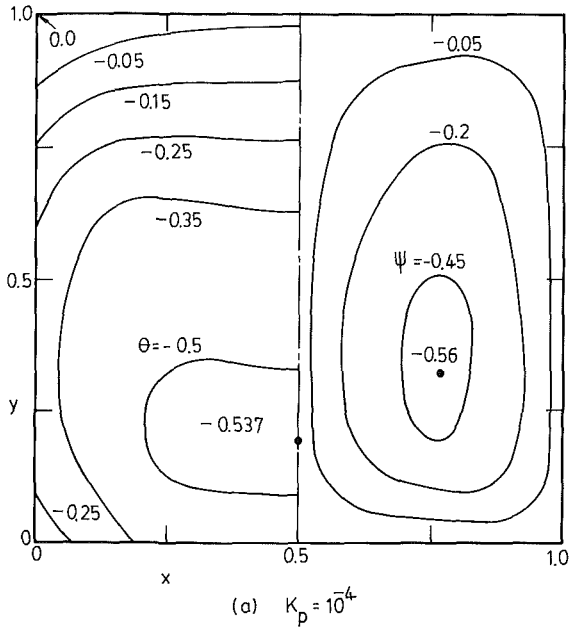

(a) $K_p = 10^{-4}$

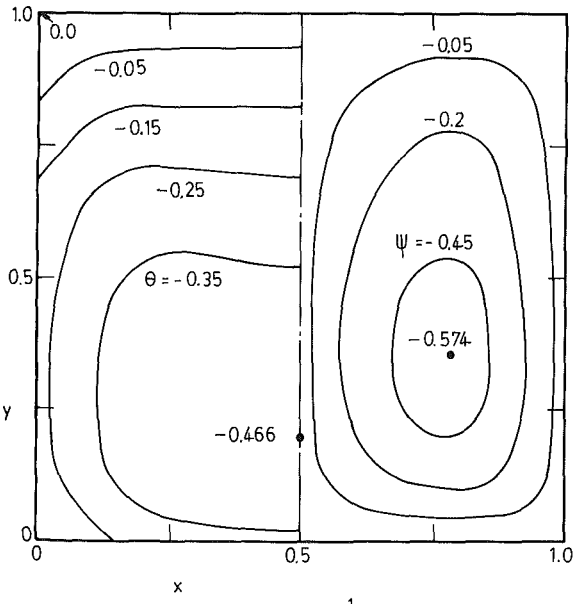

(b) $K_p = 10^{-1}$

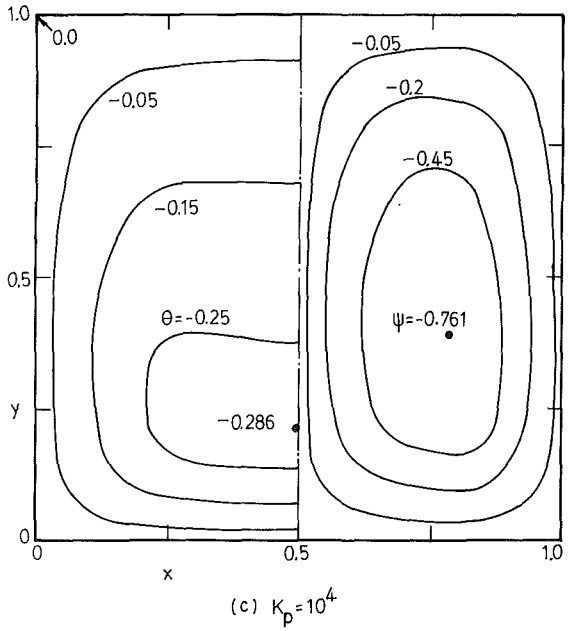

(c) $K_p = 10^4$

Fig. 2 Streamlines and isotherms for the case of $Gr^+ = 10^4$, Pr = 7.2, and $\gamma = 1$

Downloaded 17 Dec 2010 to 193.140.21.150. Redistribution subject to ASME license or copyright; see http://www.asme.org/terms/Terms_Use.cfm

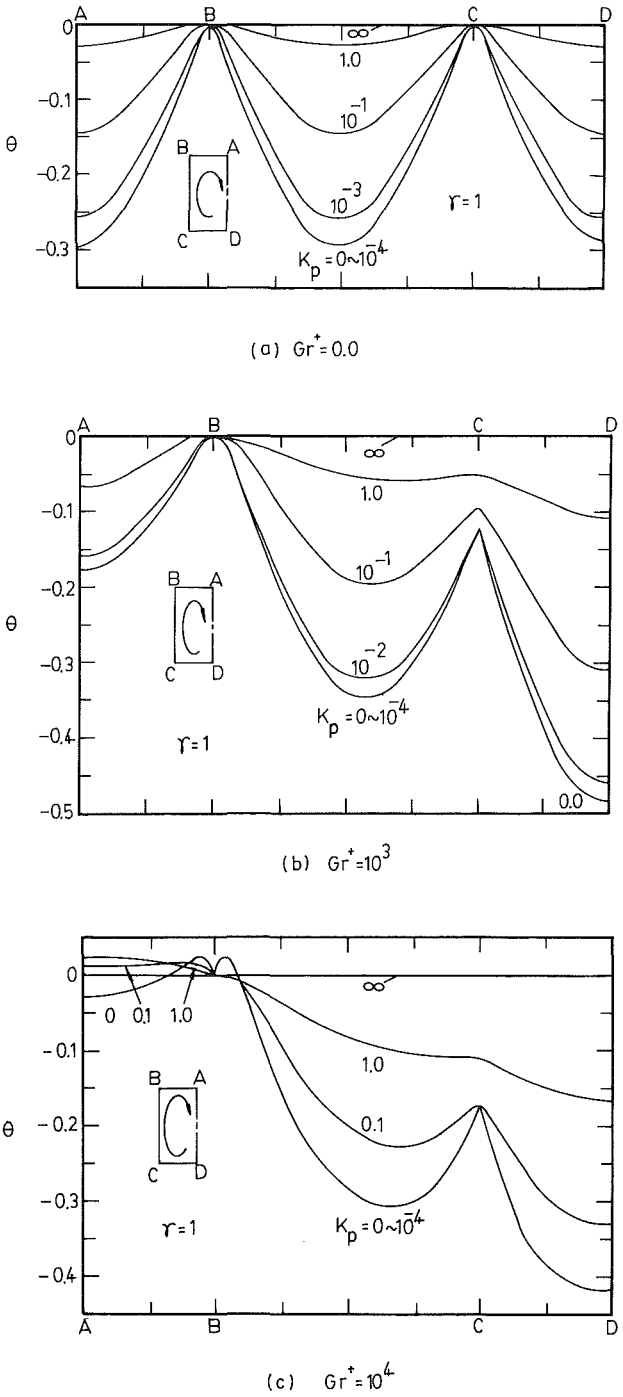

Fig. 3 Temperature distribution along the wall for Pr = 7.2 and γ = 1

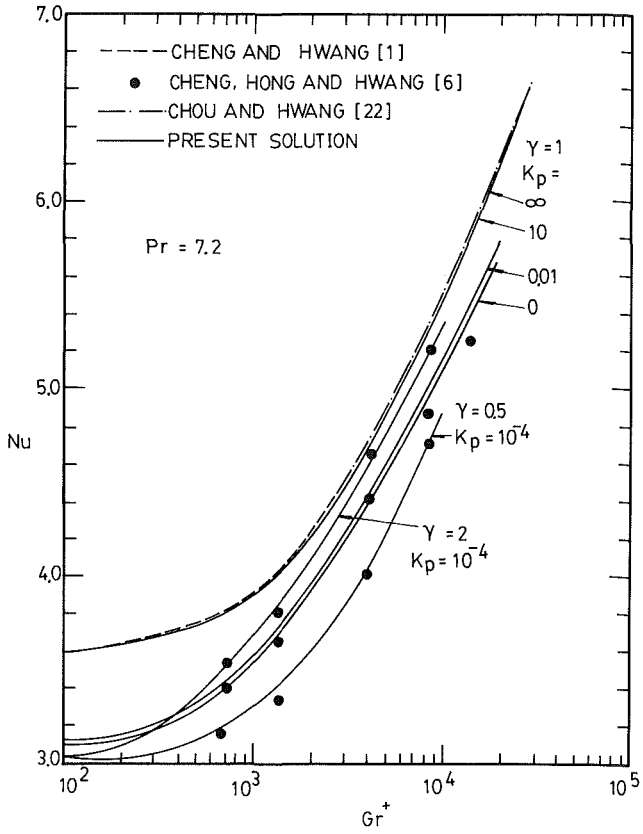

Fig. 4 Nu versus Gr^+

uniform wall temperature for the mixed convection in a horizontal square channel. It is seen in Fig. 4 that the differences between the values of Nu with $K_p = 0$ and 0.01, for $Gr^+ = 0$–2×10^4, are less than 2.1 percent. Therefore the thermal boundary condition with $K_p < 0.01$ may be considered as circumferentially uniform heat flux. Similarly the curves of $K_p = 10$ and ∞ in Fig. 4 lie close together. Therefore the thermal boundary condition with $K_p > 10$ may be considered as circumferentially uniform wall temperature.

Tables 2–4 show the numerical results of Nu and fRe versus wall conduction parameter K_p and buoyancy parameter Gr^+ for the cases of Pr = 7.2 and 0.73, with γ = 1, 0.5, and 2. It is seen that due to the reason explained in Fig. 2, the value of fRe for a higher value of K_p is greater than that for a lower value of K_p for the same value of Gr^+. Furthermore, due to the Prandtl number effect, only a few percent increase in the value of fRe is observed for Pr = 7.2 and the value of fRe is lower than that for Pr = 0.73 for the same parameters γ, K_p, and Gr^+.

Table 2 shows that the Nusselt number increases with increase in Gr^+. The values of Nu increase 64.7 and 52.8 percent for $K_p = 0$ and 10, respectively, when Gr^+ is changed from 0 to 10^4. This observation indicates that the enhancement of heat transfer rate is more effective in the case of lower K_p. As shown in Table 3, the difference between the values of Nu for $K_p = 0$ and 10^4 in the case of γ = 0.5 is larger than those in the cases of γ = 1 and 2. Table 4 summarizes the numerical results for the case of Pr = 0.73 with γ = 1, 0.5, and 2. It is seen that the value of Nu is lower in the case of Pr = 0.73 than that in the case of Pr = 7.2 for the same values of $Pr \cdot Gr^+$ and K_p.

Concluding Remarks

1 The results of the present numerical study have shown that the heat transfer characteristic of combined free and forced laminar convection in horizontal rectangular channels is affected significantly by the peripheral wall heat conduction and the buoyancy-induced secondary flow.

2 A parameter $K_p = k_w t/(k_f D_e)$ is introduced to indicate the importance of heat conduction along the channel wall. The Nusselt numbers of forced laminar convection are shown in Table 1 for channels of aspect ratio γ = 1, 0.5, and 2. By checking the values of Nu for various K_p with the two limiting Nusselt numbers, the cases of $K_p < 10^{-2}$ and $K_p > 10$ can be considered, respectively, as the thermal boundary conditions of circumferentially uniform heat flux and circumferentially uniform temperature for the case of Pr = 7.2.

Downloaded 17 Dec 2010 to 193.140.21.150. Redistribution subject to ASME license or copyright; see http://www.asme.org/terms/Terms_Use.cfm

Table 2 Numerical results for aspect ratio $\gamma = 1$ and Pr = 7.2

K_p	0		0.01		0.1		1		10		10^4	
Gr^+	Nu	fRe	Nu	fRe	Nu	fRe	Nu	fRe	Nu	fRe	Nu	fRe
0	3.098	14.24	3.138	14.24	3.324	14.24	3.548	14.24	3.599	14.24	3.610	14.24
3×10^2	–	–	3.203	14.25	3.384	14.25	3.593	14.25	–	–	–	–
10^3	3.526	14.26	3.549	14.26	3.706	14.26	3.862	14.26	3.878	14.26	3.894	14.40
3×10^3	4.191	14.29	4.229	14.29	4.412	14.30	4.527	14.31	4.498	14.33	4.500	14.34
10^4	5.103	14.36	5.183	14.37	5.440	14.37	5.569	14.40	5.499	14.48	5.498	14.46
2×10^4	5.676	14.42	5.796	14.44	–	–	6.274	14.57	–	–	–	–
3×10^4	–	–	–	–	6.536	14.57	–	–	6.662	14.73	6.652	14.72

Table 3 Numerical results for aspect ratios $\gamma = 0.5$ and 2, and Pr = 7.2

	K_p	10^{-4}		0.1		1		10^4	
	Gr^+	Nu	fRe	Nu	fRe	Nu	fRe	Nu	fRe
$\gamma=0.5$	0	3.035	15.56	3.337	15.56	3.864	15.56	4.124	15.56
	3×10^2	3.052	15.56	3.353	15.56	3.879	15.56	4.142	15.56
	10^3	3.172	15.77	3.469	15.56	3.973	15.56	4.221	15.56
	3×10^3	3.813	15.58	4.098	15.58	4.459	15.59	4.643	15.59
	10^4	4.859	15.64	5.359	15.67	5.667	15.69	5.713	15.70
	3×10^4	–	–	–	–	7.051	15.93	7.078	16.00
$\gamma=2$	0	3.035	15.56	3.337	15.56	3.864	15.56	4.124	15.56
	3×10^2	3.197	15.57	3.446	15.57	–	–	–	–
	10^3	3.681	15.57	3.869	15.57	4.117	15.57	4.248	15.57
	3×10^3	4.376	15.59	4.572	15.59	4.662	15.59	4.617	15.57
	10^4	5.333	15.63	5.558	15.64	5.569	15.65	5.385	15.67
	3×10^4	–	–	–	–	6.621	15.77	6.342	15.81

Table 4 Numerical results for $\gamma = 1$, 0.5, and 2, and Pr = 0.73

γ	1				0.5				2			
K_p	0		10^4		0		10^4		0		10^4	
Gr^+	Nu	fRe	Nu	fRe	Nu	fRe	Nu	fRe	Nu	fRe	Nu	fRe
0	3.098	14.24	3.610	14.24	3.035	15.56	4.123	15.56	3.035	15.56	4.123	15.56
1.370×10^3	3.136	14.26	3.636	14.29	3.117	15.57	4.139	15.59	3.117	15.57	4.151	15.57
6.849×10^3	3.384	14.75	3.841	14.84	3.166	15.68	4.208	15.75	3.562	15.97	4.250	15.77
1.370×10^4	3.665	15.31	4.156	15.60	3.367	15.96	4.380	16.16	3.940	16.33	4.445	16.18
4.110×10^4	4.262	16.50	4.923	17.35	3.954	16.91	5.084	17.79	4.595	17.10	4.965	17.27
6.849×10^4	4.532	17.13	–	–	4.281	17.49	–	–	–	–	–	–
8.219×10^4	–	–	5.504	18.62	–	–	5.746	19.32	–	–	5.416	18.24
1.370×10^5	–	–	5.948	19.62	–	–	6.294	20.60	–	–	5.790	19.09

3 The intensity of secondary flow increases with increase in K_p when the value of the modified Grashof number is fixed. Therefore, the values of fRe with higher values of K_p are higher than those of lower values of K_p with the same value of Gr^+.

4 The enhancement of heat transfer rate due to Gr^+ is more effective in the case of lower K_p for $\gamma = 1$ and the trend is more pronounced in the case of $\gamma = 2$. For Pr = 0.73 the value of Nu is lower than that for Pr = 7.2 with the same value of $Pr \cdot Gr^+$ and K_p.

References

1 Cheng, K. C., and Hwang, G. J., "Numerical Solution for Combined Free and Forced Laminar Convection in Horizontal Rectangular Channels," ASME Journal of Heat Transfer, Vol. 91, 1969, pp. 59-66.

2 Newell, P. H., and Bergles, A. E., "Analysis of Laminar Combined Free and Forced Convection for Fully Developed Laminar Flow in Horizontal Tubes," ASME Journal of Heat Transfer, Vol. 92, 1970, pp. 83-93.

3 Hwang, G. J., and Cheng, K. C., "Boundary Vorticity Method for Convective Heat Transfer With Secondary Flow – Application to the Combined Free and Forced Convection in Horizontal Tubes," *Heat Transfer*, Vol. 4, Elsevier Publishing Company, Amsterdam, 1970, Paper No. NC3.5.

4 Cheng, K. C., and Hong, S. W., "Combined Free and Forced Laminar Convection in Inclined Tubes," *Appl. Sci. Res.*, Vol. 27, Oct. 1972, pp. 19-38.

5 Ou, J. W., Cheng, K. C., and Lin, R. C., "Combined Free and Forced Laminar Convection in Inclined Rectangular Channels," *Int. J. Heat Mass Transfer*, Vol. 19, 1976, pp. 277-283.

6 Cheng, K. C., Hong, S. W., and Hwang, G. J., "Buoyancy Effects on Laminar Heat Transfer in the Thermal Entrance Region of Horizontal Rectangular Channels With Uniform Wall Heat Flux for Large Prandtl Number Fluids," *Int. J. Heat Mass Transfer*, Vol. 15, 1972, pp. 1819-1836.

7 Ou, J. W., Cheng, K. C., and Lin, R. C., "Natural Convection Effects on Graetz Problem in Horizontal Rectangular Channels With Uniform Wall Temperature for Large Pr," *Int. J. Heat Mass Transfer*, Vol. 17, 1974, pp. 835-843.

8 Ou, J. W., and Cheng, K. C., "Natural Convection Effects on Graetz Problem in Horizontal Isothermal Tubes," *Int. J. Heat Mass Transfer*, Vol. 20, 1977, pp. 953-960.

9 Yao, L. S., "Free-Forced Convection in the Entry Region of a Heated Straight Pipe," ASME Journal of Heat Transfer, Vol. 100, 1978, pp. 212-219.

10 Hishida, M., Nagano, Y., and Montesclaros, M. S., "Combined Forced and Free Convection in the Entrance Region of an Isothermally Heated Horizontal Pipe," ASME Journal of Heat Transfer, Vol. 104, 1982, pp. 153-159.

11 Shannon, R. L., and Depew, C. A., "Combined Free and Forced Laminar Convection in a Horizontal Tube With Uniform Heat Flux," ASME Journal of Heat Transfer, Vol. 90, 1968, pp. 353-357.

12 Bergles, A. E., and Simonds, R. R., "Combined Forced and Free Convection for Laminar Flow in Horizontal Tubes With Uniform Heat Flux," *Int. J. Heat Mass Transfer*, Vol. 14, 1971, pp. 1989-2000.

13 Sabbagh, J. A., Aziz, A., El-Ariny, A. S., and Hamad, G., "Combined Free and Forced Convection in Circular Tubes," ASME Journal of Heat Transfer, Vol. 98, 1976, pp. 322-324.

14 Depew, C. A., and August, S. E., "Heat Transfer Due to Combined Free and Forced Convection in a Horizontal and Isothermal Tube," ASME Journal of Heat Transfer, Vol. 93, 1971, pp. 380-384.

15 Patankar, S. V., Ramadhyani, S., and Sparrow, E. M., "Effect of Circumferentially Nonuniform Heating on Laminar Combined Convection in a

Downloaded 17 Dec 2010 to 193.140.21.150. Redistribution subject to ASME license or copyright; see http://www.asme.org/terms/Terms_Use.cfm

Horizontal Tube," ASME JOURNAL OF HEAT TRANSFER, Vol. 108, 1978, pp. 63-70.

16 Sparrow, E. M., and Patankar, S. V., "Relationships Among Boundary Conditions and Nusselt Numbers for Thermally Developed Duct Flows," ASME JOURNAL OF HEAT TRANSFER, Vol. 99, 1977, pp. 483-485.

17 Faghri, M., and Sparrow, E. M., "Simultaneous Wall and Fluid Axial Conduction in Laminar Pipe-Flow Heat Transfer," ASME JOURNAL OF HEAT TRANSFER, Vol. 102, 1980, pp. 58-63.

18 Shah, R. K., and London, A. L., "Thermal Boundary Conditions and Some Solutions for Laminar Duct Flow Forced Convection," ASME JOURNAL OF HEAT TRANSFER, Vol. 96, 1974, pp. 159-165.

19 Morcos, S. M., and Bergles, A. E., "Experimental Investigation of Combined Forced and Free Laminar Convection in Horizontal Tubes," ASME JOURNAL OF HEAT TRANSFER, Vol. 97, 1975, pp. 212-219.

20 Gray, D. G., and Giorgini, A., "The Validity of the Boussinesq Approximation for Liquids and Gases," *Int. J. Heat Mass Transfer*, Vol. 19, 1976, pp. 545-551.

21 Patankar, S. V., *Numerical Heat Transfer and Fluid Flow*, McGraw-Hill-Hemisphere, New York, 1980.

22 Chou, F. C., and Hwang, G. J., "Combined Free and Forced Laminar Convection in Horizontal Channels for High ReRa," *Canadian J. of Chemical Engineering*, Vol. 62, 1984, pp. 830-836.

23 Shah, R. K., and London, A. L., *Laminar Flow Forced Convection in Ducts*, Academic Press, New York, 1978.

24 Iqbal, M., Aggarwala, B. D., and Khatry, A. K., "On the Conjugate Problem of Laminar Combined Free and Forced Convection Through Vertical Non-circular Ducts," ASME JOURNAL OF HEAT TRANSFER, Vol. 94, 1972, pp. 52-56.

Downloaded 17 Dec 2010 to 193.140.21.150. Redistribution subject to ASME license or copyright; see http://www.asme.org/terms/Terms_Use.cfm

Enhanced Heat Transfer Due to Secondary Flows in Mixed Turbulent Convection

L. W. Swanson[1]

I. Catton

Mechanical, Aeronautical, and Nuclear Engineering Department, University of California, Los Angeles, Los Angeles, CA 90024

An experimental study of the fluid flow and heat transfer phenomena associated with opposing mixed turbulent convection in vertical ducts has been conducted. The duct considered had vertical and horizontal aspect ratios of 24.4 and 9.7, respectively. The working fluid was Freon-113, providing a Prandtl number of approximately 6.5. The results showed that a number of flow bifurcations occurred as Gr_{Dh}/Re^2_{Dh} was increased. The first bifurcation observed was from parallel turbulent mean flow to a large single flow cell in the x–z plane. This occurred in the neighborhood of $Gr_{Dh}/Re^2_{Dh}=2$. Further bifurcations to multiple cells and eventually pure large-scale chaos were also observed. A correlation for the enhanced heat transfer was found to be $Nu_{Dh}/Nu_{Dh,0}=1.0+0.9[ln(Gr_{Dh}/Re^2_{Dh}+1)]^{1.39}$, where $Nu_{Dh,0}$ is the Petukhov–Virillov correlation for pure forced turbulent convection.

Introduction

Combined turbulent convection refers to fluid flow influenced by both buoyancy forces and dynamic pressure forces. The buoyancy forces can act in either the same direction (aiding) or opposite direction (opposing) as the dynamic pressure forces. In heated vertical ducts with equal wall temperatures or equal wall heat fluxes symmetry can be imposed and the duct half width becomes a characteristic dimension. The density gradient across the duct half width, due to the difference in the wall and free-stream temperatures, drives the buoyant layer upward near the hot wall. This layer entrains fluid from the downward flowing free stream. The net mass flow through the duct, which remains constant, determines the magnitude of the forced flow. The main concern in these flow systems lies in how these opposing forces influence flow structure and heat transfer.

Experimental studies of mixed turbulent flows conducted over the past fifty years have dealt with either air or water flowing in horizontal or vertical ducts and tubes. Only a few of these studies are discussed although a fairly complete list is given in the references section of this paper.

Nakajima et al. (1980) examined turbulent mixed convection between parallel vertical plates for air both experimentally and theoretically. Both aiding and opposing buoyancy flows were treated for fully developed flow with $Gr/Re^2<2\times10^{-2}$. Results showed that the Nusselt number increased with increasing Gr/Re^2 (based on duct width) for forced flow with an opposing buoyancy force, and decreased with increasing Gr/Re^2 for forced flow with an aiding buoyancy force. This phenomenon was attributed to an increasing velocity fluctuation (eddy size) in opposing flow and vice versa for aiding flow.

Eckert and Diaguila (1954) conducted experiments on combined convection for air flowing through short tubes. Their heat transfer results showed mixed heat transfer coefficients up to twice as high as those for either purely free or forced convection. They attributed this increase to an increased turbulent diffusion caused by the opposing buoyancy force near the wall. Large-scale turbulence was also observed with hot-wire anemometers.

Brown and Gauvin (1965, 1966) studied the rate of heat transfer to air flowing downward at low velocities through a heated tube. They noted that the entrance region was about seven tube diameters regardless of the magnitude of the net mass flow rate. A thorough explanation of the behavior of the heat transfer in the entrance region was found in Brown and Gauvin (1966). They attributed the observed initial increase in heat transfer to an increase in the turbulent transport due to the opposing buoyancy force. They verified this by plotting the rms radial temperature fluctuation for various axial locations. They also noted that the observed decrease in heat transfer for $x/D>4.5$ was due to a reduction in the wall shear stress, also caused by buoyancy. Brown and Gauvin also suggested that the rate of heat transport in opposing convection was controlled by free convection alone.

Jackson and Fewster (1976) studied turbulent mixed convection for water flowing in vertical tubes both experimentally and theoretically. A similar theoretical approach for the same geometry has been presented by Axcell and Hall (1976) for air and Jackson (1983) for liquid metals. Jackson's method combined the buoyancy force with the shear stress by evaluating the change in shear stress across the buoyant layer given by the integral

$$\Delta\sigma_\delta=\int_0^\delta(\rho_b-\rho)g\,dy$$

Adding the change in shear stress across the buoyant layer to the shear stress at the wall yielded a modified shear stress which was used to modify the forced convection heat transfer correlation ($Nu_{Dh,0}$) of Petukhov and Kirillov (1958). By proper parameter adjustment, the correlation was made to fit data over a wide mixed flow parameter range. The correlation was found to be

$$\frac{Nu_{Dh}}{Nu_{Dh,0}}=(1+4500\overline{Gr}_{Dh}Re_{Dh}^{-21/8}Pr^{-1/2})^{0.31} \tag{1}$$

where

$$Nu_{Dh,0}=\frac{Re_{Dh}Pr\frac{C_f}{2}}{12.7\left(\frac{C_f}{2}\right)^{1/2}(Pr^{2/3}-1)+1.07} \tag{2}$$

$$C_f=\frac{1}{(3.64\log_{10}Re_{Dh}-3.28)^2}$$

$$\overline{Gr}_{Dh}=\frac{(\rho_b-\bar{\rho})gD_h^3}{\rho_b\nu^3}$$

[1]Present address: Assistant Professor, Department of Engineering, University of Denver, Denver, CO.

Contributed by the Heat Transfer Division for publication in the JOURNAL OF HEAT TRANSFER. Manuscript received by the Heat Transfer Division May 22, 1986.

 Copyright © 1987 by ASME

Downloaded 17 Dec 2010 to 193.140.21.150. Redistribution subject to ASME license or copyright; see http://www.asme.org/terms/Terms_Use.cfm

and

$$\bar{\rho} = \frac{1}{T_w - T_b} \int_{T_w}^{T_b} \rho dT \tag{3}$$

The above relationship agrees very well with data for water flowing in vertical pipes over the range $10^{-5} < \overline{\mathrm{Gr}}_{Dh}/\mathrm{Re}_{Dh}^{21/8}\,\mathrm{Pr}^{1/2} < 0.2$. The correlation moderately overpredicts the data of Watzinger and Johnson (1939) and Herbert and Sterns (1972).

All of the literature discussed to this point has dealt with either duct or pipe geometries of various vertical aspect ratios covering a fairly wide range of flow parameters. Only Eckert and Diaguila (1954) have briefly mentioned observations of large-scale turbulence via hot-wire anemometry. They apparently did not observe any flow bifurcations as the buoyancy force was increased in opposing mixed flow. In this work, an experimental study has been undertaken to gain an understanding of the fluid flow structure and heat transfer phenomena associated with opposing mixed turbulent convection in a vertical duct which has vertical and horizontal aspect ratios of 24.4 and 9.7, respectively. A description of the flow structure is provided through visual observations and a Nusselt number correlation is obtained reflecting the enhanced heat transfer over that for purely forced flows.

Experimental System

The experimental system used in this study is shown in Fig. 1. The system can be divided into two parts: the fluid flow loop and the experimental apparatus.

The fluid flow loop supplied liquid Freon-113 to the experimental apparatus at a set inlet temperature and volumetric flow rate. Freon-113 was used as the working fluid due to its favorable buoyancy properties. The Freon was stored in a 1.7-m^3 tank and its temperature was thermostatically controlled ($\pm 2.8°C$) by a 7-ton refrigeration system. Cold fluid was pumped out of the tank by a 3.73-kW Weil centrifugal pump. The volumetric flow rate to the apparatus was controlled by adjusting the globe valves in the tank recycle line and the apparatus feed line. The total inlet flow rate to the apparatus was measured with a 5.1-cm Foxboro turbine flow meter.

The fluid entered the apparatus at the flow conditioning section where perforated plates, wire screens, and gradual flow contraction flattened the velocity profile and laminarized the flow. Thus laminar plug flow at a given temperature and volumetric flow entered the buoyant layer bleed section of the apparatus. Porous plates separated the bleed chambers from the forced flow in the duct. The fluid then entered the test section of dimensions 108 cm × 2.22 cm × 43.2 cm (height (H) × half-width (D) × length (L)). These dimensions gave the test section a vertical aspect ratio ($H/2D$) of 24.4 and a horizontal aspect ratio ($L/2D$) of 9.7. Two 0.48-cm-thick polished aluminum plates served as the heated surfaces and 1.91-cm-thick plexiglass sidewalls allowed flow visualization.

EXPERIMENTAL APPARATUS

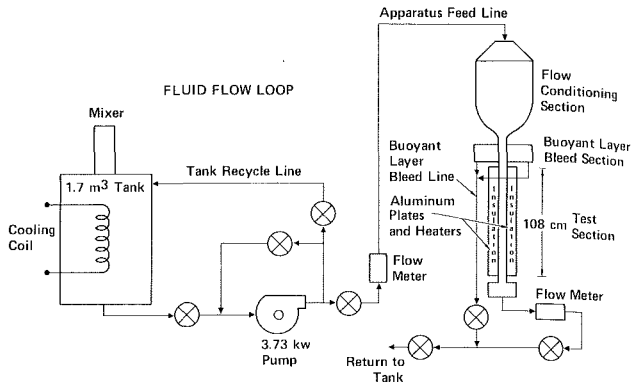

Fig. 1 Experimental system

Fifteen electrofilm strip heaters were glued to the outer surface of each aluminum plate to provide a constant wall heat flux. The amount of power supplied to the heaters was controlled with a 50-kW variac. Fiberglassed polyurethane slabs (5.1 cm thick) served as insulation and structural support for the plates. Wall thermocouples were glued with thermally conducting cement to the outside of the aluminum plates. The wall thermocouples were centered horizontally on each plate and the corresponding thermocouple probes were mounted along the duct vertical centerline. The wall/probe pairs were placed at seven equidistant locations along the duct vertical height. Output signals from the thermocouples were appropriately conditioned and transferred to a DEC PDP-11 minicomputer for data storage and reduction. Each recorded data point represented an average of five instantaneous values taken at 10-s time intervals. A 3.8-cm Flowmetrics turbine flow meter at the duct outlet allowed measurement of the net volumetric flow rate through the duct. The flow was then returned to the tank for cooling and flow loop closure. The system provided a mixed parameter range of $0.9 < \mathrm{Gr}_{Dh}/\mathrm{Re}_{Dh}^2 < 30$.

Heat transfer data were taken at each thermocouple station over the entire mixed parameter range after the system came to steady state. Initially, extra wall thermocouples were placed at various positions along the duct horizontal length to insure a constant heat flux boundary condition. The deviation from the wall thermocouple centerline temperature was found to be less than 3 percent for $\mathrm{Gr}_{Dh}/\mathrm{Re}_{Dh}^2 < 2.3$; no horizontal temperature data were taken above this point. A fully developed flow condition (ΔT approximately constant) was observed for $x/D > 5$ at all values of $\mathrm{Gr}_{Dh}/\mathrm{Re}_{Dh}^2$. The flow was observed by noticing shadows in the fluid caused by changes in the refractive index with respect to density. The average Nusselt number was calculated by averaging the values of ΔT obtained at the five inner thermocouple stations.

The systematic error in the Nusselt number was estimated based on instrumentation accuracy and conduction losses.

Nomenclature

C_f = coefficient of friction
D = duct half-width
D_h = hydraulic diameter $4D$
g = gravitational constant
Gr_{Dh} = Grashof number = $(g\beta(T_w - T_e)D_h^3/\nu^2)$
H = duct height
L = duct horizontal length
Nu_{Dh} = Nusselt number = $q_w D_h/k(T_w - T_e)$
Pr = Prandtl number = ν/α
q = heat flux
Re_{Dh} = Reynolds number = $u_{ave}D_h/\upsilon$
T = temperature
V = volumetric flow rate
α = thermal diffusivity
β = thermal expansion coefficient
δ = buoyant layer thickness
ν = kinematic viscosity
ρ = density
σ = shear stress

Subscripts

ave = average
b = bulk
Dh = hydraulic diameter
e = free stream
w = wall
0 = value for pure forced convection

Downloaded 17 Dec 2010 to 193.140.21.150. Redistribution subject to ASME license or copyright; see http://www.asme.org/terms/Terms_Use.cfm

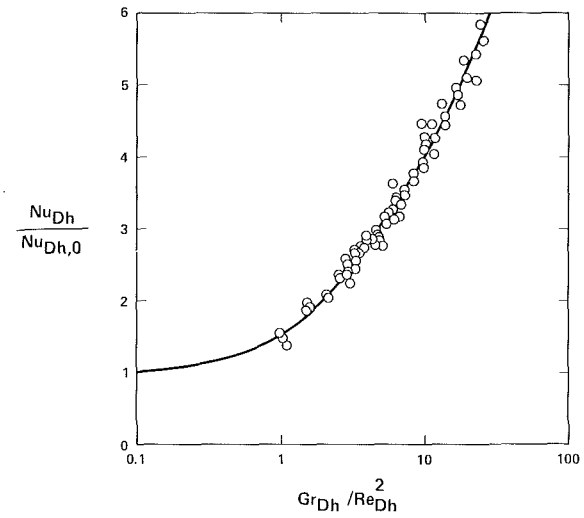

Fig. 2 Heat transfer enhancement due to buoyancy effects in forced turbulent convection in vertical ducts

Conduction losses through the plexiglass sidewalls, polyurethane insulation, and aluminum plates were less than 5 percent of q_w. Conduction in the thermocouple probes yielded a maximum error of 2 percent in ΔT. Thermocouple accuracy in an isothermal environment gave a 1 percent error in ΔT. The error in reading the power meter was approximately 2 percent of q_w. The absolute systematic error in the Nusselt number based on these estimates was found to be less than 11 percent.

The random error was evaluated based on observed variations in the wall heat flux and ΔT. Inlet fluid temperature variations ($\pm 0.56°C$ max over a 40-s sampling interval) due to the dynamics of the refrigeration system yielded a calculated maximum error of 8 percent in q_w. Individual strip heater variation in power due to fluctuations in the power supply were less than 4 percent of q_w. The maximum random error in the Nusselt number based on these estimates was found to be 12 percent.

Results and Discussion

Figure 2 depicts the experimental values of $Nu_{Dh}/Nu_{Dh,0}$ as a function of Gr_{Dh}/Re^2_{Dh}, where $Nu_{Dh,0}$ is the Petukhov-Virillov correlation given by equation (2). The curve in Fig. 2 represents a least-squares fit of the data. The resulting correlation is given as

$$\frac{Nu_{Dh}}{Nu_{Dh,0}} = 1.0 + 0.9\left[\ln\left(\frac{Gr_{Dh}}{Re^2_{Dh}} + 1\right)\right]^{1.39}$$

with a standard error of 0.14. Note the enhancement in heat transfer over that for pure forced convection with increasing Gr_{Dh}/Re^2_{Dh}, a common phenomenon associated with opposing mixed convection.

At values of Gr_{Dh}/Re^2_{Dh} less than approximately 2, two-dimensional parallel mean flow was observed and the enhanced heat transfer was caused by the increased shearing effect due to the upward flowing buoyant layer near the wall. The added shearing intensified fluid mixing which penetrated deeper into the buoyant layer as the wall heat flux was increased for a constant volumetric flow rate (increasing Gr_{Dh}/Re^2_{Dh}). The penetration continued as the heat flux was increased until the convection appeared as small clumps of fluid transported from the wall to the free stream.

The developing flow region near the upper heated edge was also on the order of one hydraulic diameter. The free stream seemed to peel off the upward flowing buoyant layer forcing the early flow development. Once developed, the buoyant layer thickness remained approximately constant throughout the duct height.

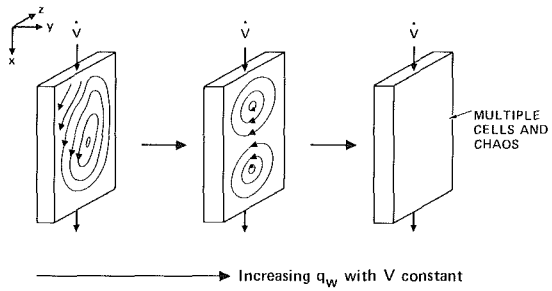

Fig. 3 Secondary flows and bifurcation phenomena observed in mixed turbulent convection for vertical ducts

At very high flow rates, upward flowing buoyant spots developed on the wall and were sheared off the wall into the free stream. The buoyant layer thickness also tended to increase as the volumetric flow rate was decreased. The interface between the buoyant layer and the free stream was wavy with vortices shedding off the layer into the free stream. The amplitude of the interfacial waves also decreased with decreasing volumetric flow rate.

Eventually, a bifurcation to a large secondary flow cell (circulation period >1 s) occurred in the neighborhood of $Gr_{Dh}/Re^2_{Dh} = 2$. This flow cell, and other observed bifurcation phenomena, are illustrated in Fig. 3. A notable characteristic of this single cell was that it definitely had a preferred flow direction (counterclockwise). The cell often attempted to reverse direction by slowing down considerably; however, no definite cell reversal was observed after the apparatus approached an average steady-state condition. The preferred flow direction was probably caused by unavoidable nonuniformities in the test section. It should also be noted that during transient heating the clockwise flow direction was predominant.

Bifurcations to multiple cells and eventually what appeared to be pure large-scale chaos were also observed as the heat flux was increased. The cells displayed chaotic behavior in flow direction with flow reversal periods that varied from seconds to minutes. No preference in flow direction was detected in this case. The pure chaotic state occurred at the largest values of Gr_{Dh}/Re^2_{Dh}. These flows were characterized by tumultuous swirling motions where huge quantities of fluid were convected up and then down the duct. This generated tremendous fluid mixing and thus higher heat transport.

Conclusions

An experimental study has been undertaken to gain an understanding of the fluid flow structure and heat transfer phenomena associated with mixed turbulent convection in vertical ducts. The duct under investigation had vertical and horizontal aspect ratios of 24.4 and 9.7, respectively. The working fluid was Freon-113, providing a Prandtl number of approximately 6.5. The results showed that a number of flow bifurcations occurred as Gr_{Dh}/Re^2_{Dh} was increased. The first bifurcation observed was from parallel turbulent mean flow to a large single flow cell in the x-z plane. This occurred in the neighborhood of $Gr_{Dh}/Re^2_{Dh} = 2$. Further bifurcations to multiple cells and eventually pure large-scale chaos were also observed. A correlation for the enhanced heat transfer was found to be

$$\frac{Nu_{Dh}}{Nu_{Dh,0}} = 1.0 + 0.9\left[\ln\left(\frac{Gr_{Dh}}{Re^2_{Dh}} + 1\right)\right]^{1.39}$$

where $Nu_{Dh,0}$ is the Petukhov-Virillov correlation for pure forced turbulent convection.

Downloaded 17 Dec 2010 to 193.140.21.150. Redistribution subject to ASME license or copyright; see http://www.asme.org/terms/Terms_Use.cfm

Acknowledgments

The authors gratefully acknowledge the support of the Electrical Power Research Institute under Project No. RP2122-9.

References

Axcell, B. P., and Hall, W. B., 1978, "Mixed Convection to Air in a Vertical Pipe," *Sixth IHTC*, Toronto, Canada, MC-7, pp. 37–42.

Brdlik, P. M., et al., 1979, "Heat Transfer Investigation for Mixed Free and Forced Turbulent Convection on Vertical Plates," *Second Symposium on Turbulent Shear Flows*.

Brown, C. K., and Gauvin, W. H., 1965, "Combined Free-and-Forced Convection," *Can. J. Chem. Engr.*, Vol. 43, pp. 306–318.

Brown, C. K., and Gauvin, W. H., 1966, "Temperature Profiles and Fluctuations in Combined Free-and-Forced Convective Flows," *Chem. Engr. Sci.*, Vol. 21, pp. 961–970.

Brown, W. G., 1960, *V.D.I. Forschungsheft*, No. 480.

Byrne, J. E., and Ejiogu, E., 1971, "Combined Free and Forced Convective Heat Transfer in a Vertical Pipe," *Symposium on Combined and Natural Convection, Inst. Mech. Engr.*, C118/71.

Carr, A. D., et al., 1973, "Velocity, Temperature, and Turbulence Measurements in Air for Pipe Flow with Combined Free and Forced Convection," ASME JOURNAL OF HEAT TRANSFER, Vol. 95, pp. 445–452.

Creveling, H. F., et al., 1975, "Stability Characteristics of a Single-Phase Free Convection Loop," *J. Fluid Mechanics*, Vol. 67, Pt. 1, pp. 65–84.

Easby, J. P., 1978, "The Effect of Buoyancy on Flow and Heat Transfer for a Gas Passing Down a Vertical Pipe at Low Turbulent Reynolds Numbers," *Int. J. Heat Mass Transfer*, Vol. 21, pp. 791–801.

Eckert, E. R., and Diaguila, A. J., 1954, "Convective Heat Transfer for Mixed, Free, and Forced Flow Through Tubes," *Trans. ASME*, Vol. 76, pp. 498–504.

Gorman, M., et al., 1984, "Chaotic Flow Regimes in a Convection Loop," *Phys. Rev. Let.*, Vol. 52, No. 25, pp. 2241–2244.

Hall, W. B., and Jackson, J. D., 1969, "Laminarization of Turbulent Pipe Flow by Buoyancy Forces," ASME Paper No. 69-HT-55.

Hall, W. B., and Price, P. H., 1970, "Mixed Forced and Free Convection From a Vertical Heated Plate to Air," *Fourth IHTC*, Paris, France, Vol. 4, NC3.3.

Hall, W. B., and Price, P. H., 1971, "Interaction between a Turbulent Free Convection Layer and a Downward Forced Flow," *Instn. Mech. Engrs.*, C113/71, pp. 6–12.

Hallman, T. M., 1956, "Combined Forced and Free Laminar Heat Transfer in Vertical Tubes With Uniform Internal Heat Generation," *Trans. ASME*, Vol. 78, pp. 1831–1841.

Herbert, L. S., and Sterns, U. J., 1972, "Heat Transfer in Vertical Tubes – Interaction of Forced and Free Convection," *Chem. Engr. J.*, Vol. 4, pp. 46–52.

Jackson, J. D., and Fewster, J., 1976, "Enhancement of Heat Transfer Due to Buoyancy for Downward Flow of Water in Vertical Tubes," *ICHMT*, International Seminar on Turbulent Buoyant Convection, Dubrovnik, Yugoslavia, pp. 759–775.

Jackson, J. D., 1983, "Turbulent Mixed Convection Heat Transfer to Liquid Sodium," *J. Heat Fluid Flow*, Vol. 4, No. 2, pp. 107–111.

Kemeny, G. A., and Somers, E. V., 1962, "Combined Free and Forced Flow in Vertical Circular Tubes – Experiments With Water and Oil," ASME JOURNAL OF HEAT TRANSFER, Vol. 84, pp. 339–346.

Kenning, D. B. R., et al., 1974, "Local Reductions in Heat Transfer Due to Buoyancy Effects in Upward Turbulent Flow," *Fifth IHTC*, Tokyo, Japan, NC4.3, pp. 139–143.

Khosla, J., et al., 1974, "Combined Forced and Natural Convection Heat Transfer to Air in a Vertical Tube," *Fifth IHTC*, Tokyo, Japan, NC4.4, pp. 144–148.

Nakajima, M., et al., 1980, "Buoyancy Effects on Turbulent Transport in Combined Free and Forced Convection between Parallel Plates," *Int. J. Heat Mass Transfer*, Vol. 23, pp. 1325–1336.

Ojalvo, M. S., et al., 1967, "Combined Forced and Free Turbulent Convection in a Vertical Circular Tube With Volume Heat Sources and Constant Wall Heat Addition," *Trans. ASME*, Nov., pp. 328–334.

Petukhov, B. S., and Kirillov, V. V., 1958, "The Problem of Heat Exchange in the Turbulent Flow of Fluids in Tubes," *Teploenegetika*, No. 4, pp. 63–68.

Petukhov, B. S., 1976, "Turbulent Flow and Heat Transfer in Pipes Under Considerable Effect of Thermogravitational Forces," *ICHMT*, International Seminar on Turbulent Buoyant Convection, Dubrovnik, Yugoslavia, pp. 701–717.

Petukhov, B. S., and Medvetskaya, N. V., 1978, "Turbulent Flow and Heat Exchange in Vertical Pipes Under Conditions of Strong Influence of Upward Forces," *Teplofizika Vysokikh Temperatur*, Vol. 16, No. 4, pp. 778–786.

Petukhov, B. S., et al., 1978, "Turbulent Flow and Heat Transfer in a Gravitational Field (Survey)," *Teplofizika Vysokikh Temperatur*, Vol. 16, No. 3, pp. 624–639.

Polyakov, A. F., 1973, "Transient Effects Due to Thermogravity in Turbulence and Heat Transfer," *Teplofizika Vysokikh Temperatur*, Vol. 11, No. 1, pp. 106–116.

Polyakov, A. F., 1974, "Mechanism and Limits on the Formation of Conditions for Impaired Heat Transfer at a Supercritical Coolant Pressure," *Teplofizika Vysokikh Temperatur*, Vol. 13, No. 6, pp. 1210–1219.

Polyakov, A. F., 1978, "Turbulent Forced Flow and Heat Transfer in Vertical Channels in Conditions of Free Convection," *Inzhenerno-Fizicheskii Zhurnal*, Vol. 35, No. 5, pp. 801–811.

Scheele, G. F., et al., 1960, "Effect of Natural Convection of Transition to Turbulence in Vertical Pipes," *Can. J. Chem. Engr.*, Vol. 38, No. 3, pp. 67–73.

Scheele, G. F., and Hanratty, T. J., 1962, "Effect of Natural Convection on the Stability of Flow in a Vertical Pipe," *J. of Fluid Mechanics*, Vol. 14, pp. 244–256.

Scheele, G. F., and Hanratty, T. J., 1961, "Effect of Natural Convection Instabilities on Rates of Heat Transfer at Low Reynolds Number," *AIChE J.*, Vol. 9, No. 2, pp. 183–185.

Watzinger, A., and Johnson, D. G., 1939, *Forschung-Ing. Wesen*, Vol. 10, pp. 182–196.

Downloaded 17 Dec 2010 to 193.140.21.150. Redistribution subject to ASME license or copyright; see http://www.asme.org/terms/Terms_Use.cfm

Win Aung
Director, Division of Mechanics, Structures, and Materials Engineering, National Science Foundation; Adjunct Professor, Department of Mechanical Engineering, Howard University, Washington, DC
Fellow ASME

G. Worku
Grove Engineering Inc., Gaithersburg, MD

Mixed Convection in Ducts With Asymmetric Wall Heat Fluxes

Results are presented of a numerical study dealing with combined free and forced laminar convection in a parallel plate vertical channel with asymmetric wall heating at uniform heat fluxes (UHF). The forced flow at the inlet is assumed to be spatially uniform and directed vertically upward. Quantitative information is provided pertaining to the effects of buoyancy and asymmetric heating on the hydrodynamic and thermal parameters. For values of Gr/Re up to 500 no flow reversal is predicted, in contrast to the case of uniform wall temperatures (UWT) recently reported. Other fundamental differences between UHF and UWT also are indicated.

Introduction

Recent technological implications have given rise to increased interest in mixed convection problems in vertical channels. The physical situations involved both buoyancy-aided and opposed cases, for laminar and turbulent flows. Consequently, the numbers of technical papers and technical sessions at professional society meetings that deal with combined free and forced convection are on the rise.

A review of the open literature, however, reveals that there has been only scant attention paid to mixed convection in vertical channels. For fully developed laminar flow, theoretical solutions have been obtained by Rao and Morris [1] for both buoyancy-assisted and opposed mixed convection under the condition that one wall is heated at uniform heat flux (UHF) and the other insulated. For assisted flow, heat transfer was found to increase with the Rayleigh number; for opposed flow the converse holds true. For hydrodynamically and thermally developing flow, Yao [2] presented an analysis of combined convection with symmetric uniform wall temperature (UWT) or UHF conditions. His study reveals the flow structure in the developing region, and leads to the conjecture that reversed flow of a periodic nature could be present in fully developed flow. For a vertical parallel plate channel with one wall at UHF and the other wall insulated, Malik and Pletcher [3] obtained theoretical results for the laminar buoyancy assisted flow of ethylene glycol, including variable property effects. The theoretical study shows that, with the onset of flow reversal adjacent to the cool wall, an increase in the heat transfer occurs.

In a recent paper [4], the present authors discussed the results of a study of laminar mixed convection in a parallel plate vertical channel in which the two walls are maintained at uniform but not necessarily equal temperatures (UWT). Buoyancy forces have been shown to introduce a distortion into the velocity profile while asymmetric heating is seen to cause a skewness that can be quite severe. For symmetric heating the distortions eventually disappear and the profile evolves into a parabolic shape at large distances from the channel entrance. For asymmetric heating the distortions, skewness, and even flow reversal are present in fully developed flow. Quantitative results on the Nusselt number and bulk temperature indicate a significant influence due to buoyancy and asymmetric heating. Finally, the hydrodynamic development length is found to increase dramatically with buoyancy, which has the opposite influence on the thermal development length.

The purpose of the present paper is to report the results of a study in which the channel walls are maintained at uniform but not necessarily equal heat fluxes. As in [4], the results are obtained by a numerical solution of the describing equations using an implicit finite difference technique. The overall investigation comprised a thesis [5] in which the objective is to secure a quantitative understanding of mixed convection in a configuration having current engineering applications, such as solar energy and electronic system cooling. In these applications, the wall heating is more nearly uniform in heat fluxes than in temperatures. A fundamental difference between the two heating conditions is that in UWT, the fluid temperatures approach constant values at large axial distances, whereas the thermal field continues to change in UHF. This phenomenon could lead to a major alteration of the structure of flow, including the occurrence of flow separation.

Table 1 Mesh sizes employed

	ΔX	ΔY
$0 \le X \le 0.0002$	0.0001	0.0125
$0.0002 \le X \le 0.0006$	0.0002	0.0125
$0.0006 \le X \le 0.001$	0.00025	0.025
$0.001 \le X \le 0.01$	0.0005	0.02
$0.01 \le X < \infty$	0.001	0.05

Theoretical Approaches

Consider the situation in which a parallel plate duct is oriented along the gravitational direction. A forced flow approaches the bottom of the duct with a flat upward (positive X direction) velocity profile and a uniform temperature. The right wall is heated uniformly by external means at a rate q_2 and the left wall heat flux is q_1. The ratio of the heat fluxes is r_H, where $0 \le r_H \le 1$, which characterizes the degree of asymmetric heating. The flow is considered laminar throughout and fluid properties are assumed constant except for the buoyancy term in the momentum equation. It is clear that the situation under consideration constitutes what is sometimes known as "aiding" flow. The dimensionless equations and the boundary conditions that describe the physical situation are

Continuity

$$\frac{\partial U}{\partial X} + \frac{\partial V}{\partial Y} = 0 \tag{1}$$

x momentum

$$U\frac{\partial U}{\partial X} + V\frac{\partial U}{\partial Y} = -\frac{\partial P}{\partial X} + \frac{Gr}{\mathrm{Re}}\theta + \frac{\partial^2 U}{\partial Y^2} \tag{2}$$

Contributed by the Heat Transfer Division for publication in the JOURNAL OF HEAT TRANSFER. Manuscript received by the Heat Transfer Division June 10, 1985.

Copyright © 1987 by ASME

Downloaded 17 Dec 2010 to 193.140.21.150. Redistribution subject to ASME license or copyright; see http://www.asme.org/terms/Terms_Use.cfm

y momentum

$$\frac{\partial P}{\partial Y}=0 \tag{3}$$

Energy

$$U\frac{\partial \theta}{\partial X}+V\frac{\partial \theta}{\partial Y}=\frac{1}{Pr}\frac{\partial^2\theta}{\partial Y^2} \tag{4}$$

$$\begin{aligned}
&\text{At } X=0, \quad 0\le Y\le 1: \quad U=1, \quad V=0, \quad \theta=0, \quad P=0\\
&\text{At } X>0, \quad Y=0: \quad U=0, \quad V=0, \quad \partial\theta/\partial Y=-r_H\\
&\text{At } X>0, \quad Y=1: \quad U=0, \quad V=0, \quad \partial\theta/\partial Y=1
\end{aligned} \tag{5}$$

Note that in addition to r_H, the nondimensional temperature and the Grashof number are defined differently than for UWT; otherwise, all parameters have the same definitions as in [4].

The describing equations are solved in conjunction with the above boundary conditions by means of a finite difference method employing an implicit differencing scheme. The method has been described in [6]; suffice it to say here that this approach transforms the differential equations into a set of algebraic equations, and the flow region is overlaid with a grid system that is spatially uniform in the transverse direction but the spacing is made smaller near the channel entrance where sharp changes in the variables are expected. Similarly, smaller axial nodal sizes are employed near the channel entrance. The numerical procedure involves a marching scheme in which the conditions specified at the channel entrance are used to calculate the values of the variables for the first row of nodes inside the channel, and these are in turn used to calculate late values for the next row. The process is repeated until a prescribed value of X is reached, or until the velocity and temperature profiles cease to change appreciably from one row to the next. Typical node spacings employed in this investigation are indicated in Table 1. As noted in [4, 5], the present approach has been subjected to a process of validation by comparison with existing results for simplified cases, giving excellent agreement and hence confidence in the validity of the new results to be presented herein.

The above describes the approach utilized to obtain the solutions for the developing flow which, as will be discussed, approaches fully developed flow (FDF) at large values of X. Results for FDF may be obtained directly from an appropriate simplification of the describing equations, starting from the fundamental condition that in FDF, $V\equiv 0$. The analysis is reported in [7].

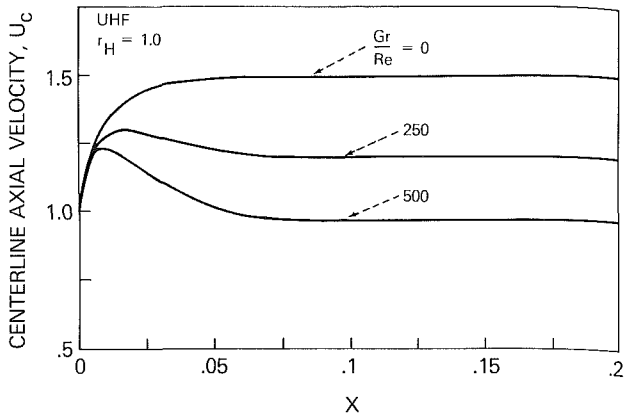

Fig. 1 Axial variation of the centerline velocity ($r_H = 1.0$)

Discussion of Results

Hydrodynamic Parameters. In the UWT case, the effect of buoyancy is most noticeable on the velocity profile. The profile in that case is highly distorted during flow development. The distortion diminishes in FDF when $r_T<1$, and completely disappears when $r_T=1$ (symmetric wall temperatures) resulting for all Gr/Re values in a parabolic profile. In the present UHF case, a similar situation exists for $r_H < 1$, but when symmetric heating occurs ($r_H=1$), the velocity becomes parabolic only for Gr/Re = 0; for Gr/Re > 0, the FDF profile is found to depend on the value of the latter parameter. Figure 1 illustrates this point using the axial variation of the centerline temperature. For symmetric heating ($r_H=1$), the centerline velocity develops into the FDF of $U_c = 1.5$ when Gr/Re = 0, and full development is accomplished at a very small value of the dimensionless distance X when compared to the UWT case. When Gr/Re > 0, the development length, as indicated by the region where U_c is changing, is increased and this trend is consistent with the UWT case; however, unlike UWT, the centerline velocity fails to develop into the universal value of 1.5, but instead assumes values progressively smaller as Gr/Re increases. Thus, a major difference between UWT and UHF (when $r_T = r_H = 1$) lies in FDF, where in UWT an identical profile is assumed by the fluid at all values of Gr/Re, whereas in UHF the profile suffers a center depression or concavity that becomes increasingly pronounced as Gr/Re increases.

For $r_H = 0.5$, the present results show that the profile at a

Nomenclature

b = duct spacing
c_p = specific heat at constant pressure
g = acceleration due to gravity
Gr = Grashof number; $g\beta q_2 b^4/\nu^2 k$ (UHF) or $g\beta(T_2 - T_0)\, b^3/\nu^2$ (UWT)
k = thermal conductivity
p' = static pressure
p'' = hydrostatic pressure
P = $(p' - p'')/\rho u_0^2$
Pr = Prandtl number = $\mu c_p/k$
q = heat transfer per unit surface area per unit time
r_H = q_1/q_2
Re = Reynolds number = $u_0 b/\nu$
T = temperature
u, v = axial or streamwise velocity and transverse velocity, respectively
U = dimensionless axial velocity = u/u_0
V = dimensionless transverse velocity = vb/ν
x, y = axial and transverse coordinates, respectively ($x=0$ at duct entrance; $y=0$ on cool wall)
X = dimensionless axial coordinate = $x/(b\text{Re})$
Y = dimensionless transverse coordinate = y/b
β = thermal expansion coefficient
μ = dynamic viscosity = $\rho\nu$
ν = kinematic viscosity
θ = dimensionless temperature = $(T - T_0)/(q_2 b/k)$

Subscripts

b = bulk condition
c = centerline value
w = condition at wall
0 = condition at entrance of duct
1 = pertaining to the cool wall
2 = pertaining to the hot wall

Downloaded 17 Dec 2010 to 193.140.21.150. Redistribution subject to ASME license or copyright; see http://www.asme.org/terms/Terms_Use.cfm

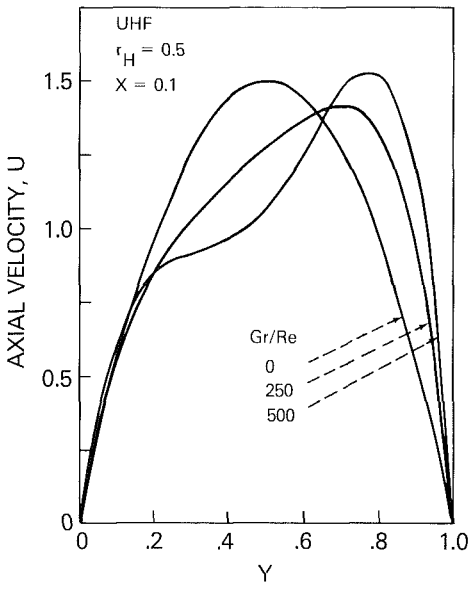

Fig. 2 Variation of the velocity profile with the buoyancy parameter ($r_H = 0.5$; $X = 0.1$)

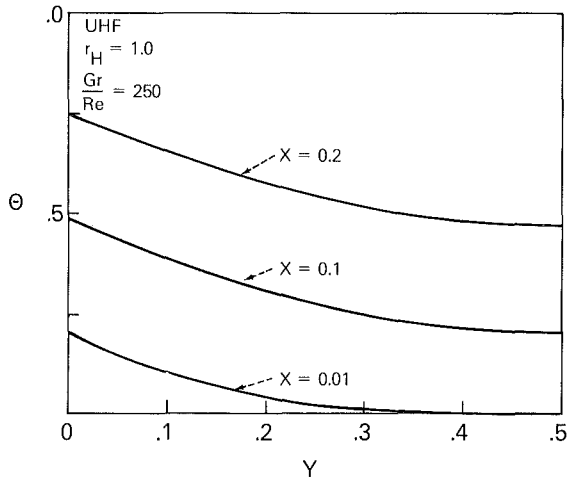

Fig. 3 Development of the temperature profile ($r_H = 1.0$; Gr/Re = 250)

relatively large value of X is not affected by the asymmetric heating when Gr/Re = 0, and a parabolic profile is attained by the fluid. This is shown in Fig. 2. The same figure also shows that for Gr/Re > 0, the fluid flow is more and more channeled toward the hot wall ($Y = 1$). There is only a negligible effect on the fluid flow near the cool wall, and at Gr/Re = 500, the maximum velocity is still not much larger than 1.5. This may be contrasted with UWT case of [4] for which the maximum fluid velocity is close to 2.0 when $r_T = 0.5$, Gr/Re = 250, and $X = 0.1$. When Gr/Re is fixed at 250, comparison of the profiles for various streamwise distances with those in [4] gives reinforcement to the inference that buoyancy has a much larger effect in UWT than in UHF. Certainly, fluid velocities are larger adjacent to the hot wall in UWT. As pointed out in [4], the large flow rates in the region near the hot wall must be augmented, in mixed convection where the rate of flow entering the channel is controlled by a blower (as opposed to a suction fan at the exit) at the entrance, by fluid flow coming down the top of the channel along the cool wall, thereby leading to the occurrence of flow separation inside the channel in UWT. The implication of the above discussion is that in UHF the likelihood of flow separation is reduced if not completely eliminated. Within the ranges of parameters studied herein, i.e., $0.3 \le r_H \le 1$, $0 \le$ Gr/Re ≤ 500, no flow reversal was observed.

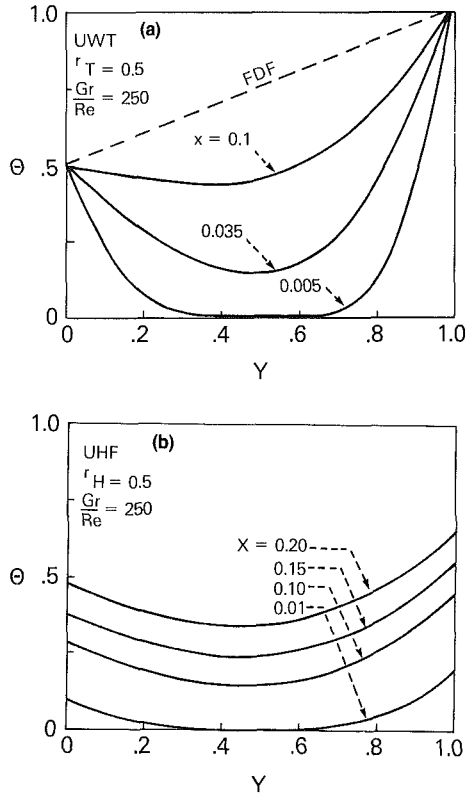

Fig. 4 Comparison of temperature development with UWT ($r_T = r_H = 0.5$; Gr/Re = 250)

The axial distribution of the dimensionless pressure for $r_H = 1$ shows a trend that is similar to that in UWT; however, here too the effect of buoyancy is not as significant. The available information suggests that even at a relatively small value of Gr/Re, the pressure P eventually becomes positive when X is sufficiently large.

Heat Transfer Parameters. In the present study, heat transfer results have been obtained for Pr = 0.72. An examination of the thermal results obtained also reveals a smaller effect due to buoyancy as compared with UWT. Figure 3 depicts typical development of the temperature profiles for $r_H = 1$ for a fixed value of Gr/Re = 250. At large X, the curves become parallel to one another, suggesting equal axial temperature gradient throughout the flow. This is of course a characteristic of thermally fully developed flow. A constrast between UHF and UWT in the thermal profiles is provided in Figs. 4(a) and 4(b). The profiles in UWT degenerate into a linear one at large X, while in UHF they maintain a self-similar concave shape in FDF.

The axial variations of the wall temperatures are given in Figs. 5(a) and 5(b) with Gr/Re as a parameter. The effect of buoyancy is to decrease the wall temperatures, but the impact on the cool wall, when $r_H = 0.5$, is negligible. This is consistent with the picture presented by the temperature distribution when X is kept fixed but Gr/Re is allowed to vary [5]. In this case, the temperature on the cool wall is found to be virtually unchanged as Gr/Re increases, but the hot wall temperature is reduced.

The wall temperatures, particularly the cool wall temperature, are sensitive to the parameter r_H. In Fig. 6(a) the cool wall temperature is plotted versus X for a fixed Gr/Re = 250, but r_H is allowed to vary. Note the drastic variation of the curves for different r_H. In Fig. 6(b), the corresponding plot for the hot wall temperature is presented. The trend is the same but the variations on the hot wall due to r_H are much smaller.

Downloaded 17 Dec 2010 to 193.140.21.150. Redistribution subject to ASME license or copyright; see http://www.asme.org/terms/Terms_Use.cfm

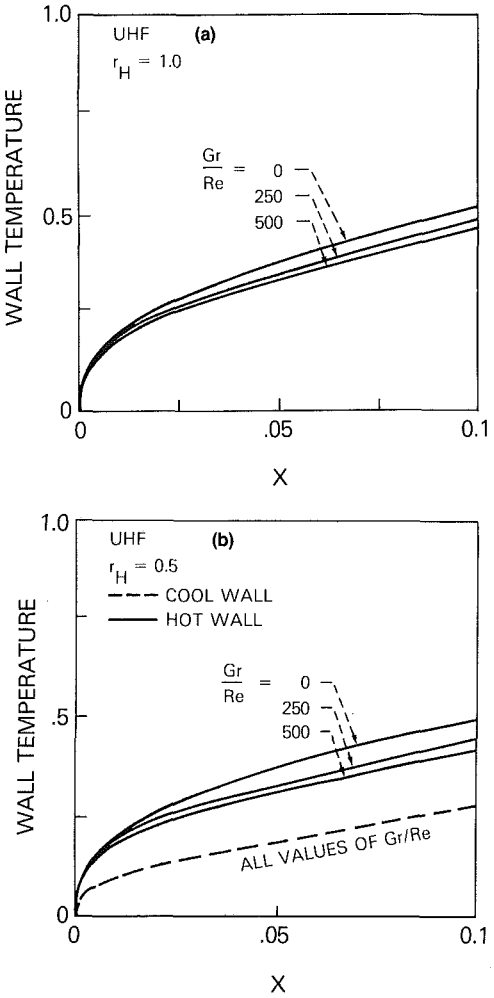

Fig. 5 Axial variation of the wall temperature for $r_H = 1.0$ and 0.5

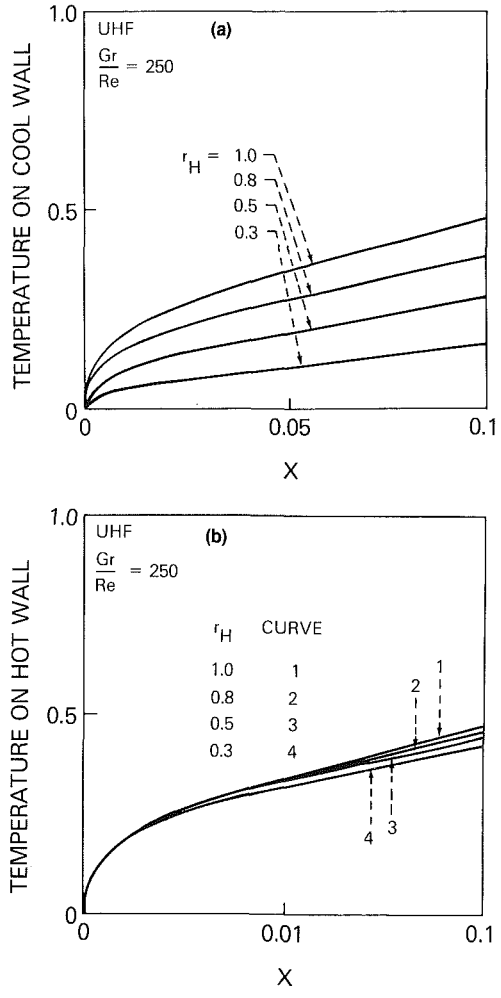

Fig. 6 Axial variations of the temperatures on the hot and cool walls for Gr/Re = 250 at different r_H (note different horizontal scales)

In engineering applications involving duct flow, a local average fluid temperature is often necessary information. A commonly employed average temperature is the bulk temperature, defined by

$$\theta_b = \frac{\int_0^1 U\theta dY}{\int_0^1 U dY}$$

In this study, this parameter is evaluated as a function of axial position. In UWT, the bulk temperature approaches a constant value at large X, and the asymptote depends on Gr/Re except when $r_T = 1$, in which the asymptote is 1 for all Gr/Re. In the present case, thermal energy is supplied to the fluid at constant rates from the two walls along the entire duct; hence θ_b varies linearly with X, and is a function only of the rate of energy input, i.e., on r_H, and not on Gr/Re. The presentation of the results can be simplified by defining the wall temperature in terms of the average of the two wall heat fluxes, instead of the hot wall temperature. Thus, the dimensionless hot wall temperature becomes

$$\bar{\theta}_2 = \frac{T_2 - T_0}{\bar{q}\, b/k}$$

where $\bar{q} = (q_1 + q_2)/2 = q_2\,(r_H + 1)/2$.

Hence,

$$\bar{\theta}_2 = \frac{2\theta_2}{(r_H + 1)}.$$

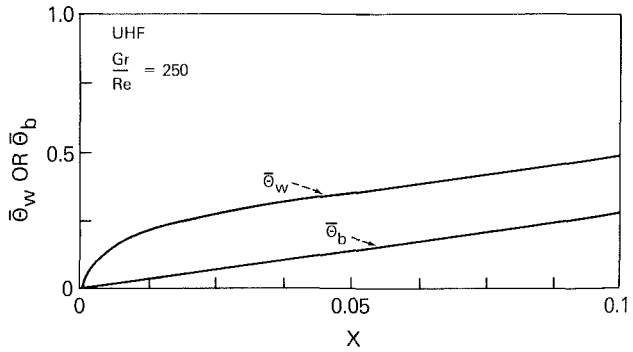

Fig. 7 Axial variations of the average wall and bulk temperatures for all values of r_H at Gr/Re = 250

Similarly,

$$\bar{\theta}_b = \frac{2\theta_b}{(r_H + 1)},$$

and the average of the two wall temperatures at position X is given by

$$\bar{\theta}_w = \frac{\theta_1 + \theta_2}{(1 + r_H)}$$

The quantities $\bar{\theta}_b$ and $\bar{\theta}_w$ are plotted in Fig. 7 for Gr/Re =

Downloaded 17 Dec 2010 to 193.140.21.150. Redistribution subject to ASME license or copyright; see http://www.asme.org/terms/Terms_Use.cfm

250. For each parameter, a universal curve valid at any value of r_H results.

Conclusions

It is evident that there are significant fundamental differences between UHF and UWT in mixed convection between asymmetrically heated vertical plates. In UHF, buoyancy introduces a lesser degree of skewness in the velocity profiles and thus exerts a lesser influence on both the hydrodynamic and thermal parameters of the problem. Similarly, flow reversal is more prone to occur in UWT than UHF; in fact, up to a value Gr/Re = 500 no flow reversal is predicted in the present analysis for any value of r_H.

References

1 Rao, T. L. S., and Morris, W. D., "Superimposed Laminar Forced and Free Convection Between Vertical Parallel Plates When One Plate is Uniformly Heated and the Other is Thermally Insulated," *Proceedings of Institution of Mechanical Engineers*, Vol. 182, Part 3H, 1967–68, pp. 374–381.

2 Yao, L. S., "Free and Forced Convection in the Entry Region of a Heated Vertical Channel," *International Journal of Heat and Mass Transfer*, Vol. 26, 1983, pp. 65–72.

3 Malik, M. R., and Pletcher, R. H., "Calculation of Variable Property Heat Transfer in Ducts of Annular Cross Section," *Numerical Heat Transfer*, Vol. 3, 1980, pp. 241–257.

4 Aung, W., and Worku, G., "Developing Flow and Flow Reversal in a Vertical Channel With Asymmetric Wall Temperatures," ASME JOURNAL OF HEAT TRANSFER, Vol. 108, 1986, pp. 299–304.

5 Worku, G., "Developing Laminar Combined Natural and Forced Convection Flow Between Vertical Parallel Plates," M.S. Thesis, Howard University, Washington, DC, 1982.

6 Aung, W., Fletcher, L. S., and Sernas, V., "Developing Laminar Free Convection Between Vertical Plates With Asymmetric Heating," *International Journal of Heat and Mass Transfer*, Vol. 15, 1972, pp. 2293–2308.

7 Aung, W., and Worku, G., "Theory of Fully Developed, Combined Convection Including Flow Reversal," ASME JOURNAL OF HEAT TRANSFER, Vol. 108, 1986, pp. 485–488.

Downloaded 17 Dec 2010 to 193.140.21.150. Redistribution subject to ASME license or copyright; see http://www.asme.org/terms/Terms_Use.cfm

Dispersion Phenomenology of LNG Vapor in the Burro and Coyote LNG Spill Experiments

D. L. Morgan, Jr.
Lawrence Livermore National Laboratory,
Livermore, CA 94550

Various physical phenomena affecting LNG vapor dispersion were observed in LNG spill experiments conducted by the Lawrence Livermore National Laboratory. Understanding the phenomena is necessary in predicting the size of the hazardous region of vapor concentration following a spill. Gravity flow of the cold dense vapor increased cloud width while density stratification and heat flow from the ground had substantial effects on the mixing rate with air. Density stratification inhibits turbulent mixing while heat flow into the cloud promotes it through a number of processes including buoyancy. Some possible instances of buoyancy were observed in the experiments, and calculations indicate that modest amount of additional heat might substantially increase cloud dispersion. In the experiments, these phenomena led to a dependence of the maximum distance £ to the lower flammability limit on source rate, wind speed, and atmospheric stability that was substantially different from the prediction of the Gaussian plume model. Including these phenomena in predictive models is important for their accuracy. Time-dependent features of the concentration field due to turbulence and rapid phase-transition explosions, which also affect £, were examined by applying a space–time interpolation scheme to the concentration data.

Introduction

Understanding the physical phenomena affecting the dispersion of LNG vapor following an LNG spill is necessary to predict the location and size of the flammable region of vapor concentration. Observation of these phenomena and the quantitative measurement of their manifestations was a major purpose of the Burro and Coyote series of liquefied natural gas (LNG) spill experiments. These DOE-sponsored experiments were conducted at China Lake, CA, in 1980 and 1981 by Lawrence Livermore National Laboratory in cooperation with the Naval Weapons Center. The experiments involved the release of LNG vapor from LNG spilled onto water at a steady rate. The spills were of sufficient duration that the resultant vapor clouds achieved steady-state conditions [1]. In their continuous nature the experiments were similar to most of the Maplin Sands LNG spill experiments [2] and different from the instantaneous heavy gas releases that constituted most of the Thorney Island experiments [3]. Koopman et al. [4, 5] and Goldwire et al. [6] give detailed descriptions of the experiments and the data collected, as well as the methods and results of the data analysis. Morgan et al. [1] describe dispersion-related features and data-model comparions, while Rodean et al. [7] analyze the data from burns of the LNG vapor cloud conducted in the Coyote experiments shortly after spill termination when steady-state conditions were present. In this report we discuss the results of studies of the phenomenology of LNG vapor dispersion as observed in these experiments.

LNG (liquefied natural gas) is composed principally of methane, with molar fractions of ethane between about 5 and 20 percent. It also contains propane and other compounds in much smaller amounts. LNG vapor poses a flammability hazard because it can ignite and burn at volume concentrations between the approximate 5 percent LFL (lower flammability limit) and the 15 percent UFL (upper flammability limit). Concentrations here and throughout are volume (molar) concentrations unless otherwise noted.

Contributed by the Heat Transfer Division for publication in the JOURNAL OF HEAT TRANSFER. Manuscript received by the Heat Transfer Division February 20, 1986. Paper No. 84-WA/HT-79.

The physical phenomena that affect dispersion of LNG vapor are due to or influenced by the fact that the vapor is initially denser and colder than air. Turbulent mixing of the vapor with air is reduced by stratification resulting from the density difference. This reduction leads to higher concentrations and a greater extent of the hazardous region, and hence a greater value of £, the maximum observed downwind distance from the source to the point at which concentration is equal to the LFL considering all times and horizontal and vertical crosswind locations. Because of the density difference between LNG vapor and air, the vapor cloud that results from mixing will undergo gravity flow. This effect can widen the vapor cloud and increase the ground area covered by the hazardous region.

LNG vapor is heavier than air only because it is cold ($-160°C$ to $-155°C$ initially, depending on ethane concentration); at ambient temperature it is lighter than air. Thus, heat flux from the surroundings, in particular from the ground, can lessen the density difference. Heat flux promotes convective turbulence, which also leads to greater mixing with the air. Both of these effects reduce the value of £. Heat flux can also lead to buoyancy of the cloud, since at equal temperatures LNG vapor is lighter than air.

Other phenomena that affect the value of £ are turbulence-induced variations in concentration and puffs of gas released from the LNG source by RPT explosions when LNG is spilled into water [8, 9]. RPT (rapid phase transition) explosions involve the sudden change of some of the LNG in the water to LNG vapor.

Experimental Observations

The data gathered in the Burro and Coyote experiments show the effects of the phenomena pertinent to LNG vapor dispersion. The effects of gravity flow, RPT explosions, turbulent variations, and possible buoyancy are directly apparent in the vapor concentration data of the experiments. We see the other heat flow phenomena and the reduction in mixing due to density stratification by their overall effects on concentration and by their effect on the way £ depends on spill and meteorological parameters (described in a later section).

Copyright © 1987 by ASME

Downloaded 17 Dec 2010 to 193.140.21.150. Redistribution subject to ASME license or copyright; see http://www.asme.org/terms/Terms_Use.cfm

Table 1 Crosswind dimensions of the Burro 8 cloud compared to predictions of the Gaussian plume model for 400 m downwind

Stability category	Half-width		Height	
	Gausssian plume	Experiment	Gaussian plume	Experimemt
D	50 m	145 m	24 m	< 8 m
E	35 m		18 m	

Since the Burro 8 experiment was characterized by one of the highest spill rates of the tests, the lowest wind speed (1.8 m/s), and the highest atmospheric stability, gravity flow effects were more pronounced in this test than in any of the others [10, 11]. Enhanced cloud width and the gravity-flow effect of cloud bifurcation were observed; the concentration was lower along the cloud centerline than in the lobes on either side. The influence of the uneven terrain on gravity flow caused the cloud to move preferentially to the lower elevations. In general, peak concentrations above any surface point were higher in Burro 8 than in any other test. This may have been partly a consequence of gravity flow, but is probably more a consequence of density stratification leading to reduced turbulent mixing, coupled with the fact that Burro 8 had the lowest ambient turbulence level of the experiments, due to low wind speed and relatively high atmospheric stability.

The effects of gravity flow on the crosswind dimensions of the Burro 8 cloud are shown in Table 1. The measured crosswind dimensions of the cloud at one third of maximum crosswind concentration are compared to predictions of the Gaussian plume model [12] which does not include the effects of gravity flow. The observed width is about three times the predicted value, while the height is less than one-half of the prediction. Burro 8 had an ambient Richardson number at 2 m of +0.121, which places the ambient stability about midway between categories D (neutral) and E (slightly stable) for a surface roughness of 2.05×10^{-4} m [4, 13]. The half-width of the Burro 8 source is estimated to be about 10 m or less; thus the point-source Gaussian plume model was employed. It was earlier shown [10] that gravity flow leads to clouds consistently wider and lower than predicted by the Germeles–Drake model [14] which includes some gravity flow effects.

Gravity flow effects are significant, but to a lesser degree than in Burro 8, at the higher wind speeds in the other experiments. As shown in Fig. 1, gravity flow increased the width of the cloud in Coyote 6 (wind speed = 4.6 m/s) over that of Coyote 5 (wind speed = 9.7 m/s). Although not directly apparent in the figure, the excess width is also present in terms of width at a given fraction of maximum crosswind concentration. For a neutrally buoyant gas cloud, width is independent of wind speed, but inversely dependent on stability. Thus, without gravity effects, the Coyote 6 cloud would be the narrower, since the Coyote 6 test was conducted under more stable conditions. Gravity-incluced spread is inversely dependent on wind speed, hence the narrower cloud of Coyote 5.

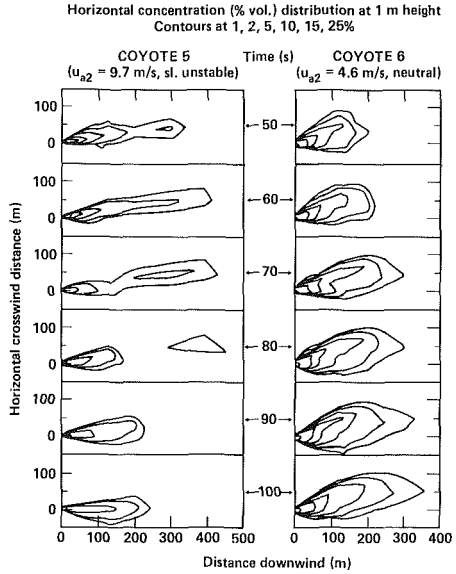

Fig. 1 The wider cloud of Coyote 6 is due to gravity flow. The high level of turbulence in Coyote 5 causes the formation of gas puffs.

Heat flow from the ground appears to have made part of the cloud buoyant in the Burro 9 experiment, as shown in Fig. 2. In this figure, approximately the same portion of the Burro 9 cloud is shown as it moves downwind and lifts off the ground. It is shown in the following section that heat from entrained air is insufficient, in itself, to make the cloud buoyant.

Buoyancy may have also occurred in the Burro 8 experiment. As shown in Fig 3, the left lobe of the cloud lifted off the ground at 400 m downwind. Liftoff of the left lobe at 400 m was present during the time concentrations exceeded 1 percent, while liftoff of the right lobe was never observed. From

Nomenclature

a, A = coefficients in fit for £
C_{pa} = air specific heat at constant pressure
C_{ps} = LNG vapor specific heat at constant pressure
C_v = volume concentration of LNG vapor
D = duration of spill
H = heat added to cloud
h = dimensionless measure of H
LFL = lower flammability limit of concentration
LNG = liquefied natural gas
M_a = molecular weight of air
M_s = molecular weight of LNG vapor
m_s = mass of LNG vapor
q = LNG spill rate
q_{gm} = geometric mean of q values
Ri_2 = ambient Richardson number at 2 m
RPT = rapid phase transition (explosion)
T_a = temperature of air
T_s = temperature of LNG vapor
t = time after spill begins
u = ambient wind speed
u_{a2} = ambient wind speed at 2 m
u_{a2gm} = geometric mean of u_{a2} values
UFL = upper flammability limit of concentration
x = downwind distance from source
α, β, γ = exponents in fit for £
λ = M_s/M_a
μ = C_{ps}/C_{pa}
ν = T_s/T_a
ρ = density of cloud
ρ_a = density of air
σ = cross-sectional area of cloud
ϕ_2 = ambient Prandtl number at 2 m
ϕ_{2gm} = geometric mean of ϕ_2 values
£ = maximum distance to the LFL

Downloaded 17 Dec 2010 to 193.140.21.150. Redistribution subject to ASME license or copyright; see http://www.asme.org/terms/Terms_Use.cfm

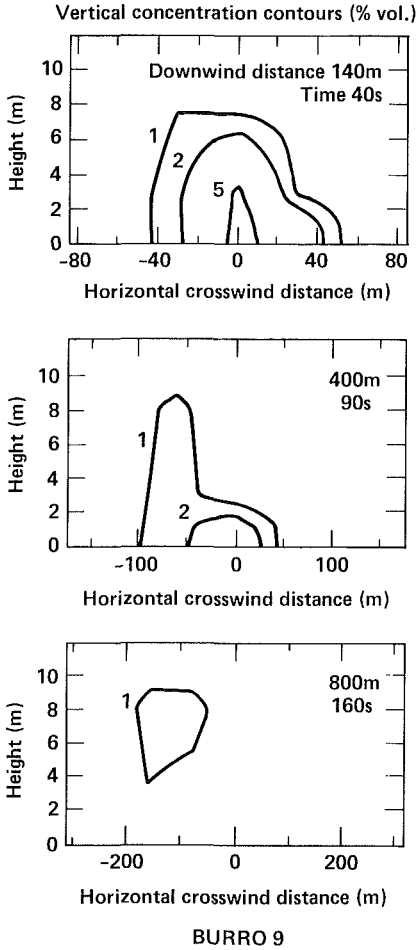

Fig. 2 Concentration in a vertical, crosswind section of a portion of the cloud as it moves downwind. This portion of the Burro 9 cloud apparently becomes buoyant.

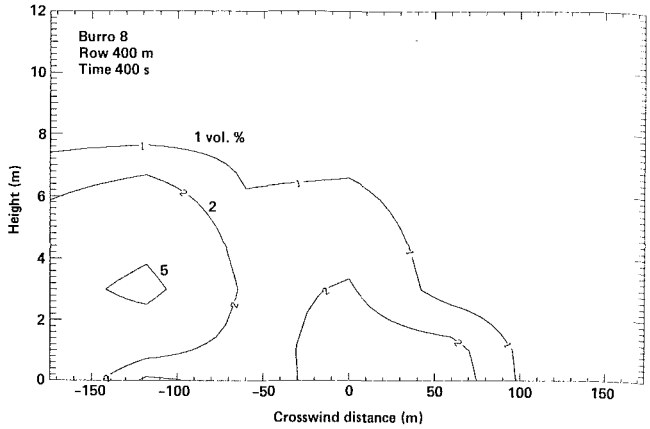

Fig. 3 Burro 8 vapor concentration (vol %) in the vertical crosswind plane at 400 m downwind of the spill. With directions defined by looking upwind, the left lobe of the cloud (left in the figure) has lifted off the ground (possible buoyancy). The centerline of the cloud is at about −50 m in the crosswind direction.

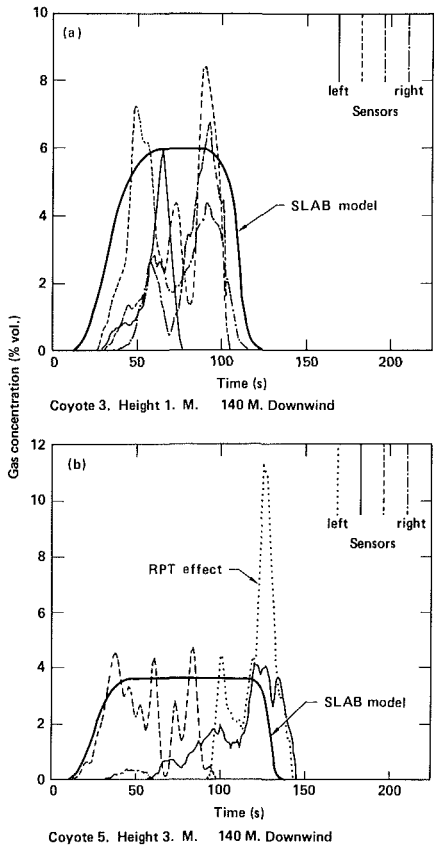

Fig. 4 Example of the effect of turbulent variation in 10-s averaged concentration time histories. The results of SLAB model simulations are included.

cloud arrival times, it appears that the left lobe was moving more slowly than the right, thus it may have absorbed more heat from the ground, in an amount sufficient to make it buoyant. (Only momentary instances of liftoff occurred at the adjacient row of sensors closer to the source at 140 m downwind. Only momentary liftoff was recorded at the next sensor row at 800 m, possibly because the major portion of the left lobe was outside the sensor array at that distance.)

A calculation of the cloud density at the point of highest concentration in the left lobe, based on measurements of concentration, temperature, and vapor composition, gives a density of about 0.7 percent less than that of the surrounding air. Estimates of rise speed for that density difference give values sufficient to account for the observed degree of liftoff, but small uncertainties in the measurements yield an uncertainty in the density that is about the same size as the calculated density difference.

An alternative explanation for the liftoff of the left lobe involves vortices along the lateral cloud edges that are generated by gravity-induced lateral flow [11, 15]. Such a vortex might entrain more air in its exterior portions resulting in higher concentrations at its center. The point of maximum concentration in Fig. 3 may be the center of a vortex. These vortices are predicted by simulations of the Burro 8 experiment by the FEM3 computer model [16] for heavy gas dispersion. FEM3 is a fully three-dimensional model that has successfully simulated cloud structure, flow, and dispersion in the Burro and Coyote experiments [1].

The only other observed case of persistent liftoff in the experiments, although somewhat erratic, occurred in Coyote 5. It occurred during the early through midportions of the time the cloud was present at downwind distances of 200 m and greater. Therefore, it may be more likely a consequence of the erratic cloud structure observed at the same time (see Figs. 1 and 8) than of buoyancy.

The effects of random and quasi-periodic turbulent variations on 10-s averaged concentration data are illustrated in Figs. 4(*a*) and 4(*b*). Here concentration time histories from sensors at different horizontal crosswind locations are superimposed. Low-frequency variations in the wind direction (periods of a few tens of seconds or greater) are responsible

Downloaded 17 Dec 2010 to 193.140.21.150. Redistribution subject to ASME license or copyright; see http://www.asme.org/terms/Terms_Use.cfm

for cloud meander in the horizontal crosswind direction, which is most apparent in 4(*b*) where the relatively narrow cloud of Coyote 5 moves from right to left (looking upwind) during the test. Higher frequency turbulent variations are also apparent. Variations of concentrations in the downwind direction are seen in Fig. 1 (see also Fig. 8) where there is a quasi-periodic formation of gas puffs at the downwind end of the Coyote 5 cloud. This phenomenon was seen to such a degree only in that test and can be associated with the fact that Coyote 5 had the highest level of ambient turbulence in the experiments.

Variability in concentration may also arise from shear instabilities and gravity waves and from variations in the source rate. One particular source rate variation is due to RPT explosions, which cause a sudden release of vapor from the spill pond. The puffs of vapor cause momentary increases in concentration as they blow downwind, in particular at the higher elevations above the surface, e.g., the large peak in Fig. 4(*b*). The effects of RPTs are discussed in more detail in [17].

In the absence of the above variations, concentration time histories would have an appearance similar to the smooth curves in Figs. 4(*a*) and 4(*b*). These curves are the cloud centerline concentrations at the indicated downwind distance and heights taken from simulations of the Coyote 3 and 5 experiments using the time-dependent SLAB computer model [1, 10, 18]. In the SLAB simulations, the fairly accurate assumption is made that the LNG evaporates as soon as it is spilled. In most cases, ensemble-averaged predictions of concentration, as SLAB makes, involve the presence of a steady state (flat tops of the curves) when the source is on at a constant rate for a sufficient time and the meteorological parameters are constant. The variations produce maximum values of concentration that exceed the mean, steady-state values, thus leading to larger values of $\mathfrak{L}$ than would be present in their absence. Hence the importance of considering and quantifying the variations [21].

The time-dependent SLAB computer code referred to above is based on a one-dimensional, quasi-three-dimensional model for heavy gas dispersion in which the effects of turbulent mixing are modeled by entrainment. The entrainment speed is calculated as a function of ambient and local-cloud variables by an expanded version of Zeman's initial formula [19] for entrainment of air into a heavy gas cloud. The expanded version adds parameterized dependence on friction velocity, velocity gradient, and convection scale velocity and is fit to relevant experimental data [20] for ranges of these quantities that occur in heavy gas releases. The rate of heat flow into the cloud is calculated by a formula due to Zeman [19] or by an experimentally based formula [4]. Time-dependent SLAB was originated by Zeman [19]. It is described in [10], and details of its current form, capabilities, and useage are given in [1, 18]. Time-dependent SLAB has been successful in calculating the values of $\mathfrak{L}$ in the Burro and Coyote experiments [1, 22].

Heat Flow and Buoyancy

Increasing temperature in the cloud reduces the density stratification (a dense cloud below lighter air), thereby bringing the initially low level of mixing closer to its ambient level and reducing lateral spread due to gravity flow. Heat flow from the surface promotes convention within the cloud which adds to the turbulent mixing rate. With sufficient heating, the cloud may become buoyant, and the upward motion lifts the cloud off the ground (away from some possible sources of ignition) and gives rise to further turbulent mixing. Thus, adding heat to the cloud has the potential for substantially reducing the hazardous area around an LNG spill.

Except for the possibility of buoyancy, it is difficult to observe directly the effects of heat flow. However, heat flow is important in explaining how cloud properties depend on spill and meteorological conditions (see following section), and its effects may be separated from those of other phenomena by the use of computer models.

In sensitivity studies based on the Burro 9 experiment [22, 23], SLAB model simulations showed that reducing the local ground-to-cloud heat flow rate from the experimentally observed amount [4] to zero increased $\mathfrak{L}$ by 60 percent and more than doubled the hazardous area. Collenbrander and Puttock [2] have noted that inclusion of heat flux from the sea surface is important in modeling the Maplin Sands LNG experiments.

The experimental results of the preceding section indicate that buoyancy was not generally an important factor to the value of $\mathfrak{L}$ in the Burro and Coyote experiments. Only for Burro 8 is it possible that buoyancy may have been significant at concentrations greater than or equal to the 5 percent LFL. For buoyancy to reduce the hazardous region, it must occur for concentrations above the LFL. However, the cases of possible buoyancy indicated in the previous section, the instances of momentary cloud liftoff, and the results of simulations of the experiments [1] indicate that the LNG clouds were frequently at least close to neutral density (about 1.003 of neutral density or less) when the concentrations were about 5 percent or less. Thus, a small amount of additional heat might have produced buoyancy and significantly reduced the hazardous areas. The amount of heat required to produce buoyancy, for concentrations of 5 percent and above in particular, may be calculated.

Under the assumptions that the ideal gas law applies and that the specific heats are constant, the ratio of dry air density ρ_a to the density ρ of a mixture of dry air and LNG vapor at the same pressure is

$$\frac{\rho_a}{\rho}=\frac{1+(\lambda\mu\nu(1+h)-1)C_v}{(1+(\lambda-1)C_v)\,(1+(\lambda\mu-1)C_v)}$$

($\rho_a/\rho > 1$ corresponds to buoyancy) where C_v is the volume (molar) concentration of LNG vapor in the mixture; where

$$\lambda=M_s/M_a,\quad \mu=C_{ps}/C_{pa},\quad \nu=T_s/T_a$$

with M_s, C_{ps}, and T_s being the mean molecular weight, mean specific heat at constant pressure, and initial temperature of the LNG vapor (source gas), and M_a, C_{pa}, and T_a being the corresponding quantities for air; and where

$$h=H/(T_sC_{ps}m_s)$$

is a dimensionless measure of the heat H, in excess of the thermal energy provided by the warmer air, that flows into the cloud from the surroundings (principally the ground and/or water surface and any artificial sources), with m_s being the mass of the parcel of LNG vapor being considered.

The value of ρ_a/ρ is shown in Fig. 5 as a function of h and C_v for

$M_a=29.0$	$M_s=16.5$
$C_{pa}=0.24$ cal/(Kg)	$C_{ps}=0.49$ cal/(Kg)
$T_a=285$ K	$T_s=125$ K

These values are intended as a rough representation of the situation sometime after a spill has begun when ethane enrichment of the remaining LNG results in an initial vapor temperature about 10 K above that at the commencement of the splll and an ethane concentration in the vapor of roughly 1 percent [4]. A more accurate calculation of ρ_a/ρ requires considering deviations from the ideal gas law, values of the specific heats as functions of temperature, density, and composition, and accurate knowledge of how vapor composition and initial temperature depend on LNG composition, and the inclusion of water vapor.

Downloaded 17 Dec 2010 to 193.140.21.150. Redistribution subject to ASME license or copyright; see http://www.asme.org/terms/Terms_Use.cfm

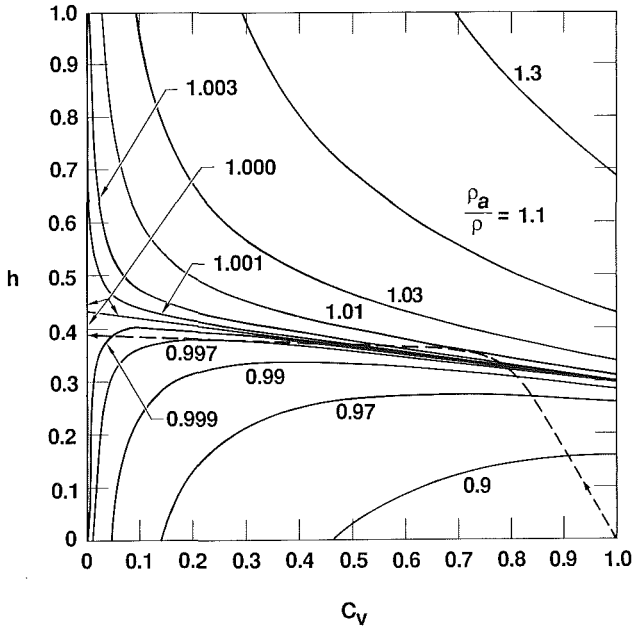

Fig. 5 Contours of ρ_a/ρ, the ratio of air density to LNG-vapor-cloud density, as a function of h, a dimensionless measure of heat added to the cloud from external sources, and C_v, the volume concentration of LNG vapor in the cloud. The cloud is buoyant for $\rho_a/\rho > 1$.

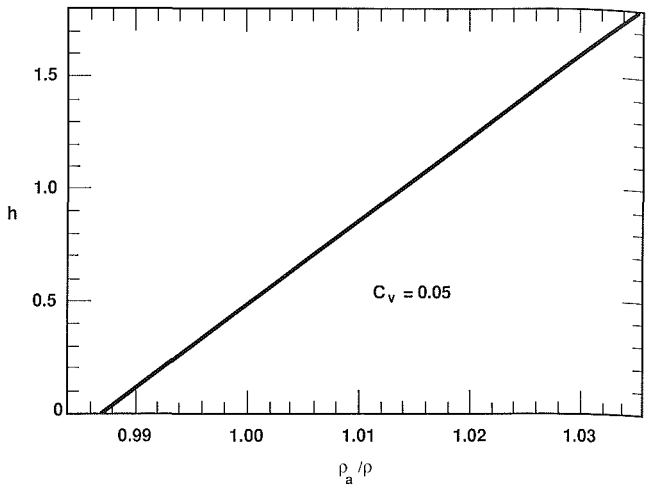

Fig. 6 The value of h required to give particular values of ρ_a/ρ for $C_v = 0.05$

The history of a portion of a cloud may be represented in Fig. 5 by a curve that begins in the lower right corner ($h = 0$, $C_v = 1$) and proceeds to the left, eventually ending somewhere on the left-hand edge where $C_v = 0$ and $\rho_a/\rho = 1$. If no external heat is added (h stays equal to zero), the curve is horizontal and proceeds to the lower left corner, never passing through the buoyant region ($\rho_a/\rho > 1$). Thus, if no external heat is added, the cloud can never be buoyant, even though the molecular weight of the LNG vapor is less than that of air. This circumstance occurs because

$$\frac{C_{ps}}{C_{pa}} \geq \frac{M_a/M_s - 1}{1 - T_s/T_a}$$

for LNG vapor. (The relation is equivalent to the derivative of ρ_a/ρ with respect to C_v being nonpositive at $C_v = 0$). Because C_{ps} is larger than C_{pa} (about twice the value), the vapor cools the air more than the air warms the vapor when they mix. This effect is sufficient to maintain $\rho_a/\rho < 1$ in spite of the lower molecular weight of LNG.

It is possible for a portion of the cloud to become buoyant as C_v decreases with mixing and then become denser than the air again as C_v proceeds to still lower values. This possibility is illustrated by the dashed curve in Fig. 5. Here a relatively high rate of heat flow while C_v is large leads to $\rho_a/\rho = 1.01$ (buoyant) at $C_v = 70$ percent. Then, with a relatively low rate of heat flow, further mixing gives $\rho_a/\rho = 0.999$ (negatively buoyant) at $C_v = 5$ percent. Thus, in this example, between $C_v = 70$ percent and $C_v = 5$ percent the density increases despite a small amount of added heat ($\Delta h \simeq 0.06$). For $M_a > M_s$, the case here, this circumstance occurs because

$$\frac{C_{ps}}{C_{pa}} > \frac{M_a}{M_s}$$

for LNG vapor (the relation is equivalent to the slope of the $\rho_a/\rho = 1$ line in Fig. 5 being negative).

The amount of heat, in terms of h, that must be added to produce a given value of ρ_a/ρ for $C_v = 5$ percent (the LFL) is shown in Fig. 6. The amount of heat that must be added to reduce $\mathfrak{L}$ and the hazardous area substantially is presently unclear. A value of $h \simeq 0.4$ (about 25 calories per gram of LNG vapor) gives $\rho_a/\rho = 1$ at $C_v = 5$ percent. If this amount of heat is added early, while $C_v \geq 70$ percent, then $\rho_a/\rho \cong 1.03$ for $C_v \cong 70$ percent (see FIg. 5) and the mean value of ρ_a/ρ is about 1.01 for C_v between 70 and 5 percent. If $h \cong 0.8$ for similar circumstances, then ρ_a/ρ varies from 1.3 to 1.01 for C_v from 70 to 5 percent with a mean ρ_a/ρ of about 1.1. If these amounts of heat were added when $C_v = 1$, they would increase the temperature of the LNG vapor by about 50 K and 100 K, respectively. The earlier the heat is added to the vapor, the more effective it is in dispersing the cloud, because higher levels of buoyancy can be achieved at higher concentrations for the same amount of heat and because buoyancy is present for a longer time. Natural sources of heat tend to add heat early due to the large temperature differences between cloud and surroundings when the vapor concentration is high.

Effect of Dispersion Phenomenology on the LFL Distance

The Burro and Coyote experiments involved a variety of values for the spill and meteorological parameters present in the tests. It is thus possible to investigate the strength of the dependence of the observed maximum LFL distance on these parameters within the respective ranges of their values over the tests. Such information can provide additional insight into the phenomenology of LNG vapor dispersion; in particular it can indicate the degree to which this dispersion differs from that of trace pollutants.

Since the experiments involved a single substance, LNG (with little significant variation in composition), and a single site, some of these parameters did not vary significantly from test to test. Among these parameters are source density, source temperature, surface roughness, and terrain features. Three parameters which varied significantly, and on which we expect to see a dependence, are source rate, wind speed, and atmospheric stability. These parameters have a strong effect on the turbulent mixing of air into the cloud, the degree to which gravity spread occurs, and the amount of surface heat flowing into the cloud. The ambient humidity was too low in all experiments and the ambient temperature too constant from experiment to experiment for either of these quantities to have a significant effect.

It should be emphasized that what is sought here is a knowledge of how strongly $\mathfrak{L}$ depended on the fundamental meteorological and spill parameters in the Burro and Coyote experiments. One might ask how $\mathfrak{L}$ depended on quantitative measures of turbulent mixing, density stratification, gravity flow, heat flow, etc., but such quantities are intermediate in the present argument in the sense that they, through the

Downloaded 17 Dec 2010 to 193.140.21.150. Redistribution subject to ASME license or copyright; see http://www.asme.org/terms/Terms_Use.cfm

physics involved, depend on the fundamental parameters. The intermediate quantities describe the physical phenomena that mediate the dependence of £ on the fundamental quantities, and these phenomena will be considered in interpreting the dependencies of £ that are found.

To determine the strength of dependence, we assume

$$£ = aq^{\alpha}u_{a2}^{\beta}\phi_2^{\gamma}$$

with (1)

$$a = A\,(q_{gm}^{\alpha}u_{a2gm}^{\beta}\phi_{2gm}^{\gamma})^{-1}$$

A, α, β, and γ are constants to be determined, q is the LNG spill rate (the liquid is assumed to evaporate as fast as it is spilled), and u_{a2} is the wind speed at a height of 2 m. The quantity ϕ_2 is a nondimensional similarity profile parameter evaluated at a height of 2 m. In our treatment of the surface boundary layer, ϕ_2 is the ambient Prandtl number at 2 m and is related to the ambient Richardson number at 2 m (Ri_2) by $\phi_2 = 1 + 5\,\mathrm{Ri}_2$ for $\mathrm{Ri}_2 \geq 0$ and $\phi_2 = (1 - 16\,\mathrm{Ri}_2)^{-1/4}$ for $\mathrm{Ri}_2 \leq 0$ [4]. The quantities q_{gm}, u_{a2gm}, and ϕ_{2gm} are the geometric means of the values of q, u_{a2}, and ϕ_2 that were present in each set of experiments to which equation (1) will be applied. Values of £, q, u_{a2}, and ϕ_2 are given in Table 2. (Spill durations, D are also included.) The values of £ are our most recent values determined from peak concentrations (for any horizontal or vertical crosswind location and any time) measured as a function of downwind distance for the 11 experiments [1]. The values of £ were determined by fitting the logarithm of the peak concentration as a function of the logarithm of x (downwind distance) for each experiment by a straight line. In each case, three or four points were used and were weighted according to the closeness to an estimated £ and reliability of the data. This procedure decreased the effects of instrumental uncertainties and of instances where cloud regions of relatively high concentration may have passed between sensors. RPT-caused concentration peaks were not considered in determining £. Previous determinations of £ used simpler procedures and included the effects of RPT explosions. These explosions occurred in three experiments [17] and led to increases in £ as high as 50 percent [1]. We estimate that the values of £ have a common one-sigma systematic uncertainty of about ± 10 percent and an approximately equal, uncorrelated random uncertainty, leading to an overall uncertainty of ± 15 percent [1].

To determine values for A, α, β, and γ in equation (1) we do a least-squares fit of a flat hypersurface in ln q, ln u_{a2} ln, ϕ_2 to the values of ln £. Besides using the set of all tests for which LFL distances could be determined (those listed in Table 2), we also used a set containing seven tests that were chosen for additional analysis [1]. Overall, these selected tests had somewhat better concentration data. Additionally, in obtaining the results which are given in Table 3, we chose a set with all 11 tests except Burro 8, because that test was unique in terms of wind speed and ambient stability.

We applied standard statistical analysis to obtain the uncertainties given in Table 3 for the 11-test case, although the uncertainty in A has been increased to include the estimated ±10 percent systematic uncertainty which is not treated by the statistical analysis. The analysis presumes that there is no significant correlation between the values of q, u_{a2}, and ϕ_2, as may be seen from Table 2. The estimated one-sigma random uncertainty of ±10 percent from the statistical analysis is in agreement with our independent estimate of the same value. The relative rms difference between the fit values of £ and the experimental values is 8 percent. As should be the case, this is close to the 10 percent magnitude of the random uncertainty. It is significant that exclusion of the parametrically unique Burro 8 test does not substantially alter the values of the quantities in Table 3. Thus, the value of its LFL can be determined to a fair accuracy using the results of the other experiments in equation (1). This fact indicates that the physical phenomena which cause Burro 8 to have such high levels of concentration are also important in the other experiments.

Using the determined values for A, α, β, and γ, equation (1) becomes

$$£ = (230 \pm 25\ \mathrm{m})\left(\frac{q}{14.0\ \mathrm{m^3/min}}\right)^{0.07\pm0.22}$$

$$\left(\frac{u_{a2}}{6.1\ \mathrm{m/s}}\right)^{-0.21\pm0.09}\left(\frac{\phi_2}{0.88}\right)^{0.57\pm0.18} \quad (2)$$

which applies only to the parameter space spanned by the Burro and Coyote experiments. Considering the ranges in values of q, u_{a2}, and ϕ_2 in the 11 tests (q varies by a factor of 1.6, u_{a2} by 5.4, and ϕ_2 by 2.5), it may be seen from equation (2) that £ depends more strongly on atmospheric stability (as represented by ϕ_2) than on either wind speed or source rate, within the parameter space of the set of 11 Burro and Coyote experiments. Further, the values and uncertainties of β (-0.21 ± 0.09) and γ (0.57 ± 0.18) make it clear that we have indeed observed a dependence of £ on both wind speed and atmospheric stability. The small value of α (0.07) relative to its uncertainty (± 0.22) shows, however, that the strength of dependence of £ on q has not been accurately determined, evidently due to the small range in values of q. Nevertheless, it is possible to put an upper limit on its value. At the 65 percent confidence level (one standard deviation) this limit is $\alpha \leq 0.29$, and at the 95 percent confidence level (two standard deviations) it is $\alpha \leq 0.51$.

To understand further the meaning of the experimentally determined dependence of £ shown in equation (2), this dependence may be compared to similar results obtained from the Gaussian plume model [12] for the dispersion of trace gases. This model includes the effects of mixing due to ambient turbulence, but does not include the alteration in mixing due to the density difference, nor the effects of gravity flow

Table 2 Values of q, u_{a2}, ϕ_2, £, and D for the set of 11 of the Burro and Coyote experiments

Experiment	q, $\mathrm{m^3/min}$	u_{a2}, m/s	ϕ_2	£, m	D s
B2	11.9	5.4	0.71	230	173
B3	12.2	5.4	0.68	180	167
B4	12.1	9.0	0.85	190	175
B5	11.3	7.4	0.81	220	190
B6	12.8	9.1	0.88	215	129
B7	13.6	8.4	0.94	240	174
B8	16.0	1.8	1.61	445	107
B9	18.4	5.7	0.95	270	79
C3	13.5	6.0	0.64	195	65
C5	17.1	9.7	0.82	205	98
C6	16.6	4.6	1.14	250	82

Table 3 Values of A, α, β, and γ of equation (1) for three combinations of Burro and Coyote tests

Test set	A	α	β	γ
Eleven tests	232 ± 25 m	0.07 ± 0.22	−0.21 ± 0.09	0.57 ± 0.18
Seven tests	243 m	0.16	−0.17	0.65
No Burro 8	217 m	0.13	−0.13	0.45

Downloaded 17 Dec 2010 to 193.140.21.150. Redistribution subject to ASME license or copyright; see http://www.asme.org/terms/Terms_Use.cfm

and heat flow from the surface. Application of the Gaussian plume model to our experiments gives [1]

$$\mathfrak{L} \simeq 118\left(\frac{q}{14.0\ \mathrm{m^3/min}}\right)^{0.53}\left(\frac{u_{a2}}{6.1\ \mathrm{m/s}}\right)^{-0.63}\left(\frac{\phi_2}{0.88}\right)^{1.29} \quad (3)$$

where the initial constant in equation (3) has the units of meters. This constant is lower in value than that in equation (2) due, at least in part, to the different averaging time for our data (10 s) and that assumed in the Gaussian plume model (roughly 10 min). Longer averaging times lead to somewhnat smaller values of average concentration [13].

It is noteworthy in comparing equation (2) to equation (3) that the observed strengths of dependence of $\mathfrak{L}$ on source rate, wind speed, and atmospheric stability are all significantly less than predicted by the Gaussian plume model. However, the Gaussian-plume results also give $\mathfrak{L}$ as being most strongly dependent on atmospheric stability (in terms of ϕ_2).

The lower dependence of $\mathfrak{L}$ on ambient stability (ϕ_2) for LNG vapor dispersion probably occurs because the mixing of air into a cloud of cold, dense gas at relatively high concentrations is influenced to a significant degree by processes involving the cloud iteself, not only by the surrounding atmosphere, while the mixing of a trace pollutant is influenced solely by the atmosphere. Parameter studies with the SLAB model showed a dependence of $\mathfrak{L}$ on atmospheric stability similar to equation (2) [22, 23, 24].

The much lessened dependence of $\mathfrak{L}$ on wind speed (u_{a2}) follows from the way in which wind speed affects turbulent mixing. For fixed values of source rate and atmospheric stability, the concentration is inversely proportional to the product of wind speed u and cross-sectional area σ in a crosswind volume element of the cloud at a fixed downwind distance x when x is sufficiently large for cloud speed to equal wind speed. In the Gaussian plume model, σ is independent of wind speed, since the speed of turbulent spread in the lateral directions is proportional to wind speed in that model. Thus, concentration is proportional to u^{-1}, and $\mathfrak{L}$ is approximately proportional to $u^{-1/2}$ (see equation (3)) since σ is approximately proportional to x^2. For cold, dense clouds, however, the speed of lateral spread is less than proportional to u [18], so σ decreases with increasing u (as can be seen in the Burro and Coyote data), leading to the dependence of $\mathfrak{L}$ on u_{a2} in equation (2). The lowered proportionality of crosswind speed to wind speed (for other parameters constant) follows from the apparent dependence of the mixing rate on wind speed when density stratification is present [18], from the dependence of mixing on the flow of heat from the surface into the cold cloud, and from the effects of gravity flow. As wind speed increases, the heating rate goes down, decreasing the contribution of convection-induced turbulence to mixing; hence less crosswind spread of the cloud. The lowered heating rate helps maintain the air/cloud density difference, and it also reduces convective mixing. Further, the contribution of gravity flow to the horizontal crosswind spread of the cloud decreases as wind speed increases.

In spite of the uncertainty in α, it is very probable that $\mathfrak{L}$ depended less strongly on source rate in the set of 11 Burro and Coyote experiments than it does in the case of a trace pollutant. One possible explanation for this difference involves gravity flow. With other parameters held constant, an increase in q would lead to an increase in cloud width due to increased effects of gravity flow. (For trace pollutant dispersion, cloud width is independent of source rate.) The consequently greater surface area of the cloud results in more air being mixed in, thus mitigating the increase in concentration from a larger q that would otherwise occur: hence the lessened dependence of $\mathfrak{L}$ on source rate. At higher spill rates than were present in the experiments, a stronger dependence on q is expected since, at any given radius from the source, the width

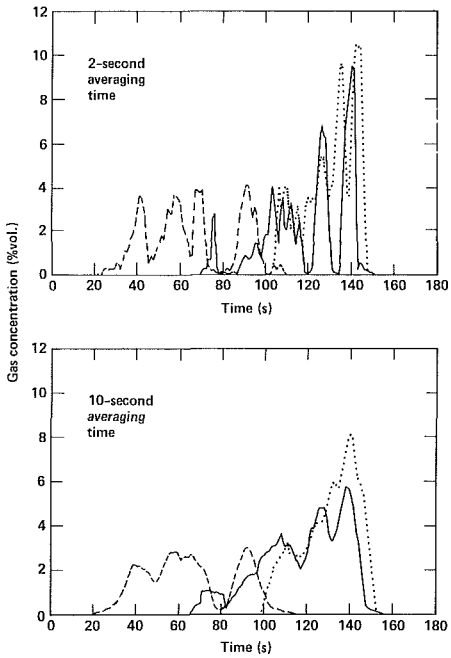

Coyote 5. Height 1. M. Downwind Distance: 200 M.

Fig. 7 Example of the effect of averaging time on concentration time histories

(along an arc) cannot increase beyond the point where the cloud completely surrounds the source, thus dampening the increase of cloud surface area with q. For such circumstances and under steady-state conditions, the area of the 5 percent (LFL) concentration surface is approximately proportional to $\mathfrak{L}^2$. The area is also proportional to q if it is assumed that the mixing rate per unit area on the 5 percent concentration surface is independent of q. Thus, if the latter assumption is correct, $\mathfrak{L}$ is then approximately proportional to $q^{0.5}$. For very small q, where the vapor would disperse as a trace pollutant (see equation (3)), α is also about equal to 0.5 (for other reasons). The set of 11 Burro and Coyote experiments was apparently conducted in a portion of parameter space where lower values of α apply.

Effects of Concentration Variation

Turbulence and other effects cause measured values of concentration to vary in time above and below their mean steady-state values. Consideration of this variation is important in determining $\mathfrak{L}$ and interpreting its meaning and in relating the concentration field to the burn characteristics of a cloud.

Because of the time variations in concentration, peak values of concentration, and hence $\mathfrak{L}$, are affected by the averaging time used for the data (see [21] for a discussion of peak-to-mean ratios). In Fig. 7 a comparison is made between concentration time histories for a 2-s averaging time and our normal 10-s averaging time. The various local maxima of concentration are up to 40 percent greater for the 2-s averaging time. Examination of all of the Coyote gas concentration data using a 2-s average instead of the normal 10-s average likewise shows increased peak concentration values reflecting the random variations in the data. Peak concentration values at the 140-m row of sensors are more influenced by the averaging interval than concentrations in the 200 and 300-m rows, which are closest to the LFL. Sample calculations give increases in $\mathfrak{L}$ that are, however, less than the 15 percent uncertainty we estimate in the experimental values of $\mathfrak{L}$.

Assessment of the effects of concentration variation in our data suffers from the fact that many of the variations, as from RPT puffs, are due to variations in cloud structure that are

Downloaded 17 Dec 2010 to 193.140.21.150. Redistribution subject to ASME license or copyright; see http://www.asme.org/terms/Terms_Use.cfm

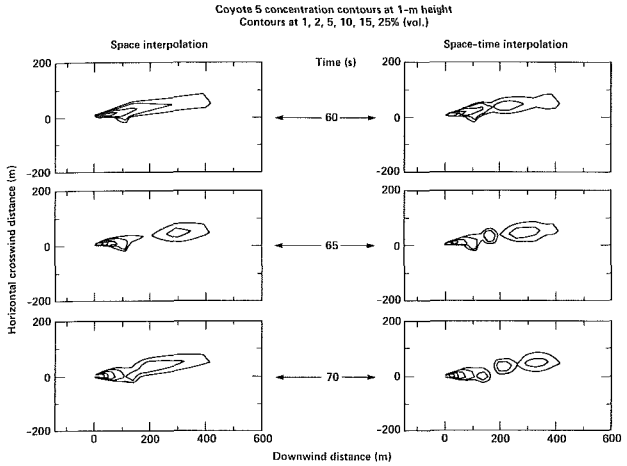

Fig. 8 Comparison of 2-s average horizontal concentration contours employing the normal space interpolation method with the space-time interpolation method

smaller in size than the downwind distances between the sensor rows in the Burro and Coyote experiments. Thus, when concentration data are interpolated between rows at a chosen time, the effect of a small-size variation may not be present because it is between the rows at the time of interpolation. This difficulty is partly overcome when determing $\mathcal{L}$, which we define as the maximum observed distance to the LFL, by basing its value on observed values of peak concentration over the duration of the experiment, irrespective of the time at which they occurred. These values are interpolated in a least-squares, log-log sense described by Morgan et al. [1] to determine $\mathcal{L}$ (summarized above). However, the values of peak concentration employed may include the effects of entirely unrelated variations, and the value of $\mathcal{L}$ so determined may not, therefore, represent an actual maximum distance to the LFL that occurred during an experiment.

An additional problem associated with these variations arises in relating characteristics of the burn regions in the Coyote experiments to the values of concentration between rows [7]. Downwind interpolation of concentration values at fixed times can give erroneous estimates of the position of the 5 percent LFL concentration contour between rows due to the small-scale variations. To overcome both of these difficulties, we have investigated a space-time interpolation scheme which appears useful in better displaying time-dependent features.

To interpolate concentration to a given value of x at time t, we use the value of concentration at the adjacent upwind row, measured at the time $t - (x - x_u)/u$ and the value of concentration measured at the adjacent downwind row at the time $t + (x_d - x)/u$, where x_u and x_d are the downwind distances of the two rows and where we assume the cloud moves at ambient wind speed u. Thus, the interpolation is carried out between two manifestations of the same physical portion of the cloud at different times as it moves downwind. Variations in concentration due to any cloud feature moving with the cloud that maintains its identity will therefore be reproduced at between-row locations. Values of $\mathcal{L}$ can then be based on the same variation as it moves downwind. In addition, the upwind and downwind edges of the cloud can be followed more accurately as well as the time-dependent position of the LFL or any other concentration contour. Because time variations at different rows now have a higher degree of correlation, a logarithmic interpolation scheme [6] can be employed more universally. With fixed-time interpolation, a logarithmic scheme can give unrealistic values when large variations are present. Space-time interpolation should be suitable, in particular, for cases involving other than LNG vapor that arise when concentrations must be measured over great distances. In such cases, the cloud may be present at only one sensor row at a time. This means of interpolation, in effect, spreads the cloud out in the downwind direction so that it occupies the full array at any one interpolation time.

Examples of space-time-interpolated horizontal concentration contours are shown in Fig. 8 where they are compared to the same results with fixed-time interpolation. Data averaged over a 2-s interval are employed. Here the time-dependent interpolation scheme was implemented by creating two rows of grid points between adjacent rows of sensors in the 140-400 m region. The concentration for the new points was calculated from the values at the adjacent up/downwind sensors by a linear interpolation of the gas data registered at the times calculated from the above formulae. The logarithms of the values were then used to obtain the contours (as employed in part in [6]). Greater detail of the turbulent eddies in the Coyote 5 experiment may be seen in the space-time-interpolated results.

Conclusions

The Burro and Coyote LNG spill experiments have permitted quantitative observation of the effects of the physical phenomena pertinent to the dispersion of LNG vapor.

Three of these phenomena occur because LNG vapor, evaporating from the cryogenic liquid, is colder and denser than air. These are gravity flow, density stratification, and heat flow from the ground. The fourth phenomenon is time-dependent variation in concentration caused by turbulence and by RPT explosions which can occur when LNG is spilled onto water. The experiments have shown that these phenomena can have a substantial effect on the size and shape of the hazardous region following a spill.

Gravity flow greatly increased the width of the cloud in the low wind-speed Burro 8 test, substantially increasing the area of the hazardous region. Significant but less pronounced effects of a similar nature were observed at higher wind speeds. Density stratification, which reduces mixing with the air, and heat flow from the ground, which enhances mixing, have significant effects along with gravity flow on $\mathcal{L}$, the maximum observed distance to the lower flammability limit. In particular, for the spill and meteorological conditions of the experiments, $\mathcal{L}$ depends on source rate, wind speed, and atmospheric stability in a substantially different manner than predicted by the Gaussian plume model, due to these particular phenomena.

Buoyancy of the cloud (possibly observed in the experiments) can lift it above sources of ignition and substantially enhance mixing. Calculations show that buoyancy can be achieved by heat, in addition to that from the mixed-in air, entering the cloud from external sources, and that only modest amounts are required.

The experimental results in regard to the phenomena important to LNG vapor dispersion are supported by studies employing the SLAB computer model in which the phenomenological effects as well as the $\mathcal{L}$ dependencies can be separated. Together, the results demonstrate the necessity for inclusion and proper treatment of the phenomena in predictive models of LNG vapor dispersion.

Time-dependent variability in concentration causes the hazardous region to vary with time and can alter the value of $\mathcal{L}$. A space-time interpolation scheme for the concentration data gives a much improved picture of the effects on the concentration data, and hence $\mathcal{L}$, of variations having a size that is about the same or less than the distance between sensor rows.

Downloaded 17 Dec 2010 to 193.140.21.150. Redistribution subject to ASME license or copyright; see http://www.asme.org/terms/Terms_Use.cfm

Acknowledgments

William Hogan and Ronald Koopman led the program that conducted the Burro and Coyote tests and analyzed the results. Koopman, Henry Goldwire, and Thomas McRae led the experimental work while Donald Ermak led the theoretical effort. Ermak provided useful discussions on a number of aspects of the work reported here, as did McRae on the effects of heat on the vapor cloud. Louise Morris was the computations scientist for the program and made various specific contributions to this article and the research required for it. This work was performed under the auspices of U.S. Department of Energy by the Lawrence Livermore National Laboratory under contract No. W-7405-ENG-48.

References

1 Morgan, D. L., Jr., Morris, L. K., Chan, S. T., Ermak, D. L., McRae, T. G., Cederwall, R. T., Koopman, R. P., Goldwire, H. C., Jr., McClure, J. W., and Hogan, W. J., *Phenomenology and Modeling of Liquefied Natural Gas Vapor Dispersion, UCRL-53581*, Lawrence Livermore National Laboratory, Livermore, CA, Apr. 1984.

2 Colenbrander, G. W., Puttock, J. S., "Maplin Sands Experiments, 1980: Interpretation and Modeling of Liquefied Gas Spill Onto the Sea," presented at the IUTAM Symposium on Atmospheric Dispersion of Heavy Gases and Small Particles, Delft, The Netherlands, Aug. 29–Sept. 2, 1983; Puttock, J. S., Blackmore, D. R., and Colenbrander, G. W., "Field Experiments on Dense Gas Dispersion," *Dense Gas Dispersion*, Elsevier Scientific Publishing Co., Amsterdam, 1982, pp. 13–41, published as a special issue of *J. Haz. Mat.*, Vol. 6, 1982, Nos. 1 and 2.

3 McQuaid, J., ed., *Heavy Gas Dispersion Trials at Thorney Island*, proceedings of a symposium held at the University of Sheffield, Great Britain, Apr. 3–5, 1984 published as a special issue of *J. Haz. Mat.*, 1985, Vol. 11; McQuaid, J., and Roebuck, B., *Large Scale Field Trials on Dense Vapor Dispersion*, final report to sponsors on the Heavy Gas Dispersion Trials at Thorney Island 1982–84, Safety Engineering Laboratory, Sheffield, United Kingdom (no date).

4 Koopman, R. P., Cederwall, R. T., Ermak, D. L., Goldwire, H. C., Jr., Hogan, W. J., McClure, J. W., McRae, T. G., Morgan, D. L., Rodean, H. C., and Shinn, J. H., "Analysis of Burro Series 40-m^3 LNG Spill Experiments," *Dense Gas Dispersion*, Elsevier Scientific Publishing Co, Amsterdam, 1982, pp. 43–82, published as a special issue of *J. Haz. Mat.*, Vol. 6, 1982, Nos. 1 and 2.

5 Koopman, R. P., Baker, J., Cederwall, R. T., Goldwire, H. C., Jr., Hogan, W. J., Kamppinen, J. M., Kiefer, R. D., McClure, J. W., McRae, T. G., Morgan, D. L., Morris, L. K., Spann, M. W., Jr., and Lind, C. D., *Burro Series Data Report LLNL/NWC 1980 LNG Spill Tests*, Lawrence Livermore National Laboratory, Livermore CA, UCID-19075, Dec. 1982.

6 Goldwire, H. C., Jr., Rodean, H. C., Cederwall, R. T., Kansa, E. J., Koopman, R. P., McClure, J. W., McRae, T. G., Morris, L. K., Kamppinen, L. M., Kiefer, R. D., Urtiew, P. A., and Lind, C. D., *Coyote Series Data Report, LLNL/NWC 1981 LNG Spill Tests, Dispersion, Vapor Burn, and Rapid-Phase-Transition*, UCID-19953, Lawrence Livermore National Laboratory, Livermore, CA, Oct. 1983.

7 Rodean, H. C., Hogan, W. J., Urtiew, P. A., Goldwire, H. C., Jr., McRae, T. G., and Morgan, D. L., Jr., *Vapor Burn Analysis for the Coyote Series of 30-m^3 LNG Spill Experiments*, Lawrence Livermore National Laboratory, Livermore, CA, UCRL-53530, Apr. 1984.

8 McRae, T. G., *Large-Scale Rapid Phase-Transition Explosions*, Lawrence Livermore National Laboratory, Livermore, CA, UCRL-88688, May 1983.

9 Reid, R. C., "Superheated Liquids: A Laboratory Curiosity and, Possibly, an Industrial Curse," *Chem. Eng. Educ., XII* (1977 Award Lecture, three-part series), 1978.

10 Ermak, D. L., Chan, S. T., Morgan, D. L., and Morris, L. K., "A Comparison of Dense Gas Dispersion Simulations With the Burro Series LNG Spill Test Results," *Dense Gas Dispersion*, Elsevier Scientific Publishing Co., Amsterdam, 1982, pp. 129–160, published as a special issue of *J. Haz. Mat.*, Vol. 6, 1982, Nos. 1 and 2.

11 Chan, S. T., Rodean, H. C., and Ermak, D. L., "Numerical Simulations of Atmospheric Releases of Heavy Gases Over Variable Terrain," *Air Pollution Modeling and Its Application, III*, Vol. 5, 1984, Plenum Press, New York, pp. 295–328.

12 Slade, D. H., ed., *Meteorology and Atomic Energy 1968*, U.S. Atomic Energy Commission, July 1968, pp. 97–116.

13 Hanna, S. R., Briggs, G. A., and Hosker, R. P., Jr., *Handbook on Atmospheric Diffusion*, DOE/TIC-11223 (DE 82002045), Technical Information Center, U.S. Department of Energy, 1982, pp. 28, 33.

14 Germeles, A. E., and Drake, E. M., *Gravity Spreading and Atmospheric Dispersion of LNG Vapor Clouds*, 4th International Symposium on Transport of Hazardous Cargoes by Sea and Inland Waterways, Jacksonville, FL, Oct. 1975.

15 Chan, S. T., and Ermak, D. L., "Recent Results in Simulating LNG Vapor Dispersion Over Variable Terrain," *Proceedings of the IUTAM Symposium on Atmospheric Dispersion of Heavy Gases and Small Particles*, Delft *Univ. of Technology, The Netherlands, Aug. 29–Sept. 2, 1983;* also UCRL-88495, Rev. 1, Lawrence Livermore National Laboratory, Livermore, CA, Nov. 1983.

16 Chan, S. T., *FEM 3—A Finite Element Model for the Simulation of Heavy Gas Dispersion and Incompressible Flows: Users Manual*, UCRL-53397, Lawrence Livermore National Laboratory, Livermore, CA, Feb. 1983.

17 McRae, T. G., Goldwire, H. C., Jr., Hogan, W. J., and Morgan, D. L., Jr., *The Effects of Large-Scale LNG/Water RPT Explosions*, ASME Paper No. 84-WA/HT-76, 1984.

18 Morgan, D. L., Jr., Morris, L. K., and Ermak, D. L., *SLAB: A Time-Dependent Computer Model for the Dispersion of Heavy Gases Released in the Atmosphere*, UCRL-53383, Lawrence Livermore National Laboratory, Livermore, CA, Jan. 1983.

19 Zeman, O., "The Dynamics and Modeling of Heavier-Than-Air Cold Gas Releases," *Atmospheric Environment*, Vol. 16, 1982, pp. 741–751.

20 Clauser, F. H., "Turbulent Boundary Layers in Adverse Pressure Gradients," *J. Aeronaut., Sci.*, Vol. 21, 1954, pp. 91–108; Bakke, P., "An Experimental Investigation of a Wall Jet," *J. Fluid Mech.*, Vol. 2, 1957, pp. 467–472; Ellison, T. H., and Turner, S. J., "Turbulent Entrainment in Stratified Flows," *J. Fluid Mech.*, Vol. 8, 1959, pp. 514–544; Lilly, D. K., "Models of Cloud-Topped Mixed Layers Under a Strong Inversion," *Quart. J. Roy. Meteorol. Soc.*, Vol. 94, 1968, pp. 292–309; Deardorf, J. W., and Willis, G. E., "Dependence of Mixed Layer Entrainment on Shear Stress and Velocity Jump," *J. Fluid Mech.*, Vol. 115, 1982, pp. 123–149.

21 Rodean, H. C.. and Cederwall, R. T., *Analysis of Turbulent Wind Velociy and Gas-Concentration Fluctuations During the Burro Series 40-m^3 LNG Spill Experiments*, UCRL-53353, Lawrence Livermore National Laboratory, Livermore, CA, Nov. 1982.

22 Morgan, D. L., Jr., Kansa, E. J., and Morris, L. K., "Simulations and Parameter Variation Studies of Heavy Gas Dispersion Using the SLAB Model," *Proceedings of the IUTAM Symposium on Atmospheric Dispersion of Heavy Gases and Small Particles*, Delft Univ. of Technology, The Netherlands, Aug. 29–Sept. 2, 1983; see also UCRL-88516, Rev. 1.

23 Morgan, D. L., Jr., Kansa, E. J., and Morris, L. K., "Simulations and Studies of Heavy Gas Dispersion Using the SLAB Model," *Extended Abstracts, Sixth Symposium on Turbulence and Diffusion*, American Meteorological Society, Boston, MA, Mar. 22–25, 1983, pp. 147–150; see also UCRL-88009.

24 Morgan, D. L., Jr., 1984 (unpublished).

Downloaded 17 Dec 2010 to 193.140.21.150. Redistribution subject to ASME license or copyright; see http://www.asme.org/terms/Terms_Use.cfm

P. R. Souza Mendes

A. C. Pinho Brasil, Jr.

Departamento de Engenharia Mecânica,
Pontifícia Universidade Católica,
Rio de Janeiro, RJ-22453
Brazil

Heat Transfer During Melting Around an Isothermal Vertical Cylinder

Introduction

Research on alternative energy resources has intensified during the past few decades as a consequence of the alarming increase in energy cost. Effective thermal energy storage systems have become a true necessity, especially in solar energy applications.

Using the phase change of some materials in thermal energy storage systems is advantageous in various ways. For example, the heat capacity of the storage reservoir is tremendously increased (on a unit volume basis), since latent heat of fusion is involved. In addition, there are advantages as far as heat transfer from and to the reservoir is concerned.

Until recently, most papers on phase change dealt exclusively with conduction heat transfer, although it has been known for some time that natural convection may play a key role during melting and freezing. Lately, however, several studies (Viskanta, 1983) considering buoyancy effects on phase-change heat transfer have been reported. Among various configurations under study, melting about a vertical plate and around a vertical cylinder are of special interest, due to their occurrence in engineering applications. In this connection, the first numerical accounting for natural convection effects is presented in Sparrow et al. (1977), where the outward melting from a vertical cylinder was investigated for an isothermal boundary condition at the cylinder surface and a no-slip condition at the top of the liquid layer. A boundary condition of timewise constant heat flux at the cylinder was studied experimentally in Kemink and Sparrow (1981), where both slip and no-slip boundary conditions were investigated.

More recently, numerical and experimental results were compared in Ho and Viskanta (1984) for melting near an isothermal vertical plate, and a moderate agreement between the experimental and analytical predictions was reported. A better agreement was obtained by Okada (1984, 1985). Kalhori and Ramadhyani (1985) presented experimental data for melting around finned and unfinned vertical tubes. They examined the case of $L/r_w = 20$, $\mathrm{Ra} = 5.85 \times 10^9$, and very large times.

The present paper reports on experimental measurements undertaken to investigate outward melting around a vertical cylinder embedded in a solid initially at its fusion temperature. The cylinder is maintained at a uniform temperature that exceeds the fusion temperature. The top and bottom of the phase-change material are adiabatic, and a small air gap provides a slip boundary condition at the top. The main objective of the research reported here was to obtain experimental data for the abovementioned configuration. It is remarkable that, although the isothermal boundary condition at the heat source has been extensively studied experimentally for melting to a vertical plate (e.g., Ho and Viskanta, 1984; Okada, 1983), there are very few experimental data available for melting to an isothermal cylinder positioned vertically.

The Experiment

The physical situation in the laboratory will now be described. An infinite horizontal layer of a phase-change material is initially solid and at its fusion temperature T_*. A vertical cylinder is embedded in the solid and is in thermal equilibrium with the phase-change medium. Both the upper and the lower surfaces of the medium are adiabatic. The upper surface is in contact with atmospheric air (no shear stress), whereas at the lower surface a no-slip boundary condition is imposed. At time $t = 0$, the cylinder temperature undergoes a step change to $T_w > T_*$. Immediately, melting begins to occur, and a solid-liquid interface starts to move outward from the cylinder.

The experiments carried out in this work were aimed at the determination of the solid-liquid interface behavior. The experimental apparatus employed in the experiments, experimental procedure, and data reduction procedure are briefly described in the following subsections. A more detailed description can be found in Pinho Brasil (1985), and in Pinho Brasil and Souza Mendes (1986).

Experimental Apparatus. Figure 1 illustrates some details of the experimental apparatus, focusing on its test section. A cylindrical container for the phase-change medium, a constant-temperature bath, and a water-heated copper tube were the basic components of the experimental apparatus. An auxiliary vacuum system was also used to stop the data runs at predetermined instants of time.

The container for the phase-change medium was a brass canister, 17 cm high and with inner diameter 15.2 cm. Its lower part was insulated by a 2.5-cm-thick layer of

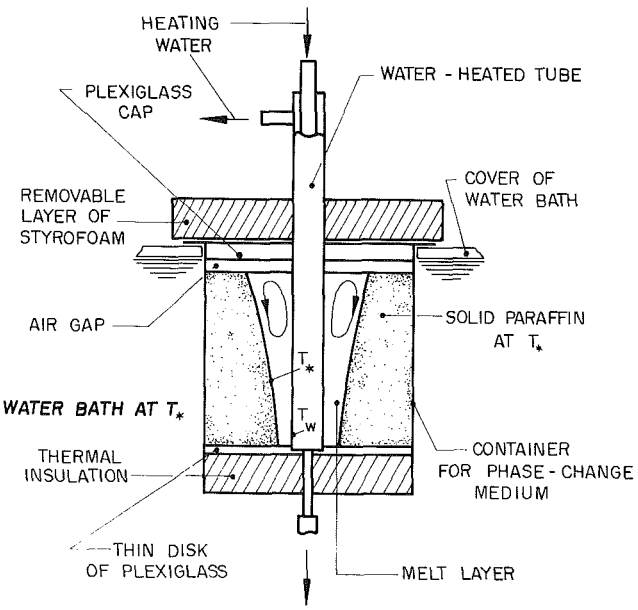

Fig. 1 The test section

Contributed by the Heat Transfer Division for publication in the JOURNAL OF HEAT TRANSFER. Manuscript received by the Heat Transfer Division April 2, 1986. Paper No. 85-WA/HT-5.

 Copyright © 1987 by ASME

Downloaded 17 Dec 2010 to 193.140.21.150. Redistribution subject to ASME license or copyright; see http://www.asme.org/terms/Terms_Use.cfm

stryrofoam, and the upper part of the container was fitted with a 1.2-cm thick cap of plexiglass.

The constant-temperature water bath provided a controlled thermal environment for the container. It consisted of an insulated tank equipped with a propeller for stirring an electric resistance, and a thermostatic device. It was very effective in maintaining the desired temperature level.

The water-heated copper tube (2.54 cm o.d.) on which the melting occurred had three thermocouples positioned respectively at 3.50, 6.35, and 9.20 cm from the bottom, and equally spaced along the circumference. Each thermocouple was situated in a longitudinal groove machined into the outer surface of the tube, and then a high-conductivity cement was employed to fill the grooves. The surface was then polished to a smooth finish.

Temperature measurements during the data runs showed that water circulation in the tube was a very effective means of providing an isothermal boundary condition at the tube surface. Experiments were performed for $T_w = 38.4$, 45.3, 51.3, 62.6, and 72.6°C.

Experimental Procedure. The phase-change material used in the experiments was *n*-eicosane paraffin, 99 percent pure, with a melting point of 36.4°C. Prior to the data runs, the paraffin was placed inside the container by pouring small portions of liquid paraffin at a time and waiting for solidification to occur. During this process, the isothermal tube was at its normal data-run position, i.e., inside the container. Both the circulating water temperature and the bath temperature were set below the paraffin melting point, to enable solidification. Two thermocouples were embedded in the phase-change medium to provide means of temperature control and selection. The final height of the phase-change medium was approximately 12.7 cm (ten times the water-heated tube radius), and a small air gap between the upper surface was kept to accommodate changes in density of the paraffin due to phase change.

Once the above-described solidification process was finished, the temperature of the heating loop and constant-temperature bath were increased to a value slightly below the melting point of the phase-change medium, in order to bring the paraffin to a temperature close to 36.4°C. After a long equilibration period, final adjustments were made to assure that the final equilibrium temperature of the phase-change medium was less than 0.5°C below its melting point.

At this point, the water-heated cylinder was withdrawn from the container and its temperature was raised to a value $T_w > T_*$. Once thermal equilibrium was achieved at the cylinder, the data run was ready to start. The cylinder was put back to its data run position, and melting was initiated immediately. During the entire period of the run, both the water bath and the heating water were maintained at their respective fixed temperatures. To terminate the data run at a preselected time, the cylinder was withdrawn from the liquid paraffin and, simultaneously, the vacuum system was activated, removing the molten mass altogether.

The final step of the experimental procedure consisted in measuring the melt-shape contour obtained from the data run. This was achieved by measuring the radial position of the interface for several axial (and angular) locations. The measurements were made with a special device designed and built for this application.

Data Reduction. The data obtained in laboratory were treated to obtain the melting patterns, molten mass, and heat transfer coefficients as functions of the relevant parameters.

The paraffin thermophysical properties were taken from Griggs and Yarbrough (1978) and Griggs and Humphries (1977), and were evaluated at the mean of T_w and T_*. The melting patterns were determined directly from the contour measurement data, whereas the molten mass of paraffin was obtained for each data run via integration of the interface curves.

The spatial-average Nusselt number at the heated cylinder surface can be related with the melting rate if the sensible heat absorbed by the liquid is neglected. The consequences of this assumption will be discussed shortly. Hence, an overall energy balance in the liquid region yields

$$\mathrm{Nu} \equiv hL/k = (L/2r_w)dM/d\tau \tag{1}$$

Therefore, the average Nusselt number at the cylinder can be evaluated based on knowledge of the melted mass behavior with time.

Uncertainty Analysis. The method of estimating uncertainties in experimental results proposed by Kline and McClintock (1953) was employed in the present work.

The uncertainty associated with the Rayleigh number was found to be 3 percent, whereas, for the dimensionless molten mass, the uncertainty estimated was under 6 percent for all cases investigated. It is worth noting that most of the results presented here depend on the dimensionless molten mass.

Results and Discussion

Experimental data were obtained for five values of the Rayleigh number Ra, namely, 7.1×10^7, 3.7×10^8, 5.7×10^8, 1.1×10^9, and 2.0×10^9. These values correspond respectively to Stefan numbers of 0.017, 0.081, 0.120, 0.213, and 0.332.

If the natural convection effects and the sensible heat absorbed by the liquid are both neglected, analytical results can be readily obtained, yielding a useful baseline case for the subsequent discussion. An overall energy balance in the melt

Nomenclature

c = specific heat
Fo = Fourier number $= \alpha t/r_w^2$
g = acceleration of gravity
h = spatial-average heat transfer coefficient at the cylinder surface
k = thermal conductivity
L = height of phase-change material layer
m = molten mass of phase-change material
M = dimensionless molten mass $= m/\rho\pi r_w^2 L$
Nu = Nusselt number at the cylinder surface $= hL/k$
r_w = radius of heated cylinder
r_* = melt layer position
R_* = dimensionless melt layer position $= r_*/r_w$
Ra = Rayleigh number $= g\beta L^3(T_w - T_*)/\nu\alpha$
Ste = Stefan number $= c(T_w - T_*)/\lambda$
t = time
T_w = surface temperature of cylinder
T_* = melting temperature
z = axial coordinate, measured upward along cylinder
Z = dimensionless axial coordinate $= z/L$
α = thermal diffusivity $= k/\rho c$
β = coefficient of thermal expansion
λ = latent heat of fusion per unit mass
ν = kinematic viscosity
ρ = density of liquid phase-change material
τ = dimensionless time = Ste·Fo
τ_c = critical dimensionless time

Downloaded 17 Dec 2010 to 193.140.21.150. Redistribution subject to ASME license or copyright; see http://www.asme.org/terms/Terms_Use.cfm

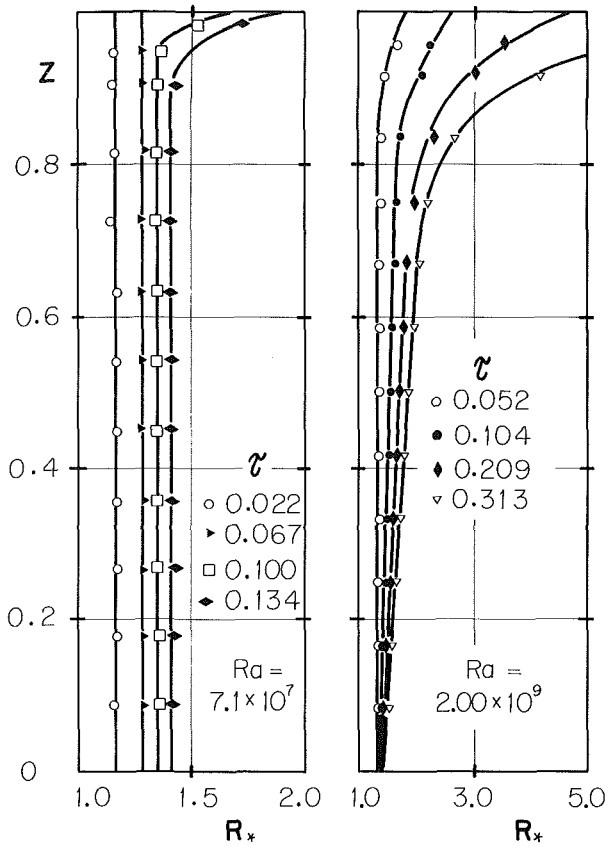

Fig. 2 Shapes of solid-liquid interface at various times

region gives $dR_*/d\tau = 1/(R_* \ln/(R_*))$, which, after integration from 0 to τ and from 1 to R_*, yields

$$R_*(\ln(R_*) - 1/2) = 2\tau - 1/2 \tag{2}$$

Equation (2) is satisfied within 1 percent by $R_* = 1.274\tau^{0.4835} + 1$, for $\tau < 0.5$.

It is interesting to note that, for Ste < 0.5, equation (2) is in very good agreement with the results found in Sparrow et al. (1978), where a more sophisticated analysis accounting for sensible heat is presented. This fact encouraged the authors to neglect sensible heat in the derivation of equation (1).

It is easy to show that $M = R_*^2 - 1$. Also, for this conduction situation, an effective heat transfer coefficient at the cylinder wall may be defined by $h(T_w - T_*) = k(T_w - T_*)/(r_w \ln(R_*))$, which yields, after rearrangement

$$\mathrm{Nu} = (L/r_w)/\ln(R_*) \tag{3}$$

Interface Movement. Figure 2 illustrates the interface movement as a function of time. It can be observed that, for low Ra, the solid-liquid interface moves parallel to the heated cylinder, except for a small deformation at the top which appears for larger times. Furthermore, the interface radial position at heights of no deformation is in close agreement with equation (2). This indicates that, for low Rayleigh numbers, the conduction mode of heat transfer is dominant.

For large values of Ra, the interface does not behave in a conduction-like manner, except for very small times. Very soon convection takes over, with melting nearly ceasing to occur at the bottom and intensifying at the top of the melt layer. This behavior is readily explained by the fact that the top is, due to gravity, a high-temperature zone, whereas, at the bottom, temperatures very close to T_* prevail.

Slightly different trends are predicted by the numerical analysis reported in Sparrow et al. (1977). For low Rayleigh numbers and dimensionless times larger than about 0.1, the mild interface slope predicted was not observed in the experiments. In addition, for high Rayleigh numbers, it seems that the melting rate predicted for the bottom region of the melt layer is somewhat larger than the ones measured during the present work.

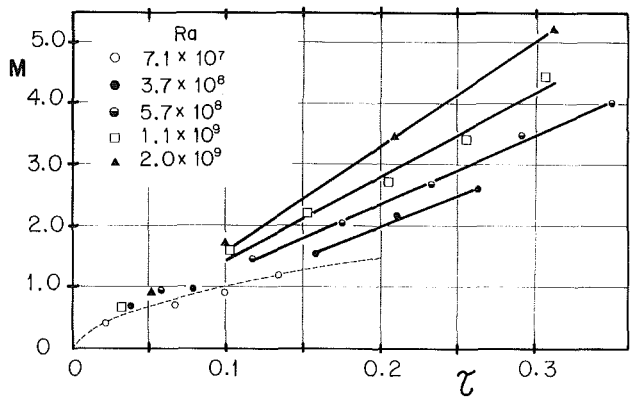

Fig. 3 Timewise variation of the molten mass for various Rayleigh numbers

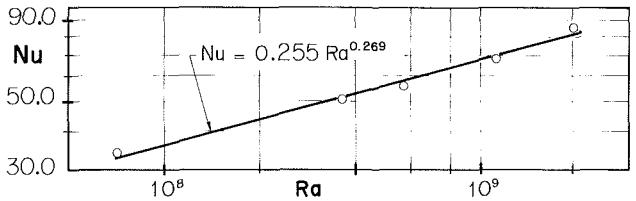

Fig. 4 Steady-state Nusselt number at the cylinder as a function of the Rayleigh number

Molten Mass. Figure 3 illustrates the dependence of the dimensionless molten mass on time, for different values of the Rayleigh number. It can be observed that, for small times, a reasonable agreement with the conduction model ($M = R_* - 1$, the dashed curve in Fig. 3) is obtained. As expected, it is observed that the experimental data for low Rayleigh numbers follow the conduction model for quite large values of τ. It is also noted that departure from the dashed curve occurs earlier for higher Rayleigh numbers.

For larger times, however, the molten mass increases linearly with time, at a rate that also increases with the Rayleigh number. This linear behavior can be explained based on the fact that, after there is enough space between the cylinder wall and the solid-liquid interface, boundary layer regimes are attained near each of the abovementioned surfaces. Therefore, radial conduction is eliminated, since a nearly uniform temperature at the core of the melt layer is attained. For this reason the melt layer thickness becomes unimportant.

Spatially Averaged Nusselt Number at the Cylinder. From the foregoing discussion on Fig. 3 and recalling that the average Nusselt number is evaluated from equation (1), it is readily seen that, for large times, Nu becomes independent of time. This behavior was also observed in Kemink and Sparrow (1981), where a boundary condition of timewise constant wall heat flux was studied. It was found there that, for large times, the cylinder wall temperature tends to a constant value and so does the average heat transfer coefficient. In the present work, a constant-wall-temperature boundary condition is imposed, and hence, as soon as conduction effects become negligible, the average heat transfer coefficient ceases to vary.

In Sparrow et al. (1977), however, the Nusselt number presented behaves in a somewhat different manner from that described above. This is probably due to the simplifying

Downloaded 17 Dec 2010 to 193.140.21.150. Redistribution subject to ASME license or copyright; see http://www.asme.org/terms/Terms_Use.cfm

Table 1 The constant C of $Nu = C\,Ra^n$ as a function of L/r_w

L/r_w	C	Reference
0	0.234	Okada (1984)
10	0.255	Present paper
20	0.393	Kemink and Sparrow (1981)

assumptions made in the governing equations to obtain the analytical solution. As mentioned before, only moderate agreements between experimental and analytical results were obtained by other researchers, and the present situation seems to be no exception.

In Fig. 4, the steady-state Nusselt number is plotted against the Rayleigh number. A least-squares line is also shown in the figure, and is represented by

$$Nu = 0.255\ Ra^{0.269} \tag{4}$$

For $Ra = 7 \times 10^7$, the above equation agrees within about 5 percent with the prediction of Sparrow et al. (1977).

It is worth noting that the exponent of Ra in equation (4) is in excellent agreement with the ones found in Kemink and Sparrow (1981) and in Okada (1984) for phase-change problems with different aspect ratios L/r_w. The coefficients found in these references, however, differ from 0.255, as illustrated in Table 1. Choosing an interpolating function of the power-law type for the values displayed in Table 1, the following expression may be written

$$Nu = (0.234 + 2.52 \times 10^{-5}(L/r_w)^{2.92})Ra^{0.269} \tag{5}$$

It is important to emphasize that the above equation was obtained for $L/r_w \leq 20$, and, even in this range, more data points are needed to validate the assumed power-law dependence of Nu on L/r_w. Nevertheless, equation (5) may be useful as a first attempt to predict such dependence.

In general, the average Nusselt number may be evaluated by equation (3) for early times, when conduction dominates, and by equation (4) after the convection regime is established. A simple criterion to estimate the critical time when equation (3) ceases to be valid, giving place to equation (4), can be developed if the time period when conduction and convection are of the same order of magnitude is neglected. In this case, the critical time is easily obtained by equating the two expressions for the Nusselt number in equations (3) and (4). The result is

$$\tau_c = 0.606(\exp(39.22\ Ra^{-0.269}) - 1)^{2.068} \tag{6}$$

It can be seen from equation (6) that τ_c decreases with the Rayleigh number, and it tends to infinity as $Ra \to 0$ (pure conduction).

As an attempt to evaluate τ_c for other values of L/r_w, the constant 39.22 in the above equation may be substituted for by $(L/r_w)/(0.234 + 2.52 \times 10^{-5}(L/r_w)^{2.92})$.

Final Remarks

Experiments were performed to study melting of a solid around a vertical cylinder embedded in it. The solid phase-change material is initially at its fusion temperature, and during the melting process, the cylinder is maintained at a uniform temperature that exceeds the melting point.

Inspection of the solid–liquid interface shapes showed that conduction heat transfer prevails initially, and the time at which natural convection becomes of importance is a function of the Rayleigh number. For high values of Ra, very soon convection takes over, and melting occurs unevenly along the z coordinate. At the bottom of the melt layer, where colder liquid tends to accumulate, very little melting occurs. The opposite is observed at the top, where the hot liquid provides plenty of energy for phase change.

A simple pure-conduction analysis predicts satisfactorily the time dependence of the molten mass for early times and low Rayleigh numbers. For larger times and high values of Ra, a linear increase is observed.

The average Nusselt number can be evaluated from results of pure-conduction analysis, provided convection is absent, i.e., early times or low Rayleigh numbers. After the onset of convection, the average Nusselt number ceases to depend on time. A correlation is presented to allow the evaluation of this steady-state Nusselt number as a function of the Rayleigh number and of the ratio L/r_w.

A simple criterion to estimate the limit of validity of the aforementioned conduction analysis is discussed, and an expression to evaluate the critical time of change in heat transfer mode is presented.

Acknowledgments

This research was performed under the auspices of the Brazilian Government (Conselho Nacional de Desenvolvimento Científico e Technológico—CNPq, Proc. No. 405945/83).

References

Griggs, E. I., and Humphries, W. R., 1977, "A Design Handbook for Phase Change Thermal Control and Energy Storage Devices," NASA Technical Paper 1074.

Griggs, E. I., and Yarbrough, D. W., 1978, "Thermal Conductivity of Solid Unbranched Alkanes From *N*-Hexadecane to *N*-Eicosane," *Proc. 14th Southeastern Seminar on Thermal Sciences*, pp. 256–267.

Ho, C.-J., and Viskanta, R., 1984, "Heat Transfer During Melting From an Isothermal Vertical Wall," ASME JOURNAL OF HEAT TRANSFER, Vol. 106, pp. 12–19.

Kalhori, B., and Ramadhyani, S., 1985, "Studies on Heat Transfer From a Vertical Cylinder, With or Without Fins, Embedded in a Solid Phase Change Medium," ASME JOURNAL OF HEAT TRANSFER, Vol. 107, pp. 44–51.

Kemink, R. G., and Sparrow, E. M., 1981, "Heat Transfer Coefficients for Melting About a Vertical Cylinder With or Without Subcooling and for Open or Closed Containment," *Int. J. Heat Mass Transfer*, Vol. 24, pp. 1699–1719.

Kline, S. J., and McClintock, F. A., 1953, "Describing Uncertainties in Single-Sample Experiments," *Mechanical Engineering*, p. 3.

Okada, M., 1983, "Melting from Vertical Plate Between Insulated Top and Bottom Surfaces," *Proc. ASME/JSME Thermal Engineering Joint Conf.*, Vol. 1, pp. 281–288.

Okada, M., 1984, "Analysis of Heat Transfer During Melting From a Vertical Wall," *Int. J. Heat Mass Transfer*, Vol. 27, pp. 2057–2066.

Okada, M., 1985, "Heat Transfer During Melting Around a Vertical Cylinder, 1st Report, Analysis and Experiments of the Melting Without Subcooling," *Bulletin of JSME*, Vol. 28, No. 243, pp. 2007–2013.

Pinho Brasil, Jr., A. C., 1985, "Transferência de Calor durante a Fusão em Geometria Cilíndrica Vertical," M.S. Thesis, PUC-RJ, Rio de Janeiro, Brazil.

Pinho Brasil, Jr., A. C., and Souza Mendes, P. R., 1985, "Outward Melting From a Vertical Cylinder With Natural Convection Effects," ASME Paper No. 85-WA/HT-5.

Sparrow, E. M., Patankar, S. V., and Ramadhyani, S., 1977, "Analysis of Melting in the Presence of Natural Convection in the Melt Region," ASME JOURNAL OF HEAT TRANSFER, Vol. 99, pp. 520–526.

Sparrow, E. M., Ramadhyani, S., and Patankar, S. V., 1978, "Effect of Subcooling on Cylindrical Melting," ASME JOURNAL OF HEAT TRANSFER, Vol. 100, pp. 395–402.

Viskanta, R., 1983, "Phase Change Heat Transfer in Solar Storage: Latent Heat Materials," G. A. Lane, ed., CRC Press, Boca Raton, FL.

Downloaded 17 Dec 2010 to 193.140.21.150. Redistribution subject to ASME license or copyright; see http://www.asme.org/terms/Terms_Use.cfm

A Study of Ice-Formation Phenomena on Freezing of Flowing Water in a Pipe

T. Hirata
Associate Professor.

H. Matsuzawa
Graduate Student.

Department of Mechanical Engineering,
Faculty of Engineering,
Shinshu University,
Nagano 380, Japan

Ice-formation phenomena in a water pipe whose wall is kept at a uniform temperature lower than the freezing temperature of water are examined under the conditions of an unstable ice-water interface. The onset conditions for a step or smooth change in ice thickness occurring with flow transition from laminar to turbulent are found to be correlated with ice thickness at the contraction region of the ice band and are expressed as a function of a pipe Reynolds number Re_D, and a cooling temperature ratio θ. It is shown that the transient freezing process depends strongly on flow as well as temperature conditions and that the typical ice shapes at steady-state conditions can be classified on a θ-Re_D coordinate system.

Introduction

Ice formation in water pipe system, is a basic engineering problem. It introduces many practical problems such as pressure drop, diminution of flow rate and, sometimes, breakage of the pipe as a result of flow blockage by ice. The problem of freezing of flowing water involves interactions among the flow, the shape of the ice, and the heat transfer at the ice-water interface. The interactions result in an instability of the interface. Under the conditions which produce thicker ice layers, the interface is unstable and the ice thickness is easily affected by a disturbance of flow as well as temperature conditions (Gilpin et al., 1980). In this case it has been reported that an ice-band structure, which shows a flow passage with a periodic variation in cross section along the length of pipe, is produced and that a high value of friction factor is brought due to a large-scale roughness caused by the undulation of ice surface (Gilpin, 1981). In the previous papers (Hirata and Ishihara, 1985; Hirata, 1986), the ice-band structure and the heat transfer coefficient at the ice-water interface were investigated and the freeze-off conditions of the water pipe system were successively revealed. It has also been found that some typical ice shapes are produced depending on experimental conditions: They are the patterns of smooth or step change in ice thickness occurring with flow transition from laminar to turbulent (Hirata et al., 1979; Seki et al., 1984), two-dimensional ice-band structure, three-dimensional ripples, and freeze-off state.

In the present study, experiments were carried out to examine the freezing phenomena in water pipes and to investigate the correlation between the typical ice shapes and the experimental conditions, particularly for the cases in which the ice layer is thick and the ice-water interface is unstable. Onset conditions for the step transition are also discussed.

Experimental Apparatus and Procedure

The experimental apparatus consisted of a test section, a refrigeration unit, and two circulation sytems of water and coolant as shown in Fig. 1. The circulation pipes of water and coolant, whose temperatures were controlled by PID-controlled heaters installed in each reservoir tank, were covered with insulation materials to decrease heat flow from the surroundings. The test section consisted of two tubes in the vertical position; the inner one was a copper tube with

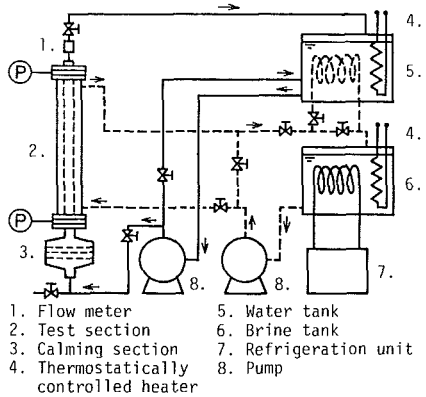

Fig. 1 Schematic illustration of experimental apparatus

$D = 19.9$ mm (or 25.4 mm) i.d., $L = 697$ mm; the outer one was a 36-mm-i.d. steel tube. The test section was installed with flange joints so that the ice in the pipe could easily be taken out for observation and measurement. The water was pumped through the copper tube and the coolant was circulated between the two tubes. The coolant was circulated at high velocity through the annulus between the two tubes to produce uniform wall temperature. The flow direction of water was in the upward vertical direction.

In order to obtain uniform velocity and uniform temperature flow at the entrance of the test section, a calming section and a contraction section (flow area ratio 16:1) were installed. It was ascertained that the Nusselt number data at the contraction region of the ice layer obtained in this experiment coincides well with Gilpin's (1979) data, which were taken under uniform velocity as well as uniform temperature profiles at the entrance of pipe. It was, therefore, deduced from that result that the velocity as well as the temperature profiles in this experiment were sufficiently uniform.

The wall temperature of the copper pipe T_w, was evaluated from three thermocouples located along the length of pipe. A small temperature difference among the three thermocouples was detected as a result of formation of a step transition pattern. The maximum temperature ratio among the three thermocouples was 0.92, for example, for $Re_D = 9500$ and $\theta = 4.1$. The water temperature in the pipe T_∞, was estimated from the mean value of the inlet and outlet of the test section.

The change of flow rate during the transient freezing process was measured at predetermined time intervals. It was

Contributed by the Heat Transfer Division for publication in the JOURNAL OF HEAT TRANSFER. Manuscript received by the Heat Transfer Division August 19, 1986.

 Copyright © 1987 by ASME

Downloaded 17 Dec 2010 to 193.140.21.150. Redistribution subject to ASME license or copyright; see http://www.asme.org/terms/Terms_Use.cfm

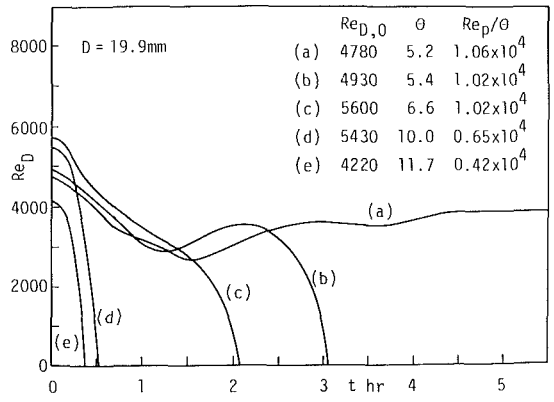

Fig. 2 Variation of flow rate with ice growth

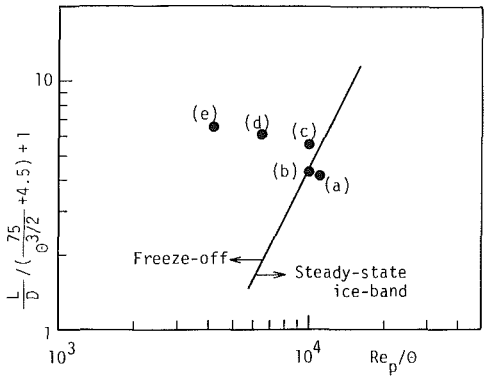

Fig. 3 Experimental conditions compared to onset of freeze-off (experimental conditions shown in Fig. 2)

assumed that a steady-state condition was attained when all temperature readings remained constant for more than 2 hr. After a steady-state condition was reached, the water and the brine in the piping system were drained and the test section was removed from the piping system. In order to remove the ice layer frozen to the pipe wall, the copper pipe was heated quickly by running tap water between the two tubes.

The distinction between a smooth and a step transition in ice

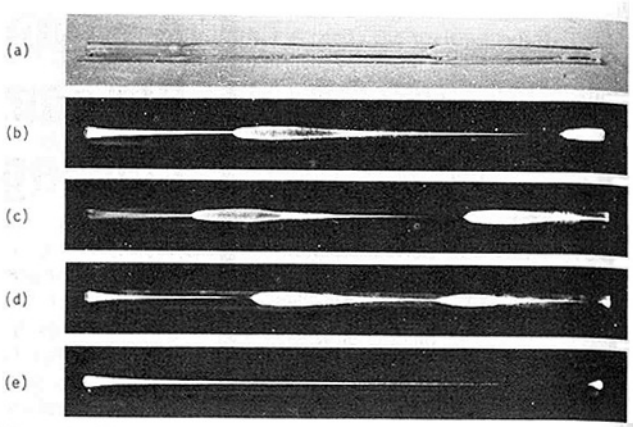

Fig. 4 Ice formation pattern (experimental conditions shown in Fig. 2)

shape was made by a visual observation of light reflected from the ice surface. When a step transition is produced, the ice thickness shows a stepped change at a separation point as shown in Fig. 6. This made the distinction between the two types of transition easy. The measurement of ice shape was done in the cooled room at temperature about 5–10°C. The removed ice layer was cut crosswise at several locations along its length and the diameter of water flow passage was measured with slide calipers. This measurement was done quickly so that the amount of melting during the measurements was negligible.

The experimental ranges covered for the two sets of test section were $0.4 \le \theta \le 11.7$, where θ is the cooling temperature ratio; $3.7\times10^3 \le Re_D \le 3.0\times10^4$ for $D = 19.9$ m and $8.0\times10^2 \le Re_D \le 2.5\times10^4$ for $D = 25.4$ mm, where Re_D is the pipe Reynolds number.

Results and Discussion

Freezing Phenomena for Thicker Ice Layers. Ice-formation phenomena during transient freezing processes depend on Reynolds number as well as temperature conditions. In order to examine the ice-formation phenomena with an unstable ice-water interface, a thicker ice layer was formed

Nomenclature

B = diameter ratio = d/D
d = minimum diameter at contraction region of ice band
d_x = diameter of flow passage at $x < L_0$
D = inside diameter of pipe
K^* = nondimensional acceleration parameter = K/St_d
L = length of pipe
L_0 = distance between the locations of pipe inlet and step transition
Nu_d = Nusselt number at contraction region = hd/λ_w
$Nu_{d,x}$ = local Nusselt number at $x < L_0$ = hd_x/λ_w
$Nu_{D,max}$ = maximum Nusselt number at reattachment point = $h_{max}D/\lambda_w$
P_0 = total pressure drop between the inlet and outlet of pipe (in this experiment P_0 is equal to total pressure at inlet of pipe when the valve at pipe outlet is shut)
Re_d, Re_D = Reynolds numbers = vd/ν, VD/ν
$Re_{D,0}$ = Reynolds number at which ice formation is initiated
Re_D^* = Reynolds number transformed from Re_p, equation (10)
Re_p = modified Reynolds number defined by $D(2P_0/\rho)^{0.5}/\nu$
St_d = Stanton number = $Nu_d/(Re_d Pr)$
t = time
T_f, T_w, T_∞ = temperatures of freezing, pipe wall, and water
v, V = mean velocities of water at contraction region, and in pipe without ice
x = distance from pipe inlet
Z^* = nondimensional distance from pipe inlet = $4L_0/(DRe_D Pr)$
θ = cooling temperature ratio = $(T_f - T_w)/(T_\infty - T_f)$
λ_i, λ_w = thermal conductivities of ice and water
λ^* = thermal conductivity ratio = λ_i/λ_w
ν = kinematic viscosity of water
ξ = friction-factor coefficient in piping system
ρ = density of water

Downloaded 17 Dec 2010 to 193.140.21.150. Redistribution subject to ASME license or copyright; see http://www.asme.org/terms/Terms_Use.cfm

under several conditions of Re_D and cooling temperature ratio, $\theta = (T_f - T_w)/(T_\infty - T_f)$. A phenomenological relevance between the variation of flow rate with ice growth and the final ice shape (in a steady-state or freeze-off condition) was investigated. Figures 2, 3, and 4 are a series of representations of the experimental results for the corresponding Re_D–θ conditions, respectively. Figure 2 gives a variation of flow rate with ice growth, where $Re_{D,0}$ is the Reynolds number at which ice formation is initiated. Figure 2(*a*) shows alternations of a decrease and increase in flow rate until a steady-state condition is reached, while Figs. 2(*b–e*) show a stoppage of flow caused by freeze-off. In Fig. 3 the experimental conditions are compared to the onset of freeze-off conditions, where Re_P is a modified Reynolds number defined by the total pressure drop between the inlet and outlet of pipe (Hirata and Ishihara, 1985). In Fig. 3 the left-hand side of the solid line is a freeze-off regime, while the right-hand side is a steady-state ice-band regime. Figures 4(*a–e*) are photographs of the final ice shapes obtained for the corresponding Re_D–θ conditions; the water flow in the photographs is from left to right. In Figs. 4(*b–e*) the flow passages are shown as light-colored areas due to rapid freezing after a flow blockage.

The transient freezing processes shown in Figs. 2, 3, and 4 can be explained from the correlations between the variations of flow rate and the final ice shapes. Figure 4(*a*) shows the ice-band structure in a steady-state condition. An insight into the behavior of Fig. 2(*a*) implies that the initial decrease of Re_D during $t = 0$–1.5 hr is due to an increase of the friction factor with ice growth throughout the inner surface of pipe. The following increase at $t = 1.5$–3 hr is caused by an abrupt expansion of the diameter of the flow passage at which the step transition of ice shape took place. The next decrease at $t = 3$ hr and increase at $t = 3.6$ hr are caused by further growth of ice thickness downstream of the step transition and by the occurrence of a new step transition, respectively. In Fig. 4(*a*) the existence of two ice bands (the one very close to the exit of the test section should be disregarded since the effect of the uncooled region downstream of the exit on the ice shape is expected) coincides with the result of Fig. 2(*a*).

The transient process shown in Fig. 4(*b*) is, in principle, the same as that of Fig. 4(*a*). In this instance the experimental conditions are very close to the onset of freeze-off, as shown in Fig. 3. Therefore, the ice layer is comparatively thicker than that of Fig. 4(*a*). The development of the second ice band (the one near the exit) brings about an increased pressure drop and finally the freeze-off is reached. It should be noted that the results of Figs. 4(*a, b*) are the cases in which the ice band is produced one after another from the upstream location along the pipe.

The freezing processes of Figs. 4(*c, d*) are different from those of Fig. 4(*a, b*). In these cases, the Re_D monotonously decreases with time until the freeze-off occurs, as can be seen in Figs. 2(*c, d*). An obvious correlation between the variation of Re_D and the occurrence of the ice band cannot be observed. Since the experimental conditions of Figs. 4(*c, d*) are in the freeze-off regime as shown in Fig. 3, the ice growth is rapid and the ice bands are produced at nearly the same time throughout the pipe length (Gilpin, 1979).

Figure 4(*e*) shows the ice shape under the most rapid conditions of freeze-off among the present experiments. As the ice growth is very rapid, the ice–water interface is kept stable during the time of freezing and the ice-band structure does not form.

Figures 5(*a, b*) are photographs for comparatively large values of Re_D and θ. In Fig. 5(*a*) it is shown that the spacing of ice bands becomes shorter near the exit of the test section. Under more unstable conditions such as in Fig. 5(*b*), a very short spacing is observed throughout the pipe length. In these cases it can be deduced from the temperature variation of pipe

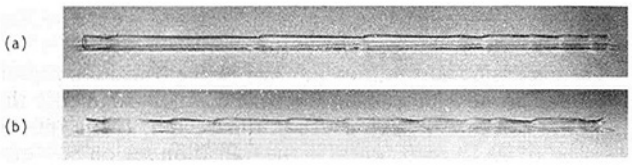

Fig. 5 Ice formation pattern at higher Reynolds numbers: (*a*) $Re_D = 17{,}800$, $\theta = 11.0$; (*b*) $Re_D = 16{,}700$, $\theta = 17.7$

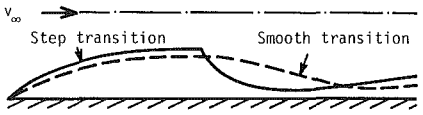

Fig. 6 Schematic drawings of smooth and step transitions

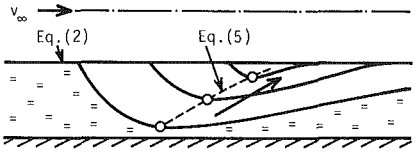

Fig. 7 Model for instability of ice–water interface

wall that the short-spacing ice bands cannot reach steady-state conditions, that is the migration does not stop. This means that an appearance and dissipation of ice bands occurs in the pipe. The formation process of these short-spacing ice bands is apparently different from those of Figs. 4(*a–d*). It has been reported by Hirata and Ishihara (1985) that a three-dimensional ripple structure is obtained at high Reynolds numbers with large turbulence. It can be considered that the ice shapes in Figs. 5(*a, b*) are also affected by a large turbulence of flow. The mechanism of that phenomenon, however, has not been fully investigated. Although three-dimensional ripples could not be obtained in the present experimental range, it can be presumed that the experimental conditions of Figs. 5(*a, b*) are close to the conditions which produce three-dimensional ripples.

Onset Conditions of Step Transition. An ice layer formed inside a water pipe, in general, increases in thickness along the length of pipe regardless of flow conditions (laminar or turbulent) at the entrance. The flow, therefore, undergoes an acceleration due to the decrease of diameter of flow passage in the flow direction. When the flow is laminar at the entrance, the Reynolds number of flow in the downstream is increased by the acceleration and the flow makes a transition to turbulent. When the flow is turbulent at the entrance, the flow is somewhat laminarized by the acceleration. As the heat transfer coefficient in the region of laminarized flow is smaller than that in a turbulent one, the local ice thickness in the laminarized region becomes larger. This brings about higher acceleration of the flow. The laminarization of the flow is, thus, promoted. In the downstream region, the Reynolds number of the flow is increased by the acceleration and the flow will make a transition to turbulent again. When the flow is turbulent at the entrance, the laminarization of flow has a significant role in order to make a flow transition in the downstream.

Because the heat transfer coefficient in a turbulent flow is larger than that in a laminar one, the local ice thickness in the turbulent region becomes smaller. At the transition region, therefore, the flow passage gradually expands in the flow direction, as shown in Fig. 6 by a dashed line. In a steady-state

Downloaded 17 Dec 2010 to 193.140.21.150. Redistribution subject to ASME license or copyright; see http://www.asme.org/terms/Terms_Use.cfm

condition, this is called a smooth transition and is obtained for the case in which the ice layer is thin.

The expansion of the flow passage in the transition region generates an adverse pressure gradient which augments the amplification rate of turbulence in this region. If the rate of decrease of ice layer thickness in the transition region becomes sufficiently large, a flow separation occurs in this region. A rapid transition of flow then occurs. Because of the flow separation in the transition region, the flow can change from a laminar flow upstream of the separation to a turbulent flow downstream of the separation in a very short distance. Because turbulence in the separated flow region produces a high heat transfer coefficient, a stepped change in ice thickness takes place at the separation point. The high heat transfer coefficient in the separated flow region melts away the rearward face of the stepped ice shape and it moves the separation point upstream. When the migration is stopped by establishing a heat balance at the ice–water interface, the final steady-state ice layer is obtained, as shown in Fig. 6 by a solid line. This is called a step transition and is obtained for the case in which the ice layer is thick.

The onset conditions of step transition are derived as follows: Let us suppose that the step shape was artificially made in the smooth ice surface as illustrated in Fig. 7 and that the heat transfer rates on the smooth surface and in the separated flow region were described by Nu_d and $\mathrm{Nu}_{D,\max}$, respectively. When the ice–water interface is unstable, the relation $\mathrm{Nu}_{D,\max} > \mathrm{Nu}_d$ must be satisfied for the step shape to continue to exist in the ice surface. On the other hand when the interface is stable, the step shape disappears gradually and the locus of the reattachment point is shown in Fig. 7 by a dashed line. The onset of step transition can, therefore, be derived by $\mathrm{Nu}_{D,\max} = \mathrm{Nu}_d$.

A heat balance at the ice–water interface in a steady-state condition yields an expression of Nusselt number as follows (Hirata and Ishihara, 1985): Assuming that heat flow in the axial direction in the ice is comparatively small than that of the radial one, we have

$$\mathrm{Nu}_d = -2\lambda^*\theta/\ln B \tag{1}$$

where $\lambda^* = \lambda_i/\lambda_w$ and $B = d/D$. In equation (1), λ^* is the thermal conductivity ratio of ice to water and B is a diameter ratio. The value of Nu_d is, therefore, obtained by measuring the diameter d of flow passage at the contraction region, and the cooling temperature ratio θ. Moretti and Kays (1965) investigated flow laminarization on a flat plate and suggested that the laminarization factor can be represented in terms of K/St, where K is an acceleration parameter defined by equation (3) and St is the Stanton number. Hirata (1987) extended their result to a pipe flow and an examination of the effect of K/St_d revealed that Nu_d was proportional to $(K/\mathrm{St}_d)^{-0.2}$ and was represented by (see the appendix)

$$\mathrm{Nu}_d = 0.8/(Z^*K^{*0.4})^{0.5} \qquad \text{for } 0.008 < K^* < 0.3 \tag{2}$$

where $Z^* = 4L_0/(D\mathrm{Re}_D\mathrm{Pr})$ and K^* is a nondimensional acceleration parameter $(=K/\mathrm{St}_d)$ derived as follows: The acceleration parameter is defined by

$$K = \frac{\nu}{v_\infty^2}\frac{dv_\infty}{dx} \tag{3}$$

Integrating equation (3) for $x = 0 \sim L_0$ and $v_\infty = V \sim v$ on the assumption that K is constant with respect to x and dividing K by St_d, we have

$$K^* = -\frac{\mathrm{Pr}}{2\lambda^*}\frac{(1-B^2)\ln B}{B}\frac{D}{\theta L_0} \tag{4}$$

On the other hand, it has been reported in the study of an ice layer grown on a cold flat plate in a water stream (Hirata et al., 1979) that the maximum Nusselt number in the reattached region is well arranged by a correlation for separated flow associated with a rearward facing step on a flat plate. In the present pipe-flow study the value of $\mathrm{Nu}_{D,\max}$ was approximated by the result for an abrupt circular-channel expansion (Zemanick and Dougall, 1970)

$$\mathrm{Nu}_{D,\max} = 0.2\,\mathrm{Re}_d^{2/3} \tag{5}$$

where Re_d is an upstream Reynolds number of the circular channel. It should be mentioned that Re_d is equivalent to the value at the contraction region in this study. Substituting equations (1) and (4) into equation (2), we have a representation of ice shape at the contraction region

$$(L_0/D)^{0.3} = 0.168\frac{B^{0.2}(-\ln B)^{0.8}}{(1-B^2)^{0.2}}\frac{\mathrm{Re}_D^{0.5}}{\theta^{0.8}} \tag{6}$$

where $\mathrm{Pr} = 13$ and $\lambda^* = 3.88$ were used. According to the abovementioned discussions a correlation for the onset of a step transition can be obtained by equating equations (2) and (5)

$$\frac{(L_0/D)^{0.6}}{\mathrm{Re}_D\theta^{0.4}} = 0.65\frac{B^{0.971}(-\ln B)^{0.743}}{(1-B^2)^{0.4}}(\mathrm{Re}_D\theta^2)^{-4/7} \tag{7}$$

Eliminating (L_0/D) from equations (6) and (7), the onset condition is derived as

$$\theta = 0.208\frac{(-\ln B)^{0.429}}{B^{0.286}}(\mathrm{Re}_D\theta^2)^{2/7} \tag{8}$$

For a given value of B, the onset condition can be represented by a relationship between Re_D and θ.

In Fig. 8 the abscissa is the nondimensional parameter on the right-hand side of equation (8). The data were taken under steady-state conditions. The solid and open circles represent step and smooth transitions, respectively. It is shown that a step transition is observed for thicker ice layer (smaller value

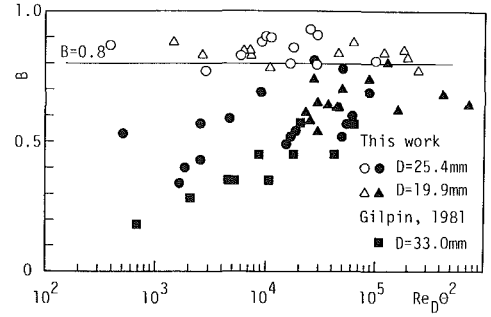

Fig. 8 Transition pattern of ice shape depending on ice thickness

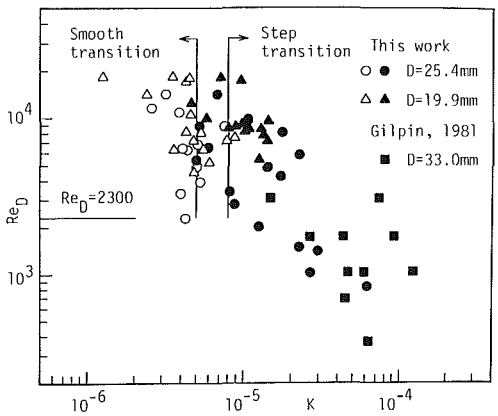

Fig. 9 Transition pattern of ice shape on Re_D–K coordinate system

Downloaded 17 Dec 2010 to 193.140.21.150. Redistribution subject to ASME license or copyright; see http://www.asme.org/terms/Terms_Use.cfm

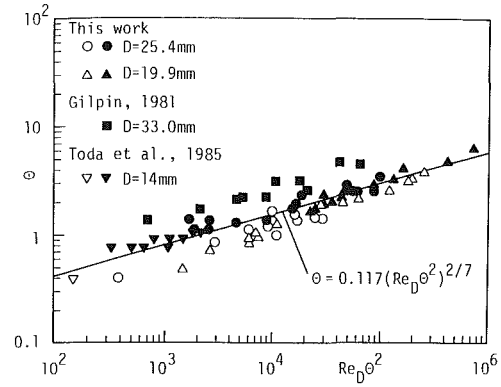

Fig. 10 Onset conditions for smooth or step transition

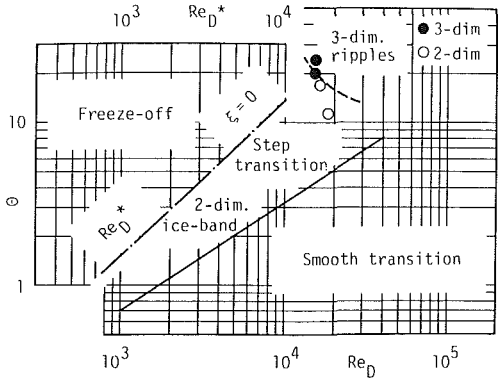

Fig. 11 Summary of different freezing phenomena on θ-Re_D coordinate system

of B) and a smooth one, for the thinner layer. As for study of a flat plate, it has been reported that the transition pattern can be described by a parameter which indicates a degree of ice thickness (Hirata et al., 1979). In the present pipe experiment a close connection between the ice thickness and the transition pattern was also obtained as shown in Fig. 8. It can be read from Fig. 8 that the onset value for the step transition is about $B=0.8$.

Figure 9 gives the map of transition pattern on an Re_D-K coordinate system obtained under steady-state conditions. Moretti and Kays (1965) suggested that a value of $K=3.3\times10^{-6}$ was sufficient to relaminarize a turbulent flow. In Fig. 9 the effect of K on the transition pattern is obvious for $Re_D>2300$. It is shown that a smooth transition occurs for $K<5\times10^{-6}$ and a step transition, for $K>8\times10^{-6}$. These results account for the consideration that a step transition results from a flow transition from laminar to turbulent flow. For $Re_D<2300$ all the experimental data shown in Fig. 9 indicate a step transition. For low-Reynolds-number flow, a higher acceleration with a thicker ice layer is required to reach the transition Reynolds number. The ice thickness at the contraction region, therefore, becomes larger and a step transition is likely to occur. This is the reason why experimental data of smooth transition cannot be obtained for $Re_D<2300$.

Figure 10 gives the results for the onset of step transition under steady-state conditions. Introducing the onset value $B=0.8$ into equation (8), we finally have

$$\theta=0.117\,(Re_D\theta^2)^{2/7} \tag{9}$$

Equation (9) is shown in Fig. 10 by a solid line. The upper part of the solid line is the step transition regime and the lower part, the smooth regime. It is noticed that some experimental data below the solid line indicate a step transition, contrary to expectations. When the experimental conditions are very close to the onset values, an initially smooth transition would change into a step pattern caused by a small disturbance of flow as well as by temperature conditions. Once the ice shape has taken a step transition, it cannot readily return to a smooth one, even if the experimental conditions are recovered. This is due to a large change in heat transfer characteristics in a separated flow region. Under the experimental conditions close to the onset values, the ice layer, therefore, tends to be a step transition.

Summary of Freezing Phenomena. In Fig. 11 the typical ice shapes are classified on a θ-Re_D coordinate system. The solid line indicates the onset of step transition and the dashed line, the onset of three-dimensional ripples supposed by previous observers (Hirata and Ishihara, 1985). The chain line represents the freeze-off conditions for the friction-factor coefficient $\xi=0$ given by Hirata and Ishihara (1985), where the onset conditions are prescribed by a modified Reynolds number, $Re_p=D(2P_0/\rho)^{0.5}/\nu$. The Re_p can be transformed into an equivalent pipe Reynolds number Re_D^* as follows:

$$Re_D^*=\frac{B^2}{[1+n(1-B^2)^2]^{0.5}}Re_p \tag{10}$$

where n is the number of ice bands in the pipe. In Fig. 11 the values of Re_D^* are used to represent the onset of freeze-off conditions. It should be noted that the freeze-off conditions are, in principle, described by Re_p, so the value of Re_D^* cannot be compared directly with that of Re_D.

As to the general nature of the freezing phenomena, it can be noted that a thinner ice layer produces a smooth transition and, with increasing ice thickness, a step transition (two-dimensional ice bands) or freeze-off occurs. A three-dimensional pattern is also observed for larger values of Re_D and θ.

Conclusions

From the present experimental studies concerning with freezing of water flowing in a pipe, the following conclusions may be drawn:

1 The formation of an ice-band structure is caused by a flow transition from laminar to turbulent flow and the transient freezing process is strongly dependent on flow as well as on temperature conditions. At higher Reynolds numbers, a large flow disturbance affects the transient freezing process and a very short spacing of ice bands is produced.

2 Equation (9) represents the onset conditions that divide a smooth transition from a step transition. These conditions are strongly affected by the thickness of the ice layer.

3 The typical ice shapes for the freezing of water flowing in a pipe are classified into the patterns of smooth or step transition, two- or three-dimensional ice band, and freeze-shut. These phenomena can be summarized on a θ-Re_D coordinate system as shown in Fig. 11.

References

Gilpin, R. R., 1979, "The Morphology of Ice Structure in a Pipe at or Near Transition Reynolds Number," *Heat Transfer*, AIChE Symposium Series 189, Vol. 75, San Diego, CA, pp. 89–94.

Gilpin, R. R., 1981, "Ice Formation in Pipe Containing Flow in the Transition and Turbulent Regimes," ASME Journal of Heat Transfer, Vol. 103, pp. 363–368.

Gilpin, R. R., Hirata, T., and Cheng, K. C., 1980, "Wave Formation and Heat Transfer at an Ice–Water Interface in the Presence of a Turbulent Flow," *Journal of Fluid Mechanics*, Vol. 99, pp. 619–640.

Hirata, T., 1986, "Effects of Friction Losses in Water-Flow Pipe Systems on the Freeze-off Conditions," *International Journal of Heat and Mass Transfer*, Vol. 29, pp. 949–951.

Hirata, T., 1987, "The Onset of Ice-Band Structure Upon the Freezing of Flowing Water in a Pipe," *Heat Transfer – Japanese Research*, in press.

Downloaded 17 Dec 2010 to 193.140.21.150. Redistribution subject to ASME license or copyright; see http://www.asme.org/terms/Terms_Use.cfm

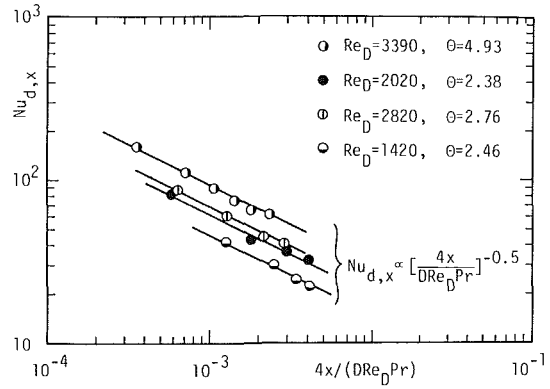

Fig. 12 Local Nusselt number at $x < L_0$ (Hirata, 1987)

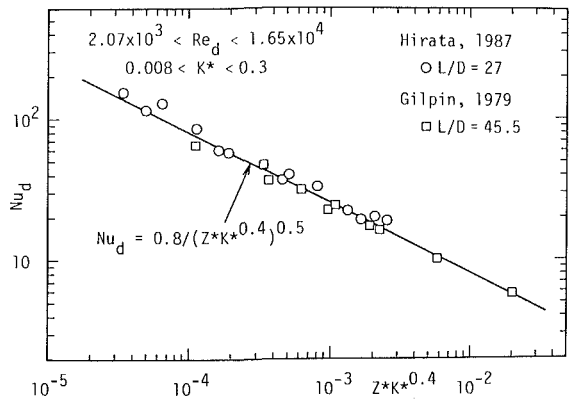

Fig. 13 Nusselt number at contraction region of ice layer (Hirata, 1987)

Hirata, T., Gilpin, R. R., and Cheng, K. C., 1979, "The Steady State Ice Layer Profile on a Constant Temperature Plate in a Forced Convection Flow – II. The Transition and Turbulent Regimes," *International Journal of Heat and Mass Transfer*, Vol. 22, pp. 1435–1443.

Hirata, T., and Ishihara, M., 1985, "Freeze-Off Conditions of a Pipe Containing a Flow of Water," *International Journal of Heat and Mass Transfer*, Vol. 28, pp. 331–337.

Moretti, P. M., and Kays, W. M., 1965, "Heat Transfer to a Turbulent Boundary Layer With Varying Free-Stream Velocity and Varying Surface Temperature – An Experimental Study," *International Journal of Heat and Mass Transfer*, Vol. 8, pp. 1187–1202.

Seki, N., Fukusako, S., and Younan, G. W., 1984, "Ice-Formation Phenomena for Water Flow Between Two Cooled Parallel Plates," ASME JOURNAL OF HEAT TRANSFER, Vol. 106, pp. 498–505.

Toda, S., Owada, H., Kurokawa, M., and Hori, Y., 1985, "Experiments on Heat Transfer and Liquid Solidification in a Tube Containing Forced Flow," *22nd National Heat Transfer Symp. of Japan* [in Japanese], Tokyo, pp. 199–201.

Zemanick, P. P., and Dougall, R. S., 1970, "Local Heat Transfer Downstream of Abrupt Circular Channel Expansion," ASME JOURNAL OF HEAT TRANSFER, Vol. 92, pp. 53–60.

APPENDIX

Equation (2) was obtained as follows (Hirata, 1987): As to the effect of flow laminarization on Nu_d, it is necessary to examine the local heat transfer coefficient for $x < L_0$, where L_0 is the distance from the pipe inlet to the location of the step transition. In Fig. 12 the local Nusselt numbers $Nu_{d,x}$ for $x < L_0$ are shown. It is seen that the value of $Nu_{d,x}$ is approximately proportional to $(Re_D D/x)^{0.5}$. This relationship can be rewritten as follows by using x as a reference length:

$$\frac{hx}{\lambda_w} = \text{const}\left(\frac{Vx}{\nu}\right)^{0.5} \frac{D}{d_x} \tag{11}$$

It is realized that the formula of equation (11) is the same as that for laminar heat transfer on a flate plate. This implies that the heat transfer rate in the region of accelerated flow for $x < L_0$ is controlled by a laminar boundary layer resistance, which coincides with the result by Gilpin (1979).

Moretti and Kays (1965) examined a flow laminarization on a flat plate and suggested that the laminarization factor can be represented in terms of K/St. Their result was extended to pipe flow, and an examination of the effect of K/St_d $(=K^*)$ on Nu_d revealed that Nu_d was proportional to $K^{*-0.2}$. Based on the results obtained, the value of Nu_d at $x = L_0$ is plotted against $Z^*K^{*0.4}$ in Fig. 13. It is shown that Gilpin's (1979) data also correlate well and that the experimental relationship of the heat transfer coefficient at $x = L_0$ can be represented by

$$Nu_d = 0.8/(Z^*K^{*0.4})^{-0.5} \tag{12}$$

where the applicable range of equation (12) is $0.008 < K^* < 0.3$.

Downloaded 17 Dec 2010 to 193.140.21.150. Redistribution subject to ASME license or copyright; see http://www.asme.org/terms/Terms_Use.cfm

D. Y. C. Wei
Materials Engineering.

B. Farouk
Mechanical Engineering and Mechanics.

D. Apelian
Materials Engineering.

Drexel University,
Philadelphia, PA 19104

Melting Powder Particles in a Low-Pressure Plasma Jet

A numerical model has been developed to predict the temperature history of metal particles injected in a low-pressure (supersonic) d-c plasma jet. The temperature and velocity fields of the plasma jet are predicted by solving the parabolized compressible Navier–Stokes equations using a spatial marching scheme. Particle trajectories and heat transfer characteristics are calculated using the predicted plasma jet temperature and velocity fields. Correction factors have been introduced to take into account the noncontinuum effects encountered in the low-pressure environment. The plasma jet profiles as well as the particle/plasma interactions under different jet pressure ratios (from underexpanded to overexpanded cases) have been investigated.

Introduction

In the plasma spraying process a d-c plasma jet is used as a heat source to melt and accelerate powder particles, which subsequently impinge and solidify on a given substrate. During the low-pressure plasma deposition (LPPD) process, the plasma jet is expanded into a low-pressure environment (40–80 torr) which results in high (supersonic) plasma jet velocities with Mach numbers ranging from 2 to 3. Previous efforts to predict heat transfer and fluid flow on atmospheric-pressure plasma spraying were based on an incompressible flow formulation employing turbulence models (Correa, 1983; McKelliget et al., 1982; El-Kaddah et al., 1984). However, these calculations are limited to the subsonic flow regime. Compressibility effects and viscous heat dissipation were neglected. In the LPPD process, the plasma jet is operated in the supersonic flow regime; therefore, the compressibility effects and viscous heat dissipation should not be considered to be negligible. One of the objectives of this work is to develop a jet model capable of predicting supersonic plasma jets operating at off-design (under or overexpanded) conditions.

Production of high-quality dense deposits requires that a large fraction of the injected particles be in a molten state when they impact the substrate. An additional objective of this work is to understand plasma/particle heat and momentum transfer since these phenomena dictate both the particle thermal history and trajectory.

Early computational work in supersonic nozzle flow fields (Cosner and Bower, 1977; Pergament et al., 1978; Holst, 1977) consisted of patching methods that divided the flow field into an inviscid free stream and viscous boundary and mixing layers. Each was analyzed independently and coupled through appropriate boundary conditions. Later schemes (Mikhail, 1979; Hasen, 1982) involved solving time-dependent, compressible Navier–Stokes equations over the entire computational domain. These schemes show a great promise for predicting flows with complex structure, and where the viscous effects become prevalent. The above schemes are, however, found to be unsuitable for supersonic jet flows exiting into a quiescent ambient environment.

In this study, a numerical model was developed to predict the thermal history of particles injected into a low-pressure plasma jet. The temperature and velocity profiles of plasma jets are predicted by solving the parabolized compressible Navier–Stokes equations using a spatial marching scheme. In the LPPD process, because of the low-pressure environment and supersonic velocity, the mean free path lengths of the plasma constituents have been calculated to be on the order of several microns. Thus, noncontinuum effects on heat and momentum transfer to the particle should be significant (Eckert and Drake, 1972; Chen and Pfender 1983). Previous work (Apelian et al., 1984) has shown that the noncontinuum interaction between the plasma gas and the injected particles is significant for the conditions encountered during LPPD. Correction factors have been introduced to take these effects into account and the results show that both heat and momentum transfer between the plasma gas and the injected particles are significantly reduced. In the particle heating model employed here, the latent heat of melting was taken into account by introducing apparent enthalpy as a function of the fraction of liquid formed which can be derived from equations describing equilibrium melting.

Model Development

The integrated process model which predicts the temperature of the injected powder particles during their flight through the plasma jet is based on models describing the plasma gas temperature and velocity, the injected particle trajectory and the heat transfer between the particles and the plasma gas. The arc region and the flow inside the plasma gun have not been considered in this study. These models are discussed in the following:

Plasma Jet Model. The following assumptions were made when formulating the jet model:

(*i*) The plasma is in local thermodynamic equilibrium. This assumption is found to be reasonable for electron densities above 10^{15}cm^{-3}. However, this assumption may not be valid at the periphery of the plasma arc where electron temperatures are much higher than the temperatures of other species.

(*ii*) The plasma jet is at steady state and possesses cylindrical symmetry.

(*iii*) The plasma is assumed to be optically thin and radiation heat transfer is negligible.

(*iv*) Ionization and recombination of ions and electrons due to shock formation are negligible.

(*v*) The plasma gas is assumed to obey the ideal gas law, and the turbulent Prandtl number is assumed to be constant (0.9).

The model considers wave/shock propagation in laminar and turbulent regions of the jet, as well as turbulent mixing in the (jet) shear layer. In addition, the model should take into account the influence of compressibility effects, pressure gradients on turbulence, and the interaction of the wave and the turbulent mixing layer. The plasma plume (jet) is described by formulating jet mixing equations using time-averaged,

Contributed by the Heat Transfer Division and presented at the ASME Winter Annual Meeting, Anaheim, California, December 1986. Manuscript received by the Heat Transfer Division September 2, 1986.

 Copyright © 1987 by ASME

Downloaded 17 Dec 2010 to 193.140.21.150. Redistribution subject to ASME license or copyright; see http://www.asme.org/terms/Terms_Use.cfm

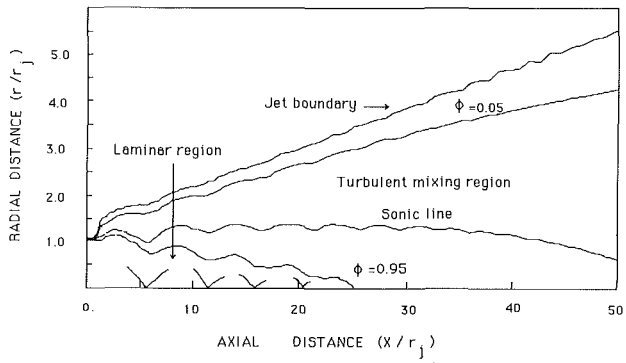

Fig. 1 Jet mixing contours for Mach 2 jet into still air ($P_j/P_\infty = 1.45$, $T_j = 1500$ K)

Reynolds decomposed, axisymmetric parabolized Navier-Stokes equations. The turbulent viscosity was obtained using the compressibility corrected k-ϵ (two equation) turbulence model (Launder, 1972).

The conservation equation for momentum, mass, and enthalpy were transformed to an x-ψ coordinate system yielding (Jennions et al., 1977):

Continuity:

$$\rho ur = \frac{\partial \psi}{\partial r}; \qquad -\rho vr = \frac{\partial \psi}{\partial x} \tag{1}$$

Streamwise momentum:

$$\frac{\partial u}{\partial x} = \frac{\partial}{\partial \psi}\left(\rho ur^2 \cdot \mu_{\text{eff}} \frac{\partial u}{\partial \psi}\right) - \frac{1}{\rho u}\frac{\partial p}{\partial x} \tag{2}$$

Lateral momentum (neglecting viscous terms):

$$\frac{\partial v}{\partial x} = -r\frac{\partial p}{\partial \psi} \tag{3}$$

Stagnation enthalpy:

$$\frac{\partial H}{\partial x} = \frac{\partial}{\partial \psi}\left(\rho ur^2 \cdot \frac{\mu_{\text{eff}}}{\sigma_H}\frac{\partial H}{\partial \psi}\right) + \frac{\partial}{\partial \psi}\left[\left(\mu_{\text{eff}} - \frac{\mu_{\text{eff}}}{\sigma_H}\right) \cdot \rho ur^2 \cdot \frac{\partial}{\partial \psi}\{(u^2+v^2)/2\}\right] \tag{4}$$

Species:

$$\frac{\partial \phi}{\partial x} = \frac{\partial}{\partial \psi}\left[\rho ur^2 \cdot \frac{\mu_{\text{eff}}}{\sigma_\phi}\frac{\partial \phi}{\partial \psi}\right] + \frac{1}{\rho u}S_\phi \tag{5}$$

where $\mu_{\text{eff}} = \mu_l + \mu_t$.

Compressibility is accounted for by making the plasma gas density depend on the pressure and temperature through the ideal gas state equation

$$p = \frac{(\gamma-1)\rho}{\gamma}\left[H - \frac{1}{2}(u^2+v^2)\right] \tag{6}$$

A parameter ϕ was introduced which ranged between 0 and 1, and was utilized to describe the extent of mixing, following Dash (1985). Argon is the only specie considered in the analysis. Essentially, the value of specie ϕ was used to locate the turbulent shear layer (Fig. 1). Following Dash (1985) the turbulent shear layer was defined in the region where ϕ ranges between 0.05 and 0.95. The two-equation (k-ϵ) turbulence model was applied in the turbulent jet mixing layer, only.

The turbulence model used in this study is the basic k-ϵ model which has been *modified* to correct for axisymmetric and weak shear flow near the centerline (Launder et al., 1972), and the viscosity formulation used takes into account compressibility of the jet (Dash et al., 1975). The latter described the observed reduced mixing rate in supersonic jets.

The formulated turbulent kinetic energy (k) and its dissipation (ϵ) equations are

$$\frac{\partial k}{\partial x} = \frac{\partial}{\partial \psi}\left(r^2 \rho u \frac{\mu_t}{\sigma_k}\frac{\partial k}{\partial \psi}\right) + (P - \epsilon) \tag{7}$$

$$\frac{\partial \epsilon}{\partial x} = \frac{\partial}{\partial \psi}\left(r^2 \rho u \frac{\mu_t}{\sigma_\epsilon}\frac{\partial \epsilon}{\partial \psi}\right) + \frac{\epsilon}{k}(C_1 P - C_2 \epsilon) \tag{8}$$

where P is the turbulent production term

$$P = \mu_t \rho u r^2 \left(\frac{\partial u}{\partial \psi}\right)^2 \tag{9}$$

The turbulent viscosity μ_t is determined from the local values of k and ϵ through the relation

$$\mu_t = C_\mu(f)\rho\frac{k^2}{\epsilon} \tag{10}$$

where $\sigma_k = 1.0$; $\sigma_\epsilon = 1.3$; $C_1 = 1.43$; $C_2 = 1.92 - 0.667f$; $C_\mu = 0.09 - 0.4f$.

The axisymmetric correction parameter f is set equal to zero in the shear layer region (before the mixing zone reaches the axis), and is defined in the downstream region as

$$f = \left[\frac{r_e}{2(u_c - u_e)}\left(\left|\frac{du_c}{dx}\right| - \frac{du_c}{dx}\right)\right]^{0.2}$$

where r_e is the width of the full mixing layer, u_c is the jet centerline velocity, and u_e is the external stream velocity.

To account further for the reduced mixing rate observed at higher Mach number jet mixing, a heuristic compressibility corrected viscosity is used

$$\mu_t = C(\mathrm{M}_\tau)C_\mu\rho\frac{k^2}{\epsilon} \tag{11}$$

where $C(\mathrm{M}_\tau)$ is the correction factor and M_τ is the

Nomenclature

a = accommodation coefficient
C_D = drag coefficient
c = speed of sound
c_P = specific heat
f_L = fraction of liquid
h = heat transfer coefficient
H = enthalpy of the gas or powder particle
k = turbulent kinetic energy
K = thermal conductivity
L = latent heat of fusion
P = turbulence production term
p = pressure
Q_0 = heat flux
r = radial distance from axis
T = temperature
t = time
S = source term
u = axial velocity
v = radial velocity
x = axial distance
γ = ratio of specific heats
ϵ = turbulent dissipation rate
μ = viscosity
ρ = density
σ = Prandtl number
ϕ = species
ψ = stream function

Subscripts

c = continuum
j = jet exit
eff = effective physical property
l = laminar state
liq = liquidus
mp = melting point
p = particle surface
r = recovery
ref = reference state
s = stagnation condition
sol = solidus
t = turbulent state
∞ = chamber condition

Downloaded 17 Dec 2010 to 193.140.21.150. Redistribution subject to ASME license or copyright; see http://www.asme.org/terms/Terms_Use.cfm

characteristic Mach number of turbulence ($M_\tau = k_{max}^{0.5}/c$), where k_{max} is the maximum value of turbulent kinetic energy k at each station, and c is the local sound speed at the grid point where k is maximum. The functional form of $C(M_\tau)$ given by Dash et al. (1975) was determined by matching calculations to observed spreading rate for isoenergetic, supersonic shear layers with one stream stationary. It should be noted that the turbulence modeling is only applied in the mixed shear layer, which is defined by the position of calculated species ratio.

A one-dimensional isentropic flow solution was calculated to obtain the mean Mach number, pressure, and the jet enthalpy at the nozzle exit based on experimentally determined operating parameters, and the critical area ratio of the nozzle (Wei, 1986). Top hat type initial conditions were used for the flow and the temperature. The initial conditions for k and ϵ are as given in Launder et al. (1977).

When performing the calculation for a jet exhausting into a quiescent stream, the imposition of the ambient pressure level along the jet edge and use of the boundary condition $u|_{\text{jet edge}} = u_\infty$ are good approximations to the problem. For the quiescent edge chamber calculation, however, the condition $u_\infty = 0$ should not be simulated numerically, since this implies vertical angles for the entrained streamline which is physically unrealistic. Instead a nominal value $u_\infty/u|_{\text{jet edge}} = 0.001$ was used to approximate the quiescent state.

The solution procedure employed a standard Patankar–Spalding parabolic marching integration to solve the equations for the streamwise velocity, total enthalpy, species, and turbulence variables. A pressure correction equation was formulated based on the compatibility of the momentum and continuity equations (Jennions et al., 1977). The pressure correction equation is solved to give the pressure variation along the cross-stream direction and to correct the flow field to satisfy continuity. Axial step size was varied in proportion to the streamline curvature. Fifty cross-stream grids were used for all calculations reported. Details of the solution procedures can be found in the references (Jennion et al., 1977; Wei, 1986). The exit plane of the plasma gun was considered as the starting plane for the solution domain. Thermophysical properties of argon were obtained from Vargaftik (1975).

Momentum and Heat Transfer Between Plasma Gas and Particles. In the LPPD process, due to the low-pressure environment and supersonic plasma velocity, the noncontinuum effects on the heat and momentum transfer to the particles become significant and should be taken into account. Single particle trajectories were calculated by solving a simplified form of the Basset–Boussinesq–Oseen equation. The equations were derived assuming that the only forces which influence the trajectory of the particles are the drag and gravity forces.

A detailed analysis of the various terms in the particle momentum and energy equations has been given by Lee et al. (1985). The Basset force term, the thermophoretic acceleration term, and the effects of gravity have been neglected considering the small size of the particles. The particles are assumed to be introduced at rest into the center of the jet. The effect of the injection gas on the plasma jet has not been considered in this analysis. The drag coefficient for the injected particles in the supersonic flow regime was calculated using the formulation suggested by Vallerani (1976). The drag coefficient for particles moving at low Reynolds and Mach numbers was calculated using an approximate solution suggested by Phillips (1975).

For particle heat transfer calculations in a plasma gas moving at high velocity, it is necessary to take into account the frictional heating of the plasma gas near the injected particulate body. Thus, the heat flow from the plasma gas to the injected particles is given by $q = h(T_r - T_p)$, where T_r is how defined as the recovery temperature and is expressed by the recovery factor r

$$r = \frac{T_r - T_p}{T_s - T_p}$$

T_s is the stagnation temperature of the plasma gas based on the relative velocity with respect to the particles. In this work, the recovery factor used was obtained from experimental results reported by Drake and Backer (1952). An experimental correction factor (Sherman, 1983) for heat transfer to bodies in subsonic flow in the transitional flow regime has been extended to the supersonic flow regime. A detailed analysis of the momentum and heat transfer to particles in jets has previously been presented by the authors (Apelian et al., 1984). An accommodation coefficient of 0.8 was used in this study.

Heat Conduction Within a Particle Undergoing a Phase Change. In evaluating heat conduction within the particles, the temperature gradient within the particle and the temperature-dependent properties of the powder particle are considered. The governing differential equations and boundary conditions for a material during the various stages of melting, i.e., (*i*) all solid, (*ii*) liquid plus solid, (*iii*) all liquid, or (*iv*) evaporating surface, have been considered. In addition, the melting model takes into account the fact that during melting of alloy particles a mushy region exists where both solid and liquid phases are present. An enthalpy method developed by Voller and Cross (1979) has been used to take into account the mushy region during melting.

For spherical particles the heating can be described by the conduction equation

$$\rho_p \frac{\partial H}{\partial t} = \frac{1}{r^2}\frac{\partial}{\partial r}\left[r^2 K_p \frac{\partial T}{\partial r}\right] \tag{12}$$

The conductivity K_p and density ρ_p are functions of temperature.

For a pure material the temperature is related to enthalpy via

$$dT = \frac{dH}{c_p} \text{ when } H < \int_{T_{\text{ref}}}^{T_{mp}} c_p dT$$

$$T = T_{mp} \text{ when } \int_{T_{\text{ref}}}^{T_{mp}} c_p dT \le H \le \int_{T_{\text{ref}}}^{T_{mp}} c_p dT$$

and

$$dT = \frac{d(H-L)}{c_p} \text{ when } H \ge \int_{T_{\text{ref}}}^{T_{mp}} c_p dT + L$$

For an alloy the relationship is as follows:

$$dT = \frac{dH}{c_p} \text{ when } H < \int_{T_{\text{ref}}}^{T_{\text{sol}}} c_p dT$$

$$dT = \frac{d(H - f_L L)}{c_p} \text{ when } \int_{T_{\text{ref}}}^{T_{\text{sol}}} c_p dT \le H \le \int_{T_{\text{ref}}}^{T_{\text{liq}}} c_p dT + L$$

$$dT = \frac{d(H-L)}{c_p} \text{ when } H \ge \int_{T_{\text{ref}}}^{T_{\text{liq}}} dT + L$$

where f_L is the liquid fraction present at temperature calculated from the alloy phase diagram.

Results and Discussion

Jet Model Confirmation. A series of calculations was performed for a cold ($T_{\text{static}} = 164$ K) Mach 2 jet into still air (having the same static temperature) at two different static pressure ratios ($P_j/P_\infty = 1.45$ and $P_j/P_\infty = 0.75$). The calcula-

Downloaded 17 Dec 2010 to 193.140.21.150. Redistribution subject to ASME license or copyright; see http://www.asme.org/terms/Terms_Use.cfm

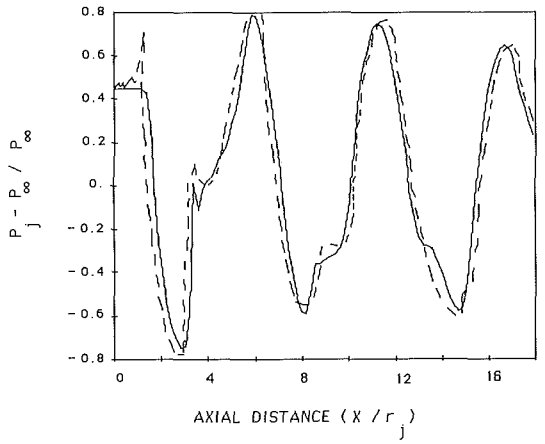

Fig. 2 Comparison of predicted and measured static pressure variations along jet axis for Mach 2 jet ($P_j/P_\infty = 1.45$) into still air; ——— predicted, ····· measured

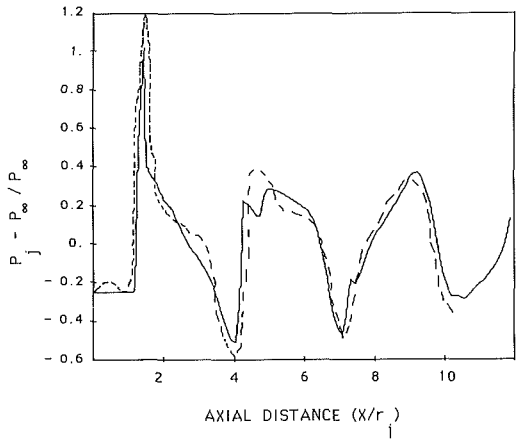

Fig. 3 Comparison of predicted and measured static pressure variations along jet axis for Mach 2 jet ($P_j/P_\infty = 0.75$) into still air; ——— predicted, ····· measured

tions simulate the experimental conditions reported by Seiner and Norum (1980). Comparisons of the predicted and measured streamwise pressure variations along the jet centerline for the two static pressure ratios are shown in Figs. 2 and 3. As can be seen, the predicted and measured pressure variations agree very well, indicating that the level of jet mixing and the attenuation of the wave intensity due to turbulent dissipation are properly modeled. The model was used to predict the rate of jet decay, and the results were compared with the measured data reported by Eggers (1966). As can be seen in Fig. 4, good agreement exists between the experimental data and the model up to 30 radii of jet axial distance.

Supersonic Plasma Jet Predictions. Having confirmed the jet model, supersonic plasma profiles describing jet mixing were generated for:

(*a*) an argon plasma exiting at Mach 2 velocity into a chamber at a reduced pressure of 40 torr ($P_j/P_\infty = 1.266$);

(*b*) an argon plasma exiting at Mach 2 velocity into a chamber at a reduced pressure of 65 torr ($P_j/P_\infty = 0.75$);

(*c*) an argon plasma exiting at Mach 3 velocity into a chamber at a reduced pressure of 40 torr ($P_j/P_\infty = 1.37$).

The nozzle exit pressure P_j was estimated using a one-dimensional isentropic flow model and a given nozzle area

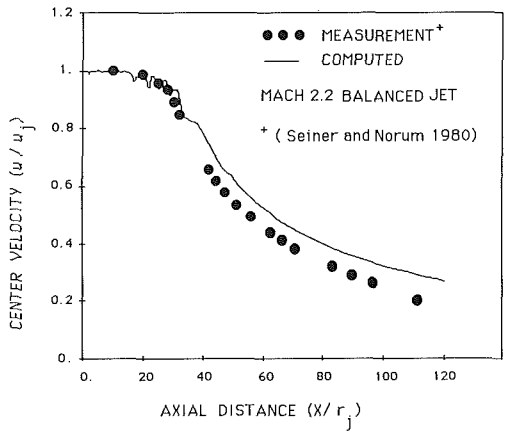

Fig. 4 Comparison between predicted and measured centerline velocity decay for a Mach 2.2 balanced jet into still air

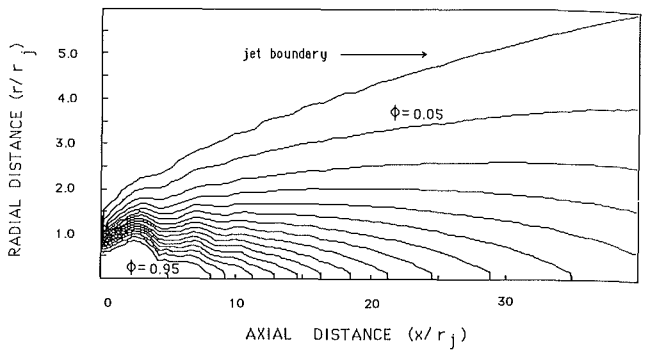

Fig. 5 Predicted degree of jet mixing contours for Mach 2 plasma conditions ($P_j/P_\infty = 1.226$)

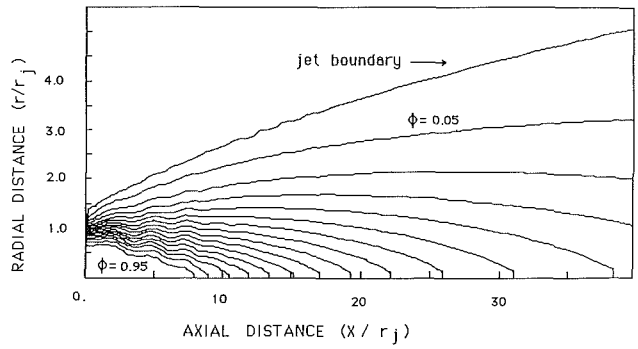

Fig. 6 Predicted jet mixing contours for Mach 2 plasma conditions ($P_j/P_\infty = 0.75$)

ratio. The inlet static temperature were taken to be 6130°K and 4584°K for the Mach 2 and Mach 3 plasma jets, respectively.

Figure 5 shows the jet mixing contours ϕ for a Mach 2 plasma operating at 40 torr. This is the situation where the jet is underexpanded, and one can clearly see the level of mixing in the plume. A strong gradient of ϕ indicates strong mixing. Moreover, one notes the deflection of the jet near the exit of the gun due to underexpansion of the jet. In contrast, when the chamber pressure is at 65 torr (the situation when we have an overexpansion of the jet), the results show distinctly different jet mixing contours, as shown in Fig. 6. The lack of deflection of the jet as it exits in a chamber at a higher pressure (65 torr) is of interest in understanding particle/plasma interaction.

Subsequently, plasma jet temperature and velocity profiles for different Mach number jets operating at a variety of different chamber pressure conditions (different values of

Downloaded 17 Dec 2010 to 193.140.21.150. Redistribution subject to ASME license or copyright; see http://www.asme.org/terms/Terms_Use.cfm

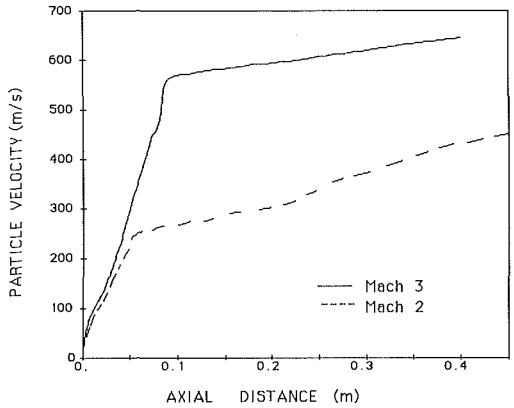

Fig. 7 Particle velocity as a function of axial distance for 30 μm Fe-20 wt percent Mn particles sprayed using Mach 3 plasma conditions ($P_j/P_\infty = 1.37$); and Mach 2 plasma conditions ($P_j/P_\infty = 1.226$); ——— Mach 3, ····· Mach 2

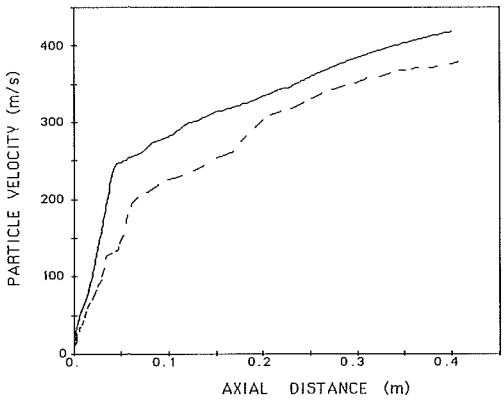

Fig. 8 Particle velocity as a function of axial distance for 30 μm Fe-20 wt percent Mn particles sprayed using Mach 2 plasma jet ($P_j/P_\infty = 1.226$, $P_j/P_\infty = 0.75$)

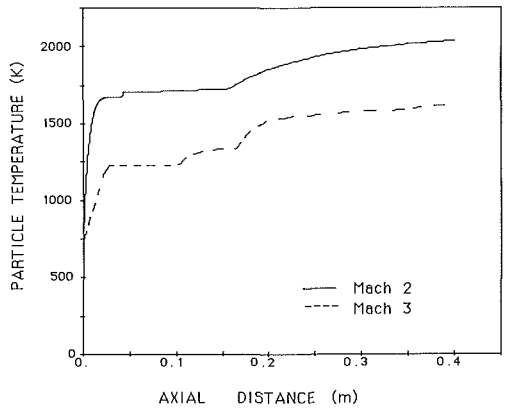

Fig. 9 Particle temperature as a function of axial distance for 30 μm Fe-20 wt percent Mn particles sprayed using Mach 2 plasma jet conditions ($P_j/P_\infty = 1.226$), and Mach 3 plasma jet conditions ($P_j/P_\infty = 1.37$); ——— Mach 2, ····· Mach 3

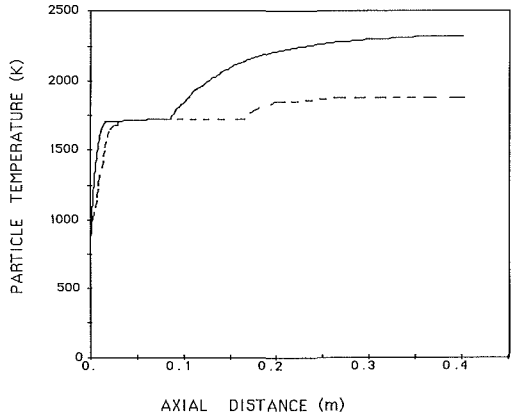

Fig. 10 Particle temperature as a function of axial distance for 30 μm Fe-20 wt percent particles sprayed using Mach 2 plasma jet ($P_j/P_\infty = 0.75$, and $P_j/P_\infty = 1.226$)

P_j/P_∞) were generated. The reader is referred to Wei (1986) for a detailed discussion and presentation of these results.

Injected Particle Velocities and Trajectories. It has been shown that in LPPD the Knudsen number ranges from 0.5 to 5 when injecting particles in the size range of 10–50 μm (Apelian, 1984). Thus noncontinuum effects on the heat and momentum transfer are substantial. The heat fluxes and the drag coefficients for injected particles in the transitional flow regimes have been reported elsewhere (Apelian, 1984). These results suggest that momentum transfer can be reduced by as much as 90 percent, and that the heat transfer can be reduced by as much as 80 percent when injecting particles in the size range of 10–50 μm in LPPD (as compared to continuum flow heat and mass transfer to particles).

Velocities of injected Fe-20 wt. percent Mn particles (30 μm diameter) as a function of the distance along the jet axis are shown in Figs. 7 and 8. The particle velocities shown in Fig. 7 are for Mach 2 and Mach 3 plasmas, both operating in a 40 torr chamber. It can be seen that momentum transfer occurs during the initial stages of flight. In addition, particle velocities in the Mach 2 plasma are much lower than in the Mach 3 plasma, giving the particles a longer residence time in the jet. The sudden change of the particle acceleration is caused by the sudden drop of gas velocity after the first shock structure. Table 1 gives calculated residence times for different plasma conditions. These results agree well with experimental data (Frind et al., 1983), which show that particle melting is more efficient in Mach 2 plasma due to larger residence times.

Injected particle velocity is further reduced when the jet is overexpanded, that is, the jet exits into a chamber which is at a higher pressure. This is seen in Fig. 8, which shows particle velocities for both underexpanded ($P_j/P_\infty = 1.226$ or 40 torr) and overexpanded ($P_j/P_\infty = 0.75$ or 65 torr) jets.

Table 1 Comparison of residence times for Fe-20 wt percent Mn particles (30 μm diameter) injected in different plasma jets

Plasma Condition	Jet Pressure Ratio	Spray Distance (m)	Residence Time (ms)
Mach 2	$P_j/P_\infty = 1.226$	0.4	1.81
	$P_j/P_\infty = 0.75$	0.4	1.96
Mach 3	$P_j/P_\infty = 1.37$	0.4	1.21

Injected Particle Temperature and Heat Transfer. Thermal histories of Fe-20 wt percent Mn particles (30 μm diameter) as a function of distance along the jet axis are shown in Figs. 9 and 10. The solidus and liquidus temperatures of the particles are 1702 K and 1725 K, respectively. The particle temperatures shown in Fig. 9 are for Mach 2 and Mach 3 plasma jets, both operating at a 40 torr chamber pressure. Figure 10 shows the mean particle temperature for two different jet pressure ratios ($P_j/P_\infty = 1.226$ or 40 torr and $P_j/P_\infty = 0.75$ or 65 torr). The plateau shown around 1700 K in the figures signifies melting of the particles. In Fig. 9 another plateau is observed near 1200 K for the Mach 3 condition. This

Downloaded 17 Dec 2010 to 193.140.21.150. Redistribution subject to ASME license or copyright; see http://www.asme.org/terms/Terms_Use.cfm

is, however, due to the temperature drop of the gas phase flow due to an expansion wave. As can be seen, particle heating is more efficient with the Mach 2 gun than with the Mach 3 gun. The Mach 2 plasma jet has a lower velocity, a higher enthalpy as well as a lower operating power level than the Mach 3 plasma jet. Powders of 30 μm size can be melted using the Mach 2 gun but are not melted using the Mach 3 gun, as shown in Fig. 9. Furthermore, particle heating is more efficient with the plasma gun operating in the overexpanded condition than the case when the plasma is in the underexpanded condition. These results are in agreement with the experimental observations previously reported (Smith, 1985).

Conclusions

The comparisons between the predictions and reported data for a supersonic jet exiting into a quiescent atmosphere have shown that the present model is capable of predicting the flow structure of high Mach number jets under moderate off-design (i.e., under or expanded) conditions. Furthermore, the strong spatial fluctuations in plasma jet properties (i.e., velocity, pressure, density, temperature) due to the imperfect expansions of the plasma jet have been explored. The present predictions of the particle temperature and velocity show close agreement with the reported data on the LPPD process (Smith, 1985) when noncontinuum effects are incorporated into the calculations. In addition, the predicted effective particle heating under the overexpanded plasma condition have also been reported by Smith (1985). Specifically, efficient melting of Rene 80 particles have been observed when a plasma jet operated at an increased chamber pressure (i.e., overexpanded condition).

It should be noticed that the present jet flow calculations were made using the radially uniform inlet condition, i.e., radial gradients for the temperature and velocities have not been considered. However, due to the strong interaction between the arc and the gas flow within the nozzle, the arc heating of plasma gas is nonuniform. Therefore, presently assumed top hat-type inlet conditions need to be investigated further. A case of dilute injection has been assumed, thus, coupling effects between plasma plume and injected particles are not considered. In addition, the contribution of ion-electron recombination on the total heat transfer (Lee et al., 1985) has been neglected.

References

Apelian, D., Wei, D., and Paliwal, M., 1984, "Particle/Plasma Interactions During Low Pressure Plasma Deposition," *Thin Solid Films*, Vol. 118, pp. 384–395.

Chen, X., and Pfender, E., 1983, "Effect of Knudsen Number on Heat Transfer of Small Particles in a Thermal Plasma," *Plasma Chem. Plasma Process*, Vol. 3, pp. 97–104.

Cosner, R. R., and Bower, W. W., 1977, "Patch Solution of the Transonic Flow Fields About an Axisymmetric Boattail," AIAA Paper No. 77-227.

Correa, S. M., 1983, "Transitional Plasma Jet Modeling," *Proceedings, 6th International Symposium on Plasma Chemistry*, M. I. Boulos and R. J. Munz, eds., Vol. 1, pp. 77–81.

Dash, S. M., 1985, "Recent Developments in the Modeling of High Speed Jets, Plumes and Wakes," AIAA Paper No. AIAA-85-1616.

Dash, S. M., Weilerstein, G., and Vaglio-Laurin, R., 1975, "Compressibility Effects in Free Turbulent Shear Flow," AFOSR-SR-75-1435, available from DTIC as AD-A016-535.

Drake, R. M., and Backer, G. H., 1952, *Trans. ASME*, Vol. 74, No. 7, pp. 1241–1253.

Eckert, E., and Drake, R., 1972, *Analysis of Heat and Mass Transfer*, McGraw-Hill, New York, pp. 467–521.

Eggers, J. M., 1966, "Velocity Profiles and Eddy Viscosity Distributions Downstream of a Mach 2.2 Nozzle Exhausting to Quiescent Air," NASA TN D-3601.

El-Kaddah, N., McKelliget, J., and Szekely, J., 1984, "Heat Transfer and Fluid Flow in Plasma Spraying," *Metall. Trans. B*, Vol. 15, pp. 59–67.

Frind, G., Goody, C. P., and Prescott, L. E., 1983, "Measurement of Particle Velocity in Two Low Pressure Jets," *Proceedings, 6th International Symposium on Plasma Chemistry*, Vol. 1, pp. 120–125.

Hasen, G. A., 1982, "Navier–Stokes Solution for an Axisymmetric Nozzle," *AIAA Journal*, Vol. 20, No. 9, pp. 1219–1231.

Holst, T., 1977, "Numerical Solution of Axisymmetric Boattail Fields With Plume Simulator," AIAA Paper No. 77-124.

Jennions, I. K., Ma, A. S., and Spalding, D. B., 1977, "A Prediction Procedure for 2-D Steady, Supersonic Flows," Imperial College of Science and Technology, Rept. No. HTS/77/24.

Launder, B. E., Morse, A., Spalding, D. B., and Rodi, W., 1972, "Prediction of Free Shear Flows: A Comparison of Six Turbulence Modes," *Free Turbulent Shear Flow*, NASA SP-321, Vol. 1, pp. 361–426.

Lee, Y. C., Chyou, Y. P., and Pfender, E., 1985, "Particle Dynamics and Particle Heat and Mass Transfer in Thermal Plasma, Part II: Particle Heat and Mass Transfer," *Plasma Chemistry and Plasma Processing*, Vol. 5, No. 4, pp. 391–398.

McKelliget, J., Szekely, J., Vardelle, M., and Fauchais, P., 1982, "The Temperature and Velocity Fields in a Gas Stream Exiting a Plasma Torch," *Plasma Chemistry and Processing Symposium*, Vol. 2, pp. 317–326.

Mikhail, A. G., 1979, "Numerical Solution of a Supersonic Nozzle Afterbody Flow With Jet Exhaust," AFFDL-TR-3078.

Pergament, H. S., Dash, S. M., and Wilmoth, R. C., 1978, "Predictions of Nearfield Jet Entrainment by an Interactive Mixing/After Burning Model," AIAA Paper No. 78-1189.

Philips, W. F., 1975, "Drag on Small Particles in a Thermal Plasma Flow," *Phys. Fluids*, Vol. 18, pp. 1089–1096.

Seiner, J. M., and Norum, T. D., 1980, "Aerodynamic Aspects of Shock Containing Jet Plume," AIAA Paper No. 80-0965.

Sherman, F. S., 1983, in: *Rarefiels Gas Dynamics*, J. A. Laurmann, ed., Academic Press, New York, Vol. 2, pp. 228–351.

Smith, R. W., 1985, "Melting and Consolidation of Ni Alloy Powders With a Plasma Jet Operating in a Low Pressure Inert Environment," Ph.D. Thesis, Drexel University, Philadelphia, PA.

Vallerani, E., 1976, "A Review of Supersonic Sphere Drag From the Continuum to Free Molecular Flow Regime," *Proc. Conf. on Aerodynamic Drag*, AGARD Conf. Proc. 124, pp. 273–284.

Vargaftik, N. B., 1975, *Tables on the Thermophysical Properties of Liquids and Gases*, Hemisphere Corp., New York.

Voller, V., and Cross, M., 1979, "Accurate Solution on Moving Boundary Problem Using the Enthalpy Method," *Int. J. Heat and Mass Transfer*, Vol. 22, pp. 749–756.

Wei, D., 1986, "Melting Powder Particle in Plasma Jet," Ph.D. Thesis, Drexel University, Philadelphia, PA.

Downloaded 17 Dec 2010 to 193.140.21.150. Redistribution subject to ASME license or copyright; see http://www.asme.org/terms/Terms_Use.cfm

Transient Radiative Cooling of a Layer Filled With Solidifying Drops

R. Siegel
NASA Lewis Research Center,
Cleveland, OH 44135
Fellow ASME

An analysis is carried out for radiative cooling of a plane layer initially filled with liquid drops that solidify and then continue to cool by loss of sensible heat. This is in connection with a proposed lightweight radiator system for heat dissipation in space. Hot liquid drops would be ejected and then cooled by direct exposure in space; they would then pass into a collector for reuse. The cooling analysis contains three transient zones. In the first, the drops cool by losing latent heat until the outermost drops become solid. Then the cooling continues by loss of both latent and sensible heat. Finally, all of the drops are solid, and they continue to cool by loss of sensible heat. A similarity behavior is eventually achieved in which the transient emittance of the layer depends only on the optical thickness.

Introduction

The generation of power for use in space applications requires a radiator for dissipation of waste heat. With increasing requirements for power generation capacity, the radiator surface area can become quite large, involving a large structural weight. A potentially light-weight radiator has been proposed (Mattick and Hertzberg, 1981) wherein streams of hot liquid drops would be passed through space where they would lose energy by transient radiative cooling. The cooled streams would then arrive at a collector to enable reuse of the coolant. Some development work on this type of system is described by Presler et al. (1986). This includes techniques for formation of droplet streams, and plans for experiments on radiative heat transfer performance. System optimization studies are given by Taussig and Mattick (1986). The radiative behavior depends on the emissive ability of a region filled with many parallel streams of drops. A detailed transient analysis of the emittance of a layer filled with drops has been given by Siegel (1987a–c) using radiative transfer theory. The previous analyses have studied the transient loss of only the sensible energy of the drops; the drops remain liquid throughout the entire cooling process. The present study will consider drops that can also solidify, thereby utilizing both their latent and sensible energy.

The transient cooling of layers that absorb, emit, and scatter radiation has been studied for the past 30 years, including some early work by Gardon (1956, 1958) on the heat treatment of glass plates that emit and absorb radiation within their volume. It is not reasonable to include a detailed literature survey here. A brief review of transient radiative cooling is given in the textbook by Siegel and Howell (1981), Chap. 18. A review of the early literature is in Viskanta and Bathla (1967), who analyzed transient cooling of an absorbing-emitting layer. A later review by Viskanta and Anderson (1975) gives results for transient radiative heating of cold plane layers and semi-infinite solids. Some references of interest on transient cooling are Bathla and Viskanta (1968) which included the effect of incident radiation from the surroundings, and Lii and Ozisik (1972) who studied the effect of reflecting boundaries on a plane layer. Kubo (1984) analyzed conditions with large scattering and small absorption.

In the preceding references, the radiating layers cooled by loss of their sensible energy. For the liquid-drop radiator it may be possible to gain some performance advantage by utilizing the latent heat of the drops as well as their sensible energy; then each drop can transport more energy to be dissipated. During the portion of the cooling process where drops are solidifying across the entire layer thickness, the layer will remain at uniform temperature. This maintains a higher layer emittance as compared with a layer in which the outer portion has become cool. Having the drops solidify is helpful in limiting evaporation losses; however, melting the drops for reuse presents a design problem not present in a fully liquid system.

To consider a case that is not overly complicated, the liquid drops are initiated at their solidification temperature. A period of transient cooling follows wherein the layer remains at uniform temperature while the drops partially solidify. An analytical solution is obtained for this period, and it yields the distribution across the layer of the liquid fraction at the time when the drops at the outer boundaries of the layer become completely solid. This liquid distribution serves as the initial condition for the next cooling region in which there is a moving boundary that separates the completely solidified outer layer at nonuniform temperature from the partially solidified inner region that is still at the solidification temperature. After solidification is complete, the entire layer continues to cool by sensible heat loss. A constant emittance condition is finally achieved, as shown by the analysis of Siegel (1986c).

Analysis

As described by Presler et al. (1986), a directed, moving layer filled with liquid drops can be produced by a drop generator. The drops exit from the generator at uniform velocity and move through space where they cool by radiative transfer. The cooling process is illustrated in Fig. 1 (shown with a highly compressed z scale). The present analysis is concerned with drops that solidify and then lose sensible heat. To consider a situation that is not overly complex, the liquid drops are assumed to leave the generator at their solidification temperature. Solidification then begins by radiative cooling while the layer remains at uniform temperature; the temperature uniformity helps maintain a high layer emittance. Unless the layer is optically very thin, the radiative cooling is more rapid in the outer regions, so that, with increasing distance from the generator, a distribution in liquid fraction develops across the layer with the smallest liquid fraction at the outer boundaries. When the distance z_0 in Fig. 1 is reached, the drops at $x=0$ and D have become solid. For larger z values, a temperature distribution begins to develop as the region in which the drops have completely solidified loses sensible heat. The center portion of the layer, which is still partially liquid, remains at the solidification temperature. The thickness of the region that is completely solid is x_s, and this thickness increases with z until the entire layer has become solidified. The entire layer then continues to cool by radiative loss of sensible energy.

Contributed by the Heat Transfer Division for publication in the JOURNAL OF HEAT TRANSFER. Manuscript received by the Heat Transfer Division August 14, 1986.

Copyright © 1987 by ASME

Downloaded 17 Dec 2010 to 193.140.21.150. Redistribution subject to ASME license or copyright; see http://www.asme.org/terms/Terms_Use.cfm

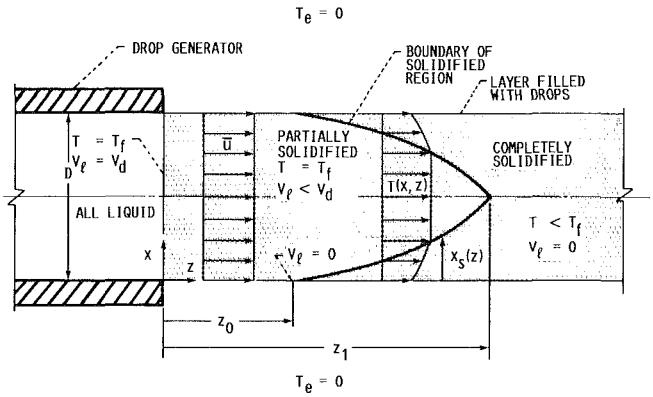

Fig. 1 Geometry of solidifying layer filled with drops

Property variations, with temperature or as a result of phase change, are neglected; they can be included later if more detailed information is needed for this type of radiator. This would include the change in radiative properties when going from liquid to solid, if the properties are known. Temperature variations within each drop are neglected; this seems reasonable for the very small drop sizes to be used in the liquid-drop radiator (diameters in the range of 100 to 200 μm).

Energy Equations. In the partially solidified region, the temperature remains uniform at T_f, and the loss of latent heat by radiative cooling is governed by the energy equation

$$\rho\lambda\bar{u}\frac{\partial\tilde{V}}{\partial z} = -\frac{\partial q_r}{\partial x} \tag{1a}$$

In the completely solidified region

$$\rho c_s\bar{u}\frac{\partial T}{\partial z} = -\frac{\partial q_r}{\partial x} \tag{1b}$$

It is assumed that temperature variations in the z direction are much more gradual than in the x direction, so that $\partial q_r/\partial z$ is neglected relative to $\partial q_r/\partial x$. Since the flow velocity of the layer is constant, it is convenient to transform the equations by letting τ be the cooling time after the droplet streams leave the generator. Then $\tau = z/\bar{u}$, and the energy equations transform to

$$\rho\lambda\frac{\partial\tilde{V}}{\partial\tau} = -\frac{\partial q_r}{\partial x} \qquad (x_s < x < D - x_s) \tag{2a}$$

$$\rho c_s\frac{\partial T}{\partial\tau} = -\frac{\partial q_r}{\partial x} \qquad (0 \le x < x_s, \quad D - x_s < x \le D) \tag{2b}$$

The droplets absorb and emit radiation. To reduce the scope of the calculations, scattering is not included in the present analysis; the effect of scattering on increasing the cooling times is shown by Siegel (1987a) for a single-phase system. Similar behavior would be expected here. Then the derivative in radiative flux is given in dimensionless form (Siegel and Howell, 1981) by:

$$\frac{1}{4\sigma T_f^4}\frac{\partial q_r}{\partial\kappa} = \tilde{T}^4(\kappa,\tilde{\tau}) - \frac{1}{2}\int_0^{\kappa_D}\tilde{T}^4(\kappa^*,\tilde{\tau})E_1(|\kappa-\kappa^*|)d\kappa^* \tag{3}$$

This assumes gray radiation, which is reasonable for many liquids and solids in the infrared region characteristic of liquid droplet radiator temperatures. Nongray calculations can be done later, if needed, after specific liquids are chosen. The absorption coefficient in a cloud of equally sized droplets of radius R_d is given by $a = E_a\pi R_d^2 N$, where N is the number of droplets per unit volume. In dimensionless form, equations (2a) and (2b) become

$$\frac{\partial\tilde{V}}{\partial\tilde{\tau}} = -\mathrm{S}\kappa_D\frac{1}{4\sigma T_f^4}\frac{\partial q_r}{\partial\kappa} \tag{4a}$$

$$\frac{\partial\tilde{T}}{\partial\tilde{\tau}} = -\kappa_D\frac{1}{4\sigma T_f^4}\frac{\partial q_r}{\partial\kappa} \tag{4b}$$

Since $\tilde{T}$ is initially unity (at $z = 0$ in Fig. 1), it is sometimes

Nomenclature

a = absorption coefficient of absorbing-emitting layer
c_s = specific heat of solidified drops
D = thickness of absorbing-emitting layer
E = latent and sensible energy in drop-filled layer
E_a = efficiency factor for absorption by a droplet
E_s = sensible energy in drop-filled layer
E_1, E_2, E_3 = exponential integral functions; $E_n(x) = \int_0^1 \mu^{n-2}\exp(-x/\mu)d\mu$
N = number of droplets per unit volume of layer
q = heat loss per unit area and time from a boundary of drop-filled layer
q_r = radiative heat flow per unit area and time
R_d = radius of spherical drop
S = Stefan number = $c_s T_f/\lambda$
T = absolute temperature; $\tilde{T} = T/T_f$
T_e = temperature of surrounding environment; $T_e = 0$
T_f = solidification temperature
T_m = spatially integrated mean temperature across layer at any time during cooling transient; $\tilde{T}_m = T_m/T_f$
T_r = reference temperature
$\bar{u}$ = uniform flow velocity of layer filled with drops
$\tilde{V}$ = local liquid fraction of drops in drop-filled layer = V_l/V_d
V_d = volume of drops per unit volume of layer
V_l = volume of liquid per unit volume of layer
X^* = dummy variable of integration
x = coordinate across width of layer; $X = x/D$
x_s = location of moving boundary of all-solid region; $X_s = x_s/D$
z = coordinate along length of layer in flow direction
z_0, z_1 = locations of beginning and end of moving boundary region
ϵ = emittance of layer
ϵ_m = emittance based on instantaneous value of T_m; $\epsilon_m = q/\sigma T_m^4$
κ = optical coordinate = ax; κ_D = optical thickness = aD; $\kappa_s = ax_s$
κ^* = dummy variable of integration
λ = latent heat per unit mass of layer filled with drops
ρ = density of layer filled with drops
ρ_d = density of droplet material
σ = Stefan–Boltzmann constant
τ = time from start of cooling = $z/\bar{u}$
$\tilde{\tau}$ = dimensionless time = $(4\sigma T_f^3/\rho c_s D)\tau$
τ_0, τ_1 = beginning and end of moving boundary region; $\tau_0 = z_0/\bar{u}$, $\tau_1 = z_1/\bar{u}$

Downloaded 17 Dec 2010 to 193.140.21.150. Redistribution subject to ASME license or copyright; see http://www.asme.org/terms/Terms_Use.cfm

more convenient and accurate to utilize the difference $1-\tilde{T}^4$ in the radiative term in equation (3). Then by adding and subtracting the integral of E_1, equation (3) becomes (the $\tilde{\tau}$ functional notation has been dropped to shorten the expressions)

$$\frac{1}{4\sigma T_f^4}\frac{\partial q_r}{\partial \kappa}=\frac{1}{2}\int_0^{\kappa_D}[1-\tilde{T}^4(\kappa^*)]E_1(|\kappa-\kappa^*|)d\kappa^* + \frac{1}{2}[E_2(\kappa)+E_2(\kappa_D-\kappa)]-[1-\tilde{T}^4(\kappa)] \tag{5a}$$

For the region between z_0 and z_1 in Fig. 1, the integral in equation (5*a*) is simplified because $1-\tilde{T}^4=0$ between $x=x_s$ and $D-x_s$. Then equation (5*a*) becomes

$$\frac{1}{4\sigma T_f^4}\frac{\partial q_r}{\partial \kappa}=\frac{1}{2}\left\{\int_0^{\kappa_s}[1-\tilde{T}^4(\kappa^*)]E_1(|\kappa-\kappa^*|)d\kappa^* + \int_{\kappa_D-\kappa_s}^{\kappa_D}[1-\tilde{T}^4(\kappa^*)]E_1(|\kappa-\kappa^*|)d\kappa^*\right\}+\frac{1}{2}[E_2(\kappa) + E_2(\kappa_D-\kappa)]-[1-\tilde{T}^4(\kappa)] \tag{5b}$$

In terms of the variable X, equation (5*b*) has the form

$$\frac{1}{\kappa_D}\frac{1}{4\sigma T_f^4}\frac{\partial q_r}{\partial X}=\frac{\kappa_D}{2}\left\{\int_0^{X_s}[1-\tilde{T}^4(X^*)]E_1(\kappa_D|X-X^*|)dX^* + \int_{1-X_s}^{1}[1-\tilde{T}^4(X^*)]E_1(\kappa_D|X-X^*|)dX^*\right\} + \frac{1}{2}\{E_2(\kappa_D X)+E_2[\kappa_D(1-X)]\}-[1-\tilde{T}^4(X)] \tag{5c}$$

The solution must consider three regions in the flow direction. For $0<z<z_0$ the entire width of the layer is partially solidified. When $z_0<z<z_1$ a portion of the width is completely solidified. For $z>z_1$ all of the drops are solid.

Analytical Solution for Region $0<z<z_0$. In this region, $\kappa_s=ax_s=0$, and since $T(x)=T_f$ throughout the region, the $1-\tilde{T}^4(\kappa)=0$. The first and last terms on the right side of equation (5*b*) are then zero. The energy equation (4*a*) applies for local liquid fraction, and it becomes

$$\frac{\partial \tilde{V}}{\partial \tilde{\tau}}=-\frac{S\kappa_D}{2}[E_2(\kappa)+E_2(\kappa_D-\kappa)] \qquad \tilde{V}(\kappa,\ \tilde{\tau}=0)=1 \tag{6}$$

We integrate with respect to $\tilde{\tau}$ and apply the initial condition to obtain

$$\tilde{V}=1-\frac{S\kappa_D}{2}[E_2(\kappa)+E_2(\kappa_D-\kappa)]\tilde{\tau} \tag{7}$$

When $\tilde{V}$ has decreased to zero at the boundaries $\kappa=0$ and κ_D, the drops are completely solidified at the edge of the layer; this is at $z=z_0$ in Fig. 1. The corresponding $\tau_0=z_0/\tilde{u}$ is found from equation (7) by letting $\tilde{V}=0$ at $\kappa=0$ to obtain

$$\tilde{\tau}_0=\frac{4\sigma T_f^3}{\rho c_s D}\frac{z_0}{\tilde{u}}=\frac{2}{S\kappa_D}\frac{1}{1+E_2(\kappa_D)} \tag{8a}$$

This $\tilde{\tau}_0$ is inserted into equation (7) to obtain the $\tilde{V}$ distribution at location z_0 as

$$\tilde{V}(\kappa,\ \tilde{\tau}_0)=1-\frac{E_2(\kappa)+E_2(\kappa_D-\kappa)}{1+E_2(\kappa_D)} = 1-\frac{E_2(\kappa_D X)+E_2[\kappa_D(1-X)]}{1+E_2(\kappa_D)} \tag{8b}$$

This distribution is shown in Fig. 2, and it serves as the initial condition for the next region in Fig. 1 where x_s is a variable. An alternative form for equation (7) is found by use of (8*a*)

$$\tilde{V}=1-\frac{E_2(\kappa)+E_2(\kappa_D-\kappa)}{1+E_2(\kappa_D)}\frac{\tilde{\tau}}{\tilde{\tau}_0} \tag{7a}$$

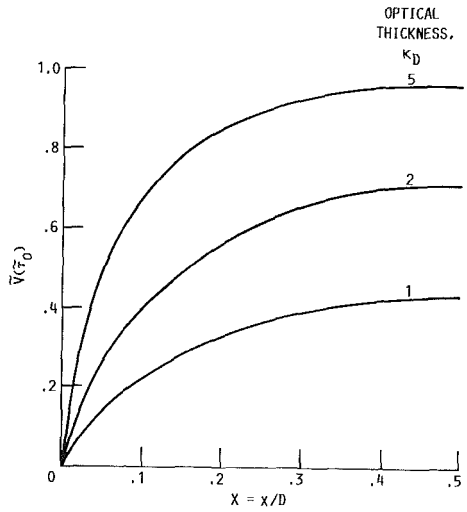

Fig. 2 Distribution of liquid fraction across layer when drops at outer edge become solid

Numerical Solution for Region $z_0<z<z_1$. Starting with equation (8*b*) as an initial distribution of $\tilde{V}(X)$, and with $\tilde{T}(X,\ \tilde{\tau}_0)=1$, equations (4*a*) and (4*b*) are integrated forward in time starting from $\tilde{\tau}_0$ to give results within the region between z_0 and z_1. The finite difference forms that were used are

$$\tilde{V}(X,\ \tilde{\tau}+\Delta\tilde{\tau})=\tilde{V}(X,\ \tilde{\tau})-\Delta\tilde{\tau}S\frac{1}{4\sigma T_f^4}\frac{\partial q_r}{\partial X}(X,\ \tilde{\tau}) \tag{9a}$$

$$\tilde{T}(X,\ \tilde{\tau}+\Delta\tilde{\tau})=\tilde{T}(X,\ \tilde{\tau})-\Delta\tilde{\tau}\frac{1}{4\sigma T_f^4}\frac{\partial q_r}{\partial X}(X,\ \tilde{\tau}) \tag{9b}$$

where $\partial q_r/\partial X$ at $(X,\ \tilde{\tau})$ is found from equation (5*c*). This was evaluated numerically by dividing the thickness of the layer into increments of size ΔX. By use of symmetry, the integration forward in $\tilde{\tau}$ was carried out only in the region of X between 0 and 1/2.

Since at τ_0 the $V(X)=0$ at $X=0$, the use of equation (9*a*) for the first time increment to obtain $\tilde{V}(X,\ \tau_0+\Delta\tau)$ yields negative $\tilde{V}$ values for small X. The ΔX interval was then located within which $\tilde{V}(X,\ \tau_0+\Delta\tau)$ changes sign, and the value of $X_s(\tilde{\tau}+\Delta\tilde{\tau})$ at which $\tilde{V}(X,\ \tau_0+\Delta\tau)=0$ was found by using Newton's divided-difference interpolating polynomial (Carnahan et al., 1969). Then equation (9*b*) was applied to obtain new temperature values, $\tilde{T}(X,\ \tilde{\tau}_0+\Delta\tilde{\tau})$, at the X mesh points where $X<X_s$. With the new set of $\tilde{T}$ values for $X<X_s$, and with $\tilde{T}=1$ for $X_s\le X\le 1/2$, new values of the radiative cooling term were found from equation (5*c*) by using symmetric values for $\tilde{T}(X)$ when $X>1/2$. The forward integration for $\tilde{V}$ and $\tilde{T}$ was continued until X_s reached 1/2 so that all the drops had become completely solidified. This occurred at $\tilde{\tau}_1$ corresponding to $\tau_1=z_1/\tilde{u}$ in the physical geometry. To illustrate the cooling process, some typical profiles of $\tilde{V}$ and $\tilde{T}$ are given in Fig. 3, and the behavior of X_s is shown in Fig. 4.

Numerical Solution for Region $z>z_1$. In this region there is only sensible heat loss from completely solidified drops, and equation (9*b*) applies. The forward integration in time was continued as previously described. With increasing $\tilde{\tau}$, the condition is reached where the layer emittance ϵ_m becomes constant. This is a consequence of the similarity solution obtained by Siegel (1987c). Typical temperature profiles during the sensible cooling process are shown in Fig. 3.

Energy Loss and Emittance of Layer. With $\tilde{V}$ and T known as a function of τ, and hence for $z=\tilde{u}\tau$ along the length of the drop-filled layer, the heat transfer characteristics of the layer can be obtained. An important quantity is the energy content of the layer as a function of z (or τ).

Downloaded 17 Dec 2010 to 193.140.21.150. Redistribution subject to ASME license or copyright; see http://www.asme.org/terms/Terms_Use.cfm

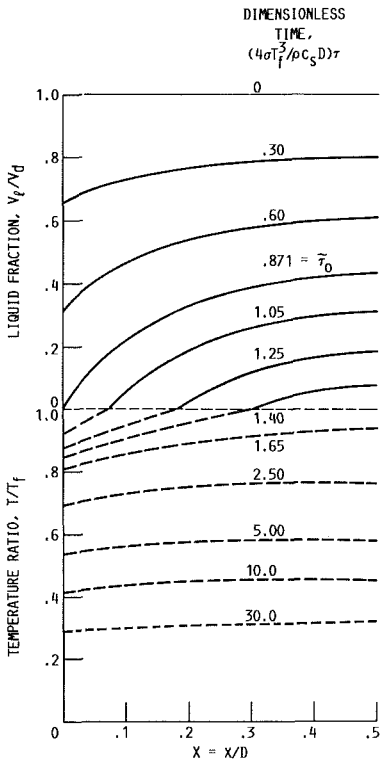

Fig. 3(*a*) Optical thickness, $\kappa_D = 1$

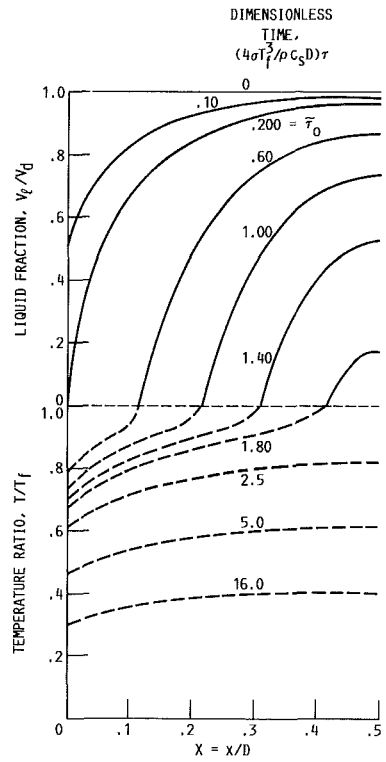

Fig. 3(*b*) Optical thickness, $\kappa_D = 5$

Fig. 3 Transient distributions of liquid fraction and temperature; Stefan number S = 2

Since the layer can cool to the temperature of space, which is close to absolute zero, the energy within the layer will be specified above this zero level. The initial energy per unit volume is $\rho(c_s T_f + \lambda)$. It is convenient to normalize the energy relative to the initial sensible energy per unit volume, $\rho c_s T_f$. Then the ratio (initial energy)/(initial sensible energy) $= 1 + 1/S$.

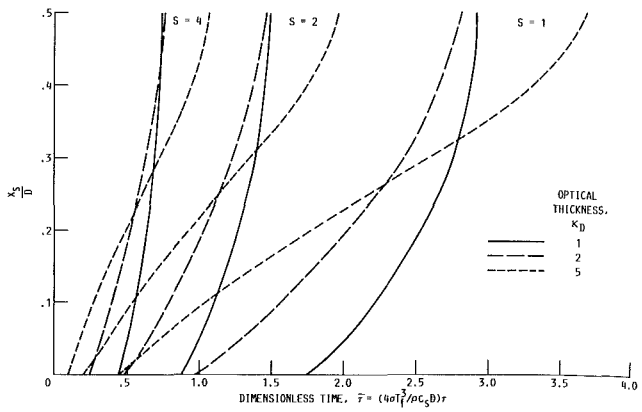

Fig. 4 Transient movement of boundary of completely solidified region

Within the region $0 < z < z_0$ $(0 < \tilde{\tau} < \tilde{\tau}_0)$, the temperature is uniform across the layer, $T = T_f$. Hence the emittance of the layer is $\epsilon = q/\sigma T_f^4 = 1 - 2E_3(\kappa_D)$, and the energy lost is constant with time. It follows that at time τ the remaining energy in a portion of the layer with unit boundary area is $\rho(c_s T_f + \lambda)D - 2[1 - 2E_3(\kappa_D)]\sigma T_f^4 \tau$. If this is divided by the initial sensible energy, the result is

$$\frac{E(\tilde{\tau})}{E_s(0)} = \frac{\text{Energy at } \tilde{\tau}}{\text{Initial sensible energy}}$$

$$= 1 + \frac{1}{S} - \frac{1}{2}[1 - 2E_3(\kappa_D)]\tilde{\tau} \qquad (0 < \tilde{\tau} < \tilde{\tau}_0) \qquad (10)$$

After solidification starts, the energy at τ in a volume of the layer bounded by a unit area of outer boundary is $2\rho[c_s \int_0^{x_s} T dx + c_s T_f (D/2 - x_s) + \lambda \int_{x_s}^{D/2} \tilde{V}\, dx]$. This can be written in the convenient form

$$\frac{E(\tilde{\tau})}{E_s(0)} = 1 - 2\int_0^{X_s(\tilde{\tau})} (1 - \tilde{T}) dX + \frac{2}{S}\int_{X_s(\tilde{\tau})}^{1/2} \tilde{V}\, dX \qquad (\tilde{\tau}_0 < \tilde{\tau}) \qquad (11)$$

When freezing is complete, the evaluation of equation (11) is simplified since $\tilde{V} = 0$ and $X_s = 1/2$.

The layer emittance, based on a reference temperature T_r, is obtained from the rate of energy change as $\epsilon = \{[E(\tau) - E(\tau + \Delta\tau)]/2\Delta\tau\}(1/\sigma T_r^4)$ which gives

$$\epsilon = \frac{2\left[\dfrac{E(\tilde{\tau})}{E_s(0)} - \dfrac{E(\tilde{\tau} + \Delta\tilde{\tau})}{E_s(0)}\right]}{\Delta\tilde{\tau}} \left(\frac{T_f}{T_r}\right)^4 \qquad (12)$$

The T_r used here will be either T_f or $T_m = (1/D)\int_0^D T\, dx$. As a check on the numerical work, the layer emittance was calculated in a second way by use of the radiative flux within a plane layer, given by Siegel and Howell (1981) as

$$q_r(\kappa, \tau) = 2\int_0^{\kappa} \sigma T^4(\kappa^*) E_2(\kappa - \kappa^*) d\kappa^* - 2\int_{\kappa}^{\kappa_D} \sigma T^4(\kappa^*) E_2(\kappa^* - \kappa) d\kappa^* \qquad (13)$$

This was evaluated at $\kappa = 0$ to obtain the boundary heat flux. Then the $q_r(0, \tau)$ was expressed as integrals over the regions $0 < \kappa < \kappa_s$ and $\kappa_D - \kappa_s < \kappa < \kappa_D$ within which $\tilde{T}$ is a variable, and over $\kappa_s < \kappa < \kappa_D - \kappa_s$ within which $\tilde{T} = 1$. This yields the emittance

$$\epsilon(\tau) = -\frac{q_r(0, \tau)}{\sigma T_r^4} = 2\left(\frac{T_f}{T_r}\right)^4 \left[\int_0^{\kappa_s} \tilde{T}^4(\kappa^*) E_2(\kappa^*) d\kappa^* + E_3(\kappa_s) - E_3(\kappa_D - \kappa_s) + \int_{\kappa_D - \kappa_s}^{\kappa_D} \tilde{T}^4(\kappa^*) E_2(\kappa^*) d\kappa^*\right] \qquad (14)$$

Downloaded 17 Dec 2010 to 193.140.21.150. Redistribution subject to ASME license or copyright; see http://www.asme.org/terms/Terms_Use.cfm

Equation (14) can also be used to check the time variation of energy within the layer to compare with equation (11). Equation (10) gives the energy variation for $\tilde{\tau}$ up to $\tilde{\tau}_0$. Using equation (8*a*) yields at $\tilde{\tau}_0$

$$\frac{E(\tilde{\tau}_0)}{E_s(0)} = 1 + \frac{1}{S} - \frac{1}{S\kappa_D}\,\frac{1-2E_3(\kappa_D)}{1+E_2(\kappa_D)} \tag{15}$$

Then by integrating the rate of energy loss obtained from equation (14) with $T_r = T_f$

$$\frac{E(\tilde{\tau})}{E_s(0)} = \frac{E(\tilde{\tau}_0)}{E_s(0)} - \frac{1}{2}\int_{\tilde{\tau}_0}^{\tilde{\tau}} \epsilon(\tilde{\tau})\,d\tilde{\tau} \qquad (\tilde{\tau}_0 < \tilde{\tau}) \tag{16}$$

Numerical Integration. For the numerical portion of the transient solution, the radiation integrals must be evaluated quite accurately. Since the exponential integral E_1 becomes infinite when its argument is zero, care must be taken when κ^* approaches κ. The quantity $-E_1$ can be integrated to obtain E_2, which is unity for a zero argument. Hence the radiation integrals can be evaluated analytically for a very small region on either side of the singularity. The numerical calculations were repeated with the size of this small region reduced until it had no effect on the results. In the regions away from the singularity, the integrations were performed with a Gaussian subroutine available on the computer system. The accuracy of some of the integrations was checked using a Simpson's-rule subroutine. Between 80 and 120 ΔX intervals were used across the layer width. The $\Delta\tilde{\tau}$ depended on κ_D and S, and was increased in size as the cooling rate decreased as the layer temperatures diminished. The calculations were repeated with smaller time increments to be sure that the results did not differ. Each transient solution required 5 min or less on an IBM 370 computer.

Results and Discussion

The layer filled with drops is moving through space with a uniform velocity, and hence the cooling results can be discussed either in terms of the distance z traveled from the droplet generator, or in terms of the time $z/\bar{u}$ following exposure to space. Both of these independent variables will be used for discussing the results. Results are given for three optical thicknesses, $\kappa_D = 1$, 2, and 5, and for S = 1, 2, 4, and ∞. Since $S = c_s T_f/\lambda$, the $S = \infty$ corresponds to the limit of zero latent heat (cooling without phase change). For materials such as water, aluminum, beryllium, and mercury, the range of S is from about 1.5 to 3.

The drops are generated in all-liquid form at the solidification temperature T_f. Radiative cooling then causes the drops to start solidifying. As long as there is some liquid throughout the entire layer cross section, it will remain at uniform temperature T_f, and the layer emittance, $1-2E_3(\kappa_D)$, depends only on the optical thickness. The energy in the layer decreases with z or τ in a linear manner until the liquid fraction in the outermost portion of the layer, which is cooling most rapidly, decreases to zero; this occurs at $\tau_0 = z_0/\bar{u}$ obtained from equation (8*a*). The distribution of liquid fraction at this time, equation (8*b*), is shown in Fig. 2 for three optical thicknesses. The distribution becomes more uniform as the optical thickness is decreased. This is because radiative energy can leave the central portions of the layer more readily, resulting in a more uniform cooling distribution throughout the layer. In the limit for a layer that is optically very thin, the layer will cool uniformly throughout its thickness.

The variation of local liquid fraction with time is given in Fig. 3 for a few values of $\tilde{\tau}$ less than $\tilde{\tau}_0$, as obtained from equation (7*a*). After solidification starts, $\tilde{V} = 0$ in the completely solidified region, $X < X_s$, while $\tilde{T} = 1$ in the partially solidified region, $X > X_s$. This is shown in Fig. 3 where typical profiles of $\tilde{V}$ and $\tilde{T}$ are given. Results are given for two optical

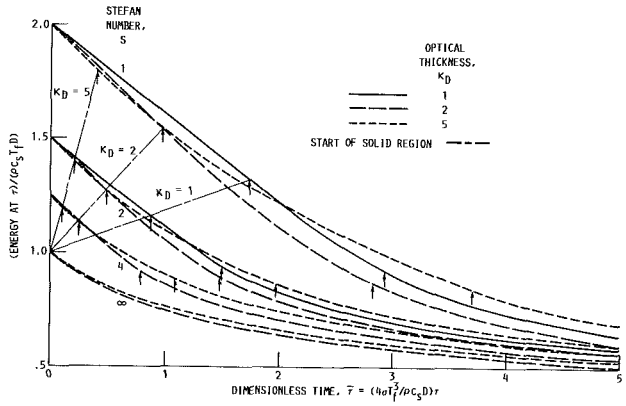

Fig. 5 Transient energy within layer, relative to initial sensible energy

thicknesses, $\kappa_D = 1$ and 5, for S = 2. The curves for the optically thick layer, $\kappa_D = 5$, show the effect of the relatively high cooling in the outer regions of the layer as compared with the slow cooling of the inner portions. The resulting profiles for $\kappa_D = 1$ are much more uniform than for $\kappa_D = 5$.

The profiles in Fig. 3 show, in a limited way, the propagation of the dividing boundary between the completely and partially solidified regions. This propagation is shown in more detail in Fig. 4. Since S is the ratio of sensible to latent heat, it is the curves for S = 1 that show the effect of the largest latent heat; this results in the slowest propagation rate. As the layer is made more optically thin, a greater portion of the latent energy can be radiated away from its interior before the outer part of the layer becomes completely solidified. Hence, after solidification starts, X_s goes from 0 to 1/2 much more rapidly when $\kappa_D = 1$ than when $\kappa_D = 5$.

The energy in the layer is shown as a function of $\tilde{\tau}$ in Fig. 5. The energy has been normalized by its initial sensible energy $\rho c_s T_f D$. For S = 1, the initial sensible and latent energies are equal so that the curves start from an energy ratio of 2. For $S = \infty$ there is no latent energy, and the curves start from unity. Each curve for S = 1, 2, and 4 starts with a linear portion within which the two-phase layer is cooling at uniform temperature and with a constant emittance. The location where this linear portion ends is marked by a small arrow. A second arrow at a larger time shows when the completely solidified region has propagated to the center of the layer. The abscissa in Fig. 5, $\tilde{\tau} = (4\sigma T_f^3/\rho c_s D)\tau$, is a convenient dimensionless variable for plotting results as it tends to confine the curves for various κ_D within the same horizontal scale. However, as pointed out in relation to the cooling curves in Siegel (1987a), the $\tilde{\tau}$ may be misleading when comparing the cooling rates for layers of various optical thicknesses. This is because quantities within the dimensionless group, $\tilde{\tau}$, may be changed as κ_D is changed. For example, a common comparison would be for two layers with different thicknesses D that contain droplets of the same size, fluid, and number density. For these conditions the absorption coefficient would remain the same and hence, in Fig. 5, the curves for $\kappa_D = 5$ would be for a layer with D that is five times larger than for the curves with $\kappa_D = 1$. Since $\tau \propto \tilde{\tau} D$ the cooling times would be much larger for $\kappa_D = 5$ as compared with $\kappa_D = 1$; however, it must be realized that the layer is five times thicker and hence contains five times as much energy. Similar behavior is obtained if D is kept constant while the droplet number density is changed. The absorption coefficient and the layer density are both proportional to number density so that the change in κ_D is accompanied by the same proportional change in τ. In Siegel (1987a) the variable $\tilde{\tau}\kappa_D/3$ was sometimes used. Since $a = E_a \pi R_d^2 N$ and $\rho = \rho_d (4/3)\pi R_d^3 N$, the $\tilde{\tau}\kappa_D/3 = (\sigma T_f^3 E_a/\rho_d c_s R_d)\tau$; the quantity in parentheses depends only on the droplet properties and not on D or N.

Downloaded 17 Dec 2010 to 193.140.21.150. Redistribution subject to ASME license or copyright; see http://www.asme.org/terms/Terms_Use.cfm

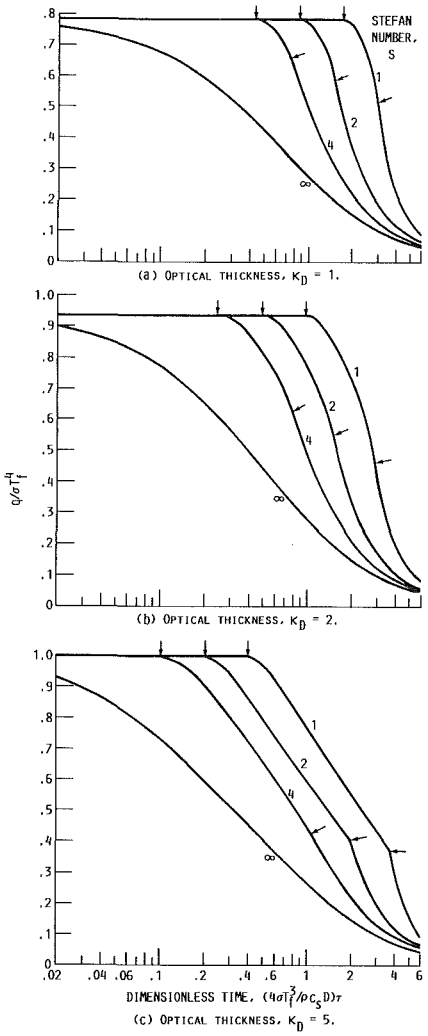

Fig. 6 Transient heat loss rates from radiating layer

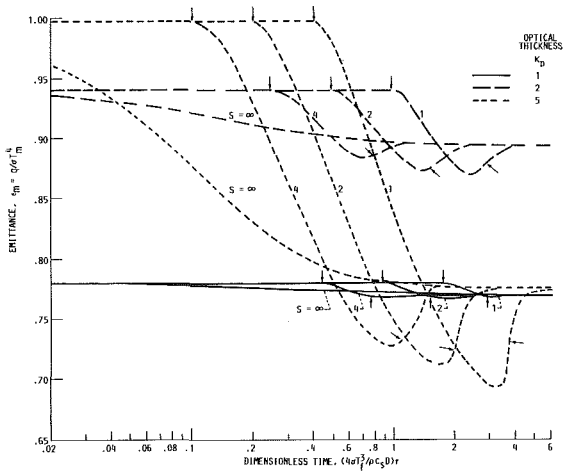

Fig. 7 Layer emittance based on instantaneous integrated mean layer temperature

The instantaneous rates of energy loss are given in Fig. 6. Each part of the figure presents results for a different κ_D. All of the curves on each part of the figure begin at the same ordinate, which is equal to the emittance of a layer at uniform temperature. The cooling rate remains at this value until the outermost portion of the layer becomes completely solid. The temperatures in the outermost region then decrease by sensible cooling, and as a result the radiative cooling rate decreases substantially.

In Fig. 7 the cooling rate is shown normalized by σT_m^4 where T_m is the integrated mean layer temperature; this normalized quantity is the emittance based on T_m. The T_m is not a very useful reference temperature since, during the two-phase portion of the cooling, it is not proportional to the energy in the layer. The reason for giving Fig. 7 is to point out that ϵ_m starts from the value for a layer at uniform temperature and then, at a time after complete solidification, arrives at a lower constant value. This is a result of the similarity solution obtained by Siegel (1987c). The curves drop below the similarity result during the two-phase cooling region, since the central part of the layer remains at uniform temperature T_f. This maintains a high value of T_m so the ϵ_m becomes smaller than the ϵ_m that is finally reached.

Concluding Remarks

An analysis was made of the transient cooling of a plane layer filled with a large number of drops that absorb and emit thermal radiation. The drops start in all liquid form at their solidification temperature and are then exposed to a space environment assumed at absolute zero temperature. For the first part of the cooling transient that follows, a convenient analytical solution is obtained. During this first portion, radiation removes latent heat from the layer, which remains at uniform temperature, and thus has a constant emittance that depends only on the optical thickness of the layer. The second portion of the transient involves loss of both latent and sensible energy. During this period the temperature decreases in the outer regions of the layer; this produces a rapid decrease in the layer emittance, and the emittance falls below the value that is reached later in the cooling process. In the final portion of the transient cooling, the drops are all solid. For the completely solidified layer, a similarity condition is ultimately reached wherein the layer emittance, based on the instantaneous heat loss and integrated mean temperature, becomes constant.

References

Bathala, P. S., and Viskanta, R., 1968, "Effect of Surroundings on the Transient Energy Transfer in a Layer of Radiating Gas," *Applied Scientific Research*, Vol. 19, pp. 182–197.

Carnahan, B., Luther, H. A., and Wilkes, J. O., 1969, *Applied Numerical Methods*, Wiley, New York.

Gardon, R., 1956, "The Emissivity of Transparent Materials," *Journal of the American Ceramic Society*, Vol. 39, No. 8, pp. 278–287.

Gardon, R., 1958, "Calculation of Temperature Distributions in Glass Plates Undergoing Heat-Treatment," *Journal of the American Ceramic Society*, Vol. 41, No. 6, pp. 200–209.

Kubo, S., 1984, "Unsteady Radiative Heat Transfer in a Scattering-Dominant Medium," *AIAA Journal*, Vol. 22, No. 12, pp. 1804–1809.

Lii, C. C., and Ozisik, M. N., 1972, "Transient Radiation and Conduction in an Absorbing, Emitting, Scattering Slab With Reflective Boundaries," *Int. Journal Heat and Mass Transfer*, Vol. 15, No. 5, pp. 1175–1179.

Mattick, A. T., and Hertzberg, A., 1981, "Liquid Droplet Radiators for Heat Rejection in Space," *Journal of Energy*, Vol. 5, No. 6, pp. 387–393.

Presler, A. F., Coles, C. E., Diem-Kirsop, P. S., and White, K. A., 1986, "Liquid Droplet Radiator Program at the NASA Lewis Research Center," ASME Paper No. 86-HT-15.

Siegel, R., and Howell, J. R., 1981, *Thermal Radiation Heat Transfer*, 2nd ed., Hemisphere Publishing Co., Washington, DC.

Siegel, R., 1987a, "Transient Radiative Cooling of a Droplet-Filled Layer," ASME JOURNAL OF HEAT TRANSFER, Vol. 109, pp. 159–164.

Siegel, R., 1987b, "Radiative Cooling of a Layer With Nonuniform Velocity–A Separable Solution," *AIAA Journal of Thermophysics and Heat Transfer*, in press.

Siegel, R., 1987c, "A Separation of Variables Solution for Nonlinear Radiative Cooling," *International Journal of Heat and Mass Transfer*, in press.

Taussig, R. T., and Mattick, A. T., 1986, "Droplet Radiator Systems for Spacecraft Thermal Control," *Journal of Spacecraft and Rockets*, Vol. 23, No. 1, pp. 10–17.

Viskanta, R., and Bathla, P. S., 1967, "Unsteady Energy Transfer in a Layer of Gray Gas by Thermal Radiation," *Zeitschrift fur Angewandte Mathematik und Physik*, Vol. 18, No. 3, pp. 353–367.

Viskanta, R., and Anderson, E. E., 1975, "Heat Transfer in Semitransparent Solids," *Advances in Heat Transfer*, Vol. 11, T. F. Irvine and J. P. Hartnett, eds., Academic Press, New York, pp. 317–441.

Downloaded 17 Dec 2010 to 193.140.21.150. Redistribution subject to ASME license or copyright; see http://www.asme.org/terms/Terms_Use.cfm

M.-C. Chyu
Assistant Professor,
Department of Mechanical Engineering,
Texas Tech University,
Lubbock, TX 79409
Assoc. Mem. ASME

A. E. Bergles
Clark and Crossan Professor
of Engineering,
Rensselaer Polytechnic Institute,
Troy, NY 12180-3590
Fellow ASME

An Analytical and Experimental Study of Falling-Film Evaporation on a Horizontal Tube

Heat transfer for saturated falling-film evaporation on a horizontal smooth tube has been studied through analysis and experimentation to investigate the effects of film flow rate, liquid feed height, and wall superheat. Two models have been proposed, both based upon three defined heat transfer regions: the jet impingement region, the thermal developing region, and the fully developed region. The model that uses an experimental correlation for heat transfer in the fully developed region compares favorably with experimental data and other predictions reported for the case where the liquid feed is in a sheet.

1 Introduction

Heat transfer through falling-film or spray-film evaporation has been widely employed in heat exchange devices in the chemical, refrigeration, petroleum refining, desalination, and food industries. In the closed-cycle ocean thermal energy conversion (OTEC) system, a horizontal-tube spray-film evaporator has been proposed to operate at the available small temperature difference. The horizontal-tube, falling-film evaporator basically consists of a bundle of horizontal tubes connected by headers at each end, as in a conventional shell-and-tube heat exchanger. The shell-side liquid is introduced through spray nozzles to the top of the bundle and falls from tube to tube. Liquid films flow and evaporate on the outside tube surfaces.

The principal advantages of horizontal-tube, falling-film evaporators are high heat transfer rates at small temperature differences and small liquid inventory as compared with flooded-bundle evaporators. Since there is no liquid pool, the effect of hydrostatic head on the heat transfer is eliminated. The horizontal-tube, falling-film evaporators also show advantages over vertical-tube evaporators in dealing with problems such as liquid distribution, leveling, noncondensable gases on the tube side, fouling, and liquid entrainment (Yundt and Rhinesmith, 1981).

Individual tube performance within the tube bundle of a horizontal-tube, multiple-effect (HTME) desalination facility was reported by Cannizzaro et al. (1974). However, flow rates over the individual tubes were not measured. The heat transfer coefficients for evaporating freshwater films on single tubes reported by Fletcher et al. (1973) were significantly lower than those obtained by Cannizzaro et al. In a subsequent effort, Fletcher et al. (1975) investigated evaporating saturated seawater films on horizontal tubes. The data obtained are 50 percent higher than those for distilled water films but still slightly lower than the seawater data reported by Cannizzaro. Parken and Fletcher (1982) observed an increase in nonboiling evaporation coefficients with increasing flow rate. However, Liu (1975) found that the heat transfer coefficient varied only with the water temperature and the liquid feed height.

The above survey of experiments suggests a need for more data, particularly to clarify the effects of film flow rate and liquid feed height. All the data reported show no influence of heat flux on heat transfer coefficient. However, a question can be raised as to the anticipated increase in heat transfer coefficient due to thinning of the film at a high heat flux. These are the issues to be investigated in this work.

With regard to prediction methods for falling-film evaporation on a horizontal tube, the correlations proposed by Owens (1978) are based upon his own experimental data plus those of Conti (1978) and Liu (1975). The semi-analytical model of Lorenz and Yung (1979) includes two distinct convective heat transfer regions: thermal developing region and fully developed region. However, the length of the developing region was found to be underestimated; also no analysis was provided for the fully developed region. Cerza and Sernas (1983) developed a mathematical model for the thermal developing region of a liquid film falling along a vertical wall with uniform heat flux. Subsequently, in a numerical approach, Parken and Fletcher (1982) considered the high local heat transfer coefficient due to the attacking liquid feed near the apex of the tube. Sabin and Poppendiek (1978) proposed a model for fully developed film evaporation based on Nusselt's (1916) film condensation work. A similar model was developed by Nakazatomi and Bergles (1981). However, as will be explained later in the analysis, errors were found in both approaches. These two models both assumed heat transferred through conduction across the liquid film and evaporation at the free surface. Agreements with experimental data were found even though the effects of jet impingement and thermal development were not considered. The question is also raised as to the importance of heat convection within the film. It is believed a pure conduction analysis is valid only if the film is thin or the flow rate is low. The effect of convection should become important at higher flow rates. An erroneous conclusion, that a Nusselt-type conduction analysis can satisfactorily predict the heat transfer without considering effects of jet impingement, thermal development, and convection, might have been drawn because of mistakes made in the analyses. It is therefore important to develop the correct solution in order to examine the limit of validity of the conduction analysis.

Two models for saturated, nonboiling, falling-film evaporation on a horizontal tube will be presented in this work, both based on three defined heat transfer regions: the jet impingement region, the thermal developing region, and the fully developed region. The only difference between the two models is the treatment of the fully developed region. One model uses a conduction solution based on Nusselt's (1916) analysis of film condensation on a horizontal tube, and the other uses an experimental correlation by Chun and Seban (1972) for fully developed film evaporation on a vertical tube.

2 Heat Transfer Models

The present analysis considers heat transfer in three distinct regions characterized as follows. When a thin film flow on the tube surface is established by supplying liquid at saturation

Contributed by the Heat Transfer Division and presented at the 23rd National Heat Transfer Conference, Denver, Colorado, August 1985. Manuscript received by the Heat Transfer Division May 5, 1986.

Copyright © 1987 by ASME

Downloaded 17 Dec 2010 to 193.140.21.150. Redistribution subject to ASME license or copyright; see http://www.asme.org/terms/Terms_Use.cfm

temperature on the top of a horizontal tube as shown in Fig. 1, there is a short jet impingement region where the heat transfer coefficient is particularly high because of impingement of the liquid. A subsequent thermal developing region is required for the film flow to be superheated to a fully developed linear profile. Although latent heat transfer occurs in this region, most of the heat transfer goes into superheating the liquid film. A fully developed region, characterized by evaporation at the free surface of the film, immediately follows the thermal developing region up to the bottom of the tube where the liquid breaks off.

2.1 Jet Impingement Region. Since the film thickness is much smaller than the tube radius, and since the impinging jet flow is expected to be influential only in a short region, the situation at the top of the horizontal tube may be considered as a liquid jet impinging on a flat plate. Heat transfer for a sheet liquid jet striking a heating surface has been studied by McMurray et al. (1966) and Miyasaka and Inada (1980). They found that the flow field can be divided into three zones: stagnation flow, impingement flow, and uniform parallel flow. As shown in Fig. 2 (Miyasaka and Inada, 1980), the stagnation flow zone is characterized by the velocity just outside the hydrodynamic boundary layer of the jet flow u_{max}, linearly proportional to the distance x from the stagnation point. The local heat transfer coefficient data in the stagnation flow zone can be correlated by the following equation:

$$h_s = 1.03\ \mathrm{Pr}^{1/3} \cdot k\left[\frac{d(u_{max}/u_j)}{d(x/w)} \cdot \frac{u_j}{\nu w}\right]^{0.5} \tag{1}$$

Since the velocity gradient is constant in the stagnation flow zone, this is also the equation for the average heat transfer coefficient $\bar{h}_s$. The jet velocity u_j for the case of a falling-film evaporator is that of a free falling body, $\sqrt{2gH}$, where H is the liquid feed height. The jet width w is calculated from the conservation of mass; i.e., $w = 2\Gamma_i/(u_j\rho)$, where Γ_i is the irrigation rate at the top of the tube. As shown in Fig. 2, the stagnation flow zone covers the region of $0 < x/w < 0.6$; therefore, the angle

$$\phi_s = 0.6\left(\frac{w}{R}\right) \tag{2}$$

is taken as the angular position at the end of the stagnation flow zone.

The impingement flow zone covers the range of $0.5 < u_{max}/u_j < 1.0$. The local heat transfer data are correlated by the following equations (Miyasaka and Inada, 1980):

$$\mathrm{Nu}_i = \frac{h_i x}{k} = 0.73\mathrm{Pr}^{1/3}\mathrm{Re}_x^{0.5} \tag{3}$$

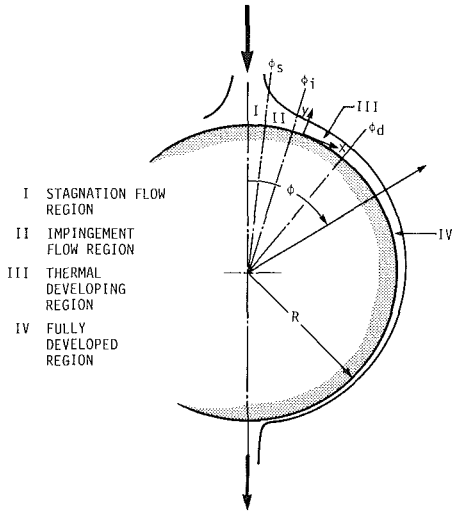

Fig. 1 Model for falling-film evaporation on a horizontal tube

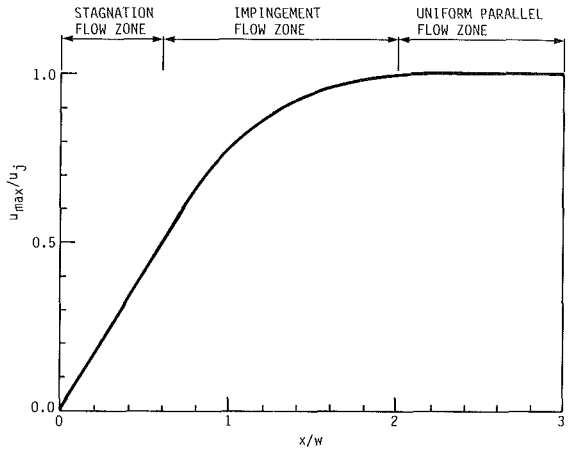

Fig. 2 Distribution of velocity just outside the hydrodynamic boundary layer in the jet impingement region

Nomenclature

C_p = constant-pressure specific heat
D = outer diameter of tube
F = coefficient defined in equation (19)
g = acceleration of gravity
H = liquid feed height
h = heat transfer coefficient
$\bar{h}$ = average heat transfer coefficient
h_{fg} = latent heat of vaporization
k = thermal conductivity
P = parameter defined in equation (20)
Pr = Prandtl number
$\overline{q''}$ = average surface heat flux
R = outer radius of tube
Re = film Reynolds number $= 4\Gamma/\mu_f$
T = temperature
ΔT = wall superheat $= T_w - T_s$
$\overline{\Delta T}$ = average wall superheat
u = velocity
$\bar{u}$ = average velocity
w = jet width
x = distance along the heating surface
y = distance in the direction normal to the heating surface
α = thermal diffusivity $= k/\rho C_p$
Γ = mass flow rate of film per unit length on one side of tube
δ = film thickness
μ = dynamic viscosity
ν = kinematic viscosity
ρ = density
σ = surface tension
τ = time
ϕ = angular position

Subscripts

c = convective
d = developing
f = liquid; film
fd = fully developed
g = gas; vapor
i = inlet condition; impingement
j = jet
s = saturation; stagnation
tr = transition
w = wall
∞ = condition well away from the heat transfer surface

Downloaded 17 Dec 2010 to 193.140.21.150. Redistribution subject to ASME license or copyright; see http://www.asme.org/terms/Terms_Use.cfm

for a laminar boundary layer, and

$$\mathrm{Nu}_i = \frac{h_i x}{k} = 0.037 \mathrm{Pr}^{1/3} \mathrm{Re}_x^{0.8} \tag{4}$$

for a turbulent boundary layer. Note that the local Reynolds number Re_x is based on the local velocity just outside the boundary layer $u_{\max}(x)$:

$$\mathrm{Re}_x = \frac{x u_{\max}(x)}{\nu} \tag{5}$$

The hydrodynamic boundary layer is laminar from the stagnation point to some critical Reynolds number Re_c, where transition to a turbulent boundary layer takes place. According to the data reported by McMurray et al. (1966), Re_c is about 4.5×10^5. The average heat transfer coefficient in the impingement flow zone $\bar{h}_i$ can be calculated numerically from the local $u_{\max}$ data given in Fig. 2. The impingement flow zone covers the range of $0.6 < x/w < 2.0$. Therefore the angle

$$\phi_i = 2.0\left(\frac{w}{R}\right) \tag{6}$$

is taken as the angular position at the end of the impingement flow zone. The flow is considered to be hydrodynamically developed at this point.

2.2 Thermal Developing Region. The analysis for the thermal developing region is based on the following assumptions:

(*a*) The entire tube surface is covered with liquid film; i.e., there is perfect wetting
(*b*) the film flow is laminar
(*c*) the film flow is steady
(*d*) the film thickness is small compared to the tube diameter
(*e*) there is no nucleate boiling within the film
(*f*) heat transfer is only by conduction across the film
(*g*) evaporation occurs on the liquid–vapor interface where the temperature is at saturation
(*h*) the wall temperature is uniform
(*i*) the drag on the liquid–vapor interface is negligible
(*j*) the fluid properties are constant
(*k*) the surface tension effect is negligible

The fully developed velocity distribution in a liquid film flowing over a horizontal tube, calculated by considering a force balance on an element of film along with the no-slip boundary condition, is

$$u_{(y,\phi)} = \frac{g(\rho_f - \rho_g)\sin\phi}{\mu}(y\delta - y^2/2) \tag{7}$$

and the mean velocity, obtained by integrating u across the thickness, is

$$\bar{u}_{(\phi)} = \frac{g(\rho_f - \rho_g)(\sin\phi)\delta^2}{3\mu} \tag{8}$$

with the film thickness

$$\delta_{(\phi)} = \left[\frac{3\mu\Gamma_{(\phi)}}{g\rho_f(\rho_f - \rho_g)\sin\phi}\right]^{1/3} \tag{9}$$

For constant Γ, this analysis leads to a nearly constant value of δ with respect to ϕ as shown in Fig. 3. The film thickness does approach infinity toward the top and the bottom of the tube. However, the thermal developing region always covers the central region where the film thickness is almost constant. The velocity and film thickness at $\phi = 90$ deg are thus used throughout the developing region.

In the thermal developing region, heat from the wall is transferred to superheat the film flow. Although latent heat transport occurs at the free surface, most of the heat goes into superheating the film. Therefore, the film flow rate can also be assumed constant throughout the region. With respect to a coordinate system moving at the same velocity as the film, the change of temperature profile in the developing region can be obtained by solving the one-dimensional transient heat conduction equation

$$\frac{\partial T}{\partial \tau} = \alpha \frac{\partial^2 T}{\partial y^2} \tag{10}$$

with the initial condition

$$T_{(0,y)} = T_s, \qquad 0 < y \le \delta \tag{11}$$

and the boundary conditions

$$T_{(\tau,0)} = T_w, \qquad \tau \ge 0 \tag{12}$$

$$T_{(\tau,\delta)} = T_s, \qquad \tau \ge 0 \tag{13}$$

Note that although the thermal developing region starts from ϕ_i, its solution is based on a starting condition of saturation temperature at the stagnation point, as given by equation (11). The heat transfer from the stagnation point to ϕ_i will be excluded in calculating heat transfer in the thermal developing region, as shown later in equation (21), because this heat transfer has been considered in the jet impingement region.

The above problem has a nonhomogeneous boundary condition at $y = 0$. The solution can be obtained by converting the nonhomogeneous problem into a homogeneous one by the

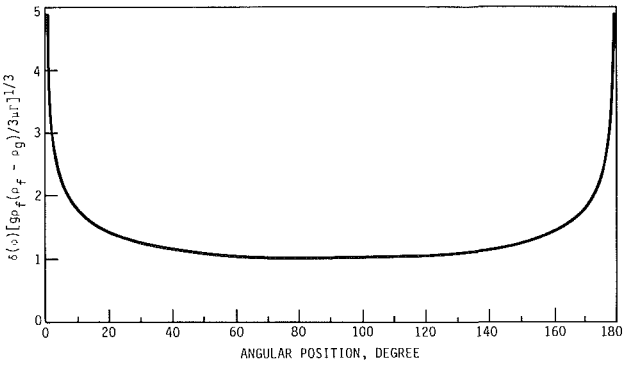

Fig. 3 Variation of film thickness with respect to angular position

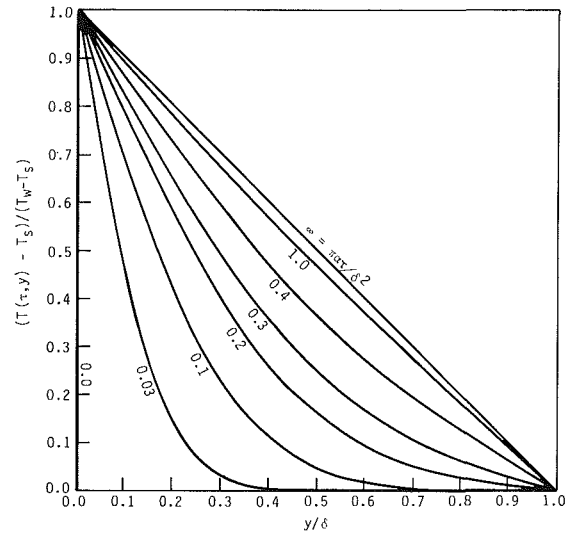

Fig. 4 Progress of temperature profile in the thermal developing region

Downloaded 17 Dec 2010 to 193.140.21.150. Redistribution subject to ASME license or copyright; see http://www.asme.org/terms/Terms_Use.cfm

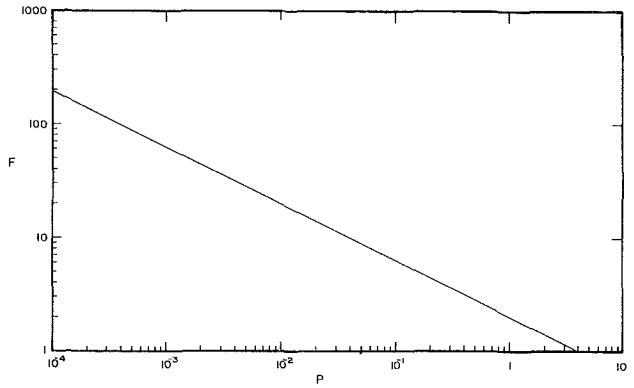

Fig. 5 Relation between the coefficient F and the parameter P

use of a partial solution to the nonhomogeneous problem. The problem also can be solved by the Laplace transformation method. The solution is given as (Myers, 1971)

$$\frac{T_{(\tau,y)}-T_s}{T_w-T_s}=1-\frac{y}{\delta}-\frac{2}{\pi}\sum_{n=1}^{\infty}\frac{\sin n\pi(y/\delta)}{n\cdot\exp\left(\frac{n^2\pi^2\alpha\tau}{\delta^2}\right)} \tag{14}$$

It is observed that the solution is composed of the steady-state solution and the transient term in the form of an infinite series. The temperature profile becomes more and more linear with time. However, theoretically it takes an infinitely long time to reach the linear temperature profile. The progress of the temperature profile in the thermal developing film is plotted in Fig. 4, which shows that the temperature profile is very close to linear for $\tau>\delta^2/\pi\alpha$. Therefore the approximate time required to reach the steady-state temperature profile is taken as

$$\tau_d=\frac{\delta^2}{\pi\alpha} \tag{15}$$

It is noted that Lorenz and Yung (1979) took $\tau_d = \delta^2/4\pi\alpha$; but the temperature profile is far from linear at that value of τ.

The average heat transfer rate in the developing region from time zero to τ is evaluated by integrating the local heat transfer rate at the wall

$$\overline{q''}_{d,(0-\tau)}=\frac{1}{\tau}\int_0^{\tau}\left(-k\frac{\partial T_{(\tau,y)}}{\partial y}\bigg|_{y=0}\right)d\tau \tag{16}$$

By substituting

$$\tau=\left(\frac{3\mu\rho}{g\Gamma^2}\right)^{1/3}R\phi \tag{17}$$

the average heat transfer rate from the top of the tube to the angular position ϕ can be expressed as

$$\overline{q''}_{d,(0-\phi)}=Fk(T_w-T_s)\left[\frac{g\rho_f(\rho_f-\rho_g)}{3\mu\Gamma_i}\right]^{1/3} \tag{18}$$

where

$$F=1+\frac{2}{\pi P}\sum_{n=1}^{\infty}\frac{1}{n^2}[1-\exp(-n^2\pi P)] \tag{19}$$

$$P=\frac{\pi\alpha\tau}{\delta^2} \tag{20}$$

The relation between the coefficient F and the parameter P is plotted in Fig. 5. For the thermal developing region from ϕ_i to ϕ_d, the average heat transfer coefficient is readily calculated from

$$\overline{h}_{d,(\phi_i-\phi_d)}=\frac{\phi_d\overline{q''}_{d,(0-\phi_d)}-\phi_i\overline{q''}_{d,(0-\phi_i)}}{(\phi_d-\phi_i)(T_w-T_s)} \tag{21}$$

The angular position at the end of the developing region ϕ_d can be obtained by substituting the time required for development τ_d into equation (17)

$$\phi_d=\frac{1}{\pi\alpha R}\left(\frac{3\mu\Gamma^4}{g\rho^5}\right)^{1/3} \tag{22}$$

Note that ϕ_d may exceed π when the film flow rate is high. This means the film flow is still developing when breaking off from the tube, and there is no fully developed region in the process. The value π should be used for ϕ_d in this case.

Lorenz and Yung (1979) calculated the total heat transfer rate by considering the enthalpy difference between the inlet and the outlet of the thermal developing region. The total heat transfer rate equals the enthalpy change only if the free surface is insulated. However, the boundary condition at the free surface is at the saturation temperature T_s. The heat transfer through evaporation at the free surface should be considered in their analysis. In the present analysis, the total heat transfer rate is calculated by integrating the local temperature gradient at the wall, as shown in equation (16).

2.3 Fully Developed Region

2.3.1 Conduction Solution. In this analysis, a linear temperature profile is assumed throughout the fully developed region. The assumptions made in the thermal developing region all apply to this fully developed solution. Heat is conducted across the film, and evaporation takes place at the free surface:

$$-h_{fg}\cdot d\Gamma=k_f\left(\frac{T_w-T_s}{\delta}\right)Rd\phi \tag{23}$$

The differential form of equation (9) can be substituted for $d\Gamma$ on the left-hand side of the equation; this leads to a differential equation of δ as a function of ϕ

$$-ed\phi=\delta d(\delta^3\sin\phi) \tag{24}$$

where

$$e=\frac{3R\mu_f k_f(T_w-T_s)}{h_{fg}g\rho_f(\rho_f-\rho_g)} \tag{25}$$

In order to solve equation (24), a nondimensional variable is introduced

$$z=\delta^4/e \tag{26}$$

and equation (24) becomes

$$\frac{3}{4}\sin\phi\frac{dz}{d\phi}+z\cos\phi+1=0 \tag{27}$$

This linear differential equation is readily solved as

$$z=\frac{-4}{3\sin^{4/3}\phi}\left(\int_0^{\phi}\sin^{1/3}\phi'd\phi'+C\right) \tag{28}$$

Assuming that the fully developed region starts at angular position ϕ_d, the integration constant C is evaluated by the boundary condition at ϕ_d, where the film thickness based on the hydrodynamics is given by equation (9). Assuming that the film flow rate at ϕ_d is Γ_i, the film thickness at ϕ_d is

$$\delta(\phi_d)=\left[\frac{3\mu_f\Gamma_i}{g\rho_f(\rho_f-\rho_g)\sin\phi_d}\right]^{1/3} \tag{29}$$

C is thus obtained as

$$C=-\frac{3}{4e}\left[\frac{3\mu_f\Gamma_i}{\rho_f g(\rho_f-\rho_g)}\right]^{4/3}-\int_0^{\phi_d}\sin^{1/3}\phi d\phi \tag{30}$$

Downloaded 17 Dec 2010 to 193.140.21.150. Redistribution subject to ASME license or copyright; see http://www.asme.org/terms/Terms_Use.cfm

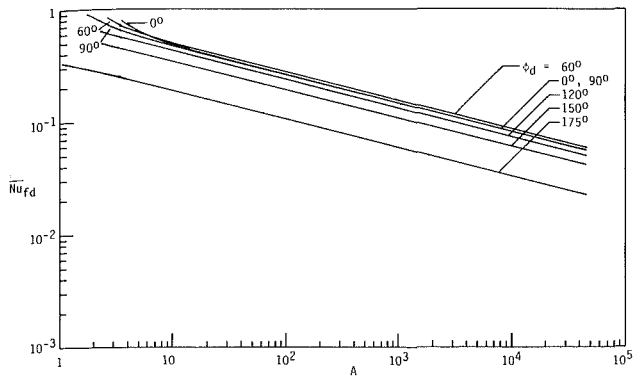

Fig. 6 Analytical predictions of Nusselt number in the fully developed region

Substituting C back into equation (28) yields the film thickness as a function of ϕ

$$\delta(\phi)=\left\{\left[\frac{3\mu_f\Gamma_i}{g\rho_f(\rho_f-\rho_g)\sin\phi}\right]^{4/3}-\frac{4e}{3\sin^{4/3}\phi}\int_{\phi_d}^{\phi}\sin^{1/3}\phi'd\phi'\right\}^{1/4} \tag{31}$$

Based on the film thickness solution, the heat transfer coefficient at angular position ϕ is calculated as

$$h_{fd}(\phi)=\frac{k_f}{\delta(\phi)}$$

$$=\frac{k_f}{\left\{\left[\frac{3\mu_f\Gamma_i}{g\rho_f(\rho_f-\rho_g)\sin\phi}\right]^{4/3}-\frac{4e}{3\sin^{4/3}\phi}\int_{\phi_d}^{\phi}\sin^{1/3}\phi'd\phi'\right\}^{1/4}} \tag{32}$$

and the mean value of the Nusselt number over the fully developed region is

$$\overline{Nu}_{fd}=\frac{\bar{h}_{fd}e^{1/4}}{k_f}=\frac{1}{\pi-\phi_d}\int_{\phi_d}^{\pi}\frac{\sin^{1/3}\phi}{\left(A-\frac{4}{3}\int_{\phi_d}^{\phi}\sin^{1/3}\phi'd\phi'\right)^{1/4}}d\phi \tag{33}$$

where the coefficient A is defined as

$$A=\left[\frac{3\mu_f\Gamma_i^4}{g\rho_f(\rho_f-\rho_g)}\right]^{1/3}\left[\frac{h_{fg}}{Rk_f(T_w-T_s)}\right] \tag{34}$$

and e is defined in equation (25). Note that $\overline{Nu}_{fd}$ is based on $e^{1/4}$.

A result similar to equation (33) was obtained by Sabin and Poppendiek (1978); however, the coefficient in the denominator of the integrand was erroneously given as $A/2^{4/3}$ because of confusion between the total mass flow rate impinging on the tube and the film flow rate on one side of the tube. This led to an overestimation of the mean fully developed heat transfer coefficient. This might explain why their prediction was found to be in reasonable agreement with the experimental data, even though the effects of the jet impingement region and the thermal developing region were not considered. The work reported by Nakazatomi and Bergles (1981) stops at the expression of film thickness. The heat transfer coefficient was then numerically calculated. However, the expression for film thickness does not appear to be correct.

It is observed that the smaller the value of A, the greater the value of $\overline{Nu}_{fd}$. The heat transfer coefficient increases because of effective heat transfer across a thin liquid film when the flow rate is small. However, a mathematical problem arises when A is smaller than $(4/3)\int_{\phi_d}^{\pi}\sin^{1/3}\phi'd\phi'$. Physically, this lower limit corresponds to incipient dryout at the bottom of the tube.

The average Nusselt number can be obtained from Fig. 6 for a known value of A. Data shown in Fig. 6 were generated by fitting a sixth-degree polynomial to the integral $\int_0^{\phi}\sin^{1/3}\phi'd\phi'$ and numerically integrating using the trapezoidal rule. It is noted that the mean fully developed heat transfer coefficient is quite constant for ϕ_d up to 90 deg. The prediction using the above solution for the fully developed region is designated as Model I.

2.3.2 Correlation Approach. For reasons of simplicity, the above analysis for the fully developed region is based on the assumption that heat transfer is only by conduction across the liquid film. An alternative approach is to adopt the following correlations by Chun and Seban (1972) which are based on experimental data for an evaporating film falling along a vertical wall:

Laminar:

$$\frac{\bar{h}_{fd}}{k}\left(\frac{\nu^2}{g}\right)^{1/3}=1.10\ \mathrm{Re}^{-1/3},\qquad \frac{\Gamma}{\mu}\le 0.61\left(\frac{\mu^4 g}{\rho\sigma^3}\right)^{-1/11} \tag{35}$$

Wavy-laminar:

$$\frac{\bar{h}_{fd}}{k}\left(\frac{\nu^2}{g}\right)^{1/3}=0.822\ \mathrm{Re}^{-0.22},\qquad 0.61\left(\frac{\mu^4 g}{\rho\sigma^3}\right)^{-1/11}<\frac{\Gamma}{\mu}\le 1450\ \mathrm{Pr}^{-1.06} \tag{36}$$

Turbulent:

$$\frac{\bar{h}_{fd}}{k}\left(\frac{\nu^2}{g}\right)^{1/3}=3.8\times10^{-3}\mathrm{Pr}^{0.65}\mathrm{Re}^{0.4},\qquad \frac{\Gamma}{\mu}>1450\mathrm{Pr}^{-1.06} \tag{37}$$

These correlations are based on the asymptotic values of the heat transfer data for a film that is thermally and hydrodynamically developed after flowing through a preheating section. The correlations are considered applicable to falling-film evaporation on a horizontal tube in view of the small film thickness compared with tube diameter. The prediction using the above correlations to calculate the mean heat transfer coefficient in the fully developed region is designated Model II.

2.4 Overall Heat Transfer Coefficient. Finally, the average heat transfer coefficient can be calculated by summing heat transfer contributions from each of the regions

$$\bar{h}=\bar{h}_s\left(\frac{\phi_s}{\pi}\right)+\bar{h}_i\left(\frac{\phi_i-\phi_s}{\pi}\right)+\bar{h}_d\left(\frac{\phi_d-\phi_i}{\pi}\right)+\bar{h}_{fd}\left(1-\frac{\phi_d}{\pi}\right) \tag{38}$$

In the range covered, the typical $\bar{h}_s$ and $\bar{h}_i$ are on the order of magnitude of 10^5 W/m^2 K, while $\bar{h}_d$ and $\bar{h}_{fd}$ are an order of magnitude smaller. However, because the jet impingement is effective in a small region, it accounts for only a small portion of the average heat transfer coefficient. The major contribution is from the fully developed region at low film flow rate and from the thermal developing region at high flow rate. Because the heat transfer in the fully developed region becomes less important as flow rate increases, data based on the two proposed models merge at a point where the film flow reaches thermal development at the bottom of the tube, or ϕ_d equals π.

Downloaded 17 Dec 2010 to 193.140.21.150. Redistribution subject to ASME license or copyright; see http://www.asme.org/terms/Terms_Use.cfm

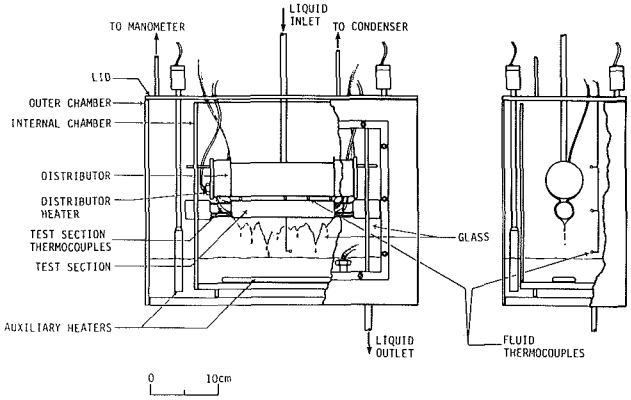

Fig. 7 Test chamber for falling-film evaporation on a horizontal cylinder

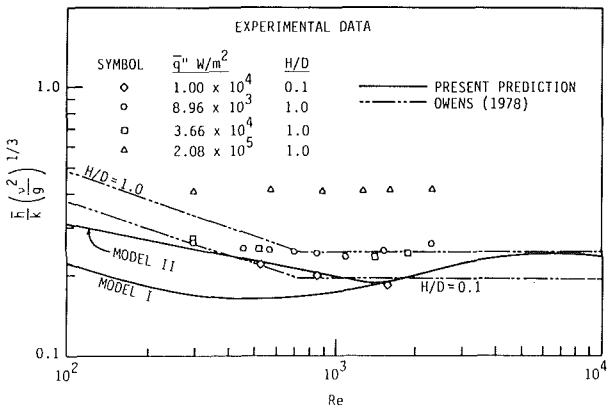

Fig. 8 Influence of film Reynolds number on the film evaporation coefficient

3 Experiment

Falling-film evaporation of water on a horizontal cylinder was tested. Experiments using electrically heated test sections with a smooth surface were conducted to investigate the effects of film flow rate, liquid feed height, and heat flux. The test facility included a circulation pump, a filter, a rotameter, flow adjusting valves, and a test chamber. The large outer test chamber has an inner chamber holding the liquid distributor, test section, and auxiliary heater (see Fig. 7). The double-chamber had an inner chamber holding the liquid distributor, test section, and auxiliary heater (see Fig. 7). The double-sulation that would have hindered visual observations. The space in the inner chamber was maintained within 0.1 K of the saturation temperature during the tests. The system pressure was atmospheric for all tests, with a typical value of 0.99 bar.

The falling liquid film was formed by distributing saturated liquid (within 0.1 K subcooling) in unsteady column jets or drips to the test cylinder. This was done by a distributor featuring a cylindrical shell enclosing an interior heater. Liquid heated by the interior heater to saturation overflowed through a slot at the top of the shell providing a film on the exterior shell wall. The liquid then detached from the bottom of the shell and impinged on the test heater. This simulated the situation in a real falling-film evaporator where the lower tube receives runoff from the tube above. A detailed configuration of the distributor is given by Chyu (1984). The liquid feed height was adjusted by moving the distributor up and down along the slots on the side walls of the inner chamber. It was observed that the liquid fed in a sheet when the gap between distributor and test cylinder was narrower than 3 mm, as shown in Fig. 7. The irrigation flow rate was measured by a rotameter at the inlet of the test chamber. The average subcooling of the liquid feed, monitored by fluid thermocouples located at the bottom of the shell, was maintained within 0.1 K.

The test cylinder was of copper, 25.4 mm in diameter and 152 mm in length. A central 12.7-mm-dia hole was provided for a cartridge heater. Six thermocouple wells of 1 mm diameter and 40 to 50 mm in depth were drilled 60 deg apart at each end, with outer edges approximately 1.5 mm from the outer surface. Failure to drill that small a hole straight along its entire depth resulted in so-called drift or runout. A novel method was developed to locate precisely the bottoms of the holes (thermocouple locations) (Chyu, 1984). This information was essential in calculating the temperature drop between the thermocouple junction and the base surface. The cartridge heater was soldered into the cylinder to minimize contact resistance. Both ends of the test cylinder were insulated with silicone seal after thermocouple installation.

The average heat flux was calculated from the active length of the cartridge heater. This calculation is justified by a conduction analysis showing that at a considerable axial distance away from the inactive zone of a cartridge heater, the heat flux in the test cylinder is essentially that of the average value based on the active length of the heater (Chyu, 1984). The wall temperature is the mean of the six wall temperatures inferred from thermocouple readings. In fact, both the experimental data and the analysis (Chyu, 1984) showed that the test cylinder was essentially isothermal at the outer surface because of its thick wall. This simulates the real situation in a spray-film evaporator by condensing steam.

The estimated uncertainties for the data presented are as follows: ± 220 W/m^2 in heat flux, $\pm$ 0.06 K in wall superheat and surface subcooling, ± 0.004 kg/s-m in film flow rate, and ± 0.1 in ratio of feed height to diameter.

4 Experimental Results and Comparison With Predictions

4.1 Influence of Film Flow Rate. In Fig. 8 the experimental data are compared with predictions based on the present models as well as on the Owens (1978) correlation. The prediction of Model II is in excellent agreement with the experimental data at $H/D = 0.1$. Model II is also in good agreement with the Owens correlation at $H/D = 0.1$ in the low and medium ranges of Reynolds number. In the high Reynolds number region, corresponding to turbulent flow, the Owens correlation predicts a constant heat transfer coefficient, while the present model predicts an increasing coefficient with Reynolds number. This is consistent with the results of Chun and Seban (1972) and Duckler (1960) for a falling film on a vertical tube wall.

Model I predicts a heat transfer coefficient 30 percent lower than Model II at low Reynolds number. This is as anticipated. Because of convection, the real temperature profile in a film flow should have a steeper gradient at the wall and, therefore, a higher heat transfer coefficient than obtained with the linear profile assumed in the conduction model. In addition, the effect of the waves that actually exist on the free surface of the film has not been considered. This contradicts the conclusion suggested by Sabin and Poppendiek (1978) and Nakazatomi and Bergles (1981) that a Nusselt-type fully developed conduction analysis can satisfactorily predict falling-film evaporation on a horizontal tube. Apparently the erroneous conclusion was due to the mistakes made in their analyses. The present analysis demonstrates that even with effects of jet impingement and thermal development taken into account, the conduction analysis fails.

The data of the two proposed models merge at Re = 1367 when there is no fully developed region in the heat transfer process. Both models show that variations in liquid feed height have little effect on the heat transfer. In fact, the

Downloaded 17 Dec 2010 to 193.140.21.150. Redistribution subject to ASME license or copyright; see http://www.asme.org/terms/Terms_Use.cfm

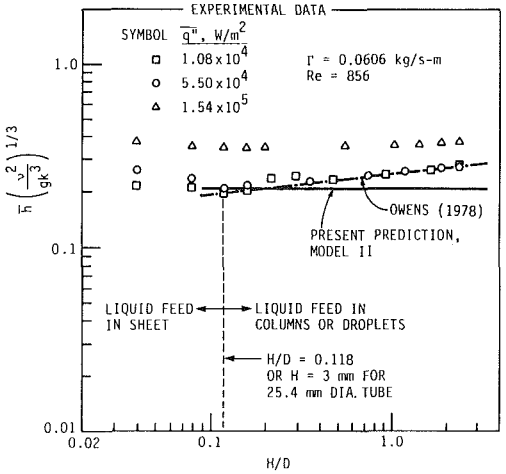

Fig. 9 Effect of liquid feed height on the falling-film evaporation heat transfer coefficient

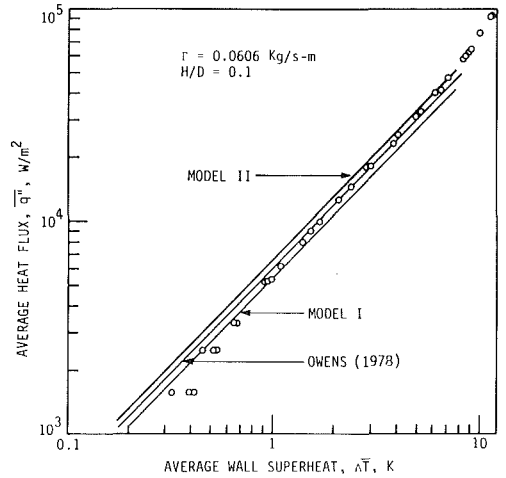

Fig. 10 Influence of wall superheat on the film evaporation coefficient

present predictions presented in Fig. 8 are valid for H/D from 0.1 to 2.5.

The experimental data at $H/D = 1.0$ are in good agreement with the Owens correlation for turbulent nonboiling films with $H/D = 1.0$ except in the low Reynolds number region. The data at $H/D = 1.0$ are significantly higher than the present predictions. It was observed that liquid feed was distributed in columns (continuous) and droplets (discontinuous) when feed height was large and in a sheet when H was no larger than 3 mm, which corresponded to H/D of approximately 0.1 based on the dimension of the test cylinder. The present analysis considers the effect of liquid feed height by assuming a two-dimensional sheet jet striking on a flat surface. Model II can predict data well at $H/D = 0.1$ when liquid feed is in a sheet. However, the prediction is lower than the data when the feed is in columns or droplets at larger H/D. The liquid columns and droplets were observed to create crests and valleys at the apex of the horizontal tube, resulting in agitation of the film flow.

At high heat flux (2.08×10^5 W/m^2), the heat transfer coefficient is very high and independent of Reynolds number. This indicates the dominance of nucleate boiling in the film.

4.2 Influence of Liquid Feed Height. The effect of variations in liquid feed height on the heat transfer was investigated at different heat flux levels. In Fig. 9, the nondimensionalized heat transfer coefficients at Re = 856 are plotted against the nondimensionalized feed height. The low heat flux data (1.080×10^4 W/m^2 and 5.503×10^4 W/m^2) show good agreement with the Owens (1978) correlation for turbulent falling film evaporation without boiling within the range of $0.1 < H/D < 2.5$. The slope of the data curve seems to agree with the 0.1 power index of the term H/D used in his correlation. However, the power index should decrease at low Re in light of the experimental data in Fig. 8, which show that heat transfer coefficient is less sensitive to the change in liquid feed height at low Reynolds numbers.

Model II predicts little influence of liquid feed height on the heat transfer coefficient. This model is based on a sheet jet of the liquid feed instead of liquid columns and droplets; apparently the liquid columns and droplets generate greater disturbance in the film than a sheet when falling from a substantial height.

The change in feed height has a weak influence on the heat transfer coefficient at high heat flux (1.54×10^5 W/m^2). This is due to nucleate boiling in the film, which dominates any change in hydrodynamics.

The present data show a minimum heat transfer coefficient at $H/D = 0.1$ or $H = 3$ mm for the 25.4-mm-dia test cylinder. As mentioned before, liquid feeds in a sheet for $H = 3$ mm or less. It was observed that bubbles were entrained from the distributor in which feed water was boiling and grew larger in the narrow space between the distributor and the test cylinder. These bubbles were apparently larger in size than those generated on the surface of the test section because of nucleate boiling. Some of them were carried with the falling film, and some of them ruptured between the distributor and the test section. These bubbles were considered to be responsible for the high heat transfer coefficients at very small H/D.

4.3 Influence of Wall Superheat. It was expected that the wall superheat has an effect on the heat transfer of film evaporation, since greater wall superheat would yield higher evaporation rate and thus an increase in heat transfer coefficient due to thinning of the film. The present analysis assumes that superheat is not a factor in the jet impingement and the thermal developing regions. As for the fully developed region, superheat participates as a variable in the conduction solution in Model I, while it does not appear in the Chun and Seban (1972) correlation used in Model II. In fact, the conduction solution in Model I also predicts negligible superheat influence on heat transfer coefficient. In Fig. 10, the experimental data follow a straight line with a slope close to unity in the q'' versus $\overline{\Delta T}$ plot. The heat transfer coefficient is quite constant with slight increase with superheat, until in the high superheat range where the data show an upswing due to nucleate boiling within the film. It is thus confirmed that the heat transfer coefficient of a nonboiling falling film is not significantly influenced by the wall superheat in the present test range. This is because convection is the major mode of heat transfer and there is not much thinning of the liquid film due to evaporation. Compared with experimental data, the Owens nonboiling correlation seems to be nearly satisfactory up to $q'' = 6 \times 10^4$ W/m^2. Data presented in Figs. 8 and 9 also show agreement with Owens correlation within this limit of heat flux.

5 Concluding Remarks

Two models have been proposed for the evaporative heat transfer of a saturated falling film on a horizontal tube. Both are based on three defined heat transfer regions: the jet impingement region, the thermal developing region, and the fully developed region. The difference between the two models is only in the fully developed region. Model I uses a conduction solution based on Nusselt's film condensation analysis; Model II uses the Chun and Seban (1972) correlation for developed film evaporation. Model II compares favorably with the ex-

Downloaded 17 Dec 2010 to 193.140.21.150. Redistribution subject to ASME license or copyright; see http://www.asme.org/terms/Terms_Use.cfm

perimental data and the Owens (1978) prediction when the liquid feed is in a sheet. Model I predicts a heat transfer coefficient lower than other predictions and experimental data at low Reynolds number because the simplified conduction solution for the fully developed region underestimates the heat transfer. The experimental heat transfer coefficients are higher than the present predictions when the liquid feeds in columns and droplets because the present predictions are based on liquid feed in a sheet. The experimental data show a weak influence of liquid feed height on heat transfer coefficient. The influence is even smaller at low Reynolds numbers. Both models and experimental data demonstrate heat transfer independent of the wall superheat. It is suggested that the effect of liquid feed in columns and droplets as observed in a real falling-film evaporator be analyzed in subsequent research.

6 Acknowledgments

This study was conducted primarily in the Heat Transfer Laboratory at Iowa State University and supported in part by the U.S. Department of Energy under Contract DE-AC22-78ET13127 and Grant DE-FG07-81ID12222. The test cylinder and technical assistance were provided by Mr. C. F. Gottzmann and Mr. P. S. O'Neill of the Linde Division of Union Carbide Corporation.

7 References

Cannizzaro, C. J., Karpf, J. Z., Kosowski, N., and Pascale, A. S., 1974, "Fourth Report on Horizontal Tube Multiple-Effect (HTME) Process Pilot Plant Test Program," *Office of Saline Water Research and Development* Progress Report No. 74-967.

Cerza, M., and Sernas, V., 1983, "Nucleate Boiling Heat Transfer in Developing Laminar Falling Water Films," *ASME-JSME Thermal Engineering Joint Conference Proceedings*, Honolulu, HI, Vol. 1, pp. 111-118.

Chun, K. R., and Seban, R. A., 1972, "Performance Prediction of Falling-Film Evaporators," ASME JOURNAL OF HEAT TRANSFER, Vol. 94, pp. 432-436.

Chyu, M.-C., 1984, "Falling Film Evaporation on Horizontal Tubes With Smooth and Structured Surfaces," Ph.D. Dissertation, Iowa State University, Ames, IA.

Conti, R. J., 1978, "Experimental Investigations of Horizontal Tube Ammonia Film Evaporators With Small Temperature Differentials," *Proceedings of the Fifth Ocean Thermal Energy Conversion Conference*, Miami Beach, FL, VI 161-VI 180.

Dukler, A. E., 1960, "Fluid Mechanics and Heat Transfer in Vertical Falling Film Systems," *Chemical Engineering Progress, Symposium Series*, Vol. 56, No. 30, pp. 1-10.

Fletcher, L. S., Sernas, V., and Galowin, L. S., 1973, "Evaporation From Thin Water Films on Horizontal Tubes," ASME Paper No. 73-HT-42.

Fletcher, L. S., Sernas, V., and Parken, W. H., 1975, "Evaporation Heat Transfer Coefficients for Thin Sea Water Films on Horizontal Tubes," *Industrial Engineering Chemistry, Process Design and Development*, Vol. 14, pp. 411-416.

Liu, P. J. P., 1975, "The Evaporating Falling Film on Horizontal Tubes," Ph.D. Thesis, University of Wisconsin, Madison, WI.

Lorenz, J. J., and Yung, D., 1979, "A Note on Combined Boiling and Evaporation of Liquid Films on Horizontal Tubes," ASME JOURNAL OF HEAT TRANSFER, Vol. 101, pp. 178-180.

McMurray, D. C., Myers, P. S., and Uyehara, O. A., 1966, "Influence of Impinging Jet Variables on Local Heat Transfer Coefficients Along a Flat Surface With Constant Heat Flux," *Proceedings of the 3rd International Heat Transfer Conference*, Chicago, Vol. II, pp. 292-299.

Miyasaka, Y., and Inada, S., 1980, "The Effect of Pure Forced Convection on the Boiling Heat Transfer Between a Two-Dimensional Subcooled Water Jet and a Heated Surface," *Journal of Chemical Engineering in Japan*, Vol. 13, No. 1, pp. 22-28.

Myers, G. E., 1971, *Analytical Methods in Conduction Heat Transfer*, McGraw-Hill, New York.

Nakazatomi, M., and Bergles, A. E., 1981, "Film Evaporation Model on Horizontal Tubes," Research Reprint of Ube Technical College, No. 27 [in Japanese].

Nusselt, W., 1916, "Die Oberflaechenkondensation des Wasserdampfes," *Zeitschrift des Vereines Deutscher Ingenieure*, Vol. 60, No. 27, pp. 541-546; 569-575.

Owens, W. L., 1978, "Correlation of Thin Film Evaporation Heat Transfer Coefficients for Horizontal Tubes," ASME Paper No. 78-WA/HT-67.

Parken, W. H., Jr., and Fletcher, L. S., 1982, "Heat Transfer in Thin Liquid Films Flowing Over Horizontal Tubes," *Heat Transfer—1982*, Proceedings of the Seventh International Heat Transfer Conference, Munich, W. Germany, Vol. 4, pp. 415-420.

Sabin, C. M., and Poppendiek, H. F., 1978, "Film Evaporation of Ammonia Over Horizontal Round Tubes," *Proceedings of the Fifth Ocean Thermal Energy Conversion Conference*, Miami Beach, FL, VI 237-VI 260.

Yundt, B., and Rhinesmith, R., 1981, "Horizontal Spray-Film Evaporation," *Chemical Engineering Progress*, Vol. 77, pp. 69-74.

Downloaded 17 Dec 2010 to 193.140.21.150. Redistribution subject to ASME license or copyright; see http://www.asme.org/terms/Terms_Use.cfm

Critical Heat Flux in Saturated Forced Convection Boiling on a Heated Disk With an Impinging Jet

M. Monde
Department of Mechanical Engineering,
Saga University,
1 Honjo Saga, 840 Japan

Critical heat flux during forced convection boiling on an open heated disk being supplied with saturated liquids through a small round jet which impinges at the center of the disk has been studied experimentally employing refrigerant R12 at comparatively high pressures from 0.6 to 2.8 MPa. Generalized correlations, predicting the CHF within an experimental range of liquid-to-vapor density ratio 5.3–41.25 and the reciprocal of Weber number 2×10^{-3}–2×10^{-7}, are given for three different characteristic regimes: V-regime where the CHF increases with an increase in the jet velocity, I-regime where the CHF is nearly constant with jet velocity, and HP-regime where the CHF appears only at high pressure and again rises with an increase in the jet velocity.

1 Introduction

Monde and Katto [1, 2] and Monde [3] proposed a generalized correlation predicting critical heat flux (CHF) in saturated forced convection boiling of water and R113 at atmospheric pressure with an impinging jet. This correlation, however, was not able to apply to the CHF data of R12 measured by Katto and Shimizu [4]. They investigated the CHF for both saturated R12 at a comparatively high pressure of 0.6 to 2.79 MPa and saturated water at atmospheric pressure using the same boiling system as that of Monde and Katto [2]. Katto and Shimizu [4] divided the CHF into two characteristic regimes and, in addition, proposed the possibility of the existence of two additional characteristic regimes. One of the two regimes is called V-regime because CHF depends on velocity; the other one is called I-regime where CHF is regarded as independent of velocity.

Recently, Katto and Haramura [5] and Katto [6] proposed a new hydrodynamic model for the CHF mechanism which is applicable to the CHF not only of pool boiling but also of forced convection boiling both on cylinders in cross flow and on flat plates submerged in a uniform flow. With the aid of their new model and dimensional analysis, Monde [7] introduced a new generalized correlation, equation (1), predicting the CHF data in the V-regime measured by Monde and Katto [1, 2], Monde [3], Katto and Kunihiro [8], Katsuta [9, 10], and Katto and Shimizu [4]

$$\frac{q_{co}}{\rho_v H_{fg} u} = 0.221 \left(\frac{\rho_l}{\rho_v}\right)^{0.645} \left(\frac{2\sigma}{\rho_1 u^2 (D-d)}\right)^{0.343} (1+D/d)^{-0.364} \quad (1)$$

It should be noted that equation (1) can predict the CHF on both upward and downward-facing heated disks because this equation is independent of the gravitational force. In addition, it may be of importance to say [7] that the effect of D/d on q_{co} is successfully correlated by the function D/d in equation (1), which is determined from the Katto and Haramura model. In addition, it is necessary to mention that the exponents of $2\sigma/\rho_l u^2 (D-d)$ and $(1+D/d)$, exactly derived from the Katto and Haramura criterion [7], and 1/3 and $-1/3$, similar to those in equation (1), while the exponent of ρ_l/ρ_v is a bit smaller than that in equation (1). However, it is pointed out in [7] that equation (1) can predict the CHF data in the V-regime only, but cannot predict the CHF in the I-regime except for the CHF in the V-regime, which is named by Katto and Shimizu [4], as well as the CHF appearing under the conditions of large D/d and low velocity u.

More recently, Monde and Okuma [11] proposed a generalized correlation for the CHF on a downward-facing heated disk when D/d is very large and velocity u is very low

$$\frac{q_{co}}{\rho_v H_{fg} u} = k \left(\frac{\rho_l}{\rho_v}\right) (d/D)^2 \quad (2)$$

where $$\frac{1}{k} = 3.89 \times 10^{-2} \left(\frac{\rho_l}{\rho_v}\right)^{0.674} \left(d/\sqrt{\sigma/g(\rho_l-\rho_v)}\right)^{1.24},$$

and the boundary between equations (1) and (2):

$$D/d = 18.4 \left(\frac{\rho_l}{\rho_v}\right)^{0.194} \left(d/\sqrt{\sigma/g(\rho_l-\rho_v)}\right)^{-0.76} (2\sigma/\rho_l u^2 (D-d))^{-0.209} \quad (3)$$

The CHF predicted by equation (2) is called the CHF in the L-regime, for simplicity.

Lienhard and Eichhorn [12] proposed a complicated correlation derived from the CHF data of Monde and Katto [1, 2] and Lienhard and Hasan [13] improved their equation to predict the CHF of R12 measured only for $D = 0.01$ m at high pressure by Katto and Shimizu [4]. It may be of interest to know that their equation is continuous for the whole experimental range of pressure although the CHF characteristic would be categorized into some groups depending on ρ_l/ρ_v, $2\sigma/\rho_l u^2 (D-d)$, and D/d according to the concept of Katto and Shimizu [4] and Monde [7]. More recently, after communication with Monde [14], Sharan and Lienhard [15] reformulated a generalized correlation as follows:

$$q_{co}/\rho_v H_{fg} u = f(r)\ (1000\ \sigma/\rho_l u^2 D)^{A(r)}\ (d/D)^{1/3} \quad (4)$$

where $f(r) = 0.00171\, r + 0.21$, and $A(r) = 0.486 + 0.06052\ (\ln r) - 0.0378\ (\ln r)^2 + 0.00362\ (\ln r)^3$. Equation (4) is valid for $(D/d)/(ud/\nu)^{1/3} < 0.40$ and $u/\sqrt{gD} > 8$. It should be necessary to elucidate the character of the function $A(r)$ being rather complicated; $A(r)$ is 0.349 or 0.329 depending on whether the density ratio r is 60 or 1603, in which CHF can be

Contributed by the Heat Transfer Division for publication in the JOURNAL OF HEAT TRANSFER. Manuscript received by the Heat Transfer Division August 20, 1985.

Copyright © 1987 by ASME

Downloaded 17 Dec 2010 to 193.140.21.150. Redistribution subject to ASME license or copyright; see http://www.asme.org/terms/Terms_Use.cfm

Table 1 Variation of the function g_2 ( ) with D/d = 5 to 60 over the range of ρ_l/ρ_v = 60 to 1600

D/d	5	10	20	40	60
g_2( )	1.039 ~ 1.057	1.071 ~ 1.080	1.096 ~ 1.100	1.120 ~ 1.122	1.134 ~ 1.135

predicted by each of equations (1) and (2), and then the minimum value of $A(r)$ attains 0.272 at r = 549.

Incidentally, it may be of interest to compare equation (1) with equation (4). Dividing equation (4) by equation (1) to eliminate q_{co} and rearranging it, we can obtain the following equation:

$$g(r,\ \sigma/\rho_l u^2\ (D-d)\ ,\ D/d) = g_1(r,\ \sigma/\rho_l u^2\ (D-d))\ g_2(r,\ D/d) \tag{5}$$

where

$$g_1(r,\ \sigma/\rho_l u^2\ (D-d)) = 38.1\, f(r)\ r^{-0.645}\ (1000\,\sigma/\rho_l u^2\ (D-d))^{A(r)-0.343} \tag{5a}$$

$$g_2(r,\ D/d) = (1+D/d)^{0.364}\ (1-d/D)^{A(r)}\ (d/D)^{1/3} \tag{5b}$$

The function g_1 $(r,\ \sigma/\rho_l u^2\ (D-d))$ gives the effect of r and $\sigma/\rho_l u^2\ (D-d)$ on the CHF, while the function g_2 $(r,\ D/d)$ gives mainly the effect of D/d on the CHF. It is not necessary to say that if g ( ) is always kept unity for the change in any parameters in equation (5), the two equations (1) and (4) are exactly the same, but it would be impossible to expect it. The values calculated over the range of r = 60 to 1600 from equation (5*b*) are listed for D/d = 5 to 60 corresponding to the existing experimental range in Table 1. Table 1 shows that the function g_2 ( ) is nearly constant with the density ratio and these values increase about 10 percent as D/d = increases from 5 to 60. It is difficult from Table 1 to determine whether equation (1) or (4) is better at predicting the effect of D/d on the CHF, for the difference of 10 percent for D/d = 5 to 60 merges into an uncertainty when measuring the CHF. It may be of importance to note that the functional form of D/d in equation (1) can be theoretically derived from the Katto and Haramura criterion [7]. Next, the values calculated from equation (5*a*) are shown for r = 60 to 1600 in Fig. 1. From Fig. 1 and Table 1, the value of function g ( ) becomes nearly unity for $2\sigma/\rho_l u^2\ (D-d) = 10^{-5}$ to 10^{-4} but tends to become larger than unity with the decrease in $2\sigma/\rho_l u^2\ (D-d)$, although the character of g_1( ) is curious. At the point r = 1600, the values of g_1( ) become the same for different values of $2\sigma/\rho_l u^2\ (D-d)$; for example, the value of g( ) is 1.007 or 1.093 depending on whether D/d is 5 or 60. Comparison of equation (4) and the CHF data measured in the present experiment at comparatively high pressure, i.e., small density ratio, will be discussed later.

The present study, therefore, involves an experiment of the CHF during forced convection boiling of saturated R12 at comparatively high pressures of 0.6 to 2.8 MPa on a downward-facing heated disk of diameter D = 0.04, 0.02, and 0.01 m. A small round impinging jet of diameter d = 0.002 m is used to measure the CHF within the wide experimental range of ρ_l/ρ_v = 5.3 to 41.25 and $2\sigma/\rho_l u^2\ (D-d) = 2 \times 10^{-3}$ to 2×10^{-7}. Furthermore, the experiments of saturated water at pressures of 0.1 to 0.6 MPa and of saturated R113 at

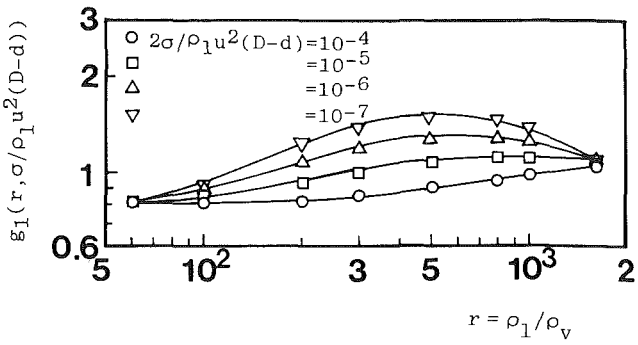

Fig. 1 Variation of the function g_1 ( ) with density ratio

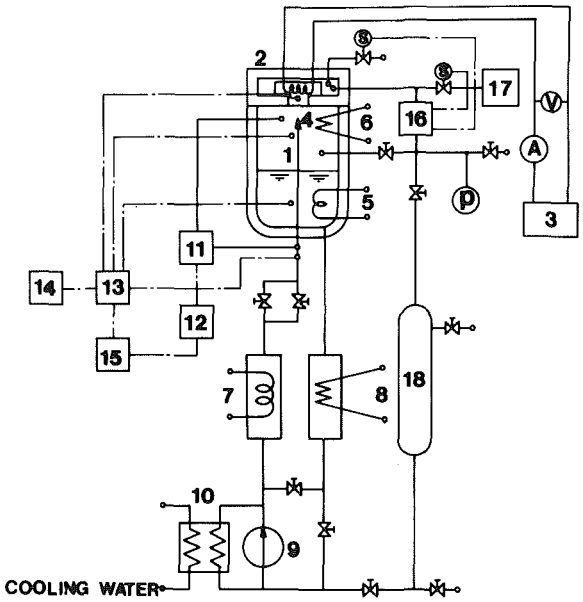

1 PRESSURE VESSEL 2 HEATING CELL 3 TRANSFORMER
4 NOZZLE 5 VESSEL-HEATER 6 COOLING COILS
7 HEATER 8 COOLER 9 PUMP
10 PUMP COOLER 11 PRESSURE TRANSDUCER
12 STRAIN AMPLIFYER 13 ICE BOX 14 RECORDER
15 DIGITAL VOLTMETER 16 DIFFERENTIAL PRESSURE GAUGE
17 N_2 TANK 18 STRAIGE TANK

Fig. 2 Schematic of the experimental apparatus

pressures of 0.1 to 0.3 MPa are also made to check the reliability of the experimental apparatus in this experiment as well as to extend the experimental range of ρ_l/ρ_v.

2 Experimental Apparatus and Method of Measuring CHF

The experimental apparatus is shown schematically in Fig. 2. At the top of a pressure vessel (1) (the details of which are shown in Fig. 3), a copper block is set up in a heating cell (2) with plate-type heaters in the upper cylindrical part, to which electric power is supplied from an a-c transformer (3). The flat

Nomenclature

D = diameter of a heated disk
d = diameter of an impinging jet
g = acceleration of gravity
H_{fg} = latent heat of evaporation
P = absolute pressure of system
q_{co} = critical heat flux for saturated boiling
r = density ratio = ρ_l/ρ_v
u = velocity of a liquid jet at nozzle exit
ρ_l = density of liquid
ρ_v = density of vapor
σ = surface tension
ν = kinematic viscosity of liquid

Downloaded 17 Dec 2010 to 193.140.21.150. Redistribution subject to ASME license or copyright; see http://www.asme.org/terms/Terms_Use.cfm

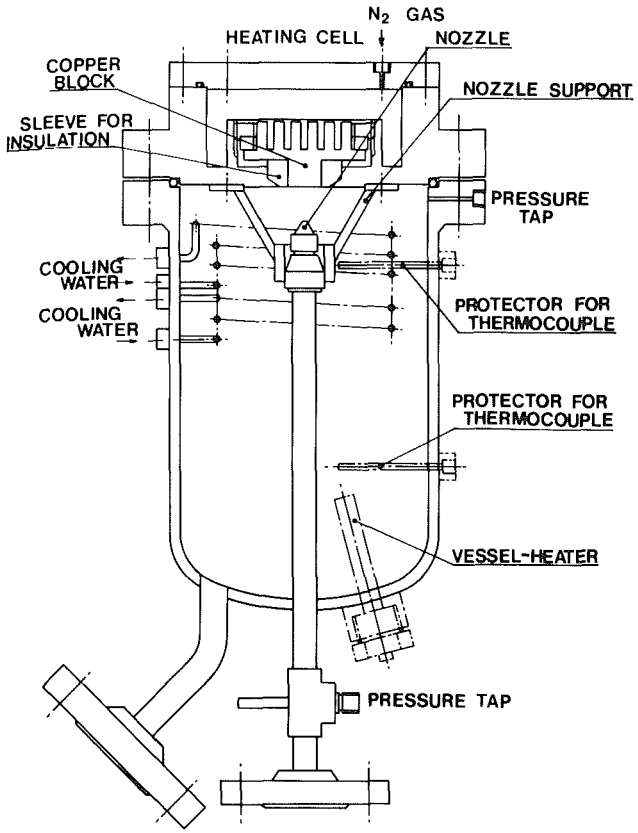

Fig. 3 Pressure vessel

end surface of the lower cylindrical part of the copper block provides a downward-facing heated circular surface. Three different diameters of D = 0.04, 0.02, and 0.01 m were employed as the heated surface. The circumferential surface of this cylindrical part is insulated with a bakelite sleeve (in the case of water, a ceramic sleeve was employed), and the clearance between the cylindrical part and the insulator is filled with plastic packing to prevent contact between the refrigerant vapor and the very high-temperature inner region of the copper block, thereby avoiding thermal decomposition of the refrigerant. The interior of the heating cell is kept at a pressure of 0.02 MPa lower than that of the inside of the pressure vessel by a N_2 tank (17) using a differential pressure gage (16) to compensate for the force acting on the copper block. The test liquid, which is pressurized by a peripheral pump (8) and then adjusted with the nozzle heater (7) up to the saturation temperature corresponding to the internal pressure of the vessel, flows out of a nozzle (4) of inner diameter d = 0.002 m, impinging at the center of the heated disk. The velocity of the liquid jet at the nozzle exit u can be determined by measuring the pressure difference between the inlet and outlet of the nozzle by means of a differential pressure transducer (11). The lower half of the inside of the pressure vessel is filled with the test liquid (about 0.4 to 0.5 m deep), which is heated by a vessel heater (5), and the vapor above the liquid is condensed by a pair of cooling coils (6). As a result, the prescribed saturation pressure inside the vessel is maintained by controlling the vessel heater as well as the cooling coils.

The heat flux across the heated disk as well as the temperature of the heated surface is determined by means of three chromel-alumel thermocouples set up at regular intervals along the axis of the cylindrical part of the copper block. The actual thermal conductivity of this copper block, which must be known to calculate the heat flux, was carefully determined in a preliminary experiment in the same way as that of [1, 2]. The heat flux can be determined with ± 5 percent from the two following observations: The values of the actual thermal for several heat fluxes in the preliminary experiment are quite in agreement within ± 5 percent, and the heat loss in the preliminary experiment is nearly equal to that in the actual experiment. In this experiment, the distance from the nozzle exit to the heated disk was always kept at 0.01 m to avoid the problem that the jet velocity can be decreased for an upward direction opposite to the gravitational force.

The critical heat flux is determined by the following means: The power to the heater in the copper block is increased in increments that are less than 5 percent of each preceding heat flux, and finally a point is reached where the heated surface temperature runs away. At this point, the CHF is determined with an uncertainty of 0 to 5 percent, apart from the uncertainty of ± 5 percent when determining the heat flux.

3 Experimental Data of CHF

Figure 4 represents a variation of the CHF data for R12 measured in this experiment with jet velocity u. The solid line in Fig. 4 is equation (1) predicting the CHF in the V-regime for each pressure. The CHF data of water and R113 obtained in this experiment are omitted here because the fact that the CHF for $\rho_l/\rho_v > 67.1$ can be predicted with deviations of ± 20 percent by equation (1) was already reported in [7].

It can be seen in Fig. 4 that at pressures of 0.57 to 2.04 MPa, corresponding to ρ_l/ρ_v = 41.25 to 8.79, the CHF data for low velocities of u are still predicted by equation (1), while CHF data for high velocities gradually deviate from the prediction of equation (1) and tend to become constant for any additional increase in the velocity. Thus, the value of q_{co} is nearly constant, independent of u. In addition, the CHF data at high pressures of P = 2.29 to 2.78 MPa (reduced pressure P_r = 0.56 to 0.67) corresponding to ρ_l/ρ_v = 7.34 to 5.29, again increase with increasing velocity u, but the tendency is a bit different from that of the CHF predicted by equation (1). In other words, two characteristic regimes, which are different from two existing ones, namely the L- and V-regimes, appear at moderate and high pressures, the one regime of CHF being approximately invariant of u and the other regime of CHF at high pressure. In this paper, for simplicity, the CHF which is approximately invariant CHF with u will be called the CHF in the same I-regime as named in [4]. Although the I-regime is named for q_{co} invariant with u in [4], the CHF which appears at high pressure and increases again with an increase in u will be called the CHF in the HP-regime. Here, the name of the I-regime was derived from the fact [4] that the q_{co} data only for D/d = 5 were invariant with u, but from Fig. 4, it is seen that the q_{co} data for D/d = 10 and 20 at moderate pressure are weekly dependent on u rather than invariant with u.

Incidentally, as for CHF in forced convection boiling in a uniformly heated tube, it may be of interest to know that the CHF characteristic changes dependent on the system pressure, the density ratio ρ_l/ρ_v, the ratio of the tube diameter to its heated length d/l, and the Weber number [16-19] and, for example, is categorized into four kinds in [17] or three kinds in [18].

4 Correlation of CHF

The CHF in the I- and HP-regimes will be discussed here since all the CHF data in the V-regime including a part of the CHF data measured in this experiment were already detailed in [7]. One may deal with the CHF data in the I- and HP-regimes on the basis of four dimensionless parameters in equation (1), which would first give a clue for analyzing the CHF data in both regimes. As a result, an equation similar in form for both CHF regimes can be given as follows:

Downloaded 17 Dec 2010 to 193.140.21.150. Redistribution subject to ASME license or copyright; see http://www.asme.org/terms/Terms_Use.cfm

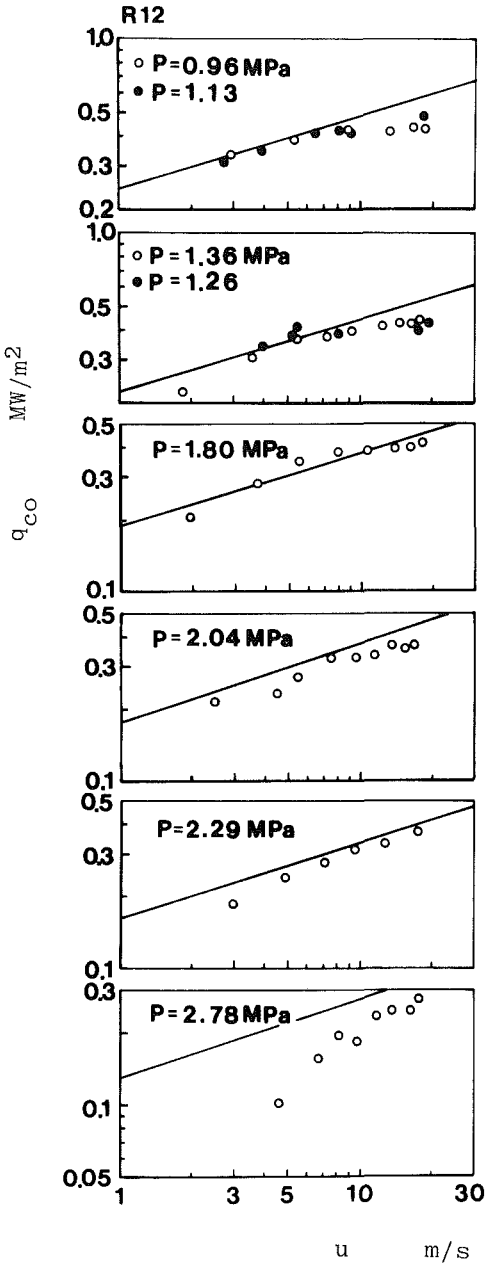

Fig. 4(*a*) Relation between CHF and jet velocity obtained for R12 (D = 0.04 m)

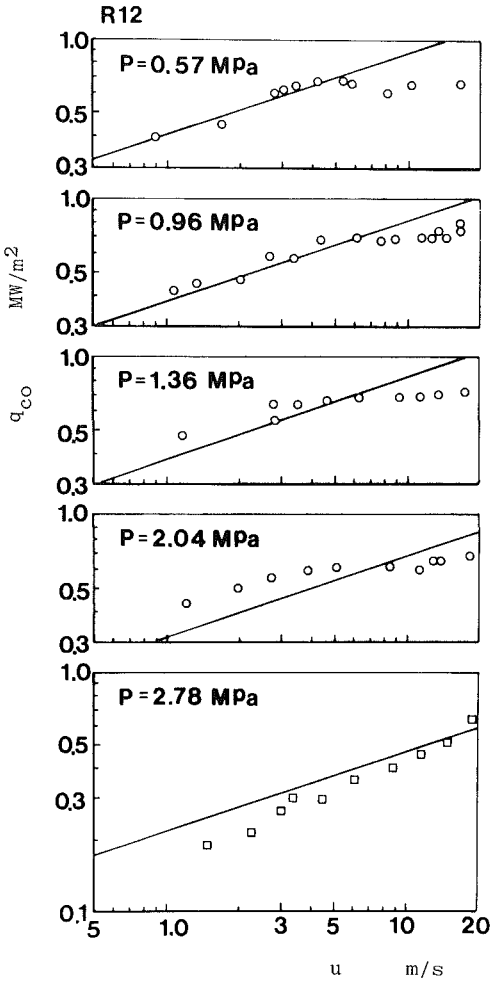

Fig. 4(*b*) Relation between CHF and jet velocity obtained for R12 (D = 0.02 m)

$$\frac{q_{co}}{\rho_l H_{fg} u} = C \left(\frac{\rho_v}{\rho_v}\right)^m \left(\frac{2\sigma}{\rho_l u^2 (D-d)}\right)^n (1+D/d)^k \qquad (6)$$

The exponents m, n, and k and the constant C can be determined by means of the least-squares method to superpose the CHF data in each regime into each single group, where the q_{co} data in the I-regime are 117 in number including 29 of the q_{co} data in [4], while the q_{co} data in the HP-regime are only 24 in number. This procedure gives $m = 0.466$, $n = 0.421$, $k = -0.303$, and $C = 0.691$ for the CHF in the I-regime and $m = 1.27$, $n = 0.28$, $k = -1.01$, and $C = 0.172$ for the CHF in the HP-regime to yield equations (7) and (8) as folows:

For the I-regime:

$$\frac{q_{co}}{\rho_v H_{fg} u} = 0.691 \left(\frac{\rho_l}{\rho_v}\right)^{0.466} \left(\frac{2\sigma}{\rho_l u^2 (D-d)}\right)^{0.421} (1+D/d)^{-0.303} \qquad (7)$$

Table 2 Exponents and constant in equation (6) for each regime

	m	n	k	C
V-regime	0.645	0.343	-0.364	0.221
I-regime	0.466	0.421	-0.303	0.691
HP-regime	1.27	0.28	-1.01	0.172

For the HP-regime:

$$\frac{q_{co}}{\rho_v H_{fg} u} = 0.172 \left(\frac{\rho_l}{\rho_v}\right)^{1.27} \left(\frac{2\sigma}{\rho_l u^2 (D-d)}\right)^{0.28} (1+D/d)^{-1.01} \qquad (8)$$

The exponents m, n, and k and the constant c are listed for each regime in Table 2 for convenience. It should be noted that the 24 data of q_{co} may be not enough to introduce equation (8).

Figures 5, 6, and 7 show a comparison of equations (1), (7), and (8) with the q_{co} data of R12 measured for D = 0.04, 0.02, and 0.01 m and with the q_{co} data of R12 measured by Katto and Shimizu [4], respectively. In Figs. 5, 6, and 7, the capital letter A gives the intersecting point between equations (1) and (7), the capital letter B between equations (7) and (8), and the capital letter C between equations (8) and (1). Light solid lines in Figs. 5, 6, and 7 are the prediction of Sharan and Lienhard's equation (4). A light solid line perpendicular to abscissa gives the limiting value on the left side of which equation (4) is applicable for predicting the CHF.

The fact that not only all the q_{co} data of ρ_l/ρ_v = 38.83 for

Downloaded 17 Dec 2010 to 193.140.21.150. Redistribution subject to ASME license or copyright; see http://www.asme.org/terms/Terms_Use.cfm

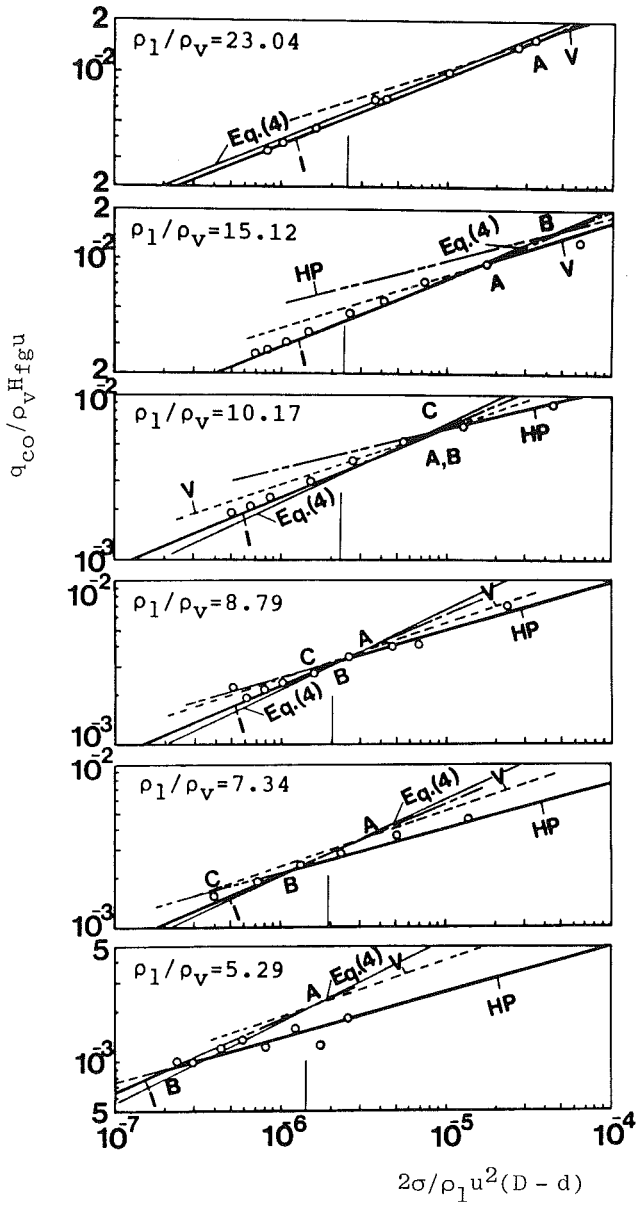

Fig. 5 Generalized graphic representation of q_{co} data for R12: V: V-regime, I: I-regime, HP: HP-regime, *A:* intersection between equations (1) and (7), *B:* intersection between equations (7) and (8), *C:* intersection between equations (8) and (1) (D = 0.04 m)

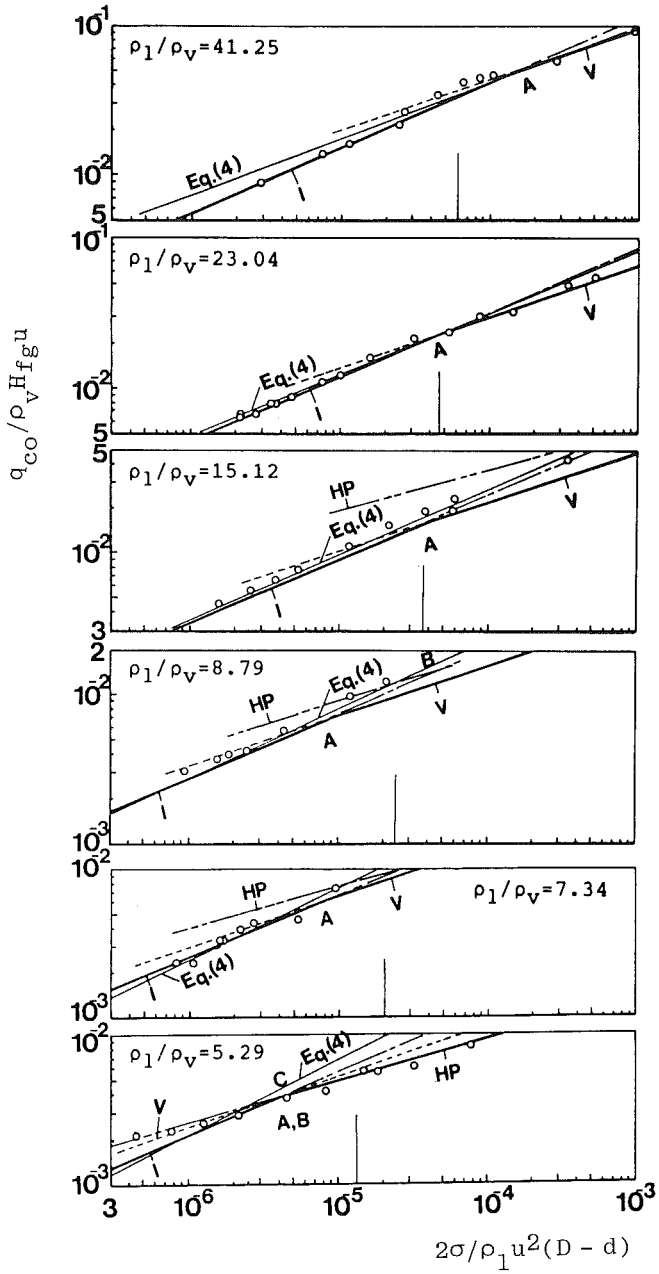

Fig. 6 Generalized graphic representation of q_{co} data for R12: V: V-regime, I: I-regime, HP: HP-regime, *A:* intersection between equations (1) and (7), *B:* intersection between equations (7) and (8), *C:* intersection between equations (8) and (1) (D = 0.02 m)

D = 0.01 m but also all the q_{co} data of $\rho_l/\rho_v > 67.1$, except for the CHF in the L-regime, are predicted by equation (1), enables us to guess that the CHF only in the V-regime takes place at larger values than a certain value of ρ_l/ρ_v which would be determined by a function of D/d and $2\sigma/\rho_l u^2(D-d)$ concerning the flow state of the vapor and liquid on the heated surface. Figures 5 and 6 show that the CHF in the V- and I-regimes coexists for $\rho_l/\rho_v < 41.25$ in the case of D = 0.02 and 0.04 m. The q_{co} data of D = 0.02 and 0.04 m in this coexisting region are predicted by the smaller one of the values calculated from equations (1) and (7). Furthermore, when the ordinate value of the point B becomes smaller than that of the point A with decreasing density ratio ρ_l/ρ_v, the CHF in the HP-regime appears in place of the CHF in the V-regime. As ρ_l/ρ_v decreases, the CHF in the HP-regime invades the CHF in the I-regime. The CHF in the HP-regime is apt to occur in the larger diameter of the heated surface. It may be of interest to find out in Figs. 5 and 6 that the q_{co} data for ρ_l/ρ_v = 5.29 and D = 0.02 m and for ρ_l/ρ_v 7.34 and D = 0.04 m seem to be predicted by equation (8), although equation (8) gives the larger value than equation (7) in the left region of the point B. It may be of interest to note that the same result was reported for the CHF in forced convection boiling in vertical uniformly heated round tubes by Katto and Ohno [17] in which such a reverse occurs at ρ_l/ρ_v = 6.67.

Next, according to the estimation from the results for D = 0.04 and 0.02 m mentioned above, the CHF for D = 0.01 m in the V- and I-regimes should coexist in the range of ρ_l/ρ_v = 18.39 to 5.29, but all the q_{co} data except for ρ_l/ρ_v = 15.12 and 8.79 fall in the CHF in the I-regime. In addition, another problem exists ion the way that the CHF in the HP-regime would take place for ρ_l/ρ_v = 5.29 when comparing Figs. 5, 6, and 7. These discrepancies should be made clear in later studies. As for the boundaries of the CHF in the respective

Downloaded 17 Dec 2010 to 193.140.21.150. Redistribution subject to ASME license or copyright; see http://www.asme.org/terms/Terms_Use.cfm

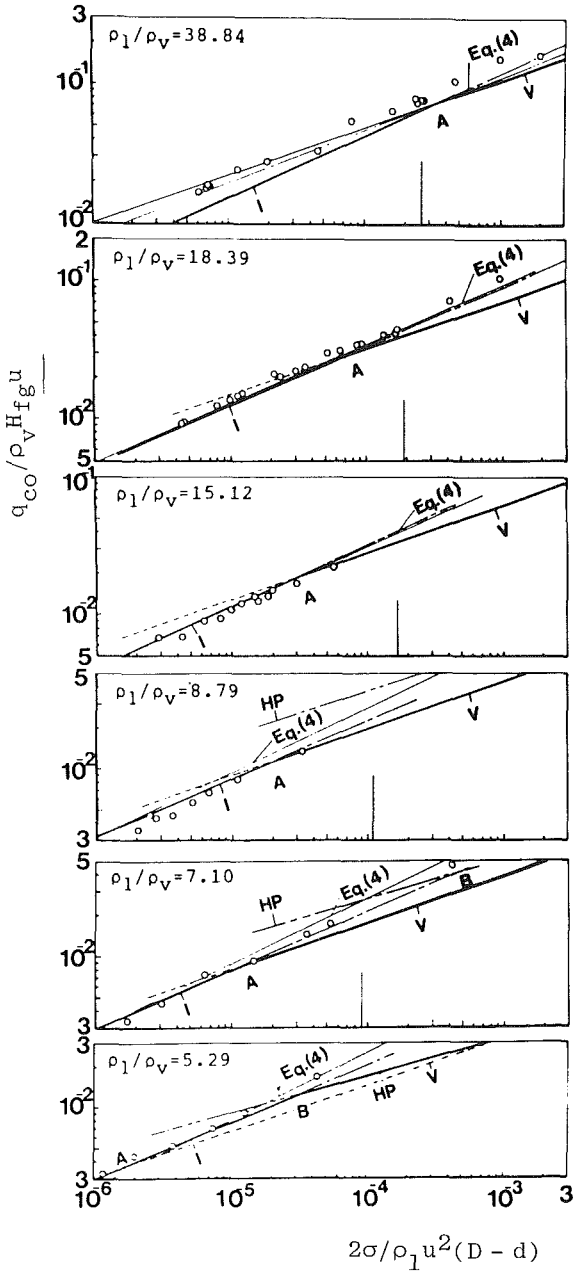

Fig. 7 Generalized graphic representation of q_{co} data for R12: V: V-regime, I: I-regime, HP: HP-regime, *A:* intersection between equations (1) and (7), *B:* intersection between equations (7) and (8), *C:* intersection between equations (8) and (1) (D = 0.01 m)

regimes, the CHF phenomenon relates closely to the flow state of vapor and liquid on the heated surface, so more advanced study will be necessary to determine the boundaries.

Incidentally, it may be of interest to compare equation (4) with the q_{co} data for $\rho_l/\rho_v < 41.25$. As shown by the light solid lines in Figs. 5, 6, and 7, equation (4) predicts the q_{co} data in the V- and I-regimes including the q_{co} data within the range where equation (4) cannot be applicable, with a tolerant agreement. In the HP-regime, however, the q_{co} value calculated from equation (4), as well as its tendency, is significantly different from those of the q_{co} data, so that it is necessary to change $A(r)$ again. The Lienhard et al. concept [12, 13, 15] that the q_{co} data are predicted by only one generalized correlation is interesting, but it would be rather difficult to elucidate its character because the CHF is related closely to the flow state where the CHF takes place.

5 Conclusions

1 The CHF in saturated forced convection boiling with an impinging jet was measured within the experimental range of the density ratio ρ_l/ρ_v = 5.3 to 41.25 and the reciprocal of the Weber number $2\sigma/\rho_l u^2(D-d) = 2 \times 10^{-7}$ to 2×10^{-3}.

2 A new type of CHF characteristic is found which is different from two existing types of CHF in the V- and L-regimes, and there seems to be a possibility that the new type of CHF can be divided into two characteristic regimes called the CHF in the I- and HP-regimes.

3 The CHF data in the I- and HP-regimes are predicted by equations (7) and (8), respectively.

Acknowledgments

The author would like to acknowledge emeritus Prof. Y. Katto, University of Tokyo, for his valuable advice during this work.

References

1 Katto, Y., and Monde, M., "Study of Mechanism of Burn-out in a High Heat-Flux Boiling System With an Impinging Jet," *Proc. 5th Int. Heat Transfer Conf.*, Paper No. B6.2, 1974, pp. 245-249.

2 Monde, M., and Katto, Y., "Burnout in a High Heat-Flux Boiling System With an Impinging Jet," *International Journal of Heat Mass Transfer*, Vol. 21, 1978, pp. 295-305.

3 Monde, M., "Burnout Heat Flux in Saturated Forced Convection Boiling With an Impinging Jet," *Heat Transfer—Japanese Research*, Vol. 9, 1980, pp. 31-41.

4 Katto, Y., and Shimizu, M., "Upper Limit of CHF in the Saturated Forced Convection Boiling on a Heated Disk With a Small Impinging Jet," ASME JOURNAL OF HEAT TRANSFER, Vol. 101, 1979, pp. 265-269.

5 Haramura, Y., and Katto, Y., "A New Hydrodynamic Model of Critical Heat Flux Applicable Widely to Both Pool and Forced Convection Boiling on Submerged Bodies in Saturated Liquids," *International Journal of Heat Mass Transfer*, Vol. 26, 1983, pp. 389-399.

6 Katto, Y., "Critical Heat Flux in Forced Convection Flow," *Proc. of ASME-JSME Thermal Engineering Joint Conference*, Vol. 3, 1983, pp. 1-10.

7 Monde, M., "Critical Heat Flux in Saturated Forced Convective Boiling on a Heated Disk With an Impinging Jet – A New Generalized Correlation," *Wärme- und Stoffübertragung*, Vol. 19, 1985, pp. 205-210.

8 Katto, Y., and Kunihiro, M., "Study of the Mechanism of Burnout in Boiling System of High Burnout Heat Flux," *Bull. JSME*, Vol. 16, 1973, pp. 1357-1366.

9 Katsuta, M., "Boiling Heat Transfer of Thin Liquid With an Impinging Jet," *Proc. of 14th National Heat Transfer Symposium of Japan*, 1980, pp. 154-157.

10 Katsuta, M., "Boiling Heat Transfer of Thin Liquid Film With an Impinging Jet," Paper No. 780-18, 1978, pp. 68-70.

11 Monde, M., and Okuma, Y., "Critical Heat Flux in Saturated Forced Convective Boiling on a Heated Disk With an Impinging Jet – CHF in L-regime, *International Journal of Heat Mass Transfer*, Vol. 28, 1985, pp. 547-552.

12 Lienhard, J. H., and Eichhorn, R., "On Predicting Boiling Burnout for Heaters Cooled Liquid Jets," *International Journal of Heat Mass Transfer*, Vol. 22, 1979, pp. 774-776.

13 Lienhard, J. H., and Hasan, M. Z., "Correlation of Burnout Data for Disk Heaters Cooled by Liquid Jets," ASME JOURNAL OF HEAT TRANSFER, Vol. 101, 1979, pp. 383-384.

14 Monde, M., Private Communications, Mar., July 1983.

15 Sharan, A., and Liehnard, J. H., "On Predicting Burnout in the Jet Configuration," ASME JOURNAL OF HEAT TRANSFER, Vol. 107, 1985, pp. 398-401.

16 Katto, Y., "Toward the Systematic Understanding of CHF of Forced Convection (Case of Uniformly Heated Round Tubes)," *Japan-US Heat Transfer Joint Seminar in Tokyo*, 1980, pp. 53-60.

17 Katto, Y., and Ohno, H., "An Improved Version of the Generalized Correlation of Critical Heat Flux for the Forced Convective Boiling in Uniformly Heated Vertical Tubes," *International Journal of Heat Mass Transfer*, Vol. 27, 1984, pp. 1641-1648.

18 Nishikawa, K., et al., "Experimental Investigation of Critical Heat Flux in Forced Convection Boiling of Freon in a Tube at High Subcritical Pressure," *Proceedings of 7th International Heat Transfer Conference*, Munich, 1982, pp. 321-326.

19 Compolunghi, F., et al., "Burn-out Power in Once-through Tubular Steam Generators," *Proceedings of 5th International Heat Transfer Conference*, Tokyo, 1974, pp. 280-284.

Downloaded 17 Dec 2010 to 193.140.21.150. Redistribution subject to ASME license or copyright; see http://www.asme.org/terms/Terms_Use.cfm

Two-Phase Boundary Layer Treatment for Subcooled Free-Convection Film Boiling Around a Body of Arbitrary Shape in a Porous Medium

A. Nakayama
Associate Professor of Energy and Mechanical Engineering.

H. Koyama
Professor of Energy and Mechanical Engineering.

F. Kuwahara
Graduate Student.

Department of Energy and Mechanical Engineering, Shizuoka University, 3-5-1 Johoku, Hamamatsu, 432 Japan

The two-phase boundary layer theory was adopted to investigate subcooled free-convection film boiling over a body of arbitrary shape embedded in a porous medium. A general similarity variable which accounts for the geometric effect on the boundary layer length scale was introduced to treat the problem once for all possible two-dimensional and axisymmetric bodies. By virtue of this generalized transformation, the set of governing equations and boundary conditions for an arbitrary shape reduces into the one for a vertical flat plate already solved by Cheng and Verma. Thus, the numerical values furnished for a flat plate may readily be tranlsated for any particular body configuration of concern. Furthermore, an explicit Nusselt number expression in terms of the parameters associated with the degrees of subcooling and superheating has been established upon considering physical limiting conditions.

Introduction

Parmentier (1979) studied free-convection film boiling over a vertical flat plate embedded in a porous medium, in terms of its application to dike intrusion in an aquifer. Upon tracing possible phase-change paths in the pressure–temperature diagram, he argued that a distinct, smooth interface exists between the vapor film and the surrounding liquid, and exploited the classical boundary layer approximations to simplify the problem. The effects of subcooling of the surrounding liquid on the boiling heat transfer characteristics were investigated by Cheng and Verma (1981) using the so-called "two-phase boundary layer concept," successfully employed by Koh (1962) and Nishikawa and Ito (1966) for film boiling on a flat plate in Newtonian fluids.

The previous studies, however, are restricted to the case of a flat plate. Since cylindrical and spherical shapes of canisters were proposed for nuclear waste disposal in subseabeds, considerable attention has been directed toward analyzing convective heat transfer from curved surfaces of heated bodies embedded in a fluid-saturated porous medium. An elegant similarity transformation was introduced by Merkin (1979) to show that a similarity solution exists for the problem of single-phase free convection flow around a two-dimensional isothermal body of arbitrary shape. This transformation has been extended by the authors (1986) to study a more general case, namely, a nonisothermal body of arbitrary shape.

In this paper, we consider the problem of subcooled free-convection film boiling over a body of arbitrary shape within a porous medium. The two-phase boundary layer treatment commonly used in Newtonian fluid flows is invoked along with a general similarity transformation procedure. It will be shown that the governing equations and boundary conditions for a two-dimensional or axisymmetric isothermal body of arbitrary shape can be transformed into those for a vertical flat plate. Thus, the numerical values furnished by Cheng and Verma (1981) for a flat plate are readily available for two-dimensional and axisymmetric bodies of arbitrary shape.

Furthermore, by considering possible physical limiting conditions, an effort is made to express the local Nusselt number explicitly in terms of the parameters associated with the degrees of subcooling and superheating, so that their effects on the heat transfer function may be appreciated more directly.

Governing Equations, Boundary and Matching Conditions

Figure 1 shows the physical model and its boundary layer coordinates (x, y). The function $r(x)$ describes the geometry of a body which may be either plane or axisymmetric, and its wall is heated up to T_w, higher than the saturation temperature T_s corresponding to its system pressure. Thus, a thin film of vapor flowing upward forms to cover the heated

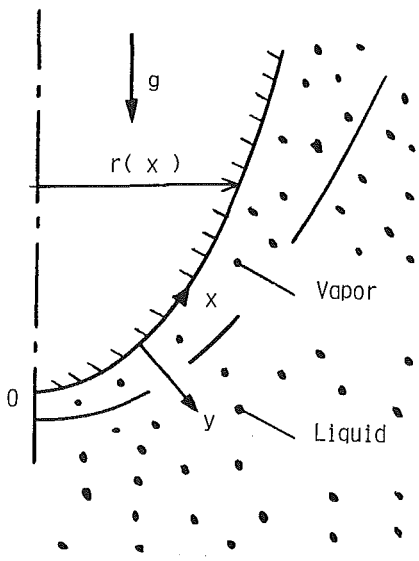

Fig. 1 Physical model and its coordinates

Contributed by the Heat Transfer Division for publication in the JOURNAL OF HEAT TRANSFER. Manuscript received by the Heat Transfer Division October 14, 1986.

 Copyright © 1987 by ASME

Downloaded 17 Dec 2010 to 193.140.21.150. Redistribution subject to ASME license or copyright; see http://www.asme.org/terms/Terms_Use.cfm

body surface. Since the surrounding liquid is subcooled to its temperature T_e ($< T_s < T_w$), a liquid boundary layer also develops adjacent to the liquid–vapor interface due to a buoyancy force. Radiation effects are assumed to be negligible.

With the usual boundary layer and Boussinesq approximations, the set of governing equations, namely, the continuity equation, Darcy's law, and the energy equation may be given for each phase as follows:

For the vapor in the porous medium ($0 \le y < \delta$):

$$\frac{\partial}{\partial x} r^* u + \frac{\partial}{\partial y} r^* v = 0 \tag{1}$$

$$u = \frac{(\rho_f - \rho) K}{\rho \nu} g_x \tag{2}$$

and

$$u \frac{\partial T}{\partial x} + v \frac{\partial T}{\partial y} = \alpha \frac{\partial^2 T}{\partial y^2} \tag{3}$$

For the liquid in the porous medium ($y > \delta$):

$$\frac{\partial}{\partial x} r^* u + \frac{\partial}{\partial y} r^* v = 0 \tag{4}$$

$$u = \frac{\beta (T - T_e) K}{\nu_f} g_x \tag{5}$$

and

$$u \frac{\partial T}{\partial x} + v \frac{\partial T}{\partial y} = \alpha_f \frac{\partial^2 T}{\partial y^2} \tag{6}$$

where

$$r^* = \begin{cases} 1 : \text{plane flow} \\ r(x) : \text{axisymmetric flow} \end{cases} \tag{7a}$$

and

$$g_x = g \left[1 - \left(\frac{dr}{dx} \right)^2 \right]^{1/2} \tag{7b}$$

The boundary conditions are given by

$$y = 0: \quad v = 0, \quad T = T_w \tag{8a,b}$$

$$y \to \infty: \quad u = 0 \quad (T = T_e) \tag{8c}$$

The matching conditions at the liquid–vapor interface ($y = \delta$) are given by

$$T = T_s \tag{9a}$$

$$\rho \left(u \frac{d\delta}{dx} - v \right) = \rho_f \left(u \frac{d\delta}{dx} - v \right)_f \tag{9b}$$

and

$$h_{fg} \rho \left(u \frac{d\delta}{dx} - v \right) = -k \frac{\partial T}{\partial y} + k_f \left(\frac{\partial T}{\partial y} \right)_f \tag{9c}$$

where equations (9*a*), (9*b*), and (9*c*) represent the continuity of temperature, conservation of mass, and energy balance at the liquid–vapor interface, respectively. In the preceding equations, u and v are the Darcian velocity components in the x and y directions and T is the local temperature. The tangential component of the acceleration due to gravity g is indicated by g_x, which is related to the local surface inclination by equation (7*b*). Furthermore, K is the permeability; k, the equivalent thermal conductivity; ν, the kinematic viscosity; α, the equivalent thermal diffusivity. The subscript f denotes the quantities associated with the surrounding liquid, while no subscript is assigned for the vapor phase. h_{fg} is the latent heat of vaporization.

Similarity Transformation and Solution

Let us introduce the stream function ψ such that the continuity equation (1) may automatically be satisfied

$$u = \frac{1}{r^*} \frac{\partial \psi}{\partial y} \tag{10a}$$

$$v = -\frac{1}{r^*} \frac{\partial \psi}{\partial x} \tag{10b}$$

Merkin (1979) introduced a similarity transformation for the single-phase problem of free convection in a porous medium. His transformation has been generalized by the authors (1986) for the case of a nonisothermal body of arbitrary shape. These transformations may be extended to the two-phase flow problem of the present concern as

$$\psi = \alpha r^* (\mathrm{Ra}_x I)^{1/2} f(\eta) \tag{11a}$$

$$T - T_s = \theta(\eta)(T_w - T_s) \tag{11b}$$

$$\eta = \frac{y}{x} (\mathrm{Ra}_x / I)^{1/2} \tag{11c}$$

where equations (11*a*), (11*b*), and (11*c*) define f, θ, and η, respectively, and

$$\mathrm{Ra}_x = \frac{K g_x x (\rho_f - \rho)}{\nu \alpha \rho} \tag{12a}$$

$$I(x) = \frac{\int_0^x g_x r^{*2} dx}{g_x r^{*2} x} \tag{12b}$$

Nomenclature

f = dimensionless stream function
g = acceleration due to gravity
h_{fg} = latent heat of vaporization
I = function associated with a body geometry
k = equivalent thermal conductivity weighted by the porosity
K = permeability
Nu_x = local Nusselt number
q_w = local surface heat flux
r = function representing wall geometry
r^* = 1 for plane flow; r for axisymmetric flow
Ra_x = local Rayleigh number
T = temperature
u, v = Darcian velocity components
x, y = boundary layer coordinates
α = thermal diffusivity $k/(\rho C_p)_{\text{fluid}}$
β = coefficient of thermal expansion
γ = ratio of a horizontal axis to a vertical axis
η = similarity variable
θ = dimensionless temperature
ν = kinematic viscosity
ρ = density
ψ = stream function

Subscripts

e = external
f = liquid
r = reference
s = saturation
w = wall
x = local

Downloaded 17 Dec 2010 to 193.140.21.150. Redistribution subject to ASME license or copyright; see http://www.asme.org/terms/Terms_Use.cfm

Ra_x is the local Rayleigh number and η is the proposed similarity variable. The function I as defined by equation (12b) adjusts the scale in the normal direction according to a given body geometry.

In terms of these transformed variables, the Darcian velocities in the vapor layer are

$$u=\frac{\alpha}{x}\,\mathrm{Ra}_x f' \tag{13a}$$

and

$$v=-\frac{\alpha}{x}(\mathrm{Ra}_x/I)^{1/2}\left[\left(I\frac{d\ln g_x r^*}{d\ln x}-\frac{1}{2}\right)\eta f'+\frac{1}{2}f\right] \tag{13b}$$

where the primes denote differentiation with respect to η. Substitution of equation (13a) into equation (2) yields

$$f'=1 \tag{14a}$$

This may readily be integrated as

$$f=\eta \tag{14b}$$

using the boundary condition

$$f(0)=0 \tag{14c}$$

which is equivalent to equation (8a) with (13b) substituted into it.

The preceding results may be substituted into the energy equation (3). After considerable manipulation, we obtain a remarkably simple expression

$$\theta''+\frac{1}{2}\eta\theta=0 \tag{15}$$

The foregoing equation is subject to the boundary conditions, namely,

$$\theta(0)=1 \tag{16a}$$

and

$$\theta(\eta_\delta)=0 \tag{16b}$$

which are equivalent to equations (8b) and (8c), respectively. The preceding equation (15) with equations (16) has the exact solution given by

$$\theta(\eta)=1-\frac{\mathrm{erf}(\eta/2)}{\mathrm{erf}(\eta_\delta/2)} \tag{17}$$

where

$$\eta_\delta=\frac{\delta}{x}(\mathrm{Ra}_x/I)^{1/2} \tag{18}$$

The unknown dimensionless vapor thickness η_δ must be determined in consideration of the liquid boundary layer covering the vapor film. The continuity equation (4) for the liquid layer may readily be satisfied as we introduce the stream function ψ as defined by equations (10). For the liquid layer, the following transformations similar to those adopted for the vapor layer are employed:

$$\psi=\alpha_f r^*(\mathrm{Ra}_{xf}I)^{1/2}f_f(\eta_f) \tag{19a}$$

$$T-T_e=\theta_f(\eta_f)(T_s-T_e) \tag{19b}$$

$$\eta_f=\frac{y}{x}(\mathrm{Ra}_{xf}/I)^{1/2} \tag{19c}$$

where equations (19a), (19b), and (19c) define f_f, θ_f, and η_f, respectively, and

$$\mathrm{Ra}_{xf}=\frac{K\beta(T_s-T_e)g_x x}{\alpha_f\nu_f} \tag{20}$$

Upon substituting equation (19a) into equations (10), we obtain

$$u=\frac{\alpha f}{x}\,\mathrm{Ra}_{xf}F_f' \tag{21a}$$

and

$$v=-\frac{\alpha_f}{x}(\mathrm{Ra}_{xf}/I)^{1/2}\left[\left(I\frac{d\ln g_x r^*}{d\ln x}-\frac{1}{2}\right)\eta_f f_f'+\frac{1}{2}f_f\right] \tag{21b}$$

The primes here indicate differentiation with respect to η_f. Using equations (21a) and (19b), the Darcy's law given by equation (5) may be transformed into

$$f_f'=\theta_f \tag{22}$$

These expressions may be substituted into the energy equation (6). After some manipulation, the energy equation may be reduced to

$$f_f'''+\frac{1}{2}f_f f_f''=0 \tag{23}$$

The boundary condition (8c) and the matching condition (9a) may be rewritten as

$$f_f'(\infty)=0 \tag{24a}$$

and

$$f_f'(\eta_{f\delta})=1 \tag{24b}$$

where

$$\eta_{f\delta}=\frac{\delta}{x}(\mathrm{Ra}_{xf}/I)^{1/2}=\left[\frac{\alpha\nu\rho\beta(T_s-T_e)}{\alpha_f\nu_f(\rho_f-\rho)}\right]^{1/2}\eta_\delta \tag{24c}$$

The matching condition for the mass flux given by equation (9b) may also be rearranged in a similar fashion. By substituting equations (13), (18), (21), and (24c) into (9b), we have

$$f_f(\eta_{f\delta})=R\eta_\delta \tag{25a}$$

where

$$R=\frac{\rho\alpha}{\rho_f\alpha_f}\left(\frac{\alpha_f\nu_f(\rho_f-\rho)}{\alpha\nu\rho\beta(T_s-T_e)}\right)^{1/2} \tag{25b}$$

is related to the ratio of the vaporization mass to the liquid mass entrained within the liquid boundary layer. The last matching condition (9c) may be transformed by substituting equation (17) as

$$\mathrm{Sup}=\sqrt{\pi}\,\exp(\eta_\delta^2/4)\mathrm{erf}(\eta_\delta/2)\left[\frac{\eta_\delta}{2}-f_f''(\eta_{f\delta})\frac{\mathrm{Sub}}{R}\right] \tag{26a}$$

where

$$\mathrm{Sup}=Cp(T_w-T_s)/h_{fg} \tag{26b}$$

and

$$\mathrm{Sub}=Cp_f(T_s-T_e)/h_{fg} \tag{26c}$$

It should be noted that the resulting set of equations, namely, equations (23), (24a), (24b), (25a), and (26a), is identical to that obtained by Cheng and Verma (1981) for the specific case of a vertical flat plate. Thus, the numerical calculation results furnished by them are directly applicable for any two-dimensional or axisymmetric shape of concern.

In principle, the differential equation (23) may be solved for a given set of parameters, namely, Sub, Sup, and R. The dimensionless vapor thickenss η_δ, however, enters into the boundary condition (25a) and the matching condition (26a) which is implicit in η_δ. (Note that $f_f''(\eta_{f\delta})$ appearing in equation (26a) is also a function of η_δ.) Such an approach will require some kind of an iterative procedure. Cheng and Verma employed an inverse method in which they determined Sup from equation (26a) after integrating equation (23) for given Sub, R, and η_δ (instead of Sup). It is also interesting to note, when integrating equation (23), we may conveniently set $\eta_{f\delta}$ = 0, since the value of $\eta_{f\delta}$ does not enter into either the differential equation or the boundary conditions.

Local Nusselt Number and Wall Heat Flux

Once the dimensionless vapor film thickness η_δ is known in this way, the local Nusselt number of interest can be evaluated from

Downloaded 17 Dec 2010 to 193.140.21.150. Redistribution subject to ASME license or copyright; see http://www.asme.org/terms/Terms_Use.cfm

$$\mathrm{Nu}_x = \frac{q_w x}{k(T_w - T_s)} = -\theta'(0)(\mathrm{Ra}_x/I)^{1/2} = \frac{(\mathrm{Ra}_x/I)^{1/2}}{\sqrt{\pi}\ \mathrm{erf}(\eta_\delta/2)} \tag{27}$$

where q_w is the wall heat flux.

By virtue of the proposed transformation, the results on a vertical flat plate can be translated to any particular two-dimensional or axisymmetric body of arbitrary shape. This can be done by evaluating the function I for the given geometry. For example, in the cases of flat plates, vertical cones, horizontal ellipses, and ellipsoids (including a horizontal circular cylinder and a sphere), we evaluate I according to its definition given by equation (12*b*) as

$$\frac{1}{I} = \begin{cases} 1\text{: vertical plates} & (28a) \\ 3\text{: vertical cones pointing downward} & (28b) \\ \dfrac{(x/L_r)\sin\phi}{(1-\cos\phi)(\sin^2\phi+\gamma^2\cos^2\phi)^{1/2}}\text{: horizontal ellipses} & (28c) \\ \dfrac{3(x/L_r)\sin^3\phi}{(\cos^3\phi-3\cos\phi+2)(\sin^2\phi+\gamma^2\cos^2\phi)^{1/2}}\text{: ellipsoids} & (28d) \end{cases}$$

where

$$\phi = \sin^{-1}(r(x)/\gamma L_r) \tag{29a}$$

and

$$x/L_r = \int_0^\phi (\sin^2\phi+\gamma^2\cos^2\phi)^{1/2}d\phi \tag{29b}$$

The lower (front) and upper (rear) stagnation points are located at $\phi = 0$ and π, respectively. The symbol L_r denotes reference lengths such as a plate height and a vertical semi-axis of an ellipse or an ellipsoid, while γ stands for the ratio of a horizontal axis to a vertical axis.

Subsequently, the local surface heat flux may be given by

$$q^* = \begin{cases} (x/L_r)^{-1/2}\text{: vertical plates} & (30a) \\ (x/3L_r)^{-1/2}\text{: vertical cones pointing downward} & (30b) \\ \dfrac{\sin\phi}{[(1-\cos\phi)(\sin^2\phi+\gamma^2\cos^2\phi)]^{1/2}}\text{: horizontal ellipses} & (30c) \\ \dfrac{\sin^2\phi}{\left[\left(\frac{1}{3}\cos^3\phi-\cos\phi+\frac{2}{3}\right)(\sin^2\phi+\gamma^2\cos^2\phi)\right]^{1/2}}\text{: ellipsoids} & (30d) \end{cases}$$

where

$$q^* \equiv \left(\frac{q_w L_r}{(T_w-T_s)k}\right)\Big/\left(\frac{K(\rho_f-\rho)gL_r}{\rho\alpha\nu}\right)^{1/2}[-\theta'(0)] \tag{31}$$

The dimensionless heat flux q^* does not depend on any of the three parameters, Sup, Sub, or R. (These parameters, of course, change the value of $\theta'(0)$.) Naturally, the q^* distribution is the same as for the case of a saturated liquid (i.e., Sub = 0). It is interesting to note that the resulting heat flux distributions (given by equations (30)) are similar to those reported in our previous work (Nakayama and Koyama, 1987) on the single-phase free convection in a porous medium. Equations (30*c*) and (30*d*) indicate that q^* for a small γ (i.e., a slender body) exhibits a pattern similar to that of a vertical flat plate or cone (as given by equations (30*a*) and (30*b*)). For a large γ (i.e., a flat body), on the other hand, q^* increases away from the front stagnation point, attains a maximum as the flow accelerates due to a significant streamwise increase in g_x, but, as the boundary layer grows thick, it decreases downstream, resulting in a nonmonotonic variation of the wall heat flux.

Asymptotic Results and an Approximate Formula

The expression for the local Nusselt number given by equation (27) is still formidable to use, since the dimensionless vapor film thickness η_δ is a complex function of the three parameters, Sub, Sup, and R. Although we may appeal to the inverse method as suggested by Cheng and Verma, a lengthy calculation procedure will be required to find η_δ for a given set of parameters. In the following, we shall establish an approximate expression for the local Nusselt number by considering possible physical limiting conditions. The resulting approximate formula will be quite accurate, and more accessible to practical heat transfer evaluations.

Let us approximate equation (25*a*) as

$$f_f(\eta_{f\delta}) = 0 \tag{32}$$

The preceding approximation, namely, setting the stream function at the interface to zero, may be justified when the vapor film is sufficiently thin that the mass flowing within the vapor layer is not significantly large. We can integrate equation (23) using equation (32) instead of equation (25*a*) to obtain

$$f_f''(\eta_{f\delta}) = -0.444 \tag{33}$$

Upon substituting this value into equation (26*a*)

$$\mathrm{Sup} = \sqrt{\pi}\ \exp(\eta_\delta^2/4)\mathrm{erf}(\eta_\delta/2)\left(\frac{\eta_\delta}{2} + 0.444\,\frac{\mathrm{Sub}}{R}\right) \tag{34}$$

Now, η_δ depends on only two parameters, namely, Sup and the lumped parameter Sub/R, which is closely related to the ratio of the subcooled energy to the vaporization energy.

In Figs. 2, the η_δ curves generated by equation (34) are compared with those based on the exact solution. As may be seen from Fig. 2(*a*), the preceding approximation results in very little loss of accuracy for the case of small R. (Note that the approximation given by equation (32) becomes exact as $R \to 0$.) Even for the case of comparatively large R, namely, R = 1.414 (as shown in Fig. 2(*b*)), the approximation leads to a reasonable estimate of η_δ for a wide range of Sup. An error due to this approximation amounts to only 6 percent at Sup = 40. Equation (26*a*) also indicates that the approximate and exact curves becomes identical for Sub = 0, irrespective of the value of R. (It should be relevant to note that, for small Sup, film boiling might give over to transition or nucleate boiling.)

The corresponding heat transfer grouping $\mathrm{Nu}_x/(\mathrm{Ra}_x/I)^{1/2}$ is plotted in Fig. 3(*a*) for small R and Fig. 3(*b*) for large R, respectively. Both figures show excellent agreement between the curves based on the preceding approximation and those from the exact solution. As might be expected, the increase in the degree of liquid subcooling, Sub, results in thinning the vapor film, hence increasing the level of the heat transfer grouping. The foregoing comparison substantiates that only the two parameters, namely, Sup and Sub/R, essentially determine the local heat transfer rate.

Although a great simplification has been made in equation (34), the equation is still implicit in η_δ, and requires some iteration if we are to determine η_δ for given Sup and Sub/R. In

Downloaded 17 Dec 2010 to 193.140.21.150. Redistribution subject to ASME license or copyright; see http://www.asme.org/terms/Terms_Use.cfm

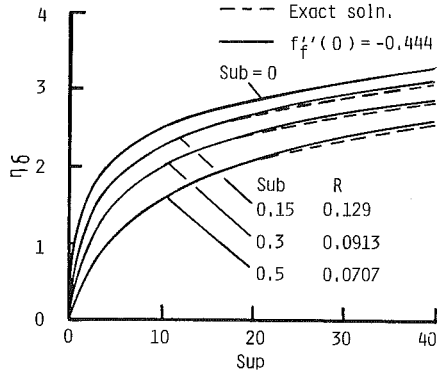

Fig. 2(a)

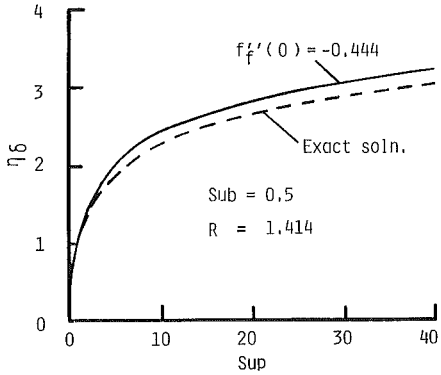

Fig. 2(b)

Fig. 2 Dimensionless vapor film thickness: (*a*) small *R*, (*b*) large *R*

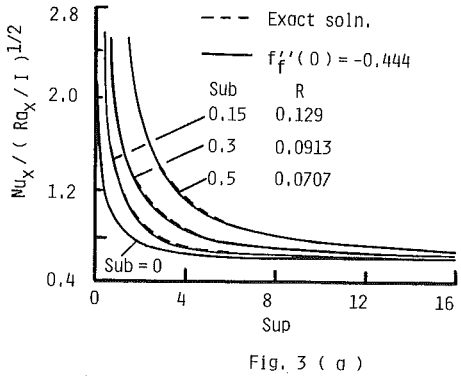

Fig. 3 (a)

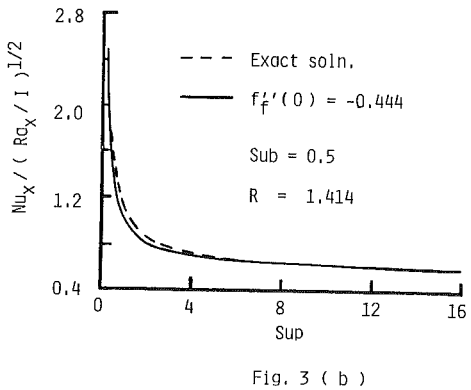

Fig. 3 (b)

Fig. 3 Local Nusselt number: (*a*) small *R*, (*b*) large *R*

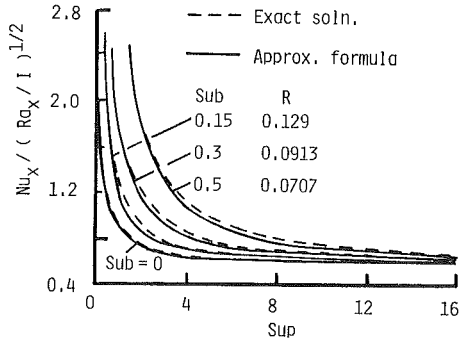

Fig. 4 Comparison of approximate formula and exact solution

order to obtain an explicit expression in terms of Sup and Sub/R, we consider two physical limiting conditions, namely, $\eta_\delta \to 0$ and $\eta_\delta \to \infty$. Under these two limiting conditions, equation (27) yields

$$\mathrm{Nu}_x/(\mathrm{Ra}_x/I)^{1/2} = \begin{cases} 1/\eta_\delta & \text{for} \quad \eta_\delta \to 0 \qquad (35a) \\ 1/\sqrt{\pi} & \text{for} \quad \eta_\delta \to \infty \qquad (35b) \end{cases}$$

The dimensionless vapor film thickness η_δ appearing in equation (35a) must be eliminated as follows. Expansion of equation (34) around $\eta_\delta = 0$ yields a quadratic equation in terms of η_δ which can readily be solved as

$$\eta_\delta = \left[2\,\mathrm{Sup} + \left(0.444\,\frac{\mathrm{Sub}}{R}\right)^2\right]^{1/2} - 0.444\,\frac{\mathrm{Sub}}{R} \qquad (36)$$

In order to obtain a general expression valid for all range of η_δ, we match the two asymptotic results using the procedure proposed by Churchill and Usagi (1972)

$$\mathrm{Nu}_x/(\mathrm{Ra}_x/I)^{1/2} = \left[\left(\frac{1}{\sqrt{\pi}}\right)^m + \left(\frac{1}{\eta_\delta}\right)^m\right]^{1/m} \qquad (37)$$

We set $m = 2$ which gives a close agreement between the approximate formula and the exact solution especially for the case of no subcooling, Sub = 0. (This value was proposed by Cheng (1981) when he matched the asymptotic results in the study of film condensation on a vertical plate in a porous medium.) Hence, we finally have

$$\mathrm{Nu}_x/(\mathrm{Ra}_x/I)^{1/2} = \left[\frac{1}{\pi} + \frac{1}{\left[\left(2\,\mathrm{Sup} + \left(0.444\,\frac{\mathrm{Sub}}{R}\right)^2\right)^{1/2} - 0.444\,\frac{\mathrm{Sub}}{R}\right]^2}\right]^{1/2} \qquad (38)$$

The curves based on the preceding explicit formula are presented in Fig. 4 along with those based on the exact solution, so as to substantiate the validity of the proposed expression. An attempt to verify the validity of the present analysis through comparison with experimental data has to be abandoned, since there are at present no experimental data available for film boiling within a saturated porous medium.

Conclusions

The problem of subcooled free-convection film boiling over a body of arbitrary shape in a porous medium has been analyzed by means of the two-phase boundary layer treatment. A general similarity transformation has been proposed to account for the geometric effect on the development of the two-phase boundary layer. It has been shown that, when the similarity variable is chosen carefully, the resulting set of

Downloaded 17 Dec 2010 to 193.140.21.150. Redistribution subject to ASME license or copyright; see http://www.asme.org/terms/Terms_Use.cfm

transformed differential equations, the boundary and matching conditions for an arbitrary shape can be reduced to the same as those for a vertical flat plate. Thus, the previous results obtained by Cheng and Verma for a flat plate may readily be translated to any particular geometry of concern.

An effort has been also made to establish an approximate formula which is more accessible for practical applications, in the sense that the heat transfer function is expressed explicitly in terms of the two parameters associated with the degrees of subcooling and superheating.

References

Cheng, P., 1981, "Film Condensation Along an Inclined Surface in a Porous Medium," *Int. J. Heat Mass Transfer*, Vol. 24, pp. 983–990.

Cheng, P., and Verma, A. K., 1981, "The Effect of Subcooled Liquid on Film Boiling About a Vertical Heated Surface in a Porous Medium," *Int. J. Heat Mass Transfer*, Vol. 24, pp. 1151–1160.

Churchill, S. W., and Usagi, R., 1972, "A General Expression for the Correlation of Rates of Heat Transfer and Other Phenomena," *AIChE J.*, Vol. 18, pp. 1121–1128.

Koh, J. C. Y., 1962, "Analysis of Film Boiling on Vertical Surfaces," ASME JOURNAL OF HEAT TRANSFER, Vol. 84, pp. 55–62.

Merkin, J. H., 1979, "Free Convection Boundary Layers on Axisymmetric and Two-Dimensional Bodies of Arbitrary Shape in a Saturated Porous Medium," *Int. J. Heat Mass Transfer*, Vol. 22, pp. 1461–1462.

Nakayama, A., and Koyama, H., 1987, "Free Convection Heat Transfer Over a Nonisothermal Body of Arbitrary Shape Embedded in a Fluid-Saturated Porous Medium," ASME JOURNAL OF HEAT TRANSFER, Vol. 109, pp. 125–130.

Nishikawa, K., and Ito, T., 1966, "Two-Phase Boundary Layer Treatment of Free Convection Film Boiling," *Int. J. Heat Mass Transfer*, Vol. 9, pp. 103–115.

Parmentier, E. M., 1979, "Two-Phase Natural Convection Adjacent to a Vertical Heat Surface in a Permeable Medium," *Int. J. Heat Mass Transfer*, Vol. 22, pp. 849–855.

Downloaded 17 Dec 2010 to 193.140.21.150. Redistribution subject to ASME license or copyright; see http://www.asme.org/terms/Terms_Use.cfm

Drag Coefficients Associated With a Moving Drop Experiencing Condensation

Lin Jie Huang

P. S. Ayyaswamy
Mem. ASME

University of Pennsylvania,
Philadelphia, PA 19104

For a moving liquid drop experiencing condensation, three different drag coefficients govern the motion and the transport. These coefficients are associated with friction, pressure, and condensation. Unlike situations involving the motion of a rigid sphere or a liquid drop without the presence of condensation, there is a large pressure recovery in the rear of a moving drop experiencing condensation. As a consequence, the pressure drag coefficient exhibits interesting behavior. While the coefficients for the friction drag and the condensation drag increase with the level of condensation, the pressure drag coefficient decreases rapidly. In this note, the roles played by the various drag forces in condensing situations are delineated. Results for the variation of average condensation heat transfer with vertical-fall height of the drop are presented.

1 Introduction

Condensation on a spray of drops occurs in a wide variety of physical situations. For example, the emergency cooling sprays of nuclear reactors, air-conditioning humidifiers, direct contact condensers in thermal power plants, atmospheric studies of raindrop growth etc., involve condensation on moving drops. The intent of this paper is to discuss the hydrodynamics and the transport phenomena associated with condensation on a single moving drop. Specifically, this paper will concern itself with the drag phenomena associated with a translating drop that experiences condensation.

There are many studies in the literature that involve heat and mass transfer and/or hydrodynamics of drop motion (Clift et al., 1978). Specifically, with regard to condensation on drops, stationary drops have been studied by Jacobs and Cook (1978). The growth rate of a water drop in a pure steam environment has been experimentally investigated by Ford and Lekic (1973). The condensation heat transfer rates for droplets moving in air–steam mixtures have been predicted using standard heat transfer correlations by (Kulic et al., 1975). In Kulic and Rhodes (1977), the authors have provided the experimentally recorded temperature-time history of a water drop experiencing condensation in a forced flow of steam and air. Condensation on slowly moving drops has been theoretically examined by Sadhal and Ayyaswamy (1983) and by Chung et al. (1984a, b). Condensation on a drop in high Reynolds number motion has been investigated by Chung and Ayyaswamy (1981a, b). Results for quasi-steady condensation heat and mass transfer appropriate to the intermediate Reynolds number range of drop motion are given by Sundararajan and Ayyaswamy (1984, 1985a). A hybrid finite-difference scheme that is suitable for solving condensation problems associated with a single moving drop has been described by Sundararajan and Ayyaswamy (1985b). In many industrial design calculations of heat and mass transfer related to moving drops experiencing condensation, the drag coefficient applicable to a rigid sphere motion is simply employed. It is shown in this paper that such an assumption may be inappropriate and may provide erroneous results.

2 Physical Description

Consider the introduction of a cold water drop of radius R_0 and initial bulk temperature T_0 into an environment consisting of a mixture of vapor (steam) and a noncondensable (air). The droplet is projected with an initial velocity $\mathbf{U}_0$ and at an angle β_0 with respect to the vertical direction (Fig. 1). The total pressure p_∞ and temperature T_∞ of the saturated mixture in the drop environment are taken to be prescribed. The drop is colder than its environment ($T_0 < T_\infty$) and condensation occurs on the drop surface.

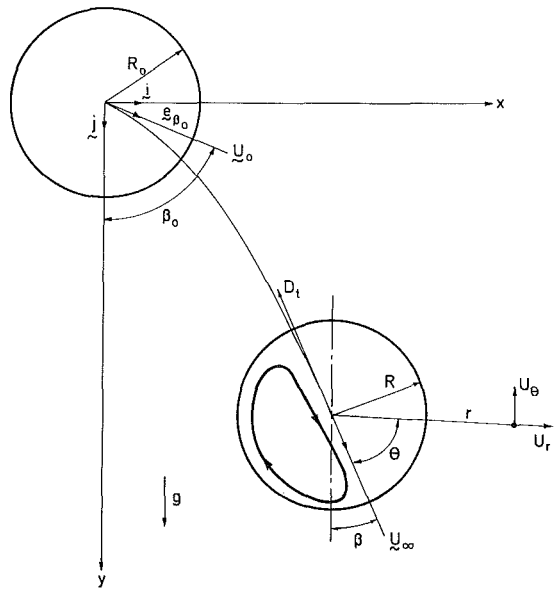

Fig. 1 Geometry of the problem

Let the instantaneous translational velocity of the drop be $\mathbf{U}_\infty$. We consider a coordinate frame that coincides with the drop center and moves with this instantaneous velocity $\mathbf{U}_\infty$ (Fig. 1). The instantaneous gaseous-phase Reynolds number of translation (hereinafter referred to as $\mathrm{Re}_g = U_\infty 2R/\nu_g$) is taken to be 0(100), but less than, say, 500. We note that in many condenser designs, Re_g may be in the range of 1000–1500. For $\mathrm{Re}_g \gtrsim 500$ flow instabilities such as drop oscillations and vortex shedding are known to occur. In this note the drop deformation due both to inertial effects (Weber number We) and to hydrostatic-pressure variation (Eötvös number Eo) are assumed to be small. We consider water drops of size 1 mm diameter or less (Eo < 0.4 and We < 0.3). We note that in many condenser designs, drops of larger sizes may have to be considered.

Contributed by the Heat Transfer Division and presented at the Winter Annual Meeting, Anaheim, California December 7–12, 1986. Manuscript received by the Heat Transfer Division May 6, 1986. Paper No. 86-WA/HT-39.

 Copyright © 1987 by ASME

Downloaded 17 Dec 2010 to 193.140.21.150. Redistribution subject to ASME license or copyright; see http://www.asme.org/terms/Terms_Use.cfm

Condensation causes a radially inward flow toward the drop surface. The nonzero mass flux at the interface alters the translational flow field and modifies the drag on the drop. Three different drag coefficients govern the motion and the transport. These coefficients are associated with friction, pressure, and condensation. The total drag coefficient which is the sum of the three coefficients may increase or decrease depending on the prevailing conditions (Reynolds number Re_g and the condensation parameter W, which represents the thermodynamic description). A correct assessment of the total drag coefficient is not only needed to establish the trajectory and the instantaneous Reynolds number for motion, but also to evaluate the transport rates accurately. Such accurate evaluations of transport rates are important in the design of direct-contact heat and mass transfer equipment.

3 Drag Coefficients

For a moving liquid drop experiencing condensation, the instantaneous total drag coefficient

$$D_t = D_p + D_f + D_c \tag{3}$$

where D_p, D_f, and D_c are the pressure-drag, friction-drag and condensation-drag coefficients, respectively (Sundararajan and Ayyaswamy, 1984). The pressure drag coefficient is

$$D_p = \int_0^\pi p^*_{g,s} \sin 2\theta \, d\theta \tag{4}$$

where the dimensionless pressure is

$$p^*_{g,s} = \frac{(p_{g,s}(\theta) - p_\infty)}{\frac{1}{2}\rho_g U_\infty^2} \tag{5}$$

The surface pressure profile is given by $p_{g,s}(\theta)$. The friction drag coefficient is defined by

$$D_f = \frac{8}{\mathrm{Re}_g} \int_0^\pi \left(\sigma^* \sin\theta - 2 \frac{\partial u^*_{g,r}}{\partial r^*}\bigg|_{r^*=1} \cos\theta \right) \sin\theta \, d\theta \tag{6}$$

In equation (6), the dimensionless surface shear stress σ^* and radius r^* are

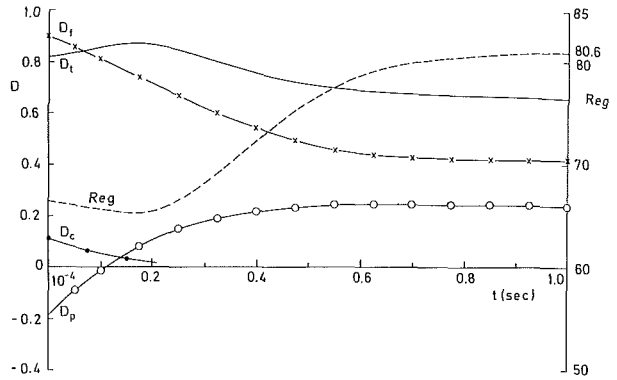

Fig. 2 Variation of Re_g, D_f, D_p, D_c and D_t with time: p_∞ = 300 kPa, T_0 = 37°C, β_0 = 0.0 deg, T_∞ = 120°C, R_0 = 250 μm, W_0 = 0.54, U_0 = 3.0 m/s, Re_{g0} = 66

$$\sigma^* = \frac{\sigma}{\mu_g U_\infty / R} \text{ and } r^* = r/R \tag{7}$$

The surface shear stress σ itself may be expressed as

$$\sigma = \mu_g \left[r \frac{\partial}{\partial r} \frac{u_{g,\theta}}{r} + \frac{1}{r} \frac{\partial u_{g,r}}{\partial \theta} \right] \Bigg|_{r=R} \tag{8}$$

In equations (6) and (8), the r and θ components of the mass average velocity $\mathbf{u}_g$ for the binary mixture of air and water vapor are represented by $u_{g,r}$ and $u_{g,\theta}$, respectively. These are scaled by U_∞ to get $u^*_{g,r}$ and $u^*_{g,\theta}$.

The condensation drag D_c arises owing to the momentum associated with the radial flow and is given by

$$D_c = 4 \int_0^\pi \left[\hat{u}^*_c \cos\theta - u^*_\theta \sin\theta \right] \hat{u}^*_c \sin\theta \, d\theta \tag{9}$$

The dimensionless condensation velocity $\hat{u}^*_c$ and the surface velocity u^*_θ are

$$\hat{u}^*_c = u^*_{g,r}|_{r^*=1} \text{ and } u^*_\theta = u^*_{g,\theta}|_{r^*=1} \tag{10}$$

Nomenclature

D = drag coefficient
D_{12} = binary diffusion coefficient
$\mathbf{e}$ = unit vector
Eo = Eötvös number = $g\Delta\rho D^2/\sigma$
g = gravitational acceleration
H = vertical fall height
$\mathbf{i}$ = unit vector in x direction
$\mathbf{j}$ = unit vector in y direction
k = thermal conductivity
m_1 = noncondensable mass fraction
p_∞ = far-stream pressure
q = dimensionless surface heat flux = $qR/\rho_g \alpha_g \lambda$
r = radial coordinate
R = radius of the drop
$\dot{R}$ = dimensionless rate of change of drop radius (scaled by U_∞)
R_∞ = radius of the outer boundary in the numerical calculation
Re = Reynolds number = $U_\infty D/\nu$
t = time
T = temperature
T_b = instantaneous bulk temperature of the drop
T_s = surface temperature of the drop
$\mathbf{u}$ = velocity
$\hat{u}_c$ = dimensionless condensation velocity
u_c = dimensionless condensation velocity at the drop surface scaled by $D_{12}/2R$
$\mathbf{U}_0$ = initial velocity of drop
$\mathbf{U}_\infty$ = far-stream translational velocity
u_r, u_θ = velocity components
w_1 = normalized mass fraction
W = condensation parameter = $1 - m_{1,\infty}/m_{1,s}$
We = Weber number = $2\rho R U_\infty^2/\sigma$
z = transformed radial coordinate = $\ln r$
α = thermal diffusivity
β = instantaneous angle of drop trajectory
$\Delta\rho$ = density difference between drop and gaseous phase
ΔT = $T_\infty - T$
θ = polar angle
θ_b = dimensionless bulk temperature
λ = latent heat of condensation
μ = dynamic viscosity
ν = kinematic viscosity
ρ = density
σ = surface tension
ϕ = azimuthal angle

Subscripts

av = average
c = condensation
f = friction
g = gas phase
h = horizontal
l = liquid phase
m = mass transfer
p = pressure
s = drop surface
t = thermal, total
v = vertical
0 = at initial time; stagnant drop
1 = noncondensable
∞ = far-stream

Superscripts

$\bar{}$ = average
$*$ = dimensionless quantity

Downloaded 17 Dec 2010 to 193.140.21.150. Redistribution subject to ASME license or copyright; see http://www.asme.org/terms/Terms_Use.cfm

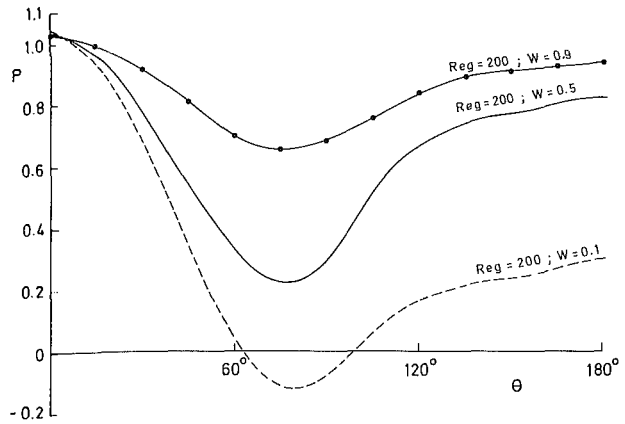

Fig. 3 Effect of condensation on the surface pressure profile: R_0 = 250 μm, β_0 = 0.0 deg

The gas-phase equations, the liquid-phase equations, and the applicable initial and boundary conditions are given by Huang and Ayyaswamy (1987a) and will not be repeated here for the sake of brevity. The details of the numerical procedure are available from Sundararajan and Ayyaswamy (1985b) and Huang and Ayyaswamy (1987b).

4 Results and Discussion

Figure 2 shows the temporal variations of Re_g, D_f, D_c, D_p, and D_t for a moving liquid drop experiencing condensation. For the parameters considered (note in particular, R_0 = 250 μm), Re_g first decreases in the immediate period following the introduction, then significantly increases. This rapid increase is followed by a gradual rate of increase until thermal equilibrium with the outside environment is achieved (condensation ceases). Beyond thermalization, the drop would translate at a fixed Re_g (constant terminal velocity). The dependence of Re_g on t may be explained as follows. Immediately upon introduction, the drop experiences vigorous condensation (large W, large ΔT). The vigorous condensation results in high values for the shear stress and momentum of the radial flow. Thus, the friction-drag coefficient D_f and the condensation drag coefficient D_c are high. However, there is a very large pressure recovery in the rear of the drop (the pressure-recovery feature is explained later by reference to the pressure profile at the drop surface in Fig. 3). The pressure-drag coefficient D_p is negative and large. With increasing time, the strength of the condensation field decreases and D_f and D_c decrease correspondingly. There is a lesser pressure recovery and a steep increase in D_p, and its influence on D_t is dominant. The total drag coefficient D_t, which is the sum of the three coefficients, increases in the period following introduction. There is a corresponding drop deceleration and Re_g decreases. A small size drop such as the one under consideration has a relatively lower heat capacity and its bulk and surface temperatures increase rapidly. The thermal driving force for condensation is reduced and the associated field strength weakens beyond this period. The D_f decreases with a steeper gradient and its influence on D is dominant. Thus, D_t decreases and $U_\infty(t)$ increases, i.e., the drop accelerates. A rapid increase in Re_g is noted. Eventually as the drop approaches thermal equilibrium with the outside, the pressure recovery is minimal and the D_f, D_t, and the corresponding Re_g are all essentially constant.

Figure 3 shows the gaseous-phase pressure profile at the drop surface. The profile changes drastically with condensation. The extent of condensation is characterized by W, the condensation parameter, given by $1-(m_{1,\infty}/m_{1,s})$. This parameter is a function of the thermodynamic conditions p_∞, T_∞, T_s, and varies from 0 to 1. The limit zero corresponds to a noncondensing situation and W = 1 to a pure-vapor environment. Recall that, for flow around liquid (solid) spheres, in the absence of condensation, there is very little pressure recovery in the rear. With condensation, however, there is a large pressure recovery, and the pressure profile is predominantly determined from a balance between the diffusive and convective transports of vorticity. For a noncondensing situation, the diffusion of vorticity away from the drop causes pressure loss in the rear. With condensation the radially inward flow counters this outward diffusion of vorticity. The pressure-drag coefficient D_p thus decreases with increasing level of condensation.

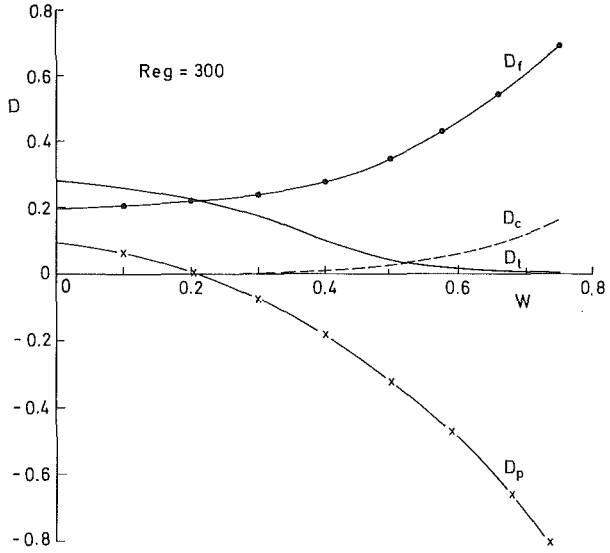

Fig. 4 Influence of condensation on drag coefficients

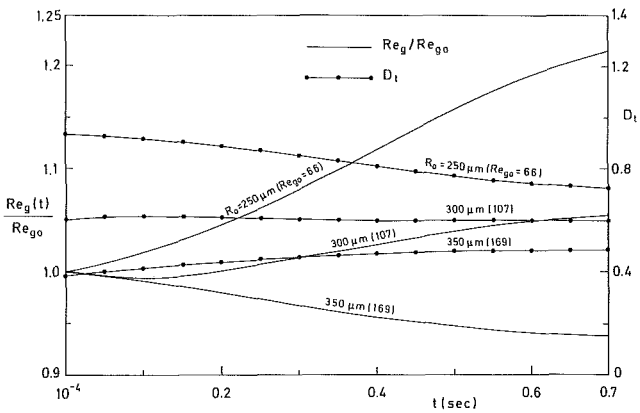

Fig. 5 The variation of $(\mathrm{Re}_g(t)/\mathrm{Re}_{g0})$ and D_t with time for drops of various sizes: p_∞ = 300 kPa, T_0 = 37°C, β_0 = 0.0 deg, T_∞ = 110°C, W_0 = 0.35

The variations in the drag coefficients with increasing condensation (W increasing) are shown in Fig. 4. For given thermodynamic conditions, large values of W correspond to the immediate period following the introduction of the drop onto the condensing environment. The pressure-drag variation becomes important at larger W (vigorous condensation), while D_f variation is important at lower values. The condensation drag needs consideration at lower Re_g or high W.

In Fig. 5, the changes in drop-motion during condensation are examined by plotting $\mathrm{Re}_g(t)/\mathrm{Re}_{g0}$ with time for various initial drop sizes. It is seen from the figure that for given p_∞, T_∞, and T_0, a small drop (R_0 = 250 μm) accelerates with time, a large drop (R_0 = 300 μm) decelerates, while a drop of in-

Downloaded 17 Dec 2010 to 193.140.21.150. Redistribution subject to ASME license or copyright; see http://www.asme.org/terms/Terms_Use.cfm

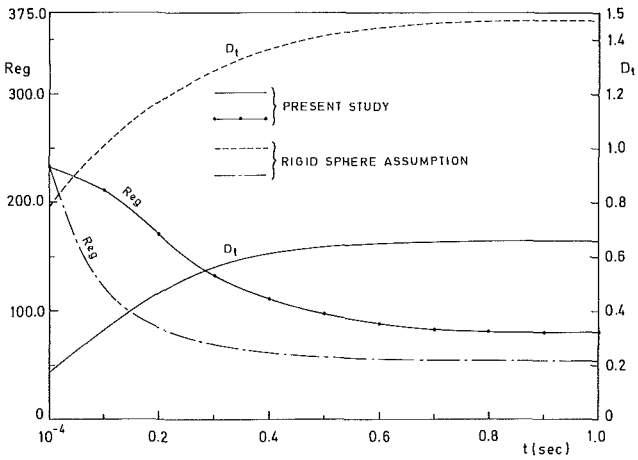

Fig. 6 Comparisons of the variations in Re_g and D_t with time: p_∞ = 300 kPa, T_0 = 37°C, β_0 = 0.0 deg, T_∞ = 120°C, R_0 = 250 μm, W_0 = 0.54, U_0 = 10.0 m/s

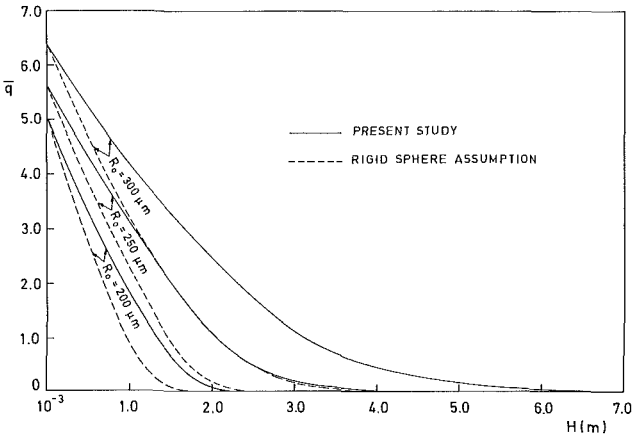

Fig. 7 The variation of $\bar{q}$ with time: p_∞ = 300 kPa, T_0 = 37°C, β_0 = 0.0 deg, T_∞ = 120°C, W_0 = 0.54, U_0 = 10.0 m/s

termediate size (R_0 = 300 μm) decelerates in the immediate transient period following introduction and then accelerates. These interesting trends may be understood by a careful examination of the drag behavior in the presence of condensation. For a large drop, D_t increases with time because D_p increases with decreasing W, although D_f and D_c decrease. As a result, the drop decelerates. For a small drop, the friction drag dominates the variation in D_t, when ΔT_0 is sufficiently small. For a drop of intermediate size, in the transient period following the introduction when W is decreasing rapidly, D_t increases due to an increase in D_p. For later times, with smaller W, D_t decreases due to the decrease in D_f (reduced shear stress). Such a drag behavior leads to an initial deceleration and a subsequent acceleration of the drop. It is also noted from the figure that there is a rapid deceleration of a large drop in the immediate transient period following introduction, whereas the acceleration of a small drop occurs almost uniformly throughout the condensation period. These trends are explained by noting that while the variation in D_p is important for large W, the variation in D_f is significant even at low values of W.

In Figs. 6 and 7, the importance of correctly estimating the drag coefficient values in condensation calculations is illustrated and emphasized. Depending on the assumptions made, the predictions of variations of Re_g and D_t with time are seen to be very different in Fig. 6. The drag coefficient for a rigid sphere used in our calculations is given by Clift and Gauvin (Clift et al., 1978). In Fig. 7, the average condensation heat transfer $\bar{q}$ ($= 0.5 \int q \sin\theta \, d\theta$) to drops of various sizes is predicted as functions of vertical fall height H. The predictions are made based both on the present development and on the assumption that the drag coefficient appropriate to a rigid sphere may be used in the calculation procedure. The latter assumption is often invoked in many industrial design calculations. The predicted fall heights are seen to be significantly different. The differences are particularly noteworthy in the design of scrubbers and containment spay systems of nuclear reactors (Huang and Ayyaswamy, 1987b).

5 Conclusions

For a moving liquid drop experiencing condensation, three different drag coefficients govern the motion and the transport. These coefficients are associated with friction, pressure, and condensation. In particular, the pressure drag coefficient exhibits interesting behavior as a consequence of the large pressure recovery in the rear of the drop. The total drag coefficient may increase or decrease depending on the prevailing conditions (Reynolds number Re_g and condensation parameter W). By simply employing the drag coefficient appropriate for a rigid sphere in design calculations involving moving drops experiencing condensation, serious errors may be committed (Huang and Ayyaswamy, 1987b).

References

Chung, J. N., and Ayyaswamy, P. S., 1981a, "Laminar Condensation Heat and Mass Transfer of a Moving Drop," *AIChE Journal*, Vol. 27, pp. 327–377.

Chung, J. N., and Ayyaswamy, P. S., 1981b, "Material Removal Associated With Condensation on a Droplet in Motion," *Int. J. Multiphase Flow*, Vol. 7, pp. 329–342.

Chung, J. N., Ayyaswamy, P. S., and Sadhal, S. S., 1984a, "Laminar Condensation on a Moving Drop. Part 1. Singular Perturbation Technique," *J. Fluid Mech.*, Vol. 139, pp. 105–130.

Chung, J. N., Ayyaswamy, P. S., and Sadhal, S. S., 1984b, "Laminar Condensation on a Moving Drop. Part 2. Numerical Solutions," *J. Fluid Mech.*, Vol. 139, pp. 131–144.

Clift, R., Grace, J. R., and Weber, M. E., 1978, *Bubbles, Drops and Particles*, Academic Press, New York.

Ford, J. S., and Lekic, A., 1973, "Rate of Growth of Drops During Condensation," *Int. J. Heat Mass Transfer*, Vol. 16, pp. 61–64.

Huang, L. J., and Ayyaswamy, P. S., 1987a, "Heat and Mass Transfer Associated With a Spray Drop Experiencing Condensation: A Fully Transient Analysis," *Int. J. Heat Mass Transfer*, in press.

Huang, L. J., and Ayyaswamy, P. S., 1987b, "Heat Transfer of a Nuclear Reactor Containment Spray Drop," *Nuclear Engineering and Design*, in press.

Jacobs, H. R., and Cook, D. S., 1978, "Direct Contact Condensation on a Non-circulating Drop," *Proc. 6th Int. Heat Transfer Conf.*, Vol. 2, Toronto, Ontario, Canada, pp. 389–393.

Kulic, E., Rhodes, E., and Sullivan, G., 1975, "Heat Transfer Rate Predictions in Condensation on Droplets From Air-Steam Mixture," *Can. J. Chem. Engrg.*, Vol. 53, pp. 252–258.

Kulic, E., and Rhodes, E., 1977, "Direct Contact Condensation From Air-Steam Mixtures on a Single Droplet," *Can. J. Chem. Engrg.*, Vol. 55, pp. 131–137.

Sadhal, S. S., and Ayyaswamy, P. S., 1983, "Flow Past a Liquid Drop With a Large Non-uniform Radial Velocity," *J. Fluid Mech.*, Vol. 133, pp. 65–81.

Sundararajan, T., and Ayyaswamy, P. S., 1984, "Hydrodynamics and Heat Transfer Associated With Condensation on a Moving Drop: Solutions for Intermediate Reynolds Numbers," *J. Fluid Mech*, Vol. 149, pp. 33–58.

Sundararajan, T., and Ayyaswamy, P. S., 1985a, "Heat and Mass Transfer Associated With Condensation on a Moving Drop: Solutions for Intermediate Reynolds Numbers by a Boundary Layer Formation," ASME JOURNAL OF HEAT TRANSFER, Vol. 107, pp. 409–416.

Sundararajan, T., and Ayyaswamy, P. S., 1985b, "Numerical Evaluation of Heat and Mass Transfer to a Moving Liquid Drop Experiencing Condensation," *Numerical Heat Transfer*, Vol. 8, No. 6, pp. 689–706.

Downloaded 17 Dec 2010 to 193.140.21.150. Redistribution subject to ASME license or copyright; see http://www.asme.org/terms/Terms_Use.cfm

Artificial Transformation of the Direct-Contact Condensation Pattern of Steam Bubbles in a Hydrophobic Liquid Medium

Y. H. Mori
Associate Professor,
Department of Mechanical Engineering,
Keio University,
Yokohama 223, Japan

When steam bubbles are released into a medium of a hydrophobic coolant, the condensate is scattered through the coolant in the form of tiny droplets. This condensation pattern is unfavorable for direct-contact condensers because it is difficult to separate the condensate and the coolant. This paper proposes a novel bubble-release device by which the condensation pattern is so transformed that the condensate remains within the confines of the bubble wall. An experimental examination with single steam bubbles released into a medium of liquid paraffin is demonstrated.

Introduction

The process of condensation of vapor bubbles in a medium consisting of an immiscible, less-volatile liquid has been studied in the last two decades by several researchers. Extensive surveys on these studies are given by Sideman and Moalem-Maron [1] and by Sudhoff et al. [2]. Fluids used or implicitly assumed in most of these studies are water as the coolant and a light hydrocarbon as the condensing fluid to be dispersed in the coolant. The selection of such a fluid combination is consistent with potential applicability of the direct-contact condensers to water desalination or geothermal heat recovery systems. Other applications are also conceivable wherein various combinations of working fluid and coolant are possible. The particular interest in the present study is in the combination of steam and a hydrophobic oil, the former being released into a medium of the latter for the purpose of water recovery and/or heating the oil.

When a bubble of a light hydrocarbon vapor condenses in water, a condensate accumulates in the confines of the bubble wall, thus forming a stable two-phase vapor/condensate bubble [1]. This condensation pattern prevails as long as the condensate wets the bubble wall relatively well. If the condensate does not wet the bubble wall well, the condensate does not always stay in the bubble throughout the condensation process; this is the case which is typified by steam bubbles condensing in a hydrophobic oil. Higeta et al. [3] reported that when a steam bubble condensed in a medium of silicone oil which was highly hydrophobic, tiny droplets of the condensate detached themselves continuously from the bubble into the silicone oil, resulting in the formation of a wake of emulsion behind the bubble. This condensation pattern is unfavorable for practical condensers because of the difficulty in separating the condensate and the medium liquid (coolant). This paper proposes a technique of transforming the condensation pattern into a completely different one in which the condensate remains within the confines of the bubble wall even if the medium liquid is highly repellent to the condensate. The basic idea is described below.

In a medium of hydrophobic oil, two-phase steam/water bubbles of any configuration are unstable [4, 5]. However, this fact does not exclude the possibility of two-phase bubbles being formed tentatively. In fact, Shimada et al. [6] observed the formation of two-phase steam/water bubbles in a liquid-paraffin layer superposed on a water layer wherein nucleate boiling occurs. Mercier et al. [7] also reported that an air bubble released in a water layer underlying a mineral oil layer penetrated into the mineral oil layer entraining some amount of water with it. Taking a hint from these studies the author has thought out a device as illustrated in Fig. 1. Steam bubbles are released not directly into a hydrophobic coolant but into a water layer which covers outlets of the steam distributor. Each steam bubble breaks through the water/coolant interface and rises in the coolant phase while encapsulated in a water shell. Although such a two-phase bubble is unstable, it does not disintegrate until the water film at the top portion of the bubble thins enough to rupture as the result of draining of water toward the lower part of the bubble. It is expected that the condensation completes within the confines of the water shell before it ruptures. If this is the case, each steam bubble turns into a water drop, which falls through the coolant phase due to density difference and then coalesces with the water layer covering the steam distributor. This idea has been examined experimentally with single steam bubbles condensing in a stagnant medium of liquid paraffin.

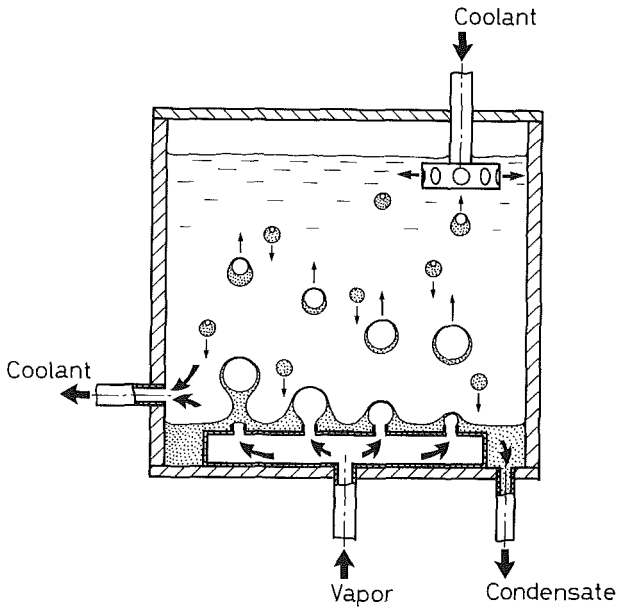

Fig. 1 Outline of a possible design of direct-contact condenser

Experimental

Experiments were so designed that single steam bubbles

Contributed by the Heat Transfer Division for publication in the JOURNAL OF HEAT TRANSFER. Manuscript received by the Heat Transfer Division June 7, 1985.

Copyright © 1987 by ASME
Downloaded 17 Dec 2010 to 193.140.21.150. Redistribution subject to ASME license or copyright; see http://www.asme.org/terms/Terms_Use.cfm

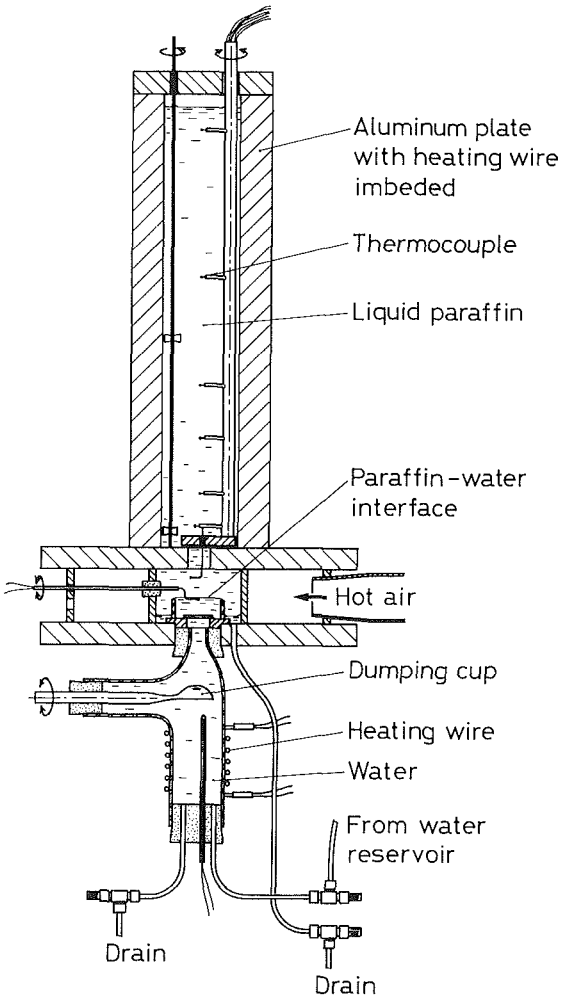

Fig. 2 Schematic of apparatus II

generated in a liquid water phase underlying a liquid paraffin phase broke into the paraffin phase entraining some amount of water. In order to make the experimental conditions simple and well-specified, some efforts were made to maintain the water adjacent to the paraffin/water interface at almost its saturation temperature and simultaneously to keep a uniform temperature in the bulk of liquid paraffin wherein bubbles would condense.

Figure 2 illustrates one of the two apparatus used in this study. We call it apparatus II hereafter. It consisted of three portions: the lower column containing water, the intermediate column in which the paraffin/water interface situated, and the upper column containing liquid paraffin. The lower column was designed as a Pyrex glass tube to minimize undesired steam-bubble generation on the column wall while the bulk of water in the column was heated up to the saturation temperature or even slightly above it. The intermediate column was a transparent polycarbonate tube of 89 mm o.d. and 50 mm high. Concentrically with this tube a glass tube of 50 mm o.d. and 15 mm high was put inside. The paraffin/water interface was supported by the top end of the glass tube. The upper column was 70 × 70 mm in cross section and 450 mm in height. The front and rear walls were built of Pyrex glass plates, and the side walls were aluminum plates. Sheathed electric heating wires were imbedded in the aluminum plates. A bakelite tube holding seven copper-constantan thermocouples was inserted in a corner of the upper column. The tube had a spatula, made of a bakelite plate, at its bottom tip. The spatula served as a cover of the center hole on the baffle plate between the upper and intermediate columns, in order to prevent mixing of cooler paraffin from the upper column with hotter paraffin from the intermediate column. By rotating the bakelite tube around its axis one can open the center hole on the baffle plate and at the same time swing the thermocouples away from the central axis of the columns.

Table 1 Some properties of water-saturated liquid paraffin at 95°C

Density[1]	854 kg/m^3
Kinematic viscosity[2]	8.41 × 10^{-6} m^2/s
Thermal conductivity[3]	0.123 W/m-K
Thermal diffusivity[4]	1.0 × 10^{-7}m^2/s

[1]Measured with a pycnometer.
[2]Measured with an Ubbelohde viscometer.
[3, 4]Measured with a transient hot-wire apparatus described in [8].

The experimental procedure was as follows. The liquid in every column was heated up to a desired level: about 102°C near the dumping cup in the lower column, 100 to 101°C at the paraffin/water interface in the intermediate column, and between 96 and 98°C in the upper column. After steady state was established, the agitator in the upper column was stopped, and the central hole on the baffle plate between the intermediate and upper columns was opened. Then a steam bubble was formed at a nucleation site on the inside surface of the Pyrex-glass dumping cup. (The nucleation site was not prepared artificially; it was probably in a fortuitously prepared tiny scratch on the glass surface. Each nucleation was readily triggered merely by giving a small impact to the handle of the dumping cup.) By turning over the dumping cup, the bubble was released and it entered the intermediate column. Then the bubble broke through the paraffin/water interface and entered the upper column. The condensation process of the bubble in the upper column was recorded by use of a photography system as described in [3].

Before constructing apparatus II, explained above, we performed some experiments with a more crude one, apparatus I. It consisted of the same upper column that we later applied to apparatus II and the lower column of aluminum plates and glass plates. The paraffin/water interface was held at 10 to 20 mm above the bottom plate of the upper column, and the temperature near the interface was not specified. However, apparatus I had an advantage: It made it possible to observe the whole process of interest, which began with the approach of each steam bubble toward the paraffin/water interface. Thus, some of the results obtained with apparatus I are also to be presented later as far as the formation of two-phase steam/water bubbles is concerned.

The water used was taken from a commercial reverse-osmosis/ion-exchange/distillation apparatus. It was boiled for the purpose of degassing just before pouring it into the lower column. The liquid paraffin was of reagent grade (Taisei Chemical Co., Ltd., Tokyo) and was saturated, before use, with water at almost the same temperature as that to be maintained in the upper column. Some properties of the liquid paraffin saturated with water were measured in our own laboratory. Their values at 95°C are listed in Table 1.

Nomenclature

D_s = equivalent spherical diameter of steam phase in two-phase bubble or of bare steam bubble
ΔT = reference temperature difference
V_{si} = initial volume of steam bubble
V_w = volume of entrained water

Downloaded 17 Dec 2010 to 193.140.21.150. Redistribution subject to ASME license or copyright; see http://www.asme.org/terms/Terms_Use.cfm

Results

Condition for Two-Phase Bubble Formation. Experiments with apparatus I showed that steam bubbles having equivalent spherical diameters less than 3.5 mm pass through the paraffin/water interface without entraining water into the paraffin phase. Most bubbles with diameters between 3.5 and 5.9 mm entrained water and rose in the paraffin phase in the form of two-phase steam/water bubbles, although some bubbles in this diameter range did not entrain any water and rose in the paraffin phase in the form of "bare" bubbles. Bubbles greater than 5.9 mm in diameter shed off the entrained water just above the interface, and then continued to rise in the paraffin phase in the form of "bare" bubbles. The above observations are generally in agreement with those of Mercier et al. [7] on the rise of air bubbles through a mineral oil/water interface.

In the above experiments with apparatus I, steam bubbles approached the interface with velocities close to their terminal velocities. We found in a side experiment using a different apparatus, however, that as the approach velocity was reduced substantially, the probability of two-phase bubble formation by medium-sized steam bubbles increased to 100 percent. Thus, in some of the experiments with apparatus II we provided an orifice of 3 mm i.d. at the bottom of the intermediate column (see Fig. 2) to reduce the approach velocity and thereby enhance the probability of two-phase bubble formation.

Condensation Behavior. Figure 3(*a*) exemplifies an almost complete history of a condensing two-phase steam/water bubble. As the condensation proceeds, the rise velocity of two-phase bubble drops because of an increase of average density in the bubble. If the initial fraction of noncondensible gas mixed in the steam is low enough, the steam/gas phase in the bubble shrinks further and thus the bubble begins to descend toward the interface. The steam/gas phase and the liquid phase separate from each other usually at this stage, as shown in Fig. 3(*b*). If the initial fraction of noncondensible gas is higher, the steam/gas phase does not shrink enough and thus the two-phase bubble continues to rise to the free surface of the paraffin, where the steam/gas phase bursts into the atmosphere leaving a water drop which then starts to fall. When a steam bubble entrains a fairly large volume of water, it often sheds off part of the water while it is rising, as shown in Fig. 3(*c*).

Figure 4 shows a sequence of rise of a "bare" steam bubble in the paraffin phase. Such a wake of emulsion as demonstrated in [3] for the case of steam bubbles released in methylphenyl silicone oil is not recognized here. It was found that when such a bare bubble burst at the free surface of the paraffin a number of water droplets with variable diameters from 0.02 to 0.14 mm were strewed into the paraffin. This fact means that the condensate droplets were conveyed by the bubble to the free surface and then spilled into the paraffin by the

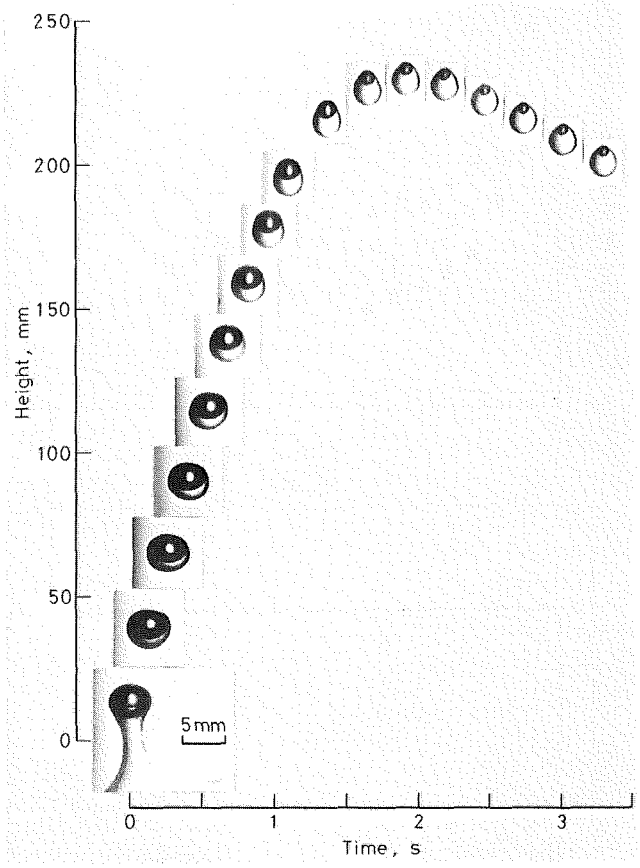

Fig. 3(*a*) Typical history of a two-phase bubble

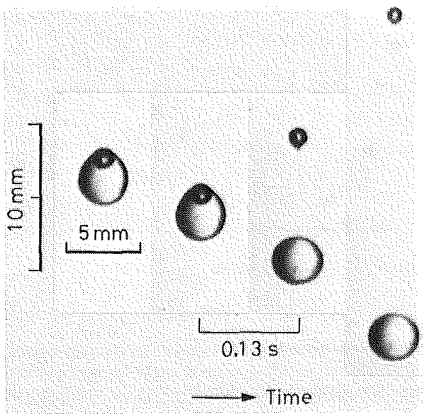

Fig. 3(*b*) Disintegration of a two-phase bubble into a bubble of noncondensible-gas/steam mixture and a water drop

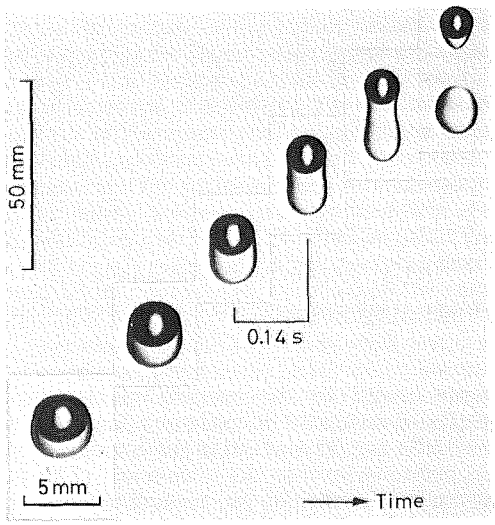

Fig. 3(*c*) Disintegration of the water phase in a two-phase bubble

Fig. 3 Photographic records of two-phase bubbles formed through the interface crossing of steam bubbles

Downloaded 17 Dec 2010 to 193.140.21.150. Redistribution subject to ASME license or copyright; see http://www.asme.org/terms/Terms_Use.cfm

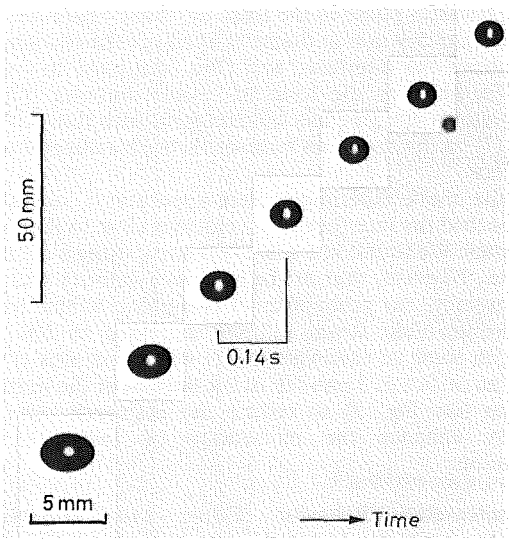

Fig. 4 Sequence of condensation of a "bare" steam bubble

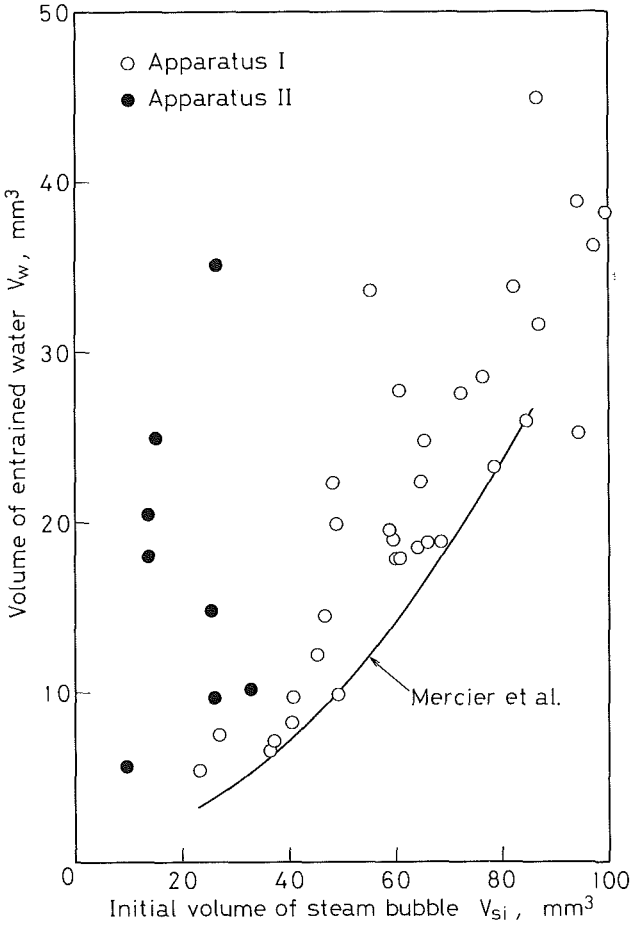

Fig. 5 Volume of entrained water versus initial volume of steam bubble

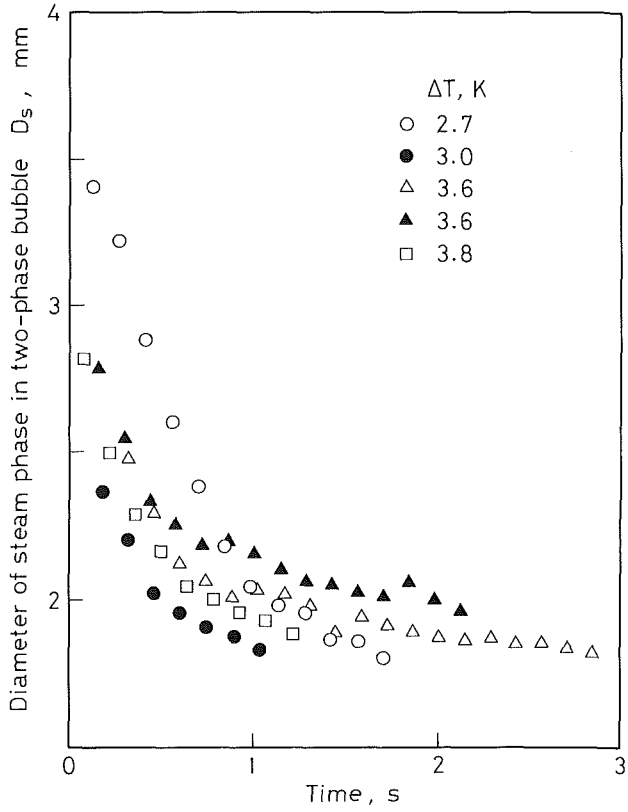

Fig. 6(a)

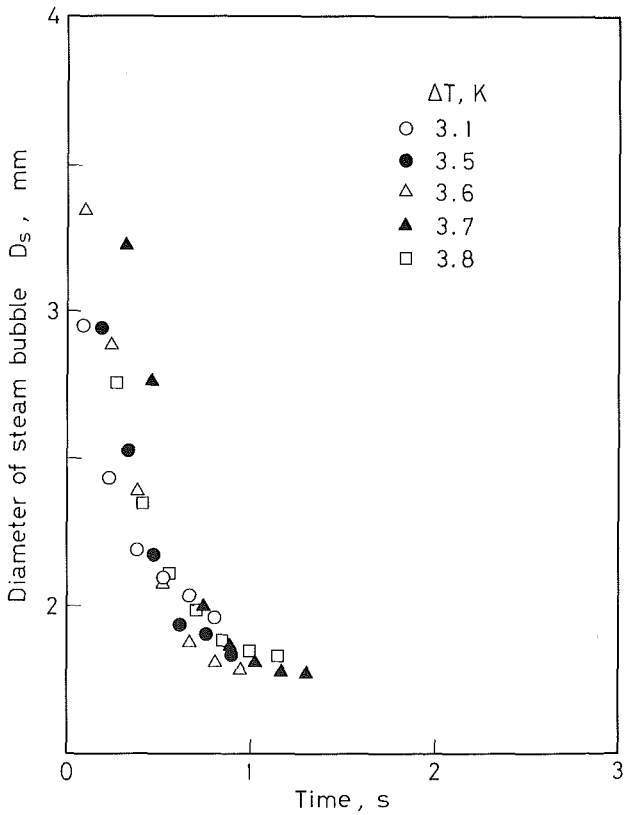

Fig. 6(b)

Fig. 6 Instantaneous equivalent spherical diameter of steam phase in two-phase bubble (*a*) or of bare steam bubble (*b*) plotted against time lapse after its entrance into the upper column of apparatus II

disturbance caused by the bursting of the bubble. The aforementioned difference in condensate appearance between the two systems may be ascribed to the liquid paraffin being a little less hydrophobic than the silicone oil. (This interpretation has not been confirmed yet, because reliable surface and interfacial tension data are available only on one of the two systems, the water/silicone oil system [9].) In any case, such tiny condensate droplets as those observed in these two systems could offer a serious problem of phase separation, ir-

Downloaded 17 Dec 2010 to 193.140.21.150. Redistribution subject to ASME license or copyright; see http://www.asme.org/terms/Terms_Use.cfm

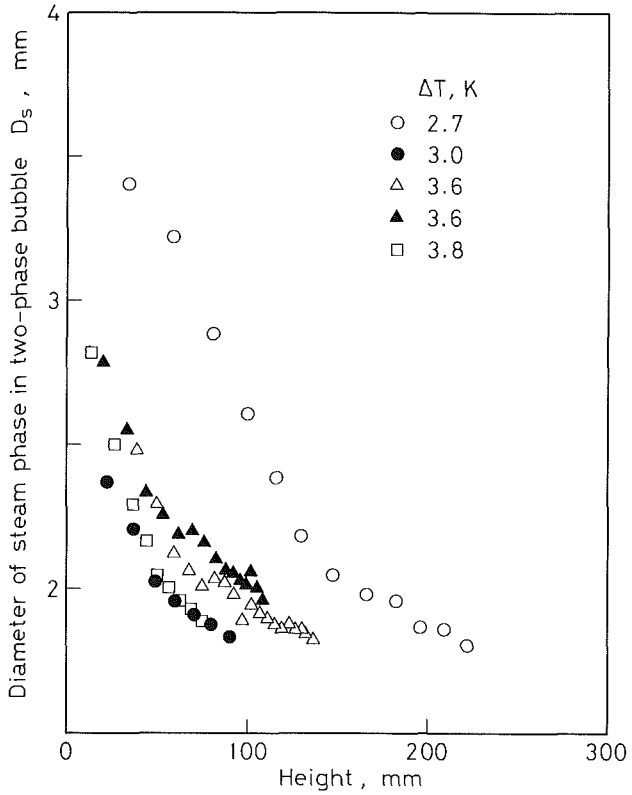

Fig. 7(a)

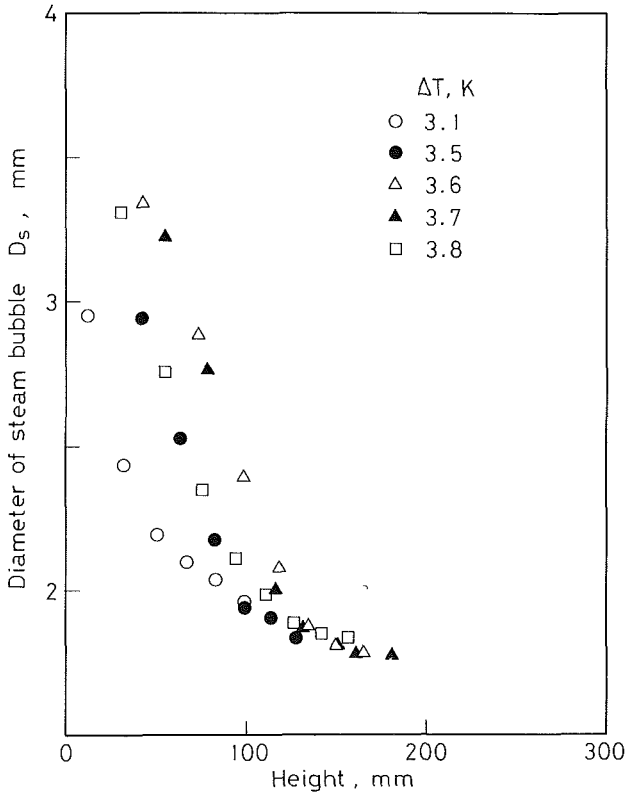

Fig. 7(b)

Fig. 7 Instantaneous equivalent spherical diameter of steam phase in two-phase bubble (a) or of bare steam bubble (b) plotted against its height above the bottom surface of the upper column of apparatus II

respective of their formation processes, which may be somewhat different from system to system depending on the properties of the medium liquid.

Volume of Entrained Water. Figure 5 shows the dependence of volume of entrained water, V_w, on the volume of steam bubble crossing the paraffin/water interface V_{si}. Since it was difficult to determine V_w directly by film analysis, this value was calculated from three volumes which were determined respectively by film analysis: the total volume of two-phase bubble, V_f, and the volume of steam/gas phase in it, V_{sf}, both being referred to completion of condensation; and V_{si}. Note that V_{si} could not be actually determined in the experiments with apparatus II because of an optical distortion; thus, the data for apparatus II were plotted on Fig. 5 by regarding as V_{si} the volume of steam (or steam/gas) phase in each two-phase bubble at the entrance of the upper column. The deviation of the data for apparatus II from those by apparatus I suggests that bubbles underwent condensation in part before they left the intermediate column. The data from apparatus I – which we believe represent more accurately the real case – approximate those by Mercier et al. [7] on the dependence of V_w on the volume of air bubbles penetrating into the mineral oil phase whose density and kinematic viscosity were, respectively, 850 kg/m^3 and 1.00×10^{-6} m^2/s.

Bubble Collapse History. Figures 6 and 7 summarize the data on collapse history of the steam (or steam/gas) phase in each two-phase bubble or of each bare steam (or steam/gas) bubble obtained with apparatus II. Figure 6(*a*) shows the change of equivalent spherical diameter D_s of the steam phase in each two-phase bubble with the time lapse after its entrance into the upper column. Figure 6(*b*) shows the same thing for bare steam bubbles. Figures 7(*a*) and 7(*b*) show the change of D_s with the height of each bubble above the bottom surface of the upper column. The initial value of D_s (or initial volume V_{si}) of each bubble cannot be specified because of the reason explained above. The reference temperature difference ΔT is defined as the excess, above the bulk temperature in the upper column, of the saturation temperature of water under the atmospheric pressure plus the hydrostatic head at the bottom of the upper column. The noncondensible gas content was presumably different from bubble to bubble; but there must be little systematic difference in the content between two-phase bubbles and bare steam bubbles, because both of them were generated in the same sets of experiments by the same procedure without intentionally distinguishing them.

The data scatter more widely in Fig. 7 than in Fig. 6. This fact is ascribed to the formation of a thermal plume, from the bottom of the upper column, after removing the cover of the central hole of the baffle plate. Depending on the time lapse, from removing the cover until the bubble release, which was not controlled exactly, the height of the growing plume which the bubble must break through to meet the cool medium was different from run to run: the higher the plume, the higher the region where the bubble underwent a significant collapse.

Because of the lack of exact controls on V_{si}, the noncondensible gas content, and the thermal-plume formation in the experiments, the bubble-collapse data presented here are unfit for any quantitative analysis of the condensation process. However, they are still sufficient for us to draw an important, though no more than qualitative, conclusion: The condensation of steam in a bubble is not hindered significantly by the entrained water shell over the bubble; in other words we can possibly overcome the problem of phase separation in direct steam/paraffin contact condensers by making bubbles entrain a water sheath in compensation for a little suppression of the condensation rate to a degree, as recognized in Fig. 6.

Discussion

In the present experiments with apparatus I and II, the entrainment of water resulting in the two-phase steam/water bubble formation was a stochastic event which depends on

Downloaded 17 Dec 2010 to 193.140.21.150. Redistribution subject to ASME license or copyright; see http://www.asme.org/terms/Terms_Use.cfm

hydrodynamic conditions such as rise velocity and shape oscillation of bubbles crossing the interface, and probably on the physicochemical nature of the interface, which in turn depends on the degree of contamination at the interface. Such a stochastic or erratic formation of two-phase bubbles is not desirable in practical condensers. However, if we employ, for example, a condenser design such as that illustrated in Fig. 1, the approach velocity of bubbles toward the interface will be suppressed substantially, and thus every medium-sized bubble will entrain some amount of water in the form of its shell.

The water entrained by a steam bubble plays a few secondary roles in the steam condensation apart from its primary role as an enclosure for confining the condensate in itself. Firstly, it eliminates the free-energy barrier for nucleation which would cause a finite supercooling of steam resulting in a decrease of the effective temperature driving force [3, 10]. Secondly, it yields some resistance to heat flow from the steam to the medium. In an early period of condensation the upper portion of a bubble was covered with a water film which was some 0.2 mm thick. The resistance afforded by such a water film is estimated to be 10 percent or less of the total resistance, if we assume a quasi-steady heat flow crossing the film. Thirdly, the entrained water serves as a sensible-heat reservoir. The data on the V_w versus V_{si} relation obtained with apparatus I (see Fig. 5) indicate that the total sensible heat which can be released from the entrained water is as much as 1.5 to 4.8 times the total latent heat which can be released from the steam phase, if the initial temperature of the entrained water is higher than the bulk temperature by, for example, 3.0 K.[1] The significant sensible-heat release from the entrained water, joining the latent-heat release from the steam phase, will certainly give a great complexity to the analytical modeling – which is not discussed in the present paper – of the process of steam condensation in each two-phase bubble.

All of the roles favorable for increasing the condensation rate of the entrained water are available as long as the water continues to envelope the steam phase throughout the condensation process. On the other hand, possibly unfavorable roles (i.e., the latter two) can become significant as V_w increases. Thus, it is desirable to minimize V_w provided the water shell does not rupture before the condensation completes, although we have not succeeded yet in any attempt at reducing V_w.

Conclusions

A novel device has been presented for preventing tiny condensate droplets from being scattered in a medium consisting of a hydrophobic coolant while steam bubbles are released in the coolant to condense. With this device steam bubbles are released into the coolant not directly but through a water layer underlying the coolant phase. Each steam bubble penetrates into the coolant phase while enveloped in a water shell. The experiments with liquid paraffin as the coolant have shown that condensation of steam in each bubble is completed within the confines of the water shell before its rupture, which results in a disintegration of the shelled bubble into a bubble of noncondensible-gas/steam mixture and a water drop in which all the condensate is dissolved. Thus, the difficulty of separating the two liquids is eliminated.

One should note, however, the disadvantages (or restrictions) of the device as well. First, the initial steam bubble size should fall in a fairly narrow range around several millimeters diameter to ensure the formation of a water shell. Second, the condensation rate is lowered a little by the presence of the water shell. The extent of these disadvantages must depend on the properties of the coolant. The subject is left for future study.

[1] This fact does not always mean that the entrained water heats the coolant in vain and retards the condensation of the steam. In steady operation of such a condenser as illustrated in Fig. 1, the entrained water can have a positive role as a sensible-heat carrier by reciprocating between the bottom water layer, where heat is possibly removed in part from the steam in bubbles in formation and also from that in the steam distributor, and the bulk of the coolant where the heat is to be released.

Acknowledgments

This study has been accomplished with a variety of assistance afforded by some students – past and present – in the Department of Mechanical Engineering, Keio University. The author expresses special thanks to T. Kojima, Y. Shimizu, H. Ogawa, and K. Inaba for their extensive efforts devoted to the experimental work. T. Nosoko and Dr. K. Higeta are acknowledged for their helpful suggestions on the apparatus and data processing. I am also grateful to Mr. N. Kawaguchi and Prof. A. Nagashima who kindly measured thermal conductivity and thermal diffusivity of the water-saturated liquid paraffin with an apparatus that they had recently developed.

References

1 Sideman, S., and Moalem-Maron, D., "Direct Contact Condensation," in: *Advances in Heat Transfer*, J. P. Hartnett and T. F. Irvine, Jr., eds., Vol. 15, Academic Press, New York, 1982, pp. 227-281.

2 Sudhoff, B., Plischke, M., and Weinspach, P.-M., "Direct Contact Heat Transfer With Change of Phase – Condensation or Evaporation of a Drobble," *German Chemical Engineering*, Vol. 15, 1982, pp. 24-43.

3 Higeta, K., Mori, Y. H., and Komotori, K., "Condensation of a Single Vapor Bubble Rising in Another Immiscible Liquid," *AIChE Symposium Series*, Vol. 75, No. 189, 1979, pp. 256-265.

4 Mori, Y. H., "Configurations of Gas-Liquid Two-Phase Bubbles in Immiscible Liquid Media," *International Journal of Multiphase Flow*, Vol. 4, 1978, pp. 383-396.

5 Mori, Y. H., "Classification of Configurations of Two-Phase Vapor/Liquid Bubbles in an Immiscible Liquid in Relation to Direct-Contact Evaporation and Condensation Processes," *International Journal of Multiphase Flow*, Vol. 11, 1985, pp. 571-576.

6 Shimada, Y., Mori, Y. H., and Komotori, K., "Heat Transfer From a Horizontal Plate Facing Upward to Superposed Liquid-Layers With Change of Phase," ASME JOURNAL OF HEAT TRANSFER, Vol. 99, 1977, pp. 568-573.

7 Mercier, J. L., da Cunha, F. M., Teixeira, J. C., and Scofield, M. P., "Influence of Enveloping Water Layer on the Rise of Air Bubbles in Newtonian Fluids," ASME *Journal of Applied Mechanics*, Vol. 41, 1974, pp. 29-34.

8 Kawaguchi, N., Nagasaka, Y., and Nagashima, A., "A Fully Automatic Apparatus to Measure the Thermal Conductivity of Liquids by the Transient Hot-Wire Method," *Review of Scientific Instruments*, Vol. 56, 1985, pp. 1788-1794.

9 Mori, Y. H., Tsui, N., and Kiyomiya, M., "Surface and Interfacial Tensions and Their Combined Properties in Seven Binary, Immiscible Liquid–Liquid–Vapor Systems," *Journal of Chemical and Engineering Data*, Vol. 29, 1984, pp. 407-412.

10 Higeta, K., Mori, Y. H., and Komotori, K., "A Novel Direct-Contact Condensation Pattern of Vapour Bubbles in an Immiscible Liquid," *The Canadian Journal of Chemical Engineering*, Vol. 61, 1983, pp. 807-810.

Downloaded 17 Dec 2010 to 193.140.21.150. Redistribution subject to ASME license or copyright; see http://www.asme.org/terms/Terms_Use.cfm

Condensation on Coolant Jets and Sheets Including the Effects of Noncondensible Gases

H. R. Jacobs
Department of Mechanical Engineering,
The Pennsylvania State University,
University Park, PA 16802
Fellow ASME

R. Nadig
The Joseph Oat Corporation,
Camden, NJ

The study of condensation of a pure vapor or a mixture of a vapor and a noncondensible gas on a laminar cylindrical jet or a falling sheet can provide the necessary information for designing cascade, curtain, or jet-type direct contact condensers. Prior to the present work the only theoretical solutions were based on the solution of the Graetz problem and were thus restricted to problems where the Jakob number is zero. Using an integral formulation of the governing equations, an extension is made which provides results for practical values of both the Jakob and Graetz numbers. For the case where noncondensibles are present, detailed results are presented for the steam–air system.

Introduction

Direct contact condensers have been built and used industrially for well over 80 years. Hausbrand's book *Evaporation, Condensing and Cooling Apparatus* appeared in its first German edition in 1900 and was later translated into English, appearing in five English language editions through 1933. Despite this early start the development of the theory for direct contact heat transfer lagged greatly behind that for surface condensers. This point is emphasized by the fact that How's article, "How to Design Barometric Condensers," published in 1956, was simply a description of rules of thumb for designing equipment.

The article by How (1956) describes a wide range of equipment, including curtain and jet condensers such as those shown in Figs. 1 and 2. As can be seen these condensers have the coolant injected as a series of jets or solid sheets which fall down through a relatively quiescent vapor or vapor–gas mixture. Typically the vapor flows upward so that a counterflow exists. However, the vapor velocity is maintained sufficiently low that no coolant is stripped from the jets or sheets.

Jet and curtain-type direct contact condensers have received considerable attention in the USSR and England (Oliker, 1976). They are being used to replace feedwater heaters and as condensers in the Heller power cycles (Bakay and Jaszay, 1978). Oliker (1976) noted a significant lack of technical data of even an experimental nature dealing with their design. He states that "the evaluation of this apparatus usually consists of determining a heat balance and the necessary flow rates of condensed steam. A calculation of the heat and mass transfer is not made." He then points out that precise evaluation of the direct contact condenser design is desirable.

The earliest theoretical treatment of curtain and jet condensers is that of Kutateladze (1952). In his work and the subsequent work of Hasson et al. (1964a, 1964b), it was assumed that the surface of the jet, which entered the vapor chamber at a temperature T_0, was suddenly changed to the saturation temperature of the vapor. The vapor induced negligible shear on the liquid; thus the velocity in the jet was essentially constant. As the resistance of the condensate was assumed negligible, the solutions were applicable only if the Jakob number, defined as

$$C_{p_l}(T_{\text{sat}} - T_0)/h_{fg}$$

was infinitesimally small. This can occur if either $(T_{\text{sat}} - T_0) \to 0$ or if $h_{fg} \to \infty$. If the former is true no condensation takes place, and the Graetz number required for complete condensation is infinite. If h_{fg} is infinite with $(T_{\text{sat}} - T_0)$ finite the Graetz number for complete utilization of the coolant tends to zero. It is thus clear that the prior theories of Kutateladze and Hasson et al. cannot be applied unless a more accurate solution is first obtained which would define where their solutions provide approximate results.

When a small amount of noncondensible gas is present in a vapor, the rate of condensation can be appreciably reduced.

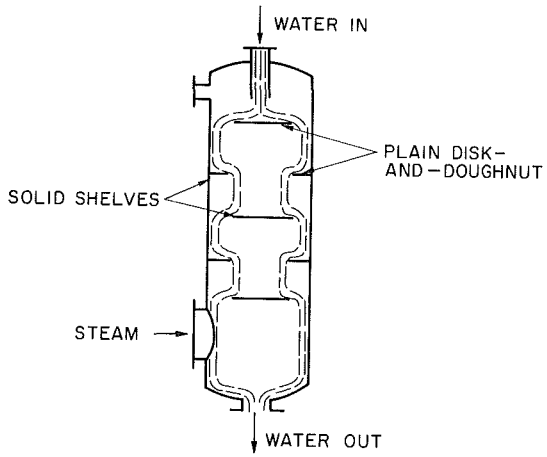

Fig. 1 "Solid curtain" condenser, condensing on a sheet

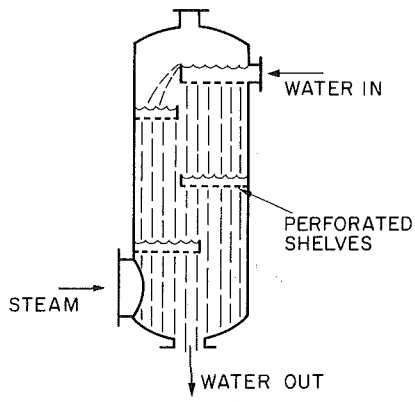

Fig. 2 Jet condenser

Contributed by the Heat Transfer Division for publication in the JOURNAL OF HEAT TRANSFER. Manuscript received by the Heat Transfer Division September 10, 1984.

Copyright © 1987 by ASME

Downloaded 17 Dec 2010 to 193.140.21.150. Redistribution subject to ASME license or copyright; see http://www.asme.org/terms/Terms_Use.cfm

This is true not only for surface condensation (Minkowycz and Sparrow, 1966), but also for direct contact condensation (Hasson et al. 1964b; Taitel and Tamir, 1969). In experiments for steam condensing on a fan jet of water, Hasson et al. (1964b) have shown that the average heat transfer coefficient could be reduced by up to 50 percent for a concentration of 1 percent air.

Taitel and Tamir (1969) were the first to consider theoretically the effects of noncondensibles for direct condensation on a sheet of coolant. Their study neglected the added resistance due to the condensate forming on the sheet. More recently Jacobs and Nadig (1983) evaluated the effects of noncondensibles on the condensation of a vapor on an immiscible liquid flowing over an adiabatic surface. They indicated that both the added mass resistance and the effect of noncondensibles were important in understanding the overall problem.

In this paper we treat the condensation of vapor on both a laminar sheet and on a jet of the same fluid, both for a pure vapor and in the presence of a noncondensible gas. For the pure vapor broadly applicable results are presented; however, for the case when noncondensibles are present, primary attention has been directed to the steam–air system. The basic models, however, are generally applicable.

General Assumptions

1 The velocity profiles in the jet or sheet are uniform. The basis for this assumption, used by the investigators mentioned above, is that the shear introduced by a low-pressure vapor on a moving liquid will be small. This is one of the classical assumptions of Nusselt (1916).

2 The other assumptions inherent in the Nusselt (1916) analysis hold, i.e., (*a*) the flow is laminar with no surface waves; (*b*) the properties of the liquid are constant.

3 The velocities in the gas–vapor phase are not influenced by gravity due to the fact that the velocity in the coolant stream is relatively high.

4 The liquid–vapor–gas interface is impermeable to the noncondensible gas. See Minkowycz and Sparrow (1966) for justification.

5 Interfacial resistance is negligible. This assumption has been shown by prior investigators, e.g., Minkowycz and Sparrow (1966), to be justifiable. The assumption substantiates the further assumption that the interface between the condensate and the vapor gas mixture is that of the local saturation temperature of the vapor, T^*. For $W_\infty = 0$ we have $T^* = T_\infty = T_{sat}$.

6 Axial conduction is negligible in the coolant stream.

7 A further assumption to be made is that the Jakob number is small or moderate in size. The Jakob number is here defined as

$$\mathrm{Ja} = C_{p_l}(T_\infty - T_0)/h_{fg}$$

The reason for this assumption is as follows: If we were to assume $W_\infty = 0$ and $T_\infty = T_{sat}$, an energy balance from where the coolant enters the condensation chamber to where its temperature is equal to T_{sat} would yield: for a jet

$$\rho_l C_{p_l} U(T_{sat} - T_0)\pi R^2 = \rho_l U h_{fg} 2\pi R\, \delta_{c_{x\to\infty}} \tag{1}$$

and for a sheet

$$\rho_l C_{p_l} U(T_{sat} - T_0)L = \rho_l U h_{fg} \delta_{c_{x\to\infty}} \tag{2}$$

Thus for a jet

$$\frac{\delta_{c_{x\to\infty}}}{R} = \frac{C_{p_l}(T_{sat} - T_0)}{2\,h_{fg}} = \frac{\mathrm{Ja}}{2} \tag{3}$$

and for a sheet

$$\frac{\delta_{c_{x\to\infty}}}{L} = \frac{C_{p_l}(T_{sat} - T_0)}{h_{fg}} = \mathrm{Ja} \tag{4}$$

It is clear that if Ja is small or moderate, the thickness of the condensate layer will be small. For a vapor condensing on its own liquid this generally means that $T_{sat} - T_0$ is of moderate size and therefore the assumption of constant properties for the liquid should be reasonable. Further, the small mass addition supports the prior assumption of uniform coolant velocity, axially as well as laterally. If the mass addition were large it would affect the inertia of the sheet or jet. Small Jakob number, for low-pressure systems, provides for negligible dynamic influences.

Mathematical Formulation and Physical Models

The basic models for condensation on a sheet or jet in the presence of a noncondensible gas are shown in Figs. 3 and 4.

Nomenclature

a, b = constants
C_{p_l} = specific heat of liquid
D = diameter
$\mathfrak{D}$ = diffusion coefficient
D_H = hydraulic diameter
Gz = Graetz number = $\mathrm{Re}_d\,\mathrm{Pr}\,D_H/s$
h = heat transfer coefficient
h_{fg} = heat of vaporization
Ja = Jakob number = $C_p\,(T_\infty - T_0)/h_{fg}$
k_l = thermal conductivity of liquid
L = thickness of sheet
M_v = molecular weight of vapor
M_g = molecular weight of gas
Nu = Nusselt number = hD_H/k
P = total pressure
Pr = Prandtl number = $C_p\,\mu/k$
P_v = vapor pressure
R = radius of jet
$\mathfrak{R}$ = universal gas constant
Re = Reynolds number
Re_{D_H} = Reynolds number based on hydraulic diameter = UD_H/ν, $U4L/\nu$ for sheet, UD/ν for jet
Sc = Schmidt number, ν/D
T_c = temperature of condensate layer
T_{CL} = centerline temperature of jet or sheet
T_i = temperature between coolant and condensate layer
T_l = temperature in sheet or jet
T_0 = inlet temperature of jet or sheet
T_{sat} = saturation temperature
U = velocity of jet or sheet
W = gas concentration
x = distance along length of jet or sheet
y = distance normal to centerline of sheet or jet
δ_t = thermal boundary layer in Region 1 of jet or sheet
δ_c = thickness of condensate film
δ_M = thickness of velocity boundary layer in vapor–gas mixture
δ_s = thickness of concentration boundary layer
θ = nondimensional temperature defined in equation (14)
μ_l = dynamic viscosity of liquid
μ_m = dynamic viscosity of vapor–gas mixture
ν_l = kinematic viscosity of liquid
ν_m = kinematic viscosity of vapor–gas mixture
ρ_l = density of liquid
ρ_m = density of vapor–gas mixture
$\bar{\ }$ = length divided by D_H

Downloaded 17 Dec 2010 to 193.140.21.150. Redistribution subject to ASME license or copyright; see http://www.asme.org/terms/Terms_Use.cfm

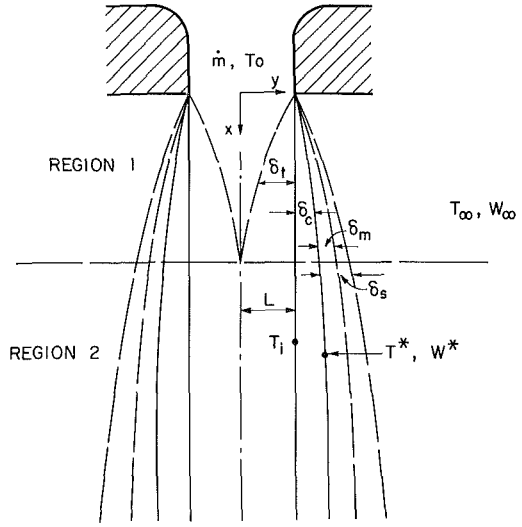

Fig. 3 Schematic model for condensation on a sheet

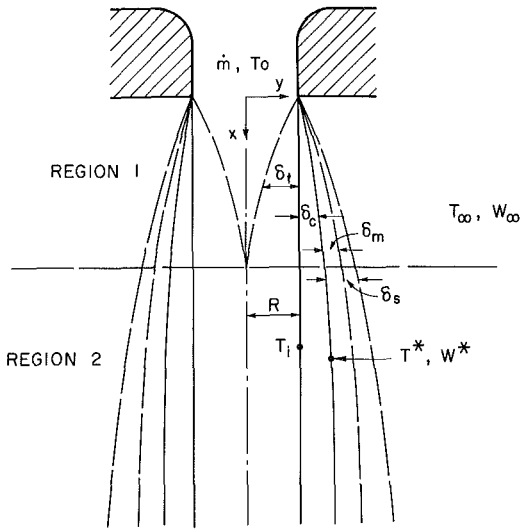

Fig. 4 Schematic model for condensation on a jet

As can be seen the sheet or jet is divided into two regions. Region 1 defines the length of sheet or jet necessary for a thermal boundary layer to grow from the condensate layer–coolant interface to the centerline of the coolant stream. Region 2 starts when the thermal boundary layer has reached the coolant centerline and continues until the condensation ceases. Outside the condensate layer of thickness δ_c, the vapor-gas mixture forms a thin boundary layer δ_m, in which the noncondensible gas concentration varies from W^* at the liquid-mixture interface to the free-stream value of W_∞. At the vapor-gas condensate interface the temperature is T^*. At the interface between the liquid coolant and the condensate layer the temperature is T_i.

A Region 1 Equations. In Region 1 the energy equation for the coolant is

$$\frac{d}{dx}\int_{L-\delta_t}^{L} \rho_l C_{p_l} U(T_l - T_0) y^n dy = k_l \left(y_n \frac{\partial T_l}{\partial y}\right)\Big|_{y=L} \tag{5}$$

For the sheet n is equal to zero and for the cylindrical jet it is equal to one. Further, for the jet $L = R$, which is the coolant radius, while for the sheet L is the half-thickness of the sheet.

In the condensate layer the assumption of small Jakob number insures that the sensible heat capacity of the condensate is small compared to the heat of vaporization and that the condensate layer is thin. These assumptions allow us to neglect the sensible heat of the condensate; thus the energy balance for the condensate layer yields for both the sheet and jet

$$h_{fg}\frac{d}{dx}\int_{L}^{L+\delta_c} \rho_l U\, y^n dy = k_l y^n \frac{\partial T_c}{\partial y}\Big|_{y=L} \tag{6}$$

The assumption of negligible thermal capacitance of the condensate layer implies a linear temperature profile across it. Thus

$$T_c = T_i + (y-L)\left(\frac{T^* - T_i}{\delta_c}\right) \tag{7}$$

The thermal capacitance of the coolant is the only heat sink to induce condensation; therefore, a more general profile is necessary. The boundary conditions are

$$T_l = T_0 \text{ and } \frac{\partial T_l}{\partial y} = 0 \text{ at } y = L - \delta_t \tag{8}$$

and $T = T_i$ at $y = L$. These conditions lead to

$$T_l = T_i + \frac{T_i - T_0}{\delta_t^2}(L^2 - 2\,\delta_t L + 2y(-L+\delta_t) + y^2) \tag{9}$$

The compatibility condition of the heat fluxes at the interface between the coolant stream and condensate film

$$\frac{\partial T_c}{\partial y}\Big|_{y=L} = \frac{\partial T_l}{\partial y}\Big|_{y=l} \tag{10}$$

leads to the following expression for the interfacial temperature:

$$T_i = \frac{T_0 + \tfrac{1}{2}\delta_t/\delta_c T^*}{1 + \tfrac{1}{2}\delta_t/\delta_c} \tag{11}$$

Substituting equations (7), (9), and (11) into equations (5) and (6) results in

$$\frac{d\bar{\delta}_t^2}{dx}\left\{\left(\frac{12}{\Pr \mathrm{Re}_{D_H}} - \frac{2\bar{\delta}_t^2}{\theta^*}\left(1-\frac{\bar{\delta}_t}{2}\right)^n \frac{d\theta^*}{dx}\right)\left(1+\tfrac{1}{2}\frac{\bar{\delta}_t}{\bar{\delta}_c}\right) + \frac{\bar{\delta}_t^2}{\bar{\delta}_c^2}\left(1-\frac{\bar{\delta}_t}{2}\right)^n \frac{d\bar{\delta}_t^2}{dx}\right\} \div \left\{(1-\bar{\delta}_t)^n\left(1+\tfrac{1}{2}\frac{\bar{\delta}_t}{\bar{\delta}_c}\right) + \left(1+\frac{\bar{\delta}_t}{2}\right)^n\right\} \tag{12}$$

and

$$\frac{d\bar{\delta}_c^2}{d\bar{x}} = \frac{2\,\mathrm{Ja}_c\theta^*}{\mathrm{Re}_{D_{H_c}}\Pr_c\left[1+\tfrac{1}{2}\frac{\bar{\delta}_t}{\bar{\delta}_c}(1+2\bar{\delta}_c)^n\right]} \tag{13}$$

where lengths have been nondimensionalized with respect to the hydraulic diameter and

$$\theta = \frac{T - T_0}{T_\infty - T_0} \tag{14}$$

In order to solve equations (12) and (13) it is first necessary to determine the value of θ^*, the nondimensional saturation temperature at the condensate vapor-gas mixture interface. This of course requires solving for the concentration of the vapor at the interface, which in turn requires the solution of the vapor gas momentum and species equations. The assumption of a small value of Jakob number and small variations in h_{fg} allows for integration of the Clausius Clapeyron equation to yield

$$\theta^* = \frac{\theta_{\mathrm{sat}_\infty} - \dfrac{T_0 T_{\mathrm{sat}_\infty} R}{h_{fg}(T_\infty - T_0)} \ln \dfrac{P_{v_\infty}}{P_v^*}}{1 + \dfrac{T_{\mathrm{sat}_\infty} R}{h_{fg}} \ln \dfrac{P_{v_\infty}}{P_v^*}} \tag{15}$$

Downloaded 17 Dec 2010 to 193.140.21.150. Redistribution subject to ASME license or copyright; see http://www.asme.org/terms/Terms_Use.cfm

The ratio of partial pressure of the vapor to total pressure

$$\frac{P_v}{P}=\frac{1-W}{1-W\left(1-\frac{M_v}{M_g}\right)} \tag{16}$$

then allows for relating the mass concentration of gas to the value of θ^*. (For the special case of $P_v/P = 1$, $W_\infty = 0$, no superheat, and thus $T_\infty = T_{\text{sat}}$, θ^* is 1.0.)

The integral forms for the momentum and species equations in the gas–vapor mixture, assuming that the condensate vapor–gas interface is impenetrable to the gas, reduce to

$$\frac{d}{dx}\int_{L+\delta_c}^{L+\delta_c+\delta_m} u^2 y^n dy + U^2(L+\delta_n)^n \frac{\rho_l}{\rho_m^*}\frac{d\delta c}{dx}$$

$$= -\nu_m\left(y^n\frac{\partial u}{\partial y}\right)\Big|_{L+\delta_c} \tag{17}$$

and

$$\frac{d}{dx}\int_{L+\delta_c}^{L+\delta_c+\delta_s}(W-W_\infty)u\, y^n dy = \mathfrak{D}\frac{W_\infty}{W^*}\left(y^n\frac{\partial W}{\partial y}\right)\Big|_{L+\delta_c} \tag{18}$$

The conditions of no slip at the condensate vapor–gas mixture interface, zero velocity in the mixture as $y \to \infty$, and the condition of $\partial u/\partial y = 0$ as $y \to \infty$ suggest that in the mixture

$$u = U\left[1-\frac{y-(L+\delta_c)}{\delta_m}\right]^2 \tag{19}$$

For the species equation with $W|_{L+\delta_c} = W^*$, $W|_{L+\delta_c+\delta_s} = W_\infty$ and $\partial W/\partial y|_{L+\delta_c+\delta_s} = 0$, we obtain

$$W-W_\infty = (W^*-W_\infty)\left(1-\frac{y-(L+\delta_c)}{\delta_s}\right)^2 \tag{20}$$

Substituting equations (19) and (20) into equations (17) and (18) and nondimensionalizing results in

$$\frac{d\bar{\delta}_m^2}{d\bar{x}}=\frac{\dfrac{12}{\mathrm{Re}_{D_H}\,\nu_l/\nu_m}-3\dfrac{\rho_l}{\rho_m}\dfrac{\bar{\delta}_m}{\bar{\delta}_c}\dfrac{d\bar{\delta}_c^2}{d\bar{x}}}{(1+\bar{\delta}_m)^n} \tag{21}$$

and

$$\frac{d}{dx}\left\{(W^*-W_\infty)\left[(\tfrac{1}{2}+\bar{\delta}_c)^n\bar{\delta}_s\left(1-\tfrac{1}{2}\frac{\bar{\delta}_s}{\bar{\delta}_m}+\frac{1}{10}\frac{\bar{\delta}_s^2}{\bar{\delta}_m^2}\right)\right.\right.$$

$$\left.\left.+\bar{\delta}_s^2\left(\frac{1}{4}-\frac{1}{5}\frac{\bar{\delta}_s}{\bar{\delta}_m}+\frac{1}{10}\frac{\bar{\delta}_s^2}{\bar{\delta}_m^2}\right)\right]\right\}$$

$$=\frac{6}{\mathrm{Re}_{D_H}\mathrm{Sc}\,\nu_l/\nu_m}(\tfrac{1}{2}+\bar{\delta}_c)^n\frac{W_\infty}{W^*}\left(\frac{W^*-W_\infty}{\bar{\delta}_s}\right) \tag{22}$$

The condition of impermeability of the condensate vapor–gas mixture interface leads to

$$W^*=\frac{W_\infty}{1-(1/4)\mathrm{Re}_{D_H}\mathrm{Sc}\dfrac{\mu_l}{\mu_m}\dfrac{\bar{\delta}_s}{\bar{\delta}_c}\dfrac{d\bar{\delta}_c^2}{d\bar{x}}} \tag{23}$$

Thus, for Region 1, equations (12), (13), (15), (16), (21), (22), and (23) completely define the condensation on a sheet or jet in the presence of a noncondensible gas, while equations (12) and (13) are sufficient for $W_\infty = 0$ and $T_\infty = T_{\text{sat}}$, with $\theta^* = 1.0$.

B Region 2 Equations. Region 2 begins when $\delta_t = L$. From this point the entire coolant stream heats up such that the centerline temperature will be continuously increasing. The energy equation for the coolant stream in Region 2 changes from that given in equation (5) only in that the limits of integration are from $y = 0$ to L. The temperature profile in the coolant must satisfy the boundary conditions

$$y=0 \qquad \frac{\partial T_l}{\partial y}=0, \quad T_l = T_{CL}$$

and

$$y=L \qquad T=T_i \tag{24}$$

These conditions are satisfied by the expression

$$T_l - T_{CL} = (T_i - T_{CL})(y/L)^2 \tag{25}$$

The governing equation and the temperature profile for the condensate layer are the same as in Region 1. Using the compatibility of heat fluxes at the interface between the original coolant stream and the condensate layer yields

$$\theta_i - \theta_{CL} = \frac{L}{2}\left(\frac{\theta^*-\theta_i}{\delta_c}\right) \tag{26}$$

Using equation (26) and the temperature profile for the coolant stream there results from the coolant energy equation

$$\frac{d\theta_i}{d\bar{x}}=\frac{\dfrac{(3/2)^n(\theta^*-\theta_i)}{\mathrm{Re}_{D_H}\mathrm{Pr}}-\tfrac{1}{2}\dfrac{\theta^*-\theta_c}{\bar{\delta}_c^2}\dfrac{d\bar{\delta}_c^2}{d\bar{x}}+\dfrac{d\theta^*}{d\bar{x}}}{8(3/2)^n\bar{\delta}_c+1} \tag{27}$$

and the condensate film energy equation remains as

$$\frac{d\bar{\delta}_c^2}{d\bar{x}}=\frac{2\ \mathrm{Ja}}{\mathrm{Re}_{D_H}\mathrm{Pr}}\frac{\theta^*-\theta_i}{(1+2\,\bar{\delta}_c)^n} \tag{28}$$

The relations defining $\bar{\delta}_m^2$, W^*, $\bar{\delta}_s^2$ remain as given for Region 1 and as expressed in equations (21), (22), and (23). The initial conditions for the θ_i, $\bar{\delta}_c^2$, θ^*, W^*, $\bar{\delta}_m^2$, and $\bar{\delta}_s^2$ for Region 2 are the conditions obtained at the end of Region 1.

C Calculation of Percent Coolant Utilized. The mean temperature of the coolant is calculated from the equation

$$T_m\int_0^L \rho_l C_{P_l} U\, y^n dy = \int_0^L \rho_l C_{p_l} U\, T_l y^n dy \tag{29}$$

For Region 1

$$\theta_m = (4/3)\theta_i\bar{\delta}_t[2(1-\bar{\delta}_t)]^n \tag{30}$$

In Region 2 for a sheet

$$\theta_m = (2/3)\theta_L + (1/3)\theta_i \tag{31}$$

and for a jet

$$\theta_m = \frac{\theta_L+\theta_i}{2} \tag{32}$$

Note that the definition of θ is as given in equation (14); thus, the value of θ_m yields the utilized fraction of the coolant capacity to absorb the heat given up by the condensation process. For direct contact condensation, it is this quantity that is important to the designer rather than the heat transfer coefficient or local Nusselt number. Thus, in this paper the percent coolant utilized is the primary factor reported. The heat transfer coefficient or Nusselt number are only reported for comparison with the results of prior studies.

Results and Discussion

A Condensation of a Pure Vapor. As noted earlier, for $W_\infty = 0$ and $T_\infty = T_{\text{sat}}$, we have the case of a pure saturated vapor condensing on a coolant stream, and need solve only

Downloaded 17 Dec 2010 to 193.140.21.150. Redistribution subject to ASME license or copyright; see http://www.asme.org/terms/Terms_Use.cfm

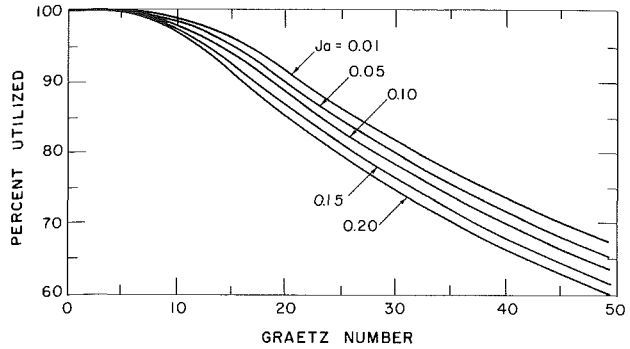

Fig. 5 Percent coolant capacity utilized for condensation of a pure saturated vapor on a sheet

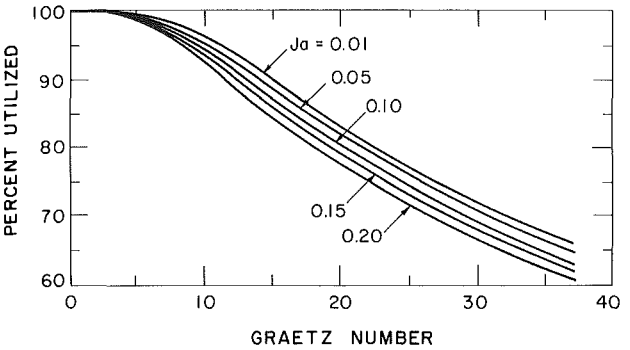

Fig. 6 Percent coolant capacity utilized for condensation of a pure vapor on a jet

equations (12) and (13) as $\theta^* = 1$. Examination of these equations indicates dependence only on Re_{D_H}, Pr, x/D_H, and Ja. For very small values of x/D_H a similarity solution exists, and δ_c and δ_t can be expressed as

$$\bar{\delta}_c|_{x\to 0} = a_0\bar{x}^{1/2} + \ldots \simeq a_0\bar{x}^{1/2}$$

and

$$\bar{\delta}_t|_{x\to 0} = b_0\bar{x}^{1/2} + \ldots \simeq b_0\bar{x}^{1/2} \tag{33}$$

Thus for small values of x it can be shown that

$$\mathrm{Nu}_{D_H}(x) = \frac{(\mathrm{Re}_{D_H}\mathrm{Pr}\, D_H/x)^{1/2}}{(3/4+2\mathrm{Ja})^{1/2}+(3/4)^{1/2}}$$

$$= \frac{\mathrm{Gz}_x^{1/2}}{(3/4+2\mathrm{Ja})^{1/2}+(3/4)^{1/2}} \tag{34}$$

for both the jet and sheet.

For the limiting case of Ja→0 and small x

$$\mathrm{Nu}_{D_H}(x) = \left(\frac{\mathrm{Gz}_x}{3}\right)^{1/2} \tag{35}$$

which is nearly equal to the results of Kutateladze (1952) and Hasson et al. (1964) for large Graetz number. The analytical Graetz problem they solve differs only in the 3 in our equation (35) being replaced by π. The difference would indicate that for large Graetz numbers the present solution gives a slightly faster heating of the coolant than the Graetz solution. The two solutions yield results within 3 percent for Jakob number less than 0.05.

As noted in the development of the governing equations, it is of more value to present the percent coolant utilized than the local or average Nusselt number when solving problems of direct contact condensation. Figures 5 and 6 present percent utilization curves from the results of our analyses for a sheet ($n = 0$) and a cylindrical jet ($n = 1$), respectively. The range of Ja covered is for values less than 0.2 while the value of the Graetz number is from 0 to 50 for the sheet and 0 to 40 for the jet. Tables 1 and 2 present tabulated values for the sheet and jet, respectively.

Table 1 Percent coolant capacity utilized for condensation on a sheet

	Percent Coolant Capacity Utilized					
Gz	Gz Sol.	Ja=0.01	Ja=0.05	Ja=0.10	Ja=0.15	Ja=0.20
78.9	50.8	53.1	51.7	50.2	48.8	47.5
56.6	59.7	62.9	61.3	59.5	57.8	56.3
49.6	63.5	67.0	65.3	63.4	61.6	60.0
44.1	66.9	70.7	68.9	66.9	65.0	63.4
39.7	70.0	73.9	72.1	70.0	68.1	66.4
36.1	72.9	76.9	74.9	72.8	70.9	69.2
33.1	75.4	79.4	77.5	75.4	73.4	71.7
30.6	77.7	81.7	79.8	77.7	75.7	73.9
28.4	79.8	83.7	81.9	79.7	77.8	75.9
26.5	81.7	85.5	83.7	81.6	79.7	77.9
24.9	83.4	87.1	85.3	83.3	81.4	79.6
24.4	84.9	88.5	86.8	84.8	82.9	81.2
22.1	86.4	89.8	88.1	86.2	84.4	82.7
19.9	88.8	91.9	90.4	88.6	86.8	85.2
18.1	90.8	93.6	92.2	90.5	88.9	87.4
17.3	91.7	94.3	93.0	91.4	89.8	88.3
15.9	93.2	95.5	94.3	92.9	91.4	90.0
13.8	95.4	97.1	96.3	95.1	93.9	92.7
12.1	96.9	98.2	97.6	96.6	95.6	94.6
10.5	98.1	99.0	98.5	97.9	97.1	96.3
8.9	99.1	99.6	99.3	98.9	98.4	97.8
7.9	99.4	99.8	99.6	99.3	98.9	98.5
7.4	99.6	99.8	99.7	99.5	99.2	98.9
6.9	99.7	99.9	99.8	99.7	99.6	99.2
6.4	99.8		99.9	99.8	99.6	99.4
6.2	99.9		99.9	99.8	99.7	99.5
5.9	99.9			99.9	99.7	99.6
5.6	99.9			99.9	99.8	99.7
5.3	99.9				99.9	99.8
5.1	99.9				99.9	99.8
4.8	99.9					99.9
4.7	99.9					99.9

Table 2 Percent coolant capacity utilized for condensation on a jet

	Percent Coolant Capacity Utilized					
Gz	Gz Sol.	Ja=0.01	Ja=0.05	Ja=0.10	Ja=0.15	Ja=0.20
58.8	51.7	53.6	52.6	51.4	50.3	49.3
45.5	57.5	60.4	59.2	57.9	56.7	55.6
37.0	62.5	66.2	64.9	63.5	62.2	61.0
31.3	66.7	71.1	69.8	68.3	66.9	65.7
27.0	70.5	75.3	73.9	72.5	71.0	69.7
23.8	73.7	78.9	77.6	76.0	74.6	73.3
21.3	76.6	81.9	80.7	79.1	77.7	76.4
19.2	79.2	84.6	83.3	81.8	80.4	79.1
17.5	81.5	86.7	85.6	84.2	82.8	81.5
16.1	83.5	88.8	87.6	86.2	84.8	83.6
14.9	85.3	90.4	89.3	87.9	86.7	85.4
13.9	86.9	91.8	90.7	89.5	88.2	87.1
12.9	88.3	92.9	92.0	90.8	89.6	88.5
12.2	89.6	94.0	93.1	91.9	90.9	89.8
11.5	90.8	94.9	94.0	92.9	91.9	90.9
10.9	91.8	95.6	94.8	93.9	92.9	91.9
10.1	93.1	96.5	95.9	94.9	94.1	93.2
9.3	94.2	97.3	96.7	95.9	95.1	94.3
8.7	95.1	97.8	97.3	96.7	95.9	95.2
8.2	95.9	98.3	97.9	97.3	96.6	95.9
7.4	96.9	98.8	98.5	98.0	97.5	96.9
6.8	97.7	99.2	98.9	98.6	98.2	97.7
6.3	98.3	99.5	99.3	98.9	98.7	98.3
5.8	98.7	99.6	99.5	99.3	99.0	98.7
5.4	99.0	99.8	99.7	99.5	99.3	99.0
5.1	99.3	99.8	99.8	99.6	99.5	99.3
4.7	99.5	99.9	99.9	99.8	99.7	99.5
4.4	99.6		99.9	99.8	99.8	99.7
4.3	99.7			99.9	99.8	99.7
4.1	99.8				99.9	99.8
3.9	99.8					99.9

The primary reason for presenting both figures and tables deals with the difficulty in obtaining accurate values for the Graetz number, and thus coolant stream length, at high degrees of coolant utilization. The curves appear to converge while in fact considerable spread is seen from the tables.

Comparison between condensation on a jet and sheet can be made by comparing values of coolant utilization shown in Tables 1 nd 2 and by examining the case of Ja = 0.05 shown in Fig. 7. For Gz → ∞ the heat transfer is the same as already noted; however, a considerable divergence of percent coolant utilized occurs for Gz < 50. For a percent coolant utilization of 99.5 percent, the jet requires a 30 percent smaller value of the Graetz number than the sheet. For equal hydraulic diameters this corresponds to a 41 percent longer coolant stream; of course, for a jet diameter equal to the sheet thickness the jet need be only 46 percent as long!

Downloaded 17 Dec 2010 to 193.140.21.150. Redistribution subject to ASME license or copyright; see http://www.asme.org/terms/Terms_Use.cfm

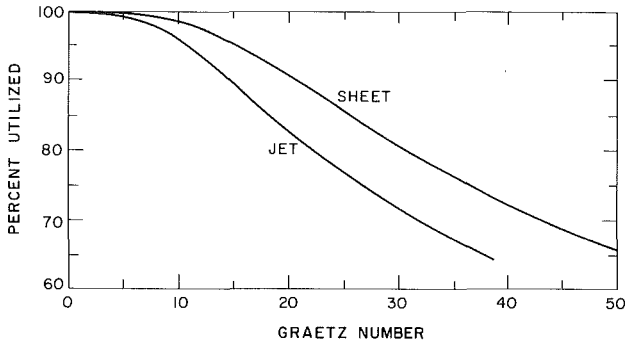

Fig. 7 Comparison of coolant capacity utilization for condensation of a pure saturated vapor on a sheet and a jet for Ja = 0.05

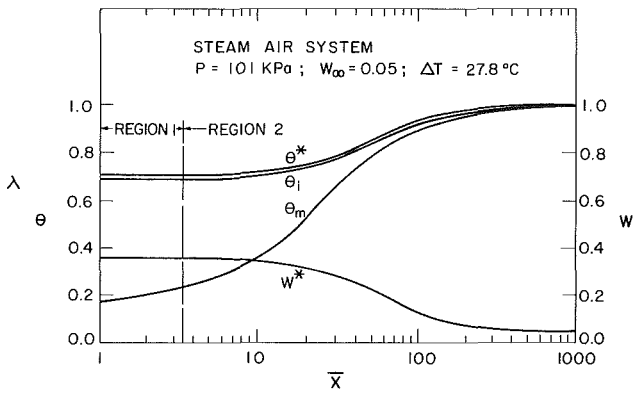

Fig. 8 Condensation of steam on a sheet of water, $W_\infty = 0.05$, P = 101 kPa

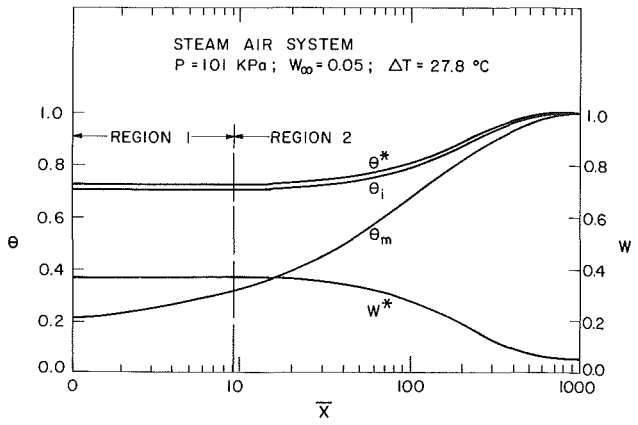

Fig. 9 Condensation of steam on a jet of water, $W_\infty = 0.05$, P = 101 kPa

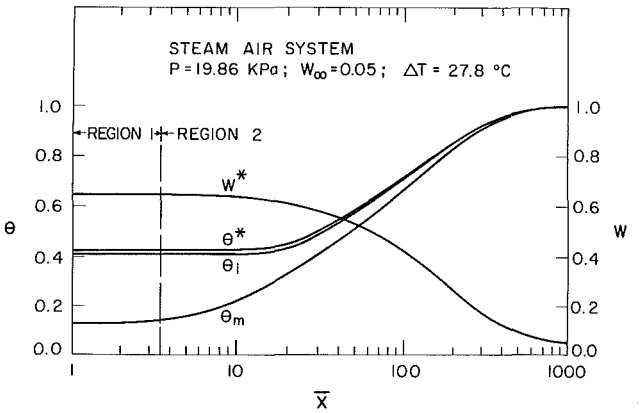

Fig. 10 Condensation of steam on a sheet of water, $W_\infty = 0.05$, P = 19.86 kPa

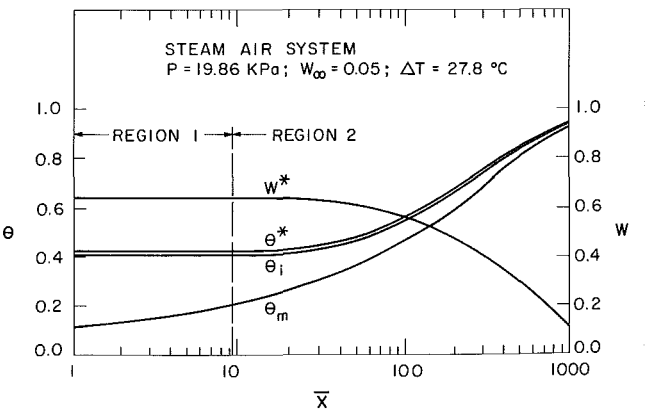

Fig. 11 Condensation of steam on a jet of water, $W_\infty = 0.05$, P = 19.86 kPa

Our results show further that for $0.01 \leq \text{Ja} \leq 0.20$ that the heat transfer for the entire range of Region 1 is well satisfied by equation (34). For the jet θ_i varied by about 5 percent over Region 1 for Jakob number of 0.2 but less than 1 percent for Jakob number of 0.01. However, to design a sheet or jet condenser the solutions for both regions must be obtained, and both θ_i and θ_{cL} vary significantly in Region 2. Thus, the tabulated values must be used.

B Condensation With Noncondensibles Present. For the case when noncondensibles are present, the governing equations indicate that all of the following parameters are of importance: Re_{D_H}, Pr, x/D_H, Ja, M_v/M_g, ρ_l/ρ_m, ν_l/ν_m, and W_∞. Due to the large number of variables, we have restricted the results to be presented in this paper to parameters which typify the problem for a steam–air system. In this way we are able to compare our results more easily with those of other investigators (Hasson et al., 1964b; Minkowycz and Sparrow, 1966; Taitel and Tamir, 1969; Jacobs and Nadig, 1983).

As noted in Region 1, a similarity solution is available for very small values of x. In fact, for the problem of the sheet, for small values of the Jakob number, the similarity solution is applicable for the entire region. For the cylindrical jet an error exists if the similarity region is used to describe the entire region. The similarity solution is satisfied by $\bar{\delta}_t = a\,\bar{x}^{1/2}$, $\bar{\delta}_c = b\bar{x}^{1/2}$, $\bar{\delta}_m = c\,\bar{x}^{1/2}$ and $\bar{\delta}_s = d\,\bar{x}^{1/2}$. These solutions indicate that W^*, θ^*, and θ_i are of constant value in Region 1. Similar results were found by Taitel and Tamir (1969) for condensation in the presence of a noncondensible gas. The extent of Region 1 is a function only of D_H and the Peclet number. For a sheet the extent of Region 1 is given by

$$\bar{x}_{D_{\text{sheet}}} = 0.083\ \text{Re}_{D_H}\text{Pr} \tag{36}$$

which is in agreement with Taitel and Tamir.

The governing equations for the cylindrical jet are highly nonlinear and do not yield a similarity solution unless $x \to 0$. Thus, the extent of Region 1 is dependent upon other parameters. However for Ja < 0.05 an approximate value of $x_{D_{\text{jet}}}$ can be obtained as the changes in θ_i, W^*, and θ^* are small. The approximate value is

$$\bar{x}_{D_{\text{jet}}} = 0.146\ \text{Re}_{D_H}\text{Pr} \tag{37}$$

Equation (30) gives the value of the mean temperature for Region 1 for the case where Ja → 0 and $W_\infty \to 0$ and θ_i goes to 1. Here $\theta_m \to 1/3$ at $\delta_t = L$ for a sheet, and $\theta_m \to 2/3$ at $\delta_t = R$ for a jet. The effect of noncondensibles is to lower the values of θ^* and θ_i even for very small values of Ja. Since θ_m is equal to the fraction of coolant cooling capacity utilized, it is

Downloaded 17 Dec 2010 to 193.140.21.150. Redistribution subject to ASME license or copyright; see http://www.asme.org/terms/Terms_Use.cfm

Table 3 Ratio of Graetz number for $W_\infty = 0$ to that for a given W_∞ for condensation on a sheet

% Util.	Pressure KPa	W_∞	Ratio of Graetz Number ΔT = 13.9°C (25°F)	ΔT = 27.8°C (50°F)	ΔT = 41.7°C (75°F)	ΔT = 55.5°C (100°F)
60	101	0.005	1.047	1.089	1.107	1.168
70	101	0.005	1.050	1.091	1.139	1.177
80	101	0.005	1.606	1.103	1.153	1.198
90	101	0.005	1.080	1.129	1.173	1.220
60	101	0.01	1.117	1.179	1.235	1.356
70	101	0.01	1.121	1.191	1.293	1.384
80	101	0.01	1.131	1.217	1.316	1.428
90	101	0.01	1.168	1.266	1.368	1.473
60	101	0.05	1.632	2.117	2.797	3.702
70	101	0.05	1.720	2.259	3.008	3.863
80	101	0.05	1.848	2.470	3.223	4.102
90	101	0.05	2.042	2.708	3.479	4.334
60	101	0.1	2.567	3.860	5.556	7.764
70	101	0.1	2.824	4.235	6.079	8.203
80	101	0.1	3.185	4.479	6.624	8.781
90	101	0.1	3.749	5.380	7.249	9.316
60	19.7	0.005	1.185	1.383	1.622	1.956
70	19.7	0.005	1.213	1.413	1.686	2.021
80	19.7	0.005	1.244	1.472	1.747	2.090
90	19.7	0.005	1.291	1.542	1.826	2.150
60	19.7	0.01	1.397	1.865	2.448	3.274
70	19.7	0.01	1.446	1.921	2.573	3.395
80	19.7	0.01	1.516	2.035	2.693	3.513
90	19.7	0.01	1.615	2.842	3.597	
60	19.7	0.05	3.596	6.698	10.840	16.309
70	19.7	0.05	3.962	7.263	11.672	16.838
80	19.7	0.05	4.439	7.997	12.357	17.460
90	19.7	0.05	5.088	8.818	13.108	17.885
60	19.7	0.1	7.573	14.944	24.508	36.916
70	19.7	0.1	8.582	16.426	26.606	38.387
80	19.7	0.1	9.884	18.322	28.444	40.164
90	19.7	0.1	11.798	20.507	30.420	41.398

Table 4 Ratio of Graetz number for $W_\infty = 0$ to that for a given W_∞ for condensation on a jet

% Util.	Pressure KPa	W_∞	Ratio of Graetz Number ΔT = 13.9°C (25°F)	ΔT = 27.8°C (50°F)	ΔT = 41.7°C (75°F)	ΔT = 55.5°C (100°F)
60	101	0.005	2.000	1.698	1.444	1.268
70	101	0.005	2.042	1.822	1.480	1.282
80	101	0.005	2.000	1.924	1.713	1.554
90	101	0.005	1.872	1.883	2.148	2.261
60	101	0.01	2.451	1.981	1.667	1.536
70	101	0.01	2.620	2.219	1.840	1.744
80	101	0.01	2.634	2.505	2.324	2.384
90	101	0.01	2.481	2.620	3.059	3.392
60	101	0.05	5.333	5.226	6.019	7.339
70	101	0.05	6.282	6.603	7.653	8.974
80	101	0.05	6.911	7.724	9.074	10.357
90	101	0.05	6.955	8.074	9.728	11.063
60	101	0.1	10.549	11.849	13.704	15.232
70	101	0.1	12.211	13.877	15.653	16.987
80	101	0.1	13.178	14.848	16.750	18.080
90	101	0.1	13.205	14.632	16.550	17.926
60	19.7	0.005	2.393	1.638	1.940	4.657
70	19.7	0.005	2.707	1.858	2.892	6.862
80	19.7	0.005	3.238	2.583	4.029	8.387
90	19.7	0.005	3.613	3.943	5.093	8.387
60	19.7	0.01	3.120	2.556	4.429	9.989
70	19.7	0.01	3.748	3.440	6.034	12.215
80	19.7	0.01	4.722	4.757	7.346	13.308
90	19.7	0.01	5.510	6.477	8.410	3.156
60	19.7	0.05	12.784	14.208	17.870	23.589
70	19.7	0.05	15.070	16.534	19.720	25.090
80	19.7	0.05	16.743	18.314	20.917	25.536
90	19.7	0.05	17.032	19.577	21.692	24.994
60	19.7	0.1	26.765	27.057	29.648	34.143
70	19.7	0.1	29.014	29.589	31.613	35.590
80	19.7	0.1	30.158	30.981	32.685	36.018
90	19.7	0.1	29.609	31.319	32.899	35.278

clear that an increase in W_∞ will decrease the fraction of coolant utilized. Thus, it is necessary, under all conditions where one wishes to utilize a major portion of the coolant capacity, to carry out the analyses for Region 2.

Typical behavior for θ_i, θ^*, θ_m, and W^* are shown in Figs. 8–11 as functions of $\bar{x}$. It is clear that the effects of the non-

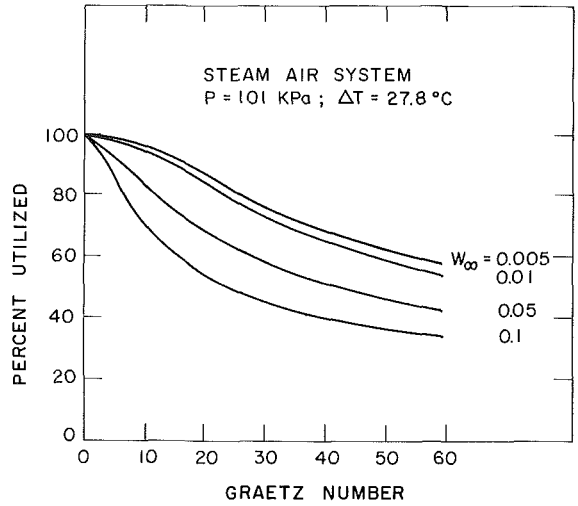

Fig. 12 Effect of W_∞ on percent coolant utilized for condensation on a sheet, P = 101 kPa

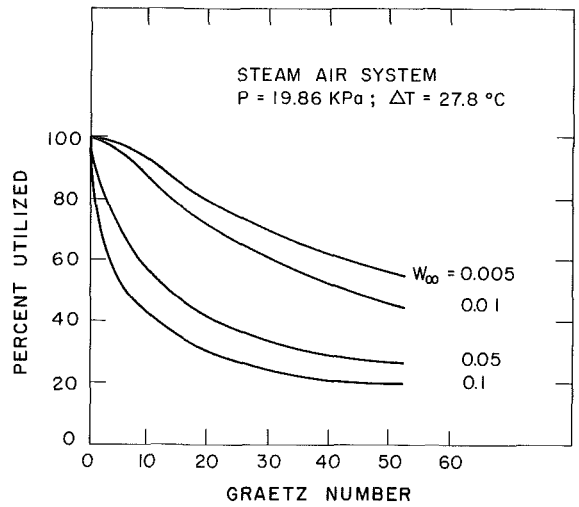

Fig. 13 Effect of W_∞ on percent coolant utilized for condensation on a sheet, P = 19.86 kPa

condensible gas are more pronounced at lower pressures. This fact was previously noted by Taitel and Tamir (1969) for condensation on a sheet and by Minkowycz and Sparrow (1966) for the case of condensation on a cooled plate. An examination of the governing equations developed in this paper would indicate that this is due to the change in ρ_l/ρ_m with pressure. As pressure decreases ρ_l/ρ_m increases, thus increasing W^*. This in turn leads to a lower value of heat transfer and extends the length of the coolant stream necessary to achieve a given coolant utilization.

In Region 2 the entire coolant stream heats up, and the rate of condensation decreases. The decrease in condensation rate brings less noncondensibles to the condensate–vapor gas interface which allows θ^* and θ_i to increase. Eventually W^* decreases to the free-stream value W_∞. The decrease in W^* leads to a "recovery" of the heat transfer coefficient above that for a pure vapor at large values of x in Region 2. However, the length of coolant stream necessary to achieve a given degree of coolant utilization for condensation is generally larger than for a pure vapor even though W_∞ might become extremely large. Jacobs and Nadig (1983) have indicated that for condensation on an immiscible thin film, it is possible for a maximum value of coolant stream length to occur. Further in-

Downloaded 17 Dec 2010 to 193.140.21.150. Redistribution subject to ASME license or copyright; see http://www.asme.org/terms/Terms_Use.cfm

creases in W_∞ would lead to a decrease in the length required for a given degree of utilization. Although for the present problem we did not observe this behavior, examination of the governing equations would indicate the possibility as P_v/P tends to zero.

For the case of steam–air, Tables 3 and 4 indicate the ratio of Gr without noncondensibles to that with noncondensibles present as a function of W_∞ and Ja for the two pressures illustrated in Figs. 8–11. Figures 12 and 13 show the results for a sheet. The experimental data of Hasson et al. (1964b) for condensation on a sheet were obtained for the pressures utilized here. They claim accuracy of ±35 percent. For $W_\infty = 0.01$ the experiments indicate a ratio of the Graetz numbers of 1.8 for effectively complete condensation. Table 3 indicates a value of 1.826 for 90 percent utilization at $P = 19.2$ KPa (2.89 psia) and $\Delta T = 41.7°C$ (75°F). At the higher pressure his ΔT was approximately 73.3°C (142°F). Extrapolation of the data of Table 3 would yield a ratio of the Graetz numbers of 1.65. These values are well within the experimental error and indicate good agreement.

Conclusions

An analysis of direct contact condensation applicable to jet and sheet condensers with and without condensibles present was carried out. For large values of Gz and very small values of Ja the results are in agreement with the work of Taitel and Tamir (1969) for condensation on a sheet. For small values of Gz the results deviate, since Taitel and Tamir neglected the influence of the condensate film.

Numerical and graphic results are presented for $0 \leq W_\infty \leq 0.05$ for $Ja \leq 0.20$ for a steam–air mixture. These results are recommended for use in atmospheric to subatmospheric conditions. The good agreement with published experimental data provides confidence in the use of the models for design purposes. It is recommended that the governing equations developed herein be used for developing design curves for other pressures and for other fluid systems. It is necessary that calculations be carried out for these cases as the solutions of the governing equations with noncondensibles present are strongly influenced by the ratio of ρ_l/ρ_m.

Acknowledgments

Support of the U.S. Department of Energy under Grant No. DEAS07761D01523 is appreciated.

References

Bakay, A., and Jaszay, T., 1978, "High Performance Jet Condensers for Steam Turbines," *Proceedings of the 6th International Heat Transfer Conference*, Vol. 2, pp. 61–65.

Hasson, D., Luss, D., and Peck, R., 1964, "Theoretical Analyses of Vapor Condensation on Laminar Jets," *International Journal of Heat and Mass Transfer*, Vol. 7, pp. 969–981.

Hasson, D., Luss, D., and Navon, V., 1964b, "An Experimental Study of Steam Condensing on a Laminar Water Street," *International Journal of Heat and Mass Transfer*, Vol. 7, pp. 983–1001.

Hausbrand, E., 1933, *Evaporating, Condensing and Coolant Apparatus*, 5th ed., D. Van Nostrand, Co., New York.

How, H., 1956, "How to Design Barometric Condensers," *Chemical Engineering*, pp. 174–182.

Jacobs, H. R., and Nadig, R., 1983, "Condensation on an Immiscible Falling Film in the Presence of a Noncondensible Gas," *Heat Exchangers for Two Phase Applications*, ASME HTD, Vol. 27, pp. 99–106.

Kutateladze, S. S., 1952, *Heat Transfer in Condensing and Boiling*, Moscow, Chapt. 7; English translation by U.S. Atomic Energy Commission, AEC-TR-3770, 2nd ed.

Minkowycz, W. J., and Sparrow, E. M., 1966, "Condensation Heat Transfer in the Presence of Noncondensibles, Interfacial Resistance, Superheating, Variable Properties and Diffusion," *International Journal of Heat and Mass Transfer*, Vol. 9, pp. 1125–1144.

Nusselt, W., 1916, "Die Oberflachenkondensation des Wasserdampfes," *Z. Ver. Deutsch Ing.*, Vol. 60, pp. 541–569.

Oliker, I., 1976, "On Calculation of Heat and Mass Transfer in Jet Type Direct Contact Heaters," ASME *National Heat Transfer Conference*, St. Louis, MO, Paper No. 76-HT-21.

Taitel, Y., and Tamir, A., 1969, "Condensation in the Presence of a Noncondensible Gas in Direct Contact," *International Journal of Heat and Mass Transfer*, Vol. 12, pp. 1157–1169.

Downloaded 17 Dec 2010 to 193.140.21.150. Redistribution subject to ASME license or copyright; see http://www.asme.org/terms/Terms_Use.cfm

Journal of Heat Transfer

Technical Notes

This section contains shorter technical papers. These shorter papers will be subjected to the same review process as that for full papers.

A Solution to Unsteady Conduction in Periodically Layered, Composite Media Using a Perturbation Method

K. D. Hagen[1]

Introduction

Heat conduction in composite media finds application in such areas as reinforced laminates, filament wound structures, and geological strata. In their classic text on heat conduction, Carslaw and Jaeger (1959) give solutions for certain two-region problems to which standard analytical techniques apply as well as problems where special forms of spatially dependent thermal properties yield the Bessel equation. Quasi-orthogonal expansion methods have been used by several investigators, e.g., Tittle (1965), Tittle and Robinson (1965), Mulholland and Cobble (1972), and more recently, Baker-Jarvis and Inguva (1985).

Perturbation techniques applied to unsteady conduction problems traditionally involve nonlinear thermal properties and boundary conditions or phase change. Aziz and Benzies (1976) give a solution for a semi-infinite region with temperature-dependent heat capacity. Temperature-dependent thermal conductivity, specific heat, and heat transfer coefficient for a finite region were managed by Olsson (1970) using a perturbation expansion. Jiji and Weinbaum (1974) use singular perturbation methods for problems involving melting and freezing. This note, however, presents a solution based on a linear perturbation series as discussed by Bellman (1964) for solving second-order differential equations having variable coefficients. The small parameter evolves from a dimensionless, spatially dependent thermal conductivity. To illustrate the technique, the example of a two-material, periodically layered semi-infinite solid is presented. The thermal conductivity is expressed as a Fourier series, while the specific heat and density of the layers are assumed equal. The perturbation expansion solution is carried out to first order, and is in good agreement with a numerical solution.

Analysis

Consider a semi-infinite medium initially at temperature T_i whose surface temperature is suddenly changed to T_s. The medium consists of alternating layers of two materials having conductivities k_1 and k_2. Each layer has a thickness l, and contact resistance at layer interfaces is neglected. The thermal conductivity can be expressed as a Fourier series

$$k(x)=\frac{k_1+k_2}{2}+\frac{2(k_1-k_2)}{\pi}\sum_{n=1}^{\infty}\frac{\sin[(2n-1)\pi x/l]}{2n-1} \tag{1}$$

The one-dimensional conduction equation with associated boundary and initial conditions is

$$\kappa(\eta)\frac{\partial^2\theta}{\partial\eta^2}+\frac{d\kappa}{d\eta}\frac{\partial\theta}{\partial\eta}-\frac{\partial\theta}{\partial\tau}=0 \tag{2}$$

$$\eta=0,\ \theta=1;\quad \eta\to\infty,\ \theta=0;\quad \tau=0,\quad \theta=0 \tag{3}$$

where the dimensionless parameters are defined as

$$\theta=\frac{T-T_i}{T_s-T_i},\quad \eta=\frac{x}{l},\quad \tau=\frac{(k_1+k_2)t}{\rho c l^2},\quad \kappa(\eta)=\frac{k(\eta)}{k_1+k_2} \tag{4}$$

Invoking a Laplace transform on equations (2) and (3) and introducing the small parameter

$$\epsilon=\frac{k_1-k_2}{k_1+k_2} \tag{5}$$

the governing equation with boundary and initial conditions becomes

$$\left[\frac{1}{2}+\frac{2\epsilon}{\pi}\sum_{n=1}^{\infty}\frac{\sin[(2n-1)\pi\eta]}{2n-1}\right]\frac{d^2\bar{\theta}}{d\eta^2}+\left[2\epsilon\sum_{n=1}^{\infty}\cos[(2n-1)\pi\eta]\right]\frac{d\bar{\theta}}{d\eta}-p\,\bar{\theta}=0 \tag{6}$$

$$\eta=0,\ \bar{\theta}=\frac{1}{p};\quad \eta\to\infty,\ \bar{\theta}=0;\quad \tau=0,\ \bar{\theta}=0 \tag{7}$$

where p is the Laplace transform variable and $\bar{\theta}$ denotes the transformed temperature. From its definition, the value of ϵ is guaranteed to satisfy $-1<\epsilon<1$, so a first-order expansion of $\bar{\theta}$ in the parameter ϵ is assumed giving

$$\bar{\theta}=\bar{\theta}_0+\epsilon\bar{\theta}_1 \tag{8}$$

Substituting equation (8) into equations (6) and (7) and inverting to the original time variable, the zero order solution is

$$\theta_0=\operatorname{erfc}\left(\frac{\eta}{\sqrt{2\tau}}\right) \tag{9}$$

which is the standard solution for a semi-infinite solid but with the conductivity replaced by an average value of $(k_1+k_2)/2$.

[1]Advanced Engineering Analysis/Design, Sperry Corporation, Salt Lake City, UT 84116.

Contributed by the Heat Transfer Division for publication in the JOURNAL OF HEAT TRANSFER. Manuscript received by the Heat Transfer Division May 12, 1986.

Copyright © 1987 by ASME

Downloaded 17 Dec 2010 to 193.140.21.150. Redistribution subject to ASME license or copyright; see http://www.asme.org/terms/Terms_Use.cfm

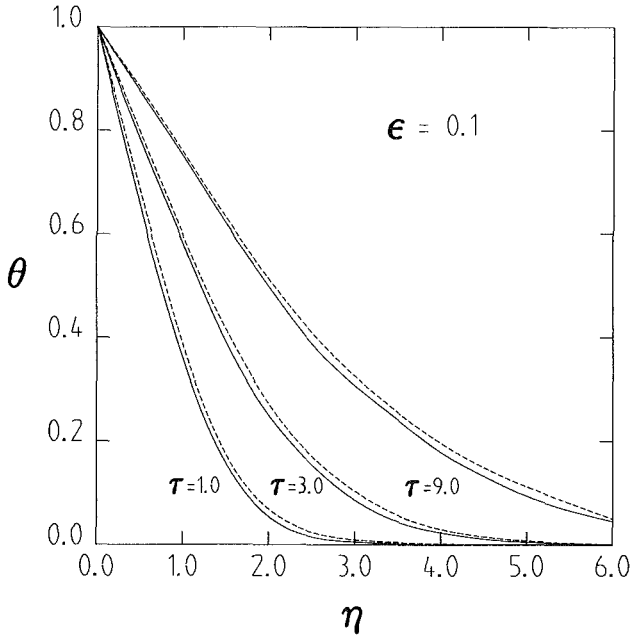

Fig. 1 Comparison of perturbation and numerical (finite difference) solutions of conduction in a two-material, periodically layered semi-infinite medium for $\epsilon = 0.1$; ---- perturbation solution; ——— numerical solution

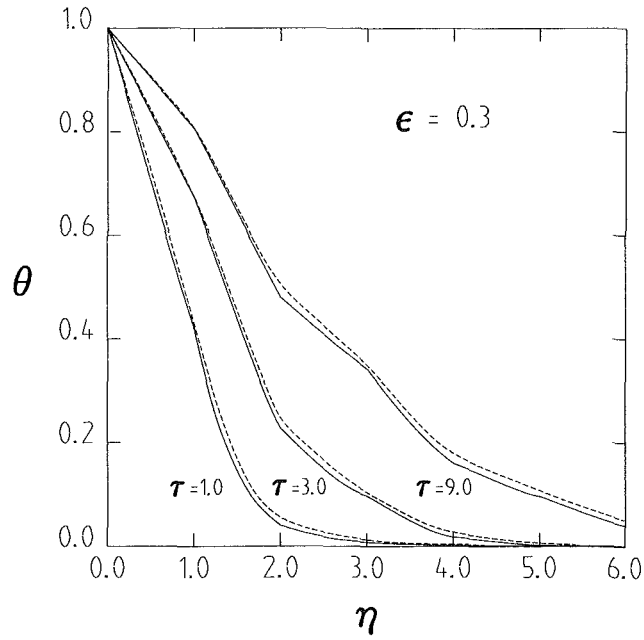

Fig. 2 Comparison of perturbation and numerical (finite difference) solutions of conduction in a two-material, periodically layered semi-infinite medium for $\epsilon = 0.3$; ---- perturbation solution; ——— numerical solution

The first-order solution is

$$\theta_1 = \frac{1}{2\pi}\left\{\frac{\eta}{\pi}\sum_{n=2}^{\infty}\frac{2(n-1)e^{-\lambda_n^2\tau}}{2n-1}A_n(\eta,\tau)\sin[(2n-1)\pi\eta] + \sum_{n=1}^{\infty}e^{-\lambda_n^2\tau}\left[\frac{2}{\pi^2}B_n(\eta,\tau)+C_n(\eta,\tau)\right]\left[1-\cos[(2n-1)\pi\eta]\right]\right\} \tag{10}$$

where

$$A_n(\eta,\tau) = \int_0^{\tau} u^{-3/2}\exp(\lambda_n^2 u - \eta^2/2u)\,du \tag{11}$$

$$B_n(\eta,\tau) = \int_0^{\tau} u^{-3/2}(\eta^2/u - 1)\exp(\lambda_n^2 u - \eta^2/2u)\,du \tag{12}$$

$$C_n(\eta,\tau) = \int_0^{\tau} u^{-1/2}\exp(\lambda_n^2 u - \eta^2/2u)\,du \tag{13}$$

and

$$\lambda_n = \frac{(2n-1)\pi}{2\sqrt{2}} \quad n = 1, 2, 3, \ldots \tag{14}$$

The integrals in equations (11), (12) and (13), which arise from performing the Laplace transform inversion, deserve some attention. Each of these integrals goes to infinity as τ approaches infinity or as an infinite number of terms is taken in the series. It can be shown, however, that the exponential terms which multiply the integrals go to zero faster than the integrals go to infinity. As τ goes to infinity, θ_1 goes to zero, leaving the zero-order solution of $\theta = 1$ for all values of η. In either case, provisions must be made in the chosen numerical integration scheme to prevent an exponential overflow and stop calculations when the exponential terms are sufficiently small. When the value of τ is of order unity or higher, fewer than ten terms are required for convergence. As η approaches infinity the integrals go to zero because of the negative exponential terms in the integrands. $A_n(\eta, \tau)$ goes to zero faster

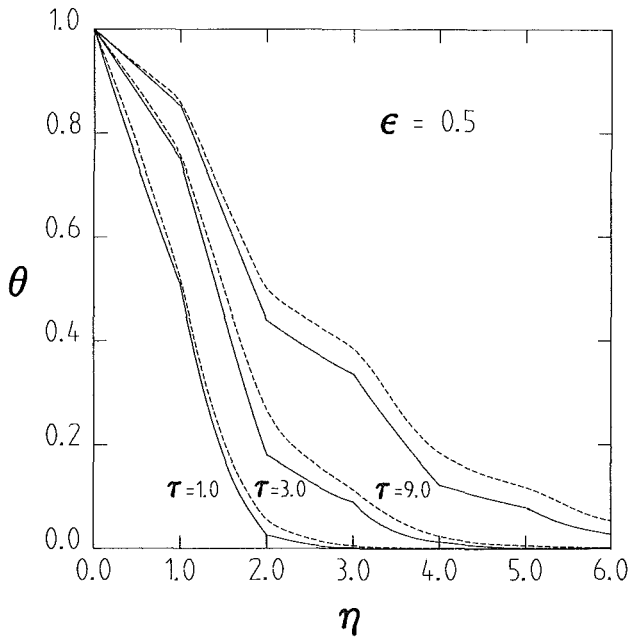

Fig. 3 Comparison of perturbation and numerical (finite difference) solutions of conduction in a two-material, periodically layered semi-infinite medium for $\epsilon = 0.5$; ---- perturbation solution; ——— numerical solution

than η in front of $A_n(\eta, \tau)$ goes to infinity making the first series of equation (10) well behaved. Hence, $\theta = 0$ for $\eta \to \infty$ as required by the second boundary condition. By inspection of equation (10), $\theta_1 = 0$ for $\eta = 0$ and $\theta = 1$ for all values of τ greater than zero as required by the first boundary condition. Finally, the integrals are identically zero for $\tau = 0$, and $\theta = 0$ for all values of η as required by the initial condition.

It should also be noted that the series involving the cosine terms in equation (6) diverges for integer values of η. Even though this seems to pose a mathematical difficulty, the

Downloaded 17 Dec 2010 to 193.140.21.150. Redistribution subject to ASME license or copyright; see http://www.asme.org/terms/Terms_Use.cfm

behavior of the first-order solution dictates that only a finite number of terms be taken, as previously discussed.

Results and Discussion

Equations (2) and (3) were solved numerically to check the accuracy of the perturbation solution. The Crank–Nicolson finite difference method was employed using step sizes of 0.1 in both space and time. Using the exact zero-order solution as a standard, the accuracy of the Crank–Nicolson scheme for these step sizes for the case of $\eta = 3$ and $\tau = 1$, 3, and 9 was found to be within 0.3 percent. The thickness of the one-dimensional region in the numerical model was made larger than the heat penetration depth for all values of τ considered, and the temperature was maintained at zero on the back side to preserve the characteristics of a semi-infinite body. Figures 1, 2, and 3 compare the perturbation and numerical solutions for $\epsilon = 0.1$, 0.3, and 0.5, respectively, for $\tau = 1.0$, 3.0, and 9.0. The perturbation solution agrees favorably with the numerical solution for small values of ϵ. The accuracy decreases, however, as ϵ increases, especially at high values of τ. Only positive values of ϵ are given here; small negative values yield similar accuracy. The perturbation solution involves less computational time compared to finite difference methods, and clearly shows the small-scale temperature variation within each layer. The curves shown for the perturbation solution were obtained using ten terms or fewer in the Fourier series for the thermal conductivity.

A linear perturbation series has been used to find the temperatures within a periodically layered, semi-infinite medium. This method is reasonably accurate for $\epsilon \leq 0.5$. Larger values of ϵ would require additional terms in the perturbation expansion at the expense of a great deal of mathematics. The technique is applicable for a range of practical problems in which the conductivities of the dissimilar layers are not drastically different, such as would be the case for insulation and metal. The mathematical approach can be applied to finite geometries and other boundary conditions, albeit the mathematics involved in finding particular integrals for the first order solution and performing the transform inversions may be complex. Neither is the method restricted to two materials or layers of equal thickness. Any periodic arrangement of layers is amenable by the technique, assuming a small thermal conductivity parameter can be derived. The spatial periodicity of density times specific heat can be handled in a similar fashion by the appropriate definition of the dimensionless time variable. In this case, a two-parameter perturbation expansion is required, one parameter for $k(x)$ and a second for $(\rho c)(x)$.

References

Aziz, A., and Benzies, J. Y., 1976, "Application of Perturbation Techniques to Heat Transfer Problems With Variable Thermal Properties," *International Journal of Heat and Mass Transfer*, Vol. 19, pp. 271–276.

Baker-Jarvis, J., and Inguva, R., 1985, "Heat Conduction in Layered, Composite Materials," *Journal of Applied Physics*, Vol. 57, No. 5, pp. 1569–1573.

Bellman, R., 1964, *Perturbation Techniques in Mathematics, Physics, and Engineering*, Holt, Reinhart and Winston, New York, pp. 9–16.

Carslaw, H. S., and Jaeger, J. C., 1959, *Conduction of Heat in Solids*, 2nd ed., Clarendon Press, Oxford, pp. 319–326, 412–415.

Jiji, L. M., and Weinbaum, S., 1974, "A Nonlinear Singular Perturbation Theory for Nonsimilar Melting or Freezing Problems," *5th International Heat Transfer Conference*, Tokyo, Paper No. Conduction Cu-3.

Mulholland, G. P., and Cobble, M. H., 1972, "Diffusion Through Composite Media," *International Journal of Heat and Mass Transfer*, Vol. 15, pp. 147–160.

Olsson, U., 1970, "Application of Perturbation Method to Heat Flow Analysis in Materials Having Temperature-Dependent Properties," *AIAA Journal*, Vol. 8, No. 10, pp. 1902–1903.

Tittle, C. W., 1965, "Boundary Value Problems in Composite Media: Quasi-Orthogonal Functions," *Journal of Applied Physics*, Vol. 36, pp. 1486–1488.

Tittle, C. W., and Robinson, V. L., 1965, "Analytical Solution of Conduction Problems in Composite Media," ASME Paper No. 65-WA-HT-52.

An Apparatus to Measure the Maximum Heat Transfer Rate in Heat Pipes

J. H. Ambrose,[1] L. C. Chow,[1] and J. E. Beam[2]

Introduction

In an earlier investigation of evaporative heat transfer in low-temperature heat pipes, it was concluded (Ambrose et al., 1985) that nucleate boiling was the dominating mechanism for heat removal from the wall. Experimental data for vaporization of water and freon in screen wicks was shown to agree well with a boiling correlation. Data used in the correlation were obtained from Abhat and Seban (1974) for a water/screen wick vaporization experiment and from Ponnappan and Mahefkey (1983) for a copper/water double-wall artery heat pipe.

During verification testing of this heat pipe, heat input to the evaporator was provided by electrical resistance heating. In such cases the evaporator wall heat flux is the independent parameter and the temperature drop across the evaporator is measured as a function of applied heat flux. The temperature drop is given by $T_w - T_s$, where T_w is the wall temperature and T_s is the saturated vapor temperature. The criterion used to signify that the maximum heat flux had been reached was an observed evaporator temperature drop larger than 10°C.

Nucleate boiling in a heat pipe wick shows similarities to conventional nucleate pool boiling. For a constant heat flux boundary condition, the temperature drop $T_w - T_s$ increases monotonically with increasing heat flux. For heat fluxes equal to or greater than the maximum heat flux q_{max}, the heated surface becomes partially exposed to vapor, resulting in a drastic decrease in the heat transfer coefficient. For pool boiling, the maximum heat flux is a result of Helmholtz instability of the vapor jets leaving the heated surface. In low-temperature heat pipes, before the boiling limit is reached, dryout will usually occur due to the inability of the wick to pump sufficient liquid to the evaporator (capillary limit). The capillary limit Q_{max} is a limitation on total heat input rate Q for a given heat pipe.

Temperatures in the heat pipe evaporator increase rapidly if the maximum heat input rate is maintained, and the rise in internal pressure may cause failure of the container material. This is especially true for high-vapor-pressure working fluids such as ammonia and freon.

In the experiment of Ponnappan and Mahefkey (1983), the reported maximum heat input rate was approximately 20 percent less than the predicted capillary limit to heat transport. It is possible that the maximum heat input was not actually reached in their experiment in order to avoid a severe dryout. In this paper, a unique apparatus is used to control the wall temperature of the heat pipe evaporator independently. With this method, an increase in T_w above that corresponding to Q_{max} can only cause a decrease in Q. Although it is more difficult to control the temperature than the heat flux, this method allows a more accurate determination of Q_{max} and precludes the possibility of runaway temperature.

[1]Mechanical Engineering Department, University of Kentucky, Lexington, KY.

[2]Power Technology Branch, Air Force Aero Propulsion Laboratory, Wright-Patterson Air Force Base, OH.

Contributed by the Heat Transfer Division and presented at the AIAA/ASME Thermophysics and Heat Transfer Conference, Boston, Massachusetts, June 2-4, 1986. Manuscript received by the Heat Transfer Division November 20, 1985.

Downloaded 17 Dec 2010 to 193.140.21.150. Redistribution subject to ASME license or copyright; see http://www.asme.org/terms/Terms_Use.cfm

behavior of the first-order solution dictates that only a finite number of terms be taken, as previously discussed.

Results and Discussion

Equations (2) and (3) were solved numerically to check the accuracy of the perturbation solution. The Crank–Nicolson finite difference method was employed using step sizes of 0.1 in both space and time. Using the exact zero-order solution as a standard, the accuracy of the Crank–Nicolson scheme for these step sizes for the case of $\eta = 3$ and $\tau = 1$, 3, and 9 was found to be within 0.3 percent. The thickness of the one-dimensional region in the numerical model was made larger than the heat penetration depth for all values of τ considered, and the temperature was maintained at zero on the back side to preserve the characteristics of a semi-infinite body. Figures 1, 2, and 3 compare the perturbation and numerical solutions for $\epsilon = 0.1$, 0.3, and 0.5, respectively, for $\tau = 1.0$, 3.0, and 9.0. The perturbation solution agrees favorably with the numerical solution for small values of ϵ. The accuracy decreases, however, as ϵ increases, especially at high values of τ. Only positive values of ϵ are given here; small negative values yield similar accuracy. The perturbation solution involves less computational time compared to finite difference methods, and clearly shows the small-scale temperature variation within each layer. The curves shown for the perturbation solution were obtained using ten terms or fewer in the Fourier series for the thermal conductivity.

A linear perturbation series has been used to find the temperatures within a periodically layered, semi-infinite medium. This method is reasonably accurate for $\epsilon \leq 0.5$. Larger values of ϵ would require additional terms in the perturbation expansion at the expense of a great deal of mathematics. The technique is applicable for a range of practical problems in which the conductivities of the dissimilar layers are not drastically different, such as would be the case for insulation and metal. The mathematical approach can be applied to finite geometries and other boundary conditions, albeit the mathematics involved in finding particular integrals for the first order solution and performing the transform inversions may be complex. Neither is the method restricted to two materials or layers of equal thickness. Any periodic arrangement of layers is amenable by the technique, assuming a small thermal conductivity parameter can be derived. The spatial periodicity of density times specific heat can be handled in a similar fashion by the appropriate definition of the dimensionless time variable. In this case, a two-parameter perturbation expansion is required, one parameter for $k(x)$ and a second for $(\rho c)(x)$.

References

Aziz, A., and Benzies, J. Y., 1976, "Application of Perturbation Techniques to Heat Transfer Problems With Variable Thermal Properties," *International Journal of Heat and Mass Transfer*, Vol. 19, pp. 271–276.

Baker-Jarvis, J., and Inguva, R., 1985, "Heat Conduction in Layered, Composite Materials," *Journal of Applied Physics*, Vol. 57, No. 5, pp. 1569–1573.

Bellman, R., 1964, *Perturbation Techniques in Mathematics, Physics, and Engineering*, Holt, Reinhart and Winston, New York, pp. 9–16.

Carslaw, H. S., and Jaeger, J. C., 1959, *Conduction of Heat in Solids*, 2nd ed., Clarendon Press, Oxford, pp. 319–326, 412–415.

Jiji, L. M., and Weinbaum, S., 1974, "A Nonlinear Singular Perturbation Theory for Nonsimilar Melting or Freezing Problems," *5th International Heat Transfer Conference*, Tokyo, Paper No. Conduction Cu-3.

Mulholland, G. P., and Cobble, M. H., 1972, "Diffusion Through Composite Media," *International Journal of Heat and Mass Transfer*, Vol. 15, pp. 147–160.

Olsson, U., 1970, "Application of Perturbation Method to Heat Flow Analysis in Materials Having Temperature-Dependent Properties," *AIAA Journal*, Vol. 8, No. 10, pp. 1902–1903.

Tittle, C. W., 1965, "Boundary Value Problems in Composite Media: Quasi-Orthogonal Functions," *Journal of Applied Physics*, Vol. 36, pp. 1486–1488.

Tittle, C. W., and Robinson, V. L., 1965, "Analytical Solution of Conduction Problems in Composite Media," ASME Paper No. 65-WA-HT-52.

An Apparatus to Measure the Maximum Heat Transfer Rate in Heat Pipes

J. H. Ambrose,[1] L. C. Chow,[1] and J. E. Beam[2]

Introduction

In an earlier investigation of evaporative heat transfer in low-temperature heat pipes, it was concluded (Ambrose et al., 1985) that nucleate boiling was the dominating mechanism for heat removal from the wall. Experimental data for vaporization of water and freon in screen wicks was shown to agree well with a boiling correlation. Data used in the correlation were obtained from Abhat and Seban (1974) for a water/screen wick vaporization experiment and from Ponnappan and Mahefkey (1983) for a copper/water double-wall artery heat pipe.

During verification testing of this heat pipe, heat input to the evaporator was provided by electrical resistance heating. In such cases the evaporator wall heat flux is the independent parameter and the temperature drop across the evaporator is measured as a function of applied heat flux. The temperature drop is given by $T_w - T_s$, where T_w is the wall temperature and T_s is the saturated vapor temperature. The criterion used to signify that the maximum heat flux had been reached was an observed evaporator temperature drop larger than 10°C.

Nucleate boiling in a heat pipe wick shows similarities to conventional nucleate pool boiling. For a constant heat flux boundary condition, the temperature drop $T_w - T_s$ increases monotonically with increasing heat flux. For heat fluxes equal to or greater than the maximum heat flux q_{max}, the heated surface becomes partially exposed to vapor, resulting in a drastic decrease in the heat transfer coefficient. For pool boiling, the maximum heat flux is a result of Helmholtz instability of the vapor jets leaving the heated surface. In low-temperature heat pipes, before the boiling limit is reached, dryout will usually occur due to the inability of the wick to pump sufficient liquid to the evaporator (capillary limit). The capillary limit Q_{max} is a limitation on total heat input rate Q for a given heat pipe.

Temperatures in the heat pipe evaporator increase rapidly if the maximum heat input rate is maintained, and the rise in internal pressure may cause failure of the container material. This is especially true for high-vapor-pressure working fluids such as ammonia and freon.

In the experiment of Ponnappan and Mahefkey (1983), the reported maximum heat input rate was approximately 20 percent less than the predicted capillary limit to heat transport. It is possible that the maximum heat input was not actually reached in their experiment in order to avoid a severe dryout. In this paper, a unique apparatus is used to control the wall temperature of the heat pipe evaporator independently. With this method, an increase in T_w above that corresponding to Q_{max} can only cause a decrease in Q. Although it is more difficult to control the temperature than the heat flux, this method allows a more accurate determination of Q_{max} and precludes the possibility of runaway temperature.

[1]Mechanical Engineering Department, University of Kentucky, Lexington, KY.

[2]Power Technology Branch, Air Force Aero Propulsion Laboratory, Wright-Patterson Air Force Base, OH.

Contributed by the Heat Transfer Division and presented at the AIAA/ASME Thermophysics and Heat Transfer Conference, Boston, Massachusetts, June 2-4, 1986. Manuscript received by the Heat Transfer Division November 20, 1985.

Copyright © 1987 by ASME

Downloaded 17 Dec 2010 to 193.140.21.150. Redistribution subject to ASME license or copyright; see http://www.asme.org/terms/Terms_Use.cfm

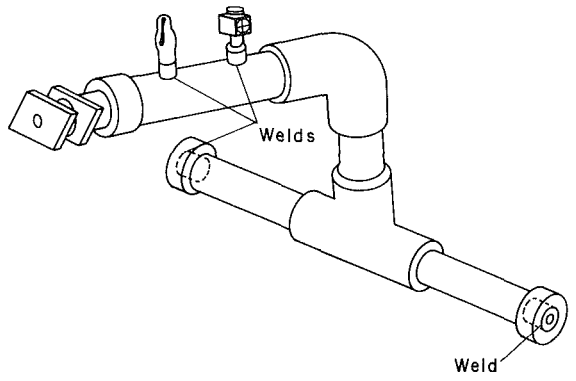

(a) Pictorial View

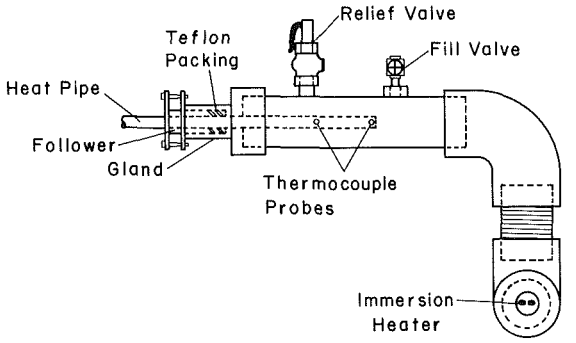

(b) Schematic

Fig. 1 Steam-generation vessel

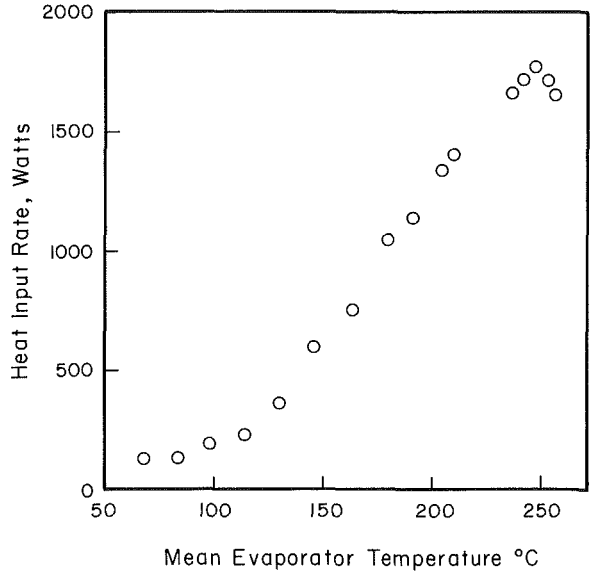

Fig. 2 Heat input rate versus mean evaporator temperature

Experimental Apparatus

The goal of the present work is to design and build an apparatus which allows an accurate measurement of Q_{max} for a low-temperature heat pipe. Direct condensation of steam on the evaporator wall is the means chosen to provide the high heat fluxes with excellent thermal stability. A controlled temperature boiler was designed by a group of mechanical engineering seniors as part of the requirements for a Thermal Systems Design course at Washington State University. It consists of a steam-generation vessel and a feedback control system.

The steam-generation vessel is shown in Fig. 1. It is constructed of standard 7.62 cm (3 in.) schedule 80 forged steel pipe with screwed fittings. Its configuration allows the heat pipe to be tested either horizontally or at positive tilt angles (condenser end raised) of up to 90 deg. Two 240 V, 2500 W immersion heaters are screwed into the lower legs of the vessel (one heater in each leg) and provide all necessary power. The heat pipe is inserted through a simple gland seal which is welded to the end cap of the upper leg of the vessel. Braided teflon packing is compressed in the gland seal around the heat pipe. With different followers and packing the vessel can accommodate varying heat pipe diameters of 1.5 to 3 cm. Screwed fittings welded to the upper leg are used to mount a 5.5 MPa (800 psi) relief valve and a 1.27 cm (1/2 in.) forged steel gate valve. The gate valve is for evacuation and filling purposes. The entire vessel is wrapped with 10.2 to 15.2 cm (4 to 6 in.) of fiberglass insulation to reduce the heat loss.

For each test run, the steam vessel is thoroughly evacuated before filling with degassed, distilled water. Slightly over 4 liters of liquid is added so that the liquid level will remain above the two immersion heaters and the upper pipe will be filled with steam. Saturated conditions are verified by measuring the pressure and temperature of the steam.

Steady-state heat losses from the steam vessel are measured by blocking the heat pipe gland seal with a short steel bar. Heat losses are plotted as a function of internal steam-vessel temperature, and the appropriate heat losses obtained from this curve are subtracted from each heat input rate reported.

The feedback control system accurately maintains a given temperature in the steam vessel by thermostatically controlling one immersion heater. A key element to maintaining a constant vessel temperature is the large latent heat of the fluid, which acts as a buffer against the on and off pulses of the intermittent heater. The other heater is set at a constant power level dependent upon the desired temperature. Feedback control is facilitated by a microcomputer. Four type-K thermocouple probes, inserted through screwed compression fittings, sample the temperature of the heat pipe wall. The four temperature measurements are averaged every 20 s. If the difference between the desired and average temperatures is greater than 0.28°C the intermittent heater is turned either on or off as required. Once set, the control system will maintain the mean evaporator temperature to within 0.6°C. The actual limits of deviation of the mean vessel temperature are more than those of the control system due to thermal lag. Both heaters are wired through rheostats so that the power levels may be varied between 0 and 2500 W. The total on time of the intermittent heater is recorded to calculate the average power input over the test period of 20 min.

The heat pipe used for the tests is a double-wall artery heat pipe designed and fabricated at the Air Force Aero Propulsion Laboratory (Ponnappan and Mahefkey, 1983). The heat pipe is 1.20 m (47.2 in.) long and 2.22 cm (7/8 in.) in diameter, with 20.32 cm (8 in.) long evaporator and condenser sections. It has a unique inner tube which separates the liquid and vapor flow paths, prohibiting entrainment of liquid by the vapor flow. Arteries are machined into the outer surface of the inner tube to provide low flow resistance for the liquid return. A 100 mesh screen wick located in the annulus between the inner and outer tubes is responsible for the capillary pumping.

Nine thermocouples are attached to the pipe along the adiabatic and condenser sections to monitor the axial temperature profile. Cooling is accomplished with a forced air/water droplet system.

Downloaded 17 Dec 2010 to 193.140.21.150. Redistribution subject to ASME license or copyright; see http://www.asme.org/terms/Terms_Use.cfm

Results and Discussion

Experimental data for horizontal operation of the heat pipe are given in Fig. 2. In this figure, the heat input rate (corrected for heat loss to the ambient) is plotted versus the evaporator wall temperature. The measured maximum value of 1768 W agrees well with the predicted value of 1790 W for Q_{max}. The measured value of Q_{max} is approximately 20 percent greater than that reported earlier by Ponnappan and Mahefkey (1983), which was measured by controlling the heat flux. There are two contributing factors to this difference. The first is the previously mentioned difficulty associated with maintaining heat input rates near Q_{max}. The second is that Q_{max} can be larger for the case of constant wall temperature than for constant wall heat flux. Q_{max} depends on the external evaporator boundary condition. A constant heat flux case is more severe since it requires that the same amount of liquid be supplied everywhere along the heated wall. Certain locations in the evaporator, such as the upper portion of the wall, have larger pumping requirements and will dryout first. For constant wall temperature, the heat flux and liquid supply may vary along the evaporator. With the constant-temperature boundary condition, the heat flux distribution will adjust itself so that heat is transferred in regions where liquid is available. This fact contributes to the larger Q_{max} obtained with the constant wall temperature boundary condition.

Experimental Uncertainty

The uncertainty limits for the evaporator, adiabatic, and condenser thermocouples are 0.6°C. The uncertainty limit of the heat input rate measurement is 13 W (at 1770 W). As a result of possible poor contact between the probe tips and the wall, the mean evaporator wall temperatures include an added uncertainty. Between tests, the heat pipe was removed from the steam vessel and replaced, causing reduced contact between the thermocouple probes and the evaporator wall in the higher-temperature test runs. A difference of 6–11°C between the four probe readings was observed for later tests, whereas during earlier tests, these were within 2–3°C. For each probe, the maximum estimated error due to poor probe contact is 20°C. This value is an estimate of the temperature drop across a condensate layer formed on the evaporator wall at the maximum heat input rate. Condensate layer thickness is based on laminar film condensation on a horizontal cylinder and found to be approximately 0.1 mm for this condition. Abscissas of the five highest temperature data points in Fig. 2 (all taken with constant probe positions) should be reduced by roughly the same amount. This error in wall temperature is in all cases positive and relatively constant because the thermal resistance of the condensate layer varies only slightly over the range of interest. Despite this error, the existence of the maximum heat input rate in Fig. 2 is established.

Acknowledgments

This work was supported by the Air Force Aero Propulsion Laboratory and was performed at Washington State University, Pullman, WA.

References

Abhat, A., and Seban, R. A., 1974, "Boiling and Evaporation From Heat Pipe Wicks With Water and Acetone," ASME JOURNAL OF HEAT TRANSFER, Vol. 96, pp. 331–337.

Ambrose, J. H., Chow, L. C., Ponnappan, R., Beam, J. E., and Mahefkey, E. T., 1985, "A Boiling Heat Transfer Correlation for Heat Pipes," *SAE Transactions*, Vol. 94, Sect. 5, pp. 161–167.

Ponnappan, R., and Mahefkey, E. T., 1983, "Development of a Double-Wall Artery High-Capacity Pipe," *Progress in Astronautics and Aeronautics*, Vol. 86, P.E. Bauer and H. E. Collicott, eds., pp. 202–221.

Some Studies of the Effects of Axial Conduction in a Tube Wall on the Steady-State Laminar Convective Heat Transfer

N. K. Anand[1] and D. R. Tree[2]

Nomenclature

- Gz = Graetz number $= 4R^2\bar{U}/\alpha L$
- K = ratio of the thermal conductivity of the wall to thermal conductivity of the fluid
- K_f = thermal conductivity of the fluid
- K_w = thermal conductivity of the solid
- L = tube length
- Pe = Peclet number $= 2R\bar{U}/\alpha$
- q = heat flux
- q' = increased heat flux at center of tube
- r = radial distance from the tube centerline
- R = tube radius
- t = tube thickness
- T = fluid temperature
- T_e = entrance temperature of the fluid
- T_w = tube wall temperature
- u = local velocity of the fluid $= 2\bar{U}(1-r^2/R^2)$
- $\bar{U}$ = mean velocity of the fluid
- X = dimensionless axial distance $= z/L$
- z = axial distance from the tube entrance
- α = thermal diffusivity of the fluid
- β = dimensionless number $= K\phi\epsilon$
- γ = ratio of increased heat flux to heat flux $= q'/q$
- ϵ = tube thickness to length ratio $= t/L$
- η = dimensionless radial distance $= r/R$
- θ = dimensionless fluid temperature $= (T-T_e)/qR/K_f$
- θ_w = dimensionless wall temperature $= (T_w-T_e)/qR/K_f$
- ϕ = ratio of tube radius to length $= R/L$

Subscripts

- b = bulk
- W = wall

Introduction

Whenever a superheated fluid flowing inside a tube is cooled to its saturated state, there is a sudden and significant increase in the heat transfer coefficient at the solid–fluid interface. Since the temperature of the fluid remains almost constant, this causes a step change in heat flux at the tube wall. This increased heat flux will increase the temperature of the tube wall. Even for thin wetted tubes, this temperature increase can cause considerable heat flow along the axial direction of the tube.

This axial conduction in the tube wall may have an influence on the rate of condensation of the fluid and the amount of

[1]Assistant Professor, Department of Mechanical Engineering, Texas A&M University, College Station, TX.

[2]Professor and Assistant Head, School of Mechanical Engineering, Purdue University, West Lafayette, IN.

Contributed by the Heat Transfer Division for publication in the JOURNAL OF HEAT TRANSFER. Manuscript received by the Heat Transfer Division August 4, 1983.

Downloaded 17 Dec 2010 to 193.140.21.150. Redistribution subject to ASME license or copyright; see http://www.asme.org/terms/Terms_Use.cfm

Results and Discussion

Experimental data for horizontal operation of the heat pipe are given in Fig. 2. In this figure, the heat input rate (corrected for heat loss to the ambient) is plotted versus the evaporator wall temperature. The measured maximum value of 1768 W agrees well with the predicted value of 1790 W for Q_{max}. The measured value of Q_{max} is approximately 20 percent greater than that reported earlier by Ponnappan and Mahefkey (1983), which was measured by controlling the heat flux. There are two contributing factors to this difference. The first is the previously mentioned difficulty associated with maintaining heat input rates near Q_{max}. The second is that Q_{max} can be larger for the case of constant wall temperature than for constant wall heat flux. Q_{max} depends on the external evaporator boundary condition. A constant heat flux case is more severe since it requires that the same amount of liquid be supplied everywhere along the heated wall. Certain locations in the evaporator, such as the upper portion of the wall, have larger pumping requirements and will dryout first. For constant wall temperature, the heat flux and liquid supply may vary along the evaporator. With the constant-temperature boundary condition, the heat flux distribution will adjust itself so that heat is transferred in regions where liquid is available. This fact contributes to the larger Q_{max} obtained with the constant wall temperature boundary condition.

Experimental Uncertainty

The uncertainty limits for the evaporator, adiabatic, and condenser thermocouples are 0.6°C. The uncertainty limit of the heat input rate measurement is 13 W (at 1770 W). As a result of possible poor contact between the probe tips and the wall, the mean evaporator wall temperatures include an added uncertainty. Between tests, the heat pipe was removed from the steam vessel and replaced, causing reduced contact between the thermocouple probes and the evaporator wall in the higher-temperature test runs. A difference of 6–11°C between the four probe readings was observed for later tests, whereas during earlier tests, these were within 2–3°C. For each probe, the maximum estimated error due to poor probe contact is 20°C. This value is an estimate of the temperature drop across a condensate layer formed on the evaporator wall at the maximum heat input rate. Condensate layer thickness is based on laminar film condensation on a horizontal cylinder and found to be approximately 0.1 mm for this condition. Abscissas of the five highest temperature data points in Fig. 2 (all taken with constant probe positions) should be reduced by roughly the same amount. This error in wall temperature is in all cases positive and relatively constant because the thermal resistance of the condensate layer varies only slightly over the range of interest. Despite this error, the existence of the maximum heat input rate in Fig. 2 is established.

Acknowledgments

This work was supported by the Air Force Aero Propulsion Laboratory and was performed at Washington State University, Pullman, WA.

References

Abhat, A., and Seban, R. A., 1974, "Boiling and Evaporation From Heat Pipe Wicks With Water and Acetone," ASME JOURNAL OF HEAT TRANSFER, Vol. 96, pp. 331–337.

Ambrose, J. H., Chow, L. C., Ponnappan, R., Beam, J. E., and Mahefkey, E. T., 1985, "A Boiling Heat Transfer Correlation for Heat Pipes," *SAE Transactions*, Vol. 94, Sect. 5, pp. 161–167.

Ponnappan, R., and Mahefkey, E. T., 1983, "Development of a Double-Wall Artery High-Capacity Pipe," *Progress in Astronautics and Aeronautics*, Vol. 86, P.E. Bauer and H. E. Collicott, eds., pp. 202–221.

Some Studies of the Effects of Axial Conduction in a Tube Wall on the Steady-State Laminar Convective Heat Transfer

N. K. Anand[1] and D. R. Tree[2]

Nomenclature

- Gz = Graetz number $= 4R^2\bar{U}/\alpha L$
- K = ratio of the thermal conductivity of the wall to thermal conductivity of the fluid
- K_f = thermal conductivity of the fluid
- K_w = thermal conductivity of the solid
- L = tube length
- Pe = Peclet number $= 2R\bar{U}/\alpha$
- q = heat flux
- q' = increased heat flux at center of tube
- r = radial distance from the tube centerline
- R = tube radius
- t = tube thickness
- T = fluid temperature
- T_e = entrance temperature of the fluid
- T_w = tube wall temperature
- u = local velocity of the fluid $= 2\bar{U}(1-r^2/R^2)$
- $\bar{U}$ = mean velocity of the fluid
- X = dimensionless axial distance $= z/L$
- z = axial distance from the tube entrance
- α = thermal diffusivity of the fluid
- β = dimensionless number $= K\phi\epsilon$
- γ = ratio of increased heat flux to heat flux $= q'/q$
- ϵ = tube thickness to length ratio $= t/L$
- η = dimensionless radial distance $= r/R$
- θ = dimensionless fluid temperature $= (T-T_e)/qR/K_f$
- θ_w = dimensionless wall temperature $= (T_w-T_e)/qR/K_f$
- ϕ = ratio of tube radius to length $= R/L$

Subscripts

- b = bulk
- W = wall

Introduction

Whenever a superheated fluid flowing inside a tube is cooled to its saturated state, there is a sudden and significant increase in the heat transfer coefficient at the solid–fluid interface. Since the temperature of the fluid remains almost constant, this causes a step change in heat flux at the tube wall. This increased heat flux will increase the temperature of the tube wall. Even for thin wetted tubes, this temperature increase can cause considerable heat flow along the axial direction of the tube.

This axial conduction in the tube wall may have an influence on the rate of condensation of the fluid and the amount of

[1]Assistant Professor, Department of Mechanical Engineering, Texas A&M University, College Station, TX.

[2]Professor and Assistant Head, School of Mechanical Engineering, Purdue University, West Lafayette, IN.

Contributed by the Heat Transfer Division for publication in the JOURNAL OF HEAT TRANSFER. Manuscript received by the Heat Transfer Division August 4, 1983.

Copyright © 1987 by ASME

Downloaded 17 Dec 2010 to 193.140.21.150. Redistribution subject to ASME license or copyright; see http://www.asme.org/terms/Terms_Use.cfm

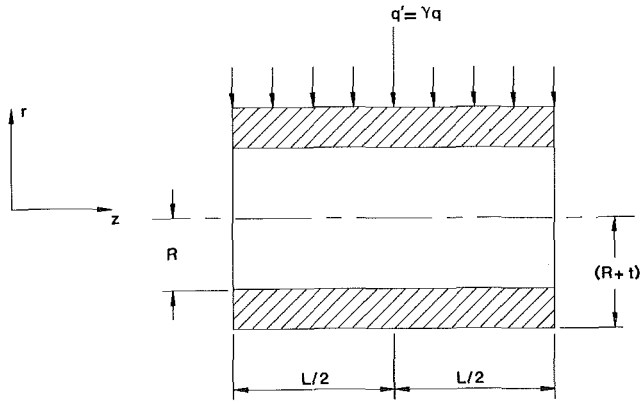

Fig. 1 Model

heat removed from the fluid flowing inside the tube. There are other situations, such as in power plants, where a step increase in heat flux to the tube may occur. Therefore, a detailed study of this effect of a step increase in heat transfer at a given location was initiated.

A careful examination of the literature reveals that a considerable amount of work has been done in the area of conjugate heat transfer in channel flows [1–7]. The present investigation was prompted by the increase in heat transfer near the condensation point of a superheated vapor being cooled inside a circular pipe. The conjugate heat transfer with the added complexity of a two-phase flow prevented this exact problem from being solved. In order to reduce the complexity of the problem, the effects of axial tube wall conduction on the steady-state, laminar, convective heat transfer of a single-phase fluid with a step change in heat flux were studied.

Formulation of the Problem and Solution Technique

Figure 1 shows a schematic diagram of the model used for the analysis. In this investigation, consideration is given to the heat transfer process of a single-phase fluid flowing inside a thin circular tube; the tube thermal resistance in the radial direction is neglected. The external surface of the tube wall is subjected to a constant heat flux q along its length except at the midpoint location. At this location an increased heat flux at the wall caused by a change of phase of the fluid is simulated by imposing an increased heat flux q', where $q' = \gamma q$ = 1, 10, 100, 1000, and 10,000. The increased heat flux is applied at the midpoint of the tube so that the effect of preheating on the wall temperature and the bulk temperature of the fluid upstream of the midpoint can be studied.

The single-phase flow inside the tube is treated to be steady, laminar, and incompressible. In this investigation consideration is given to flows where Pe > 100, so that axial heat diffusion in the fluid along the direction of the fluid flow is neglected. Since only thin tubes are analyzed in this study, the tube end surface areas are negligibly small and are assumed to be adiabatic. With these simplifying assumptions, the energy equation for the tube wall in dimensionless form is

$$\beta\frac{d^2\theta_w}{dX^2}+\gamma(1+\epsilon/\phi)-\frac{\partial\theta}{\partial\eta}\bigg|_{\eta=1}=0 \tag{1}$$

with the following boundary conditions

$$\frac{d\theta_w}{dX}\bigg|_{x=0}=\frac{d\theta_w}{dX}\bigg|_{x=1}=0 \tag{2}$$

In addition $\gamma = 1$ except at $x = 0.5$ where $\gamma \geq 1$. The energy equation for the fluid in dimensionless form is

$$\frac{\mathrm{Gz}}{2}(1-\eta^2)\frac{\partial\theta}{\partial X}=\frac{1}{\eta}\frac{\partial\theta}{\partial\eta}+\frac{\partial^2\theta}{\partial\eta^2} \tag{3}$$

with the initial and boundary conditions

$$\begin{aligned}&\frac{\partial\theta}{\partial\eta}\bigg|_{\eta=0}=0 \text{ for all } X\\ &\theta(X,1)=\theta_w(X), \qquad X\geq 0\\ &\theta(0,\eta)=0, \qquad X<0\end{aligned} \tag{4}$$

The two energy equations (1) and (3) are coupled by the source term $\partial\theta/\partial\eta\,|_{\eta=1}$ in the tube wall energy equation and the boundary condition $\theta(X, 1) = \theta_w(X)$ in the fluid energy equation. In order to solve the fluid energy equation, a solution to the tube energy equation is needed and vice versa. This problem is solved numerically using a finite difference method.

An iterative approach was used to solve this conjugate heat transfer problem. The iteration procedure at the nth step is started by guessing the temperature field for both the tube wall and the fluid. The temperature field for the fluid at the $(n+1)$th iteration step is computed (solving equation (3)) by using the temperature field for the tube wall at the nth iteration step. The temperature field for the tube wall at the $(n+1)$th iteration step is computed (solving equation (1)) using the temperature field for the fluid at the $(n+1)$th iteration step. The temperature field for the fluid at the (n + 2)th iteration step is computed by using the temperature field for the tube wall at the $(n+1)$th iteration step. This process was continued until both temperature fields cease to vary by more than 10^{-6} for any two successive steps of iteration. The details of the computational algorithm are discussed in the following paragraph.

The energy equation for the fluid field equation (3) is parabolic in the axial coordinate X and elliptic in the radial coordinate η. This makes it possible to use a marching-type technique. The solution to the fluid energy equation is obtained by marching along the X direction, using a fully implicit method. The finite difference form of the fluid energy equation is obtained by replacing derivatives in the radial direction with the central difference and derivative in the axial direction with the up-wind difference. This type of discretization requires a solution for a set of simultaneous linear algebraic equations at each marching station. The tridiagonal matrix algorithm was used to solve the set of algebraic equations.

The energy equation for the tube wall is elliptic in nature. The diffusion term in the X direction is replaced by the central difference. The heat input term $\partial\theta/\partial\eta\,|_{\eta=1}$ is replaced with the first-order difference (using two points). The finite difference equations for the nodes at the boundary were obtained by making an energy balance over each boundary control volume. These simultaneous equations are solved using the tridiagonal matrix algorithm.

Results and Discussion

The independent parameters governing this conjugated heat transfer problem are: thickness-to-length ratio of the tube ($\epsilon = t/L$), radius-to-length ratio of the tube ($\phi = R/L$), ratio of the thermal conductivity of the tube wall to that of the fluid flowing inside the tube ($K = K_w/K_f$), ratio of the increased heat flux applied at the midpoint of the tube to the heat flux applied on the rest of the tube ($\gamma = q'/q$), and the Graetz number ($\mathrm{Gz} = 2\phi\mathrm{Pe}$).

As stated earlier, consideration is given to thin tubes and conduction heat transfer in the fluid along the direction of the fluid flow is neglected. Hence, the Peclet number Pe was fixed at 500 and ϵ was fixed at 0.001. The remaining parameters are ϕ, K, and γ. The study of this problem for different values of these three independent parameters requires prohibitively large amounts of computation time, which was not available

Downloaded 17 Dec 2010 to 193.140.21.150. Redistribution subject to ASME license or copyright; see http://www.asme.org/terms/Terms_Use.cfm

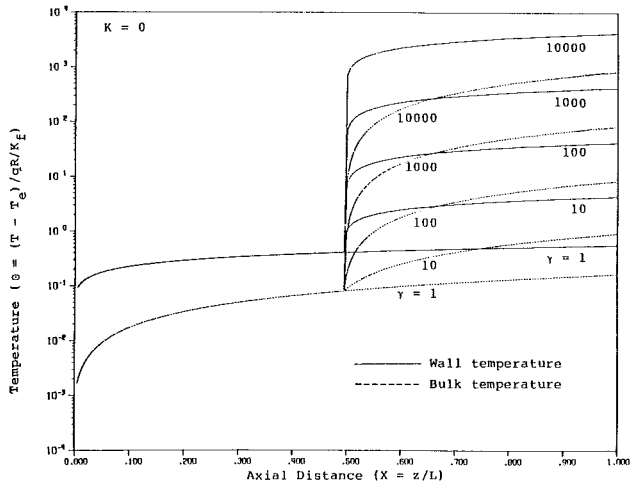

Fig. 2 Temperature variation

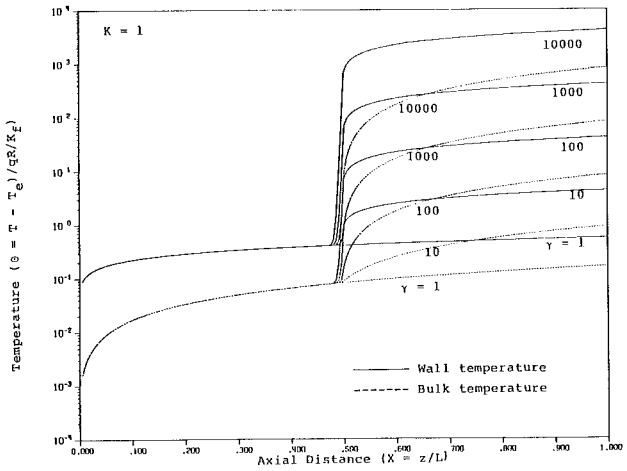

Fig. 3 Temperature variation

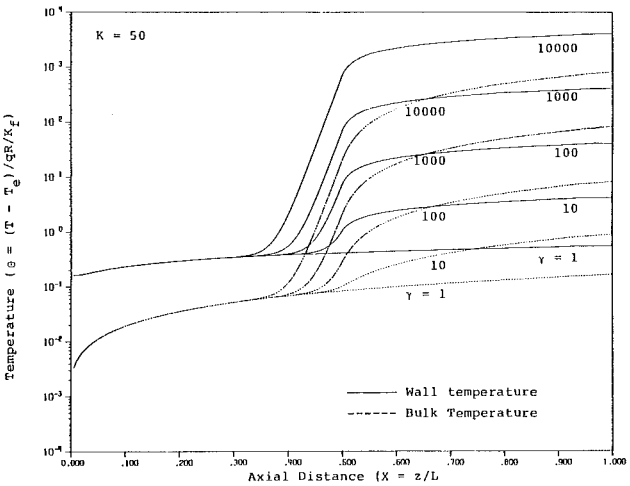

Fig. 4 Temperature variation

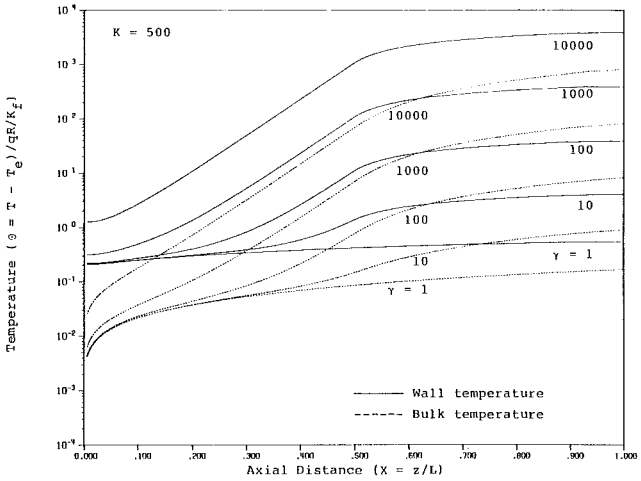

Fig. 5 Temperature variation

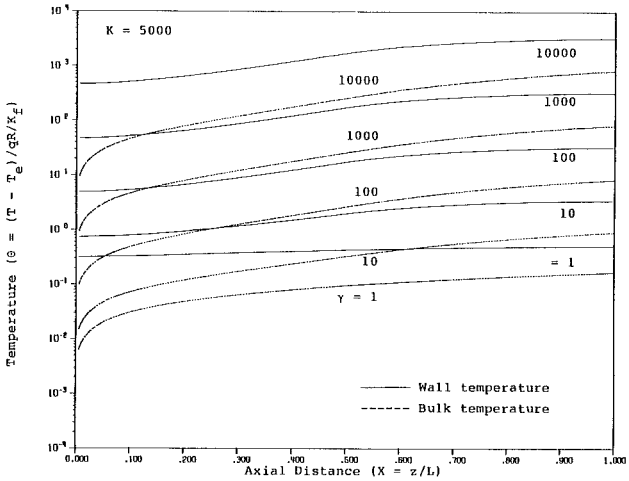

Fig. 6 Temperature variation

for this investigation. Mori et al. [7] concluded that, for $\phi = 0.05$ or less, the effect of wall conduction on convection was insignificant. In order to investigate the effect of axial wall conduction due to a step change in heat flux, ϕ was set at 0.05. This fixes the Graetz number at 50. The thermal conductivity ratio ($K = K_w/K_f$) varied from 0 to 5000 and γ is varied from 1 to 10,000.

After a series of numerical experiments where the grid size was varied over a wide range, it was determined that 41 was a sufficient number of grid points in the radial direction and 201 in the axial direction. Uniform grid spacing was used, although the use of a nonuniform grid size may have saved some computer time. The accuracy of the computational algorithm developed in this investigation was tested by comparing it with the results obtained by Siegel et al. [8] for laminar pipe flow with an inactive wall. The details of the comparison studies are discussed in [9]. For all values of X, the results of this work are within 4 percent of those obtained by Siegel et al. [8]. For higher values of X, the comparison is even better.

Variations of the wall and the fluid bulk temperature for different values of K are shown in Figs. 2–6. The increased heat flux ($\gamma = 1$, 10, 100, 1000, 10,000) is imposed at the midpoint of the tube. Henceforth, regions to the left and right of the midpoint will be referred to as upstream and downstream regions. Heat is transported downstream by advection. Inside the tube wall heat is transported both upstream and downstream by the axial conduction. At lower values of K, advection dominated the axial conduction inside the tube wall. As advection occurs always from an upstream to a downstream direction, only the wall and the fluid bulk

Downloaded 17 Dec 2010 to 193.140.21.150. Redistribution subject to ASME license or copyright; see http://www.asme.org/terms/Terms_Use.cfm

temperatures downstream are affected at low values of K. As the K value increases, a considerable amount of heat is transported upstream by conduction inside the tube wall. This causes the tube and the fluid bulk temperatures to increase upstream and to decrease downstream.

As expected, both tube wall and the fluid bulk temperatures increase with an increase in γ. This behavior is observed in both upstream and downstream regions. A detailed discussion of the variation of the local Nusselt number at the solid fluid interface is given in [9].

The results for $K=0$ represent the case of a nonparticipating wall. The comparison of the tube wall temperature and the bulk temperature of the fluid for $K=0$ and $K=5000$ shows that they are significantly different for 1, but are not much different for $\gamma=1$. This finding re-establishes the conclusion drawn by Mori et al. [7]. Hence, it is concluded that neglecting conduction effects in the analysis of the conjugate heat transfer problem inside a circular duct for cases of $\gamma>1$ could be erroneous.

The computational algorithm developed in this investigation was used to make spot checks for different values of Gz and ϵ. At extremely high values of Gz and for extremely low values of ϵ, solutions were found to be unstable. However, all stable solutions behaved in the same manner as results for $Gz=50$ and $\epsilon=0.001$.

Some of the conclusive results obtained in this investigation can be qualitatively extrapolated to a case of a heat exchanger in which the fluid flowing inside a tube is undergoing a phase change. These extrapolations show that axial conduction heat transfer inside the tube wall preheats the fluid upstream. If superheated vapor were to condense inside the tube, the preheating effect will shift the condensation further downstream. Now, the area of the tube exposed to a two-phase region is reduced, and hence to maintain the same heat transfer rate as in the absence of preheating, larger heat transfer area is needed. If a subcooled liquid were to evaporate inside the tube, the effect of preheating would be the reverse of the condensing case. Hence, it is recommended that tube materials with low thermal conductivity in the axial direction be used in condensers and those with high thermal conductivity be used in evaporators. However, in both cases, the radial conduction resistance should be negligibly small.

References

1 Davis, E. J., and Gill, W. N., "The Effects of Axial Conduction in the Wall on Heat Transfer With Laminar Flow," *International Journal of Heat and Mass Transfer*, Vol. 13, 1970, pp. 459–470.

2 Mori, S., Shinke, T., Sakakibara, M., and Tanimoto, A., "Steady Heat Transfer to Laminar Flow Between Parallel Plates With Conduction in Wall," *Heat Transfer Research*, Vol. 5, No. 4, 1976, pp. 17–25.

3 Povarnitsyn, M. S., and Yurova, E. V., "Calculation of the Temperature Field in a Plane Channel With Nonuniform Heating of Thermally Conducting Walls," *Inzhenerono-Fizicheskii Zhurnal*, Vol. 10, No. 1, 1966, pp. 120–126.

4 Luikov, A. V., Aleksashenko, V. A., and Aleksashenko, A. A., "Analytical Methods of Solution of Conjugated Heat Transfer," *International Journal of Heat and Mass Transfer*, Vol. 14, 1971, pp. 1047–1056.

5 Aleksashenko, V. A., "Conjugated Stationary Problem of Heat Transfer With a Moving Fluid in a Semi-infinite Tube allowing for Viscous Dissipation," *Inzhenerno-Fizicheskii Zhurnal*, Vol. 14, No. 1, 1968, pp. 100–107.

6 Faghri, M., and Sparrow, E. M., "Simultaneous Wall and Fluid Axial Conduction in Laminar-Pipe Flow Heat Transfer," ASME JOURNAL OF HEAT TRANSFER, Vol. 102, 1980, pp. 58–63.

7 Mori, S., Sakakibara, M., and Tanimoto, A., "Steady Heat Transfer to Laminar Flow in a Circular Tube With Conduction in the Tube Wall," *Heat Transfer—Japanese Research*, Vol. 3, No. 2, 1974, pp. 37–46.

8 Siegel, R., Sparrow, E. M., and Hallman, T. M., "Steady Laminar Heat Transfer in a Circular Tube With Prescribed Wall Heat Flux," *Applied Science Research*, Section A, Vol. 7, 1958, pp. 386–392.

9 Anand, N. K., "Numerical Simulation of Single Tube Heat Exchangers," Ph.D. Thesis, Purdue University, 1983.

Comparison of Turbulent Thermal Entrance Regions for Pipe Flows With Developed Velocity and Velocity Developing From a Sharp-Edged Inlet

E. M. Sparrow[1] and M. M. Ohadi[1]

Introduction

The thermal entrance region for turbulent flow in a circular tube has been analytically investigated for two types of velocity distributions (Kays and Crawford, 1980). In one case, the flow is hydrodynamically developed throughout the entire length of the thermal entrance region. In the other, the velocity is uniform at the inlet of the heated section, so that there is a hydrodynamic development of the flow which occurs simultaneously with the thermal development. The latter situation is rarely, if ever, encountered in practice and is, in fact, difficult to achieve in a laboratory experiment.

The effect of various types of velocity distributions on the turbulent heat transfer coefficients in the thermal entrance region of an isothermal-walled tube was investigated experimentally by Boelter et al. (1948). The different velocity distributions were attained by use of different configurations of the inlet of the heated section. As noted in Kays and Crawford (1980), the insufficiencies of the experimental technique used by Boelter et al. (1948) suggest that the results be regarded as qualitative rather than quantitative.

The objective of the present research is to provide definitive thermal entrance region heat transfer results for an isothermal-walled tube for two types of turbulent velocity distributions that are of practical relevance. The two sets of results will be compared to yield the quantitative response of the thermal entrance region to the nature of the velocity condition at the tube inlet. The work to be reported here is experimental and covers the Reynolds number range from approximately 5000 to 85,000.

For one of the two investigated velocity distributions, the heated tube was preceded by an unheated hydrodynamic development tube. This setup yielded a fully developed velocity profile at the inlet of the heated tube. The second case is that of the commonly encountered sharp-edged inlet. In particular, the inlet was situated at the center of a large circular plate which simulated the downstream wall of a large plenum chamber. As is well established, the presence of a sharp-edged inlet gives rise to flow separation.

A major issue in the attainment of accurate heat transfer coefficients in the immediate neighborhood of the inlet of the heated tube is the suppression of extraneous heat losses. Without special precautions, such extraneous losses would occur between the heated tube and the hydrodynamic development tube, and between the heated tube and the circular plate which framed the sharp-edged inlet. To eliminate the losses totally, the experiments were performed using the naphthalene sublimation technique. The use of this technique also enabled the attainment of the isothermal-wall boundary condition (actually, the mass transfer equivalent) while permitting local transfer coefficients to be measured.

Experiments

The respective experimental setups for the mass transfer tube fed by an upstream hydrodynamic development tube and for the mass transfer tube with a sharp-edged inlet are shown schematically in Fig. 1. The mass transfer tube was common

[1]Department of Mechanical Engineering, University of Minnesota, Minneapolis, MN 55455.

Contributed by the Heat Transfer Division for publication in the JOURNAL OF HEAT TRANSFER. Manuscript received by the Heat Transfer Division October 29, 1986.

Downloaded 17 Dec 2010 to 193.140.21.150. Redistribution subject to ASME license or copyright; see http://www.asme.org/terms/Terms_Use.cfm

temperatures downstream are affected at low values of K. As the K value increases, a considerable amount of heat is transported upstream by conduction inside the tube wall. This causes the tube and the fluid bulk temperatures to increase upstream and to decrease downstream.

As expected, both tube wall and the fluid bulk temperatures increase with an increase in γ. This behavior is observed in both upstream and downstream regions. A detailed discussion of the variation of the local Nusselt number at the solid fluid interface is given in [9].

The results for $K=0$ represent the case of a nonparticipating wall. The comparison of the tube wall temperature and the bulk temperature of the fluid for $K=0$ and $K=5000$ shows that they are significantly different for 1, but are not much different for $\gamma=1$. This finding re-establishes the conclusion drawn by Mori et al. [7]. Hence, it is concluded that neglecting conduction effects in the analysis of the conjugate heat transfer problem inside a circular duct for cases of $\gamma>1$ could be erroneous.

The computational algorithm developed in this investigation was used to make spot checks for different values of Gz and ϵ. At extremely high values of Gz and for extremely low values of ϵ, solutions were found to be unstable. However, all stable solutions behaved in the same manner as results for $Gz=50$ and $\epsilon=0.001$.

Some of the conclusive results obtained in this investigation can be qualitatively extrapolated to a case of a heat exchanger in which the fluid flowing inside a tube is undergoing a phase change. These extrapolations show that axial conduction heat transfer inside the tube wall preheats the fluid upstream. If superheated vapor were to condense inside the tube, the preheating effect will shift the condensation further downstream. Now, the area of the tube exposed to a two-phase region is reduced, and hence to maintain the same heat transfer rate as in the absence of preheating, larger heat transfer area is needed. If a subcooled liquid were to evaporate inside the tube, the effect of preheating would be the reverse of the condensing case. Hence, it is recommended that tube materials with low thermal conductivity in the axial direction be used in condensers and those with high thermal conductivity be used in evaporators. However, in both cases, the radial conduction resistance should be negligibly small.

References

1 Davis, E. J., and Gill, W. N., "The Effects of Axial Conduction in the Wall on Heat Transfer With Laminar Flow," *International Journal of Heat and Mass Transfer*, Vol. 13, 1970, pp. 459–470.

2 Mori, S., Shinke, T., Sakakibara, M., and Tanimoto, A., "Steady Heat Transfer to Laminar Flow Between Parallel Plates With Conduction in Wall," *Heat Transfer Research*, Vol. 5, No. 4, 1976, pp. 17–25.

3 Povarnitsyn, M. S., and Yurova, E. V., "Calculation of the Temperature Field in a Plane Channel With Nonuniform Heating of Thermally Conducting Walls," *Inzhenerono-Fizicheskii Zhurnal*, Vol. 10, No. 1, 1966, pp. 120–126.

4 Luikov, A. V., Aleksashenko, V. A., and Aleksashenko, A. A., "Analytical Methods of Solution of Conjugated Heat Transfer," *International Journal of Heat and Mass Transfer*, Vol. 14, 1971, pp. 1047–1056.

5 Aleksashenko, V. A., "Conjugated Stationary Problem of Heat Transfer With a Moving Fluid in a Semi-infinite Tube allowing for Viscous Dissipation," *Inzhenerno-Fizicheskii Zhurnal*, Vol. 14, No. 1, 1968, pp. 100–107.

6 Faghri, M., and Sparrow, E. M., "Simultaneous Wall and Fluid Axial Conduction in Laminar-Pipe Flow Heat Transfer," ASME JOURNAL OF HEAT TRANSFER, Vol. 102, 1980, pp. 58–63.

7 Mori, S., Sakakibara, M., and Tanimoto, A., "Steady Heat Transfer to Laminar Flow in a Circular Tube With Conduction in the Tube Wall," *Heat Transfer—Japanese Research*, Vol. 3, No. 2, 1974, pp. 37–46.

8 Siegel, R., Sparrow, E. M., and Hallman, T. M., "Steady Laminar Heat Transfer in a Circular Tube With Prescribed Wall Heat Flux," *Applied Science Research*, Section A, Vol. 7, 1958, pp. 386–392.

9 Anand, N. K., "Numerical Simulation of Single Tube Heat Exchangers," Ph.D. Thesis, Purdue University, 1983.

Comparison of Turbulent Thermal Entrance Regions for Pipe Flows With Developed Velocity and Velocity Developing From a Sharp-Edged Inlet

E. M. Sparrow[1] and M. M. Ohadi[1]

Introduction

The thermal entrance region for turbulent flow in a circular tube has been analytically investigated for two types of velocity distributions (Kays and Crawford, 1980). In one case, the flow is hydrodynamically developed throughout the entire length of the thermal entrance region. In the other, the velocity is uniform at the inlet of the heated section, so that there is a hydrodynamic development of the flow which occurs simultaneously with the thermal development. The latter situation is rarely, if ever, encountered in practice and is, in fact, difficult to achieve in a laboratory experiment.

The effect of various types of velocity distributions on the turbulent heat transfer coefficients in the thermal entrance region of an isothermal-walled tube was investigated experimentally by Boelter et al. (1948). The different velocity distributions were attained by use of different configurations of the inlet of the heated section. As noted in Kays and Crawford (1980), the insufficiencies of the experimental technique used by Boelter et al. (1948) suggest that the results be regarded as qualitative rather than quantitative.

The objective of the present research is to provide definitive thermal entrance region heat transfer results for an isothermal-walled tube for two types of turbulent velocity distributions that are of practical relevance. The two sets of results will be compared to yield the quantitative response of the thermal entrance region to the nature of the velocity condition at the tube inlet. The work to be reported here is experimental and covers the Reynolds number range from approximately 5000 to 85,000.

For one of the two investigated velocity distributions, the heated tube was preceded by an unheated hydrodynamic development tube. This setup yielded a fully developed velocity profile at the inlet of the heated tube. The second case is that of the commonly encountered sharp-edged inlet. In particular, the inlet was situated at the center of a large circular plate which simulated the downstream wall of a large plenum chamber. As is well established, the presence of a sharp-edged inlet gives rise to flow separation.

A major issue in the attainment of accurate heat transfer coefficients in the immediate neighborhood of the inlet of the heated tube is the suppression of extraneous heat losses. Without special precautions, such extraneous losses would occur between the heated tube and the hydrodynamic development tube, and between the heated tube and the circular plate which framed the sharp-edged inlet. To eliminate the losses totally, the experiments were performed using the naphthalene sublimation technique. The use of this technique also enabled the attainment of the isothermal-wall boundary condition (actually, the mass transfer equivalent) while permitting local transfer coefficients to be measured.

Experiments

The respective experimental setups for the mass transfer tube fed by an upstream hydrodynamic development tube and for the mass transfer tube with a sharp-edged inlet are shown schematically in Fig. 1. The mass transfer tube was common

[1]Department of Mechanical Engineering, University of Minnesota, Minneapolis, MN 55455.

Contributed by the Heat Transfer Division for publication in the JOURNAL OF HEAT TRANSFER. Manuscript received by the Heat Transfer Division October 29, 1986.

Copyright © 1987 by ASME

Downloaded 17 Dec 2010 to 193.140.21.150. Redistribution subject to ASME license or copyright; see http://www.asme.org/terms/Terms_Use.cfm

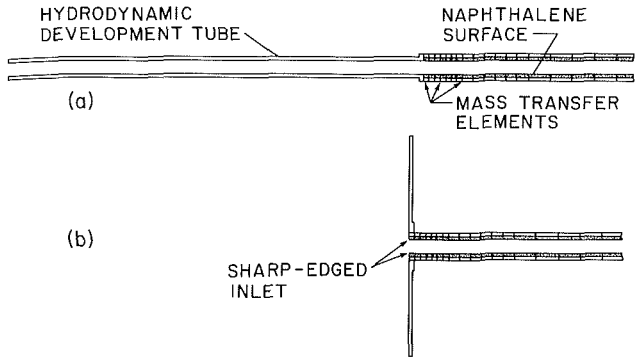

Fig. 1 Experimental setups for mass transfer in a tube with (*a*) hydrodynamically developed flow throughout and (*b*) a sharp-edged inlet

to both setups. It had an internal diameter D of 3.175 cm (1.250 in.) and an overall length of $20.4D$ ($20.5D$ for the sharp-edged case). The tube was an assemblage of 21 mass transfer elements, of which numbers 1 through 7 each had an axial length of $0.4D$, 8 through 13 a length of $0.8D$, and 14 through 21 a length of $1.6D$ (the first element for the sharp-edged case was $0.5D$ in length). The use of shorter elements at the upstream end of the tube and longer elements farther downstream was in recognition of the relatively rapid variations of the transfer coefficient which occur near the inlet and the gradual variations which occur in the downstream region.

Each element consisted of a shell-like metallic exterior and an internal annular layer of naphthalene that was created by a casting procedure. The inner surface of the naphthalene (i.e., the surface which bounded the flow passage) was hydrodynamically smooth, having been cast against a highly polished and lapped brass shaft. The successive elements were interconnected by interlocking tongues and recesses that had been machined into the metallic portions, in a manner similar to that illustrated in Fig. 1 of Molki and Sparrow (1983). However, the mass transfer elements used here had longer tongues and recesses to ensure more precise axial alignment. Axial alignment (i.e., straightness) was further assured by the use of an adjustable support beneath the tube. Once the elements were assembled, the assembly was made into a single unit by pressure applied by quick-acting clamps. To seal against leaks, highly adhesive tape was applied to the outside of the tube at the interfaces of the successive elements.

Two of the elements, numbers 1 and 21, were equipped with fine, precalibrated thermocouples that were cast in place such that the junctions were situated at the bounding surface of the flow passage.

The detailed configuration of the mass transfer elements, their fabrication, and their assembly is described by Ohadi (1986). The casting procedure used here is generally similar to that of Molki and Sparrow (1983) and illustrated in Fig. 2 of that reference. Refinements of the casting equipment and procedure are set forth by Ohadi (1986).

The condition of hydrodynamically developed flow throughout the mass transfer section was achieved by means of an upstream-positioned tube that did not participate in the mass transfer (Fig. 1*a*). Nonparticipation was assured by making the tube from a metal, specifically, aluminum. The diameter of the upstream tube was identical to that of the mass transfer tube (3.175 cm), and its length was $30D$. To hasten hydrodynamic development, the inlet to the upstream tube was sharp-edged. Taps installed in the tube indicated a linear decrease of pressure with distance, thereby confirming hydrodynamic development. The two tubes were mated via a special flange which guaranteed colinearity.

For the sharp-edged case (Fig. 1*b*), the tube inlet was framed by a circular aluminum plate whose diameter was equal to $16D$. With the plate in place, air was supplied to the mass transfer tube from the space upstream of the inlet, which thereby served as a large plenum chamber. The upstream face of the first mass transfer element was shielded from exposure to the airflow by a thin metal sheet (thickness = $0.02D$).

The apparatus was operated in the suction mode, with air drawn from the temperature-controlled laboratory and with the naphthalene-enriched discharge vented outside the building. The mass of each mass transfer element was measured before and after each data run to determine the per-element mass transfer rate $\dot{M}$. A painstaking experimental technique was developed and employed as set forth by Ohadi (1986). The accuracy of the Sherwood number data is estimated to be about 2 percent.

Results and Discussion

For any element i, the mass transfer coefficient K_i and Sherwood number Sh_i were evaluated by

$$K_i = \dot{M}_i / A_i (\rho_{nw} - \rho_{nb,i}), \quad \mathrm{Sh}_i = K_i D / \mathfrak{D} \tag{1}$$

where the bulk density of the naphthalene vapor at i is given by

$$\rho_{nb,i} = \sum_{j=1}^{i-1} \dot{M}_j / \dot{Q} + (\dot{M}_i / \dot{Q})/2 \tag{2}$$

in which A_i is the transfer surface area of element i, $\dot{Q}$ is the volumetric flow rate, and $\mathfrak{D}$ is the mass diffusion coefficient. The naphthalene vapor ρ_{nw} at the tube wall was computed from the measured uniform wall temperature of the naphthalene in conjunction with the vapor pressure/temperature relation (Sogin, 1958) and the perfect gas law. The mass diffusion coefficient was eliminated via the relation $\mathfrak{D} = \nu/\mathrm{Sc}$, where the Schmidt number is 2.5 (Sogin, 1958) and ν is the kinematic viscosity of air.

The Reynolds number Re is that for a conventional tube flow

$$\mathrm{Re} = 4\dot{w}/\mu\pi D \tag{3}$$

where $\dot{w}$ is the mass flow rate and D is the inside diameter of the tube.

The Sherwood number results determined as described in the foregoing are plotted in Figs. 2 and 3 as a function of the dimensionless axial coordinate x/D, where x is measured from the beginning of the mass transfer section. Each data point represents the Sherwood number for an individual mass transfer element, and the point is plotted at the x/D value at the axial midpoint of the element. Although the data are quasi-local rather than strictly local, the selected sizes and positioning of the mass transfer elements are most than sufficient to resolve the Sh versus x/D distribution.

Figure 2 conveys results for the lower end of the investigated Reynolds number range (5000-15,000) while Fig. 3 is for the higher end of the range (24,000-84,000). For each Reynolds number, the open symbols are for the case of the sharp-edged inlet, while the black symbols are for the case of the tube-fed inlet (i.e., hydrodynamically developed flow). For all Reynolds numbers except the lowest, the respective Re values for the two cases coincide within 0.8-1.6 percent. However, at the lowest Reynolds number, there is a 5 percent spread in the Re values. As will be seen shortly, this spread will affect the appearance, but not the substance, of the Sh comparison between the cases.

All of the axial distributions for the tube-fed-inlet case share a common shape, while those for the sharp-edged-inlet case have a different common shape. For the former, the maximum value of the transfer coefficient is attained at the inlet of

Downloaded 17 Dec 2010 to 193.140.21.150. Redistribution subject to ASME license or copyright; see http://www.asme.org/terms/Terms_Use.cfm

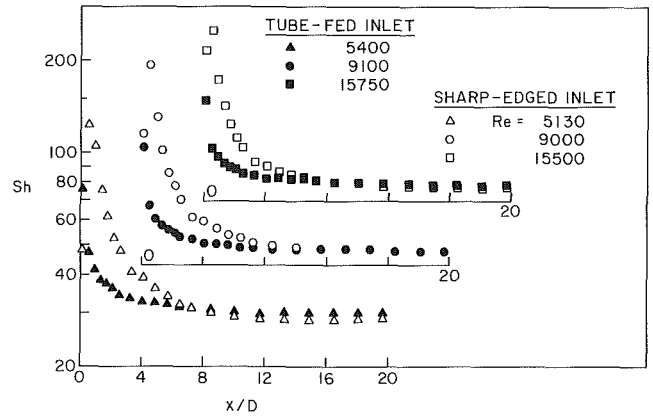

Fig. 2 Sherwood number distributions for the lower range of Reynolds numbers

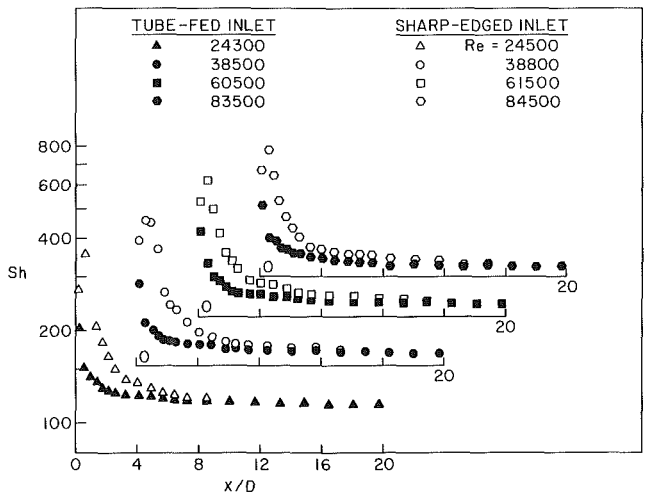

Fig. 3 Sherwood number distributions for the higher range of Reynolds numbers

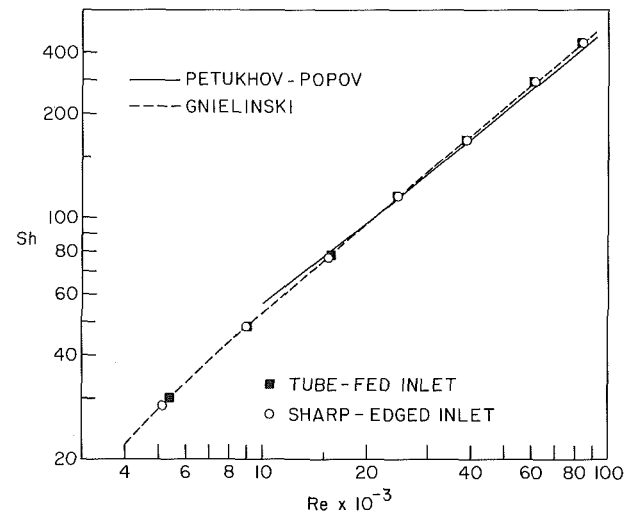

Fig. 4 Fully developed Sherwood numbers

the mass transfer tube, and with increasing downstream distance the coefficient decreases monotonically to a constant, fully developed value. This pattern reflects the orderly growth of the thermal boundary layer. The Sh distribution for the sharp-edged case is characterized by an initial sharp rise, the attainment of a maximum at $x/D \sim 0.65$, and a decrease which ultimately levels off to a fully developed value. This behavior is characteristic of flow separation and reattachment, and post-separation redevelopment.

In the mass transfer entrance region, the transfer coefficients for the sharp-edged-inlet case always exceed those for the tube-fed-inlet case. The greatest deviations occur at the axial station where the coefficients for the former attain their maximum, i.e., at $x/D \sim 0.65$. At that station, the ratio of the sharp-edged Sh to the tube-fed Sh takes on the values 2.6, 2.8, 2.5, 2.3, 2.2, 2.1, and 1.9 as Re ranges from the lowest to the highest of the investigated values. Thus, there are major deviations between the two cases – factors of two or three. Except at the lowest Reynolds number, the aforementioned ratio decreases monotonically with Re. The exception may be due to the imperfect match of the Reynolds numbers (5130 versus 5400).

Significant but much smaller deviations occur at the first measurement station, $x/D \sim 0.2$. For Reynolds numbers of 15,000 and higher, the sharp-edged Sh exceed the tube-fed Sh by 30-40 percent. At the lower Re, the differences are quite small.

Downstream of the maximum of the sharp-edged Sh distribution, the two Sh distributions begin to draw together. At $x/D \sim 2.2$, the sharp-edged Sh exceed the tube-fed Sh by 45 to 20 percent as Re increases over the investigated range. These deviations are still appreciable but their magnitudes, relative to those at the maximum, reflect the drawing together of the curves.

The deviations between the two distributions diminish to about 5 percent at $x/D \sim 6$, so that significant effects of the velocity distribution on the local Sherwood numbers are confined to $0 \leq x/D \leq 6$. Complete overlap of the distributions occurs for $x/D > 10$ for Re up to 25,000 and for $x/D > 12$ at higher Re.

The attainment of the same fully developed Sh values for the two cases is expected. The fact that this expectation was fulfilled in the experiments reinforces the experimental technique. The noncoincidence at the lowest Reynolds number is due to the imperfect matching of the respective Re values.

The fully developed Sherwood numbers are compared in Fig. 4 with the well-established correlation of Petukhov-Popov (1970), which applies for $Re \geq 10{,}000$, and with its generalization by Gnielinski (1976) into the low-Re turbulent range. The agreement of the data with the correlations is excellent, thereby lending further support to the accuracy of the experimental results.

References

Boelter, L. M. K., Young, G., and Iversen, H. W., 1948, "An Investigation of Aircraft Heaters – XXVII. Distribution of Heat Transfer Rate in the Entrance Region of a Circular Tube," NACA TN 1451.

Gnielinski, V., 1976, "New Equations for Heat and Mass Transfer in Turbulent Pipe and Channel Flow," *International Chemical Engineering*, Vol. 16, pp. 359-368.

Kays, W. M., and Crawford, M. E., 1980, *Convective Heat and Mass Transfer*, 2nd ed., McGraw-Hill, New York.

Molki, M., and Sparrow, E. M., 1983, "In-Tube Heat Transfer for Skewed Inlet Flow Caused by Competition Among Tubes Fed by the Same Plenum," ASME JOURNAL OF HEAT TRANSFER, Vol. 105, pp. 870-877.

Ohadi, M. M., 1986, "Turbulent Swirl-Affected Heat Transfer and Pressure Drop Characteristics in a Straight Tube Situated Downstream of a Bend," Ph.D. Thesis, Department of Mechanical Engineering, University of Minnesota, Minneapolis, MN.

Petukhov, B. S., 1970, "Heat Transfer and Friction in Turbulent Pipe Flow With Variable Physical Properties," *Advances in Heat Transfer*, Vol. 6, pp. 503-564, equations (48) and (50).

Sogin, H. H., 1958, "Sublimation From Disks to Air Streams Flowing Normal to Their Surfaces," *ASME Transactions*, Vol. 80, pp. 61-71.

Downloaded 17 Dec 2010 to 193.140.21.150. Redistribution subject to ASME license or copyright; see http://www.asme.org/terms/Terms_Use.cfm

Instabilities of Mixed Convection Flows Adjacent to Inclined Plates

H. I. Abu-Mulaweh,[1] B. F. Armaly,[1] and T. S. Chen[1]

Introduction

The measurements by Sparrow and Husar (1969) and by Lloyd and Sparrow (1970) established that the onset of instability (transition from laminar to turbulent) in free convection boundary layer flow above an inclined heated plate is predominated by the wave mode of instability for inclination angles less than 14 deg, as measured from the vertical, and by the vortex mode of instability for angles greater than 17 deg. The transition Grashof number decreased as the angle of inclination increased. The predictions of Chen and Tzuoo (1982) for this flow provide trends that are similar to measured values, but the predicted critical Grashof numbers deviate significantly (three orders of magnitude smaller) from measured values. The instability of mixed convection boundary layer flow adjacent to inclined heated plates have also been treated numerically by Chen and Mucoglu (1979) for wave instability and by Chen et al. (1982) for vortex instability. Comparisons with measurements could not be done in these studies because measurements of instability in mixed convection flow adjacent to inclined plates were not available in the literature. It is anticipated, however, that these predictions will underestimate the actual onset of instability, as in the free convection case. The lack of measurements in this flow domain for this geometry has motivated the present study.

The onset of instability in mixed convection flow adjacent to an isothermally heated inclined plate was determined in this study through flow visualization. The buoyancy-assisting and buoyancy-opposing flow cases were examined for the flow both above and below the heated plate. The critical Grashof–Reynolds number relationships for the onset of instability in this flow domain are reported in this paper.

Apparatus and Procedure

This flow visualization study was performed in an open circuit wind tunnel which could be rotated and fixed at any desired inclination angle from 0 to 360 deg. The free-stream flow remains laminar and parallel to the heated plate at any angle of inclination. Details of the tunnel, heated plate, and other instrumentation have been described by Ramachandran et al. (1985). The free-stream velocity in the tunnel could be varied between 0.3–3 m/s and the plate temperature could be maintained at a uniform and constant value in the range of 20°–100°C. The uncertainty associated with the temperature measurements was determined to be 0.1°C, and for the velocity measurements it was 2 percent. Flow visualizations were performed by using a 15 W collimated white light beam, 2.5 cm in diameter. The flow was seeded by glycerin particles, 2–5 μm in diameter, which served as scattering centers for visualizing the flow. These particles also served as seeds for the measurements of the free-stream velocity by a laser-Doppler velocimeter.

The onset of instability was determined through flow visualization at different inclination angles, in 15 deg increments, throughout the entire 360 deg rotation domain of the tunnel. The procedure consisted of the following steps. The tunnel was fixed at a selected inclination angle and the plate was heated to a desired fixed and uniform temperature, while a particular constant free-stream velocity was maintained in the tunnel. Flow visualization started after steady-state conditions were achieved (steady state required approximately 4 hours of operation). The collimated light beam, which was placed parallel to the heated surface and perpendicular to the direction of the flow, was traversed in the direction of the flow and away from the leading edge of the heated plate, until an instability was detected visually inside the boundary layer. The scattered light beam, which crossed the width of the heated plate, was viewed perpendicularly from a downstream location, which made the detection of a small disturbance in the flow possible. The start of instability was established as the plane on which the two-dimensional flow was transformed to a three-dimensional vortex flow. The location of the plane (critical distance) along with the plate temperature and the free-stream velocity were used to calculate the critical Grashof and Reynolds numbers. The uncertainty and the repeatability of this critical distance as determined from the flow visualization are within the 2 percent. The thermophysical properties that were used in these calculations were evaluated at the average film temperature. For a given inclination angle, four different free-stream velocities, in the range of 0.3–1.2 m/s, were examined for each fixed plate temperature. Similarly, for each inclination angle four different plate temperatures, in the range of 35° – 75°C, were examined while room temperature was maintained at 21°C. These observations generated a large set of data documenting the influence of the various parameters on the instability of such a flow.

Results and Discussion

A sample of the flow visualization patterns obtained in this study is shown in Fig. 1 for the case of flow above a horizontal heated plate. Each image in that figure represents a view of the flow at the planes indicated (X = 12.7 cm, 22.9 cm, 25.4 cm, and 30.5 cm) as seen from a downstream location in the test section. The collimated light beam and the seeded air flow provide the light scattering required at the plane for flow visualization. Any disturbance that is responsible for secondary motion in the flow can be easily detected by the presence of a darker background indicating the pattern of the secondary flow. The figure clearly illustrates a region of two-dimensional laminar and stable flow at small downstream

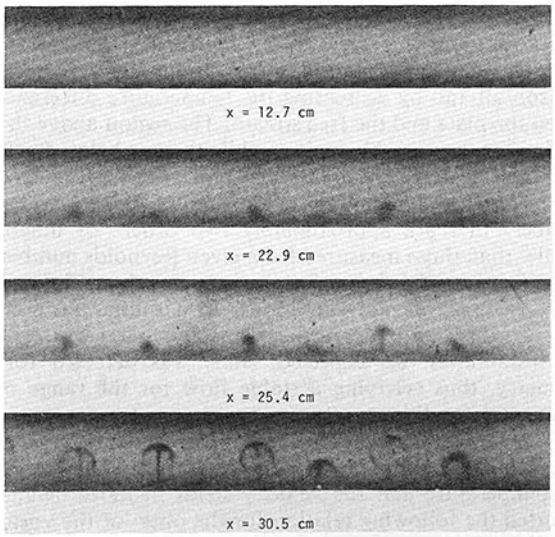

Fig. 1 Incipience and growth of vortex rolls in flow above horizontal heated plate; $U_\infty = 0.34$ m/s, $(T_w - T_\infty) = 30$°C

[1]Department of Mechanical and Aerospace Engineering, University of Missouri – Rolla, Rolla, MO 65401.

Contributed by the Heat Transfer Division for publication in the JOURNAL OF HEAT TRANSFER. Manuscript received by the Heat Transfer Division June 30, 1986.

Copyright © 1987 by ASME

Downloaded 17 Dec 2010 to 193.140.21.150. Redistribution subject to ASME license or copyright; see http://www.asme.org/terms/Terms_Use.cfm

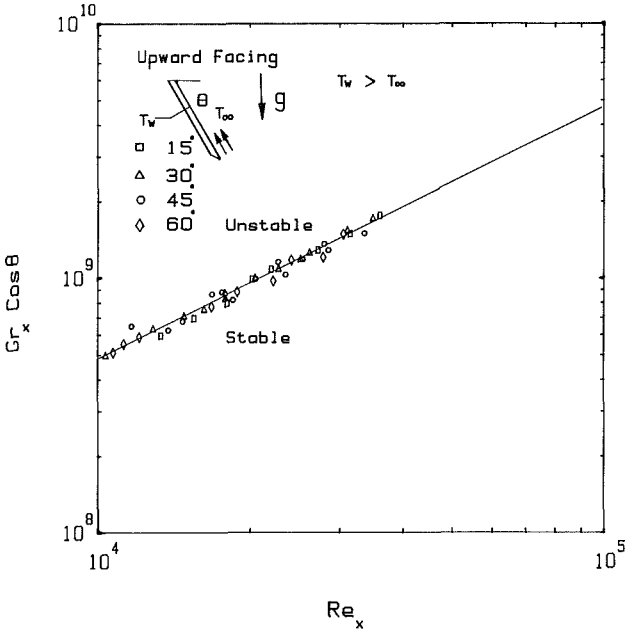

Fig. 2 Onset of vortex instability for an upward-facing buoyancy-assisting flow

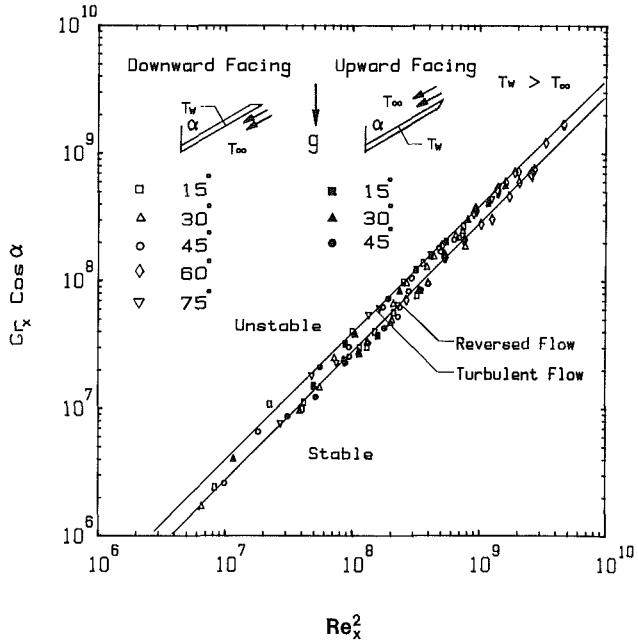

Fig. 3 Onset of instability for upward and downward-facing buoyancy-opposing flow

distances from the leading edge, followed by the onset of vortices which breaks the two-dimensional nature of the flow, and followed further by a region where the vortices develop and grow until they break down (not shown in this figure), thus developing into a two-dimensional turbulent flow domain. The start/onset of the instability, which is the important parameter for this study, can clearly be identified from this flow visualization technique.

The critical Reynolds and Grashof numbers for an upward-facing buoyancy-assisting flow as determined from flow visualization are presented in Fig. 2. The results for inclination angles 15 deg $< \theta <$ 60 deg, as measured from the horizontal axis, can be correlated by the following linear relation

$$Gr_x \cos\theta = 4.7 \times 10^4 \, Re_x \tag{1}$$

The critical Grashof and Reynolds numbers have the standard definition and are based on the critical streamwise location identifying the onset of vortex instability. The critical Reynolds and Grashof number ranges which were used to establish this correlation are $8 \times 10^3 < Re_x < 3 \times 10^4$ and $4 \times 10^8 < Gr_x < 3 \times 10^9$. The results indicate that the onset of vortex instability is delayed by increasing the free-stream velocity or the inclination angle (as measured from the horizontal) and by decreasing the temperature difference between the plate and the free stream. The region above the line in Fig. 2 is the unstable region, while the one below the line is the stable region. The numerical predictions of Chen et al. (1982) provide similar trends, but predict transition Grashof numbers that are approximately two orders of magnitude smaller than those measured for a given Reynolds number. Instability was not detected for angles larger than 60 deg in the range of experimental conditions. In a similar fashion, the downward-facing buoyancy-assisting flow case was explored for instabilities. As expected, none was detected for this geometry, thus verifying a stable flow for the range of experimental conditions.

The case of the upward-facing horizontal heated plate is not included in the above correlation. Moharreri (1986) examined the temperature and the velocity fields in more detail, and reported the following relation for the onset of the vortex instability

$$Gr_x = 100 \, Re_x^{1.5} \tag{2}$$

This relation is similar to the one proposed by Wu and Cheng (1976) for water flow above a horizontal heated plate. The critical Reynolds and Grashof number ranges which were used to establish this correlation are $2 \times 10^3 < Re_x < 2 \times 10^4$ and $6 \times 10^6 < Gr_x < 2 \times 10^8$.

The buoyancy-opposing flow with inclination angles of 15 deg $< \alpha <$ 75 deg for downward-facing plate and inclination angles of 15 deg $< \alpha <$ 45 deg for upward-facing plate (as measured from the vertical axis) displayed similar behavior by developing a region of flow reversal inside the boundary layer which starts at some critical streamwise location from the leading edge. The reversed flow region was confined to a shallow layer of a certain length, i.e., a recirculating pocket within the boundary layer. Beyond that region the flow displayed turbulent flow characteristic without any reversed flow region. The critical Grashof and Reynolds numbers identifying the start of the reversed flow region and the start of the turbulent flow region are presented for different inclination angles in Fig. 3. These results can be correlated by the following relations:

For the start of reversed flow region

$$Gr_x \cos\alpha = 0.270 \, Re_x^2 \tag{3}$$

For the start of turbulent flow region

$$Gr_x \cos\alpha = 0.365 \, Re_x^2 \tag{4}$$

The region presented below these lines in Fig. 3 is the stable region. The length of the stable region, as measured from the leading edge of the heated plate, increases as the free-stream velocity or the inclination angle α increases and as the temperature difference between the plate and the free stream decreases. The critical Reynolds and Grashof number ranges which were used to establish the above two correlations are $2.5 \times 10^3 < Re_x < 7 \times 10^4$ and $2 \times 10^6 < Gr_x < 3.5 \times 10^9$.

The upward-facing buoyancy-opposing flows with inclination angles α greater than 45 deg, as measured from the vertical, displayed different transition characteristics than the previously discussed case of inclination angles that are smaller or equal to 45 deg. The flow displayed a vortex mode of instability with the critical Grashof and Reynolds numbers as presented in Fig. 4. These results can be correlated by the following relation:

Downloaded 17 Dec 2010 to 193.140.21.150. Redistribution subject to ASME license or copyright; see http://www.asme.org/terms/Terms_Use.cfm

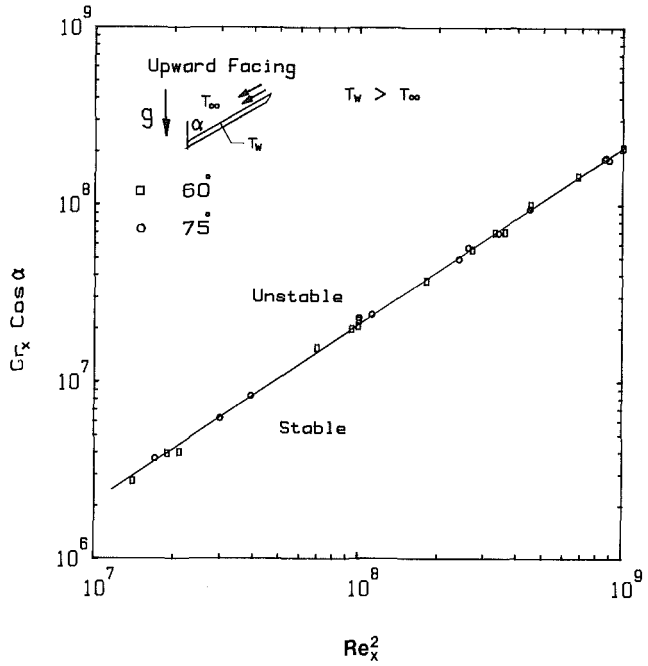

Fig. 4 Onset of vortex instability for upward-facing buoyancy-opposing flow

$$\mathrm{Gr}_x \cos\alpha = 0.210\,\mathrm{Re}_x^2 \tag{5}$$

The region below the line is the stable region which is influenced, in the same way as discussed in the previous paragraph, by the magnitude of the free-stream velocity, the inclination angle, and the temperature difference. The critical Reynolds and Grashof number ranges which were used to establish the above correlation are $4\times10^3 < \mathrm{Re}_x < 3.5\times10^4$ and $1.5\times10^7 < \mathrm{Gr}_x < 5\times10^8$.

Conclusions

The onset of instability in mixed convection flow adjacent to isothermal heated inclined plates was determined for buoyancy-assisting and buoyancy-opposing flows and for flow above and below the heated plate. The results are summarized in terms of simple correlations between the critical Grashof and Reynolds numbers. The length of the stable region increases by increasing the free-stream velocity and the inclination angle, θ or α, but decreases as the temperature difference between the plate and the free stream increases. The results presented should aid in limiting the applicability of the two-dimensional, laminar mixed convection flow solutions to this flow geometry.

Acknowledgments

The work reported in this paper was supported in part by a grant (NSF MEA 83-00785) from the National Science Foundation and by the University of Missouri Weldon Spring Endowment Fund.

References

Chen, T. S., and Mucoglu, A., 1979, "Wave Instability of Mixed Convection Flow Over a Horizontal Flat Plate," *International Journal of Heat and Mass Transfer*, Vol. 22, pp. 185–196.

Chen, T. S., Mucoglu, A., and Armaly, B. F., 1982, "Thermal Instability of Mixed Convection Flow Over Inclined Surfaces," *Numerical Heat Transfer*, Vol. 5, pp. 343–352.

Chen, T. S., and Tzuoo, K. L., 1982, "Vortex Instability of Free Convection Flow Over Horizontal and Inclined Surfaces," ASME JOURNAL OF HEAT TRANSFER, Vol. 104, pp. 637–643.

Moharreri, S., 1986, "Laser-Doppler and Hot-Wire Measurements in Convective Flows," M.S. Thesis, Department of Mechanical and Aerospace Engineering, University of Missouri – Rolla.

Lloyd, J. R., and Sparrow, E. M., 1970, "On the Instability of Natural Convection Flow on Inclined Plates," *Journal of Fluid Mechanics*, Vol. 42, pp. 465–470.

Ramachandran, N., Armaly, B. F., and Chen, T. S., 1985, "Measurements and Predictions of Laminar Mixed Convection Flow Adjacent to a Vertical Surface," ASME JOURNAL OF HEAT TRANSFER, Vol. 107, pp. 636–641.

Sparrow, E. M., and Husar, R. B., 1969, "Longitudinal Vortices in Natural Convection Flow on Inclined Plates," *Journal of Fluid Mechanics*, Vol. 37, pp. 251–255.

Wu, R. S., and Cheng, K. C., 1976, "Thermal Instability of Blasius Flow Along Horizontal Plates," *International Journal of Heat and Mass Transfer*, Vol. 19, pp. 907–913.

Mixed Convection Flow About Slender Bodies of Revolution

J. L. S. Chen[1]

1 Introduction

Heat transfer from a thin needle or a slender body of revolution has been studied by many investigators for the case of either forced convection [1, 2] or free convection [3–6]. The problem of heat transfer by combined free and forced convection from vertical thin needles with the surfaces maintained at a uniform temperature or uniform heat flux has been analyzed by Narain and Uberoi [7, 8].

This paper deals with the subject of combined convection heat transfer in laminar axial boundary-layer flows about vertical slender bodies of revolution with variable surface temperature or variable surface heat flux. The analysis is directed toward the aspect of similarity flow of the subject problem. It has been found that similarity solutions exist when (*i*) the surface temperature varies as $x^{(2m-1)}$, and (*ii*) the surface heat flux varies as $x^{(5m-3)/2}$, where x is the axial coordinate measured from the front stagnation of the body and m is an arbitrary constant. Similarity velocity and temperature profiles as well as local skin-friction coefficient and Nusselt number have been obtained for various shapes and sizes of the body and presented in graphic forms.

2 Similarity Analysis

Consider a steady-state, incompressible, laminar flow past a thin vertical axisymmetric body. The free-stream velocity is assumed to vary according to x^m. The ambient fluid is maintained at a constant temperature T_∞, while the body surface is at either variable temperature $T_w(x)$ or variable heat flux $q_w(x)$. It is assumed that the heat is transferred from the body to the fluid so that the buoyancy force aids the forced convection in the same direction. Under the assumption of constant fluid properties except for density change due to temperature change, the conservation equations for the axisymmetric boundary layers may be written as

$$\frac{\partial(ru)}{\partial x}+\frac{\partial(rv)}{\partial r}=0 \tag{1}$$

$$u\frac{\partial u}{\partial x}+v\frac{\partial u}{\partial r}=U\frac{dU}{dx}+g\beta(T-T_\infty)+\frac{\nu}{r}\frac{\partial}{\partial r}\left(r\frac{\partial u}{\partial r}\right) \tag{2}$$

$$u\frac{\partial T}{\partial x}+v\frac{\partial T}{\partial r}=\frac{\alpha}{r}\frac{\partial}{\partial r}\left(r\frac{\partial T}{\partial r}\right) \tag{3}$$

where (x, r) are the axial and radial coordinates, respectively, with the origin placed at the front stagnation point of the

[1]Associate Professor, Department of Mechanical Engineering, University of Pittsburgh, PA 15261; Mem. ASME.

Contributed by the Heat Transfer Division for publication in the JOURNAL OF HEAT TRANSFER. Manuscript received by the Heat Transfer Division April 18, 1985.

Downloaded 17 Dec 2010 to 193.140.21.150. Redistribution subject to ASME license or copyright; see http://www.asme.org/terms/Terms_Use.cfm

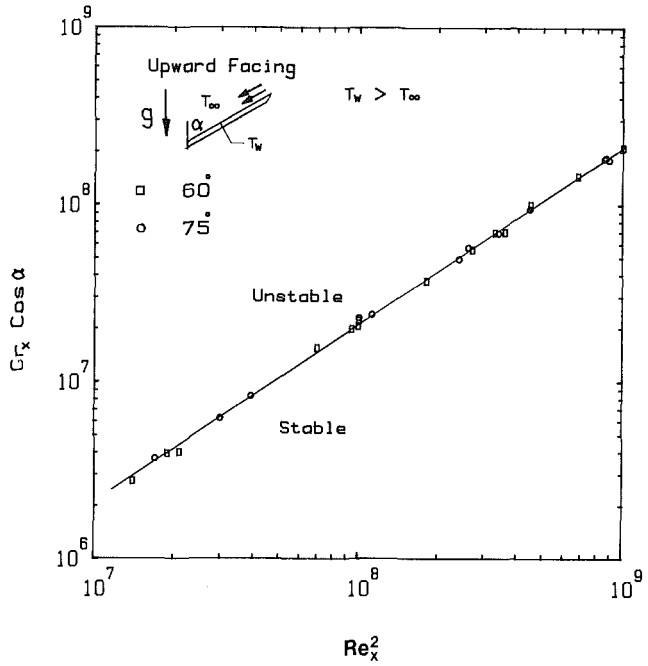

Fig. 4 Onset of vortex instability for upward-facing buoyancy-opposing flow

$$\mathrm{Gr}_x \cos\alpha = 0.210\,\mathrm{Re}_x^2 \tag{5}$$

The region below the line is the stable region which is influenced, in the same way as discussed in the previous paragraph, by the magnitude of the free-stream velocity, the inclination angle, and the temperature difference. The critical Reynolds and Grashof number ranges which were used to establish the above correlation are $4\times10^3 < \mathrm{Re}_x < 3.5\times10^4$ and $1.5\times10^7 < \mathrm{Gr}_x < 5\times10^8$.

Conclusions

The onset of instability in mixed convection flow adjacent to isothermal heated inclined plates was determined for buoyancy-assisting and buoyancy-opposing flows and for flow above and below the heated plate. The results are summarized in terms of simple correlations between the critical Grashof and Reynolds numbers. The length of the stable region increases by increasing the free-stream velocity and the inclination angle, θ or α, but decreases as the temperature difference between the plate and the free stream increases. The results presented should aid in limiting the applicability of the two-dimensional, laminar mixed convection flow solutions to this flow geometry.

Acknowledgments

The work reported in this paper was supported in part by a grant (NSF MEA 83-00785) from the National Science Foundation and by the University of Missouri Weldon Spring Endowment Fund.

References

Chen, T. S., and Mucoglu, A., 1979, "Wave Instability of Mixed Convection Flow Over a Horizontal Flat Plate," *International Journal of Heat and Mass Transfer*, Vol. 22, pp. 185–196.

Chen, T. S., Mucoglu, A., and Armaly, B. F., 1982, "Thermal Instability of Mixed Convection Flow Over Inclined Surfaces," *Numerical Heat Transfer*, Vol. 5, pp. 343–352.

Chen, T. S., and Tzuoo, K. L., 1982, "Vortex Instability of Free Convection Flow Over Horizontal and Inclined Surfaces," ASME JOURNAL OF HEAT TRANSFER, Vol. 104, pp. 637–643.

Moharreri, S., 1986, "Laser-Doppler and Hot-Wire Measurements in Convective Flows," M.S. Thesis, Department of Mechanical and Aerospace Engineering, University of Missouri – Rolla.

Lloyd, J. R., and Sparrow, E. M., 1970, "On the Instability of Natural Convection Flow on Inclined Plates," *Journal of Fluid Mechanics*, Vol. 42, pp. 465–470.

Ramachandran, N., Armaly, B. F., and Chen, T. S., 1985, "Measurements and Predictions of Laminar Mixed Convection Flow Adjacent to a Vertical Surface," ASME JOURNAL OF HEAT TRANSFER, Vol. 107, pp. 636–641.

Sparrow, E. M., and Husar, R. B., 1969, "Longitudinal Vortices in Natural Convection Flow on Inclined Plates," *Journal of Fluid Mechanics*, Vol. 37, pp. 251–255.

Wu, R. S., and Cheng, K. C., 1976, "Thermal Instability of Blasius Flow Along Horizontal Plates," *International Journal of Heat and Mass Transfer*, Vol. 19, pp. 907–913.

Mixed Convection Flow About Slender Bodies of Revolution

J. L. S. Chen[1]

1 Introduction

Heat transfer from a thin needle or a slender body of revolution has been studied by many investigators for the case of either forced convection [1, 2] or free convection [3–6]. The problem of heat transfer by combined free and forced convection from vertical thin needles with the surfaces maintained at a uniform temperature or uniform heat flux has been analyzed by Narain and Uberoi [7, 8].

This paper deals with the subject of combined convection heat transfer in laminar axial boundary-layer flows about vertical slender bodies of revolution with variable surface temperature or variable surface heat flux. The analysis is directed toward the aspect of similarity flow of the subject problem. It has been found that similarity solutions exist when (*i*) the surface temperature varies as $x^{(2m-1)}$, and (*ii*) the surface heat flux varies as $x^{(5m-3)/2}$, where x is the axial coordinate measured from the front stagnation of the body and m is an arbitrary constant. Similarity velocity and temperature profiles as well as local skin-friction coefficient and Nusselt number have been obtained for various shapes and sizes of the body and presented in graphic forms.

2 Similarity Analysis

Consider a steady-state, incompressible, laminar flow past a thin vertical axisymmetric body. The free-stream velocity is assumed to vary according to x^m. The ambient fluid is maintained at a constant temperature T_∞, while the body surface is at either variable temperature $T_w(x)$ or variable heat flux $q_w(x)$. It is assumed that the heat is transferred from the body to the fluid so that the buoyancy force aids the forced convection in the same direction. Under the assumption of constant fluid properties except for density change due to temperature change, the conservation equations for the axisymmetric boundary layers may be written as

$$\frac{\partial(ru)}{\partial x}+\frac{\partial(rv)}{\partial r}=0 \tag{1}$$

$$u\frac{\partial u}{\partial x}+v\frac{\partial u}{\partial r}=U\frac{dU}{dx}+g\beta(T-T_\infty)+\frac{\nu}{r}\frac{\partial}{\partial r}\left(r\frac{\partial u}{\partial r}\right) \tag{2}$$

$$u\frac{\partial T}{\partial x}+v\frac{\partial T}{\partial r}=\frac{\alpha}{r}\frac{\partial}{\partial r}\left(r\frac{\partial T}{\partial r}\right) \tag{3}$$

where (x, r) are the axial and radial coordinates, respectively, with the origin placed at the front stagnation point of the

[1]Associate Professor, Department of Mechanical Engineering, University of Pittsburgh, PA 15261; Mem. ASME.

Contributed by the Heat Transfer Division for publication in the JOURNAL OF HEAT TRANSFER. Manuscript received by the Heat Transfer Division April 18, 1985.

 Copyright © 1987 by ASME

Downloaded 17 Dec 2010 to 193.140.21.150. Redistribution subject to ASME license or copyright; see http://www.asme.org/terms/Terms_Use.cfm

body; (u, v) are the velocity components in these directions; g is the gravitational acceleration; β is the coefficient of thermal expansion, ν the kinematic viscosity, and α the fluid thermal diffusivity; $U(x) = u_1 x^m$ is the mainstream velocity; and T is the fluid temperature. It is noted that the axial pressure gradient term UdU/dx in equation (2) is externally imposed which, for example, may result from the contouring of a channel wall afar from the body [9]. The boundary conditions at the outer edges of the boundary layers are

$$r \to \infty: \quad u = U(x); \quad T = T_\infty \tag{4}$$

and at the body surface

$$r = R(x): \quad u = v = 0; \quad T = T_w, \quad \text{or} \quad \frac{\partial T}{\partial r} = -\frac{q_w(x)}{k} \tag{5}$$

where $R(x)$ prescribes the surface shape of the axisymmetric body; $T_w(x)$ and $q_w(x)$ are the wall temperature and wall heat flux, respectively; and k is the thermal conductivity of the fluid.

To transform equation (1) to (5), we first introduce an axisymmetric stream function ψ and a similarity variable z defined by

$$\psi = \nu x f(z) \tag{6}$$

$$z = (u_1/\nu) x^{m-1} r^2 \tag{7}$$

Setting $z = a$, where a is a constant and is numerically small for a slender body, equation (7) prescribes both shape and size of the body with its surface given by

$$R(x) = \left(\frac{\nu}{u_1} a\right)^{\frac{1}{2}} x^{\frac{1-m}{2}} \tag{8}$$

Of practical interest are pointed bodies and cylinders for which we must have, from equation (8), $m \le 1$. For example, the body is a cylinder when $m = 1$, a paraboloid when $m = 0$, and a cone when $m = -1$.

The continuity equation (1) is identically satisfied if the velocity components are expressed as

$$u = 2Uf', \quad v = -\frac{\nu}{r}[f + (m-1)zf'] \tag{9}$$

where the primes denote differentiation with respect to z. What follows are two sets of transformations for the two cases under consideration.

Bodies With Variable Wall Temperature. Define a dimensionless temperature

$$\theta(z) = \frac{T - T_\infty}{T_w - T_\infty} \tag{10}$$

It can be readily shown that, using equations (6), (7), and (9), the governing equations (2) and (3) reduce to ordinary differential equations in z if

$$T_w = T_\infty + T_1 x^s \tag{11}$$

and

$$s = 2m - 1 \tag{12}$$

The resulting transformed equations are

$$8zf''' + 4(2+f)f'' + \lambda\theta + m[1 - 4(f')^2] = 0 \tag{13}$$

$$2z\theta'' + (2 + \mathrm{Pr} f)\theta' - s\mathrm{Pr} f'\theta = 0 \tag{14}$$

with the boundary conditions

$$f(a) = f'(a) = 0; \quad f'(\infty) = \frac{1}{2} \tag{15}$$

$$\theta(a) = 1; \quad \theta(\infty) = 0 \tag{16}$$

where

$$\mathrm{Pr} = \frac{\nu}{\alpha}, \quad \lambda = \frac{\mathrm{Gr}}{\mathrm{Re}^2} = \frac{\beta g T_1}{u_1^2}, \quad \mathrm{Gr} = \frac{\beta g (T_w - T_\infty) x^3}{\nu^2},$$

$$\mathrm{Re} = \frac{Ux}{\nu} \tag{17}$$

Thus, for the mixed convection problem under consideration, similarity solutions exist only for a restricted power-law surface temperature distribution given by equation (11) with the restriction (12). For the case of pure forced convection, however, Chen and Smith [2] have shown that restriction (12) is not necessary, i.e., s is independent of m and may be an arbitrary constant. On the other hand, the mixed convection parameter λ is an indicator of the relative effect of buoyancy upon forced convection. When $\lambda = 0$ equations (13)–(16) are reduced to those for the case of pure forced convection reported in [2].

It is noted that the transformation that led to equations (13)–(17) was patterned after that for pure forced convection. When the buoyancy effect becomes increasingly large, so does the value of λ. In the limit as $\lambda \to \infty$, pure free convection exists. Numerical integrations of equations (13)–(17) become increasingly difficult with larger values of λ. To minimize this difficulty, we may, alternatively, employ the following transformation patterned after that for pure free convection:

$$\psi_0 = \nu x f_0(z_0), \quad z_0 = \frac{c}{\nu} x^{m-1} r^2 \tag{18a}$$

$$u = 2\lambda^{1/2} U f_0', \quad v = -\frac{\nu}{r}[f_0 + (m-1) z_0 f_0'] \tag{18b}$$

$$\theta_0(z_0) = \frac{T - T_\infty}{T_w - T_\infty} \tag{18c}$$

where $c = (g\beta T_1)^{1/2}$, and the primes now denote differentiation with respect to z_0. Substituting equation (18) into (2)–(5) yields

$$8z_0 f_0''' + 4(2 + f_0) f_0'' + \theta_0 - 2(s+1)(f_0')^2 + \frac{m}{\lambda} = 0 \tag{19}$$

$$2z_0\theta_0'' + (2 + \mathrm{Pr} f_0)\theta_0' - s\mathrm{Pr} f_0'\theta_0 = 0 \tag{20}$$

with

$$f_0(a_0) = f_0'(a_0) = ; \quad f_0'(\infty) = \frac{1}{2}\lambda^{-1/2} \tag{21}$$

$$\theta_0(a_0) = 1; \quad \theta_0(\infty) = 0 \tag{22}$$

When $\lambda \to \infty$, equations (19)–(22) reduce to those for the case of pure free convection obtained by Chen [5]. During the course of numerical integrations, equations (13)–(16) will be used for small and intermediate values of λ and the alternate set of equations (19)–(22) for intermediate and large values of λ. The two sets of equations should give the same results.

The local skin-friction coefficient is given by

$$C_f = 2\nu\left(\frac{\partial u}{\partial r}\right)_{z=a} \Big/ U^2 = 8a^{1/2}\mathrm{Re}^{-1/2} f''(a) \tag{23}$$

and the local Nusselt number is

$$\mathrm{Nu} = \frac{-x\left(\frac{\partial T}{\partial r}\right)_w}{T_w - T_\infty} = -2(a\mathrm{Re})^{1/2}\theta'(a) \tag{24}$$

It is noted that, owing to the familiar boundary layer approximations that both the viscous and thermal diffusions in the flow direction are small as compared to those in the direction normal to the flow, the use of $\partial u/\partial r$ and $\partial T/\partial r$ instead of $\partial u/\partial n$ and $\partial T/\partial n$ (where n is normal to the body surface) in equations (23) and (24), respectively, has been made.

Downloaded 17 Dec 2010 to 193.140.21.150. Redistribution subject to ASME license or copyright; see http://www.asme.org/terms/Terms_Use.cfm

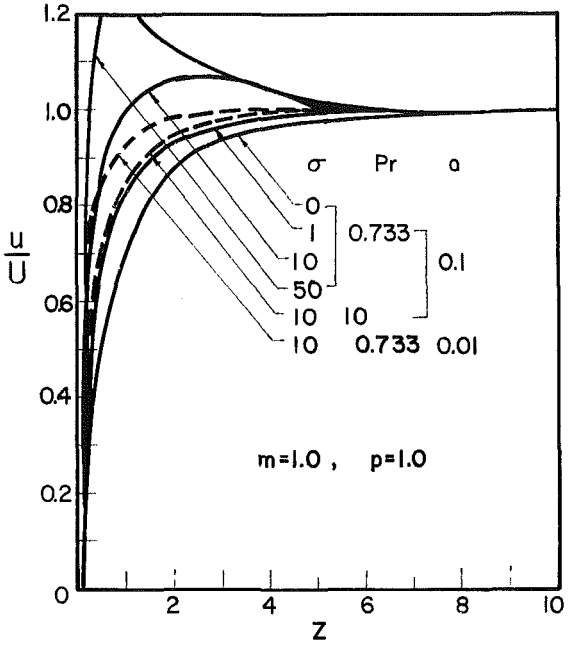

Fig. 1 Axial velocity profiles for slender cylinders with linear wall heat flux distribution

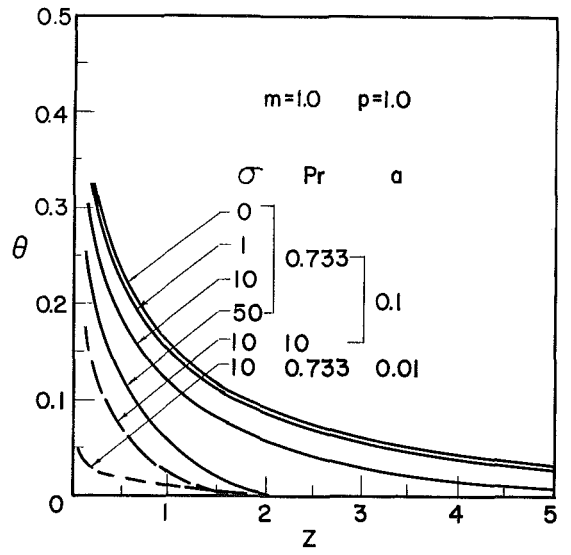

Fig. 2 Temperature profiles for slender cylinders with linear wall heat flux distribution

Bodies With Variable Wall Heat Flux. In this case we define a dimensionless temperature

$$\theta(z) = 2(a\mathrm{Re})^{1/2}\frac{k(T-T_\infty)}{xq_w} \tag{25}$$

It can be shown that if

$$q_w = q_1 x^p \text{ and } p = \frac{5m-3}{2} \tag{26}$$

the similarity equations are

$$8zf''' + 4(2+f)f'' + \sigma\theta + m[1-4(f')^2] = 0 \tag{27}$$

$$2z\theta'' + (2+\mathrm{Pr}f)\theta' - (2m-1)\mathrm{Pr}f'\theta = 0 \tag{28}$$

with

$$f(a) = f'(a) = 0; \quad f'(\infty) = \frac{1}{2} \tag{29}$$

$$\theta'(a) = -1; \quad \theta(\infty) = 0 \tag{30}$$

in which

$$\sigma = \frac{\mathrm{Gr}_m}{\mathrm{Re}^2} = \left(\frac{c_0}{u_1}\right)^2, \quad \mathrm{Gr}_m = \frac{\beta g q_w x^4}{2k\nu^2}(a\mathrm{Re})^{-1/2} \tag{31}$$

$$c_0 = \left(\frac{\beta g q_1}{2k}\right)^{1/2}\left(\frac{\nu}{au_1}\right)^{1/4}$$

The parameter σ, similar to λ in the preceding case, measures the relative importance of free convection over forced convection. It is noted that when $p=0$, equations (26)–(31) are reduced to the special case of uniform wall heat flux treated by Narain and Uberoi [8]. When $\sigma=0$, the heat transfer mode is pure forced convection, and equations (27)–(30) are the same as those obtained in [2].

For large σ, a set of alternate similarity equations may be obtained by using the transformations (18*a*) and (18*b*) modified by replacing λ by σ and c by c_0. The transformed equations are

$$8z_0 f_0''' + 4(2+f_0)f_0'' + \theta_0 - 4m(f_0')^2 + \frac{m}{\sigma} = 0 \tag{32}$$

$$2z_0\theta_0'' + (2+\mathrm{Pr}f_0)\theta_0' - (2m-1)\mathrm{Pr}f_0'\theta_0 = 0 \tag{33}$$

with

$$f_0(a_0) = f_0'(a_0) = 0; \quad f_0'(\infty) = \frac{1}{2}\sigma^{-1/2} \tag{34}$$

$$\theta_0'(a_0) = -\sigma^{-1/2}; \quad \theta_0(\infty) = 0 \tag{35}$$

By setting $\sigma\to\infty$, the problem described by equations (32)–(35) becomes the case of pure free convection reported by Chen [6].

The local skin-friction coefficient and Nusselt number are given by, respectively,

$$C_f = 8a^{1/2}\mathrm{Re}^{-1/2}f''(a) \tag{36}$$

$$\mathrm{Nu} = \frac{xq_w}{k(T_w - T_\infty)} = 2(a\mathrm{Re})^{1/2}\theta^{-1}(a) \tag{37}$$

3 Results and Discussion

Derived in the preceding section are two sets of similarity equations each for the variable wall temperature and variable wall heat flux cases. As was stated earlier, to facilitate numerical computation, the alternate sets are employed for intermediate and large λ (or σ) and the other sets for small and intermediate λ (or σ). It has been verified that the two sets yield the same results. Some representative results are presented as follows.

Variable Wall Heat Flux Cases. Figures 1 and 2 show, respectively, the dimensionless axial velocity profiles and dimensionless temperature distributions for an accelerating flow ($m=1.0$) past a vertical slender cylinder with a linear surface heat flux variation ($p=1.0$) along the axis. The mixed convection parameter σ is a measure of the relative importance of the free convection and forced convection contributions for the case of variable wall heat-flux bodies. It may be observed from Fig. 1 that the overshoot, due to buoyancy effect, of the axial velocity beyond its free-stream value depends upon not only σ but also Pr and the body size parameter a. When $\sigma=10$, the overshoot (approximately 7 percent) takes place for the case of $\mathrm{Pr}=0.733$ and $a=0.1$, but not for the other two cases for $\mathrm{Pr}=10$ with $a=0.1$ and $\mathrm{Pr}=0.733$ with $a=0.01$. The effects of body size are such that the more slender the body, the thinner the velocity and thermal boundary layers; and it also plays a role in the control of velocity overshoot. It is interesting to note that in the case of a two-dimensional body or an axisymmetric body where the radius of its transverse cur-

Downloaded 17 Dec 2010 to 193.140.21.150. Redistribution subject to ASME license or copyright; see http://www.asme.org/terms/Terms_Use.cfm

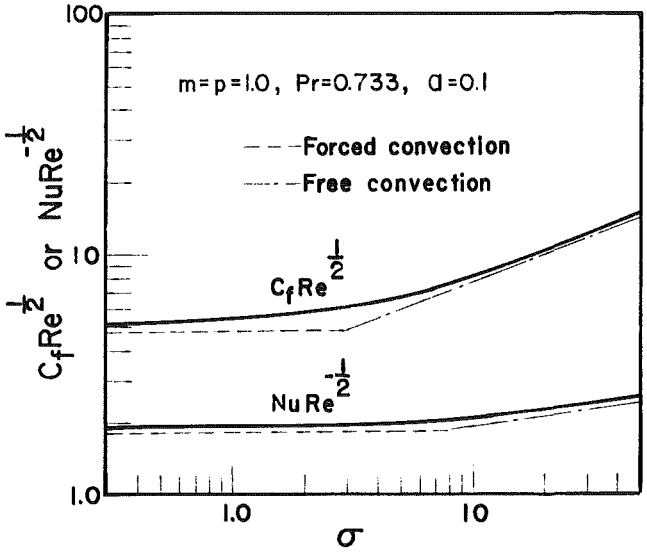

Fig. 3 Buoyancy effects on skin friction and heat transfer (wall heat flux case)

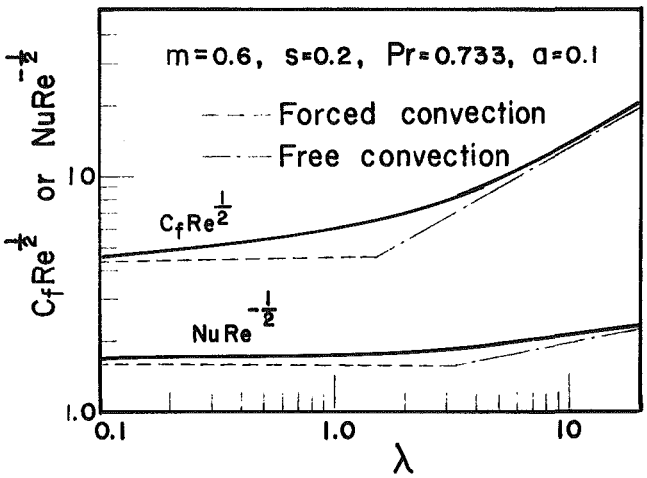

Fig. 4 Buoyancy effects on skin friction and heat transfer (wall temperature case)

vature is much greater than the boundary-layer thickness, the velocity overshoot is controlled only by σ and Pr.

The effects of σ on skin friction and heat transfer are illustrated in Fig. 3, which shows a typical trend that is common to all of the parameters studied herein. As $\sigma \to \infty$ the results tend to the asymptotes for pure free convection as shown in the figure. Thus, in the situation of aiding mixed convection considered here, both the skin-friction coefficient and Nusselt number are higher than they would be in either of the corresponding component flows alone.

Variable Wall Temperature Cases. The buoyancy effects on skin friction and heat transfer are shown in Fig. 4 for an accelerating flow ($m = 0.6$) past a needle-shaped body, of which the surface is prescribed by $R = (a\nu/u_1)^{1/2} x^{1/5}$ and subject to a temperature distribution with $s = 0.2$. Examination of the results reveals that the effects of Pr, a, and λ on the flow and heat transfer are qualitatively similar to those in the case of variable wall heat flux. However, it is noted that quantitatively the two cases require separate attention, unlike the free-convection cases where the results for a uniform heat flux flat plate (or cylinder) can be closely correlated with those for a uniform wall temperature plate (or cylinder) [10, 11].

References

1 Narain, J. P., and Uberoi, M. S., "Forced Heat Transfer Over Thin Needles," ASME JOURNAL OF HEAT TRANSFER, Vol. 94, 1972, pp. 240–242.

2 Chen, J. L. S., and Smith, T. M., "Forced Convection Heat Transfer From Non-isothermal Thin Needles," ASME JOURNAL OF HEAT TRANSFER, Vol. 100, 1978, pp. 358–362.

3 Van Dyke, M., "Free Convection From a Vertical Needle," in: *Problems of Hydrodynamics and Continuum Mechanics*, I. E. Block, ed., 1970, pp. 748–761.

4 Narain, J. P., and Uberoi, M. S., "Laminar Free-Convection From Thin Vertical Needles," *Physics of Fluids*, Vol. 15, 1972, pp. 928–929.

5 Chen, J. L. S., "Natural Convection From Needles With Variable Wall Temperature," ASME Paper No. 80-HT-72, 1980.

6 Chen, J. L. S., "Natural Convection From Needles With Variable Wall Heat Flux," ASME JOURNAL OF HEAT TRANSFER, Vol. 105, 1983, pp. 403–406.

7 Narain, J. P., and Uberoi, M. S., "Combined Forced and Free-Convection Heat Transfer From Thin Needles in a Uniform Stream," *Physics of Fluids*, Vol. 15, 1972, pp. 1879–1882.

8 Narain, J. P., and Uberoi, M. S., "Combined Forced and Free-Convection Over Thin Needles," *Int. Journal of Heat and Mass Transfer*, Vol. 16, 1973, pp. 1505–1511.

9 Sparrow, E. M., Eichhorn, R., and Gregg, J. L., "Combined Forced and Free Convection in a Boundary Flow," *Physics of Fluids*, Vol. 2, 1959, pp. 319–328.

10 Sparrow, E. M., and Gregg, J. L., "Laminar Free Convection From a Vertical Plate With Uniform Surface Heat Flux," *Trans. ASME*, Vol. 78, 1956, pp. 435–440.

11 Nagendra, H. R., Tirunarayanan, M. A., and Ramachandran, A., "Laminar Free Convection From Vertical Cylinders With Uniform Heat Flux," ASME JOURNAL OF HEAT TRANSFER, Vol. 92, 1970, pp. 191–194.

Correlations for Laminar Mixed Convection in Boundary Layers Adjacent to Horizontal, Continuous Moving Sheets

N. Ramachandran,[1,4] T. S. Chen,[2,4] and B. F. Armaly[3,4]

Introduction

In industrial processes such as the extrusion of metals and plastics, the cooling and/or drying of paper and textiles, and material handling operations, heat transfer is frequently encountered in boundary layers adjacent to continuous sheets moving in an otherwise quiescent medium. The buoyancy forces arising from the heating or cooling of these sheets modify the flow and thermal fields and thereby the heat transfer characteristics of the process. Such boundary layer problems have been analyzed by several investigators. For example, combined forced and free convection adjacent to continuous, moving sheets has been studied numerically by Chen and Strobel (1980) for horizontal geometry and by Strobel and Chen (1980) for inclined geometry. These two studies also included mass diffusion effects in boundary layers. The aim of the present investigation is to develop useful correlations for the local and average Nusselt numbers in laminar boundary layers along a horizontal, continuous sheet moving in an otherwise quiescent environment. Such correlations have not been presented in the past. The available results have been extended to cover higher buoyancy parameter values and a wider range of Prandtl numbers. Both the uniform wall temperature (UWT) and the uniform surface heat flux (UHF) cases are examined in this study.

[1]Assoc. Mem. ASME.

[2]Fellow ASME.

[3]Mem. ASME.

[4]Department of Mechanical and Aerospace Engineering, University of Missouri—Rolla, Rolla, MO 65401.

Contributed by the Heat Transfer Division for publication in the JOURNAL OF HEAT TRANSFER. Manuscript received by the Heat Transfer Division March 31, 1986.

Downloaded 17 Dec 2010 to 193.140.21.150. Redistribution subject to ASME license or copyright; see http://www.asme.org/terms/Terms_Use.cfm

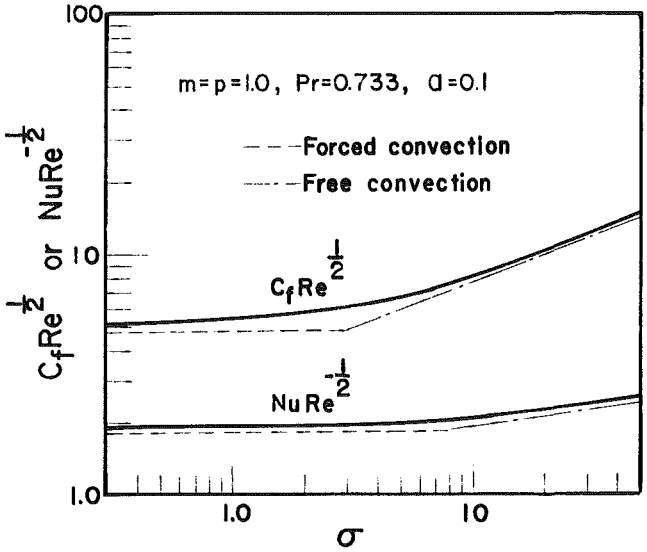

Fig. 3 Buoyancy effects on skin friction and heat transfer (wall heat flux case)

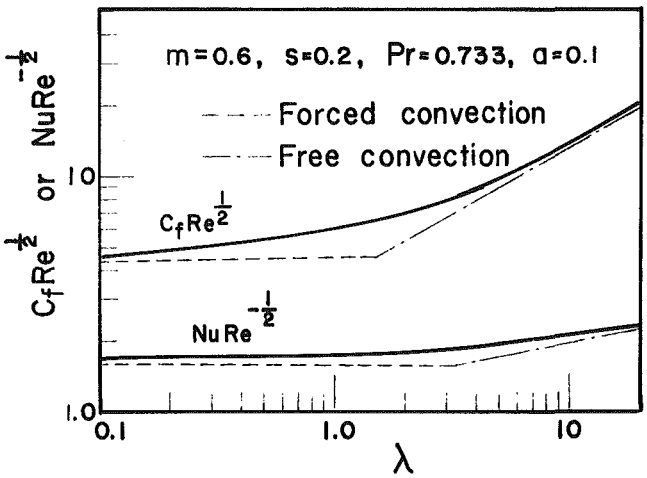

Fig. 4 Buoyancy effects on skin friction and heat transfer (wall temperature case)

vature is much greater than the boundary-layer thickness, the velocity overshoot is controlled only by σ and Pr.

The effects of σ on skin friction and heat transfer are illustrated in Fig. 3, which shows a typical trend that is common to all of the parameters studied herein. As $\sigma \to \infty$ the results tend to the asymptotes for pure free convection as shown in the figure. Thus, in the situation of aiding mixed convection considered here, both the skin-friction coefficient and Nusselt number are higher than they would be in either of the corresponding component flows alone.

Variable Wall Temperature Cases. The buoyancy effects on skin friction and heat transfer are shown in Fig. 4 for an accelerating flow ($m = 0.6$) past a needle-shaped body, of which the surface is prescribed by $R = (a\nu/u_1)^{1/2} x^{1/5}$ and subject to a temperature distribution with $s = 0.2$. Examination of the results reveals that the effects of Pr, a, and λ on the flow and heat transfer are qualitatively similar to those in the case of variable wall heat flux. However, it is noted that quantitatively the two cases require separate attention, unlike the free-convection cases where the results for a uniform heat flux flat plate (or cylinder) can be closely correlated with those for a uniform wall temperature plate (or cylinder) [10, 11].

References

1 Narain, J. P., and Uberoi, M. S., "Forced Heat Transfer Over Thin Needles," ASME JOURNAL OF HEAT TRANSFER, Vol. 94, 1972, pp. 240–242.

2 Chen, J. L. S., and Smith, T. M., "Forced Convection Heat Transfer From Non-isothermal Thin Needles," ASME JOURNAL OF HEAT TRANSFER, Vol. 100, 1978, pp. 358–362.

3 Van Dyke, M., "Free Convection From a Vertical Needle," in: *Problems of Hydrodynamics and Continuum Mechanics*, I. E. Block, ed., 1970, pp. 748–761.

4 Narain, J. P., and Uberoi, M. S., "Laminar Free-Convection From Thin Vertical Needles," *Physics of Fluids*, Vol. 15, 1972, pp. 928–929.

5 Chen, J. L. S., "Natural Convection From Needles With Variable Wall Temperature," ASME Paper No. 80-HT-72, 1980.

6 Chen, J. L. S., "Natural Convection From Needles With Variable Wall Heat Flux," ASME JOURNAL OF HEAT TRANSFER, Vol. 105, 1983, pp. 403–406.

7 Narain, J. P., and Uberoi, M. S., "Combined Forced and Free-Convection Heat Transfer From Thin Needles in a Uniform Stream," *Physics of Fluids*, Vol. 15, 1972, pp. 1879–1882.

8 Narain, J. P., and Uberoi, M. S., "Combined Forced and Free-Convection Over Thin Needles," *Int. Journal of Heat and Mass Transfer*, Vol. 16, 1973, pp. 1505–1511.

9 Sparrow, E. M., Eichhorn, R., and Gregg, J. L., "Combined Forced and Free Convection in a Boundary Flow," *Physics of Fluids*, Vol. 2, 1959, pp. 319–328.

10 Sparrow, E. M., and Gregg, J. L., "Laminar Free Convection From a Vertical Plate With Uniform Surface Heat Flux," *Trans. ASME*, Vol. 78, 1956, pp. 435–440.

11 Nagendra, H. R., Tirunarayanan, M. A., and Ramachandran, A., "Laminar Free Convection From Vertical Cylinders With Uniform Heat Flux," ASME JOURNAL OF HEAT TRANSFER, Vol. 92, 1970, pp. 191–194.

Correlations for Laminar Mixed Convection in Boundary Layers Adjacent to Horizontal, Continuous Moving Sheets

N. Ramachandran,[1,4] T. S. Chen,[2,4] and B. F. Armaly[3,4]

Introduction

In industrial processes such as the extrusion of metals and plastics, the cooling and/or drying of paper and textiles, and material handling operations, heat transfer is frequently encountered in boundary layers adjacent to continuous sheets moving in an otherwise quiescent medium. The buoyancy forces arising from the heating or cooling of these sheets modify the flow and thermal fields and thereby the heat transfer characteristics of the process. Such boundary layer problems have been analyzed by several investigators. For example, combined forced and free convection adjacent to continuous, moving sheets has been studied numerically by Chen and Strobel (1980) for horizontal geometry and by Strobel and Chen (1980) for inclined geometry. These two studies also included mass diffusion effects in boundary layers. The aim of the present investigation is to develop useful correlations for the local and average Nusselt numbers in laminar boundary layers along a horizontal, continuous sheet moving in an otherwise quiescent environment. Such correlations have not been presented in the past. The available results have been extended to cover higher buoyancy parameter values and a wider range of Prandtl numbers. Both the uniform wall temperature (UWT) and the uniform surface heat flux (UHF) cases are examined in this study.

[1]Assoc. Mem. ASME.

[2]Fellow ASME.

[3]Mem. ASME.

[4]Department of Mechanical and Aerospace Engineering, University of Missouri—Rolla, Rolla, MO 65401.

Contributed by the Heat Transfer Division for publication in the JOURNAL OF HEAT TRANSFER. Manuscript received by the Heat Transfer Division March 31, 1986.

Copyright © 1987 by ASME

Downloaded 17 Dec 2010 to 193.140.21.150. Redistribution subject to ASME license or copyright; see http://www.asme.org/terms/Terms_Use.cfm

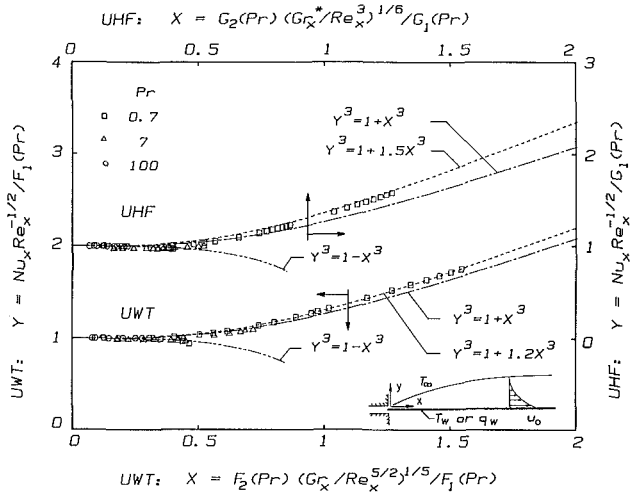

Fig. 1 A comparison between the predicted and correlated local Nusselt numbers for the UWT and UHF cases

Analysis

The boundary layer along a semi-infinite continuous sheet, issuing from a slot and moving in an otherwise quiescent medium, develops from the opening of the slot along the direction of motion as depicted schematically in the inset of Fig. 1. The heat transfer in such a boundary layer flow is physically different from that for the classical forced convection along a stationary semi-infinite flat plate. The heat transfer rate from the moving sheet is higher than that from a stationary flat plate due to the higher transfer rate in the vicinity of the moving wall.

The boundary layer equations for a horizontal, continuous moving sheet which is either heated isothermally (UWT) or maintained at a constant surface heat flux (UHF) are the same as those stated by Chen et al. (1977) and are hence not repeated here. However, the following modifications in the boundary conditions from the aforementioned study have to be incorporated. For the flow field, $u = u_0$ at $y = 0$ (where u_0 is the velocity of the moving sheet) and $u \to 0$ as $y \to \infty$, and for the thermal field under the UHF condition $q_w = -k\partial T/\partial y =$ const at $y = 0$. The governing equations and boundary conditions are transformed from the (x, y) primitive variables to the (ξ, η) or (ξ_1, η) coordinate system for the UWT or UHF case. In this note, the transformed equations and boundary conditions are listed for completeness and the correlation equations for the local and average Nusselt numbers are presented, respectively, for the UWT and UHF cases.

Uniform Wall Temperature (UWT) Case. The transformed equations and boundary conditions for mixed convection along a horizontal continuous, moving sheet are (Chen and Strobel, 1980)

$$f''' + \frac{1}{2} ff'' \pm \frac{1}{2} \xi \left[\eta\theta + \int_\eta^\infty \theta d\eta + \xi \int_\eta^\infty \frac{\partial \theta}{\partial \xi} d\eta \right] = \frac{1}{2} \xi \left(f' \frac{\partial f'}{\partial \xi} - f'' \frac{\partial f}{\partial \xi} \right) \quad (1)$$

$$\frac{1}{\Pr} \theta'' + \frac{1}{2} f\theta' = \frac{1}{2} \xi \left(f' \frac{\partial \theta}{\partial \xi} - \theta' \frac{\partial f}{\partial \xi} \right) \quad (2)$$

$$f(\xi, 0) = 0, \quad f'(\xi, 0) = 1, \quad \theta(\xi, 0) = 1$$
$$f'(\xi, \infty) = 0, \quad \theta(\xi, \infty) = 0 \quad (3)$$

where the primes denote partial differentiation with respect to $\eta = y(u_0/\nu x)^{1/2}$, and the plus and minus signs in front of the third term on the left-hand side of equation (1) are, respectively, for buoyancy-assisting and opposing conditions. The buoyancy parameter $\xi(x)$, the reduced stream function $f(\xi, \eta)$, and the dimensionless temperature $\theta(\xi, \eta)$ are given, respectively, by

$$\xi(x) = \mathrm{Gr}_x/\mathrm{Re}_x^{5/2}, \quad f(\xi, \eta) = \psi(x, y)/(\nu u_0 x)^{1/2},$$
$$\theta(\xi, \eta) = (T - T_\infty)/(T_w - T_\infty) \quad (4)$$

where ψ is the stream function and the local Grashof and Reynolds numbers are defined in the usual manner as $\mathrm{Gr}_x = g\beta(T_w - T_\infty)x^3/\nu^2$ and $\mathrm{Re}_x = u_0 x/\nu$. The local Nusselt number $\mathrm{Nu}_x = hx/k$ has the expression

$$\mathrm{Nu}_x \mathrm{Re}_x^{-1/2} = -\theta'(\xi, 0) \quad (5)$$

and the average Nusselt number $\overline{\mathrm{Nu}} = \bar{h}L/k$ is given by

$$\overline{\mathrm{Nu}} \mathrm{Re}_L^{-1/2} = 2\xi_L^{-1} \int_0^{\xi_L} [-\theta'(\xi, 0)] d\xi \quad (6)$$

where ξ_L is the buoyancy parameter based on a certain characteristic length L.

Correlation equations for the local Nusselt number in mixed convection are developed along the same line as proposed by Churchill (1977). Thus, the mixed convection local Nusselt number Nu_x can be written as a combination of the local Nusselt numbers, Nu_F for pure forced convection and Nu_N for pure free convection, in the form

$$\mathrm{Nu}_x^n = \mathrm{Nu}_F^n \pm \mathrm{Nu}_N^n \quad (7)$$

In this equation n is a constant and the plus and minus signs pertain to buoyancy-assisting and opposing conditions, respectively. Equation (7) can be written in the form

$$Y^n = 1 \pm X^n \quad (8)$$

where

$$Y = Nu_x/\mathrm{Nu}_F, \quad X = \mathrm{Nu}_N/\mathrm{Nu}_F \quad (9)$$

Equations (8) and (9) also apply to the average Nusselt number $\overline{\mathrm{Nu}}$ if the local quantities Nu_x, Nu_F, and Nu_N are replaced with the corresponding average quantities $\overline{\mathrm{Nu}}$, $\overline{\mathrm{Nu}}_F$, and $\overline{\mathrm{Nu}}_N$, respectively.

The local Nusselt number results from the present calculations for pure forced convection in laminar boundary layer adjacent to an isothermal, continuous moving sheet can be correlated by the equation

$$\mathrm{Nu}_F = F_1(\mathrm{Pr})\mathrm{Re}_x^{1/2} \quad (10)$$

where

$$F_1(\mathrm{Pr}) = 1.8865\ \mathrm{Pr}^{13/32} - 1.4447\ \mathrm{Pr}^{1/3} \quad (11)$$

which is accurate to within 5 percent for $0.1 \le \mathrm{Pr} \le 100$. From the analysis of Chen et al. (1986) the corresponding expression for free convection along an upward-facing heated, horizontal flat plate maintained at a uniform wall temperature is given by

$$\mathrm{Nu}_N = F_2(\mathrm{Pr})(\mathrm{Gr}_x)^{1/5} \quad (12)$$

where

$$F_2(\mathrm{Pr}) = (\mathrm{Pr}/5)^{1/5}\mathrm{Pr}^{1/2}[0.25 + 1.6\ \mathrm{Pr}^{1/2}]^{-1} \quad (13)$$

The pure free convection limit for this problem, it is noted, corresponds to the case when both the semi-infinite sheet and the ambient fluid are at rest simultaneously and hence there is no externally forced flow. Physically, this implies that the velocity (of the sheet) u_0 becomes so small that it is insignificant in comparison to large thermal buoyancy forces. As in the case of a stationary horizontal flat plate, the free convection boundary layer will exist for a short length before a

Downloaded 17 Dec 2010 to 193.140.21.150. Redistribution subject to ASME license or copyright; see http://www.asme.org/terms/Terms_Use.cfm

buoyant plume is formed downstream. The local mixed convection Nusselt number for a horizontal, isothermal, continuous moving sheet can then be expressed according to equation (8) as

$$\mathrm{Nu}_x\mathrm{Re}_x^{-1/2}/F_1(\mathrm{Pr}) = \{1 \pm [F_2(\mathrm{Pr})(\mathrm{Gr}_x/\mathrm{Re}_x^{5/2})^{1/5}/F_1(\mathrm{Pr})]^n\}^{1/n} \tag{14}$$

Similarly, the corresponding average mixed convection Nusselt number can be correlated as

$$\overline{\mathrm{Nu}}\mathrm{Re}_L^{-1/2}/2F_1(\mathrm{Pr}) = \{1 \pm [5F_2(\mathrm{Pr})(\mathrm{Gr}_L/\mathrm{Re}_L^{5/2})^{1/5}/6F_1(\mathrm{Pr})]^n\}^{1/n} \tag{15}$$

Equations (14) and (15) have the form $Y = (1 \pm X^n)^{1/n}$. As will be seen later when results are presented, $n = 3$ provides a good correlation.

Uniform Surface Heat Flux (UHF) Case. The transformed equations and boundary conditions for mixed convection in laminar boundary layer along a horizontal, continuous moving sheet subjected to a uniform surface heat flux are given by (Mucoglu and Chen, 1978)

$$f_1''' + \frac{1}{2} f_1 f_1'' \pm \frac{1}{2}\xi_1\left[\eta\phi + 2\int_\eta^\infty \phi d\eta + 2\xi_1\int_\eta^\infty \frac{\partial\phi}{\partial\xi_1} d\xi_1\right] = \xi_1\left(f_1' \frac{\partial f_1'}{\partial\xi_1} - f_1'' \frac{\partial f_1}{\partial\xi_1}\right) \tag{16}$$

$$\frac{1}{\mathrm{Pr}}\phi'' + \frac{1}{2} f_1\phi' - \frac{1}{2} f_1'\phi = \xi_1\left(f_1' \frac{\partial\phi}{\partial\xi_1} - \phi' \frac{\partial f_1}{\partial\xi_1}\right) \tag{17}$$

$$f_1(\xi_1, 0) = 0, \quad f_1'(\xi_1, 0) = 1, \quad \phi'(\xi_1, 0) = -1$$
$$f_1'(\xi_1, \infty) = 0, \quad \phi(\xi_1, \infty) = 0 \tag{18}$$

where the primes again denote partial differentiation with respect to η. The reduced stream function $f_1(\xi_1, \eta)$, the dimensionless temperature $\phi(\xi_1, \eta)$, and the buoyancy parameter $\xi_1(x)$ for this case are defined as

$$f_1(\xi_1, \eta) = \psi(x, y)/(\nu u_0 x)^{1/2},$$
$$\phi(\xi_1, \eta) = (T - T_\infty)\mathrm{Re}_x^{1/2}/(q_w x/k), \tag{19}$$
$$\xi_1(x) = \mathrm{Gr}_x^*/\mathrm{Re}_x^3$$

where $\mathrm{Gr}_x^* = g\beta q_w x^4/k\nu^2$ is the modified local Grashof number. The expressions for the local and average Nusselt numbers are, respectively,

$$\mathrm{Nu}_x\mathrm{Re}_x^{-1/2} = 1/\phi(\xi_1, 0) \tag{20}$$

and

$$\overline{\mathrm{Nu}}\mathrm{Re}_L^{-1/2} = \xi_{1L}^{-1/2}\int_0^{\xi_{1L}} [1/\phi(\xi_1, 0)]\xi_1^{-1/2} d\xi_1 \tag{21}$$

where ξ_{1L} is ξ_1 based on a certain characteristic length L.

Correlations for the UHF case can be expressed in the same form as that of equations (7)–(9). For laminar forced convection adjacent to a moving sheet under the UHF case, the local Nusselt number results from the present calculations can be correlated by the equation

$$\mathrm{Nu}_F = G_1(\mathrm{Pr})\mathrm{Re}_x^{1/2} \tag{22}$$

where

$$G_1(\mathrm{Pr}) = 2.8452\ \mathrm{Pr}^{13/32} - 2.0947\ \mathrm{Pr}^{1/3} \tag{23}$$

which has an error of less than 4 percent for $0.1 \le \mathrm{Pr} \le 100$. The corresponding free convection case is given by the following correlation from the analysis of Armaly et al. (1987)

$$\mathrm{Nu}_N = G_2(\mathrm{Pr})(\mathrm{Gr}_x^*)^{1/6} \tag{24}$$

where

$$G_2(\mathrm{Pr}) = (\mathrm{Pr}/6)^{1/6}\mathrm{Pr}^{1/2}[0.12 + 1.2\ \mathrm{Pr}^{1/2}]^{-1} \tag{25}$$

The local and average mixed convection Nusselt number for the horizontal moving sheets can then be written according to equation (8) as follows:

$$\mathrm{Nu}_x\mathrm{Re}_x^{-1/2}/G_1(\mathrm{Pr}) = \{1 \pm [G_2(\mathrm{Pr})(\mathrm{Gr}_x^*/\mathrm{Re}_x^3)^{1/6}/G_1(\mathrm{Pr})]^n\}^{1/n} \tag{26}$$

and

$$\overline{\mathrm{Nu}}\mathrm{Re}_L^{-1/2}/2G_1(\mathrm{Pr}) = \{1 \pm [3G_2(\mathrm{Pr})(\mathrm{Gr}_L^*/\mathrm{Re}_L^3)^{1/6}/4G_1(\mathrm{Pr})]^n\}^{1/n} \tag{27}$$

Again, equations (26) and (27) have the form $Y = (1 \pm X^n)^{1/n}$. As will be seen later, $n = 3$ also provides a good correlation for the UHF case.

It is noted that alternate correlation equations for both the UWT and UHF cases for free convection from a horizontal flat plate have been presented by Churchill (1983). They may also be used in correlating the mixed convection Nusselt number in place of equations (12), (13) and (24), (25).

Results and Discussion

The correlation equations (14) and (26) along with the calculated results for Prandtl numbers of 0.7, 7, and 100 are presented in the Y versus X form for both the buoyancy-assisting and opposing conditions, respectively, in Fig. 1 for the UWT and UHF cases. Computations were extended to higher values of the buoyancy parameter than the work of Chen and Strobel (1980) and to cover an additional Prandtl number of 100 for the UWT case. New results were generated for both the buoyancy-assisting and opposing conditions for the UHF case. As is evident from the figure, an exponent value of $n = 3$ correlates rather well (with errors of less than 10 percent) for both the heating conditions and for both the buoyancy-assisting and opposing situations. The average Nusselt numbers as calculated by equations (6) and (21) for the UWT and UHF cases, respectively, were then correlated with the respective equations (15) and (27), and good agreement was found to exist between the calculated and the correlated results. Thus a separate figure for the average Nusselt number correlations is not presented. Instead, Fig. 1 may be utilized for this purpose provided the Y and X coordinates in these figures (for the appropriate heating condition) are represented by those given in equations (15) and (27).

Better correlation equations for Pr = 0.7 under the buoyancy-assisting case are shown by dashed lines in Fig. 1 for both the UWT and UHF cases. They have the form $Y^n = 1 + aX^n$ in which $a = 1.2$ for the UWT case and $a = 1.5$ for the UHF case, with $n = 3$.

It must be pointed out that the correlation equations presented in this note were based on the results from the numerical solution of the governing laminar boundary layer equations. As such they do not account for effects that may be caused, for example, by buoyancy-induced instability and transition or plume-like behaviors downstream due to strong buoyancy forces. Thus, these correlation equations should be used with caution, pending experimental determination of the validity regime. It may be suggested, however, that they perhaps should be restricted in their applications to $X < 1$.

Conclusion

Simple and accurate correlation equations have been developed and presented for estimating the local and average Nusselt numbers in mixed convection adjacent to horizontal, continuous moving sheets whose surface is maintained either at a constant temperature or at a constant heat flux. The correlations presented for a Prandtl number range of $0.7 \le \mathrm{Pr} \le 100$ and for both buoyancy-assisting and opposing conditions agree very well with the analytically predicted values.

Downloaded 17 Dec 2010 to 193.140.21.150. Redistribution subject to ASME license or copyright; see http://www.asme.org/terms/Terms_Use.cfm

Acknowledgments

The present study was supported in part by a grant from the National Science Foundation (NSF MEA 83-00785).

References

Armaly, B. F., Chen, T. S., and Ramachandran, N., 1987, "Correlations for Laminar Mixed Convection on Vertical, Inclined, and Horizontal Flat Plates With Uniform Surface Heat Flux," *International Journal of Heat and Mass Transfer*, Vol. 30, pp. 405–408.

Chen, T. S., Armaly, B. F., and Ramachandran, N., 1986, "Correlations for Laminar Mixed Convection Flows on Vertical, Inclined, and Horizontal Flat Plates," ASME JOURNAL OF HEAT TRANSFER, Vol. 108, pp. 835–840.

Chen, T. S., Sparrow, E. M., and Mucoglu, A., 1977, "Mixed Convection in Boundary Layer Flow on a Horizontal Plate," ASME JOURNAL OF HEAT TRANSFER, Vol. 99, pp. 66–71.

Chen, T. S., and Strobel, F. A., 1980, "Buoyancy Effects on Heat and Mass Transfer in Boundary Layer on a Continuous, Moving Horizontal Plate," *Numerical Heat Transfer*, Vol. 3, pp. 115–130.

Churchill, S. W., 1977, "A Comprehensive Correlating Equation for Laminar Assisting, Forced and Free Convection," *AIChE Journal*, Vol. 23, pp. 10–16.

Churchill, S. W., 1983, "Combined Free and Forced Convection Around Immersed Bodies," in: *Heat Exchanger Design Hand Book*, Hemisphere Publishing, Washington, DC, Chap. 2.5.9.

Mucoglu, A., and Chen, T. S., 1978, "Mixed Convection on a Horizontal Plate With Uniform Surface Heat Flux," *Proceedings of the 6th International Heat Transfer Conference*, Vol. 1, pp. 85–90.

Strobel, F. A., and Chen, T. S., 1980, "Buoyancy Effects on Heat and Mass Transfer in Boundary Layers Adjacent to Inclined, Continuous, Moving Sheets," *Numerical Heat Transfer*, Vol. 3, pp. 461–481.

Boundary Effects in Laminar Mixed Convection Flow Through an Annular Porous Medium

M. Parang[1] and M. Keyhani[2]

Nomenclature

c_1, c_2, c_3, c_4 = constants in equation (6)
d = diameter
Da = Darcy number = K/l^2
Gr = Grashof number = $g\beta l^3\ (q_i d_i + q_o d_o)/\nu^2 k$
H = parameter defined before equation (5)
K = permeability of the medium
k = fluid thermal conductivity
l = hydraulic radius = $r_o - r_i$
Nu = Nusselt number
P = pressure
Re = Reynolds number = $u_m l/\nu$
q = surface heat flux rate
Q = heat flux ratio = q_i/q_o
r = dimensionless radial coordinate
R = radius ratio = r_o/r_i
S = dimensionless pressure loss
T = dimensionless temperature
u = dimensionless volume-averaged axial velocity
u_m = bulk mean velocity
z = axial coordinate
α = parameter defined before equation (5)
β = fluid coefficient of volume expansion
γ_1, γ_2 = parameters defined after equation (6)
ϵ = porosity of the medium
ν = kinematic viscosity
ρ_m = bulk fluid density

Subscripts

i = inner surface
m = mixed Darcy flow regime (for Nusselt number)
o = outer surface

[1]Associate Professor, Mechanical and Aerospace Engineering Department, University of Tennessee, Knoxville, TN 37996; Mem. ASME.

[2]Assistant Professor, Mechanical and Aerospace Engineering Department, University of Tennessee, Knoxville, TN 37996; Mem. ASME.

Contributed by the Heat Transfer Division and presented at the AIAA/ASME Heat Transfer and Thermophysics Conference, Boston, Massachusetts, June 2–4, 1986. Manuscript received by the Heat Transfer Division March 10, 1986.

Introduction

The influence of the Brinkman and Forchheimer terms in forced convection over a flat plate has been investigated by Vafai and Tien (1981). A similar study was reported by Ranganathan and Viskanta (1984) discussing the wall and inertia effects in mixed-convection flow over a flat plate. Tong and Subramanian (1985) have reported a study of the wall effect on natural convection in a vertical enclosure. Their results indicate that the viscous term should be considered when the Darcy number is greater than 10^{-5}. Similar results are obtained by Lauriat and Prasad (1986) in natural convection in a vertical porous cavity. They also found that the wall effect is negligible for Darcy number below 10^{-5}.

This study addresses the Brinkman-extended Darcy model (Brinkman flow) of a laminar mixed-convection flow in an annular porous region. The primary objective of the present study is to help clarify the conditions under which the Brinkman term can be neglected in this flow without producing an unacceptable error. The simple geometry considered and the closed-form nature of the solution are advantageous in the demonstration of the importance of the wall effect. The results of this study can also be used in the evaluation of the accuracy of the numerical computations in more complex non-Darcian annular flows in the limiting case of the fully developed flow.

Analysis

The geometry of the problem under consideration is shown in Fig. 1. A vertically oriented annulus region is filled with a fluid-saturated porous medium. An upward (opposite to the gravity vector) forced flow is combined with mixed convection which is present due to uniform heat flux at the boundaries. The heat flux rates at the inner and outer walls are q_i and q_o, respectively. The thermal and velocity fields are assumed fully developed.

Assuming an isotropic, homogeneous porous medium and

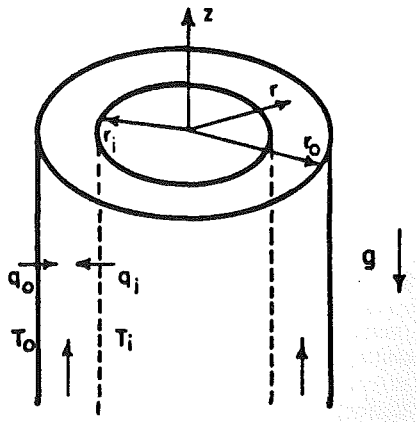

Fig. 1 Geometry of the problem

Downloaded 17 Dec 2010 to 193.140.21.150. Redistribution subject to ASME license or copyright; see http://www.asme.org/terms/Terms_Use.cfm

Acknowledgments

The present study was supported in part by a grant from the National Science Foundation (NSF MEA 83-00785).

References

Armaly, B. F., Chen, T. S., and Ramachandran, N., 1987, "Correlations for Laminar Mixed Convection on Vertical, Inclined, and Horizontal Flat Plates With Uniform Surface Heat Flux," *International Journal of Heat and Mass Transfer*, Vol. 30, pp. 405–408.

Chen, T. S., Armaly, B. F., and Ramachandran, N., 1986, "Correlations for Laminar Mixed Convection Flows on Vertical, Inclined, and Horizontal Flat Plates," ASME JOURNAL OF HEAT TRANSFER, Vol. 108, pp. 835–840.

Chen, T. S., Sparrow, E. M., and Mucoglu, A., 1977, "Mixed Convection in Boundary Layer Flow on a Horizontal Plate," ASME JOURNAL OF HEAT TRANSFER, Vol. 99, pp. 66–71.

Chen, T. S., and Strobel, F. A., 1980, "Buoyancy Effects on Heat and Mass Transfer in Boundary Layer on a Continuous, Moving Horizontal Plate," *Numerical Heat Transfer*, Vol. 3, pp. 115–130.

Churchill, S. W., 1977, "A Comprehensive Correlating Equation for Laminar Assisting, Forced and Free Convection," *AIChE Journal*, Vol. 23, pp. 10–16.

Churchill, S. W., 1983, "Combined Free and Forced Convection Around Immersed Bodies," in: *Heat Exchanger Design Hand Book*, Hemisphere Publishing, Washington, DC, Chap. 2.5.9.

Mucoglu, A., and Chen, T. S., 1978, "Mixed Convection on a Horizontal Plate With Uniform Surface Heat Flux," *Proceedings of the 6th International Heat Transfer Conference*, Vol. 1, pp. 85–90.

Strobel, F. A., and Chen, T. S., 1980, "Buoyancy Effects on Heat and Mass Transfer in Boundary Layers Adjacent to Inclined, Continuous, Moving Sheets," *Numerical Heat Transfer*, Vol. 3, pp. 461–481.

Boundary Effects in Laminar Mixed Convection Flow Through an Annular Porous Medium

M. Parang[1] and M. Keyhani[2]

Nomenclature

c_1, c_2, c_3, c_4 = constants in equation (6)
d = diameter
Da = Darcy number = K/l^2
Gr = Grashof number = $g\beta l^3\ (q_i d_i + q_o d_o)/\nu^2 k$
H = parameter defined before equation (5)
K = permeability of the medium
k = fluid thermal conductivity
l = hydraulic radius = $r_o - r_i$
Nu = Nusselt number
P = pressure
Re = Reynolds number = $u_m l/\nu$
q = surface heat flux rate
Q = heat flux ratio = q_i/q_o
r = dimensionless radial coordinate
R = radius ratio = r_o/r_i
S = dimensionless pressure loss
T = dimensionless temperature
u = dimensionless volume-averaged axial velocity
u_m = bulk mean velocity
z = axial coordinate
α = parameter defined before equation (5)
β = fluid coefficient of volume expansion
γ_1, γ_2 = parameters defined after equation (6)
ϵ = porosity of the medium
ν = kinematic viscosity
ρ_m = bulk fluid density

Subscripts

i = inner surface
m = mixed Darcy flow regime (for Nusselt number)
o = outer surface

Introduction

The influence of the Brinkman and Forchheimer terms in forced convection over a flat plate has been investigated by Vafai and Tien (1981). A similar study was reported by Ranganathan and Viskanta (1984) discussing the wall and inertia effects in mixed-convection flow over a flat plate. Tong and Subramanian (1985) have reported a study of the wall effect on natural convection in a vertical enclosure. Their results indicate that the viscous term should be considered when the Darcy number is greater than 10^{-5}. Similar results are obtained by Lauriat and Prasad (1986) in natural convection in a vertical porous cavity. They also found that the wall effect is negligible for Darcy number below 10^{-5}.

This study addresses the Brinkman-extended Darcy model (Brinkman flow) of a laminar mixed-convection flow in an annular porous region. The primary objective of the present study is to help clarify the conditions under which the Brinkman term can be neglected in this flow without producing an unacceptable error. The simple geometry considered and the closed-form nature of the solution are advantageous in the demonstration of the importance of the wall effect. The results of this study can also be used in the evaluation of the accuracy of the numerical computations in more complex non-Darcian annular flows in the limiting case of the fully developed flow.

Analysis

The geometry of the problem under consideration is shown in Fig. 1. A vertically oriented annulus region is filled with a fluid-saturated porous medium. An upward (opposite to the gravity vector) forced flow is combined with mixed convection which is present due to uniform heat flux at the boundaries. The heat flux rates at the inner and outer walls are q_i and q_o, respectively. The thermal and velocity fields are assumed fully developed.

Assuming an isotropic, homogeneous porous medium and

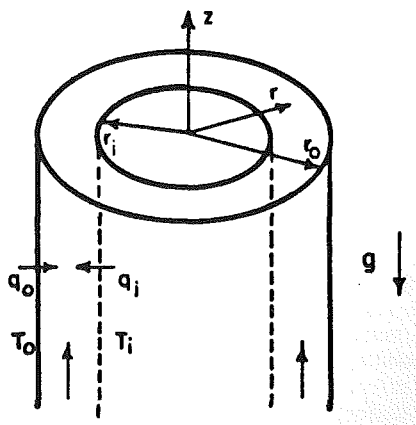

Fig. 1 Geometry of the problem

[1]Associate Professor, Mechanical and Aerospace Engineering Department, University of Tennessee, Knoxville, TN 37996; Mem. ASME.

[2]Assistant Professor, Mechanical and Aerospace Engineering Department, University of Tennessee, Knoxville, TN 37996; Mem. ASME.

Contributed by the Heat Transfer Division and presented at the AIAA/ASME Heat Transfer and Thermophysics Conference, Boston, Massachusetts, June 2–4, 1986. Manuscript received by the Heat Transfer Division March 10, 1986.

Copyright © 1987 by ASME

Downloaded 17 Dec 2010 to 193.140.21.150. Redistribution subject to ASME license or copyright; see http://www.asme.org/terms/Terms_Use.cfm

incompressible, constant-property laminar flow, and invoking Boussinesq approximation, the governing conservation laws in nondimensional form are (Parang and Keyhani, 1986)

$$\left(\frac{\mathrm{Da}}{\epsilon}\right)(R-1)^2D^2u-u+\left(\frac{\mathrm{GrDa}}{\mathrm{Re}}\right)\frac{1}{R^2-1}T=S \qquad (1)$$

$$D^2T=u \qquad (2)$$

In these equations Da, Gr, Re, and R are Darcy number, Grashof number, Reynolds number, and radius ratio, respectively. The differential operator D^2 and nondimensional pressure term S are defined, respectively, as

$$D^2=\frac{1}{r}\frac{d}{dr}\left(r\frac{d}{dr}\right), \quad S=\left(\frac{1}{\rho_m}\frac{dp}{dz}+g\right)\frac{l}{u_m^2}\mathrm{ReDa}$$

The nondimensional constant-heat flux boundary conditions are

$$r=1 \qquad u=0 \qquad \frac{dT}{dr}=-\frac{R^2-1}{2}\frac{1}{1+R/Q} \qquad (3)$$

$$r=R \qquad u=0 \qquad \frac{dT}{dr}=\frac{R^2-1}{2}\frac{1}{R+Q} \qquad (4)$$

where $Q=q_i/q_o$ is the ratio of heat fluxes at the walls.

Equations (1) and (2) show the characteristic dimensionless parameters of the problem. The wall effect is manifested through the parameter Da/ϵ. The inclusion of this term results in Brinkman modification of the Darcy flow model. The relative importance of the buoyancy (mixed convection) effect is represented by the dimensionless flow parameter GrDa/Re. A more algebraically convenient form of presenting these two effects is obtained if we define the following parameters

$$H^2=\frac{\mathrm{GrDa}}{\mathrm{Re}}\frac{1}{R^2-1}, \qquad \alpha^2=\frac{\epsilon}{\mathrm{Da}(R-1)^2}$$

The set of equations (1) and (2), with the boundary conditions (3) and (4), was solved for velocity and temperature profiles in terms of the modified Bessel functions I_o and K_o. They are

$$u=c_1I_o(\gamma_1r)+c_2K_o(\gamma_1r)+c_3I_o(\gamma_2r)+c_4K_o(\gamma_2r) \qquad (5)$$

$$T=S/H^2+c_1a_1I_o(\gamma_1r)+c_2a_1K_o(\gamma_1r)+c_3a_2I_o(\gamma_2r)+c_4a_2K_o(\gamma_2r) \qquad (6)$$

where

$$\gamma_1=\sqrt{\frac{\alpha^2}{2}[1+\sqrt{1-4H^2/\alpha^2}]},$$

$$\gamma_2=\sqrt{\frac{\alpha^2}{2}[1-\sqrt{1-4H^2/\alpha^2}]}$$

$$a_1=\frac{1-\gamma_1^2/\alpha^2}{H^2}, \qquad a_2=\frac{1-\gamma_2^2/\alpha^2}{H^2}$$

The special form of the velocity and temperature solutions for various limiting cases of the above two effects are omitted here for brevity of space (see Parang and Keyhani, 1986). The constants c_1, c_2, c_3, and c_4 are algebraically involved and are not presented here.

The Nusselt numbers at the inner and outer walls are

$$\mathrm{Nu}_i=\frac{(R-1)^2(R+1)}{2T_i(1+R/Q)}, \quad \mathrm{Nu}_o=\frac{(R-1)^2(R+1)}{2T_o(R+Q)}$$

where T_i and T_o are temperatures at the inner and outer boundaries, respectively.

Typical velocity and temperature profiles, the Nusselt number results, the effect of mixed convection, and the boundary effect are presented and discussed briefly in the following section. A more detailed discussion can be found in Parang and Keyhani (1986).

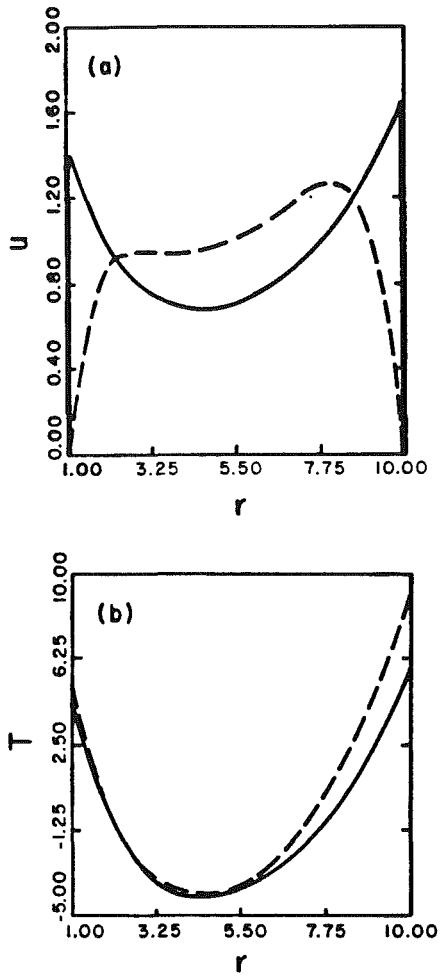

Fig. 2 Velocity (*a*) and temperature (*b*) profiles for Brinkman flow with $R=10$, $Q=2$, GrDa/Re = 10; ·····: $\mathrm{Da}/\epsilon=10^{-2}$, ———: $\mathrm{Da}/\epsilon=10^{-6}$

Table 1 Variation of normalized Nusselt number at the inner and outer walls with radius ratio and Da/ϵ with $Q=2$ and GrDa/Re = 10

Da/ϵ	$\mathrm{Nu}_i/\mathrm{Nu}_{im}$			$\mathrm{Nu}_o/\mathrm{Nu}_{om}$		
	R			R		
	2	5	10	2	5	10
10^{-6}	0.997	0.997	0.997	0.990	0.993	0.993
10^{-4}	0.973	0.972	0.973	0.910	0.934	0.935
10^{-2}	0.831	0.843	0.880	0.574	0.637	0.637

Results and Discussion

The velocity and temperature profiles with $Q=2$, $R=10$, and GrDa/Re = 10 are presented in Figs. 2(*a*) and 2(*b*) for the two values $\mathrm{Da}/\epsilon=10^{-2}$ and 10^{-6}. As expected the velocity gradient at the wall is substantially higher at the smaller Da/ϵ value. For a given GrDa/Re, it is observed (Parang and Keyhani, 1986) that for $\mathrm{Da}/\epsilon=10^{-6}$ the velocity profile is indistinguishable from that of the mixed convection Darcy flow ($\mathrm{Da}/\epsilon=0$), and the region where velocity drops to zero is so thin that it cannot be shown in the figure. The relatively lower velocity at the wall for large Da/ϵ results in higher temperature at the wall as shown in Fig. 2(*b*). This effect is more pronounced at the outer wall.

The results for Nusselt number are normalized with respect to mixed convection Darcy flow ($\mathrm{Da}/\epsilon=0$) Nusselt number (i.e., Nu_{im} and Nu_{om} for inner and outer walls, respectively) and are presented in Table 1 for $Q=2$, GrDa/Re = 10, and various values of Da/ϵ and R. It is obvious that in this case the

Downloaded 17 Dec 2010 to 193.140.21.150. Redistribution subject to ASME license or copyright; see http://www.asme.org/terms/Terms_Use.cfm

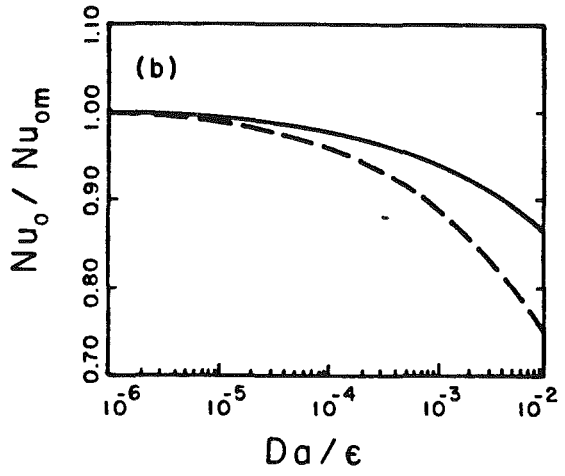

Fig. 3 Comparison of wall effect on heat transfer coefficient with $R = 2$; ·····: GrDa/Re = 10; ———: GrDa/Re = 1.0, for the outer wall ($Q = 0$)

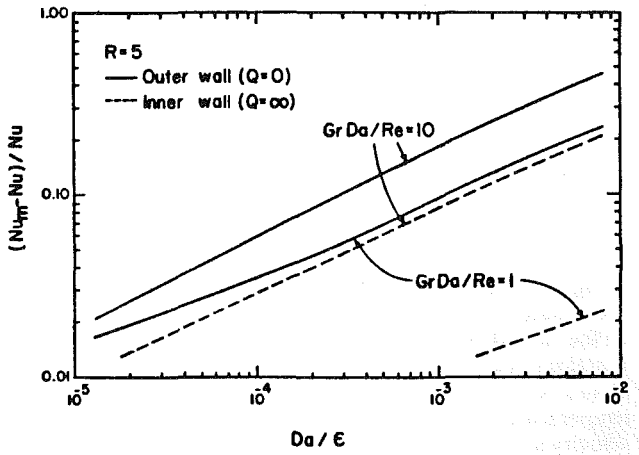

Fig. 4 Comparison of the Nusselt number for Brinkman (Nu) and Darcy (Nu_m) flow regimes as a function of Da/ϵ for $R = 5$

inclusion of the Brinkman term has no appreciable effect on heat transfer coefficient at $Da/\epsilon = 10^{-6}$ (less than 1 percent). Furthermore, an increase of two orders of magnitude in Da/ϵ shows less than 9 percent change in the Nusselt number. However, the boundary effect becomes significant at higher values of Da/ϵ. For example for $Da/\epsilon = 10^{-2}$ the exclusion of the Brinkman term can result in more than 70 percent error in the Nusselt number. For a given radius ratio the heat transfer coefficient decreases with increase in Da/ϵ on both walls. It is also observed that for a given Da/ϵ, Nusselt number improves with increase in radius ratio R.

The buoyancy effect on heat transfer coefficient in the Brinkman flow is similar to the Darcy flow regime discussed in Parang and Keyhani (1986). For example, with $R = 10$, $Q = 2$, and $GrDa/Re = 10$, the outer wall Nusselt number improves relative to the forced Brinkman flow ($GrDa/Re = 0$) results by 44, 40, and 22 percent for $Da/\epsilon = 10^{-6}$, 10^{-4}, and 10^{-2}, respectively.

The velocity and temperature profiles with $R = 2$ and $GrDa/Re = 10$ for the fundamental solutions (i.e., $Q = 0$, $Q = \infty$) have characteristics similar to those presented in Figs. 2(*a*) and 2(*b*) except with a more pronounced skew of the flow velocity near the heated wall (Parang and Keyhani, 1986). The Nusselt number (normalized as before by Nu_{im} and Nu_{om}) for these fundamental solutions are similar to those discussed in Table 1. The wall effect is observed to have a significant impact on the heat transfer coefficient at the outer wall and is increasingly more important at higher radius ratios. However the impact of boundary effect on the inner wall remains relatively small at even high values of Da/ϵ.

The boundary effect is observed to be more important with increase in the flow parameter GrDa/Re. This phenomenon is illustrated in Fig. 3 where the normalized Nusselt number of one of the fundamental solutions ($Q = 0$) is shown for $GrDa/Re = 1$ and 10. Furthermore, the effect of the mixed convection on the heat transfer coefficient becomes increasingly more important with higher Da/ϵ due to the interaction of buoyancy and wall effect. The error in the Nusselt number due to the omission of the Brinkman term as a function of Da/ϵ for various values of the flow parameter and typical values of the radius ratio are presented in Fig. 4.

Conclusion

Several important conclusions can be drawn from the discussion in the previous section. The present results, along with those of Lauriat and Prasad (1986) and Tong and Subramanian (1985), indicate that the Brinkman term may be neglected without an appreciable loss of accuracy for $Da/\epsilon \leq 10^{-5}$. Since the other two studies are for natural convection in vertical enclosures with boundary conditions different from the present study, this limit on the importance of wall effect seems to be applicable to problems with different geometry and thermal boundary conditions. Moreover, for moderate values of the relevant flow parameters, the present conclusion may be applicable to forced, mixed, and natural convection flow regimes. Finally, it is also found that the wall effect is more pronounced at the outer wall in annular porous flows. That is, for a given GrDa/Re and radius ratio the exclusion of the Brinkman term will result in a higher error in the heat transfer coefficient of the outer cylinder relative to that of the inner cylinder.

References

Lauriat, G., and Prasad, V., 1986, "Natural Convection in a Vertical Porous Cavity: A Numerical Study for Brinkman-Extended Darcy Formulation," ASME HTD-Vol. 56, pp. 13–22.

Parang, M., and Keyhani, M., 1986, "Boundary Effects in Laminar Mixed Convection Flow Through an Annular Porous Medium," ASME HTD-Vol. 56, pp. 117–125.

Ranganathan, P., and Viskanta, R., 1984, "Mixed Convection Boundary-Layer Flow Along a Vertical Surface in a Porous Medium," *Num. Heat Transfer*, Vol. 7, pp. 305–317.

Tong, T. W., and Subramanian, E., 1985, "A Boundary-Layer Analysis for Natural Convection in Vertical Porous Enclosures – Use of the Brinkman-Extended Darcy Model," *Int. J. Heat Mass Transfer*, Vol. 28, No. 3, pp. 563–571.

Vafai, V., and Tien, C. L., 1981, "Boundary and Inertial Effects on Flow and Heat Transfer in Porous Media," *Int. J. Heat Mass Transfer*, Vol. 24, pp. 195–204.

A General Similarity Transformation for Combined Free and Forced-Convection Flows Within a Fluid-Saturated Porous Medium

A. Nakayama[1] and H. Koyama[1]

Nomenclature

f = dimensionless stream function
g = acceleration due to gravity
I = function associated with a deviation from unity
k = thermal conductivity
K = permeability

[1]Department of Energy and Mechanical Engineering, Shizuoka University, Hamamatsu, 432 Japan.

Contributed by the Heat Transfer Division for publication in the JOURNAL OF HEAT TRANSFER. Manuscript received by the Heat Transfer Division June 16, 1986.

Downloaded 17 Dec 2010 to 193.140.21.150. Redistribution subject to ASME license or copyright; see http://www.asme.org/terms/Terms_Use.cfm

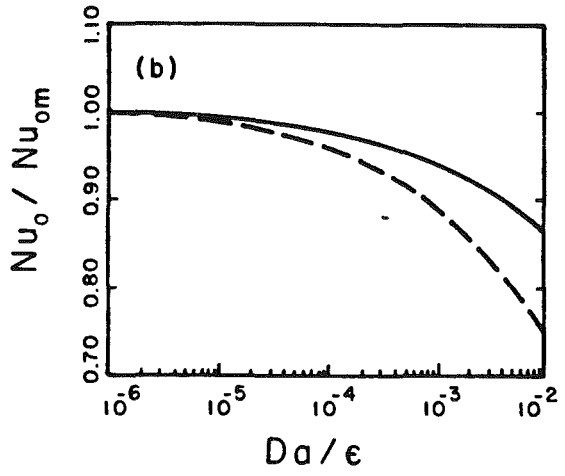

Fig. 3 Comparison of wall effect on heat transfer coefficient with $R = 2$; ·····: GrDa/Re = 10; ———: GrDa/Re = 1.0, for the outer wall ($Q = 0$)

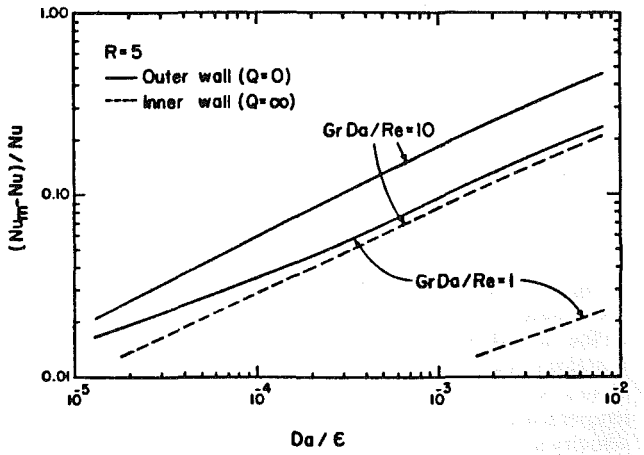

Fig. 4 Comparison of the Nusselt number for Brinkman (Nu) and Darcy (Nu_m) flow regimes as a function of Da/ϵ for $R = 5$

inclusion of the Brinkman term has no appreciable effect on heat transfer coefficient at $Da/\epsilon = 10^{-6}$ (less than 1 percent). Furthermore, an increase of two orders of magnitude in Da/ϵ shows less than 9 percent change in the Nusselt number. However, the boundary effect becomes significant at higher values of Da/ϵ. For example for $Da/\epsilon = 10^{-2}$ the exclusion of the Brinkman term can result in more than 70 percent error in the Nusselt number. For a given radius ratio the heat transfer coefficient decreases with increase in Da/ϵ on both walls. It is also observed that for a given Da/ϵ, Nusselt number improves with increase in radius ratio R.

The buoyancy effect on heat transfer coefficient in the Brinkman flow is similar to the Darcy flow regime discussed in Parang and Keyhani (1986). For example, with $R = 10$, $Q = 2$, and $GrDa/Re = 10$, the outer wall Nusselt number improves relative to the forced Brinkman flow ($GrDa/Re = 0$) results by 44, 40, and 22 percent for $Da/\epsilon = 10^{-6}$, 10^{-4}, and 10^{-2}, respectively.

The velocity and temperature profiles with $R = 2$ and $GrDa/Re = 10$ for the fundamental solutions (i.e., $Q = 0$, $Q = \infty$) have characteristics similar to those presented in Figs. 2(*a*) and 2(*b*) except with a more pronounced skew of the flow velocity near the heated wall (Parang and Keyhani, 1986). The Nusselt number (normalized as before by Nu_{im} and Nu_{om}) for these fundamental solutions are similar to those discussed in Table 1. The wall effect is observed to have a significant impact on the heat transfer coefficient at the outer wall and is increasingly more important at higher radius ratios. However the impact of boundary effect on the inner wall remains relatively small at even high values of Da/ϵ.

The boundary effect is observed to be more important with increase in the flow parameter GrDa/Re. This phenomenon is illustrated in Fig. 3 where the normalized Nusselt number of one of the fundamental solutions ($Q = 0$) is shown for $GrDa/Re = 1$ and 10. Furthermore, the effect of the mixed convection on the heat transfer coefficient becomes increasingly more important with higher Da/ϵ due to the interaction of buoyancy and wall effect. The error in the Nusselt number due to the omission of the Brinkman term as a function of Da/ϵ for various values of the flow parameter and typical values of the radius ratio are presented in Fig. 4.

Conclusion

Several important conclusions can be drawn from the discussion in the previous section. The present results, along with those of Lauriat and Prasad (1986) and Tong and Subramanian (1985), indicate that the Brinkman term may be neglected without an appreciable loss of accuracy for $Da/\epsilon \leq 10^{-5}$. Since the other two studies are for natural convection in vertical enclosures with boundary conditions different from the present study, this limit on the importance of wall effect seems to be applicable to problems with different geometry and thermal boundary conditions. Moreover, for moderate values of the relevant flow parameters, the present conclusion may be applicable to forced, mixed, and natural convection flow regimes. Finally, it is also found that the wall effect is more pronounced at the outer wall in annular porous flows. That is, for a given GrDa/Re and radius ratio the exclusion of the Brinkman term will result in a higher error in the heat transfer coefficient of the outer cylinder relative to that of the inner cylinder.

References

Lauriat, G., and Prasad, V., 1986, "Natural Convection in a Vertical Porous Cavity: A Numerical Study for Brinkman-Extended Darcy Formulation," ASME HTD-Vol. 56, pp. 13–22.

Parang, M., and Keyhani, M., 1986, "Boundary Effects in Laminar Mixed Convection Flow Through an Annular Porous Medium," ASME HTD-Vol. 56, pp. 117–125.

Ranganathan, P., and Viskanta, R., 1984, "Mixed Convection Boundary-Layer Flow Along a Vertical Surface in a Porous Medium," *Num. Heat Transfer*, Vol. 7, pp. 305–317.

Tong, T. W., and Subramanian, E., 1985, "A Boundary-Layer Analysis for Natural Convection in Vertical Porous Enclosures—Use of the Brinkman-Extended Darcy Model," *Int. J. Heat Mass Transfer*, Vol. 28, No. 3, pp. 563–571.

Vafai, V., and Tien, C. L., 1981, "Boundary and Inertial Effects on Flow and Heat Transfer in Porous Media," *Int. J. Heat Mass Transfer*, Vol. 24, pp. 195–204.

A General Similarity Transformation for Combined Free and Forced-Convection Flows Within a Fluid-Saturated Porous Medium

A. Nakayama[1] and H. Koyama[1]

Nomenclature

f = dimensionless stream function
g = acceleration due to gravity
I = function associated with a deviation from unity
k = thermal conductivity
K = permeability

[1]Department of Energy and Mechanical Engineering, Shizuoka University, Hamamatsu, 432 Japan.

Contributed by the Heat Transfer Division for publication in the JOURNAL OF HEAT TRANSFER. Manuscript received by the Heat Transfer Division June 16, 1986.

Copyright © 1987 by ASME

Downloaded 17 Dec 2010 to 193.140.21.150. Redistribution subject to ASME license or copyright; see http://www.asme.org/terms/Terms_Use.cfm

Nu_x = local Nusselt number
Pe_x = local Peclet number
q_w = local surface heat flux
r = function representing wall geometry
r^* = 1 for plane flow and r for axisymmetric flow
Ra_x = local Rayleigh number
T = temperature
u, v = Darcian velocity components
x, y = boundary layer coordinates
α = thermal diffusivity
β = coefficient of thermal expansion
η = similarity variable
θ = dimensionless temperature
λ = exponent associated with wall temperature distribution
ν = kinematic viscosity
ξ = transformed variable in the streamwise direction
ϕ = circumferential angle
ψ = dimensionless stream function

Subscripts

e = boundary layer edge
w = wall

Introduction

Convective heat transfer within a fluid-saturated porous medium is of great interest, especially in the petroleum and geothermal industries. Considerable attention has been directed toward understanding the transport properties of porous media subjected to free, forced, or mixed convection.

Analytical studies of free convection based on the boundary layer concept were reported on a vertical plate (Avduyevskiy et al., 1976; Cheng and Minkowycz, 1977), and a horizontal circular cylinder and sphere (Nilson, 1981). Merkin (1979) proposed a similarity transformation which can deal with isothermal two-dimensional and axisymmetric bodies of arbitrary shape. Fand et al. (1986) applied Merkin's analysis to the specific case of free convection around a horizontal isothermal circular cylinder. The transformation suggested by Merkin has recently been extended to the general case of nonisothermal bodies of arbitrary shape by the authors (Nakayama and Koyama, 1986). The problem of combined free and forced convection (mixed convection) in a porous medium also has many important applications such as in geothermal reservoirs where a pressure gradient exists due to withdrawal or reinjection of fluids. Cheng (1977) studied mixed convection on a flat plate, and obtained similarity solutions for the special case where the free-stream velocity and wall temperature distributions of an inclined plate (a wedge) vary according to the same power function of distance. Subsequently, Cheng (1982) found similarity solutions for mixed convection over an isothermal horizontal cylinder and sphere. So far, only simple geometries were treated in combined convection.

It is the purpose of the present paper to introduce a general transformation procedure appropriate to the problem of combined free and forced convection in a porous medium. It will be shown that particular transformations proposed in the previous papers by Cheng (1982) and Minkowycz and coworkers (1985) are simply the specific forms of the present general transformation. Pure forced convection will be treated first as a limiting case of combined free and forced convection. The analysis reveals that any two-dimensional or axisymmetric body of arbitrary shape possesses its corresponding class of wall temperature distributions which permit similarity solutions. Secondly, combined free and forced convection will be considered to seek similarity solutions. It is found that, unlike in pure forced convection, similarity solutions in mixed convection are possible only when the external free-stream velocity varies everywhere in proportion to the product of the streamwise component of the gravity force and the wall–ambient temperature difference.

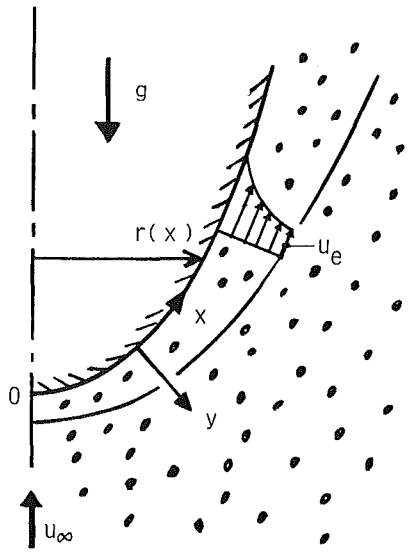

Fig. 1 Physical model and coordinate system

Governing Equations

Figure 1 shows the physical model and its boundary layer coordinates (x, y). The geometry and surface wall temperature of the heated body in a porous medium are specified by the functions $r(x)$ and $T_w(x)$, respectively. The wall temperature $T_w(x)$ is assumed to be everywhere higher than the ambient temperature of a porous medium T_e. The boundary layer edge velocity $u_e(x)$ may be obtained from the potential flow theory once the geometric configuration is known. In common with prior boundary layer studies of this kind, we limit our analysis to cases where a boundary layer structure exists in the system.

Under the usual boundary layer approximations along with the Boussinesq approximation, the governing equations, namely, the equation of continuity, Darcy's law,[2] and the energy equation are given by

$$\frac{\partial}{\partial x} r^* u + \frac{\partial}{\partial y} r^* v = 0 \tag{1}$$

$$\frac{\partial u}{\partial y} = \frac{K\beta}{\nu} g_x \frac{\partial T}{\partial y} \tag{2}$$

and

$$u \frac{\partial T}{\partial x} + v \frac{\partial T}{\partial y} = \alpha \frac{\partial^2 T}{\partial y^2} \tag{3}$$

where

$$r^* = \begin{cases} 1 & \text{plane flow} \\ r(x) & \text{axisymmetric flow} \end{cases} \tag{4a}$$

and

$$g_x = g\left[1 - \left(\frac{dr}{dx}\right)^2\right]^{1/2} \tag{4b}$$

In the foregoing equations, u and v are the Darcian velocity components in the x and y directions and T is the local

[2] We assume that the flow is slow or the pores are small enough that the Darcy law is valid.

Downloaded 17 Dec 2010 to 193.140.21.150. Redistribution subject to ASME license or copyright; see http://www.asme.org/terms/Terms_Use.cfm

temperature. The tangential component of the acceleration due to gravity g is indicated by g_x, which is related to the local surface inclination through equation (4*b*). K is the permeability; ν, the kimematic viscosity; α the equivalent thermal diffusivity of the porous medium; and β, the coefficient of thermal expansion. The appropriate boundary conditions for the problem are

$y=0$:

$$v=0, \tag{5a}$$

$$T=T_w(x) \tag{5b}$$

$y\to\infty$:

$$u=u_e(x), \tag{5c}$$

$$T=T_e \tag{5d}$$

where the subscripts w and e refer to the wall and boundary layer edge, respectively. The continuity equation (1) can automatically be satisfied by introducing the stream function ψ such that

$$u=\frac{1}{r^*}\frac{\partial\psi}{\partial y} \tag{6a}$$

$$v=-\frac{1}{r^*}\frac{\partial\psi}{\partial x} \tag{6b}$$

Transformation

We now introduce the following transformation:

$$\psi=\alpha r^*(\mathrm{Pe}_x I)^{1/2} f(x,\eta) \tag{7a}$$

$$T-T_e=\Delta T_w\theta(x.\eta) \tag{7b}$$

$$\eta=\frac{y}{x}(\mathrm{Pe}_x/I)^{1/2} \tag{7c}$$

where

$$\Delta T_w(x)=T_w-T_e \tag{8a}$$

$$\mathrm{Pe}_x=\frac{u_e x}{\alpha} \tag{8b}$$

$$I(x)=\frac{\int_0^x u_e r^{*2}\Delta T_w^2\,dx}{u_e r^{*2}\Delta T_w^2\,x} \tag{8c}$$

Pe_x is the local Peclet number and η is the proposed pseudo-similarity variable. The function I as defined in equation (8*c*) adjusts the scale in the normal direction according to a given body geometry and its surface temperature distribution. Obviously, the function I reduces to unity for the special case of an isothermal vertical flat plate. Substitution of equations (7) into (2)–(6) yields

$$f''=(\mathrm{Ra}_x/\mathrm{Pe}_x)\theta' \tag{9a}$$

and

$$\theta''+(\tfrac{1}{2}-nI)f\theta'-nIf'\theta=-xI\left(\theta'\frac{\partial f}{\partial x}-f'\frac{\partial\theta}{\partial x}\right) \tag{9b}$$

with boundary conditions given by

$\eta=0$:

$$f=0, \tag{10a}$$

$$\theta=1 \tag{10b}$$

$\eta\to\infty$:

$$f'=1, \tag{10c}$$

$$\theta=0 \tag{10d}$$

and the Darcian velocities are

$$u=(\alpha/x)\mathrm{Pe}_x f' \tag{11a}$$

and

$$v=(\alpha/x)(\mathrm{Pe}_x/I)^{1/2}\left[(nI-\tfrac{1}{2})f-Ix\frac{\partial f}{\partial x}-\left(I\frac{d\ln u_e r^*}{d\ln x}+nI-\tfrac{1}{2}\right)\eta f'\right] \tag{11b}$$

where

$$n(x)=\frac{d\ln\Delta T_w}{d\ln x} \tag{12a}$$

$$\mathrm{Ra}_x=\frac{K\beta\Delta T_w g_x x}{\nu\alpha} \tag{12b}$$

The primes in the foregoing equations denote differentiation with respect to η. Equation (9*a*) may readily be integrated with equations (10*c*) and (10*d*) as

$$f'=1+(\mathrm{Ra}_x/\mathrm{Pe}_x)\theta \tag{13}$$

Pure Forced Convection

Let us consider the limiting case $\mathrm{Ra}_x/\mathrm{Pe}_x\to 0$, namely, the case of pure forced convection. Equation (13) with the boundary conditions given by equation (10*a*), for this case, gives

$$f=\eta \tag{14}$$

The energy conservation equation (9*b*) reduces to

$$\theta''+(\tfrac{1}{2}-nI)\eta\theta'-nI\theta=xI\frac{\partial\theta}{\partial x} \tag{15}$$

It is interesting to note that similarity solutions to equation (15) exist when the product nI remains constant in the streamwise direction. Similarity solutions for pure forced convection around a nonisothermal circular cylinder or sphere were reported by Minkowycz et al. (1985). The more general case of pure forced convection from nonisothermal curved surfaces of arbitrary shape, however, has not been treated yet. Thus, to seek such possible similarity solutions, we rewrite the lumped parameter nI using a transformed variable ξ as

$$nI=\frac{d\ln\Delta T_w}{d\ln x}\frac{\int_0^x u_e r^{*2}\Delta T_w^2 dx}{u_e r^{*2}\Delta T_w^2 x}=\frac{d\ln\Delta T_w}{d\ln\xi}\frac{\int_0^\xi\Delta T_w^2 d\xi}{\Delta T_w^2\xi} \tag{16a}$$

where

$$\xi=\int_0^x u_e r^{*2}dx \tag{16b}$$

The preceding equation (16*a*) suggests that the product nI is constant provided that the wall temperature varies according to

$$\Delta T_w\propto\xi^\lambda \tag{17}$$

Substitution of equation (17) into (16*a*) gives a simple relation between the lumped parameter nI and te constant exponent λ as

$$nI=\frac{\lambda}{1+2\lambda} \tag{18}$$

Hence, equation (15) reduces to

$$\theta''+\frac{1}{2(1+2\lambda)}\eta\theta'-\frac{\lambda}{1+2\lambda}\theta=0 \tag{19}$$

Equation (19) appears to be identical to the one derived by Cheng (1977) for the specific case of a flat plate (a vertical wedge) with its wall temperature varying as $\Delta T_w\propto x^\lambda$. (Note that η in their work corresponds to $\eta/(1+2\lambda)^{1/2}$ in our notation.) Thus, numerical values furnished for the case of a flat plate are now applicable to all two-dimensional and axisym-

Downloaded 17 Dec 2010 to 193.140.21.150. Redistribution subject to ASME license or copyright; see http://www.asme.org/terms/Terms_Use.cfm

metric bodies of arbitrary shape, by virtue of equations (16*b*) and (17).

Once the θ distribution for a given value of λ is determined by a standard shooting procedure, the local Nusselt number of our primary concern may be evaluated from

$$\mathrm{Nu}_x \equiv \frac{q_w x}{\Delta T_w k} = -\theta'(0)(\mathrm{Pe}_x/I)^{1/2}$$

$$= -\theta'(0)(1+2\lambda)^{1/2}\left(\frac{d\ln\xi}{d\ln x}\mathrm{Pe}_x\right)^{1/2} \tag{20}$$

In the above expression, the geometric effect is included in ξ or $(d\ln\xi/d\ln x)$ to be precise, which, for example, correspond to

$\xi \propto x^{1+n_v}$ $\left(\lambda = \dfrac{n}{1+n_v}\right)$:

a vertical wedge pointing downward (21*a*)

$\xi \propto x^{3+n_v}$ $\left(\lambda = \dfrac{n}{3+n_v}\right)$:

a vertical cone pointing downward (21*b*)

$\xi \propto 1-\cos\phi$:

a horizontal circular cylinder (21*c*)

$\xi \propto \cos^3\phi - 3\cos\phi + 2$:

a sphere (21*d*)

and

$$\frac{d\ln\xi}{d\ln x} = \begin{cases} 1+n_v\text{: a vertical wedge} & (22a) \\ 3+n_v\text{: a vertical cone} & (22b) \\ \dfrac{\phi\sin\phi}{1-\cos\phi}\text{: a horizontal circular cylinder} & (22c) \\ \dfrac{3\phi\sin^3\phi}{\cos^3\phi-3\cos\phi+2}\text{: a sphere} & (22d) \end{cases}$$

where the potential flows are assumed for $u_e(x)$, namely,

$$u_e \propto x^{n_v}\text{: a wedge or a cone} \tag{23a}$$

and

$$u_e \propto \sin\phi\text{: a cylinder or a sphere} \tag{23b}$$

Equation (20) along with (22) reveals that the surface wall heat flux over a wedge or cone varies according to $q_w \propto x^{(2n+n_v-1)/2}$, while the circumferential variation of q_w on a horizontal circular cylinder of a sphere with a radius L_r is given by

$$q^* = -\theta'(0)(1+2\lambda)^{1/2}\left(\frac{2}{1-\cos\phi}\right)^{1/2-\lambda}\sin\phi\text{:}$$

a horizontal cylinder (24*a*)

and

$$q^* = -\theta'(0)(1+2\lambda)^{1/2}\left(\frac{9}{8}\right)^{1/2}$$

$$\left(\frac{4}{\cos^3\phi-3\cos\phi+2}\right)^{1/2-\lambda}\sin^2\phi\text{: a sphere} \tag{24b}$$

where

$$q^* \equiv \frac{q_w L_r}{\Delta T_{wr} k}\Big/\left(\frac{u_\infty L_r}{\alpha}\right)^{1/2} \tag{24c}$$

u_∞ is the approaching free-stream velocity and ΔT_{wr} is the wall-ambient temperature difference at the rear stagnation point. Both equations (24*a*) and (24*b*) suggest that, for a positive exponent λ, q_w increases away from the front stagnation point as a result of an increase in ΔT_w, attains a maximum, then decreases towards the rear stagnation point as the boundary layer grows thick.

The foregoing results on pure forced convection heat transfer are plotted in Fig. 2 in terms of the grouping $\mathrm{Nu}_x/((d\ln\xi/d\ln x)\mathrm{Pe}_x)^{1/2}$ for universal use.

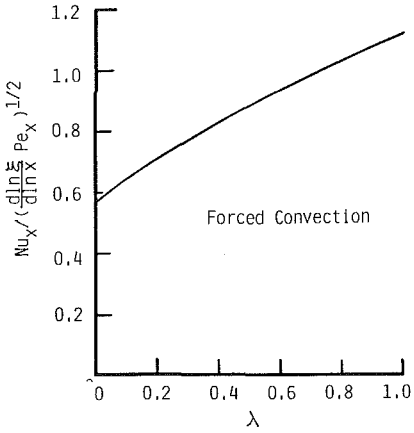

Fig. 2 Heat transfer results on pure forced convection

Combined Free and Forced Convection

For the general case of combined free and forced convection, we substitute equation (13) into (9*b*) to eliminate θ. After some manipulation, we have

$$f''' + (\tfrac{1}{2} - nI)ff'' - nI(f'-1)f' = xI\left(f'\frac{\partial f'}{\partial x} - f''\frac{\partial f}{\partial x}\right.$$

$$\left. - f'(f'-1)\frac{d}{dx}\ln(\mathrm{Ra}_x/\mathrm{Pe}_x)\right) \tag{25}$$

with the boundary conditions given by

$$\eta = 0\text{: } f = 0,\ f' = 1 + (\mathrm{Ra}_x/\mathrm{Pe}_x) \tag{26a}$$

$$\eta \to \infty\text{: } f' = 1 \tag{26b}$$

Equation (25) indicates that similarity solutions exist when

$$\mathrm{Ra}_x/\mathrm{Pe}_x \propto \frac{q_x \Delta T_w}{u_e} = \text{const.} \tag{27a}$$

and

$$nI = \frac{d\ln\Delta T_w}{d\ln x}\frac{\int_0^x u_e r^{*2}\Delta T_w^2 dx}{u_e r^{*2}\Delta T_w^2 x} = const. \tag{27b}$$

or by combining equation (27*a*) with (27*b*),

$$nI = \frac{d\ln\Delta T_w}{d\ln x}\frac{\int_0^x g_x r^{*2}\Delta T_w^3 dx}{g_x r^{*2}\Delta T_w^3 x} = \frac{d\ln\Delta T_w}{d\ln\xi}\frac{\int_0^\xi \Delta T_w^3 d\xi}{\Delta T_w^3 \xi} \tag{27c}$$

where the transformed variable ξ, for this time, should be defined as

$$\xi = \int_0^x g_x r^{*2} dx \tag{28}$$

Thus, similarity solutions exist when the boundary layer edge velocity $u_e(x)$ varies everywhere in proportion to the product $g_x\Delta T_w$, and at the same time, ΔT_w varies in accord with a power function of the new variable ξ

$$\Delta T_w \propto \xi^\lambda \tag{29}$$

which yields a simple relation, namely,

Downloaded 17 Dec 2010 to 193.140.21.150. Redistribution subject to ASME license or copyright; see http://www.asme.org/terms/Terms_Use.cfm

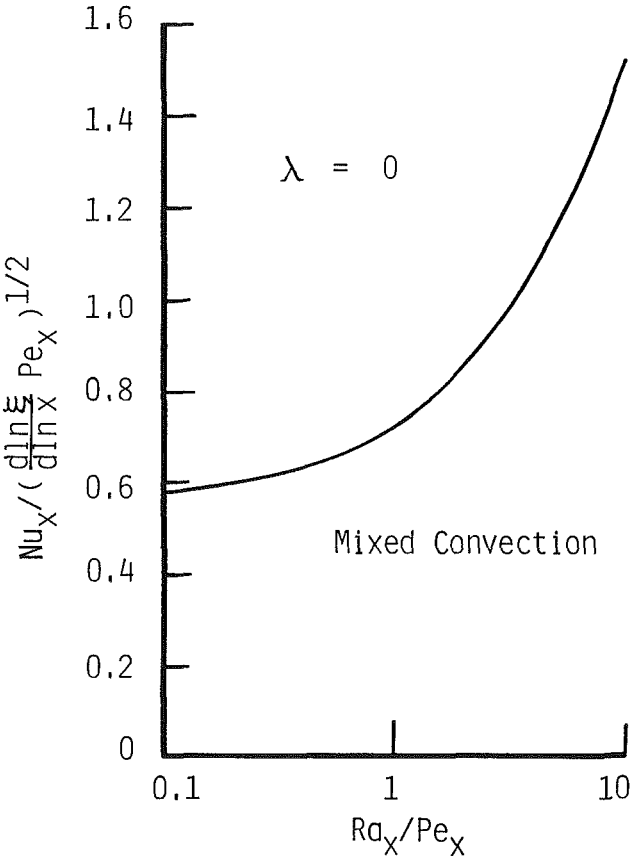

Fig 3 Heat transfer results on combined free and forced convection

$$nI = \frac{\lambda}{1+3\lambda} \tag{30}$$

and equation (25) reduces to

$$f''' + \frac{1+\lambda}{2(1+3\lambda)} ff'' - \frac{\lambda}{1+3\lambda} f'(f'-1) = 0 \tag{31}$$

The resulting equation is identical to the one reported by Cheng (1977) for combined free and forced convection on a flat plate assuming $\Delta T_w \propto x^{\lambda}$. Therefore, his numerical results are readily applicable to the present general case of combined free and forced convection. Two kinds of possible situations in which the aformentioned requirements for similarity are satisfied seem to exist as follows:

For the case of constant gravitational force, g_x = const, the proportional relation requires $u_e \propto \Delta T_w$. Thus, similarity solutions exist for a vertical wedge or cone only when its surface wall temperaure ΔT_w varies with the same power index as that of the boundary layer edge velocity u_e, namely, $n = n_v$.

On the other hand, for the case of constant wall temperature, namely, $n = 0$, we must have $u_e \propto g_x$ for similarity to hold. The case corresponds to an isothermal horizontal circular cylinder and an isothermal sphere, since we have $u_e \propto g_x \sin\phi$ according to the potential theory.

Upon solving equation (31) with the boundary conditions given by equations (26), the local Nusselt number may readily be evaluated from

$$Nu_x = -\frac{f''(0)}{(Ra_x/Pe_x)} (1+3\lambda)^{1/2} \left(\frac{d\ln\xi}{d\ln x} Pe_x\right)^{1/2} \tag{32}$$

where the variable ξ defined by equation (28) for combined free and forced convection corresponds to

$\xi \propto x (\lambda = n)$: a vertical wedge (33*a*)

$\xi \propto x^3 (\lambda = n/3)$: a vertical cone (33*b*)

$\xi \propto 1 - \cos\phi$: a horizontal circular cylinder (33*c*)

$\xi \propto \cos^3\phi - 3\cos\phi + 2$: a sphere (33*d*)

and

$$\frac{d\ln\xi}{d\ln x} = \begin{cases} 1: \text{ a vertical wedge} & (34a) \\ 3: \text{ a vertical cone} & (34b) \\ \dfrac{\phi\sin\phi}{1-\cos\phi}: \text{ a horizontal circular cylinder} & (34c) \\ \dfrac{3\phi\sin^3\phi}{\cos^3\phi - 3\cos\phi + 2}: \text{ a sphere} & (34d) \end{cases}$$

Since $u_e \propto g_x$ for a cylinder or a sphere, the transformed variable ξ for combined convection on an isothermal cylinder or sphere is proportional to that for pure forced convection on a cylinder or a sphere (defined by equation (16*b*)). Naturally, the circumferential variation of the surface wall heat flux for these geometries is similar to that for the case of pure forced convection subjected to $\lambda = 0$.

For illustrative purposes, the heat transfer grouping $Nu_x/((d\ln\xi/d\ln x)Pe_x)^{1/2}$ is presented in Fig. 3, where the abscissa variable is set to (Ra_x/Pe_x) to see its effect on local heat transfer rates.

References

Avduyevskiy, V. S., Kalashnik, V. N., and Kopyatevich, R. M., 1976, "The Investigation of Free-Convection Heat Transfer in Gas-Filled Porous Media at High Pressures," *Heat-Transfer—Soviet Research*, Vol. 10, pp. 136–144.

Cheng, P. 1977, "Combined Free and Forced Convection Flow About Inclined Surfaces in Porous Media," Vol. 2, pp. 807–814.

Cheng, P., 1982, "Mixed Convection About a Horizontal Cylinder and a Sphere in a Fluid-Saturated Porous Medium," *Int. J. Heat Mass Transfer*, Vol. 25, pp. 1245–1247.

Cheng, P., and Minkowycz, W. J., 1977, "Free Convection About a Vertical Flat Plate Embedded in a Saturated Porous Medium With Application to Heat Transfer from a Dike," *J. Geophysics Research*, Vol. 82, pp. 2040–2044.

Fand, R. M., Steinberger, T. E., and Cheng, P., 1986, "Natural Convection Heat Transfer From a Horizontal Cylinder Embedded in a Porous Medium," *Int. J. Heat Mass Transfer*, Vol. 29, pp. 119–133.

Merkin, J. H., 1979, "Free Convection Boundary Layers on Axisymmetric and Two-Dimensional Bodies of Arbitrary Shape in a Saturated Porous Medium," *Int. J. Heat Mass Transfer*, Vol. 22, pp. 1461–1462.

Minkowycz, W. J., Cheng, P., and Chang, C. H., 1985, "Mixed Convection About a Nonisothermal Cylinder and Sphere in a Porous Medium," *Numerical Heat Transfer*, Vol. 8, pp. 349–359.

Nakayama, A., and Koyama, H., 1987, "Free Convective Heat Transfer Over a Nonisothermal Body of Arbitrary Shape Embedded in a Fluid-Saturated Porous Medium," ASME JOURNAL OF HEAT TRANSFER, Vol. 109, pp. 125–130.

Nilson, R. H., 1981, "Natural Convective Boundary Layer on Two-Dimensional and Axisymmetric Surfaces in High-Pr Fluids or in Fluid Saturated Porous Media," ASME JOURNAL OF HEAT TRANSFER, Vol. 103, pp. 803–807.

An Analytical Study of the Effect of the Darcy and Fick Laws on the Sublimation of a Frozen Semi-infinite Porous Medium

Y. C. Fey[1] and M. A. Boles[1,2]

Nomenclature

C = molar concentration of moisture
C_0 = molar concentration of frozen bounded substance

[1]Mechanical and Aerospace Engineering Department, North Carolina State University, Raleigh, NC 27695-7910.

[2]Mem. ASME.

Contributed by the Heat Transfer Division for publication in the JOURNAL OF HEAT TRANSFER. Manuscript received by the Heat Transfer Division October 24, 1985.

Downloaded 17 Dec 2010 to 193.140.21.150. Redistribution subject to ASME license or copyright; see http://www.asme.org/terms/Terms_Use.cfm

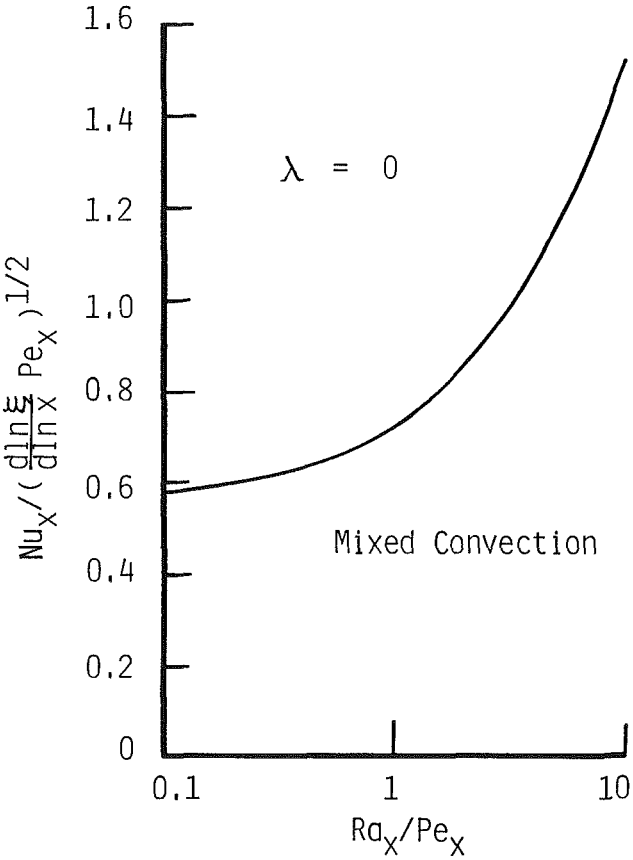

Fig 3 Heat transfer results on combined free and forced convection

$$nI=\frac{\lambda}{1+3\lambda} \tag{30}$$

and equation (25) reduces to

$$f'''+\frac{1+\lambda}{2(1+3\lambda)}ff''-\frac{\lambda}{1+3\lambda}f'(f'-1)=0 \tag{31}$$

The resulting equation is identical to the one reported by Cheng (1977) for combined free and forced convection on a flat plate assuming $\Delta T_w \propto x^{\lambda}$. Therefore, his numerical results are readily applicable to the present general case of combined free and forced convection. Two kinds of possible situations in which the aformentioned requirements for similarity are satisfied seem to exist as follows:

For the case of constant gravitational force, g_x = const, the proportional relation requires $u_e \propto \Delta T_w$. Thus, similarity solutions exist for a vertical wedge or cone only when its surface wall temperaure ΔT_w varies with the same power index as that of the boundary layer edge velocity u_e, namely, $n = n_v$.

On the other hand, for the case of constant wall temperature, namely, $n = 0$, we must have $u_e \propto g_x$ for similarity to hold. The case corresponds to an isothermal horizontal circular cylinder and an isothermal sphere, since we have $u_e \propto g_x \sin\phi$ according to the potential theory.

Upon solving equation (31) with the boundary conditions given by equations (26), the local Nusselt number may readily be evaluated from

$$\mathrm{Nu}_x=-\frac{f''(0)}{(\mathrm{Ra}_x/\mathrm{Pe}_x)}(1+3\lambda)^{1/2}\left(\frac{d\ln\xi}{d\ln x}\mathrm{Pe}_x\right)^{1/2} \tag{32}$$

where the variable ξ defined by equation (28) for combined free and forced convection corresponds to

$\xi \propto x(\lambda=n)$: a vertical wedge (33*a*)

$\xi \propto x^3(\lambda=n/3)$: a vertical cone (33*b*)

$\xi \propto 1-\cos\phi$: a horizontal circular cylinder (33*c*)

$\xi \propto \cos^3\phi-3\cos\phi+2$: a sphere (33*d*)

and

$$\frac{d\ln\xi}{d\ln x}=\begin{cases}1\text{: a vertical wedge} & (34a)\\ 3\text{: a vertical cone} & (34b)\\ \dfrac{\phi\sin\phi}{1-\cos\phi}\text{: a horizontal circular cylinder} & (34c)\\ \dfrac{3\phi\sin^3\phi}{\cos^3\phi-3\cos\phi+2}\text{: a sphere} & (34d)\end{cases}$$

Since $u_e \propto g_x$ for a cylinder or a sphere, the transformed variable ξ for combined convection on an isothermal cylinder or sphere is proportional to that for pure forced convection on a cylinder or a sphere (defined by equation (16*b*)). Naturally, the circumferential variation of the surface wall heat flux for these geometries is similar to that for the case of pure forced convection subjected to $\lambda = 0$.

For illustrative purposes, the heat transfer grouping $\mathrm{Nu}_x/((d\ln\xi/d\ln x)\mathrm{Pe}_x)^{1/2}$ is presented in Fig. 3, where the abscissa variable is set to $(\mathrm{Ra}_x/\mathrm{Pe}_x)$ to see its effect on local heat transfer rates.

References

Avduyevskiy, V. S., Kalashnik, V. N., and Kopyatevich, R. M., 1976, "The Investigation of Free-Convection Heat Transfer in Gas-Filled Porous Media at High Pressures," *Heat-Transfer—Soviet Research*, Vol. 10, pp. 136–144.

Cheng, P. 1977, "Combined Free and Forced Convection Flow About Inclined Surfaces in Porous Media," Vol. 2, pp. 807–814.

Cheng, P., 1982, "Mixed Convection About a Horizontal Cylinder and a Sphere in a Fluid-Saturated Porous Medium," *Int. J. Heat Mass Transfer*, Vol. 25, pp. 1245–1247.

Cheng, P., and Minkowycz, W. J., 1977, "Free Convection About a Vertical Flat Plate Embedded in a Saturated Porous Medium With Application to Heat Transfer from a Dike," *J. Geophysics Research*, Vol. 82, pp. 2040–2044.

Fand, R. M., Steinberger, T. E., and Cheng, P., 1986, "Natural Convection Heat Transfer From a Horizontal Cylinder Embedded in a Porous Medium," *Int. J. Heat Mass Transfer*, Vol. 29, pp. 119–133.

Merkin, J. H., 1979, "Free Convection Boundary Layers on Axisymmetric and Two-Dimensional Bodies of Arbitrary Shape in a Saturated Porous Medium," *Int. J. Heat Mass Transfer*, Vol. 22, pp. 1461–1462.

Minkowycz, W. J., Cheng, P., and Chang, C. H., 1985, "Mixed Convection About a Nonisothermal Cylinder and Sphere in a Porous Medium," *Numerical Heat Transfer*, Vol. 8, pp. 349–359.

Nakayama, A., and Koyama, H., 1987, "Free Convective Heat Transfer Over a Nonisothermal Body of Arbitrary Shape Embedded in a Fluid-Saturated Porous Medium," ASME JOURNAL OF HEAT TRANSFER, Vol. 109, pp. 125–130.

Nilson, R. H., 1981, "Natural Convective Boundary Layer on Two-Dimensional and Axisymmetric Surfaces in High-Pr Fluids or in Fluid Saturated Porous Media," ASME JOURNAL OF HEAT TRANSFER, Vol. 103, pp. 803–807.

An Analytical Study of the Effect of the Darcy and Fick Laws on the Sublimation of a Frozen Semi-infinite Porous Medium

Y. C. Fey[1] and M. A. Boles[1,2]

Nomenclature

C = molar concentration of moisture
C_0 = molar concentration of frozen bounded substance

[1]Mechanical and Aerospace Engineering Department, North Carolina State University, Raleigh, NC 27695-7910.

[2]Mem. ASME.

Contributed by the Heat Transfer Division for publication in the JOURNAL OF HEAT TRANSFER. Manuscript received by the Heat Transfer Division October 24, 1985.

Copyright © 1987 by ASME

Downloaded 17 Dec 2010 to 193.140.21.150. Redistribution subject to ASME license or copyright; see http://www.asme.org/terms/Terms_Use.cfm

$\bar{C}$ = C/C_3 = nondimensional molar concentration of vapor
$\bar{C}_0$ = C_0/C_3 = nondimensional molar concentration of frozen bounded substance
E = $C_3 M_m \alpha_2 l \epsilon/(T_3 K_1)$ = nondimensional porosity
K = effective thermal conductivity
K_{21} = K_2/K_1 = thermal conductivity ratio
l = latent heat of sublimation
L = $l/(R_0 T_3)$ = nondimensional latent heat of sublimation
Lu = α_m/α_2 = Luikov moisture diffusivity
Lu_p = α_p/α_2 = Luikov filtration diffusivity
P = pressure
$\bar{P}$ = P/P_3 = nondimensional pressure
R = $C_3 R_0 T_3/P_3$ = *nondimensional* gas constant
R_0 = universal gas constant
$s(t)$ = position of sublimation interface
t = time
T = temperature
T_0 = initial temperature
x = space coordinate
$Z(\eta)$ = $P(\eta) + \beta C(\eta)$ = transformation variable
α = effective thermal diffusivity
α_m = effective moisture diffusivity
α_p = filtration motion diffusion coefficient of vapor
α_{21} = α_2/α_1 = thermal diffusivity ratio
β = $(\alpha_m - \alpha_p)/\kappa$
Δ = $\kappa P_3/[(\alpha_p - \alpha_m)C_3]$ or $-P_3/(\beta C_3)$ = nondimensional permeability
ϵ = porosity
θ = T/T_3 = nondimensional temperature
θ_0 = T_0/T_3 = nondimensional initial temperature
κ = permeability
λ = $s(t)/(2\sqrt{\alpha_2 t})$ = nondimensional position of sublimation interface

Subscripts

1 = frozen region, $s(t) < x < \infty$
2 = dried region, $0 < x < s(t)$
3 = at triple point of bounded substance
s = at surface, $x=0$
v = at interface of sublimation, $x = s(t)$

Introduction

Many applications of the vacuum sublimation process for freeze-drying products exist. For instance, the food, medical, and chemical industries use the sublimation process to maintain the shape and quality of heat-sensitive products during the drying process. The application of the vacuum sublimation process has received considerable attention over the past 20 years. Theoretically, it is assumed that the vapor transfer in the dried region is governed by diffusional (Fick) flow and/or hydrodynamic (Darcy) flow. Thus vapor movement in porous media is due to the concentration and/or pressure gradients. Recently Lin (1981, 1982) analyzed the sublimation process in a semi-infinite porous medium by considering the transient heat equations in both the dried and frozen regions and by assuming the vapor transfer in the dried region to be the result of the concentration gradient only. In addition, by relating the conditions of the interface to the Clapeyron equation coupled with the heat and mass balances at the interface, Lin obtained the values of temperature and concentration at the interface and the exact solution for the problem.

Luikov (1966, 1975) formulated the system of equations for heat and mass transfer in the capillary-porous media which included the effect of pressure gradients and the equation of pressure field. In the present work, we present a more complete description of the vacuum sublimation process for which an exact analytical solution is obtained. The present formulation is based upon the Luikov system and the fact that the vapor flow in the dried region results from both moisture concentration and pressure gradients in the porous medium.

Statement of the Problem

A semi-infinite frozen porous medium is exposed to an environment where the pressure and vapor concentration are maintained below the triple point of the bounded substance, and the temperature is higher than the initial temperature of the porous medium. The porous medium is assumed to be composed of very small solid particles of the same size. Also, the medium is isotropic, homogeneous, and rigid. Figure 1 shows a semi-infinite frozen porous medium where the temperature and mass content are initially constant throughout the medium. At time greater than zero the temperature, vapor concentration, and pressure of the surface at $x=0$ are maintained at constant values and the sublimation process begins. Since the vapor is transferred outwardly, the dried region and frozen region are formed and are separated by a distinct, sharply thin, moving interface defined by $x = s(t)$. The temperature, vapor concentration, and pressure at the interface are in equilibrium and unknown, but are assumed to have constant values which will be determined later. There are no moisture concentration or pressure gradients in the frozen region. In the dried region vapor concentration flows occur as a result of the interactions of temperature, vapor concentration, and pressure gradients.

To formulate the theoretical model of the vacuum sublimation problem, additional assumptions are made as follows:

1 The one-dimensional heat and mass transfer is considered. Both the Darcy and Fick laws for vapor transfer are valid through the dried region.

2 The heat radiation, heat convection, thermal expansion of the medium, condensation, Soret and Dufour effects are assumed small and negligible.

3 The dried region contains the vapor resulting from the sublimation process and a small amount of residual air as compared to the vapor mass.

4 The thermophysical properties remain constant but may be different for different regions.

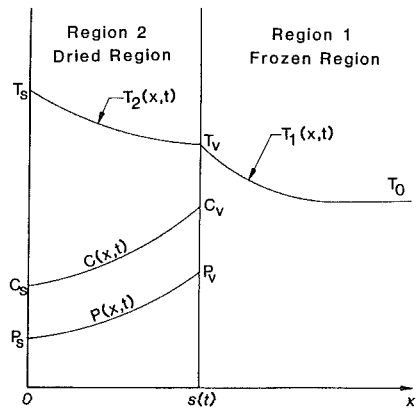

Fig. 1 Schematic description for the sublimation problem

Downloaded 17 Dec 2010 to 193.140.21.150. Redistribution subject to ASME license or copyright; see http://www.asme.org/terms/Terms_Use.cfm

5 The Clapeyron equation and ideal gas law are assumed valid at the interface.

From the above assumptions, the sublimation process can be formulated by the following equations:

$$\frac{\partial T_1(x,t)}{\partial t}=\alpha_1\frac{\partial^2 T_1(x,t)}{\partial x^2},\qquad s(t)<x<\infty \tag{1}$$

$$\frac{\partial T_2(x,t)}{\partial t}=\alpha_2\frac{\partial^2 T_2(x,t)}{\partial x^2},\qquad 0<x<s(t) \tag{2}$$

$$\frac{\partial C(x,t)}{\partial t}=\alpha_m\frac{\partial^2 C(x,t)}{\partial x^2}+\kappa\frac{\partial^2 P(x,t)}{\partial x^2},\qquad 0<x<s(t) \tag{3}$$

$$\frac{\partial P(x,t)}{\partial t}=\alpha_p\frac{\partial^2 P(x,t)}{\partial x^2},\qquad 0<x<s(t) \tag{4}$$

where equations (1) and (2) describe the temperature distribuiton in the frozen and dried regions, respectively. Equations (3) and (4), based on the theories described above and Luikov system (Luikov, 1966, 1975), describe the concentration and pressure fields in the dried region, respectively. It should be noted that the first term and second term on the right side of equation (3) represent the Fick and Darcy laws, respectively.

The boundary and initial conditions are

$$T_1(x,0)=T_1(\infty,t)=T_0 \tag{5}$$

$$T_2(0,t)=T_s \tag{6}$$

$$C(0,t)=C_s \tag{7}$$

$$P(0,t)=P_s \tag{8}$$

At the sublimation interface the conditions are

$$T_1(s,t)=T_2(s,t)=T_v \tag{9}$$

$$C(s,t)=C_v \tag{10}$$

$$P(s,t)=P_v \tag{11}$$

where T_v, C_v, and P_v are the interface temperature, concentration, and pressure, respectively, and are assumed to be constant but unknown.

The Clapeyron equation relating the latent heat of sublimation to the interface conditions, from equation (8) in (Lin, 1982), is

$$\frac{C_vT_v}{C_3T_3}=\exp\left[\frac{l}{R_0}\left(\frac{1}{T_3}-\frac{1}{T_v}\right)\right] \tag{12}$$

By applying the ideal gas law at the interface, we have

$$P_v=C_vR_0T_v \tag{13}$$

The energy and moisture balances at the interface yield

$$-K_2\frac{\partial T_2(s,t)}{\partial x}+K_1\frac{\partial T_1(s,t)}{\partial x}=\epsilon C_0M_ml\frac{ds(t)}{dt} \tag{14}$$

$$\alpha_m\frac{\partial C(s,t)}{\partial x}+\kappa\frac{\partial P(s,t)}{\partial x}=(C_0-C_v)\frac{ds(t)}{dt} \tag{15}$$

Solution of the Problem

We introduce the nondimensional similarity variable

$$\eta=\frac{x}{2\sqrt{\alpha_2 t}} \tag{16}$$

into equations (1)–(15) and define a new variable $Z(\eta)$ as given in (Boles and Ozisik, 1983) which decouples equations (3) and (4)

$$Z(\eta)=P(\eta)+\beta C(\eta) \tag{17}$$

where

$$\beta=\frac{\alpha_m-\alpha_p}{\kappa} \tag{18}$$

The location of the interface is assumed to be given by

$$s(t)=2\lambda\sqrt{\alpha_2 t} \tag{19}$$

where λ is an unknown constant to be determined during the solution.

With the introduction of the new variables η and λ, we note that the dried region corresponds to $0<\eta<\lambda$, and the frozen region corresponds to $\lambda<\eta<\infty$. The problem is transformed to a system of ordinary differential equations for T_1, T_2, P, Z with variable coefficients subject to the transformed boundary and interface conditions. This system can be solved exactly, and the solution for $C(\eta)$ is obtained from equation (17). After substituting the above solutions into the interface equations and performing the necessary manipulations, we obtain the four transcendental interface equations. By using the nondimensional parameters defined in the nomenclature, the solutions are presented as follows:

$$\theta_1(\eta)=\theta_0+(\theta_v-\theta_0)\frac{\operatorname{erfc}(\sqrt{\alpha_{21}}\eta)}{\operatorname{erfc}(\sqrt{\alpha_{21}}\lambda)},\qquad \lambda<\eta<\infty \tag{20}$$

$$\theta_2(\eta)=\theta_s+(\theta_v-\theta_s)\frac{\operatorname{erf}(\eta)}{\operatorname{erf}(\lambda)},\qquad 0<\eta<\lambda \tag{21}$$

$$\bar{P}(\eta)=\bar{P}_s+(\bar{P}_v-\bar{P}_s)\frac{\operatorname{erf}\left(\frac{\eta}{\sqrt{\mathrm{Lu}_p}}\right)}{\operatorname{erf}\left(\frac{\lambda}{\sqrt{\mathrm{Lu}_p}}\right)},\qquad 0<\eta<\lambda \tag{22}$$

$$\bar{C}(\eta)=\bar{C}_s+[\Delta(\bar{P}_s-\bar{P}_v)+(\bar{C}_v-\bar{C}_s)]\frac{\operatorname{erf}\left(\frac{\eta}{\sqrt{\mathrm{Lu}}}\right)}{\operatorname{erf}\left(\frac{\lambda}{\sqrt{\mathrm{Lu}}}\right)}+\Delta(\bar{P}_v-\bar{P}_s)\frac{\operatorname{erf}\left(\frac{\eta}{\sqrt{\mathrm{Lu}_p}}\right)}{\operatorname{erf}\left(\frac{\lambda}{\sqrt{\mathrm{Lu}_p}}\right)},\qquad 0<\eta<\lambda \tag{23}$$

The interface conditions of energy and moisture become

$$K_{21}\left(\frac{\theta_s-\theta_v}{\theta_v-\theta_0}\right)\frac{e^{-\lambda^2}}{\operatorname{erf}(\lambda)}-\sqrt{\alpha_{21}}\frac{e^{-\alpha_{21}\lambda^2}}{\operatorname{erfc}(\sqrt{\alpha_{21}}\lambda)}=\frac{\sqrt{\pi}\bar{C}_0E\lambda}{\theta_v-\theta_0} \tag{24}$$

$$\frac{\sqrt{\mathrm{Lu}}[\Delta(\bar{P}_s-\bar{P}_v)+(\bar{C}_v-\bar{C}_s)]e^{-\frac{\lambda^2}{\mathrm{Lu}}}}{\operatorname{erf}\left(\frac{\lambda}{\sqrt{\mathrm{Lu}}}\right)}+\frac{\Delta(\bar{P}_v-\bar{P}_s)\sqrt{\mathrm{Lu}_p}e^{-\frac{\lambda^2}{\mathrm{Lu}_p}}}{\operatorname{erf}\left(\frac{\lambda}{\sqrt{\mathrm{Lu}_p}}\right)}=\sqrt{\pi}(\bar{C}_0-\bar{C}_v)\lambda \tag{25}$$

The Clapeyron equation becomes

$$\bar{C}_v\theta_v=\exp\left[L\left(1-\frac{1}{\theta_v}\right)\right] \tag{26}$$

and the ideal gas law becomes

$$\bar{P}_v=\bar{C}_vR\theta_v \tag{27}$$

Downloaded 17 Dec 2010 to 193.140.21.150. Redistribution subject to ASME license or copyright; see http://www.asme.org/terms/Terms_Use.cfm

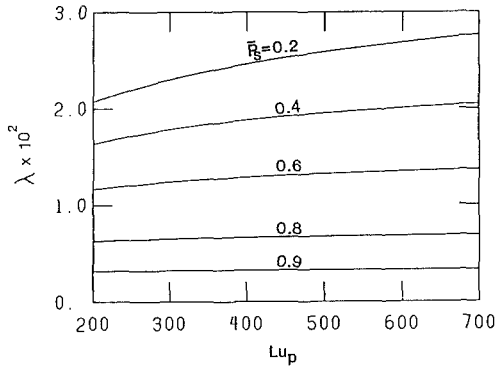

Fig. 2 Effect of surface pressure on nondimensional position of sublimation interface

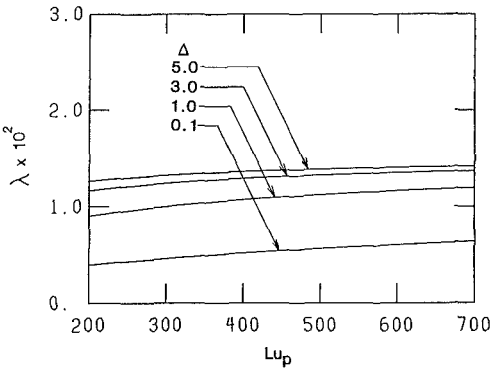

Fig. 3 Effect of permeability on nondimensional position of sublimation interface

The nondimensional constant λ and nondimensional temperature θ_v, pressure $\bar{P}_v$, molar concentration $\bar{C}_v$ at the interface are then obtained by numerically solving the simultaneous equations (24)–(27). Once the interface constants are known, equations (20)–(23) readily yield the exact solution to the sublimation problem.

Results and Discussion

To study the effects of the Darcy and Fick laws on the vacuum sublimation process, the effects of the surface pressure and permeability on the nondimensional interface position λ are illustrated as a function of the Luikov filtration diffusivity Lu_p. The general trend is that λ increases as Lu_p increases. On the figures presented in this study, only the parameters whose values are different from the reference values are indicated. The selected reference values are: $K_{21} = 0.037$, $\alpha_{21} = 0.134$, $\Delta = 3$, $Lu_p = 300$, $\bar{C}_0 = 1.9 \times 10^5$, $Lu = 0.1$, $\bar{C}_s = 0.2$, $\theta_0 = 0.9$, $\theta_s = 1.0$, $\bar{P}_s = 0.6$, $E = 0.36 \times 10^{-5}$, $L = 22.5$, $R = 0.987$.

Figure 2 illustrates the effects of the nondimensional surface pressure $\bar{P}_s$ on the sublimation front position. Decreasing the surface pressure causes a higher pressure gradient through the dried region and increases the sublimation rate. The effects are very pronounced which reveal that Darcy flow is a significant component in the vapor transfer process. Lowering the surface pressure is an efficient way to accelerate the sublimation process.

Figure 3 illustrates the effects of the nondimensional permeability Δ on the sublimation front position. A porous medium with high permeability allows the vapor to move easily through the medium and the sublimation process will take place more rapidly. This figure also shows that the Darcy law is a significant driving force for the sublimation process.

It is noted that the sublimation front position is little affected by a wide range of variation of Lu. This reveals that the Fick flow is less important in the vacuum sublimation process.

In conclusion the mechanisms of vapor transfer are governed by both the Darcy and Fick laws. However, in the vacuum sublimation drying case the Darcy law is the dominant driving force. To accelerate the sublimation dehydration, the ambient pressure and vapor concentration should be maintained at low values. Also, we note that the present system accounting for the Darcy and Fick laws simultaneously is a more complete model of the vacuum sublimation dehydration problem.

References

Boles, M. A., and Ozisik, M. N., 1983, "Exact Solution for Freezing in Cylindrically Symmetric, Porous, Moist Media," ASME JOURNAL OF HEAT TRANSFER, Vol. 105, pp. 401-403.

Dyer, D. F., and Sunderland, J. E., 1968, "Heat and Mass Transfer Mechanisms in Sublimation Dehydration," ASME JOURNAL OF HEAT TRANSFER, Vol. 90, pp. 379-384.

Harper, J. C., 1962, "Transport Properties of Gases in Porous Media at Reduced Pressures With Reference to Freeze-Drying," *AIChE Journal*, Vol. 8, No. 3, pp. 298-302.

Katayama, K., and Hayashi, Y., 1972, "Researches on Vacuum Freeze-Drying," *Bull. of JSME*, Vol. 15, No. 81, pp. 344-353.

Lin, S., 1981, "An Exact Solution of the Sublimation Problem in a Porous Medium," ASME JOURNAL OF HEAT TRANSFER, Vol. 103, pp. 165-168.

Lin, S., 1982, "An Exact Solution of the Sublimation Problem in a Porous Medium, Part II—With an Unknown Temperature and Vapor Concentration at the Moving Sublimation Front," ASME JOURNAL OF HEAT TRANSFER, Vol. 104, pp. 808-811.

Luikov, A. V., 1966, *Heat and Mass Transfer in Capillary-Porous Bodies*, Pergamon Press, Oxford.

Luikov, A. V., 1975, "Systems of Differential Equations of Heat and Mass Transfer in Capillary-Porous Bodies (Review)," *Int. J. Heat Mass Transfer*, Vol. 18, pp. 1-14.

Discrete-Ordinate Solutions of the Radiation Transport Equation

J. S. Truelove[1]

Introduction

Over the past decade, the discrete-ordinate method (Chandrasekhar, 1960) has been used by a number of researchers to solve multidimensional radiation transport problems in the field of engineering heat transfer (Hyde and Truelove, 1977; Truelove, 1978; Fiveland, 1984; Jamaluddin and Smith, 1986). The method is based on a discrete representation for the angular variation in the radiation intensity. The angular quadrature is arbitrary, although restrictions arise from the need to preserve symmetries and invariance properties of the physical system. Moment-matching, completely symmetric quadratures are frequently selected because of their generality (Carlson and Lathrop, 1968). However, some quadratures do not match half-range moments, in particular the half-range first moment which is related to the one-way radiation flux. It is the purpose of this note to point out that low-order discrete-ordinate solutions of the transport equation may be significantly improved when the quadrature is chosen to match the half-range first moment. These improvements are illustrated for the specific case of radiation in a two-dimensional rectangular enclosure, examined recently by Fiveland (1984).

Analysis

Discrete-Ordinate Equations. Discrete-ordinate equations in multidimensional geometry are derived elsewhere (Hyde and Truelove, 1977. Briefly, the radiation transport equation for the intensity $I(\mathbf{r}, \Omega)$ is replaced by a set of equations for the intensities $I_i(\mathbf{r})$ in a finite number of discrete directions Ω_i.

[1]Department of Chemical and Materials Engineering, University of Newcastle, NSW 2308, Australia.

Contributed by the Heat Transfer Division for publication in the JOURNAL OF HEAT TRANSFER. Manuscript received by the Heat Transfer Division November 10, 1986.

Downloaded 17 Dec 2010 to 193.140.21.150. Redistribution subject to ASME license or copyright; see http://www.asme.org/terms/Terms_Use.cfm

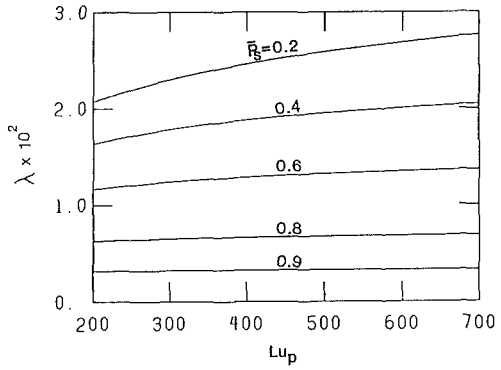

Fig. 2 Effect of surface pressure on nondimensional position of sublimation interface

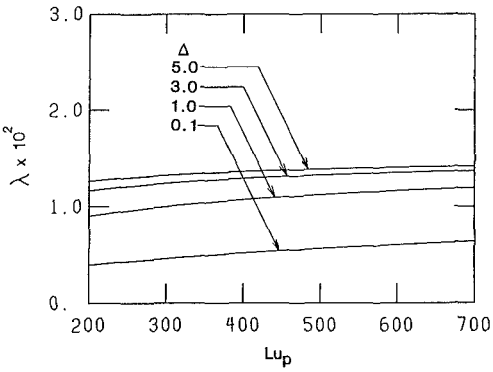

Fig. 3 Effect of permeability on nondimensional position of sublimation interface

The nondimensional constant λ and nondimensional temperature θ_v, pressure $\bar{P}_v$, molar concentration $\bar{C}_v$ at the interface are then obtained by numerically solving the simultaneous equations (24)–(27). Once the interface constants are known, equations (20)–(23) readily yield the exact solution to the sublimation problem.

Results and Discussion

To study the effects of the Darcy and Fick laws on the vacuum sublimation process, the effects of the surface pressure and permeability on the nondimensional interface position λ are illustrated as a function of the Luikov filtration diffusivity Lu_p. The general trend is that λ increases as Lu_p increases. On the figures presented in this study, only the parameters whose values are different from the reference values are indicated. The selected reference values are: $K_{21} = 0.037$, $\alpha_{21} = 0.134$, $\Delta = 3$, $Lu_p = 300$, $\bar{C}_0 = 1.9 \times 10^5$, $Lu = 0.1$, $\bar{C}_s = 0.2$, $\theta_0 = 0.9$, $\theta_s = 1.0$, $\bar{P}_s = 0.6$, $E = 0.36 \times 10^{-5}$, $L = 22.5$, $R = 0.987$.

Figure 2 illustrates the effects of the nondimensional surface pressure $\bar{P}_s$ on the sublimation front position. Decreasing the surface pressure causes a higher pressure gradient through the dried region and increases the sublimation rate. The effects are very pronounced which reveal that Darcy flow is a significant component in the vapor transfer process. Lowering the surface pressure is an efficient way to accelerate the sublimation process.

Figure 3 illustrates the effects of the nondimensional permeability Δ on the sublimation front position. A porous medium with high permeability allows the vapor to move easily through the medium and the sublimation process will take place more rapidly. This figure also shows that the Darcy law is a significant driving force for the sublimation process.

It is noted that the sublimation front position is little affected by a wide range of variation of Lu. This reveals that the Fick flow is less important in the vacuum sublimation process.

In conclusion the mechanisms of vapor transfer are governed by both the Darcy and Fick laws. However, in the vacuum sublimation drying case the Darcy law is the dominant driving force. To accelerate the sublimation dehydration, the ambient pressure and vapor concentration should be maintained at low values. Also, we note that the present system accounting for the Darcy and Fick laws simultaneously is a more complete model of the vacuum sublimation dehydration problem.

References

Boles, M. A., and Ozisik, M. N., 1983, "Exact Solution for Freezing in Cylindrically Symmetric, Porous, Moist Media," ASME JOURNAL OF HEAT TRANSFER, Vol. 105, pp. 401-403.

Dyer, D. F., and Sunderland, J. E., 1968, "Heat and Mass Transfer Mechanisms in Sublimation Dehydration," ASME JOURNAL OF HEAT TRANSFER, Vol. 90, pp. 379-384.

Harper, J. C., 1962, "Transport Properties of Gases in Porous Media at Reduced Pressures With Reference to Freeze-Drying," *AIChE Journal*, Vol. 8, No. 3, pp. 298-302.

Katayama, K., and Hayashi, Y., 1972, "Researches on Vacuum Freeze-Drying," *Bull. of JSME*, Vol. 15, No. 81, pp. 344-353.

Lin, S., 1981, "An Exact Solution of the Sublimation Problem in a Porous Medium," ASME JOURNAL OF HEAT TRANSFER, Vol. 103, pp. 165-168.

Lin, S., 1982, "An Exact Solution of the Sublimation Problem in a Porous Medium, Part II—With an Unknown Temperature and Vapor Concentration at the Moving Sublimation Front," ASME JOURNAL OF HEAT TRANSFER, Vol. 104, pp. 808-811.

Luikov, A. V., 1966, *Heat and Mass Transfer in Capillary-Porous Bodies*, Pergamon Press, Oxford.

Luikov, A. V., 1975, "Systems of Differential Equations of Heat and Mass Transfer in Capillary-Porous Bodies (Review)," *Int. J. Heat Mass Transfer*, Vol. 18, pp. 1-14.

Discrete-Ordinate Solutions of the Radiation Transport Equation

J. S. Truelove[1]

Introduction

Over the past decade, the discrete-ordinate method (Chandrasekhar, 1960) has been used by a number of researchers to solve multidimensional radiation transport problems in the field of engineering heat transfer (Hyde and Truelove, 1977; Truelove, 1978; Fiveland, 1984; Jamaluddin and Smith, 1986). The method is based on a discrete representation for the angular variation in the radiation intensity. The angular quadrature is arbitrary, although restrictions arise from the need to preserve symmetries and invariance properties of the physical system. Moment-matching, completely symmetric quadratures are frequently selected because of their generality (Carlson and Lathrop, 1968). However, some quadratures do not match half-range moments, in particular the half-range first moment which is related to the one-way radiation flux. It is the purpose of this note to point out that low-order discrete-ordinate solutions of the transport equation may be significantly improved when the quadrature is chosen to match the half-range first moment. These improvements are illustrated for the specific case of radiation in a two-dimensional rectangular enclosure, examined recently by Fiveland (1984).

Analysis

Discrete-Ordinate Equations. Discrete-ordinate equations in multidimensional geometry are derived elsewhere (Hyde and Truelove, 1977. Briefly, the radiation transport equation for the intensity $I(\mathbf{r}, \Omega)$ is replaced by a set of equations for the intensities $I_i(\mathbf{r})$ in a finite number of discrete directions Ω_i.

[1]Department of Chemical and Materials Engineering, University of Newcastle, NSW 2308, Australia.

Contributed by the Heat Transfer Division for publication in the JOURNAL OF HEAT TRANSFER. Manuscript received by the Heat Transfer Division November 10, 1986.

Copyright © 1987 by ASME

Downloaded 17 Dec 2010 to 193.140.21.150. Redistribution subject to ASME license or copyright; see http://www.asme.org/terms/Terms_Use.cfm

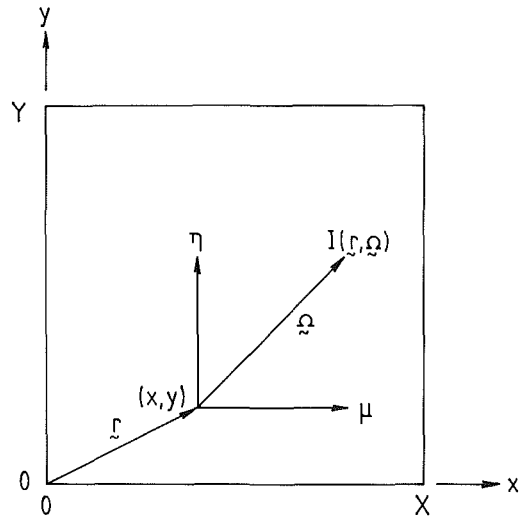

Fig. 1 Two-dimensional rectangular geometry

Angular integrals involving the intensity are approximated by angular quadrature. Here the equations are presented for two-dimensional rectangular geometry; the coordinate system is illustrated in Fig. 1.

The discrete-ordinate representation of the radiation transport equation for an absorbing-emitting grey medium can be written as

$$\mu_i \frac{\partial I_i}{\partial x} + \eta_i \frac{\partial I_i}{\partial y} = -KI_i + KI_{b,g} \tag{1}$$

where I_i [$\equiv I(x, y; \Omega_i)$] is the total radiation intensity at position (x, y) in the discrete direction Ω_i [$\equiv (\mu_i, \eta_i, \xi_i)$], K is the absorption coefficient of the medium, and $I_{b,g}$ is the total black-body radiation intensity at the temperature of the medium.

If the surface bounding the medium is grey and emits and reflects diffusely then the radiation boundary conditions for equation (1) are given by

$$\text{at } x=0: \quad I_i = \epsilon I_{b,w} + (1-\epsilon)/\pi \sum_{\mu_j<0} w_j |\mu_j| I_j; \quad \mu_i > 0 \tag{2a}$$

$$\text{at } x=X: \quad I_i = \epsilon I_{b,w} + (1-\epsilon)/\pi \sum_{\mu_j>0} w_j \mu_j I_j; \quad \mu_i < 0 \tag{2b}$$

$$\text{at } y=0: \quad I_i = \epsilon I_{b,w} + (1-\epsilon)/\pi \sum_{\eta_j<0} w_j |\eta_j| I_j; \quad \eta_i > 0 \tag{2c}$$

$$\text{at } y=Y: \quad I_i = \epsilon I_{b,w} + (1-\epsilon)/\pi \sum_{\eta_j>0} w_j \eta_j I_j; \quad \eta_i < 0 \tag{2d}$$

where I_i is the intensity of radiation leaving the surface, ϵ is the surface emissivity, $I_{b,w}$ is the total black-body radiation intensity at the temperature of the surface, and w_j is the angular quadrature weight associated with the direction Ω_j.

The equation for conservation of energy in the medium is given by

$$4\pi K I_{b,g} - K \sum_i w_i I_i = \dot{q} \tag{3}$$

where $\dot{q}$ is the volumetric rate at which energy is generated within the medium by modes of energy transport other than radiation.

The net radiant heat flux vector is given by

$$\mathbf{q} = \sum_i w_i \Omega_i I_i \tag{4}$$

Table 1 Angular quadrature schemes for two-dimensional rectangular geometry (one μ–η quadrant only)

Designation	Ω			w
	μ	η	ξ	
S_4	0.295876	0.295876	0.908248	$\pi/3$
	0.295876	0.908248	0.295876	$\pi/3$
	0.908248	0.295876	0.295876	$\pi/3$
S_2	0.500000	0.500000	0.707107	π
S_4'	0.333333	0.333333	0.881917	$\pi/3$
	0.333333	0.881917	0.333333	$\pi/3$
	0.881917	0.333333	0.333333	$\pi/3$
S_2'	0.577350	0.577350	0.577350	π

Angular Quadrature Scheme. The choice of quadrature scheme is arbitrary, although restrictions on the directions Ω_i and weights w_i arise from the need to preserve symmetries and invariance properties of the physical system. Since there is no optimum general quadrature, moment-matching, completely symmetric quadratures are frequently selected because of their generality and any degrees of freedom are used to satisfy special conditions. If the geometric dimensionality is reduced, the restriction to complete symmetry can be relaxed.

The following summation condition is satisfied by all quadrature schemes:

$$\sum_i w_i = 4\pi \tag{5}$$

The half-range-flux and diffusion-theory conditions are given by

$$\sum_{\mu_i>0} w_i \mu_i = \pi \tag{6}$$

$$\sum_i w_i \mu_i^2 = 4\pi/3 \tag{7}$$

together with similar relations involving η_i and ξ_i in the case of fully symmetric schemes.

The S_2 and S_4 quadrature schemes used in this work are given in Table 1. The S_4 quadrature is formed by the moment-matching method suggested by Carlson and Lathrop (1968), the single degree of freedom, namely the selection of μ_1, being used to satisfy the condition of equation (6). The scheme is fully symmmetric and satisfies both the half-range-flux and diffusion-theory conditions. The S_2 quadrature scheme is symmetric in the (x, y) plane and satisfies the half-range-flux condition but not the diffusion-theory condition. Also shown in Table 1 are the S_2 and S_4 quadrature schemes used by Fiveland (1984), designated S_2' and S_4', respectively. Both schemes are fully symmetric and satisfy the diffusion-theory condition. However, neither scheme satisfies the half-range-flux condition, the errors being 15 and 3 percent for S_2' and S_4', respectively.

A wide variety of angular-quadrature schemes (including those used in this work) have been presented by Lathrop and Carlson (1965).

Solution of Discrete-Ordinate Equations. The numerical solution procedure is based on the method of Carlson and Lathrop (1968) and is described in detail by Hyde and Truelove (1977). Briefly, the radiation transport equations for the intensities $I_i(x, y)$ are reduced to conservative finite-difference form using the control-volume method and weighted-diamond-difference relations. The equations are solved by recursive evaluation, the direction of integration being in accord with the direction of physical propagation of the radiation beam as defined by Ω_i, with iterative recalculation of boundary conditions and sources which depend upon the intensity distribution.

Downloaded 17 Dec 2010 to 193.140.21.150. Redistribution subject to ASME license or copyright; see http://www.asme.org/terms/Terms_Use.cfm

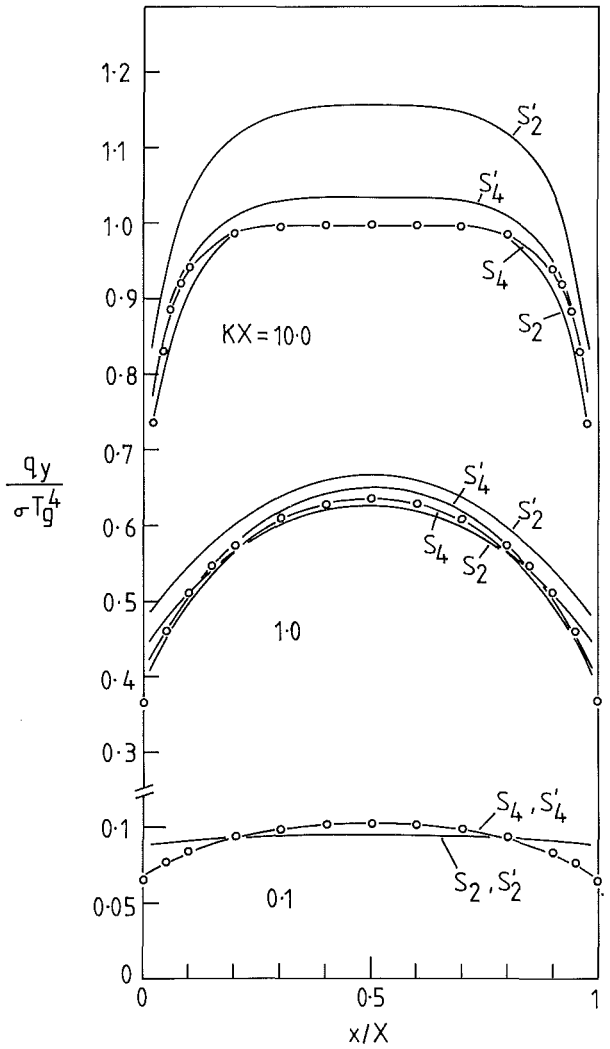

Fig. 2 Nondimensional wall heat flux profile at different optical thicknesses *KX*. Square enclosure (side *X*), black walls at zero temperature, absorbing-emitting medium at uniform temperature T_g. Exact solution (○) reported by Fiveland (1984).

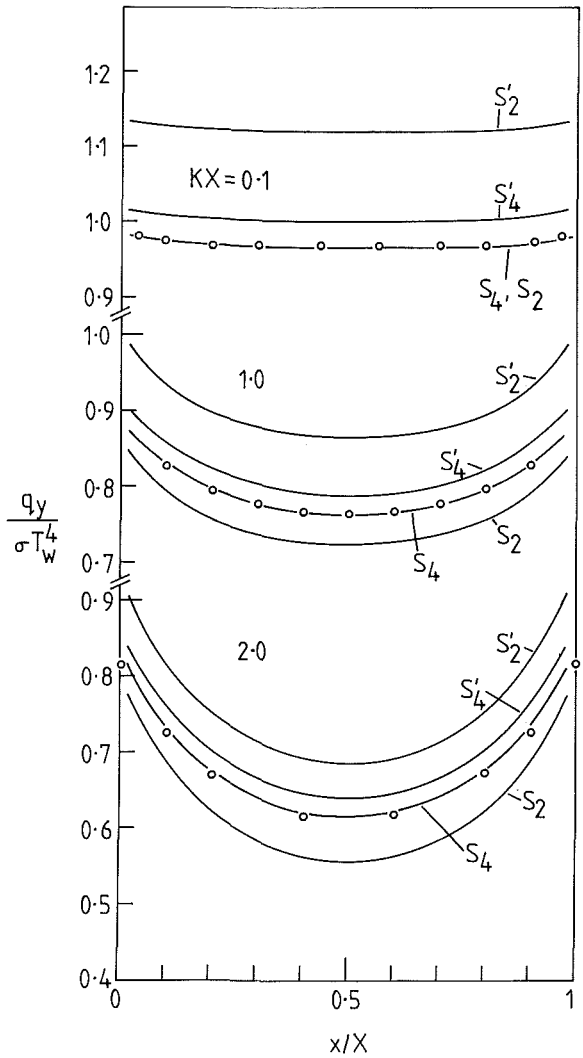

Fig. 3 Nondimensional wall heat flux profile at different optical thicknesses *KX*. Square enclosure (side *X*), black walls: one hot at temperature T_w and three at zero temperature, absorbing-emitting medium in radiative equilibrium. Heat flux at hot wall. Exact (finite-element) solutions (○) reported by Razzaque et al. (1983).

Results and Discussion

Two cases of radiation heat transfer in the two-dimensional rectangular enclosure (Fig. 1) are examined. The particular test cases were selected because exact, or at least very precise, solutions of the radiation transport equation exist for comparison with the discrete-ordinate solution.

Figure 2 shows the wall heat flux profile for a square enclosure with cold black walls and absorbing-emitting medium at uniform temperature. This configuration has also been used as a test case by Fiveland (1984). The results are presented for three values of the optical thickness *KX*, namely 0.1, 1.0, and 10.0. As noted by Fiveland, the S_2' solution deviates significantly from the exact solution at each optical thickness. Furthermore, the S_4' solution also deviates from the exact solution, particularly at the higher optical thicknesses. By comparison, the S_2 and S_4 solutions are in good agreement with the exact solution over the range of optical thicknesses. At the highest optical thickness, the S_2' and S_4' solutions overestimate the heat flux at the center of the wall by 15 and 3 percent, respectively. These discrepancies, erroneously attributed to the "ray effect" by Fiveland, are in fact due to the failure of the S_2' and S_4' quadrature schemes to satisfy the half-range-flux conditions. Interestingly, the present S_4 solutions are also superior to Fiveland's S_6 solution.

Figure 3 shows the wall heat flux profile for a square enclosure with black walls, one of which is hot, and absorbing-emitting medium in radiative equilibrium ($\dot{q} = 0$). The results are presented at three optical thicknesses, namely 0.1, 1.0, and 2.0, for which precise finite-element solutions exist. Only the S_4 solution is in good agreement with the exact solution at each optical thickness. The S_2' and S_4' solutions deviate from the exact solution for the reasons stated above, while the S_2 solution departs from the exact solution at the higher optical thicknesses because the S_2 quadrature scheme does not satisfy the diffusion-theory conditions.

Conclusions

Discrete-ordinate solutions of the radiation transport equation have been obtained with an S_4 quadrature scheme constructed so as to satisfy both the half-range-flux and diffusion-theory conditions. The solutions are superior to those obtained with an alternative S_4 quadrature which fails to satisfy the half-range-flux condition.

The results of the present evaluation of the S_4 discrete-ordinate method in two-dimensional geometry are supported by the previous investigations of Hyde and Truelove (1977) for more complex multidimensional geometries. The discrete-ordinate method can be readily applied to problems involving absorbing-emitting-scattering media. The method yields substantial savings in computer time compared to zonal and

Downloaded 17 Dec 2010 to 193.140.21.150. Redistribution subject to ASME license or copyright; see http://www.asme.org/terms/Terms_Use.cfm

finite-element methods while at the same time achieving acceptable engineering precision.

Acknowledgments

The continuing support of the National Energy Research Development and Demonstration Programme of Australia is gratefully acknowledged.

References

Carlson, B. G., and Lathrop, K. D., "Transport Theory—The Method of Discrete Ordinates," in: *Computing Methods in Reactor Physics*, H. Greenspan, C. N. Kelber, and D. Okrent, eds., Gordon and Breach, New York.

Chandrasekhar, S., 1960, *Radiative Transfer*, Dover Publications, New York.

Fiveland, W. A., 1984, "Discrete-Ordinates Solutions of the Radiative Transport Equation for Rectangular Enclosures," ASME JOURNAL OF HEAT TRANSFER, Vol. 106, pp. 699–706.

Hyde, D. J., and Truelove, J. S., 1977, "The Discrete-Ordinates Approximation for Multidimensional Radiant Heat Transfer in Furnaces," UKAEA Report No. AERE-R8502.

Jamaluddin, A. S., and Smith, P. J., 1986, "Prediction of Radiative Heat Transfer in Cylindrical Furnaces," Technical Report No. WSS/CI 86-60, Western States Section of the Combustion Institute.

Lathrop, K. D., and Carlson, B. G., 1965, "Discrete Ordinates Angular Quadrature of the Neutron Transport Equation," LASL Report No. LA-3186.

Razzaque, M. M., Klein, D. E., and Howell, J. R., 1983, "Finite-Element Solution of Radiative Heat Transfer in a Two-Dimensional Rectangular Enclosure With Grey Participating Medium," ASME JOURNAL OF HEAT TRANSFER, Vol. 105, pp. 933–936.

Truelove, J. S., 1978, "Evaluation of a Multi-flux Model for Radiative Heat Transfer in Cylindrical Furnaces," UKAEA Report No. AERE-R9100.

Dynamic Response of a Liquid–Vapor Interface During Flow Film Boiling From a Sphere

J. Orozco,[1] R. Stellman,[1] and D. Poulikakos[1]

Nomenclature

B_0 = constant, equation (24)
B_1 = constant, equation (24)
B_2 = constant, equation (24)
B_3 = constant, equation (24)
g = acceleration of gravity
h'_{fg} = modified heat of vaporization
k = thermal conductivity
$\dot{m}$ = mass flow rate
P_L = liquid-side pressure at interface
P_{ST} = liquid static pressure at point (r, θ)
P_{STAG} = liquid hydrostatic pressure at stagnation point of liquid–vapor interface
q' = surface heat flux
r = radial distance from stagnation point, Fig. 1(a)
R = sphere radius
R_m = mean heater radius
t = time
T = temperature
ΔT_v = vapor superheat
ΔT_L = liquid subcooling
u = vapor velocity in the r direction
U_L = liquid velocity at the liquid–vapor interface
U_∞ = liquid free-stream velocity
v = vapor velocity in the z direction
V = vaporization velocity
z = normal distance from stagnation point, Fig. 1(a)
α = thermal diffusivity
δ = vapor layer thickness
δ_0 = equilibrium vapor layer thickness
$\dot{\delta}$ = interface velocity
$\ddot{\delta}$ = interface acceleration
ϵ_{peak} = average peak-to-peak roughness height
θ = angle measured from stagnation point
ν = vapor kinematic viscosity
ρ = density
ϕ = function, equation (11)
ψ = function, equation (15)
$\Delta\delta_0$ = change in vapor layer equilibrium position
Δ = displacement of vapor layer interface

Subscripts

L = liquid
V = vapor
STAG = stagnation
ST = static
0 = equilibrium

[1]Department of Mechanical Engineering, University of Illinois at Chicago, Chicago, IL 60680

Contributed by the Heat Transfer Division for publication in the JOURNAL OF HEAT TRANSFER. Manuscript received by the Heat Transfer Division May 30, 1986.

1 Introduction

Film boiling is the mode of boiling during which the hot surface is separated from the vaporizing liquid by a nearly continuous film of vapor. Film boiling is usually considered a very undesirable boiling regime since it is a relatively quiet and inefficient mode of heat transfer, particularly as compared to nucleate boiling. It is customary to analyze the two-phase flow regime of laminar flow film boiling by assuming an idealized vapor film flow characterized by a smooth liquid–vapor interface. Since Bromley's (1950) first analytical approach to film boiling, various solutions have been presented for simple geometric configurations by Witte (1968), Epstein and Hauser (1980), and Witte and Orozco (1984). However, during stable flow film boiling, the wavy nature of the liquid–vapor interface and its role in local heat and mass transport have been largely ignored.

The vapor interface is rarely stationary. Interfacial waves may substantially augment the heat transfer rates throughout the layer. Sheppard and Bradfield (1972) have shown experimentally that the laminar film boiling regime during pool boiling around the forward stagnation point on a vertically oriented hemisphere-cylinder exhibits a continuously wavy interface for fluids near their saturation temperature, and that these waves emanate from the stagnation point region. The same authors developed an analytical solution for the liquid–vapor interface oscillation during pool boiling of Freon-11 near saturation assuming viscous dominance in the vapor layer and employing the concept of a load-per-unit-area on a stagnation-point interface element. They also obtained expressions for the mean vapor layer thickness, the oscillation frequency, and the mean heat flux.

The present analysis treats stagnation point flow film boiling on a sphere immersed in a subcooled liquid. The effect of system parameters on the dynamic behavior of the liquid–vapor interface as well as the response to step changes in the temperature and velocity fields are investigated.

This study corrects and extends the theoretical analysis previously developed by Sheppard and Bradfield (1972). The new theoretical model not only allows for the influence of liquid velocity, vapor superheat, and liquid subcooling on the wavy nature of the liquid–vapor interface, but it also sheds

Downloaded 17 Dec 2010 to 193.140.21.150. Redistribution subject to ASME license or copyright; see http://www.asme.org/terms/Terms_Use.cfm

finite-element methods while at the same time achieving acceptable engineering precision.

Acknowledgments

The continuing support of the National Energy Research Development and Demonstration Programme of Australia is gratefully acknowledged.

References

Carlson, B. G., and Lathrop, K. D., "Transport Theory—The Method of Discrete Ordinates," in: *Computing Methods in Reactor Physics*, H. Greenspan, C. N. Kelber, and D. Okrent, eds., Gordon and Breach, New York.

Chandrasekhar, S., 1960, *Radiative Transfer*, Dover Publications, New York.

Fiveland, W. A., 1984, "Discrete-Ordinates Solutions of the Radiative Transport Equation for Rectangular Enclosures," ASME JOURNAL OF HEAT TRANSFER, Vol. 106, pp. 699–706.

Hyde, D. J., and Truelove, J. S., 1977, "The Discrete-Ordinates Approximation for Multidimensional Radiant Heat Transfer in Furnaces," UKAEA Report No. AERE-R8502.

Jamaluddin, A. S., and Smith, P. J., 1986, "Prediction of Radiative Heat Transfer in Cylindrical Furnaces," Technical Report No. WSS/CI 86-60, Western States Section of the Combustion Institute.

Lathrop, K. D., and Carlson, B. G., 1965, "Discrete Ordinates Angular Quadrature of the Neutron Transport Equation," LASL Report No. LA-3186.

Razzaque, M. M., Klein, D. E., and Howell, J. R., 1983, "Finite-Element Solution of Radiative Heat Transfer in a Two-Dimensional Rectangular Enclosure With Grey Participating Medium," ASME JOURNAL OF HEAT TRANSFER, Vol. 105, pp. 933–936.

Truelove, J. S., 1978, "Evaluation of a Multi-flux Model for Radiative Heat Transfer in Cylindrical Furnaces," UKAEA Report No. AERE-R9100.

Dynamic Response of a Liquid–Vapor Interface During Flow Film Boiling From a Sphere

J. Orozco,[1] R. Stellman,[1] and D. Poulikakos[1]

Nomenclature

B_0 = constant, equation (24)
B_1 = constant, equation (24)
B_2 = constant, equation (24)
B_3 = constant, equation (24)
g = acceleration of gravity
h'_{fg} = modified heat of vaporization
k = thermal conductivity
$\dot{m}$ = mass flow rate
P_L = liquid-side pressure at interface
P_{ST} = liquid static pressure at point (r, θ)
P_{STAG} = liquid hydrostatic pressure at stagnation point of liquid–vapor interface
q' = surface heat flux
r = radial distance from stagnation point, Fig. 1(a)
R = sphere radius
R_m = mean heater radius
t = time
T = temperature
ΔT_v = vapor superheat
ΔT_L = liquid subcooling
u = vapor velocity in the r direction
U_L = liquid velocity at the liquid–vapor interface
U_∞ = liquid free-stream velocity
v = vapor velocity in the z direction
V = vaporization velocity
z = normal distance from stagnation point, Fig. 1(a)
α = thermal diffusivity
δ = vapor layer thickness
δ_0 = equilibrium vapor layer thickness
$\dot{\delta}$ = interface velocity
$\ddot{\delta}$ = interface acceleration
ϵ_{peak} = average peak-to-peak roughness height
θ = angle measured from stagnation point
ν = vapor kinematic viscosity
ρ = density
ϕ = function, equation (11)
ψ = function, equation (15)
$\Delta\delta_0$ = change in vapor layer equilibrium position
Δ = displacement of vapor layer interface

Subscripts

L = liquid
V = vapor
STAG = stagnation
ST = static
0 = equilibrium

[1]Department of Mechanical Engineering, University of Illinois at Chicago, Chicago, IL 60680

Contributed by the Heat Transfer Division for publication in the JOURNAL OF HEAT TRANSFER. Manuscript received by the Heat Transfer Division May 30, 1986.

1 Introduction

Film boiling is the mode of boiling during which the hot surface is separated from the vaporizing liquid by a nearly continuous film of vapor. Film boiling is usually considered a very undesirable boiling regime since it is a relatively quiet and inefficient mode of heat transfer, particularly as compared to nucleate boiling. It is customary to analyze the two-phase flow regime of laminar flow film boiling by assuming an idealized vapor film flow characterized by a smooth liquid–vapor interface. Since Bromley's (1950) first analytical approach to film boiling, various solutions have been presented for simple geometric configurations by Witte (1968), Epstein and Hauser (1980), and Witte and Orozco (1984). However, during stable flow film boiling, the wavy nature of the liquid–vapor interface and its role in local heat and mass transport have been largely ignored.

The vapor interface is rarely stationary. Interfacial waves may substantially augment the heat transfer rates throughout the layer. Sheppard and Bradfield (1972) have shown experimentally that the laminar film boiling regime during pool boiling around the forward stagnation point on a vertically oriented hemisphere-cylinder exhibits a continuously wavy interface for fluids near their saturation temperature, and that these waves emanate from the stagnation point region. The same authors developed an analytical solution for the liquid–vapor interface oscillation during pool boiling of Freon-11 near saturation assuming viscous dominance in the vapor layer and employing the concept of a load-per-unit-area on a stagnation-point interface element. They also obtained expressions for the mean vapor layer thickness, the oscillation frequency, and the mean heat flux.

The present analysis treats stagnation point flow film boiling on a sphere immersed in a subcooled liquid. The effect of system parameters on the dynamic behavior of the liquid–vapor interface as well as the response to step changes in the temperature and velocity fields are investigated.

This study corrects and extends the theoretical analysis previously developed by Sheppard and Bradfield (1972). The new theoretical model not only allows for the influence of liquid velocity, vapor superheat, and liquid subcooling on the wavy nature of the liquid–vapor interface, but it also sheds

Copyright © 1987 by ASME

Downloaded 17 Dec 2010 to 193.140.21.150. Redistribution subject to ASME license or copyright; see http://www.asme.org/terms/Terms_Use.cfm

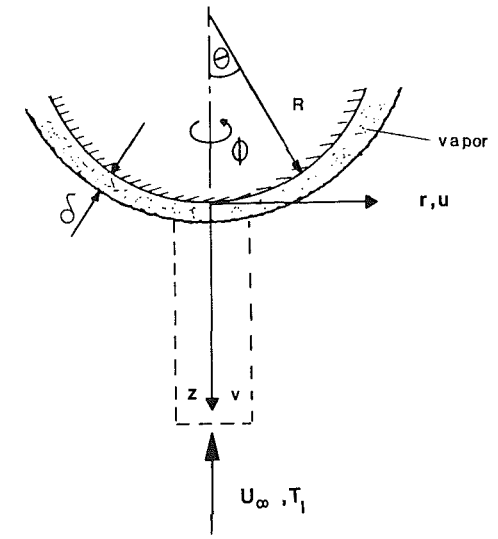

Fig. 1(a)

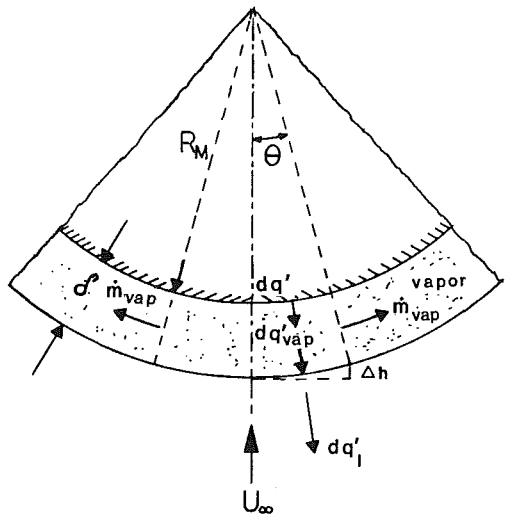

Fig. 1(b)

Fig. 1 Model and coordinate system

some light on the response of the system to perturbations in heat flux and superheat and into the conditions leading toward instances of liquid–solid contact during stable flow film boiling.

Theoretical Model

The basic flow model is shown in Fig. 1(*a*). The system can be idealized as a fluid mass moving in opposition to a gas layer spring and damper with the wave generation phenomenon and accompanying heat pulses serving as forcing functions. The model includes the following simplifications:

- Pure incompressible liquid and vapor
- Uniform body surface temperature
- Vapor film thin compared to radius of the sphere
- Negligible buoyant forces
- Negligible surface tension effects
- Negligible inertia effects in the vapor
- Heat transfer from the heater to the interface by conduction only, with a linear temperature profile

As suggested by Bradfield (1965), the equation of motion for the liquid–vapor interface resulting from a balance of forces in the vicinity of the lower stagnation point is

$$\frac{P_{ST}}{g}\ddot{\delta} = -P_L + p \tag{1}$$

where P_{ST} is the liquid-side static pressure at the interface, P_L is liquid-side total pressure, and p is the pressure distribution in the vapor layer.

The liquid velocity at the liquid-vapor interface is obtained from

$$U_L(\theta) = (3/2)U_\infty \sin\theta \tag{2}$$

This assumption is rather common in studies of forced convection film boiling. It simply implies that the drag of the vapor film upon the adjacent liquid is negligibly small. In the stagnation point neighborhood, the liquid-side total pressure (Fig. 1*b*) at a point (r, θ) on the interface can be written as

$$P_L = P_{ST}(r, \theta) + 1/2\rho_L(U_\infty^2 - U_L^2(\theta)) \tag{3a}$$

or in terms of the stagnation pressure and by using equation (2)

$$P_L = (P_{\text{STAG}} - \Delta h \rho_L g) + \frac{\rho_L U_\infty^2}{2}\left(1 - \frac{9}{4}\sin^2\theta\right) \tag{3b}$$

For any angle θ, Δh and y can be written, respectively, as

$$\Delta h = \frac{(R+\delta)\sin^2\theta}{1+\cos\theta} \quad \text{and} \quad r = (R+\delta)\sin\theta \tag{4}$$

In the vicinity of the forward stagnation point Δh can be approximated by

$$\Delta h \cong \frac{r^2}{2(R+\delta)} \tag{5}$$

Equation (5) differs from Bradfield's result by a factor of 1/2, due to an algebraic error we discovered in his analysis. Thus, the liquid-side pressure at a point (r, θ) can be written as

$$P_L = \left(P_{\text{STAG}} - \frac{r^2}{2(R+\delta)}\rho_L g\right) + \frac{\rho_L U_\infty^2}{2}\left(1 - \frac{9}{4}\frac{r^2}{(R+\delta)^2}\right) \tag{6}$$

Taking into account the fact that $\delta << R$, the equation of motion for the liquid–vapor interface results after combining equations (1) and (6)

$$p = P_{\text{STAG}}\left(1 + \frac{\ddot{\delta}}{g}\right) + \frac{\rho_L U_\infty^2}{2} - \frac{r^2\rho_L}{R}\left(\frac{g+\ddot{\delta}}{2} + \frac{9}{8}\frac{U_\infty^2}{R}\right) \tag{7}$$

In the stagnation-point region, the vapor velocity field can be expected to be dominated by the mass addition at the evaporating interface. Hence, the assumption is made that the vertical component v of the vapor layer velocity is independent of r. Considering a cylindrical coordinate system (Fig. 1*a*), the Navier–Stokes equations read

Continuity

$$\frac{1}{r}\frac{\partial}{\partial r}(ru) + \frac{\partial v}{\partial z} = 0 \tag{8}$$

r-momentum

$$\frac{\partial u}{\partial t} + u\frac{\partial u}{\partial r} + v\frac{\partial u}{\partial z} = -\frac{1}{\rho}\frac{\partial p}{\partial r} + \nu\left[\frac{\partial}{\partial r}\left(\frac{1}{r}\frac{\partial(ru)}{\partial r}\right) + \frac{\partial^2 u}{\partial z^2}\right] \tag{9}$$

z-momentum

$$\frac{\partial v}{\partial t} + u\frac{\partial v}{\partial r} + v\frac{\partial v}{\partial z} = -\frac{1}{\rho}\frac{\partial p}{\partial z} + \nu\left[\frac{\partial}{\partial r}\left(r\frac{\partial v}{\partial r}\right) + \frac{\partial^2 v}{\partial z^2}\right] \tag{10}$$

The solution for the vapor layer pressure evaluated at the interface δ must match the vapor-side pressure in equation (1). This matching requirement yields an equation of motion for the liquid–vapor interface which can then be solved for the equilibrium vapor thickness and heat flux. Assuming that v is not a function of radial position or that

Downloaded 17 Dec 2010 to 193.140.21.150. Redistribution subject to ASME license or copyright; see http://www.asme.org/terms/Terms_Use.cfm

$$v \neq v(r); \qquad \frac{\partial v}{\partial z} = \phi(z, t) \tag{11}$$

where $\phi(z, t)$ is an arbitrary function of z and time. From continuity we obtain that

$$u = -\frac{r}{2}\phi(z, t) \tag{12}$$

With the help of the momentum equations on the other hand, we develop a viscous solution for the vapor pressure subject to the following boundary conditions:

$$\begin{aligned} &\text{at } r = 0: \quad u = 0 \\ &\text{at } z = 0: \quad u = 0, \ v = 0 \\ &\text{at } r = 0 \text{ and } z = \delta: \quad u = 0, \ v = \ddot{\delta} - V \end{aligned} \tag{13}$$

Thus, the vapor-side pressure reads

$$p = \frac{\rho r^2}{4}\psi(t) + \rho c(z, t) \tag{14}$$

where c is an arbitrary function of z and time, and $\psi(t)$ is given by

$$\psi(t) = \frac{\partial \phi}{\partial t} - \frac{1}{2}\phi^2 + v\frac{\partial \phi}{\partial z} - \nu\frac{\partial^2 \phi}{\partial z^2} \tag{15}$$

Comparing the coefficient of the r^2 term in equation (14) with that of equation (7), we obtain with the use of equation (15) that

$$\frac{\partial \phi}{\partial t} - \frac{1}{2}\phi^2 + v\frac{\partial \phi}{\partial z} - \nu\frac{\partial^2 \phi}{\partial z^2} = -\frac{4}{R}\frac{\rho_L}{\rho}\left[\frac{g + \ddot{\delta}}{2} + \frac{9}{8}\frac{U_\infty^2}{R}\right] \tag{16}$$

Neglecting the unsteady and inertial terms and applying the boundary conditions at $z = 0$ and $z = \delta$, equation (13), equation (16) becomes

$$\nu(\dot{\delta} - V) = -\frac{\delta^3}{12}\left[\frac{4}{R}\left(\frac{\rho_L}{\rho}\right)\left(\frac{g + \ddot{\delta}}{2} + \frac{9}{8}\frac{U_\infty^2}{R}\right)\right] \tag{17}$$

after integrating thrice with respect to z.

Attention is now turned to performing an energy balance on a differential film element as shown in Fig. 1(b). This balance yields

$$dq' = dq'_{\text{vap}} + dq'_L \tag{18}$$

where dq'_{vap} is the energy required to form vapor, and dq'_L is the energy conducted into the subcooled liquid when $T_L < T_{\text{sat}}$. In the vicinity of the forward stagnation point, equation (18) can be expanded as

$$k\frac{\Delta T_v}{\delta} = h'_{fg}\rho V - k_L\frac{\partial T}{\partial z}\bigg|_{z=\delta} \tag{19}$$

The heat transferred into the bulk liquid is obtained by using the solution to the energy equation according to Sideman (1966). Sideman's solution is based on the notion that the heat transfer in the liquid is confined to a thin layer near the liquid-vapor interface. Thus, the temperature gradient $\partial T/\partial z\,|_{z=\delta}$ is given by

$$\frac{\partial T}{\partial z}\bigg|_{z=\delta} = \frac{-\Delta T_L \sin^2\theta}{\left[\pi\frac{2}{3}\frac{R\alpha}{U_\infty}\left(\frac{2}{3} - \cos\theta + \frac{1}{3}\cos^3\theta\right)\right]^{1/2}} \tag{20}$$

In the limit as $\theta \to 0$ equation (20) reduces to

$$\frac{\partial T}{\partial z}\bigg|_{z=\delta} = \frac{-2\Delta T_L}{\left(\pi\frac{2}{3}\frac{R\alpha}{U_\infty}\right)^{1/2}} \tag{21}$$

Therefore, the velocity of vaporization becomes (equation (19))

$$V = \frac{1}{h'_{fg}\rho}\left[k\frac{\Delta T_v}{\delta} - \frac{2k_L\Delta T_L}{\left(\pi\frac{2}{3}\frac{R\alpha}{U_\infty}\right)^{1/2}}\right] \tag{22}$$

Finally, substitution of equation (22) into equation (17) yields the viscous dominant equation of motion for the liquid-vapor interface

$$\ddot{\delta} + B_0\frac{\dot{\delta}}{\delta^3} + B_1\frac{1}{\delta^3} - B_2\frac{1}{\delta^4} + B_3 = 0 \tag{23}$$

where

$$\begin{aligned} B_0 &= 6\nu R\left(\frac{\rho}{\rho_L}\right) & B_1 &= \frac{12\nu R k_L \Delta T_L}{\rho_L h'_{fg}\left(\pi\frac{2}{3}\frac{R\alpha}{U_\infty}\right)^{1/2}} \\ B_2 &= \frac{6\nu R k \Delta T_v}{h'_{fg}\rho_L} & B_3 &= g + \frac{9}{4}\frac{U_\infty^2}{R} \end{aligned} \tag{24}$$

The equilibrium vapor layer thickness is given by the solution to

$$\delta_0^4 + \frac{B_1}{B_3}\delta_0 - \frac{B_2}{B_3} = 0 \tag{25}$$

Equation (25) is obtained directly from equation (23) by neglecting the terms with time derivatives. Note that setting $U_\infty = 0$ and $\Delta T_L = 0$ one obtains that the saturated pool boiling equilibrium thickness is given by

$$\delta_0 = 1.19\left[\frac{3\nu R K \Delta T_v}{\rho h'_{fg} g}\right]^{1/4} \tag{26}$$

This result is 19 percent higher than Bradfields's solution. Bradfield did not account properly for the liquid-side hydrostatic pressure at point (r, θ) as previously explained.

The dynamic behavior of the film thickness is determined by solving equation (23) numerically with the help of the fourth-order Runge-Kutta method (Wolford, 1970). The step size used was continuously checked to avoid any numerical errors since the frequency of oscillation of the liquid-vapor interface is very sensitive to changes in system parameters.

Results and Discussion

Figures 2(a) and 2(b) illustrate the dynamic response of the liquid-vapor interface to a step change in heater temperature for both pool boiling and flow boiling of Freon-11 at saturation, respectively. In response to a change in vapor superheat, the liquid-vapor interface shows an oscillatory behavior around a new equilibrium vapor thickness. It is worth noting that for the case of flow boiling (Fig. 2b) the equilibrium vapor layer is thinner than that of pool boiling (Fig. 2a). The liquid velocity also causes a decrease in the amplitude and an increase in the frequency of oscillation of the vapor layer. Consequently, equilibrium is reached faster.

Figures 2(a) and 2(b) also illustrate the effect of a step change in vapor superheat on the heat transfer coefficient at the surface of the heater. Since the heat transfer coefficient is inversely proportional to δ (the vapor layer thickness) higher heat transfer coefficients are obtained for the case of flow

Downloaded 17 Dec 2010 to 193.140.21.150. Redistribution subject to ASME license or copyright; see http://www.asme.org/terms/Terms_Use.cfm

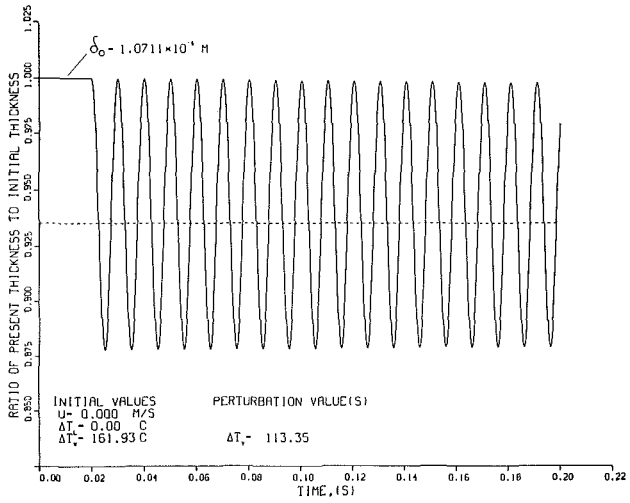

Fig. 2(a)

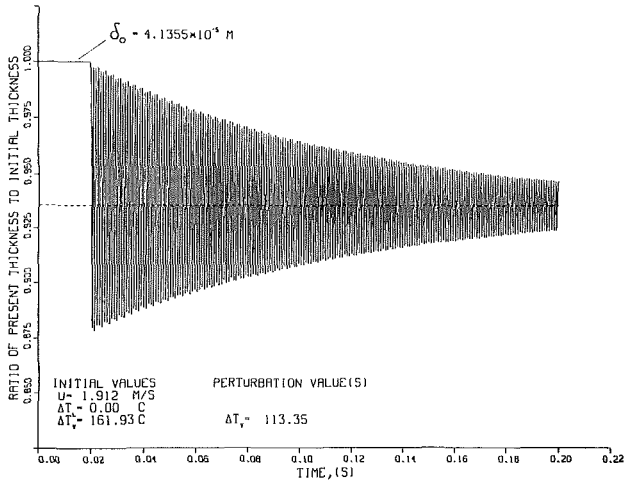

Fig. 2(b)

Fig. 2 Dynamic response of the liquid-vapor interface to a step change in heater temperature for both pool boiling and flow boiling of Freon-II at saturation

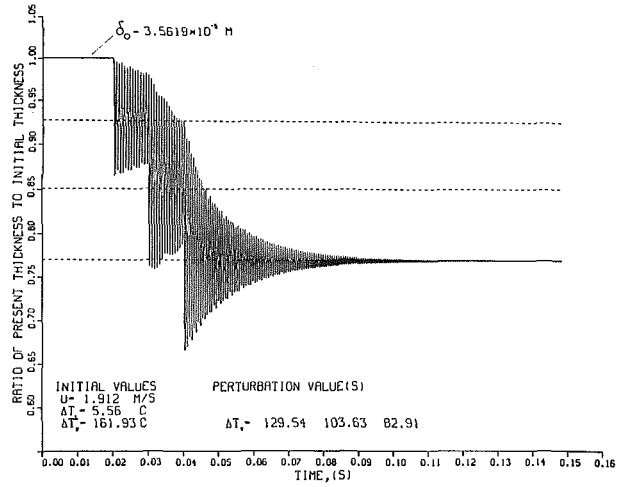

Fig. 3(a)

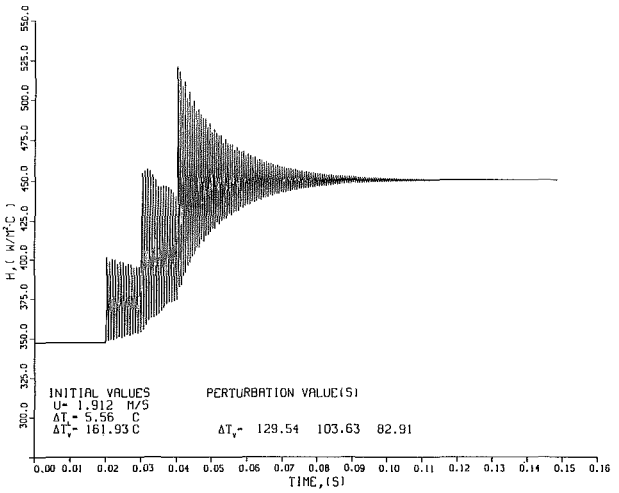

Fig. 3(b)

Fig. 3 Dynamic response of both vapor film layer and heat transfer coefficient triggered by a series of step changes in heater temperature during flow film boiling

boiling. Liquid subcooling has the same relative effect, but to a lesser degree.

Figures 3(*a*) and 3(*b*) show the oscillatory behavior of the liquid-vapor interface triggered by a series of step changes in heater temperature during flow boiling. The response of the vapor layer is very sensitive to the degree of excitation (current value of the amplitude of oscillation) of the vapor layer at the time of change in system parameter (velocity or temperature). For instance, the largest amplitude of oscillation toward the heated surface is obtained if a decrease in vapor superheat or an increase in either liquid velocity or subcooling is imposed at the time when the vapor layer is at the farthest position from the sphere surface. It was also found (Fig. 3*a*) that the amplitude of oscillation around the equilibrium position is not symmetrical. This lack of symmetry is attributed to the fact that as the liquid-vapor interface moves toward the heated surface, higher heat fluxes accompanied by higher viscous dissipation occur. As the vapor interface moves toward the liquid, the viscous dissipation in the vapor layer decreases; thus, larger amplitudes of oscillation are produced as the liquid-vapor interface moves away from the heated surface. Based on the above, it is understood that a prediction of the amplitude of oscillation of the vapor film due to a change in system parameters is dependent on the degree of excitation of the vapor layer. As long as the disturbances in both the temperature and velocity fields are small, the vapor layer will oscillate very close to its equilibrium position. The driving force that sets the interface in motion would have to be proportional to a change in equilibrium position ($\Delta\delta_0$). Figure 4(*a*) illustrates how the vapor layer reacts to changes in equilibrium position $\Delta\delta_0$. The symbol Δ stands for the displacement that the interface undergoes in response to changes in system parameters, and is taken as positive toward the heated surface. Thus, if the condition of the heated surface is characterized by assigning it a surface roughness (Fig. 4*b*), the magnitude of the oscillations created by changes in equilibrium position would allow one to predict whether instances of liquid-solid contacts are possible. These instances of liquid-solid contact would enhance the heat transfer rates and could also lead toward the collapse of the vapor layer.

Conclusion

Overall, the simple model presented in this study in connection to flow film boiling from a sphere can be used to reveal a number of important characteristics relevant to the dynamic response of a liquid-vapor interface. It was shown that changes (controlled or undesired) in the liquid velocity or the vapor superheat initiate large oscillations in the vapor film thickness and the heat transfer coefficient. In addition to the obvious fact that these oscillations affect the heat transfer pro-

Downloaded 17 Dec 2010 to 193.140.21.150. Redistribution subject to ASME license or copyright; see http://www.asme.org/terms/Terms_Use.cfm

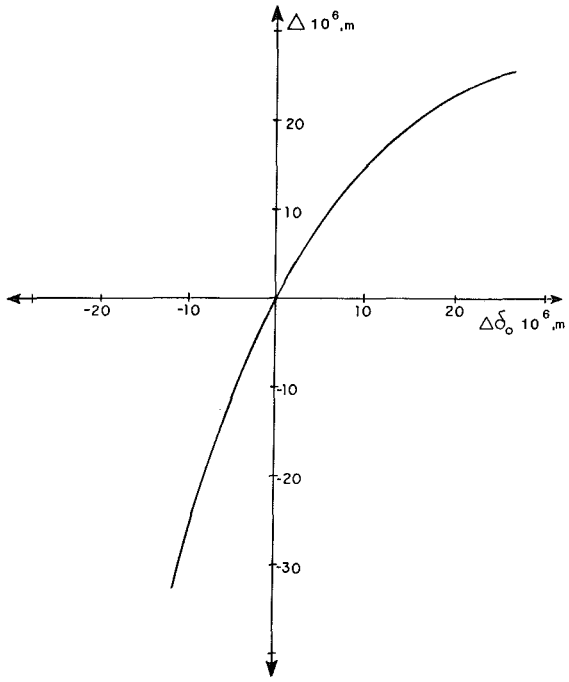

Fig. 4(*a*) Vapor layer response to changes in equilibrium position

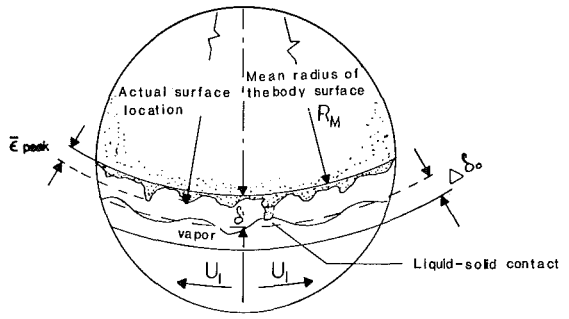

Fig. 4(*b*) Model of liquid-solid contact

cess from the sphere to the liquid, they might create contact "spots" between the liquid and the heater. The realization of this fact depends on the surface characteristics of the sphere. For prescribed surface roughness for example, Fig. 4 can be used to predict if contact spots between the liquid and the sphere surface are likely to occur. The model does not account for cases where the response is unstable. We believe that if the initial response of the vapor layer to a given perturbation is such that the amplitude of oscillation exceeds the equilibrium thickness, it is possible for the vapor layer to collapse.

Acknowledgments

The authors would like to thank the University of Illinois Research Board and Amoco Research for their support of this research.

References

Bromley, L. A., 1950, "Heat Transfer in Stable Film Boiling," *Chemical Engineering Progress*, Vol. 6, pp. 221-227.

Bradfield, W. S., 1965, "Wave Generation at a Stagnation Point in Stable Film Boiling," *Proceedings Two-Phase Flow Symposium*, University of Exeter, England.

Epstein, M., and Hauser, G., 1980, "Subcooled Forced Convection Film Boiling in the Forward Stagnation Region of a Sphere or Cylinder," *International Journal of Heat and Mass Transfer*, Vol. 23, pp. 179-184.

Sheppard, J. J., and Bradfield, W. S., 1972, "Stagnation Point Free-Convection Film Boiling on a Hemisphere," *Progress in Heat and Mass Transfer*, Vol. 6, Pergamon Press, New York, pp. 227-293.

Sideman, S., 1966, "The Equivalence of the Penetration Theory and Potential Flow Theory," *I. and E.C.*, Vol. 58, No. 2, pp. 54-68.

Witte, L. C., 1968, "Film Boiling From a Sphere," *I. and E.C. Fundamentals*, Vol. 7, pp. 510-517.

Witte, L. C., and Orozco, J., 1984, "The Effect of Vapor Velocity Profile Shape on Flow Film Boiling From Submerged Bodies," ASME JOURNAL OF HEAT TRANSFER, Vol. 106, pp. 191-197.

Wolford, J. C., 1970, *Applied Numerical Methods for Digital Computation With Fortran*, International Textbook Company, Scranton, PA.

Sidewall and Immersion-Depth Effects on Pool Boiling Burnout for Horizontal Cylindrical Heaters

Y. Elkassabgi[1,3] and J. H. Lienhard[2,3]

Nomenclature

D = diameter of cylindrical heater
g = acceleration of gravity
H = depth of heater
q_{max}, $q_{max,\infty}$ = saturated peak pool boiling heat flux; q_{max} in deep, unobstructed liquid
R = radius of a horizontal cylindrical heater $= D/2$
R' = Laplace number $= R[g(\rho_f - \rho_g)/\sigma]^{1/2}$
W = distance between sidewalls
x = $H/D - 25 + 1.23(W/D)$
y = $\dfrac{q_{max}/q_{max,\infty}}{0.58 - 0.029(W/D)}$
ρ_f, ρ_g = saturated liquid and vapor densities
σ = surface tension

Introduction

The horizontal cylinder is the geometry in which the problem of evaluating the peak nucleate boiling heat flux q_{max} (commonly called the *burnout* heat flux) has been most studied. Countless data have been presented but many are subject to a variety of nuisance variables. The objective of the present work is to identify experimentally the range of influence of two of these nuisance variables: sidewall blockage and immersion depth.

The existing hydrodynamic predictions of q_{max} envision either an infinite flat plate beneath an infinitely deep liquid bath, or a finite heater immersed in a bath of infinite extent (see, e.g., reviews by Lienhard and Dhir, 1973, and by Lienhard and Witte 1985). Attention has been given to such effects in other geometries (for example, Westwater et al., 1986, have looked at sidewall blockage effects on spheres and immersion effects on large flat plates). However, the effect of nearby walls or depth of immersion on a horizontal cylinder has not been systematically documented.

Our aim here is to determine, experimentally, how q_{max} is altered when a long horizontal cylinder of diameter D is centered between vertical sidewalls separated by a distance W and located a distance H below the liquid surface.

[1]Graduate Student, Student Mem. ASME.

[2]Professor, Fellow ASME.

[3]Heat Transfer/Phase-Change Laboratory, Mechanical Engineering Department, University of Houston – University Park, Houston, TX 77004.

Contributed by the Heat Transfer Division for publication in the JOURNAL OF HEAT TRANSFER. Manuscript received by the Heat Transfer Division December 5, 1986.

Downloaded 17 Dec 2010 to 193.140.21.150. Redistribution subject to ASME license or copyright; see http://www.asme.org/terms/Terms_Use.cfm

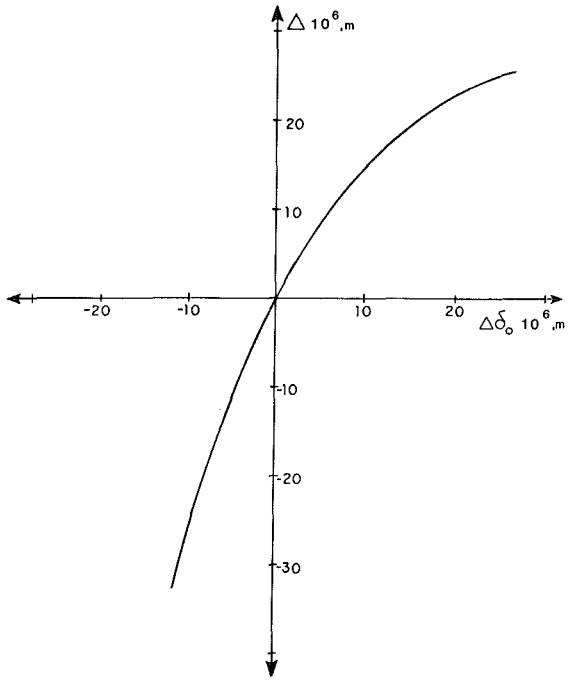

Fig. 4(*a*) Vapor layer response to changes in equilibrium position

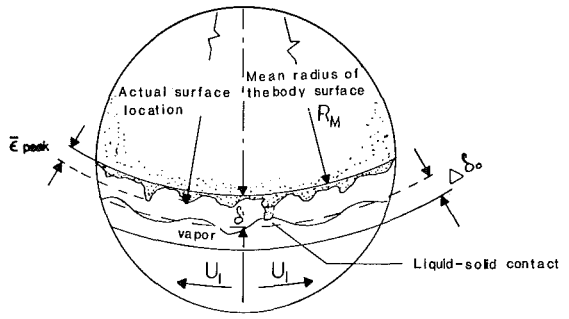

Fig. 4(*b*) Model of liquid-solid contact

cess from the sphere to the liquid, they might create contact "spots" between the liquid and the heater. The realization of this fact depends on the surface characteristics of the sphere. For prescribed surface roughness for example, Fig. 4 can be used to predict if contact spots between the liquid and the sphere surface are likely to occur. The model does not account for cases where the response is unstable. We believe that if the initial response of the vapor layer to a given perturbation is such that the amplitude of oscillation exceeds the equilibrium thickness, it is possible for the vapor layer to collapse.

Acknowledgments

The authors would like to thank the University of Illinois Research Board and Amoco Research for their support of this research.

References

Bromley, L. A., 1950, "Heat Transfer in Stable Film Boiling," *Chemical Engineering Progress*, Vol. 6, pp. 221-227.

Bradfield, W. S., 1965, "Wave Generation at a Stagnation Point in Stable Film Boiling," *Proceedings Two-Phase Flow Symposium*, University of Exeter, England.

Epstein, M., and Hauser, G., 1980, "Subcooled Forced Convection Film Boiling in the Forward Stagnation Region of a Sphere or Cylinder," *International Journal of Heat and Mass Transfer*, Vol. 23, pp. 179-184.

Sheppard, J. J., and Bradfield, W. S., 1972, "Stagnation Point Free-Convection Film Boiling on a Hemisphere," *Progress in Heat and Mass Transfer*, Vol. 6, Pergamon Press, New York, pp. 227-293.

Sideman, S., 1966, "The Equivalence of the Penetration Theory and Potential Flow Theory," *I. and E.C.*, Vol. 58, No. 2, pp. 54-68.

Witte, L. C., 1968, "Film Boiling From a Sphere," *I. and E.C. Fundamentals*, Vol. 7, pp. 510-517.

Witte, L. C., and Orozco, J., 1984, "The Effect of Vapor Velocity Profile Shape on Flow Film Boiling From Submerged Bodies," ASME JOURNAL OF HEAT TRANSFER, Vol. 106, pp. 191-197.

Wolford, J. C., 1970, *Applied Numerical Methods for Digital Computation With Fortran*, International Textbook Company, Scranton, PA.

Sidewall and Immersion-Depth Effects on Pool Boiling Burnout for Horizontal Cylindrical Heaters

Y. Elkassabgi[1,3] and J. H. Lienhard[2,3]

Nomenclature

D = diameter of cylindrical heater
g = acceleration of gravity
H = depth of heater
q_{max}, $q_{max,\infty}$ = saturated peak pool boiling heat flux; q_{max} in deep, unobstructed liquid
R = radius of a horizontal cylindrical heater $= D/2$
R' = Laplace number $= R[g(\rho_f - \rho_g)/\sigma]^{1/2}$
W = distance between sidewalls
x = $H/D - 25 + 1.23(W/D)$
y = $\dfrac{q_{max}/q_{max,\infty}}{0.58 - 0.029(W/D)}$
ρ_f, ρ_g = saturated liquid and vapor densities
σ = surface tension

Introduction

The horizontal cylinder is the geometry in which the problem of evaluating the peak nucleate boiling heat flux q_{max} (commonly called the *burnout* heat flux) has been most studied. Countless data have been presented but many are subject to a variety of nuisance variables. The objective of the present work is to identify experimentally the range of influence of two of these nuisance variables: sidewall blockage and immersion depth.

The existing hydrodynamic predictions of q_{max} envision either an infinite flat plate beneath an infinitely deep liquid bath, or a finite heater immersed in a bath of infinite extent (see, e.g., reviews by Lienhard and Dhir, 1973, and by Lienhard and Witte 1985). Attention has been given to such effects in other geometries (for example, Westwater et al., 1986, have looked at sidewall blockage effects on spheres and immersion effects on large flat plates). However, the effect of nearby walls or depth of immersion on a horizontal cylinder has not been systematically documented.

Our aim here is to determine, experimentally, how q_{max} is altered when a long horizontal cylinder of diameter D is centered between vertical sidewalls separated by a distance W and located a distance H below the liquid surface.

[1]Graduate Student, Student Mem. ASME.

[2]Professor, Fellow ASME.

[3]Heat Transfer/Phase-Change Laboratory, Mechanical Engineering Department, University of Houston – University Park, Houston, TX 77004.

Contributed by the Heat Transfer Division for publication in the JOURNAL OF HEAT TRANSFER. Manuscript received by the Heat Transfer Division December 5, 1986.

Copyright © 1987 by ASME

Downloaded 17 Dec 2010 to 193.140.21.150. Redistribution subject to ASME license or copyright; see http://www.asme.org/terms/Terms_Use.cfm

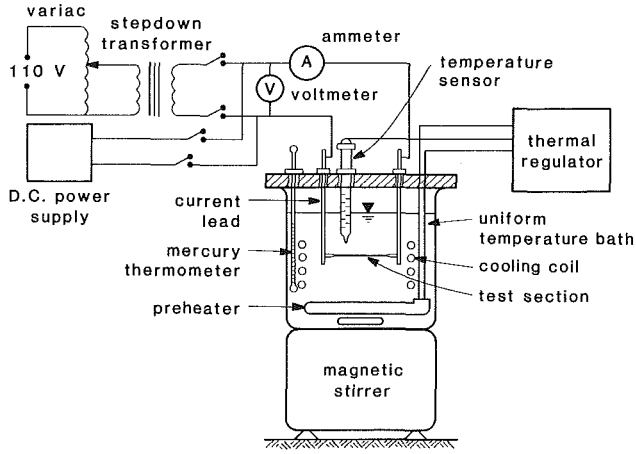

Fig. 1 Schematic representation of the experimental apparatus

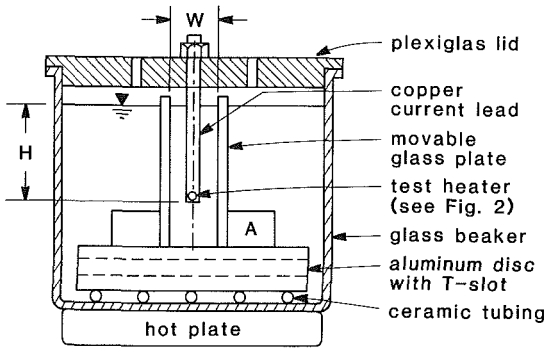

(a) Detail of the test section showing end view of test heater and the variable-gap walls.

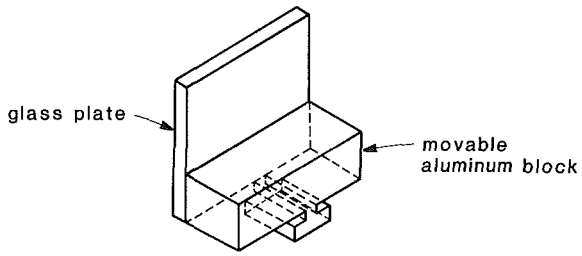

(b) Detail of mounting A

Fig. 2 Detail of the heater mounting

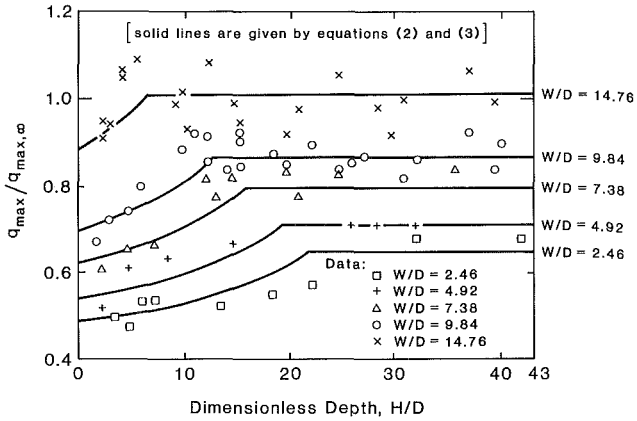

Fig. 3 Uncorrelated data showing the influences of both sidewalls and immersion depth

Experiment and Results

Figure 1 shows the relatively conventional apparatus that we used to measure q_{max} in methanol at 1 atm, using 0.813-mm-dia Nichrome wires as electric resistance heaters. The heaters were mounted as shown in Fig. 2 and supplied with d-c power. Tapered copper electrodes were electroplated on the ends of each wire to eliminate vapor hangup around the ends, and to guarantee that burnout occurred at random locations on the wire. Each wire was inspected for flaws, washed with detergent soap, rinsed in water, and finally rinsed with the fluid to be boiled, before it was installed. The distance between the heater and the bottom of the slot was $>>D$, H, or W, and liquid was admitted to the test region through the bottom.

The liquid was preheated to saturation with a hot plate, which was turned off about a half minute before each reading. The heater was then rapidly powered up to about 90 percent of q_{max}, and finally brought to burnout over another 15 to 30 s. The probable error of the q_{max} data was always within 3.6 percent.

Seventy-three such observations were made, with only two or three observations on any one heating element. Complete details of the experiment are given by Elkassabgi (1986).

The Laplace number R', based on the cylinder radius R

$$R' \equiv R[g(\rho_f - \rho_g)/\sigma]^{1/2} \tag{1}$$

was 0.157 for the heaters. ρ_f and ρ_g are the saturated liquid and vapor densities, respectively, g is the acceleration of gravity, and σ is the surface tension. This value is in a range where the hydrodynamic theory of burnout is completely applicable.

The uncorrelated data are shown in Fig. 3. The ordinate has been normalized using the measured value of $q_{max,\infty} = 0.765$ MW/m^2, in the unobstructed container – an average of eight observations which gave an rms deviation of only 4.5 percent.

Correlation of Results

To help make the pattern of these seemingly scattered data in Fig. 3 more evident, we include lines that display their trends. (The lines shown here are not our original guesses, but rather representations of the final correlation developed below.)

It is clear that, at each value of W/D, there is a value of H/D above which H/D ceases to influence $q_{max}/q_{max,\infty}$. We determine, by least-squares fitting, that in this deep-liquid region

$$\frac{q_{max,\infty}}{q_{max}} = 0.58 + 0.029\frac{W}{D} \tag{2}$$

with an rms deviation of only ±5.25 percent. This expression is valid only up to $q_{max}/q_{max,\infty} = 1$, which occurs when $W/D = 14.76$. For larger values of W/D, the data show that the sidewall effect is abruptly lost, for the deep-liquid data. Equation (2) is restricted to the deep-liquid range of $H/D \geq (25 - 1.23W/D)$.

Using a new independent variable, $x \equiv (H/D - 25 + 1.23W/D)$, suggested by the shift of the deep-liquid limit, we then correlate all the data as shown in Fig. 4. The data for which x is negative in Fig. 5 are ones that *are* influenced by H/D. A final least-squares fit of these data yields

$$y \equiv 0.70 + (1 - 0.70)e^{0.08x} \tag{3}$$

which represents them within an rms deviation of only ±5.62 percent. It is restricted to the ranges $2.46 \leq W/D \leq 14.76$ and $1.85 \leq H/D \leq (25 + 1.23W/D)$, where the lower bound is set by the limits of our data, and the upper bound is set by a change in the process.

Downloaded 17 Dec 2010 to 193.140.21.150. Redistribution subject to ASME license or copyright; see http://www.asme.org/terms/Terms_Use.cfm

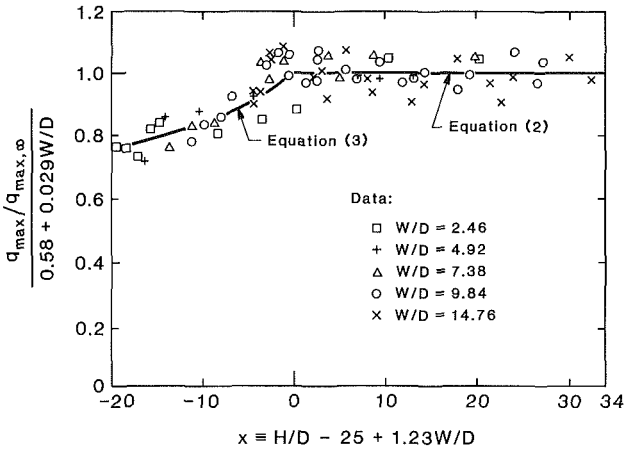

Fig. 4 Correlation of the data for $2.46 \leq W/D \leq 14.76$ and $1.85 \leq H/D$

Discussion

The correlations above are strictly empirical and not based on any physical considerations. It therefore behooves us to ask what they suggest about the physical character of the problem.

The influence of sidewalls is to reduce q_{max}, but only when they are less than 14.76D apart. It is entirely likely that the escaping vapor jets are reduced in size in a confined space, increasing the vapor velocity at a given heat flux and hastening the Helmholtz collapse of the jets.

However, the apparent linearity of the effect must surely cease when the walls are placed very close to the heater – as W/D approaches 1. Therefore we strongly warn against using the present results for W/D below the limits of the present data (our apparatus did not permit us to go to W less than $2.46D$).

One would expect a very small H/D to give the jets direct access through the liquid into the vapor region above. However, to predict the effect (upon the hydrodynamic stability of the jet) of providing them with this escape route becomes quite complicated when the dynamics of the vapor jet wall become coupled with those of the horizontal free surface.

The depth effect is very small by the time W/D reaches 14.76, and our experiments show that it cannot be discerned at all in an open bath. We also note that the immersion-depth effect becomes stronger when it is coupled with the sidewall effect.

Conclusions

1 When $H/D \geq (25 - 1.23W/D)$ and $2.46 \leq W/D \leq 14.76$, q_{max} is given by equation (1).

2 When $1.85 \leq H/D \leq (25 - 1.23W/D)$ and $W/D \leq 15.76$, q_{max} is given by equation (3).

3 When $W/D \geq 14.76$, q_{max} appears to be uninfluenced by the bath depth or width.

Acknowledgments

This work has received support under NSF Grant No. MEA-8218708.

References

Elkassabgi, Y., 1986, "The Peak Pool Boiling Heat Flux From Horizontal Cylinders in Subcooled Liquids," Doctoral Dissertation, Mech. Engr. Dept., Univ. of Houston, Houston, TX.

Lienhard, J. H., and Dhir, V. K., 1973, "Extended Hydrodynamic Theory of the Peak and Minimum Pool Boiling Heat Fluxes," NASA CR-2270.

Lienhard, J. H., and Witte, L. C., 1985, "An Historical Review of the Hydrodynamic Theory of Boiling," *Chem. Engr. Revs.*, Vol. 3, No. 3, pp. 187–280.

Westwater, J. W., Hwalek, J. J., and Irving, M. E., 1986, "Suggested Standard Method for Obtaining Boiling Curves by Quenching," *I&EC Fundamentals*, Vol. 25, pp. 685–692.

Additional Data on Subcooled Boiling of Heptane

H. Müller-Steinhagen[1]

In a recent publication, Müller-Steinhagen et al. (1986) reported an investigation on forced convective heat transfer to subcooled heptane for two different heater geometries, namely for a heated rod in an annulus and for a heated coiled wire in crossflow. Additional experiments were performed extending the range of Reynolds numbers by more than one order of magnitude to lower Reynolds numbers and higher Reynolds numbers for the annulus and the coiled wire, respectively.

Annular Flow

Figure 1 shows measured and calculated heat transfer coefficients α for the annulus as a function of the heat flux $\dot{q}$. The experiments were performed for a bulk temperature $T_b = 37°C$ and a system pressure $p = 1.07$ bar with mass velocities $\dot{m}$ between 10 kg/m^{2}s and 20 kg/m^{2}s. A convective heat transfer region and a subcooled boiling region can be distinguished according to the influence of heat flux on the heat transfer coefficient. While it is well known (for example Collier, 1972) that the fully developed subcooled boiling heat transfer coefficient is quite independent of mass velocity, it is noteworthy to comment on the fact that for the present measurements the *convective* heat transfer coefficient depends on the heat flux rather than on the mass velocity. With the Grashof number being much larger than the Reynolds number ($Gr/Re^2 > 100$ for all annular measurements), the influence of forced convection may be neglected as compared to the influence of natural convection. This result is also demonstrated in Fig. 3, curve I, which shows that for the annular flow assembly, forced convection is only of minor influence, as long as the Reynolds number is sufficiently small.

One of the motivations for the present investigation was to verify whether the developed subcooled boiling heat transfer coefficient at high heat fluxes remains constant, even if the flow velocity is varied over a wide range and the hydrodynamic conditions change from turbulent to laminar flow. In Fig. 3, curve II, measured heat transfer coefficients for fully developed subcooled boiling are shown over a wide range of Reynolds numbers ranging from 4 to 35,000. No influence of the Reynolds number on the coefficients is to be noticed. The opposite result is predicted by a correlation published by Shah (1983). The correlation suggested by Chen (1963), which already agreed favorably with previous data reported by Müller-Steinhagen et al. (1986), was also in good agreement with the present data, if the appropriate correlation for convective heat transfer is used. Since natural convection was the dominant convective heat transfer mechanism for the present measurements with annular flow, the correlation for the local Nusselt number Nu_x by Touloukian et al. (1948)

$$Nu_x = 0.5545(Gr\ Pr)^{0.25}$$

may be applied to predict the heat transfer coefficients (see Fig. 1).

Figure 1 shows furthermore that the measured data for medium heat fluxes are higher than the calculated values. This and the observation that boiling started at surface temperatures well below the saturation temperature are attributed to residual dissolved gases (see Müller-Steinhagen et al., 1986) in the heptane, which was not completely degassed

[1]Department of Chemical and Materials Engineering, School of Engineering, University of Auckland, Auckland, New Zealand.

Contributed by the Heat Transfer Division for publication in the JOURNAL OF HEAT TRANSFER. Manuscript received by the Heat Transfer Division March 12, 1986.

Downloaded 17 Dec 2010 to 193.140.21.150. Redistribution subject to ASME license or copyright; see http://www.asme.org/terms/Terms_Use.cfm

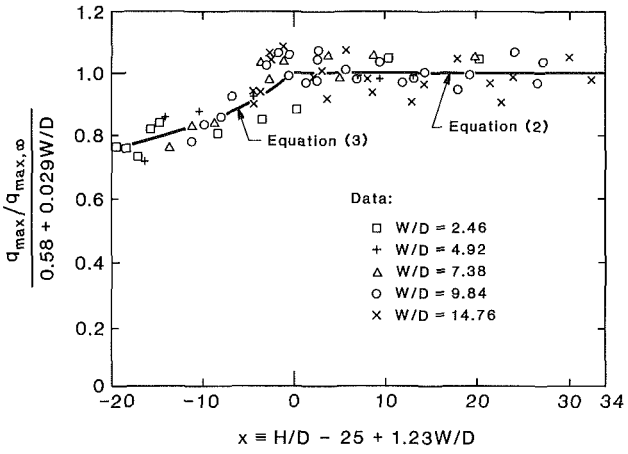

Fig. 4 Correlation of the data for $2.46 \leq W/D \leq 14.76$ and $1.85 \leq H/D$

Discussion

The correlations above are strictly empirical and not based on any physical considerations. It therefore behooves us to ask what they suggest about the physical character of the problem.

The influence of sidewalls is to reduce q_{max}, but only when they are less than 14.76D apart. It is entirely likely that the escaping vapor jets are reduced in size in a confined space, increasing the vapor velocity at a given heat flux and hastening the Helmholtz collapse of the jets.

However, the apparent linearity of the effect must surely cease when the walls are placed very close to the heater – as W/D approaches 1. Therefore we strongly warn against using the present results for W/D below the limits of the present data (our apparatus did not permit us to go to W less than $2.46D$).

One would expect a very small H/D to give the jets direct access through the liquid into the vapor region above. However, to predict the effect (upon the hydrodynamic stability of the jet) of providing them with this escape route becomes quite complicated when the dynamics of the vapor jet wall become coupled with those of the horizontal free surface.

The depth effect is very small by the time W/D reaches 14.76, and our experiments show that it cannot be discerned at all in an open bath. We also note that the immersion-depth effect becomes stronger when it is coupled with the sidewall effect.

Conclusions

1 When $H/D \geq (25 - 1.23W/D)$ and $2.46 \leq W/D \leq 14.76$, q_{max} is given by equation (1).

2 When $1.85 \leq H/D \leq (25 - 1.23W/D)$ and $W/D \leq 15.76$, q_{max} is given by equation (3).

3 When $W/D \geq 14.76$, q_{max} appears to be uninfluenced by the bath depth or width.

Acknowledgments

This work has received support under NSF Grant No. MEA-8218708.

References

Elkassabgi, Y., 1986, "The Peak Pool Boiling Heat Flux From Horizontal Cylinders in Subcooled Liquids," Doctoral Dissertation, Mech. Engr. Dept., Univ. of Houston, Houston, TX.

Lienhard, J. H., and Dhir, V. K., 1973, "Extended Hydrodynamic Theory of the Peak and Minimum Pool Boiling Heat Fluxes," NASA CR-2270.

Lienhard, J. H., and Witte, L. C., 1985, "An Historical Review of the Hydrodynamic Theory of Boiling," *Chem. Engr. Revs.*, Vol. 3, No. 3, pp. 187–280.

Westwater, J. W., Hwalek, J. J., and Irving, M. E., 1986, "Suggested Standard Method for Obtaining Boiling Curves by Quenching," *I&EC Fundamentals*, Vol. 25, pp. 685–692.

Additional Data on Subcooled Boiling of Heptane

H. Müller-Steinhagen[1]

In a recent publication, Müller-Steinhagen et al. (1986) reported an investigation on forced convective heat transfer to subcooled heptane for two different heater geometries, namely for a heated rod in an annulus and for a heated coiled wire in crossflow. Additional experiments were performed extending the range of Reynolds numbers by more than one order of magnitude to lower Reynolds numbers and higher Reynolds numbers for the annulus and the coiled wire, respectively.

Annular Flow

Figure 1 shows measured and calculated heat transfer coefficients α for the annulus as a function of the heat flux $\dot{q}$. The experiments were performed for a bulk temperature $T_b = 37°C$ and a system pressure $p = 1.07$ bar with mass velocities $\dot{m}$ between 10 kg/m^{2}s and 20 kg/m^{2}s. A convective heat transfer region and a subcooled boiling region can be distinguished according to the influence of heat flux on the heat transfer coefficient. While it is well known (for example Collier, 1972) that the fully developed subcooled boiling heat transfer coefficient is quite independent of mass velocity, it is noteworthy to comment on the fact that for the present measurements the *convective* heat transfer coefficient depends on the heat flux rather than on the mass velocity. With the Grashof number being much larger than the Reynolds number ($Gr/Re^2 > 100$ for all annular measurements), the influence of forced convection may be neglected as compared to the influence of natural convection. This result is also demonstrated in Fig. 3, curve I, which shows that for the annular flow assembly, forced convection is only of minor influence, as long as the Reynolds number is sufficiently small.

One of the motivations for the present investigation was to verify whether the developed subcooled boiling heat transfer coefficient at high heat fluxes remains constant, even if the flow velocity is varied over a wide range and the hydrodynamic conditions change from turbulent to laminar flow. In Fig. 3, curve II, measured heat transfer coefficients for fully developed subcooled boiling are shown over a wide range of Reynolds numbers ranging from 4 to 35,000. No influence of the Reynolds number on the coefficients is to be noticed. The opposite result is predicted by a correlation published by Shah (1983). The correlation suggested by Chen (1963), which already agreed favorably with previous data reported by Müller-Steinhagen et al. (1986), was also in good agreement with the present data, if the appropriate correlation for convective heat transfer is used. Since natural convection was the dominant convective heat transfer mechanism for the present measurements with annular flow, the correlation for the local Nusselt number Nu_x by Touloukian et al. (1948)

$$Nu_x = 0.5545(Gr\ Pr)^{0.25}$$

may be applied to predict the heat transfer coefficients (see Fig. 1).

Figure 1 shows furthermore that the measured data for medium heat fluxes are higher than the calculated values. This and the observation that boiling started at surface temperatures well below the saturation temperature are attributed to residual dissolved gases (see Müller-Steinhagen et al., 1986) in the heptane, which was not completely degassed

[1]Department of Chemical and Materials Engineering, School of Engineering, University of Auckland, Auckland, New Zealand.

Contributed by the Heat Transfer Division for publication in the JOURNAL OF HEAT TRANSFER. Manuscript received by the Heat Transfer Division March 12, 1986.

Copyright © 1987 by ASME

Downloaded 17 Dec 2010 to 193.140.21.150. Redistribution subject to ASME license or copyright; see http://www.asme.org/terms/Terms_Use.cfm

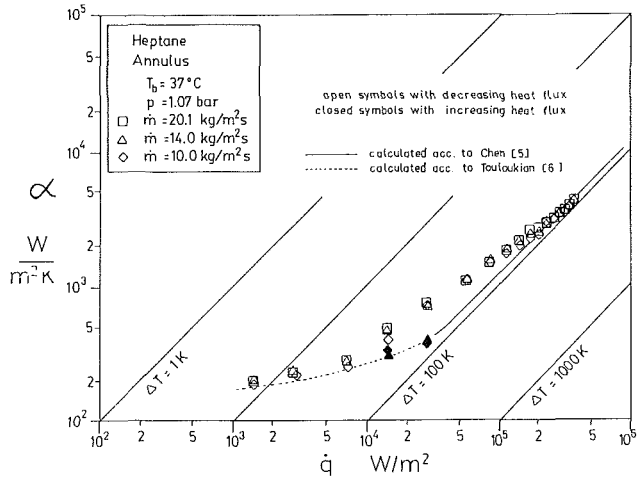

Fig. 1 Heat transfer coefficient for annular flow as a function of heat flux

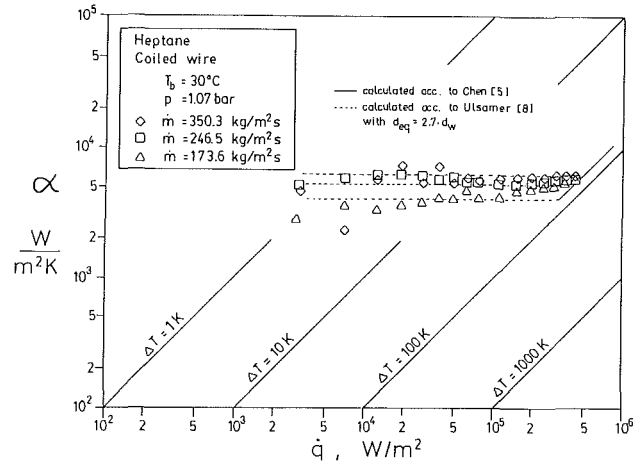

Fig. 2 Heat transfer coefficient for flow past the coiled wire as a function of heat flux

before the experiments. At low heat fluxes (no boiling) and at high heat fluxes (fully developed subcooled boiling) measurements and calculated values are in good agreement.

Most of the measurements presented in this note were measured with decreasing heat flux; however, there are some data given in Fig. 1 that were obtained with increasing heat flux. These data show the presence of a boiling hysteresis which could not be detected during the previous measurements with higher Reynolds numbers. This observation is a further support for the hypothesis stated by Murphy et al. (1972) and Müller-Steinhagen et al. (1986) that hysteresis effects decrease with increasing flow velocity.

Coiled Wire

For the coiled wire, a widely extended range of convective heat transfer is observed in Fig. 2, as compared with the previous experiments at lower Reynolds numbers. A transition

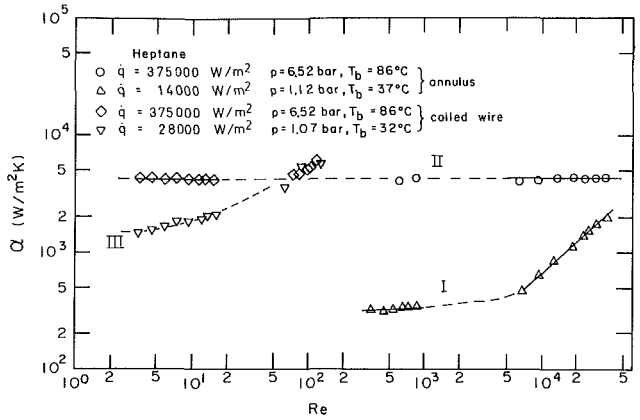

Fig. 3 Influence of Reynolds number on convective heat transfer and subcooled boiling heat transfer

to subcooled boiling may only be detected at the highest heat fluxes, where the influence of mass velocity gradually diminishes. Figure 3, curve III, presents the influence of the Reynolds number on the heat transfer coefficients for the coiled wire, indicating laminar flow as the exponent n in $\alpha \sim \mathrm{Re}^n$ is always less than or equal to 0.5.

The measurements presented in the previous report (Müller-Steinhagen et al., 1986) could be predicted with satisfactory accuracy using the entrance region solution for flow past flat plates. For the data measured at higher Reynolds numbers, this procedure is not successful, since flow separation occurs along the wire circumference. Correlations derived for the flow past cylinders by McAdams (1954) also fail in predicting correct values for the coil, if either wire diameter d_w or equivalent diameter d_{eq} is used as a basis in the Reynolds and Nusselt numbers. In order to obtain satisfactory results, a diameter which is approximately 2.7 times the wire diameter has to be used in these correlations. It is felt that this result must depend on the dimensions of the coil, such as wire diameter, coil diameter, and number of coils per unit length. This should be determined in future investigations.

References

Chen, J. G., 1963, "A Correlation for Boiling Heat Transfer to Saturated Fluids in Convective Flow," *Proceedings, 6th Nat. Heat Transfer Conference*, Boston, MA.

Collier, J. G., 1972, *Convective Boiling and Condensation*, McGraw-Hill, New York.

McAdams, W., 1954, *Heat Transmission*, McGraw-Hill, New York.

Murphy, R. W., and Bergles, A. E., 1972, "Subcooled Flow Boiling of Fluorocarbons—Hysteresis and Dissolved Gas Effects on Heat Transfer," *Proceedings, Heat Transfer and Fluid Mechanics Inst.*, Stanford University, Stanford, CA.

Müller-Steinhagen, H. M., Watkinson, A. P., and Epstein, N., 1986, "Subcooled-Boiling and Convective Heat Transfer to Heptane Flowing Inside an Annulus and Past a Coiled Wire. Part I: Experimental Results; Part II: Correlation of Data," ASME JOURNAL OF HEAT TRANSFER, Vol. 108, pp. 922–933.

Shah, M., 1983, "Generalized Prediction of Heat Transfer During Subcooled Boiling in Annuli," *Heat Transfer Engineering*, Vol. 4, No. 1, pp. 24–31.

Touloukian, Y. S., Hawkins, G. A., and Jakob, M., 1948, "Heat Transfer by Free Convection From Heated Vertical Surfaces to Liquids," *Trans. ASME*, Vol. 70, pp. 13–18.

Downloaded 17 Dec 2010 to 193.140.21.150. Redistribution subject to ASME license or copyright; see http://www.asme.org/terms/Terms_Use.cfm